UNIVERSITÀ DEGLI STUDI DI PALERMO

Dottorato di Ricerca in Scienze Fisiche e Chimiche

Dipartimento di Fisica e Chimica ”Emilio Segrè”

XXXV Ciclo

The mass determination challenge for exoplanetary science

IL DOTTORE

Claudia Di Maio

IL COORDINATORE

Prof. Marco Cannas

IL TUTOR

Dott.ssa Giuseppina Micela

IL CO TUTOR

Prof.ssa Costanza Argiroffi

ANNO CONSEGUIMENTO TITOLO 2023

Acknowledgements

Here is my gratitude to the most important people in my life who have been part of this journey. I have written them in Italian because I would like them to be able to understand. I apologize.

I ringraziamenti dopo un percorso così lungo sono d'obbligo, ma nel mio caso sono più che dovuti e sentiti. Partiamo dalla mia "capa" Giusi. Ma che ti devo dire che già non sai? La parola "Grazie" è veramente riduttiva. Mi hai sopportato, mi hai cresciuto aggiungerei, scientificamente parlando ma non solo, e proprio per questo i ringraziamenti non saranno mai abbastanza. Mi hai insegnato davvero tanto, hai provato a farmi credere un pò di più in me stessa (ci sto lavorando ma è un percorso più lungo di un dottorato). Ci hai pensato tu a credere in me e non puoi immaginare quanto ti devo. Da un anno all'altro ho percepito la mia crescita, spaventosa. Tra tutto quello che in questi tre lunghi anni mi porterò ci sarà sicuramente il rapporto umano, più importante a mio avviso di molte altre cose, non scontato e per questo prezioso. Sei un punto di riferimento per tutti. Spero di riuscire a somigliarti un pò... magari prima o poi. Grazie.

Ai ringraziamenti aggiungo TUTTE, nessun escluso, le persone che vivono in Osservatorio, dai ricercatori all'amministrazione. Andare a lavoro in osservatorio ogni mattina è stata una gioia, ogni giorno, perchè sapevo di trovare degli amici. Trovare un ambiente lavorativo così è cosa rara. Come ho già detto, siamo una bellissima famiglia ed è un privilegio farne parte. Spero di rimanere a lungo a rompervi le scatole.

Grazie a Serena, Laura, Antonino, Salvo, Jesus per avermi aiutata in tutto e aver condiviso con me questo percorso. Grazie.

Grazie agli amici che mi sono stati vicini, al gruppo dei 49, dei Giampaoli, a tutti. Grazie ad Alice, so di poter contare su di te sempre, e non serve altro.

Grazie alla mia famiglia, che ha sempre gioito con me dei miei successi ed è sempre stata al mio fianco nelle mie cadute. Grazie alla mia famiglia acquisita. Mi avete accolta come se fossi vostra figlia, siete speciali e vi voglio bene. Grazie a mia madre, per te non dirò altro perchè non ci sono parole che potrebbero descrivere quanto ti amo. Sappi solo che andrà tutto bene perchè ci sono io.

E poi, grazie a Giuseppe. Senza di te non sarei riuscita a fare niente e a scrivere nemmeno una parola di tutto ciò. Sei il primo a credere in me, più di quanto ci creda io, e l'ultimo a lasciare perdere; pronto a sorreggermi e consolarmi sempre,

a sopportare i miei scleri e le mie paranoie. Sono pazza ma mi ami lo stesso, cosa potrei volere di più. Hai sconvolto le mie priorità e la mia visione della vita, che ormai non esiste senza di te. Ti amo. Punto.

E adesso, visto che, come disse una volta qualcuno, "sbattivu", si comincia....

Abstract

The mass of an exoplanet is a key parameter for the characterisation of the internal structure of a planet, as well as the study of the formation and the evolution of the planet, and of its atmosphere. The radial velocity technique allows measuring the planetary mass from the radial velocity variation of its parent star. However, limitations in the property determination of exoplanets, particularly in their masses, can arise from various sources especially from astrophysical noise due to stellar variability, caused by magnetic activity, which affects the detection and characterisation of exoplanets.

This PhD thesis aims to understand the impact of our knowledge of the planetary mass in the planetary atmospheric characterisation and to reduce the sources of uncertainty by a deep study of the stellar activity and by developing new techniques for stellar variability filtering.

To this end, I analysed the impact of the planetary mass uncertainties of atmospheric retrievals of multiple targets from the mission reference sample of Ariel, the forthcoming ESA M4 mission aimed at studying planetary atmospheres. I simulated different spectra as observed by Ariel, assuming a primordial or secondary atmosphere of hot Jupiters, and sub-Neptunes or super-Earths, respectively, under different cloudy configurations. I estimated both the accuracy and precision necessary for each analysed target, testing also the capability of retrieval in the case of incorrect mass estimation. I verified that one of the most crucial issues is the presence of high-altitude clouds, in particular in the secondary atmosphere cases. For this reason, I tested the capability to retrieve the cloudy configuration or the presence of a secondary atmosphere during the first tier of the Ariel mission, to take an informed decision if including the planet in the Tier-2 sample. In the second part of this thesis, I described `SpotCCF`, a photospheric stellar model that I developed to optimise the radial velocity extraction in fast-rotating stars. This model, based on the cross-correlation function technique, takes into account the contribution of stellar activity by considering the presence of multiple spots on the stellar surface that caused deformation of the profile of the cross-correlation function. I applied this model to the HARPS-N observations of V1298 Tau, a very active K1 star, which shows strongly deformed cross correlation function (CCF) profiles. The `SpotCCF` model is also able to give information about the spot configuration (latitude, longitude and area covered by the spot). In the end, I also focused my study

on understanding stellar activity in M dwarfs, which is crucial for improving our understanding of the physics of stellar atmospheres and for planet search programs. Specifically, I analysed HARPS and HARPS-N observation of AD Leonis, measuring the line profiles and intensities of sensitive activity indicators, and evaluating the correlations between them.

Globally, the PhD thesis highlights the importance of planetary mass characterisation and the complexity of their determination due to the effects of stellar variability. In the context of the Ariel mission, it highlights the importance of a detailed and individual analysis of each target of the mission reference sample, to be able to accurately select the Tier-2 targets and characterise their planetary atmosphere, and represents a step forward towards the preparation of the ESA M4 Ariel mission. It also shows how this work cannot be disentangled from a detailed study of the stellar variability that is crucial in the determination of the planetary mass, both in its accuracy and precision.

Contents

List of Figures

List of Tables

Acronyms

Ariel	Atmospheric Remote sensing Infrared Exoplanet Large Survey.
ArielRad	Ariel radiometric model.
CCF	cross correlation function.
CIA	collision-induced absorption.
CoRoT	COnvection ROtation and planetary Transits.
DRS	Data Reduction Software.
ESA	European Space Agency.
ESO	European Southern Observatory.
ESPRESSO	Echelle SPectrograph for Rocky Exoplanets and Stable Spectroscopic Observations.
EW	Equivalent width.
ExoMol	Molecular line lists for exoplanet atmospheres.
FAP	false alarm probability.
GAPS	Global Architecture of Planetary System.
GLS	generalised Lomb-Scargle.
HARPS	High Accuracy Radial velocity Planet Searcher.
HARPS-N	High Accuracy Radial velocity Planet Searcher for the Northern emisphere.
HITEMP	High-temperature molecular spectroscopic database.
HITRAN	High-resolution transmission molecular absorption database.
HST	Hubble Space Telescope.
IAU	International Astronomical Union.
JWST	James Webb Space Telescope.
KS test	Kolmogorov-Smirnov test.
MAP	maximum-a-posteriori.
MCMC	The Markov Chain Monte Carlo.
MRS	Mission reference sample.
NASA	National Aeronautics and Space Administration.
NS	Nested Sampling.

RMS root mean square.
RV Radial velocity.
SNR signal-to-noise ratio.
TauREx Tau Retrieval for Exoplanets.
TERRA Template-Enhanced Radial velocity Re-analysis Application.
TESS Transiting Exoplanet Survey Satellite.
TNG Telescopio Nazionale Galileo.
TTVs Transit Timing Variations.
VLT Very Large Telescope.

CHAPTER 1

Introduction

The discovery of new other worlds and the possibility of life on other planets are among the main subjects within astrophysical science that excite the public and the entire science community.

The Solar System planets have been a favoured target for backyard astronomers for centuries.

Since 2006, the International Astronomical Union (IAU) has defined a planet (in the Solar System) as being a celestial body that fulfils the following requirements:

- it orbits around the Sun;
- it has sufficient mass for its self-gravity to overcome rigid body forces and to assume a hydrostatic equilibrium (a spherical shape);
- it has "cleared the neighbourhood" around its orbit.

There are eight bodies in the Solar System that meet the above requirements and can therefore be classified as planets: Mercury, Venus, Mars, Jupiter, Saturn, Uranus, Neptune and of course Earth. A non-satellite body that fulfils the first two requirements of the IAU definition of the planet, is classified as a *dwarf planet*.

For centuries, astronomers studied the planet formation by observing celestial bodies within our own Solar System. However, the first discoveries of exoplanets (Wolszczan and Frail, 1992; Mayor and Queloz, 1995) revealed that our Solar System is not unique in its abundance of planets, and opened up a new way to understand the planetary formation and evolution. Since then, astronomers have been focused on discovering new exoplanets and improving their detection techniques.

Exoplanets have been found orbiting around different types of stars and in different regions of the galaxy. They exhibit diverse characteristics in comparison to our own planets. To date, a variety of exoplanets has been discovered, with wide ranges of masses, radii, densities and compositions, also considering the intrinsic degeneracy between these parameters (i.e. multiple combinations of mass and radius may lead to the same density, which could also be explained by different chemical compositions).

Characterising exoplanets by estimating their masses, radii, temperature, and atmospheric composition provide information about their formation and evolution, as the diversity of these planets suggests different pathways to their formation. However, the large number of detected exoplanets has only recently enabled meaningful statistical analyses and searches for structures in the planetary parameter space. The main goal is to determine the frequency of exoplanets and the distribution of their parameters relevant to our understanding of planet formation, but this task is challenging as each detection method has its own biases, sensitivities, and limitations in measuring planet properties. To increase our sensitivity to detect and characterise exoplanets, different techniques are being developed.

Additionally, the accuracy and precision of our estimations depend on the properties of the host stars, which are often young and characterised by strong magnetic activity that can limit our detection capabilities. Determining the properties of host stars, such as their mass, can also be expensive but is a crucial parameter for the planetary systems they host. Therefore, a multi-approach study in the exoplanetary field, which includes the study of host stars and the stellar activity in addition to the detection and characterisation of planets, is necessary.

To date, there is no formally accepted definition of exoplanets. In August 2018, the IAU Commision F2: Exoplanets and the Solar System adopted a working definition of an exoplanet. The current official working definition is as follows (Lecavelier des Etangs and Lissauer, 2022):

- *objects with true masses below the limiting mass for thermonuclear fusion of deuterium (currently calculated to be 13 Jupiter masses for objects of solar metallicity - Spiegel et al. (2011)) that orbit stars, brown dwarfs or stellar remnants and that have a mass ratio with the central object below the L4/L5*[1] *instability* $\left(M/M_{central} < \frac{2}{(25+\sqrt{621})} \approx \frac{1}{25}\right)$ *are "planets" (no matter how they formed). The minimum mass/size required for an extrasolar object to be considered a planet should be the same as that used in our Solar System* [2].

- *Substellar objects with true masses above the limiting mass for thermonuclear fusion of deuterium are "brown dwarfs", no matter how they formed nor where they are located.*

- *Free-floating objects in young star clusters with masses below the limiting mass for thermonuclear fusion of deuterium are not "planets", but are "sub-brown dwarfs" (or whatever name is most appropriate).*

[1] Lagrangian points

[2] defined in the second criterion of the definition of a planet in the Solar System

1.1 A BRIEF HISTORY OF THE SEARCH FOR EXOPLANETS

The first exoplanet was discovered in the early 1990s by Wolszczan and Frail (1992) who detected periodic variations in the arrival time of emitted beams from pulsar PSR B1257+12. Three years later, Mayor and Queloz (1995) made the first radial velocity planetary detection (see radial velocity technique in Section 1.2.2) discovering a Jupiter sized object around the main sequence star 51 Peg with a much closer orbit to its host star than previously thought possible. This discovery was followed by many similar detections, resulting from a re-analysis of previous datasets (Marcy and Butler, 1996; Butler and Marcy, 1996; Butler et al., 1997). These discoveries led to new theories about the possible migration of giant planets from the outer regions where they are thought to be formed (Ward, 1997; Bryden et al., 1999; Nelson et al., 2000).

The initial planetary systems discovered using the radial velocity technique consisted of a single hot Jupiter and its host star, as they were easier to detect. Butler et al. (1997) and then Butler et al. (1999) found the first evidence of an exoplanetary system, around υ Andromedae, containing multiple planets.

In 2000, Mazeh et al. (2000) showed, through a radial velocity analysis of HD 209458, that the plane of the hot Jupiter orbit was very near edge-on, implying that the planet may appear to cross the star disc at some point during its orbit. The first planetary transit (see Section 1.2.1 for more information about this technique) was observed simultaneously by Charbonneau et al. (2000) and Henry et al. (2000), who witnessed a period decrease in the star brightness during the planet inferior conjunction in its radial velocity orbit. Since 1999, several ground-based transit searches have been conducted, but, the most significant discoveries of transiting planets have been done from space-based observations, such as the COnvection ROtation and planetary Transits (CoRoT) satellite (Baglin et al., 2007), which discovered 24 transiting planets during its mission from 2007 to 2012, and the NASA's Kepler satellite (Koch et al., 2007), which discovered 151 confirmed planets and potentially thousands more yet to be confirmed[3] from 2009 to 2013, during its main mission and many more during the K2 phase.

Alongside transiting and radial velocity searches, there have been many attempts to directly image exoplanet systems using both space and ground-based equipment. The sub-stellar object 2M1207b and its brown dwarf companion were observed by Chauvin et al. (2005), and the first image was produced using the NACO adap-

[3] An exoplanets candidate is a likely planet discovered by a telescope but has not yet been proven to actually exist. A planet is considered "confirmed" once it is verified through additional observations with different techniques.

tive optics near-infrared instrument of the European Southern Observatory (ESO)'s Very Large Telescope (VLT). The microlensing technique has also produced several exoplanet detections, the first discovered by Bond et al. (2004). This method relies on the planet passing in front of a background star light and causing a distinct brightness increase.

A more detailed description of the main exoplanetary detection methods is provided in the following section.

1.2 Exoplanet detection and characterisation methods

Exoplanets can be detected through multiple methods, each with its own advantages and disadvantages. To date[4], 5272 exoplanets have been discovered, primarily through the radial velocity (1027) and transit (3945) methods. The cumulative distribution of exoplanets detected over time by each method is shown in Figure 1.1.

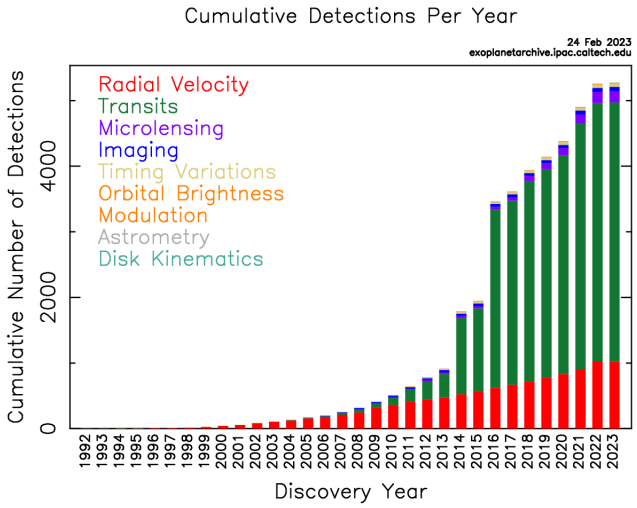

Figure 1.1: *Detected exoplanets over the years colour coded by detection methods. Image credit: NASA Exoplanet Archive.*

Exoplanets are found around stars of different ages, masses, metallicities, and regions of the galaxy, allowing us to understand the formation of planets on a larger scale. Although great leaps in knowledge have been made as to the diversity and architecture of planetary systems, the connection between the formation process and environment and the observed planetary systems remains a mystery.

In the context of understanding the exoplanet structure and the formation processes that lead to the present-day architecture of host star systems, the most important methods of detection are those that allow us also to determine precisely and

[4] As of February 24, 2023 - NASA Exoplanet Archive

accurately the exoplanets fundamental properties, such as mass and radius, in order to perform further analysis. Relevant properties for this study include planet mass, radius, orbital distance and period, and host star properties that shape the architecture of a planetary system.

1.2.1 TRANSIT DETECTION AND RADIUS DETERMINATION

With 3945 confirmed exoplanet[4], the *transit method* has been the most prolific detection technique. This method detects the slight change in flux of a host star as a planet passes in front of it. If the orbital plane of a planetary system is nearly edge on ($i \approx 90$ degrees, having defined the inclination i as the angle formed by the line of sight and the perpendicular to the orbital plane) relative to the observer, the planets will periodically transit its parent star. The geometry is illustrated in Figure1.2.

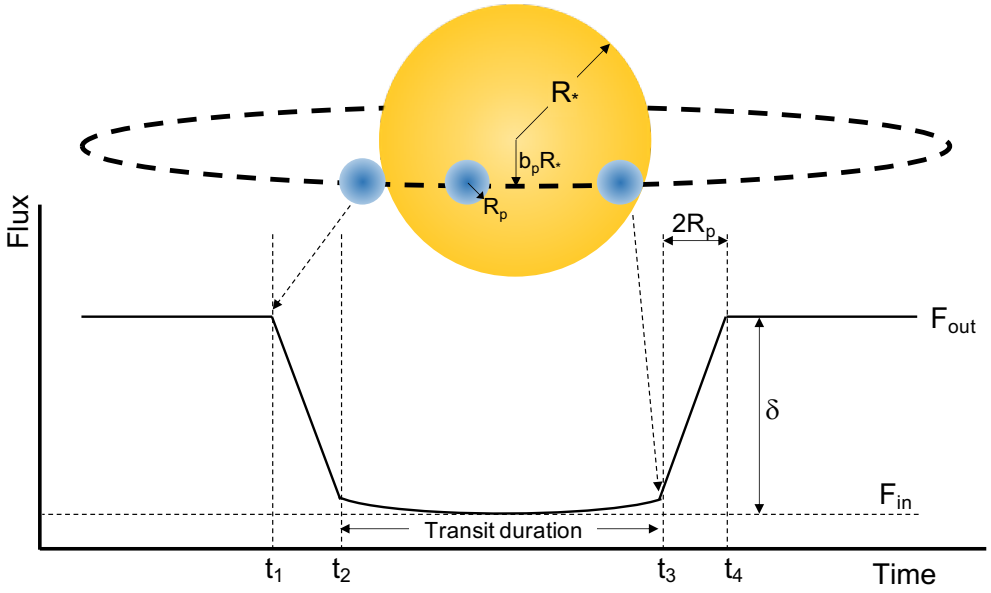

FIGURE 1.2: *Illustration of the transit method for detection exoplanets. If the orbital plane of a system appears nearly edge-on, planet will cross the disk of the star.*

The observable for transit surveys is the stellar flux variation over time. When a planet transits, it causes a decrease in the stellar flux due to the planet blocking some of the light. For some planets, an "eclipse" can also be observed when the planet passes behind the star. This is because the planet also contributes a small amount of the unresolved total light (combining star and planet) that is maximum just before and after the eclipse. The planet signal can come from either the reflection of the stellar light in the visible wavelengths or the planet thermal emission in the infrared. Both transits and eclipses (as shown in Figure 1.3) have measurable effects on the

total observed flux and can provide information regarding the planet atmospheric properties.

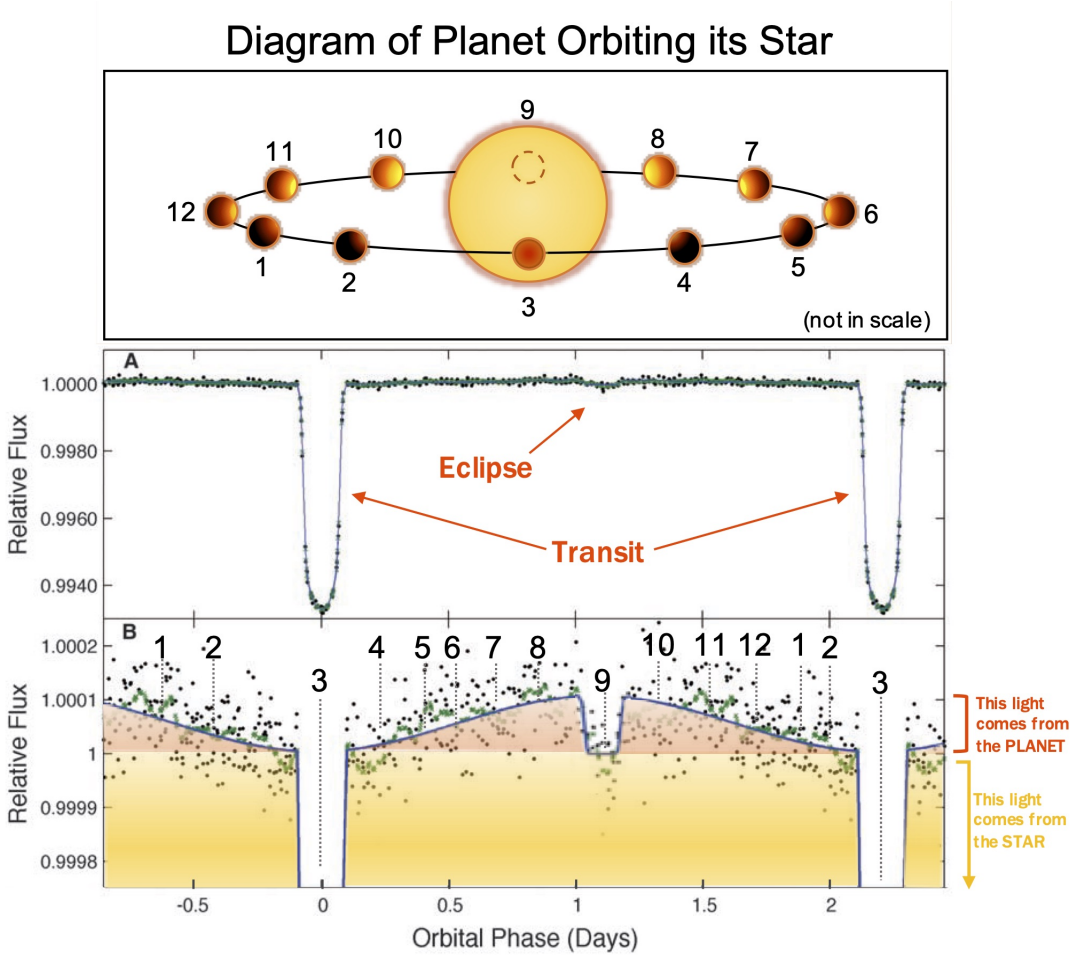

Figure 1.3: *Top panel: Diagram of a planet orbiting its star. Middle panel: Phase curve observation of HAT-P-7 b by the Kepler space telescope. Bottom panel: Expanded view. Adapted from Borucki et al. (2009).*

To a first approximation, the transit depth δ, which is the fraction of stellar flux blocked by the planet, is given by the ratio of the projected planetary and stellar areas:

$$\delta = \frac{F_{out} - F_{in}}{F_{out}} \approx \left(\frac{R_p}{R_*}\right)^2 \tag{1.1}$$

where F_{out} and F_{in} are the fluxes outside and during the transit, and R_p and R_* are the planetary and stellar radii. This expression assumes uniform brightness on the stellar surface (i.e. neglects limb darkening and all phenomena connected to the stellar activity), a full overlap of the planet and star, and the perfect opacity of the planet.

From Equation 1.1, by measuring the flux variation during a transit, knowing the

stellar radius, we can estimate the planetary radius. When observing stars similar in size to the Sun, the decrease in flux for giant planets like Jupiter, Saturn or planet orbiting HD 209458 is approximately 1% (see Figure 1.4). Photometric transit detections for these planets can be made using ground-based telescopes. For planets like Uranus and Neptune, the transit depth is about 0.1%, while for Earth-size planets it is about 0.01%, requiring high-quality space-based observations. The radius of the star also plays a crucial role in the transit depth, making accurate star size determination important. Equation 1.1 shows that for smaller stars such as M dwarfs ($R_* \approx 0.1 R_\odot$), the transit depth of an Earth-size planet is around 1%.

Observations of multiple transits allow for the measure of the orbital period, and then the determination of the orbit, which can be calculated using the known mass of a host star and the Third Kepler Law

$$\frac{a_p^3}{P_p^2} = \frac{GM_*}{4\pi^2} \tag{1.2}$$

where a_p is the semi-major axis, P_p is the period of the planet, G is the gravitational constant, and M_* is the mass of the host star (where we assume $M_p << M_*$).

However, this method is limited to detecting only those planets whose orbits bring them in front of their stars when viewed from Earth, which is, assuming random orientation, about 0.5% of all star system for a case like an Earth-Sun transit (Johnson, 2016). Despite this, with a large number of monitored stars, this method has led to the discovery of about 3500 exoplanets, including small, rocky terrestrial planets.

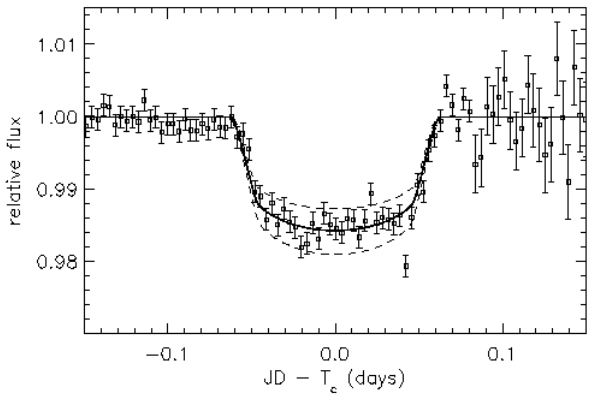

Figure 1.4: *Transit of the hot Jupiter HD 209458b, the first known transiting exoplanet discovered by Charbonneau et al. (2000).*

The total transit duration (T_{dur}) is defined as the time during which any part of the planet blocks the star disc (see points t_1 and t_4 in Figure 1.2), and it depends on

the planet transit path across the host star disc.

The arc length between points P and Q is α, and the straight-line distance between P and Q is $2l$ (see the star-planet geometry in Figure 1.5). From the triangle formed by P, Q (first and fourth contact[5]) and the centre of the star, $\sin\left(\frac{\alpha}{2}\right) = \frac{l}{a}$; which gives the expression for the total transit duration:

$$T_{dur} = P\frac{\alpha}{2\pi} = \frac{P}{\pi}\sin^{-1}\left(\frac{l}{a}\right) = \frac{P}{\pi}\sin^{-1}\left(\frac{\sqrt{(R_* + R_p)^2 - (b_p R_*)^2}}{a}\right) \tag{1.3}$$

The total transit duration is heavily dependent on the impact parameter b_p, which is defined as the sky-projected distance between the centre of the stellar disc and the centre of the planetary disc at conjunction. Assuming a circular orbit of semi-major axis a, and inclination i, the impact parameter is expressed as (see Figure 1.5):

$$b_p = \frac{a\cos i}{R_*} \tag{1.4}$$

The condition for a transit to occur is then $b_p < 1 + R_p/R_*$. The longest transit occurs when the exoplanet crosses the centre of the star disc ($b_p = 0$), while a shorter transit duration occurs when $b_p \neq 0$. Assuming a circular orbit, the total distance around the orbit is $2\pi a$, where a is the radius of the orbit.

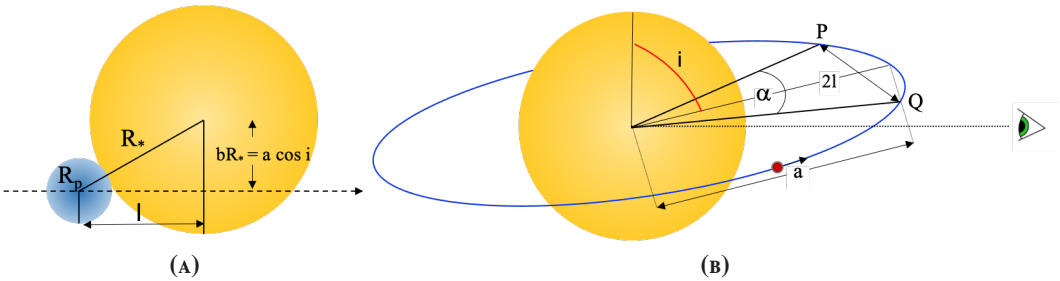

Figure 1.5: *Illustrations of the star-planet geometry showing the distance traversed by the planet, $2l$ from different points of view. The left panel shows the plane-of-sky projection of the star-planet system, hence as a view from the observer. The right panel shows the lateral view of the star-planet system, with the observer on the right*

If a planet is located at an orbital radius a in a system viewed at an inclination angle i, part of the planet will intersect the star disc if $\cos i \leq (R_p + R_*)/a$. The probability of a transit occurring, P_{tr}, for randomly oriented orbits can be calculated as:

$$P_{tr} = \frac{R_p + R_*}{a} \tag{1.5}$$

[5]points at which the planet disc is just touching the outer edge of the star, in the ingress and the egress of transit respectively

Equation 1.5 shows that close-in planets orbiting larger stars are more likely to exhibit transits. For example, Earth-sized planets around solar-like stars have a low transit probability of $P_{tr} = 0.5\%$, while hot Jupiters with a < 0.05 AU have a higher transit probability of $P_{tr} = 10\%$.

1.2.2 Radial velocity detection method and mass determination

The Radial velocity (RV) method was the first widely used technique for discovering exoplanets and is based on the Doppler effect. It has been responsible for detecting the majority of the first 100 exoplanets discovered, and today[4], over 1027 exoplanets have been discovered using RV measurements.

The RV method detects exoplanets by observing the gravitational effect they have on their host star. As a planet orbits a star, the star revolves around the centre of mass of the system, causing periodic changes in the star radial velocity.

The radial component of the star motion, v_r, along the line of sight causes a periodic Doppler shift in the stellar spectrum received on Earth, which is given by $\left(\frac{\Delta\lambda(t)}{\lambda} = \frac{v_r(t)}{c}\right)$. This motion is a result of the gravitational pull of the planet on the star, causing the star to wobble back and forth, as illustrated in Figure 1.6, due to both bodies moving in an r^{-1} gravitational potential and orbiting their common centre of mass on elliptical orbits, as predicted by Newtonian mechanics.

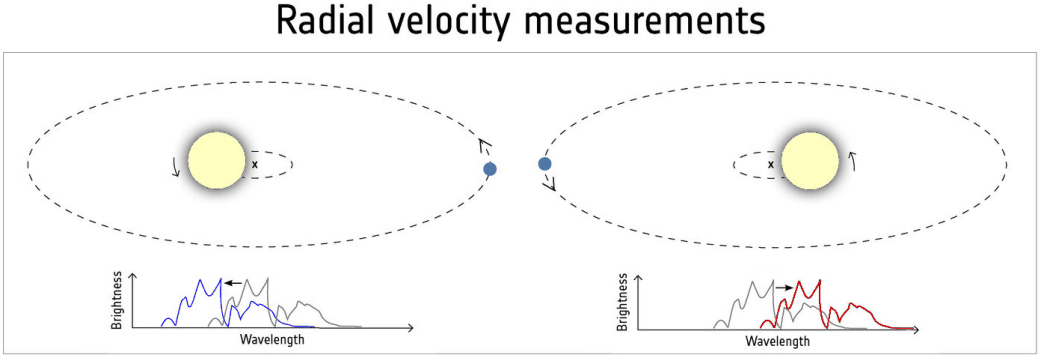

Figure 1.6: *Illustration of the radial velocity method. The stellar spectrum seen by an observer is blueshifted (left) and redshifted (right) as the star orbits the system barycentre. Credit: eso.org*

The magnitude of this effect is determined by the semi-amplitude of the star motion along the line of sight to Earth, denoted by K_*. In a single planet system, the characteristic amplitude of the radial velocity variations of the star is given by:

$$K_* = \frac{M_p \sin i}{(M_* + M_p)^{2/3}} \left(\frac{2\pi G}{P}\right)^{1/3} \frac{1}{\sqrt{1 - e^2}} \tag{1.6}$$

which can be derived from Kepler's laws. Here, M_p and M_* represent the planetary and the stellar masses, respectively, i is the inclination angle between the orbital plane and the plane of the sky, G is the universal gravitational constant, P is the orbital period, and e is the orbital eccentricity.

If the orbit is circular, the radial velocity variations are sinusoidal and reach a maximum value of K_* (see an example of RV time series in Figure 1.7). Stellar mass can typically be estimated through mass-spectral type relationships or by using other observables. Therefore, by knowing the M_* and P values and measuring K_*, by using Equation 1.6, we can calculate $M_p \sin i$. However, without knowledge of the inclination of the system, and since $\sin i \leq 1$, this technique usually only provides in most cases an upper limit for the planetary mass.

Equation 1.6 also indicates that for a given star, radial velocity semi-amplitudes are maximised for planets with high mass and low orbital periods.

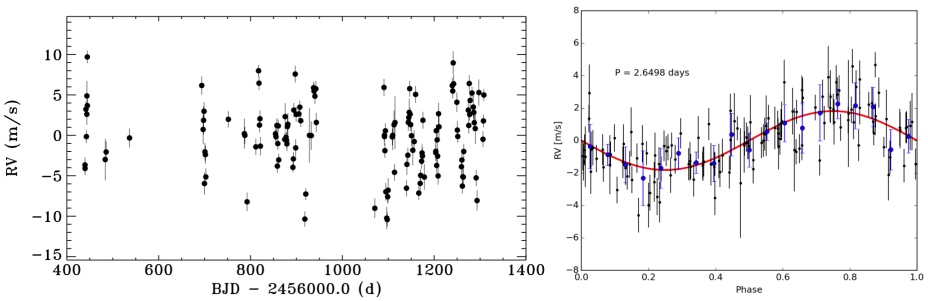

(A) (B)

Figure 1.7: *(A) Radial velocity time series for GJ 3998 measured with the TERRA pipeline. (B) RV data folded at the best-fit orbital period of the inner planet GJ 3998 b. Blue dots show the mean values in bins of amplitude 0.05. The red solid line indicates the best-fit orbital solution. Figures adapted from Affer et al. (2016).*

Currently, the most sensitive spectrographs for detecting exoplanets are the High Accuracy Radial velocity Planet Searcher (HARPS) spectrograph (Pepe et al., 2000) on the 3.6m telescope at La Silla Observatory in Chile, its northern hemisphere counterpart, the HARPS-N (Cosentino et al., 2012), installed on the Telescopio Nazionale Galileo (TNG) telescope in La Palma, Spain, and the recent Echelle SPectrograph for Rocky Exoplanets and Stable Spectroscopic Observations (ESPRESSO) spectrograph (Pepe et al., 2021), at the VLT in Paranal, Chile.

Another method for determining the planetary masses is the Transit Timing Variations (TTVs). TTVs occur in multi-planetary systems where one or more planets transit, and their gravitational attraction causes variations in the timing of transits. If a single planet were to follow a Keplerian orbit with regular transit times, the presence of additional bodies would cause deviations from this strict periodic-

ity. TTVs are sensitive to the masses and orbital configurations of the interacting planets, making TTVs analysis a powerful tool for mass determination.

1.2.3 Other techniques to detect exoplanets

The methods discussed above have led most of the exoplanet discoveries to date. However, other techniques, such as direct imaging and micro-gravitational lensing, have also been used to detect exoplanets, although they have contributed to a smaller number of discoveries. Each detection method has sensitivity to specific ranges or types of planets and plays an important role in discovering exoplanets. A diverse range of techniques provides comprehensive coverage of the parameter space and access to complementary information. To provide a complete overview, I will briefly mention these other methods here.

Direct imaging (62 discovered exoplanets[4])

The goal of direct imaging is to observe the exoplanet thermal emission directly by spatially resolving it as a separate point source from the host star. This is achieved by using a coronagraph to block the direct light from the host star, allowing nearby objects to be resolved (as shown in Figure 1.8). This method is sensitive to young, massive planets that are still retaining the thermal heat from their formation, and typically found in face-on orbits at large separations (Traub and Oppenheimer, 2010).

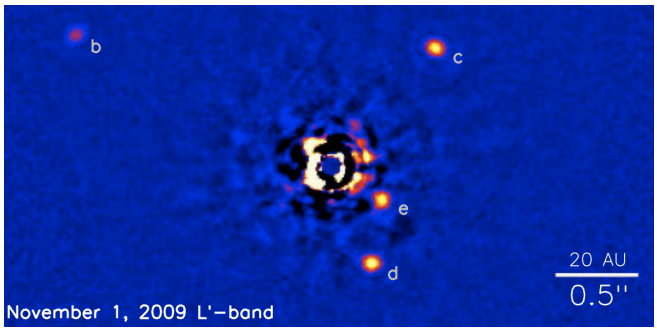

Figure 1.8: *Direct image with the Keck II telescope of the HR-8799 system, composed of 4 giant planets. Figure taken from Marois et al. (2010).*

Gravitational microlensing (176 discovered exoplanets[4])

Gravitational microlensing, which was first proposed as a method for exoplanet detection by Mao and Paczynski (1991) and Gould and Loeb (1992), uses the general relativistic deflection of light in curved space-time to detect distant exoplanets.

When a distant star passes close to a nearer star from the perspective of an observer, the light rays from the background star that traverse the gravitational field of the foreground "lensing" star change their trajectory. This bending of the light rays into the line of sight results in extended, intensified images of the background star. In practice, we observe and measure from the ground only the magnification of the source star flux as a function of time. By plotting the magnification as a function of time we produce a light curve, the shape of which depends on the stellar objects that cause the magnification of the source. For a single star that does not host any planet we have a single lensing event and the light curve has just one wide peak while for a planet orbiting the lens star we have a wide peak with a blip (close-in planet, see Figure 1.9) or double lensing event (planet in a distant orbit).

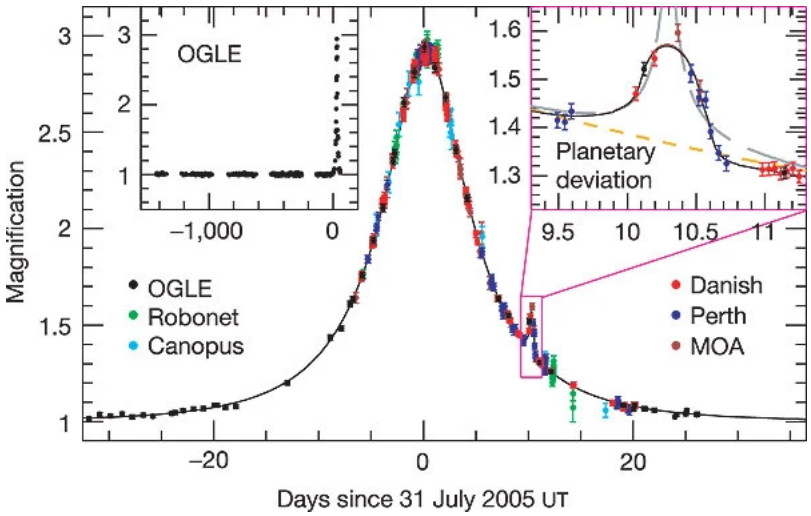

Figure 1.9: *Light curve of the microlensing event of OGLE-2005-BLG-390Lb, showing the presence of a planetary signal lasting for about a day. Figure extracted from Beaulieu et al. (2006).*

Astrometry (2 discovered exoplanets[4])

As in the case of radial velocity method, astrometry quantifies the gravitational perturbation of the host star caused by an orbiting companion by measuring the relative position of the star Perryman (2014). The elliptical motion of the star has a angular semi-major axis α given by

$$\alpha = \left(\frac{M_p}{M_*}\right)\left(\frac{a}{1AU}\right)\left(\frac{d}{1pc}\right)^{-1} \text{arcsec} \tag{1.7}$$

where a is the semi-major axis of the planet orbit (assumed circular), d the distance of the object from the observer. This astrometric signature α is the observable for the astrometric planet detection. As seen in Equation 1.7, the amplitude of the

astrometric signature is proportional to M_p and a, and inversely to d, hence the astrometry technique is more sensitive to long period systems (P $\geq$ 1 year), but is limited by the accuracy of the positional measurement of the star.

1.3 THE OBSERVED POPULATION OF PLANETS

The various observing techniques mentioned have resulted today[4] in detecting over 5200 exoplanets orbiting different types of stars. According to statistical estimates based on different discovery methods, there is on average at least one planetary companion for every star in the galaxy, as suggested by Howard et al. (2010) and Batalha (2014). This indicates the possibility of billions of planets existing in the Milky Way alone. Figure 1.10 illustrates a comparison between the known exoplanet population and the solar system planets in terms of mass (panel A) and radius (panel B) versus semi-major axis.

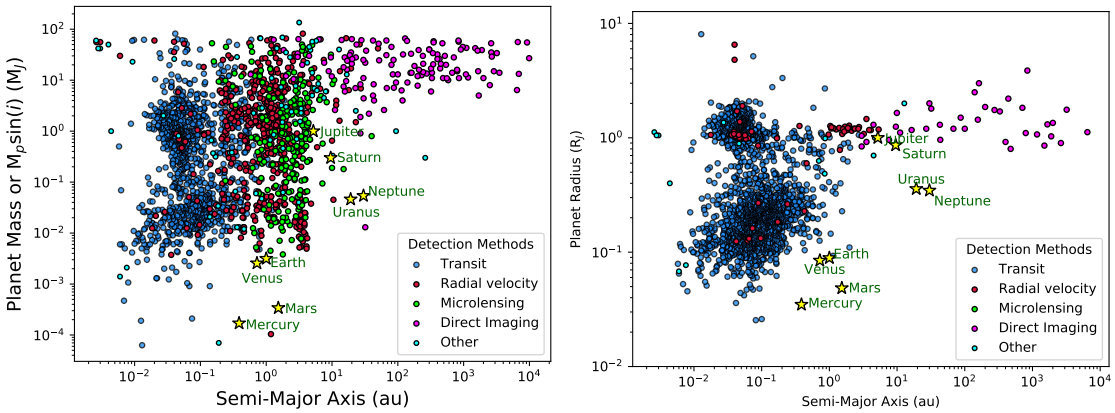

(A) (B)

FIGURE 1.10: *Left: exoplanets with known M_p (or $M_p \sin i$, for non-transiting planets) and semi-major axis. Right: exoplanets with known R_p versus semi-major axis. In both panel, the points are coloured according to the detection method. The planets of our solar system (gold star) are reported for comparison. Data from exoplanet.eu database (as of 31 January 2023).*

These representations indicate a wide range of observed exoplanets, highlighting that the demographics of planetary systems differ significantly from our own solar system.

Exoplanet detection methods are typically biased towards large planets located close to their stars, as these are easier to detect, leading to over-representation in known exoplanet catalogues. Moreover, certain groups of planets outside or below current survey detection limits are fundamentally invisible. Figure 1.10 demonstrates that transit surveys detect the smallest exoplanets, ranging in size from that

of the smaller planets in our solar system at 0.01 AU from their star to slightly larger than Jupiter at 1 AU. Radial velocity surveys detect Earth-mass exoplanets at 1 AU and planets two orders of magnitude more massive than Jupiter at 10 AU, while microlensing surveys can detect Jupiter-mass at 5 AU. Beyond 10 AU, direct imaging surveys mainly detect super-Jupiters.

Combining different detection methods provides a consistent picture of planet populations even if observation biases should be taken into account. According to radial velocity and transit surveys, the most commonly known types of exoplanets are super-Earths and sub-Neptunes, located within 1 AU. Giant planets, mostly located between 1 and 10 AU, orbit a smaller fraction of stars. For the purpose of this thesis, Hot Jupiters and smaller planets, such as super-Earths and sub-Neptunes, will be briefly discussed.

1.3.1 Hot-Jupiters

Hot Jupiters are giant planets with masses similar to Jupiter's ($M_p \sim 0.3$ - $3\ M_J$, Stevens and Gaudi 2013) and average radii ($R_p \sim 0.2$ - $2\ R_J$, Stevens and Gaudi 2013) that orbit their star with periods of less than 10 days. They are located very close to their star ($a < 0.1$ AU), and therefore receive strong stellar irradiation, leading to equilibrium temperatures ranging from 800 - 4000 K. Hot Jupiters dominated planet discoveries for a least one decade, as they are easiest exoplanets to detect via transits and RV methods.

Since massive planets cannot form in the high-temperature inner regions of the protoplanetary disk, multiple early evolution mechanisms have been proposed to explain their short orbital periods. Hot Jupiters could have migrated via gas disc migration, in which a giant planet migrates before the dispersal of the protoplanetary gas disc by exchanging angular momentum with the disc (Goldreich and Tremaine, 1980; Ida and Lin, 2008; Baruteau et al., 2014), or through high-eccentricity migration, a process by which planets or other celestial objects with high eccentric orbits can migrate and change their orbits over time due to interactions with other objects in the system, such as other planets or gas and dust in the disc (Rasio and Ford, 1996; Kozai, 1962).

Hot Jupiters are intrinsically rare, despite being the easiest to find. Their occurrence rate - the average number of planets per star satisfying a given range of properties - around main sequence stars is only about 0.5 - 1% (Wright et al., 2012; Fressin et al., 2013; Deleuil et al., 2018). The occurrence rate of hot Jupiters is highly dependent on the metallicity of the host star, as metal-rich stars are more likely to host a gas giant planet (Fischer and Valenti, 2005; Sousa et al., 2011). Host

star metallicity may be linked to the amount of material available on the protoplanetary disc for giant planet formation via core accretion (Johnson et al., 2010).

In the atmospheres of hot Jupiters, hydrogen and helium are dominant, as they are in the giant planets of our solar system. The fractions of these molecules are likely to be similar to their parent star value. In addition to these two main constituents, other molecules, such as oxygen, carbon, and nitrogen species, are also predicted to be present in the atmospheres (Sharp and Burrows, 2007).

1.3.2 Super-Earths and Sub-Neptune

One of Kepler's most surprising findings was the abundance of planets between 1-4 $R_\oplus$, absent from our solar system, making them particularly interesting to study their formation and evolution paths. This category includes both Neptune-like gaseous planets and smaller rocky super-Earths. About 50% of solar-type stars host at least one planet smaller than the size of Neptune (Fressin et al., 2013). The occurrence rate of planets with $R_p \sim R_\oplus$ is relative insensitive to stellar metallicity, as opposed to the clear trend seen for giant planets (Buchhave et al., 2012), but increases for short-period (10-100 days) planets (1.7 - 4.0 $R_\oplus$) around metal-rich stars (Petigura et al., 2018). These planets display a more varied bulk density distribution than hot Jupiters (Lopez and Fortney, 2013; Weiss et al., 2013; Weiss and Marcy, 2014). The most likely scenario that explains their formation is by core accretion of solids beyond several AU, followed by migration through the gas disc. After the gas disc disperses, these planets continue to evolve under several mechanisms which will determine their final masses, leading to diverse compositions. These planets can have a solid surface and no atmosphere or a tiny envelope, mainly composed of a significant fraction of elements such as Si, Mg, Fe, C, O. Alternatively, they may be "transitional planets" with either a rocky core with an H-rich envelope or a significant fraction of H_2O-dominated ices/fluids. Their atmosphere can be primordial or evolved to a secondary atmosphere. They could have atmospheres with a larger fraction of water vapour but also retained some hydrogen and helium.

1.3.3 Exoplanetary Atmospheres

Since the first detection of atmospheric absorption from a transiting exoplanet by Charbonneau et al. (2002), and the subsequent detection of thermal emission from another transiting exoplanet (Charbonneau et al., 2005), atmospheric observations have been reported for over fifty transiting exoplanets. These observations, when combined with their bulk parameters and host star properties, can provide valuable

insights into the atmospheric and interior properties, formation, and evolution histories of exoplanets.

Moreover, planetary atmospheres can be broadly classified as either "primary" or "secondary". Primary atmospheres originate from the accretion of gases from the nebula and are mainly composed of hydrogen and helium. On the other hand, secondary atmospheres are formed by the outgassing of volatiles from the planet interior. The composition of the atmosphere of planets with masses ranging from 1-15 $M_\oplus$ can be diverse and may either be predominantly primary, predominantly secondary, or a mixture of both.

The composition of a planet interior has a significant impact on the characteristics of its atmosphere. Five broad categories of planetary atmospheres can be defined:

- *H and He dominated atmospheres*: These atmospheres contain mostly hydrogen and helium in cosmic proportions, indicating that the planet captured its atmosphere from the protoplanetary nebula.

- *Outgassed atmospheres with hydrogen*: Planets that have atmospheres resulting from outgassing, rather than being captured from the protoplanetary nebula, will typically contain some amount of hydrogen in the form of H_2. The specific quantity of H_2 will depend on the composition of the planetesimals that contributed to the planet formation (Elkins-Tanton and Seager, 2008). Such planets in the range of 10-30 $M_\oplus$ may be massive and cold enough to retain hydrogen in their atmospheres against atmospheric escape, resulting in H-rich atmospheres that are distinct from the CO_2- or N_2-dominated atmospheres of Solar System terrestrial planets. Some super-Earths may have particularly thick outgassed atmospheres of up to 50% by mass of H, up to a few percent of the planet mass. Additionally, some planets may feature massive water vapour atmospheres (e.g., Rogers and Seager, 2010).

- *Outgassed atmospheres dominated by CO_2*: On Earth, CO_2 dissolved in the ocean and was sequestered in limestone sedimentary rocks, which left N_2 as the dominant atmospheric gas. This category of atmospheres is characterised by the absence of H and He, and the presence of H_2O may suggest the existence of a liquid water ocean.

- *Hot super-Earth atmospheres lacking volatile*: Planets with atmospheric temperatures exceeding 1500 K are likely to have lost not only H but also other volatiles such as C, N, O, and S. The resulting atmosphere would consist of

silicates enriched in more refractory elements like Ca, Al, and Ti (Schaefer and Fegley, 2009).

- *Atmosphereless planets*: These are hot planets that have lost their entire atmosphere.

Giant planets outside our solar system are expected to have primary atmospheres composed largely of H and He (e.g., Seager et al., 2007). These atmospheres are also expected to contain a number of less abundant molecular and atomic species made up of heavier elements (e.g. O, C, N) in proportions governed by the primordial abundances (Burrows and Sharp, 1999). These "trace species" are responsible for the dominant features of giant planet spectra.

On the other hand, super-Earths have no analogues in our solar system, as their masses are intermediate between those of terrestrial planets and ice giants. It is presently unknown if super-Earths are sub-Neptunes with H/He-rich atmospheres, or are scaled up terrestrial planets with atmospheres dominated by heavy molecules (e.g., H_2O, CO_2).

In principle, H-rich atmospheres could be easily distinguished from those dominated by heavier molecules. However, it is important to consider the role of clouds, which may originate from condensation of silicates or other refractory "rocky" materials, or from photochemical processes. They are generally grey absorbers or scatterers, and could also obscure transmission spectrum features (Fortney, 2005; Morley et al., 2013). However, transmission spectrum observations with a high enough SNR should be able to recover a wealth of atmospheric information (Benneke and Seager, 2012).

1.4 This thesis

1.4.1 Motivations

The radius and mass of an exoplanet are the basic quantities that determine the properties and the evolution of a planet. They can be determined by measuring the flux and the radial velocity variation of its parent star caused by the planet orbit. Improving the precision of observational planet masses and radii is crucial for understanding planet structure and formation models. Both are key parameters for studying the internal structure of a planet, its formation and evolution and to derive atmospheric properties.

In this context, accurate estimation of both the radius and mass of a planet can be essential in retrieving the planetary atmospheric composition. However, the uncer-

tainty in the mass measurement, which typically has an error bar from a minimum value of 10% for planets with $M > 0.1\ M_J$ but much larger for smaller planets (often greater than 50% or even only estimated from models), can contribute to the degeneracy in retrieving the mean molecular weight of the atmosphere, especially in the presence of clouds.

On the other hand, as mentioned in Section 2.5, limitations in the characterisation of exoplanets, particularly in their masses, can arise from various sources especially from stellar noise due to stellar variability, due to magnetic activity, which creates noise and affect the detection and characterisation of exoplanets. Therefore, it is important to not only detect and characterise exoplanets but also study and characterise their host stars, especially when they are M or young stars.

1.4.2 Plan of the thesis

In Chapter 2, I introduce the atmospheric characterisation of exoplanets through transmission spectroscopy, the challenges for the detection and characterisation of exoplanets and the main instruments, data reduction techniques and analysis tools relevant for this thesis. In Chapter 3, I analyse the impact of uncertainties in the planetary mass on the atmospheric retrieval. In Chapter 4 I extend this analysis to a sub-sample from the Ariel MRS proving a receipt for each analysed target. In Chapter 5, I present a method for optimizing the radial velocity extractions for fast-rotating stars using the cross-correlation function (CCF) technique, which takes into account stellar activity by considering the presence of spots on the stellar surface. In Chapter 6, I measure activity indicators at visible wavelength for the very active star AD Leonis, observed with HARPS and HARPS-N, to better understand the behaviour of chromospheres in M stars, characterise their variability, and find correlations among them. Conclusions and future prospectives follows in Chapter 7.

CHAPTER 2

Instruments and analysis methods

The aim of this chapter is to provide essential information for the full comprehension of the subsequent chapters. Firstly, I introduce the main instruments used for detecting and characterising exoplanets, which are relevant to this thesis. I also discuss the main software used for reducing HARPS/HARPS-N spectra and some tools that will aid in the data analysis. Next, I introduce the characterisation of the exoplanetary atmosphere through transmission spectroscopy and the powerful retrieval framework TauREx (Al-Refaie et al., 2021). Finally, I discuss the main challenges associated with exoplanet detection and characterisation.

2.1 Instruments for the detection and characterisation of exoplanets relevant for this thesis

2.1.1 HARPS-N

High Accuracy Radial velocity Planet Searcher for the Northern emisphere (HARPS-N) is an echelle spectrograph located at the 3.6m Telescopio Nazionale Galileo (TNG), La Palma. It covers a wavelength range of 383 to 693 nm and has a spectral resolution R = 115000 (Cosentino et al., 2012). Figure 2.1 shows an image of the spectrograph. It is designed to obtain high-precision radial velocity measurements while avoiding spectral drifts due to temperature and air pressure variations, thanks to very accurate control of pressure and temperature. HARPS-N if fiber-fed by the Nasmyth B Focus of the 3.6 INAF - TNG telescope through a Front End Unit (FEU). The two fibers (A and B, used for the target and to obtain the sky spectrum or a simultaneous calibration lamp, respectively) have an aperture on the sky of 1"; this produces a resolving power of 115000 in the spectrograph. The spectrum is projected onto an e2V CCD 231 detector, which allows 69 spectral orders.

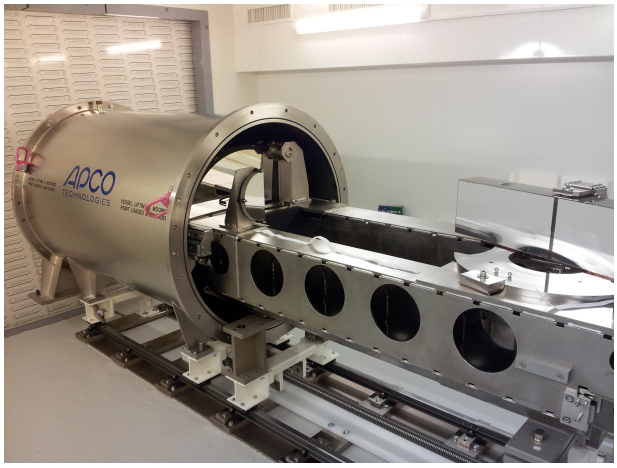

Figure 2.1: *HARPS-N echelle spectrograph. Figure is taken from TNG website.*

2.1.2 Space-based Photometry

Precise photometry from NASA's Kepler (Borucki et al., 2010), K2 (Howell et al., 2011), and TESS (Ricker et al., 2015) missions over the last two decades has revolutionised exoplanet science and stellar astrophysics.

In March 2009, the NASA Kepler Mission launched into a stable, Earth-trailing heliocentric orbit and stared continuously at a single patch of the sky for more than 4 years, monitoring the flux of 200,000 stars. Its goal was to quantify the occurrence rate of Earth-like planets, or planets discovered orbiting near the habitable zone of their host star, using the transit method. The Kepler spacecraft was pointed at a region in the sky known for its abundance of FGK main-sequence stars similar to the Sun, out of the galactic plane and between the constellations of Cygnus and Lyra.

Unfortunately, the mission concluded with a malfunction in two reaction-wheels, which nullified the spacecraft ability to remain focused on a single patch of the sky for an extended period. An alternative plan was established, and in May 2016, the K2 mission was approved. K2 (Howell et al., 2011) used solar wind pressure to balance the third dimension of the spacecraft, allowing for stable pointing for up to 2-3 months along the ecliptic. In October 2018, after having observed 20 fields along the ecliptic during its K2 mission, the Kepler spacecraft ran out of fuel, and NASA announced that the telescope had officially been retired.

In September 2018, the Transiting Exoplanet Survey Satellite (TESS) (Ricker et al., 2015) achieved first light. The spacecraft observes large portions of the night sky over an extended period of time. It observes a hemisphere of the night sky for a full year and then switches to the other hemisphere for the next year. This allows TESS to observe most stars for at least 27 days at a time but can observe some stars

for a full year if they are located near the north and south ecliptic poles.

2.1.3 Ariel

The ESA Atmospheric Remote sensing Infrared Exoplanet Large Survey (Ariel) space telescope is a 0.64m^2 telescope, planned to be launched in 2029. It will be the first telescope dedicated to studying the atmosphere of a large population of exoplanets, characterising their thermal structures, chemical compositions, cloud properties and dynamical processes as a function of longitude, latitude and altitude for about 1000 exoplanets ranging from Jupiters and Neptunes down to super-Earth size orbiting different types of stars. The mission will use transit, eclipse and phase curve techniques and revisit some planets with multiple techniques at different times. It will use simultaneously observations obtained in three photometric bands in the visible/near-infrared and three spectroscopic channels in the infrared (1.10-7.80 μm). A detailed description of the Ariel Mission is provided in the Ariel Red Book (ESA/SCI(2020)1).

The observations are separated into "Tiers" (Tinetti et al., 2016, 2018), each with different goals:

- **Tier 1 Reconnaissance survey**: These observations will use a low spectral resolution (4 spectral resolution elements covering the 1.10 - 7.80 μm range, with an average SNR $\geq$ 7) to characterise about 1000 transiting planets. They aim to answer basic questions through the large statistical sample of observed planets, such as determining the fraction of planets that have cloudy atmospheres, the fraction of small planets that have retained their primary envelope, removing mass-radius degeneracies to constrain planet interiors, obtaining rough estimates of planet properties like temperature, albedo or the presence of main molecules, and classifying the planets through colour-colour diagrams. The Ariel Tier 1 survey mode will also allow for rapid and broad characterisation of planets so that decisions can be made about priorities for future observation with Tier 2 and Tier 3. The necessary performance can be reached in less than 10 transits/eclipses for the majority of targets.

- **Tier 2 Deep survey**: This tier uses a higher spectral resolution (R$\sim$ 10 for 1.10 $< \lambda <$ 1.95 μm; R$\sim$ 50 for 1.95 $< \lambda <$ 3.90 μm; R$\sim$ 15 for 3.90 $< \lambda <$ 7.80 μm; with an average SNR $\geq$ 7) on a sub-sample of about 500 planets, which constitutes the core of the mission. Tier 2 spectroscopic observations will be essential for uncovering atmospheric structure and composition (main components and trace gases), as well as searching for potential correlations

Table 2.1: *Summary of the Ariel required spectral coverage and resolving power. The key scientific motivations are listed in the right column (Tinetti et al., 2018).*

Wavelength range	Resolving power	Scientific motivation
VISPhot 0.50 - 0.60 μm	Integrated band	• Correction stellar activity • Measurement of planetary albedo • Detection of Rayleigh scattering/hazes
FGS1 0.60 - 0.80 μm	Integrated band	• Correction stellar activity • Measurement of planetary albedo • Detection/characterisation of clouds/hazes
FGS2 0.80 - 1.10 μm	Integrated band	• Correction stellar activity • Detection/characterisation of clouds/hazes
NIRSpec 1.10 - 1.95 μm	R $\geq$ 15	• Correction stellar activity • Detection/characterisation of clouds/hazes • Detection of molecules (e.g. H_2O,TiO,VO, metal hydrides) • Measurement of planet temperature • Retrieval of molecular abundances • Retrieval of vertical and horizontal thermal structure • Detection temporal variability (weather/cloud distribution)
IR spectrograph (AIRS) 1.95 - 7.8 μm	R $\geq$ 100 (below 3.9 μm) R $\geq$ 30 (above 3.9 μm)	• Detection of atmospheric chemical components • Measurement of planet temperature • Retrieval of molecular abundances • Retrieval of vertical and horizontal thermal structure • Detection temporal variability (weather/cloud distribution)

between atmospheric chemistry and basic parameters like planetary radius, density, temperature, stellar type and metallicity.

- **Tier 3 Benchmark planets**: These observations will focus on studying the variability through time and space of exoplanet atmospheres. This tier is dedicated to planets for which the maximum Ariel spectral resolving power and SNR ≥ 7 can be reached in one or two observations (e.g. 10% sample). Ariel Tier 3 observations will identify variations in the thermal vertical and horizontal structure through time. The results will be used to quantify, for the first time, the uncertainty introduced when we obtain only disc and time-integrated spectra. Additionally, by combining all observations obtained over time for a Tier 3 planet, unprecedented SNR will be achieved, enabling an extremely detailed study of atmospheric chemistry and dynamics.

- **Tier 4 Phase-curves and bespoke observations**: This is a special tier for targets of particular interests even if non-transiting. Custom observations with individualised requirements, such as phase curves, can be carried out in Tier 4. Phase-curve analysis, which involves tracking the scattered or emitted light of a planet along its entire orbit, enables the extraction of valuable information about the chemistry, thermal structure, and cloud properties. Furthermore, by combining analyses at different phases of the orbit, it becomes possible to map the dynamics of the planetary atmosphere, identifying features such as hot-spots or cloudy regions (e.g., Changeat, 2022).

Table 2.2: *Summary of the science requirements for the survey tiers given in Tinetti et al. (2021).*

Tier name	Science requirements
Tier 1 Reconnaissance Survey	- All planets in the sample - 5+ spectral resolution elements covering the 1.10 – 7.80 μm range) measurements with average SNR $\geq$ 7 - Transit or eclipse
Tier 2 Deep Survey	- Spectroscopic measurements for a subsample (e.g. 50% of sample) - R $\sim$ 10 for 1.10 $< \lambda <$ 1.95 μm; R $\sim$50 for 1.95 $< \lambda <$ 3.90 μm; R$\sim$15 for 3.90 $< \lambda <$ 7.80 μm; with average SNR $\geq$ 7 - Transit and/or eclipse
Tier 3 Benchmark planets	- Spectroscopic measurements for a subsample (e.g. 10% of sample) - R $\sim$ 15 for 1.10 $< \lambda <$ 1.95 μm; R $\sim$100 for 1.95 $< \lambda <$ 3.90 μm; R$\sim$30 for 3.90 $< \lambda <$ 7.80 μm; with average SNR $\geq$ 7 achievable in 1-2 observations - Transit and/or eclipse, repeated in time
Tier 4 Phase-curves and bespoke obs.	- Phase-curves, eclipse mapping, bespoke observations - Multiple-band photometry/spectroscopy with SNR $\geq$ 10

Ariel observations will simultaneously cover the wavelengths from 0.5 μm to 7.8 μm. The telescope has 3 photometers (a Visible Photometer, VISPhot, and two Fine Guidance Sensors, FGS1 and FGS2), and two spectrometers (the Near Infrared Spectrometer, NIRSpec, and the Ariel Infrared Spectrometer, AIRS) with varying resolution depending on the Tier level. Table 2.1 summarises the Ariel required spectral coverage, resolving power and the key scientific motivations, while Table 2.2 outlines the science requirements for each survey tier.

2.2 Data Reduction

In this thesis, I analysed HARPS and HARPS-N spectra. In Chapter 5. HARPS and HARPS-N spectra were used to measure the RVs, while in Chapter 6, HARPS and HARPS-N spectra were used to analyse time-series variations in activity-sensitive lines, such as Ca II H & K and Hα.

All spectra were automatically reduced using the Data Reduction Software (DRS) (Cosentino et al., 2012), which also extracts the radial velocities. However, another approach to derive the RVs is available, namely the Java-based Template-Enhanced Radial velocity Re-analysis Application (TERRA) (Anglada-Escudé and Butler, 2012).

2.2.1 Data Reduction Software (DRS)

The DRS handles all the aspects of the scientific reduction of the raw data. It applies the classical optimal extraction method described by Horne (1986), which includes

bias and background subtraction, flat fielding, and delivers spectra that are both cosmic ray corrected and wavelength calibrated. The DRS also calculates radial velocities (RVs) using the cross correlation function (CCF) method (Baranne et al., 1996; Pepe et al., 2002).

Cross-correlation function (CCF) approach

The RV of a star with respect to the system barycentre can be inferred from by the Doppler shift in the wavelength of the stellar spectrum, which is given by:

$$\Delta\lambda = \lambda_{obs} - \lambda_{em} \tag{2.1}$$

where λ_{obs} is the observed wavelength in the star-planet barycentre and λ_{em} is the emitted wavelength. The velocity is related to $\Delta\lambda$ by:

$$v_R = \left(\frac{\Delta\lambda}{\lambda_{em}}\right)c. \tag{2.2}$$

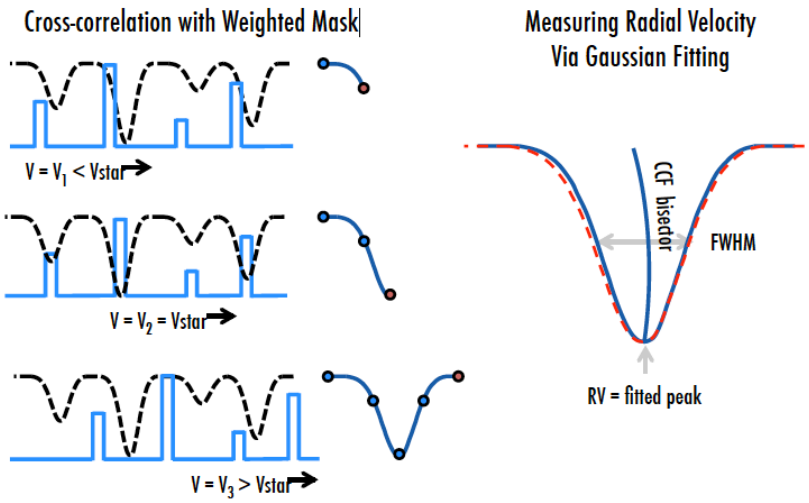

Figure 2.2: *Illustration of the construction of the cross-correlation function.*

We can obtain Doppler shift measurement from every single line of each order of the spectrum. However, to determine accurate and precise RV measurement from the spectrum, the DRS used the cross correlation function (CCF) method. The CCF technique, first proposed by Fellgett (1955), and developed by Griffin (1967). Schematically, it is based on obtaining a mean-line profile of the spectrum by cross-correlating the stellar spectrum with a binary mask, defined to be 1 if $\lambda = \lambda_{em} \pm \Delta_{width}$ and zero otherwise, optimised for the specific spectral type. A number in the interval between 0 and 1 can be given to the mask to assign different weights to different

parts of the spectrum (for example dependent on the SNR). To calculate the total flux that is not blocked by the mask, the mask is shifted in increments of step size Δ_v, and the spectrum is multiplied by the mask at each velocity step until the cross-correlation function (CCF) is obtained. A diagram illustrating this process is shown in Figure 2.2.

If S is the observed spectrum, the CCF is given by:

$$CCF(v) = S(\lambda) \times M[\lambda(1 + v/c)]w \tag{2.3}$$

In practice, to calculate the CCF, an array of velocities v= [-v_A,v_A] is defined with step size of Δ_v. The observed spectra are computed in the range $\lambda_{em}(1 + v/c) \pm \Delta_{width}$ for each velocity element v, and S and M are correlated for the different velocity elements, for which w will be either 0 or 1. The RV is obtained as the centroid of a Gaussian function fitted to the CCF profile. The DRS provides the CCF for each spectral order, but the RV of a specific observation is calculated as the weighted average of the RVs from individual spectral orders, where the weights are determined by the SNR of each order. An example of CCF profile is shown in Figure 2.3.

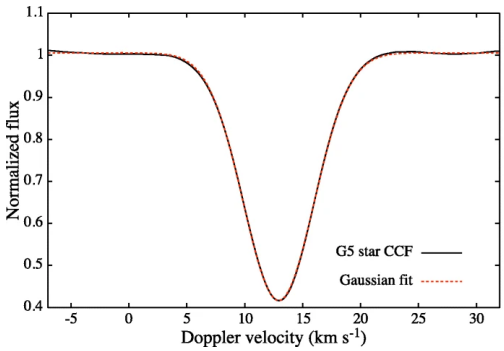

Figure 2.3: *CCF created by DRS for a G5 star using the G2 mask and relative Gaussian fit. From: Rainer et al. (2020)*

2.2.2 Template-Enhanced Radial velocity Re-analysis Application (TERRA)

TERRA algorithm is used to extract the RVs using a template matching approach.

Given a wavelength calibrated observation and a stable instrumental profile, the observed spectrum differs from the template only by a Doppler shift (due to Earth motion around the Sun and/or the presence of companions) and a flux normalization function (most likely due to observational and instrumental effects).

The TERRA algorithm involves building a high-SNR template T by combining all of the observed spectra, and then finding the parameters that minimise the difference between the observed spectrum S and the template T. Specifically, the goal is to minimise R, the residuals at each pixel i, which are defined as follows:

$$R(\lambda_i) = T[\alpha_v \lambda] - S[\lambda] \sum_{m=0}^{M} \alpha_m (\lambda - \lambda_c)^m \tag{2.4}$$

Here, λ is the wavelength of the observation transformed to the solar system barycentre reference frame. The parameter α_v represents the Doppler shift between the template and the observed spectrum, while α_m are the parameters of the flux normalisation function, which is an M-degree polynomial that accounts for time-dependent observational and instrumental effects. Therefore, the Doppler shift and the other α_i parameters are obtained for each spectral order by minimising:

$$\chi^2 = \sum_{i=1}^{N_{pixel}} \omega_i R^2(\lambda_i) \tag{2.5}$$

where ω_i represents the weight assigned to each pixel at wavelength λ_i. The final RV is calculated as the weighted mean of the values obtained for each spectral order. This method has been demonstrated to work particularly well for M dwarfs, or stars with broad lines.

2.3 Method of statistical analyses and analytical tools

This section aims to introduce some key statistical and numerical methods and tools used in this thesis. Firstly, I introduce the widely popular tools classified as periodograms. In the context of exoplanetary science, their main application is to study the presence of periodic signals in time-series, but they can also be used to define detection limits for planetary companions. Next, I introduce TauREx (Al-Refaie et al., 2021), a powerful retrieval framework that provides extremely fast-forward models for spectroscopic transmission and emission. Finally, I present a brief discussion of posterior sampling methods such as The Markov Chain Monte Carlo (MCMC) and Nested Sampling, used to fit data to specific models.

2.3.1 Periodograms

The first technique defined as a periodogram was introduced by Arthur Schuster (Schuster, 1898). It is based on the discrete-time Fourier transform and represents

one of the most widely adopted methods for analysing periodic variations in time-series. Unfortunately, it requires continuous sampling of the signal with even time intervals, and therefore, it is usually unsuitable for exoplanet searches involving low-cadence data with irregular time sampling. A generalisation of the Schuster periodogram known as the Lomb-Scargle algorithm (Barning, 1963; Lomb, 1976; Scargle, 1982) was developed in order to handle the irregular time sampling. This is achieved by using a pair of phase offset sinusoidal basis orthogonal functions. It is equivalent to fitting time-series data with sine waves of the form $y = a\sin(\omega t + \phi) = b\sin\omega t + c\cos\omega t$. However, this method has two major shortcoming when used to analyse time-series in the exoplanetary context. Firstly, it assumes that the observations are noise-free and hence the measurements errors are not taken into account. Secondly, it assumes that the data has zero mean, implying that the mean of the data and the mean of the sinusoids are the same. The generalised Lomb-Scargle (GLS) periodogram, which accounts for measurement errors and non-zero mean, was introduced by Zechmeister and Kürster (2009). Following their notation, for a time-series (t_i, y_i) with N observations and errors σ_i, we fit the following model:

$$y(t) = a\sin\omega t + b\cos\omega t + c \tag{2.6}$$

Hence, minimise the following function:

$$\chi^2 = \sum_{i=1}^{N} \frac{|y_i - y(t_i)|^2}{\sigma_i^2} = W\sum w_i[y_i - y(t_i)]^2 \tag{2.7}$$

where the observations are weighted by inverse-variance as:

$$w_i = \frac{1}{W}\frac{1}{\sigma_i^2} \qquad \left(W = \sum \frac{1}{\sigma_i^2} \quad \sum w_i = 1\right) \tag{2.8}$$

This formulation will be used in the following chapters.

Figure 2.4 shows a generalised Lomb-Scargle (GLS) periodogram and the false alarm probability (FAP), which determines the statistical significance of the periodic signals. In particular, in period analysis techniques the lower the FAP for a given period P, the more likely P is a significant period (FAP values are expressed as a number between 0 and 1).

It is also important to identify the nature of the several peaks in the periodogram that may have stellar, instrumental, or observational origins, rather than being caused by a planet.

Unfortunately, the GLS periodogram relies on a few fundamental assumptions

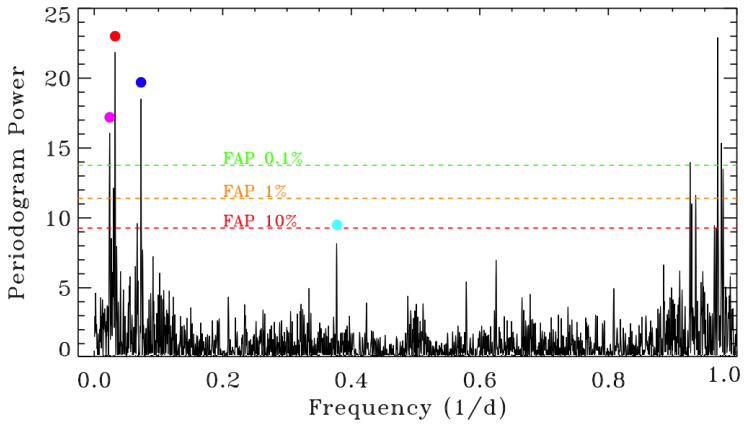

Figure 2.4: *GLS periodogram of the radial velocities of GJ 3998, of the original data. The dashed lines indicate the 0.1%, 1%, and 10% levels of false-alarm probability. Adapted from Affer et al. (2016)*

that are not always met, which can make the results unreliable. It assumes that the studied signal is a single sinusoid affected by Gaussian noise, requiring not only a strictly periodic signal, but also that it is represented by a sine/cosine function. This might apply to a single planet on a circular orbit, but not to general Keplerian signals, which are often non-sinusoidal and affected by multiple interferences, including quasi-periodic activity-induced signals and the astrophysical window functions. The time sampling of observations is also crucial for the robustness of any detection, as "ghost" signals can be observed due to the sparse and irregular time sampling. Proper testing for these biases is necessary to avoid distorted results.

Despite these limitations, the GLS periodogram is widely used in the astrophysics community due to its convenience and efficiency, and it is one of the most commonly used tools in exoplanet studies, including Doppler spectroscopy. GLS periodograms are often used to estimate the stellar rotation period of stars from the time curves of their activity indicators, which can help distinguish between stellar and planetary signals and "clean" the RV time-series.

2.3.2 Numerical methods

All retrieval codes share a common underlying structure, consisting of a forward model framework responsible for constructing the spectrum that will be used as a model (referred to as the *forward model*), and a retrieval framework that fits the forward model to observations to determine the optimal set of parameters that accurately describe the data. During the retrieval step, different methods may be employed to establish parameter constraints and derive posterior distributions.

The *retrieval problem*, also known as the *inverse problem*, consists in defining

the state vector of a model based on a data vector. The data or measurement vector, represented by a vector **y**, and a set of physical parameters pertinent to our model, represented by a state vector **x** (such as gas mixing ratios and temperature at each atmospheric level in the case of atmospherical retrieval, or the latitude, longitude and filling factor of spots in the case of a spot model), can be related as follows:

$$\mathbf{y} = \mathcal{M}(\mathbf{x}) + \epsilon \tag{2.9}$$

Here, the error vector $\boldsymbol{\epsilon}$ encapsulates all the errors, and $\mathcal{M}(\mathbf{x})$ is the *forward model* - a function that captures our understanding of the physics of the measurements.

This relationship enables an accurate solution to the inverse problem when the input parameters that best describe the scenario are precisely known, or when the underlying physics are well known a priori, and the data have extremely high signal-to-noise ratios. In such cases, $\mathcal{M}(\mathbf{x})$ can be expanded around an initial guess for the true state, denoted as $\mathbf{x}_0$, using one step of a Taylor series. Specifically, we can write:

$$(\mathbf{y}) - \mathcal{M}(\mathbf{x}_0) = \frac{\delta \mathcal{M}(x)}{\delta \mathbf{x}}(\mathbf{x} - \mathbf{x}_0) + \epsilon = \mathbf{J}(\mathbf{x} - \mathbf{x}_0) + \epsilon \tag{2.10}$$

where **J** is the Jacobian matrix, a weighting function matrix that describes how sensitive the model is to perturbations in each state vector parameter at each wavelength position.

However, in some cases, the inputs are uncertain and the initial assumption that $\mathbf{y} = \mathcal{M}(\mathbf{x}) + \epsilon$ may not be entirely valid. In such situations, *Bayesian inference* is a more effective statistical tool as it allows us to constraint the physical state while accounting for the large uncertainties in the measurements, and also allows us to impose minimal prior knowledge on the physical state.

To apply Bayesian inference, we treat **x**, **y** and ϵ as random variables and determine the joint probability distribution of (**x**,**y**). We then define the "solution" to the inverse problem as the probability distribution of **x** given **y**, denoted as **x**|**y**. This approach enables us to model the noise, even if we do not know the exact nature of the noise that affects the given data. It also allows us to specify a priori the form of solutions that we believe to be more likely, thereby enabling us to assign weights to multiple solutions which explain the data. This is the Bayesian approach to inverse problems.

Bayes' theorem explains the relationship between the probability density function of the data vector, **y**, and the probability density function of the state vector, **x**,

given a forward model, $\mathcal{M}$. The theorem is expressed as:

$$\mathcal{P}(\mathbf{x}|\mathbf{y},\mathcal{M}) = \frac{\mathcal{P}(\mathbf{y}|\mathbf{x},\mathcal{M})\mathcal{P}(\mathbf{x},\mathcal{M})}{\mathcal{P}(\mathbf{y}|\mathcal{M})} \tag{2.11}$$

Here, $\mathcal{P}(\mathbf{x}|\mathbf{y},\mathcal{M})$ represents the posterior distribution of the state vector when the measurement is given, while $\mathcal{P}(\mathbf{x},\mathcal{M})$ is the prior distribution representing our knowledge of the state vector before the measurement is taken. The likelihood function, $\mathcal{P}(\mathbf{y}|\mathbf{x},\mathcal{M})$, quantifies the probability of observing the data vector, given a particular state vector and forward model. The denominator $\mathcal{P}(\mathbf{y}|\mathcal{M})$, is the *Bayesian evidence* ($\mathscr{E}$), which is obtained by integrating $\mathcal{P}(\mathbf{y}|\mathbf{x},\mathcal{M})$ $\mathcal{P}(\mathbf{x},\mathcal{M})$ over all states vectors.

Different Bayesian inference methods, such as The Markov Chain Monte Carlo (MCMC) and Nested Sampling (NS), use different approaches to sample parameter space of the model and estimate the posterior distributions and evidences.

Markov Chain Monte Carlo (MCMC)

The The Markov Chain Monte Carlo (MCMC) method was developed in the 1940s and 1950s and is one of the most widely used Bayesian inference methods in astronomy (Trotta, 2017).

Consider the expected value of the state vector $\mathbf{x}$ with probability distribution $f(\mathbf{x})$:

$$\mathbb{E}(\mathbf{x}) = \int \mathbf{x} f(\mathbf{x})\, d\mathbf{x} \tag{2.12}$$

By using the Monte Carlo integration technique, it is possible to approximate the unknown integral by producing a reasonable number of random vectors $\mathbf{x}_i$. In other words, Monte Carlo methods allow us to approximate the values of integrals against probability density functions with finite sums over N_{samp} samples:

$$\mathcal{J} = \int h(\mathbf{x}) f(h(\mathbf{x}))\, dh(\mathbf{x}) \longrightarrow \hat{\mathcal{J}} = \frac{1}{N_{samp}} \sum_{i}^{N_{samp}} h(\mathbf{x}_i) f(h(\mathbf{x}_i)) \quad \text{(for large } N_{samp}\text{)} \tag{2.13}$$

where $h(\mathbf{x}_i)$ is a sample drawn from f. In Bayesian inference, we can replace $f(h(\mathbf{x}))$ with the posterior distribution, $\mathcal{P}(\mathbf{x}|\mathbf{y},\mathcal{M})$, and make $h(\mathbf{x})$ a function of the unknown parameter. The resulting expected values is:

$$\mathbb{E}(h(\mathbf{x})|\mathbf{y}) = \int \mathcal{P}(\mathbf{y}|\mathbf{x},\mathcal{M}) h(\mathbf{x})\, d\mathbf{x} \approx \frac{1}{N_{samp}} \sum_{i=1}^{N_{samp}} h(\mathbf{x}) \tag{2.14}$$

and the sample variance is:

$$\mathrm{var}(\mathcal{J}) = \frac{1}{N_{samp}(N_{samp}-1)} \sum_{i=1}^{N_{samp}} (\mathbf{x}_i - \mathcal{J})^2 \tag{2.15}$$

One of the major challenges of the Monte Carlo integration method is efficiently generating the samples $\mathbf{x}_i$. This can be addressed using a *Markov chain*. Markov chains are stochastic processes where the probability distribution of the future state depends only on the current state and not past states (see e.g. Line et al. (2013); Trotta (2017)). This property is known as the *Markovian property* (Markov et al., 1954) and can be thought of as a property of "mild non-independence", as the chain exhibits only one-step dependence.

A sequence of random variable $X_0, X_1, ...$ that takes values in the likelihood space of 1,2,... is known as a *Markov chain* if, for all $n \geq 0$, the following condition holds:

$$\mathcal{P}(X_{n+1} = j | X_n = i, X_{n-1} = i_{n-1}, ..., X_0 = i_0) = \mathcal{P}(X_{n+1} = j | X_n = 1) \tag{2.16}$$

In this expression, $\mathcal{P}(X_{n+1} = j | X_n = 1)$ is referred to as the *transition probability* or *transition kernel* from state i to state j.

The MCMC method has been widely used for exoplanetary atmospheric retrievals and exoplanet detections (Madhusudhan et al., 2011; Benneke and Seager, 2012; Line et al., 2013; Hou et al., 2012; Blunt et al., 2019; Nowak et al., 2020). The method allows for efficient and extensive sampling of the posterior distribution and enables the specification of prior distributions of the parameters, where applicable. Despite its capabilities, the MCMC method has some limitations, particularly in complex parameter spaces. For example, the MCMC method is not optimised for calculating the evidence, which is computationally demanding. While this is acceptable for parameter estimation of a given model, it makes it challenging to conduct model comparisons when multiple models are plausible.

Nested Sampling

The Nested Sampling (NS) method has emerged as a powerful alternative to the MCMC method in Bayesian inference (Skilling, 2004, 2006; Feroz et al., 2009) and has been promptly adopted in exoplanetary atmospheric retrieval codes (e.g., Benneke and Seager, 2012; Line et al., 2015; Waldmann et al., 2015b; Lavie et al., 2017; MacDonald and Madhusudhan, 2017; Gandhi and Madhusudhan, 2018). Standard MCMC methods can lead to problems in efficient sampling from multi-modal pos-

terior distributions or those with large and curved degeneracies between parameters (Feroz et al., 2010, 2019). Convergence can also be problematic for MCMC. The NS algorithm and the MultiNest implementation (Feroz et al., 2009) aim to solve both problems. Indeed, MultiNest is optimised for highly degenerate and multi-modal posteriors and has found extensive applications in the astrophysical context (Skilling, 2004; Feroz et al., 2009, 2010, 2011a,b; Bridges et al., 2009; Graff et al., 2012; Karpenka et al., 2013).

Let us first remind that the evidence for a set of parameters $\mathbf{x}$ is:

$$\mathscr{E} = \int \mathcal{P}(\mathbf{y}|\mathbf{x}, \mathcal{M})\mathcal{P}(\mathbf{x}, \mathcal{M})\, d\mathbf{x} \tag{2.17}$$

where $\mathscr{E} = \mathcal{P}(\mathbf{y}|\mathcal{M})$. In NS, this multidimensional integral is transformed into a one-dimensional integral by exploiting the relation between the likelihood and prior volume. The prior volumes is defined by (Feroz and Hobson, 2008):

$$\mathscr{X}(\xi) = \int_{\mathcal{P}(\mathbf{y}|\mathbf{x},\mathcal{M})>\xi} \mathcal{P}(\mathbf{x}, \mathcal{M})\, d\mathbf{x} \tag{2.18}$$

where the integral extends over all regions for which the likelihood function is contained within the iso-likelihood contour $\mathcal{P}(\mathbf{y}|\mathbf{x}, \mathcal{M}) = \xi$. Assuming that the inverse of this equation is monotonically decreasing function of $\mathscr{X}$, the evidence, defined by the Equation 2.17, can be written as:

$$\mathcal{P}(\mathbf{y}|\mathcal{M}) = \int_0^1 \mathcal{P}(\mathscr{X})\, d\mathscr{X} = \mathscr{E} \tag{2.19}$$

The evidence can then be approximated numerically using standard quadrature methods. If the likelihood values $\mathcal{P}(\mathscr{X}_j)$ can be evaluated at a sequence of decreasing values $1 = X_0 > X_1 > X_2 > ... > X_M > 0$, we have:

$$\mathcal{P}(\mathbf{y}|\mathcal{M}) = \sum_{i=1}^{M} \mathcal{P}(\mathscr{X}_i) w_i \tag{2.20}$$

where the weights w_i are obtained using the simple trapezium rule:

$$w_i = \frac{1}{2}(X_{i-1} - X_{i+1}) \tag{2.21}$$

The summation in Equation 2.20 is performed by drawing N_{live} "live" random samples (live points) from the full prior $\mathcal{P}(\mathbf{x}, \mathcal{M})$, so that the initial prior volume $\mathscr{X}_0$ is unity (Feroz et al., 2009).

These samples are sorted in order of their likelihood values, and the sample with the smallest likelihood $\mathcal{P}(\mathscr{X}_0)$ is removed from the live set. This sample corresponds to the case with the worst fit to the data, and it is replaced by a point drawn from the prior distributions, provided that its likelihood is larger than $\mathcal{P}(\mathscr{X}_0)$. The new prior volume contained within this iso-likelihood contour is a random variable given by $X_1 = t_1 X_0$, where t_1 has a distribution $\mathcal{P}(t) = N_{live} t^{N_{live}-1}$. This is the probability distribution for the largest of N_{live} samples drawn uniformly from the interval [0,1], and it represents the shrinkage in prior volume between consecutive likelihood contours. The process is repeated as the contours sweep through the parameter space, and as the prior volume reduces in size, the algorithm travels through "nested shells" of iso-likelihood contours, identifying the regions of highest likelihood. The algorithm then stops when the product of the remaining prior volume and maximum-likelihood value does not change by more than a specified tolerance. Once the evidence is determined, the posterior distributions are computed using the full set of discarded points (i.e., the points with the lowest-likelihood value at each iteration i). Each of these points is assigned a weight:

$$w_{\text{discarded},i} = \frac{\mathcal{P}(\mathbf{y}|\mathbf{x}, \mathcal{M}) w_i}{\mathcal{P}(\mathbf{y}|\mathcal{M})} \tag{2.22}$$

These samples can be used to infer the mean, standard deviations, covariances etc., of the retrieved parameters or to compute marginalised posterior distributions. Also, from posterior distribution can be obtained the maximum-a-posteriori (MAP) estimate, as the mode of the posterior distribution.

The NS method has several advantages over other Bayesian inference methods. One of the main advantages of the NS method is that it is designed to be highly efficient for computing the Bayesian evidence for a given model, making it particularly desirable when comparing multiple models. By efficiently exploring the model parameter space to compute the Bayesian evidence with high accuracy, the NS method also naturally allows for high-density sampling of the posterior distribution. This makes the NS method especially suited for handling complex model parameter space with multimodal and non-Gaussian posterior distributions. Furthermore, the optimisation algorithm is naturally parallelised, thereby significantly reducing computation time.

Model selection

The Bayesian evidence allows us to select the best model, which is the one that strikes the best balance between quality of fit and model complexity. By apply-

ing the principle of Occam's razor, we should avoid added complexity in a model whenever a simpler model gives an adequate fit to the observations. In the Bayesian framework, a more complicated model will have higher evidence only if it fits the data significantly better than a simpler theory (Trotta, 2007).

To compare two models, $\mathcal{M}_0$ and $\mathcal{M}_1$, we can define the ratio of the models' probabilities, or *Bayes factor*:

$$\mathcal{B}_{21} = \frac{\mathcal{P}(\mathcal{M}_2|\mathbf{y})}{\mathcal{P}(\mathcal{M}_1|\mathbf{y})} = \frac{\mathcal{P}(\mathcal{M}_2)}{\mathcal{P}(\mathcal{M}_1)} \frac{\mathcal{P}(\mathbf{y}|\mathcal{M}_2)}{\mathcal{P}(\mathbf{y}|\mathcal{M}_1)} = \frac{\mathcal{P}(\mathcal{M}_2)}{\mathcal{P}(\mathcal{M}_1)} \frac{\mathscr{E}_2}{\mathscr{E}_1} \tag{2.23}$$

Assuming the model priors are identical ($\mathcal{P}(\mathcal{M}_2) = \mathcal{P}(\mathcal{M}_1)$), we can simplify Equation 2.23 to:

$$\mathcal{B}_{21} = \frac{\mathscr{E}_2}{\mathscr{E}_1} = \frac{\mathcal{P}(\mathbf{y}|\mathcal{M}_2)}{\mathcal{P}(\mathbf{y}|\mathcal{M}_1)} \tag{2.24}$$

This is the ratio of the models' evidence, and a value of $\mathcal{B}$ greater (less) than unity represents an increase (decrease) in support in favour of model 2 over model 1. Using Jeffrey's scale (Jeffreys, 1998), an empirically calibrated scale shown in Table 2.3, it is possible to qualitatively determine whether a more complex model is strongly favoured, weakly favoured, or inconclusive. Such scale will be used in the following chapter.

Table 2.3: *Jeffreys'scale and translation to frequentist significance values in favour of a more complex model. Adapted from Trotta (2008).*

$\lvert\ln \mathcal{B}_{21}\rvert$	Probability	"sigma"	Interpretation
< 1.0	< 0.750	$< 2\sigma$	Inconclusive
1.0	0.750	2.1σ	Weak evidence
2.5	0.923	2.7σ	Moderate evidence
5.0	0.993	3.6σ	Strong evidence

For example, in the context of atmospheric retrievals, model selection can be used to estimate the detection significance of detecting a specific molecular constituent in a Bayesian framework. The Bayes factor between two models, including (or excluding) a range of molecules, can be used to assess the preference for adding, or removing, a given molecule.

2.4 Atmospherical characterisation through transmission spectroscopy

The spectrum of an exoplanet can be obtained using different techniques (see Figure 2.5). The primary transit allows us to obtain transmission spectra that probes the

terminator region of the exo-atmosphere, which is the atmospheric region between the irradiated and the dark side of the exoplanet. As the orbit continues, we can monitor the received flux for different planetary orbital phases to characterise the illuminated hemisphere gradually. Before and after the secondary eclipse we can compare the flux received from the star with and without the exoplanet contribution to obtain the emission spectrum from the dayside of the latter. Additionally, some systems allow for a direct imaging of the exoplanets, providing an isolated measurement of the exoplanetary atmosphere.

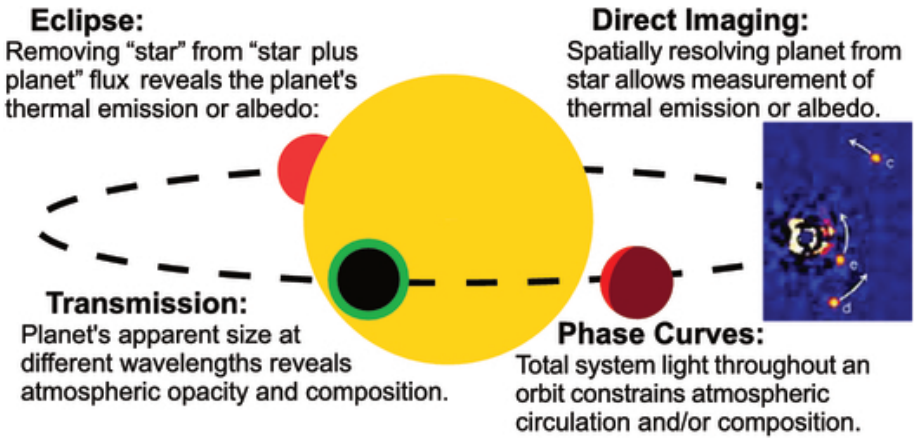

Figure 2.5: *Observational approaches used to characterise the atmospheres of extrasolar planets. Credit: Crossfield et al. (2015).*

Understanding a planet atmosphere is not only crucial for comprehending the planet itself, but also for gaining insight into its formation, structure, evolution, and potential for sustaining life.

Over the past few decades, multiple techniques have been developed to study the atmospheres of planets within our solar system, using both high- and low-resolution spectroscopic measurements obtained from telescopes and spacecraft and in situ measurements (e.g., Irwin et al., 2008).

However, analysing the atmospheres of exoplanets presents unique challenges when compared to those within our solar system, because exoplanets can be obtained only remotely and are inherently disk-averaged over the spatially unresolved planet. Furthermore, exoplanetary spectra are very faint, resulting in lower signal-to-noise ratio (SNR). In some cases, the planet-star contrast is comparable to the noise level, which strongly limits our sensitivity. Finally, the parameter space of exoplanetary atmospheres is much wider than that of solar system planets. For example, the equilibrium temperatures of most solar system planets lie below 300 K, while those of exoplanets extend until $\sim$ 3000 K. Similarly, all other atmospheric parameters have a wide range, implying an enormous complexity and diversity in

exoplanetary atmospheres that go beyond what we have experienced in the solar system.

From the spectrum of an exoplanet, obtained for example from transmission spectroscopy, we can extract information about the chemical compositions, temperature profiles, clouds/hazes, and energy circulation. These properties, in turn, can provide key insights into the atmospheric physical and chemical processes of exoplanets, as well as their formation mechanisms.

This is where "atmospheric retrieval" comes in. Atmospheric retrieval techniques are nowadays commonly used to interpret the observed data, and with the new data provided by JWST and future dedicated missions, such as Ariel, this approach will be even more fundamental to characterise exoplanets atmospheres.

In the following sections, I will discuss the use of retrieval methods to interpret transmission spectroscopy. In particular, I will present TauREx (Al-Refaie et al., 2021), a novel inverse retrieval code for exoplanetary atmospheres.

2.4.1 Transmission spectroscopy

As the exoplanet transits between its parent star and the observer, some of the light from the host star passes through the exoplanet atmosphere and is both scattered and absorbed by the molecules contained within. A differential spectroscopy approach is used to obtain the transmission spectrum that encodes the absorption from the exoplanet and the composition of the upper layer of the terminator. Essentially, the exoplanetary spectrum is derived by subtracting the *out-transit* spectrum from the *in-transit* spectrum, and then normalising it by the *out-transit* spectrum. The resulting observed transmission spectrum therefore carries with it the signatures of that planet atmospheric contents. The transit geometry enables us to investigate a small yet crucial fraction of the exoplanetary atmosphere, specifically the annulus that corresponds to the *terminator* region, that lies between the day and night side of the exoplanet.

The stellar wavelength-dependent intensity I_λ, crossing the medium will be altered by its interaction with matter. The intensity I_λ is defined as the amount of radiant energy dE_λ per time interval dt and wavelength interval $d\lambda$, crossing an element of area dA, in the direction of a differential solid angle $d\Omega$, at an angle θ to the normal of dA. This is expressed as:

$$I_\lambda = \frac{dE_\lambda}{\cos\theta \, d\Omega \, d\lambda \, dt \, dA} \tag{2.25}$$

The general form of the radiative transfer equation Chandrasekhar (1950) de-

scribes the amount of change in radiation dI_λ along a small distance dl

$$dI_\lambda = -I_\lambda \sigma_\lambda \rho_N dl + j_\lambda \rho_N dl \tag{2.26}$$

where I_λ is the intensity of the radiation, ρ_N is the number density of the medium, and σ_λ is the absorption or extinction cross-section for radiation of wavelength λ, j_λ is the emission coefficient. The first part of the right-hand side term is the reduction in radiation intensity through the gas, and the second part is the strengthening of the signal due to contributing emission sources within the gas.

The radiative transfer equation can be written as:

$$\frac{dI_\lambda}{\sigma_\lambda \rho_N dl} = -I_\lambda + J_\lambda \tag{2.27}$$

Where the source function, J_λ, is defined as the ratio of emission and absorption in the gas:

$$J_\lambda = \frac{j_\lambda}{\sigma_\lambda} \tag{2.28}$$

Considering only the extinction properties of a gas, the wavelength-dependent radiation change through a medium can be expressed as:

$$\frac{dI_\lambda}{\sigma_\lambda \rho_N dl} = -I_\lambda \tag{2.29}$$

This relation expressed the attenuation of the stellar radiation traversing the planet due to the interaction with the atmospheric matter during transit.

The solution to this equation for the intensity at a distance l is:

$$I_\lambda(l_1) = I_\lambda(l_0)\, exp\Big(- \int_{l_0}^{l_1} \sigma_\lambda \rho_N dl \Big) \tag{2.30}$$

We can define the wavelength dependant global optical depth τ_λ, at a given wavelength λ as:

$$\tau_\lambda = \int_{l_0}^{l_1} \sigma_\lambda \rho_N \, dl \tag{2.31}$$

If we consider a given altitude z above $\mathrm{R}_p = z(p_0)$ in the atmosphere of the planet, the simple expression of the Beer-Bouguet-Lambert law is derived:

$$I_\lambda(\tau_\lambda(z)) = I_\lambda(\tau_\lambda(0)) e^{-\tau_\lambda(z)} \tag{2.32}$$

The optical depth at the altitude z along a certain path can be described as:

$$\tau_\lambda(z) = \sum_{i=1}^{N_{gas}} \left(\int_0^{l(z)} \sigma_{i,\lambda}(z')\chi_i(z')\rho_N(z')\, dl \right) \tag{2.33}$$

where N_{gas} is the total number of molecules in the atmosphere, χ_i is the mixing ratio of molecule i, $\sigma_{i,\lambda}$ is the absorption cross section of molecule i at wavelength λ, and ρ_N is the number density in m^{-3}.

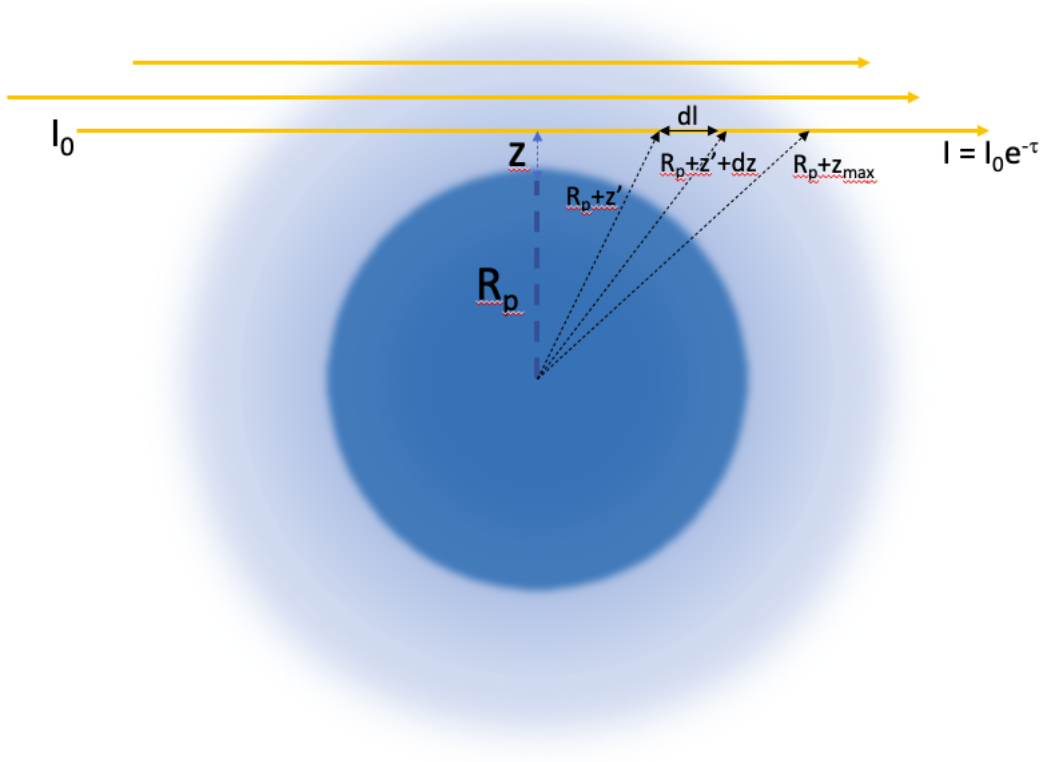

Figure 2.6: *Illustration of the paths of the stellar photons filtered through the planetary atmosphere during a primary transit observation. Adapted from Tinetti et al. (2012).*

The path followed by the stellar photons can be easily calculated using the geometry shown in Figure 2.6, where:

$$dl = 2\left(\sqrt{(R_p + z' + dz')^2 - (R_p + z)^2} - \sqrt{(R_p + z')^2 - (R_p + z)^2} \right) \tag{2.34}$$

with R_p, z, z' and dz defined in Figure 2.6. This leads to:

$$l(z) = \int dl = \sqrt{(R_p + z_{max})^2 - (R_p + z)^2} \tag{2.35}$$

Finally, Equation 2.33 can be converted to an equivalent area, $A(\lambda)$, by integrat-

ing along all viewing paths:

$$A(\lambda) = 2 \int_0^{z_{max}} (R_p + z)\left(1 - e^{-\tau(\lambda,z)}\right) dz \tag{2.36}$$

When the equivalent area $A(\lambda)$ is computed, the total transit depth as a function of wavelength can be expressed as:

$$\mathrm{k}(\lambda) = \frac{R_p^2 + A(\lambda)}{R_*^2} \tag{2.37}$$

where R_p and R_* represent the planet and star radius, respectively (Tinetti et al., 2012).

2.4.2 Spectral retrieval of exoplanetary atmosphere

Atmospheric retrieval techniques for exoplanets have been developed to address the "degeneracy problem". Initial molecular detections were based on few channels of infrared photometry and low-resolution spectrophotometry with low SNR (e.g., Barman, 2007; Tinetti et al., 2007; Grillmair et al., 2008; Swain et al., 2008). Temperature inversions in hot Jupiters were initially identified through broadband photometric observations (e.g., Knutson et al., 2008, 2009; Burrows et al., 2007, 2008). These deductions were made using a limited set of forward models that assumed temperature profiles and molecules that qualitatively matched the data. To overcome these limitations and provide a more robust framework for deriving atmospheric properties of exoplanets, the concept of atmospheric retrieval was introduced (Madhusudhan and Seager, 2009).

Retrieval is synonymous with fitting an atmospheric model to an observed spectrum and estimating the model parameters along with uncertainties.

Figure 2.7 shows a schematic representation of atmospheric retrieval for exoplanets. The retrieval process comprises two separate frameworks: the *forward model framework* responsible for constructing the forward model, and the *retrieval framework* responsible for fitting the forward model to observations. The forward model acts as a bridge between these two frameworks.

The atmospheric spectrum is mainly determined by the pressure-temperature (P-T) profile and the chemical composition of the atmosphere. These are calculated under equilibrium conditions in such models, with the possibility of including clouds.

An atmospheric retrieval code has two main components:

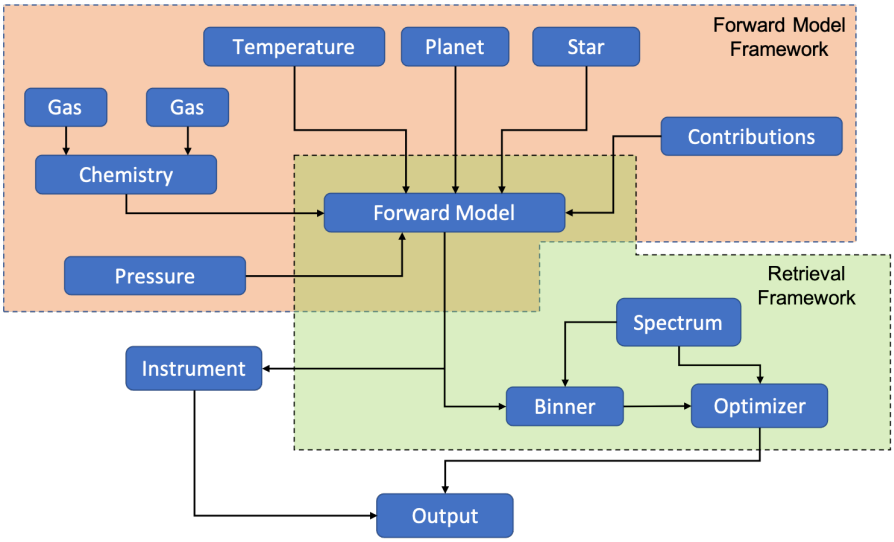

Figure 2.7: *The overall structure of atmospheric retrieval. Highlighted is the two framework structure of the complete framework: the forward model framework responsible of the construction of the forward model and the retrieval framework responsible for the fit of forward model against an observation (spectrum). Figure adapted from Al-Refaie et al. (2021).*

- a parametric model to compute the atmospheric spectrum for given atmospheric parameters;
- an optimisation algorithm, which is a statistical inference method that explores the model parameter space in search of models that fit the data. In the process, it creates posterior probability distributions of all the model parameters.

The parameters for forward models used in retrievals correspond to three broad properties: chemical composition, P-T profile and clouds/hazes. The chemical composition of the atmosphere is represented by the volume mixing ratio of the species, such as the number density of each species relative to the total number density. Typically, for H_2-rich species, the prominent absorbers such as H_2O, CO, CH_4, CO_2, Na, K, etc. are included. The mixing ratios are usually assumed to be uniform in the region of the atmosphere probed by the observations. The model may also account for opacity due to the presence of clouds or hazes in the atmosphere (Benneke and Seager, 2012; Kreidberg et al., 2014; Barstow et al., 2017; MacDonald and Madhusudhan, 2017; Line et al., 2015).

In the following, I will introduce TauREx (Waldmann et al., 2015b,a), a retrieval code used to analyse exoplanetary transmission and emission spectra. It has been widely applied in the study of exoplanetary atmospheres, as evidenced by several applications (e.g., Tsiaras et al., 2019; Rocchetto and Waldmann, 2015; Drossart et al., 2022; Zhou et al., 2022; Bocchieri et al., 2022).

2.4.3 TauREx: A retrieval code for exoplanetary atmospheres

Tau Retrieval for Exoplanets (TauREx) is a radiative transfer fully Bayesian retrieval framework commonly used to model and analyse exoplanetary atmosphere spectra (Waldmann et al., 2015b,a). The code has undergone several optimisations and improvements, culminating in a major release (Al-Refaie et al., 2021). It can be used to simulate different atmospheric configurations with various star-planet systems and perform retrievals using highly accurate line lists from the ExoMol (Tennyson et al., 2016), HITEMP (Rothman and Gordon, 2014) and HITRAN (Gordon et al., 2016) database to build forward and retrieval models.

A schematic view of input parameters and their dependencies within the forward model is shown in Figure 2.8.

Figure 2.9 presents an example of a high-resolution spectrum (in blue) and a low-resolution spectrum (in orange). The low-resolution spectrum is obtained by convolving the high-resolution spectrum with an instrumental model, simulating how it would appear when observed by Ariel.

The one-dimensional radiative transfer models included in TauREx assume a plane-parallel atmosphere and consider molecular absorption, Rayleigh scattering, collision-induced absorption, and flat opacity clouds.

To determine the altitude profile z at each layer l, TauREx employs the following equations:

$$z_l = z_{l-1} + \Delta z_l \tag{2.38}$$

$$\Delta z_l = -H_{l-1} \log\left(\frac{P_l}{P_{l-1}}\right) \tag{2.39}$$

$$H_l = \frac{k_B T_l}{\mu_l g_l} \tag{2.40}$$

$$z_0 = 0 \tag{2.41}$$

Here, P_l, T_l, μ_l, g_l and H_l are the pressure, temperature, mean molecular weight, acceleration due to gravity, and scale-height at layer l, respectively. Δz_l denote the change in altitude from layer $l-1$ to l, and $l = 0$ represents the bottom of the atmosphere, where TauREx defines the planetary radius (Al-Refaie et al., 2021).

By assuming hydrostatic equilibrium and applying the ideal gas law, the number density at each atmospheric level l can be computed as:

$$\rho_{N,l} = \frac{P_l}{k_B T_l} \tag{2.42}$$

where k_B is the Boltzmann constant.

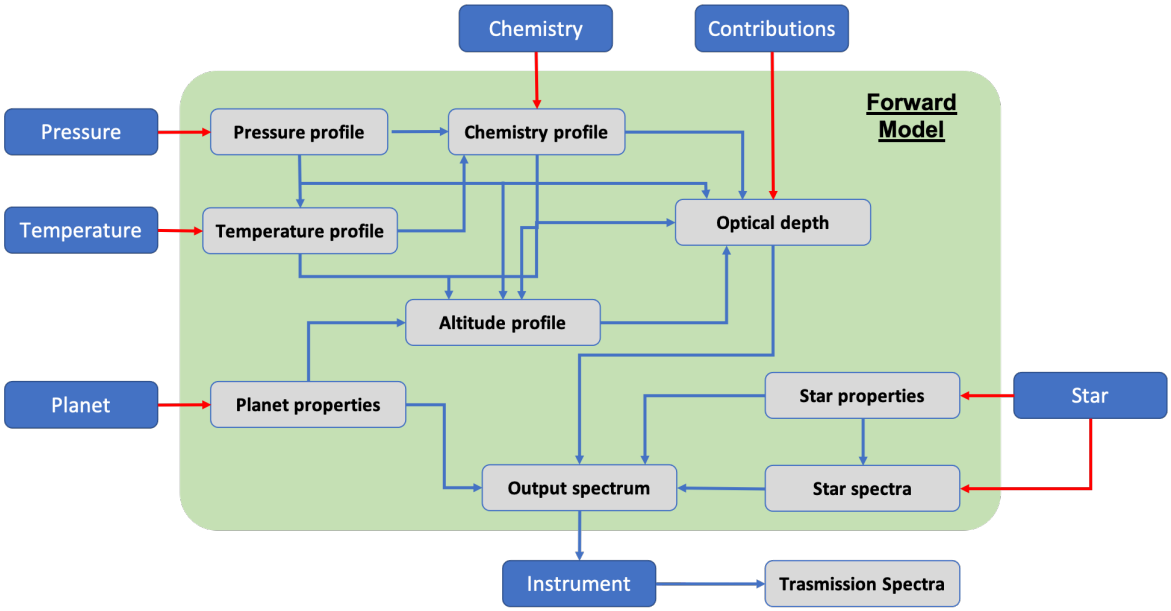

Figure 2.8: *A flow graph describing the input parameters and their dependencies within the forward model. The large blue boxes describe the class of TauREx in which we have to set the parameters and the red arrows describe the property they provide to the forward model. The grey boxes describe atmospheric properties produced within the forward model. Figure adapted from Al-Refaie et al. (2021).*

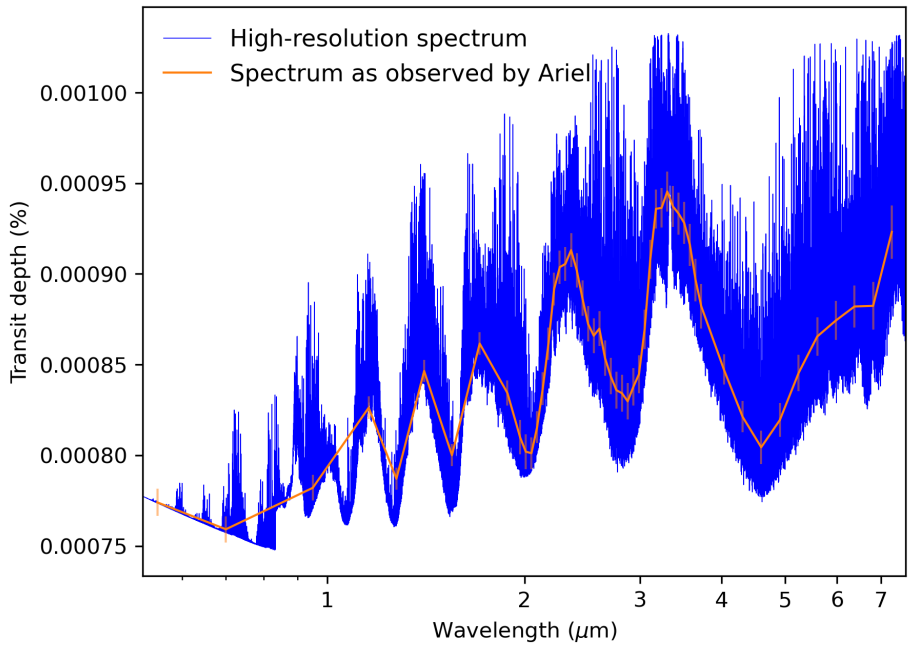

Figure 2.9: *Example of a high-resolution spectrum obtained with TauREx forward mode (in blue) and a low-resolution spectrum obtained convolving the high-resolution spectrum through an instrumental model in order to obtain a spectrum as observed by Ariel (in orange). The errorbars were obtained simulating the noise with ArielRad taking into account the number of transit required for the Tier-2.*

The scale height at each atmospheric level l is determined by Equation 2.40, while the mean molecular weight is calculated as:

$$\mu_l = \sum_{n}^{N_{gas}} \chi_{n,l} m_{mol,n} \tag{2.43}$$

where N_{gas} is the number of molecular species in the atmosphere, while $\chi_{n,l}$, and $m_{mol,n}$ are the mixing ratio at layer l and the molecular weight of species n, respectively.

Furthermore, the gravity is given by:

$$g_l = \frac{GM_p}{(R_p + z_l)^2} \tag{2.44}$$

where z_l is the altitude at the l-th layer, R_p and M_p are the radius and the mass of the planet, and G is the gravitational constant.

In order to calculate the altitude at each pressure level (see Equations 2.38 and 2.39), it is necessary to compute the scale height (Equation 2.40), which requires the computation of the gravity (Equation2.44), which, in turn, requires the computation of the altitude. This can only be achieved with an iterative process. In TauREx, the gravity and scale height of the zeroth layer are firstly computed. Then, the change in altitude of the next layer is simply given by Equation 2.39. Using the value of Δz for the zero-th layer, the gravity and scale height at the top of the zero-th layer (and, equivalently, bottom of the first layer) can be computed. This computation is then repeated iteratively until the top of the atmosphere is reached.

Rayleigh scattering and collision-induced absorption for H_2-H_2 and H_2-He pairs are also taken into account by simply including these two sources of opacity in the computation of the optical depth for each path length using pre-computed cross sections and relative abundances of each species. Collision induced absorption cross sections are taken from HITRAN (Richard et al., 2012; Gordon et al., 2016) as well as from Borysow et al. (2001) and Borysow (2002).

As shown in the equation above, the scale height can be expressed as:

$$H_l = \frac{k_B T_l (R_p + z)^2}{\mu M_p G} \tag{2.45}$$

and can be used to predict the degeneracies expected in retrieval simulations. Changeat et al. (2020) discussed that in the case of a cloudy atmosphere, degeneracies may exist as R_p cannot be accurately detected below the cloud deck. Additionally, for the secondary atmosphere, a wider range of main atmospheric components may exist,

and therefore μ is degenerate with M_p. In Chapter 3 I investigated the relevance of planetary mass knowledge in spectral retrievals, identifying the cases in which mass measurements are required for clear or cloudy, primary or secondary atmospheres, as well as the required precision, in the context of the ESA M4 Ariel Mission.

2.5 Challenges for the detection and characterisation of exoplanets

In the previous sections, the importance of characterising both exoplanets and their host stars in terms of their masses and radii has been emphasised. For instance, accurate estimates of planetary mass and radius through radial velocity and transit techniques rely on precise measurements of the stellar mass and radius. However, limitations in the detection and characterisation of an exoplanet can arise from various sources, which depend on the specific planet, star, and instrument used. For instance, some stellar systems may mimic planetary transits, creating false alarms in the search for transiting exoplanets. Also, non-white noise components due to atmospheric effects, such as telluric or moon contamination, can limit ground-based observations, while instrumental effects, such as hot pixels caused by cosmic rays or telescope jitter due to thermal shocks, can affect space- or ground-based observations.

Additionally, precise and accurate characterisation of exoplanets cannot be dissociated from the characterisation of their host stars. For example, the transit measurements only provide us with the planet-to-star radius ratio, while the mass provided by radial velocity measurements is dependent on the stellar mass. The derivation of these important planetary parameters, which are fundamental for testing theoretical predictions of planetary structure, are strongly connected to the effective temperature (T_{eff}), surface gravity (log g), and the metallicity of the star.

2.5.1 Influence of host stars parameter estimates on the exoplanets characterisation

The characterisation of planets, including their mass, radius, density and age, depends on the characterisation of their host star. The accuracy and the precision of the planet properties fundamentally rely on the achieved accuracy and precision of the host star properties. Unfortunately, direct measurements of the physical properties of stars are rare and only feasible for specific targets. The physical properties of host stars are typically derived by using theoretical stellar evolutionary models.

Therefore, the final accuracy and precision of stars and their planets strongly depend on the uncertainties in the stellar model parameters. However, in exceptional cases, planetary properties can be derived without using stellar models.

Precise dynamical masses can be obtained for double-lined and single-lined eclipsing binaries, as well as for non-eclipsing double-lined spectroscopic binaries if astrometric orbits of the star are known (Torres et al., 2010). The spectroscopic surface gravity and luminosity of the star, given the effective temperature is known, can also be used to estimate the stellar mass with good precision (Sousa et al., 2011), as well as mass-luminosity relations with a precision below 10% (Xia and Fu, 2010). Finally, stellar masses can be determined by comparing the observed stellar properties with stellar evolutionary tracks (e.g., Johnson et al., 2010; Sousa et al., 2015).

Concerning the stellar radius, interferometry is one of the most accurate methods for determining the radii of stars by measuring their angular size. This technique provides direct radius measurements with a precision of 1-3% on the angular diameter (Boyajian et al., 2013). Lunar occultations can also be used to determine the angular size and linear radii of stars, albeit it is limited to specific cases, providing radii with a precision down to 3% (Richichi, 1997). Furthermore, the stellar radii can be obtained from stellar evolution models by using the luminosity and the effective temperature of the stars (e.g., Torres et al., 2006), or for transiting systems, from the stellar density derived directly from the light curve and the T_{eff} (e.g., Sozzetti et al., 2007). In addition, asteroseismic quantities combined with T_{eff} and stellar metallicity can be used to derive the radii of exoplanet hosts, providing stellar radii with a precision of 2-4% (e.g., Chaplin et al., 2014).

Direct measurement of stellar ages is not possible, and therefore, the use of stellar models is typically required to estimate ages. The most common methods used for this purpose are isochrone placement and asteroseismology (e.g., Takeda et al., 2007; Campante et al., 2015), with precision levels of around 20-30% for isochrone placement and 10-20% for asteroseismology. However, both methods rely on knowledge of the atmospheric parameters of the star. Alternatively, empirical relations calibrated between age and rotation period (e.g., Barnes, 2007), age and chromospheric activity (e.g., Mamajek and Hillenbrand, 2008), or age and chemical abundance ratios (e.g., Nissen, 2015) can be used to derive stellar ages.

Accurate and precise determination of stellar atmospheric parameters, including effective temperature (T_{eff}), surface gravity (log g), and metallicity/chemical abundances, is crucial for fully characterising exoplanet host stars. The most commonly used and accurate techniques for deriving these parameters rely on stellar

spectroscopy, with main spectral analysis techniques such as the Equivalent width (EW) method and the spectral synthesis method. In addition, precise determination of individual heavy element abundances and specific elemental ratios in stars with planets is also important, as they are expected to influence the structure and composition of terrestrial planets (e.g., Grasset et al., 2009; Dorn et al., 2015).

2.5.2 Stellar activity

Stellar variability is one of the sources of correlated noise that can strongly contaminate the planet signal in the stellar light curve and radial velocity time-series. The main cause of stellar variations is stellar magnetic activity.

Stars that have a convective envelope are capable of generating and amplifying magnetic fields. The stellar magnetic field is believed to be produced and maintained by a dynamo that arises from the coupling between differential rotation and convection in the inner layers of stars. These magnetic fields, produced within the stars, also emerge outside of them (Wright and Drake, 2016).

Therefore, stars exhibit magnetic activity resulting from the interaction between their own stellar magnetic field and the plasma present in the photosphere, chromosphere, and corona, giving rise to a class of phenomena such as stellar flares, spots, faculae, and prominences, observed in a wide range of stars.

Magnetic activity is a characteristic of late-type stars, such as those with a mass similar to or less than that of the Sun, including M stars, which have a convective envelope. Substellar objects, such as brown dwarfs, also show signs of magnetic activity, although weaker than solar-type stars or M stars, showing a strong dependence on the mass and age of the star (e.g., Stelzer et al., 2006). The most significant magnetic activity is observed in young main-sequence stars (e.g., Pizzolato et al., 2003; Järvinen et al., 2007; Brown et al., 2022).

The evidence of stellar magnetic activity phenomena is mostly indirect and manifests itself through the presence of typical spectral characteristics and variability. From an observational standpoint, stellar magnetic activity appears as an excess of emission compared to stellar photospheric radiation with contributions throughout the electromagnetic spectrum, from radio to X-ray regimes. These emissions are associated with plasma heated through magnetic processes at temperatures ranging from 10^4 K in the chromosphere to over 10^6 K in the corona (Güdel, 2004). In the optical band, different behaviours are seen in spectral lines due, for example, to the presence of spots.

Only in the Sun, thanks to its spatial resolution, is it possible to understand the complex inhomogeneity that characterises magnetic activity. Phenomena of mag-

netic activity are connected and determined by the surface magnetic fields located in sunspots, active regions, faculae, flares, and coronal loop structures (Houdebine et al., 2009).

These phenomena produce photometric and spectroscopic stellar variability on time scales ranging from a few tens of seconds, in the case of flares, to days to weeks (stellar rotations), and from months to years (stellar activity cycles). The amplitudes of these variations are maybe comparable to or larger than the amplitude of planetary signals.

Stellar activity depends on stellar type/mass, and rotation that evolves with age. The dependence on stellar age comes from the stellar rotation rate driving the differential rotation between the stellar core and the convective envelope, which is the magnetic field production mechanism for main sequence stars. Stars rotating faster display a higher activity level. Young stars have larger rotation rates (i.e., are more active) as they have gained angular momentum through contraction under gravity. The slight dependence on mass also comes from star ability to form a radiative core, as radiative pressure will halt the stellar contraction. The stars then stop gaining angular momentum, and the dissipation of its angular momentum through magnetic breaking will force the star to spin down, thus reducing the activity level for older stars (see Favata and Micela (2003); Schrijver and Zwaan (2000)).

The photometric and radial velocity amplitude of stellar variability can easily be larger than the amplitude of the signal of a planet, affecting the detection of the latter by creating false alarms and impacting the amplitude of the real signal, especially for small planets. Stellar variability also hinders the characterisation of the detected planets as it adds correlated noise to the planet signal, reducing the precision and altering the accuracy of the derived planet parameters.

For example, as a star rotates, a stellar spot on its surface can hide a part of the stellar surface rotating towards us, and then a part rotating away from us, creating red-shifted and blue-shifted perturbations respectively. This can mimic the presence of a planet, altering the radial velocity time-series. The stellar activity component due to spots and plages is difficult to remove, as their amplitude in radial velocity can be larger than that of the planet signal. Techniques to identify radial velocity variations due to stellar activity at long times scales include photometric observations of the star simultaneous with the radial velocity measurements, the analysis of the correlation between the radial velocity variations and the variations in the bisector of the cross-correlation peak of the stellar spectra, or with the variations in Ca II H&K lines, Hα line and He I line. In this thesis, I will deal with spot influence on radial velocity determination in Chapter 5, and I will study the principal activity

indicators in Chapter 6.

Activity indicators

Some lines, including some in the optical band, are indicators of chromospheric activity and represent a fundamental diagnostic of the structure and variability of this region. These lines have sufficiently high absorption coefficients, so that a significant portion of the line originates in the outer layers of the atmosphere, particularly in the chromosphere. Therefore, the study of these lines allows us to monitor the amount of material present in the chromosphere, its physical conditions, and how it is affected by magnetic activity.

The Ca II H (λ = 3968 Å) and K (λ = 3933 Å) lines, and the Mg II h (λ = 2803 Å) and k (λ = 2796 Å) lines are the indicators of chromospheric brightness and activity traditionally studied in cool stars. Other indicators of chromospheric gas are represented by hydrogen lines, in particular the Hα line at 6563 Å, the Ca II triplet (λ = 8498 Å, λ = 8542 Å, λ = 8662 Å) in the infrared, and the He I lines (λ = 5876 Å and λ = 10830 Å) (Schöfer et al., 2019).

In the solar chromosphere, the most intense lines are represented by Ca II, while Balmer emission in M stars is much greater than the other chromospheric lines (Linsky et al., 1982; West et al., 2004). Together with the low emissivity of M stars in the blue, this makes the Hα line the main chromospheric activity indicator in stars of this spectral type. Some M stars also have an intense Ca II line, in particular, the Ca II K line. Particularly active M stars have the Hα line in emission.

Hα and Ca II *K correlation*

The Hα and Ca II K lines are two of the most intense emission lines in the optical band in the spectra of active M stars (Sundland et al., 1988; Mauas and Falchi, 1994).

Within the M spectral class, there is a high variability in the emission intensity of the Ca II K line and a wide variety of spectra in which the Hα line may appear in absorption or emission (Walkowicz and Hawley, 2009). The Hα line, particularly the core of the line, is an indicator of the hottest regions of the chromosphere ($\approx$ 7000 K), while the emission component of the Ca II K line is formed in the cooler regions, between the minimum temperature and 6000 K (Giampapa et al., 1982; Walkowicz and Hawley, 2009). Together, the Hα and Ca II K lines offer complementary information about the chromospheric structure (Walkowicz and Hawley, 2009).

The topic of an ongoing discussion is the "zero point" of chromospheric activity, which allows us to define a criterion for identifying chromospheres with minimal magnetic activity. Young et al. (1984) argue that the zero point of chromospheric activity is defined by an intense Hα absorption line. In contrast, Stauffer and Hartmann (1986) claim that the evolution of the line as a function of chromospheric activity can go from an absorption line that becomes increasingly intense and only begins to fill gradually with emission at higher levels of activity. In this scenario, stars that do not have a chromospheric contribution, in which there are no intense absorption lines, and stars with moderate magnetic activity, in which the line is partially filled but still in absorption, both present a weak Hα absorption line. Therefore, without the use of additional indicators of chromospheric activity, such as Ca II K, it is difficult to distinguish between stars with intermediate activity and inactive stars.

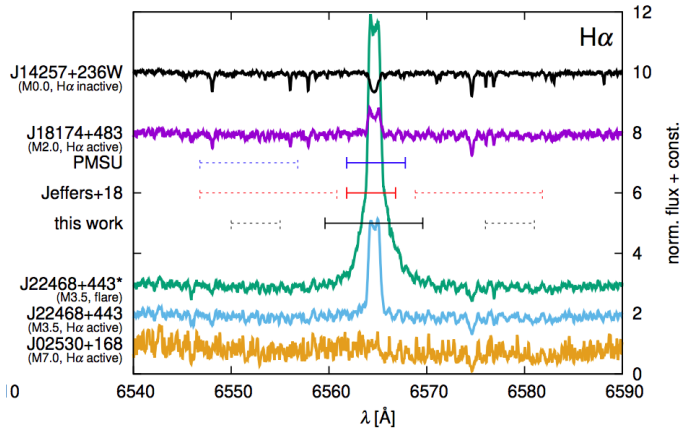

Figure 2.10: *Selection of spectra around the Hα line: an inactive M0.0 star (J14257+236W, in black), a moderately active M2.0 star (J18174+483, in purple), an active M3.5 star (J22468+443) during a flare (in green), in quiescent state (in light blue), a moderately active M7.0 star (J02530+168, in orange). Adapted from Schöfer et al. (2019)*

Figure 2.10 shows the diversity of the Hα line in M stars with different activity levels. In inactive stars (black spectrum), the line appears in absorption, while it becomes an emission line for moderately active stars (purple spectrum). Furthermore, it is evident how the intensity of the line also varies with the level of activity of the same star, showing greater intensity during a flare (green spectrum) compared to its quiescent state (light blue spectrum).

Several previous studies have investigated the correlation between the Hα and Ca II K lines in various M stars (Robinson et al., 1990; Rauscher and Marcy, 2006; Cincunegui et al., 2007). However, both Robinson et al. (1990) and Cincunegui et al. (2007) argue that time-resolved observations of the Hα and Ca II K lines are not always positively correlated, and that the correlation is due to the spectral type

of the sampled stars rather than the properties of their chromospheres (Walkowicz and Hawley, 2009).

Additionally, previous studies have analysed this correlation using observations obtained at different epochs of a particular star. However, in active M stars, both Ca II K and Hα vary on timescales ranging from minutes to decades. Therefore, comparing line measurements obtained from non-simultaneous observations can lead to inaccurate results. For these reasons, the relationship between these important activity indicators is still uncertain.

Walkowicz and Hawley (2009) conducted a study using simultaneous observations to verify whether the observed correlation between these activity indicators is due to a continuum effect, i.e., related to the different T_{eff}, or if there is actually a relationship between these lines in particularly active chromospheres. This study showed that for stars with weak or intermediate activity, there is a range of variability in the equivalent width of the Ca II K emission line corresponding to less variability in the Hα absorption line. It is also observed that the Hα line may appear in absorption in stars with low activity, and it increases along with the Ca II K line with increasing stellar activity. The Hα line, therefore, fills up until it becomes in emission in more active stars, as observed by Stauffer and Hartmann (1986).

The positive correlation between Ca II K and Balmer emission in individual observations of active stars does not necessarily imply that these chromospheric indicators are always positively correlated over time for every star. In the scenario proposed by Walkowicz and Hawley (2009), increased chromospheric emission would correspond to a greater presence of active regions on the stellar surface due to a stronger influence of the magnetic field. If Ca II K and Hα are produced by cool and hot components, respectively, one would expect that greater chromospheric heating would result in increased emission in both lines, with a greater contribution from the hotter component. The relationship between the two lines will become more decoupled as the hotter active component becomes more prominent (Walkowicz and Hawley, 2009).

In a study by Scandariato et al. (2017), the correlation between the total flux of Ca II H&K lines and the flux of the Hα line was analysed for a sample of 41 stars with varying metallicity and temperature.

In the left panel of Figure 2.11, the emission flux of the Hα line, $F_{H\alpha}$, is shown as a function of the irradiated flux of the Ca II H&K doublet, F_{HK}, obtained by summing the fluxes of the H and K lines. The central panel shows the same plot using the average values of the measured fluxes of these lines in question. In the right panel, a similar graph shows the trend of the fluxes of the mentioned lines, separat-

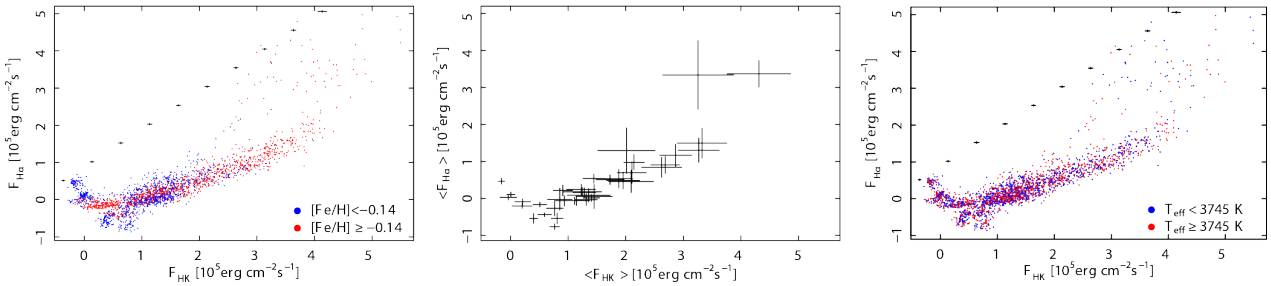

Figure 2.11: *Left: close-up view of the F_{HK} vs. $F_{H\alpha}$ diagram. Colours code the metallicity of the stars as shown in the legend. Black crosses represent the typical measurement uncertainties at different activity levels. Middle: same as in the left panel for the median of the flux measurements. For each star, the error bars represent the median absolute deviation of the measurements shown in the left panel. Right: the same as in the left panel, representing each star with the corresponding linear fit to its flux-flux values. Gray lines mark best fits with low statistical significance, while black lines represent p-values lower than 1% based on Spearman's correlation test. Adapted from Scandariato et al. (2017)*

ing the sample of analysed stars according to a threshold temperature value of T_{eff} = 3745 K. In this study, an increase in F_{HK} with fixed $F_{H\alpha}$, as a function of metallicity, is not evident. Similarly, the trend of the line fluxes does not seem to be correlated with the temperature of the star. Probably, the range of metallicity and temperature of the analysed stars is not wide enough to highlight significant correlations with these parameters (Scandariato et al., 2017). However, this study shows that the relationship between the fluxes of the Hα and Ca II H&K lines is not monotonic. In fact, observing the central panel shown in Figure 2.11, it can be noted that the flux of the Hα line initially has a decreasing trend as the Ca II H&K flux increases, then it goes below zero for values $< F_{HK} > 10^{-5}$ erg cm^{-2} s^{-1}, and finally has an increasing trend along with the F_{HK} flux. Similar results have been obtained by Robinson et al. (1990). From a theoretical point of view, these results are predicted by chromospheric models (Cram and Mullan, 1979; Cram and Giampapa, 1987; Houdebine and Stempels, 1997). According to these models, the most plausible scenario is that the Ca II H&K emission lines are collisionally dominated, so the irradiated flux increases with increasing pressure. On the other hand, the Hα line is dominated by radiation; the increase in optical thickness initially leads to a deeper absorption line until the electron density is high enough to bring the line into a collision-dominated formation regime that fills the line (Scandariato et al., 2017). Active stars therefore exhibit both the Ca II K and Hα emission lines, and the most active stars have a more intense emission in both lines.

CHAPTER 3

Exploring the effects of planetary mass on atmospheric retrieval

The content of this chapter has been published in the journal *Astronomy & Astrophysics*, volume 669, as the article with the title "Analysis of the planetary mass uncertainties on the accuracy of atmospherical retrieval" (Di Maio, C. et al., 2023).

3.1 Introduction

In the last decade, our knowledge of exoplanet atmospheres has been revolutionised. The majority of planets for which detailed atmospheric information is available have been shown to transit their parent star. The atmospheres of about sixty exoplanets have been observed using transmission spectroscopy. By modelling the transmission spectra of exoplanets, we are able to extract information about various properties and processes in the atmosphere (Charbonneau et al., 2002; Tinetti et al., 2007; Swain et al., 2008; Kreidberg et al., 2014; Schwarz et al., 2015; Sing et al., 2016; Hoeijmakers et al., 2018; de Wit et al., 2018; Tsiaras et al., 2019; Brogi and Line, 2019; Welbanks et al., 2019; Edwards et al., 2020; Changeat and Edwards, 2021; Changeat et al., 2022; Roudier et al., 2021; Yip et al., 2021a). This is commonly done through a forward model, which generates a spectrum from atmospheric parameters, and a parameter estimation scheme, which samples the parameter space to calculate the probability distribution of the set of parameters. This method, called "atmospheric retrieval", has become a fundamental tool for explaining individual observations from transit, eclipse, and phase curve spectroscopy at both low and high resolution.

With NASA's Kepler (Borucki et al., 2010) and Transiting Exoplanet Survey Satellite (TESS, Ricker et al. (2015)) the numbers of transiting planets is increased significantly and a number of them have been already identified a large number of targets suitable for atmospheric characterisation with the Hubble Space Telescope (HST), Spitzer, as well as the James Webb Space Telescope (JWST, Greene et al. (2016)). A new generation of observatories from space and the ground and dedi-

cated missions will come online in the next years, offering broader spectral coverage, and higher SNR, allowing us to study a significantly larger number of targets. The ESA-Ariel mission (alone) was designed for this purpose: it will provide transit, eclipse, and phase-curve spectra of about one thousand of planets. It is expected to revolutionise our understanding of the physical and chemical properties of a large and diverse sample of extrasolar worlds. To maximise the science return of Ariel, the observations will be performed in four tiers with more demanding objectives (Tinetti et al., 2021), each one with different binning of the spectra in order to reach the required signal-to-noise ratio, and for a decreasing number of targets aiming to obtain both an unprecedented statistics of planetary atmospheres and their full characterisation for a number of benchmark cases.

Most of the planets with mass measurements, mainly coming from radial velocity follow-up confirmations, have typical error bars of the order of 10%, in particular for planets with M > 0.1 M_J. Planets smaller than Neptune have larger mass errors, often larger than 40-50%; while in a number of cases, the mass planet is completely unknown. Given the role of mass in the scale height of an atmosphere (eq. 2.40), this uncertainty may contribute to the degeneracy in retrieving the mean molecular weight of the atmosphere, especially when clouds are present (Batalha et al., 2019). In addition, de Wit and Seager (2013) showed that the next-generation of transmission spectra would contain the information necessary to independently constrain the mass of an exoplanet based on its temperature, pressure, and composition profile.

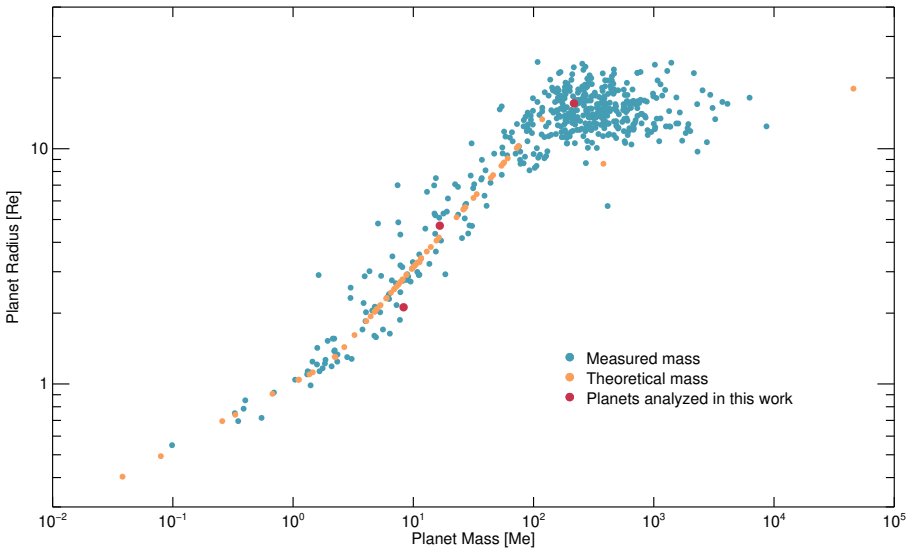

Figure 3.1: *Mass-Radius distribution of the planets of the Mission reference sample (MRS) for which we have an estimation of the mass. In red we highlighted the targets analysed in this work (data courtesy of Edwards).*

In a previous work, Changeat et al. (2020) using a set of simulations performed

an atmospheric retrieval to study the influence of the knowledge of the planetary mass on the retrieved parameters. In particular, these authors found that for clear-sky gaseous atmospheres, the results obtained when the mass is known or retrieved as a free parameter are indistinguishable. In the case of secondary atmospheres, the retrievals are more challenging due to the higher degree of freedom for the atmospheric main components. In cases where clouds are added, the mass uncertainties may substantially impact the retrieval due to the degeneracy with the mean molecular weight.

In this context, I aim to understand how precisely we ought to measure the planetary mass in order to robustly characterise the atmosphere.

According to Edwards and Tinetti (2022), the Mission reference sample (MRS) of Ariel will contain a selection of planets that could be observed in the prime mission lifetime. About 2000 will be included in the MRS and about half of them will be actually investigated by Ariel. Today about 570 of them are confirmed planets and for $\sim$ 500 of them, we have an estimate of the mass. In Fig. 3.1 I reported the mass-radius relation for the planets that have a measured mass (blue dots), and a theoretical mass (orange dots) and I highlighted with the targets analysed in this work red dots.

The results of this work could provide input for the radial velocity campaigns that should therefore prioritise the most impacted planets. This paper is organised as follows. I refer the reader to the previous Sections 2.1.3 and 2.4.1 for an overview of the ESA M4 Ariel Mission, and the transit spectroscopy and to Section 2.4.2 for an overview of the atmospheric retrieval. I describe the methodology used for the retrieval analysis in Section 3.2.1. In Section 3.2.2 I present the analysis performed for the primordial atmosphere cases. The impact of the signal-to-noise ratio on the atmospheric retrieval is discussed in Sect. 3.2.3. Section 3.2.4 and Section 3.2.5 present the retrieval analysis of the clear and cloudy secondary atmosphere cases. The conclusions and a summary of this work follow in Section 3.2.6.

Specific analysis of a sample of planets that will be observed by Ariel is the subject of Chapter 4.

3.2 Retrieval Analysis

3.2.1 Methodology

In order to analyse the atmospheric retrieval accuracy and how this depends on the planetary mass uncertainties I used the open-source TauREx 3.1, the new version

of TauREx (Waldmann et al., 2015a,b). This fully Bayesian inverse atmospheric retrieval framework (Al-Refaie et al., 2021), is useful in simulating different atmospheric configurations with different star-planet systems and performing retrievals (see Section 2.4.3 for a detailed description of TauREx). It uses the highly accurate line lists from the ExoMol (Tennyson et al., 2016), HITEMP (Rothman and Gordon, 2014) and HITRAN (Gordon et al., 2016) database to build forward and retrieval models. In my study, the molecular cross sections were taken from ExoMol (H_2O, Polyansky et al. (2018); CO, Li et al. (2015); CH_4, Yurchenko et al. (2017)).

For each tested case I used TauREx in forward mode to generate a high-resolution theoretical spectrum. I focused only on transit spectra. I specified the main properties of the star and the planet and the main constituents of the atmosphere using their relative abundances. Then, by convolving the high-resolution spectrum through the instrument model (ArielRad v. 2.4.6, Mugnai et al. (2020), Ariel Payload v. 0.0.5, ExoRad v. 2.1.94), I simulated a spectrum as observed by Ariel and used it as the input of the retrieval. The instrument model was obtained for each target and to simulate the Ariel Tier-2 performance, I took into account the number of transit required for the Tier-2 to obtain the adequate SNR. I investigated the parameter space

Table 3.1: *Planetary and stellar parameters used to produce the forward models and the prior boundary used in our retrieval analyses for the primordial atmosphere of the Hot-Jupiter and the Neptunian planet.*

Hot-Jupiter case				
HD 209458		HD 209458b		
Stellar Parameters	Input	Planetary Parameters	Input	Boundary
Sp. type	G0 V	R_p (R_J)	1.39	(0.9,1.5)
R_s ($R_\odot$)	$1.19^{(a)}$	M_p (M_J)	0.73	(0.5,1)
M_s ($M_\odot$)	$1.23^{(a)}$	T_p (K)	1450	(100,4000)
T_s (K)	$6091^{(a)}$			
d (pc)	$48^{(a)}$			
m_v	$7.65^{(b)}$			
Hot-Neptune case				
HD 219666		HD 219666b		
Stellar Parameters	Input	Planetary Parameters	Input	Boundary
Sp. type	G5 V	R_p (R_J)	0.42	(0.4,0.44)
R_s ($R_\odot$)	$1.03^{(c)}$	M_p (M_J)	0.05	(0.02,0.07)
M_s ($M_\odot$)	$0.92^{(c)}$	T_p (K)	1041	(100,4000)
T_s (K)	$5527^{(c)}$			
d (pc)	$94^{(c)}$			
m_v	$9,81^{(d)}$			

Notes. $^{(a)}$ Stassun et al. (2017) $^{(b)}$ del Burgo and Allende Prieto (2016) $^{(c)}$ Esposito et al. (2019) $^{(d)}$ Høg et al. (2000) .

with the nested sampling algorithm MultiNest (Feroz et al., 2009) with 500 live points and an evidence tolerance of 0.5.

In Section 3.2.2, I tested the case of a hypothetical hot-Jupiter, with parameters based on HD 209458b (see Table 3.1). In order to investigate the benefits of increased accuracy in the planetary mass estimation, I performed the retrieval when the mass is totally unknown and, thus, retrieved as a free parameter, and when the mass is known with an uncertainty of 40% and 10%. Also, in order to test the atmospheric retrieval for a smaller planet, I performed a retrieval for a hot-Neptune around a G star, with parameters based on HD 219666b (see Table 3.1) considering (even in this case) a mass uncertainty of 40% and 10%.

In Sec.3.2.3, I also discussed the importance of guaranteeing an adequate SNR value by performing the retrieval for the same cases but considering 10.5th-magnitude stars. Furthermore, I compared the retrieval performed on the same object considering different uncertainties at different wavelength ranges to investigate whether the retrieval is more sensitive to a specific range of the spectrum.

In Section 3.2.4, I investigated the case of a hypothetical super-Earth, with parameters based on HD 97658b (see Table 3.2), one of the targets of the Ariel Target List (Edwards et al., 2019).

Table 3.2: *Planetary and stellar parameters used to produce the forward models for the secondary atmosphere of a Super-Earth planet.*

Secondary Atmosphere				
HD 97658		HD 97658b		
Stellar Parameters	Input	Planetary Parameters	Input	Boundary
Sp. type	K1 V	R_p (R_J)	0.189	(0.9,1.5)
R_s ($R_\odot$)	$0.73^{(a)}$	M_p (M_J)	0.02611	variable (see text)
M_s ($M_\odot$)	$0.85^{(a)}$	T_p (K)	720.33	(100,4000)
T_s (K)	$5212^{(b)}$			
d (pc)	$21.546^{(b)}$			
m_v	$7.78^{(b)}$			

Notes. $^{(a)}$ Howard et al. (2011) $^{(b)}$ Ellis et al. (2021) .

I tested three different atmospheric configurations by considering a heavy atmosphere containing a significant fraction of H_2O, CO and N_2, respectively. Also, in order to test the impact of the mass uncertainties onto the retrieval of the atmospheric properties I considered in my analysis three different mass uncertainties (10%, 30%, 50%). In Section 3.2.5, I investigated the case of cloudy N_2-dominated secondary atmospheres. In order to test the advantage in the retrieval of a atmosphere dominated by active gases, which are characterised by traceable molecular

features directly observable in the spectrum, I analysed two other different scenarios where I considered a H_2O- and a CO-dominated atmosphere.

For all the tested cases, I assumed a planetary atmosphere constituted by 100 layers in a plane-parallel geometry, uniformly distributed in log space between 10^{-6} and 10^{1} bar. The temperature structure was modelled with an isothermal $T - p$ profile. The trace gases considered were allowed to vary freely between 10^{-12} and 10^{-2} in volume mixing ratio.

Regarding the processes in the atmosphere that contribute to the optical depth to be considered, I set the molecular profile of each species to be constant at each atmospheric layer. Also, I took into account the collision-induced absorption (CIA) from H_2-H_2 (Abel et al., 2011; Fletcher et al., 2018), and H_2-He (Abel et al., 2012), as well as Rayleigh scattering for all molecules.

3.2.2 Primordial Atmosphere

To investigate the contribution of the planetary mass uncertainties to the retrieval of a primary atmosphere, I simulated a spectrum of a Hot-Jupiter based on HD 209458b and its parent star.

In previous work, Changeat et al. (2020) already performed a retrieval on this object, comparing the case where the planetary mass is assumed to be known to one where it is retrieved as a free parameter. In particular, they found that for a clear sky atmosphere (10^{1} bar), the knowledge of the mass does not impact the results. However, if clouds are modelled, some discrepancies appear only in the retrieval of the radius when the cloud pressure gets closer to 10^{-3} bar and the retrieved mass also becomes less accurate.

Here, I want to investigate the benefits of increased accuracy in the planetary mass estimation on atmospheric retrieval. I adopted the same parameters used by Changeat et al. (2020). In particular, for trace gases, I included H_2O, CH_4, and CO, with mixing ratios of 10^{-5}, 5×10^{-6} and 10^{-4}, respectively. I first simulated a clear sky atmosphere case and then tested the behaviour of the retrievals when clouds are present with four different configurations (P_{clouds} = 10^{-1}, 10^{-2}, 5×10^{-2} and 10^{-3} bar for the worst-case scenario). For each scenario, I performed the retrieval for three cases: in the first case, the planetary mass is retrieved as a free parameter (I used a large boundary range, by supposing a mass uncertainty of about 100%); in the second, I supposed to know the mass with an uncertainty of 40%; and in the third case, I applied an uncertainty of 10%.

I also performed the retrieval for a Neptunian planet around a G star to investigate how the retrieval depends on the planet characteristics.

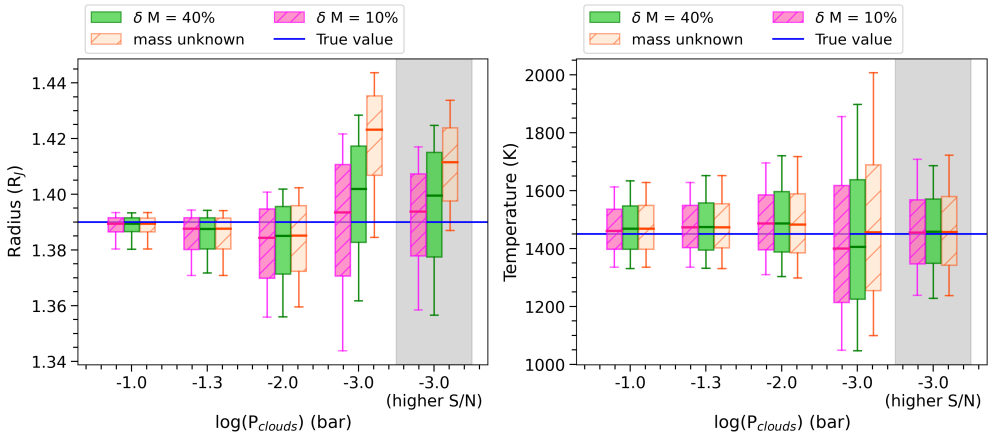

(A) *Radius*

(B) *Temperature*

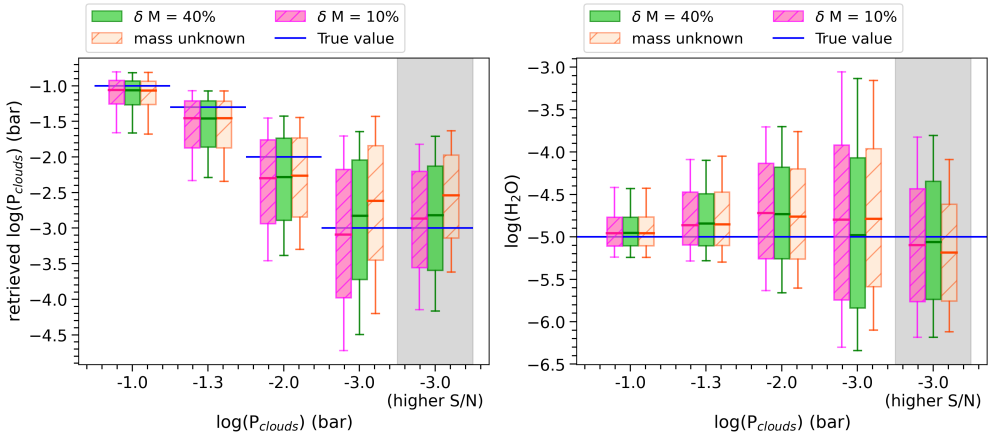

(C) *Clouds*

(D) *H_2O mixing ratio*

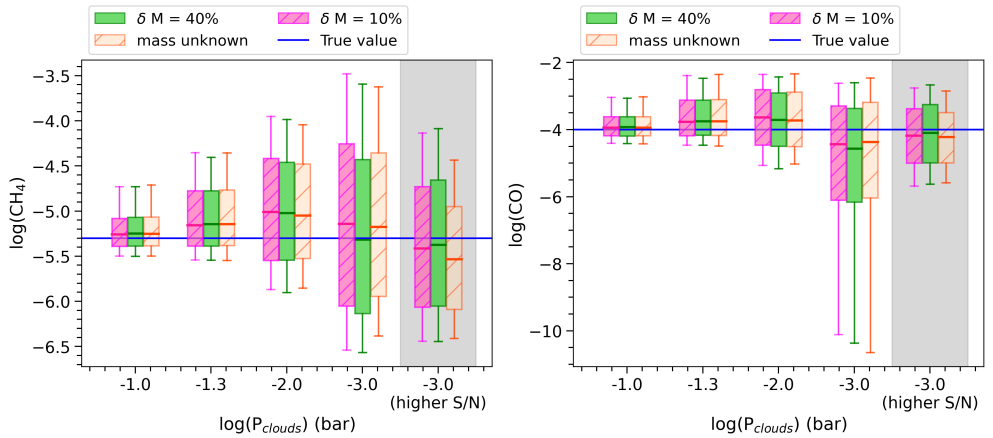

(E) *CH_4 mixing ratio*

(F) *CO mixing ratio*

Figure 3.2: *Comparison between the results obtained from the retrieval performed for the case of a hot-Jupiter around a G star when the mass is known with an uncertainty of 100% (in orange), 40% (in green), and of 10% (in magenta) as a function of cloud pressure. In the grey area, we reported the results obtained for a $P_{clouds} = 10^{-3}$ bar assuming noise decreased by a factor of two. The size of the box and the error bar represent the points within 1σ and 2σ of the median of the distribution (highlighted with solid lines), respectively. The blue line is the input value.*

The parameters used to generate the forward model and the prior bounds employed for each fitted parameter are reported in Table 3.1.

In Fig. 3.2 I compare the results obtained for a hot-Jupiter orbiting around a G star, as a function of cloud pressure, in the case when we know the mass with an uncertainty of 100% (in orange), 40% (in green), and of 10% (in magenta). The discrepancies in the retrieval of the radius, which appear when the cloud pressure gets closer to 10^{-3} bar, and which are the same as obtained by Changeat et al. (2020), disappear when I performed the retrieval while considering a mass uncertainty of about 40% or less. In these cases, the retrieved radius for high-altitude clouds is within 1σ of the true value. Also, for all the parameters, I obtained a more accurate and precise retrieval when we know the mass with an uncertainty of 40% in the case of high-altitude clouds as well.

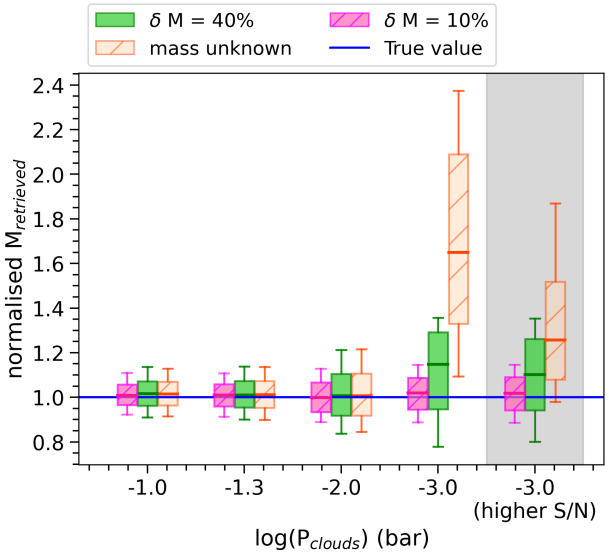

FIGURE 3.3: *Comparison between the normalised retrieved mass in the case of a hot-Jupiter around a G star when the mass is estimated with an uncertainty of 100% (in orange), 40% (in green), and of 10% (in magenta) as a function of cloud pressure. In the grey area, we reported the results obtained for a $P_{clouds} = 10^{-3}$ bar considering a noise decreased by a factor of two. The size of the box and the error bar represent the points within 1σ and 2σ of the median of the distribution (highlighted with solid lines), respectively. The blue line is the input value.*

Focusing on the retrieval of the mass, in Fig. 3.3 I compare the results of the normalised retrieved mass of each tested case obtained for the mass as totally unknown and for the mass with an uncertainty of 40% and 10%. The mass is well retrieved for all cases with clouds at low altitudes even when we totally unknown the mass. The retrieved mass becomes less accurate when the cloud pressure is lower than 10^{-3} bar. With a mass uncertainty of 40%, I significantly increase the accuracy and precision in the normalised retrieved mass. Indeed, in this case, the mass is well retrieved even for high-altitude clouds and the retrieved values are within 1σ with

the true values. Additionally, it can be seen that while a better estimation of the mass (mass uncertainty of 10%), could allow us to retrieve the mass and the radius with more precision also in the cases with high altitude clouds, I do not observe a significant difference between the results obtained with a mass uncertainty of 40% and 10% of all the other parameters.

Furthermore, I performed the retrieval for the worst cloudy case ($P_{clouds} = 10^{-3}$ bar) considering an increased SNR (see the results in the grey part of the plots in Fig. 3.2). To this purpose, I considered four times as many observations, so I decreased the noise by a factor of 2. From this test, it is clear that for the worst scenario, where the contribution of the clouds determines a less accurate estimate of the retrieved parameters, an increased SNR could help to better estimate the parameter and, in particular, the trace composition of the atmosphere.

From these results, it is clear that we could use TauREx as a tool to estimate the mass of hot-Jupiters with more precision than what we already know. In particular, with an initial mass uncertainty of 40%, I could be able to retrieve the mass with an uncertainty of about 15%.

To test the atmospheric retrieval in the case of a smaller planet, I simulated a spectrum of a Neptunian planet, based on HD 219666b around its host star (Table 3.1). I used the same parameters of the hot-Jupiter case for the atmospheric composition. From Fig. 3.4 we can note that in this case some discrepancies appear in the atmospheric retrieval, in particular for the CH_4 and CO mixing ratios, when the cloud pressure gets closer to 10^{-3} bar. All the other parameters are well retrieved even for high altitude clouds. Focusing on the retrieval of the mass (see Fig. 3.5), it can be seen that the mass is well retrieved for all the cases at lower altitudes, while the retrieved mass becomes less accurate when the cloud pressure decreases. In all tested cases for neptunian planets, the mass is refined to within 20% provided the initial mass uncertainty is $\leq 40\%$.

Additionally, the discrepancies obtained in the atmospheric retrieval at high altitude clouds does not disappear when the mass in known with an uncertainty of 10%. In this case while the retrieval of the mass increase in precision, as expected, the mass knowledge does not seem to impact the retrieval of the atmospheric composition and hence the results obtained from the retrieval are correlated with the SNR.

The results obtained from the retrieval of the analysed cases are summarised in Table A.1 and Table A.2 reported in Sec. A.3 of Appendix A.

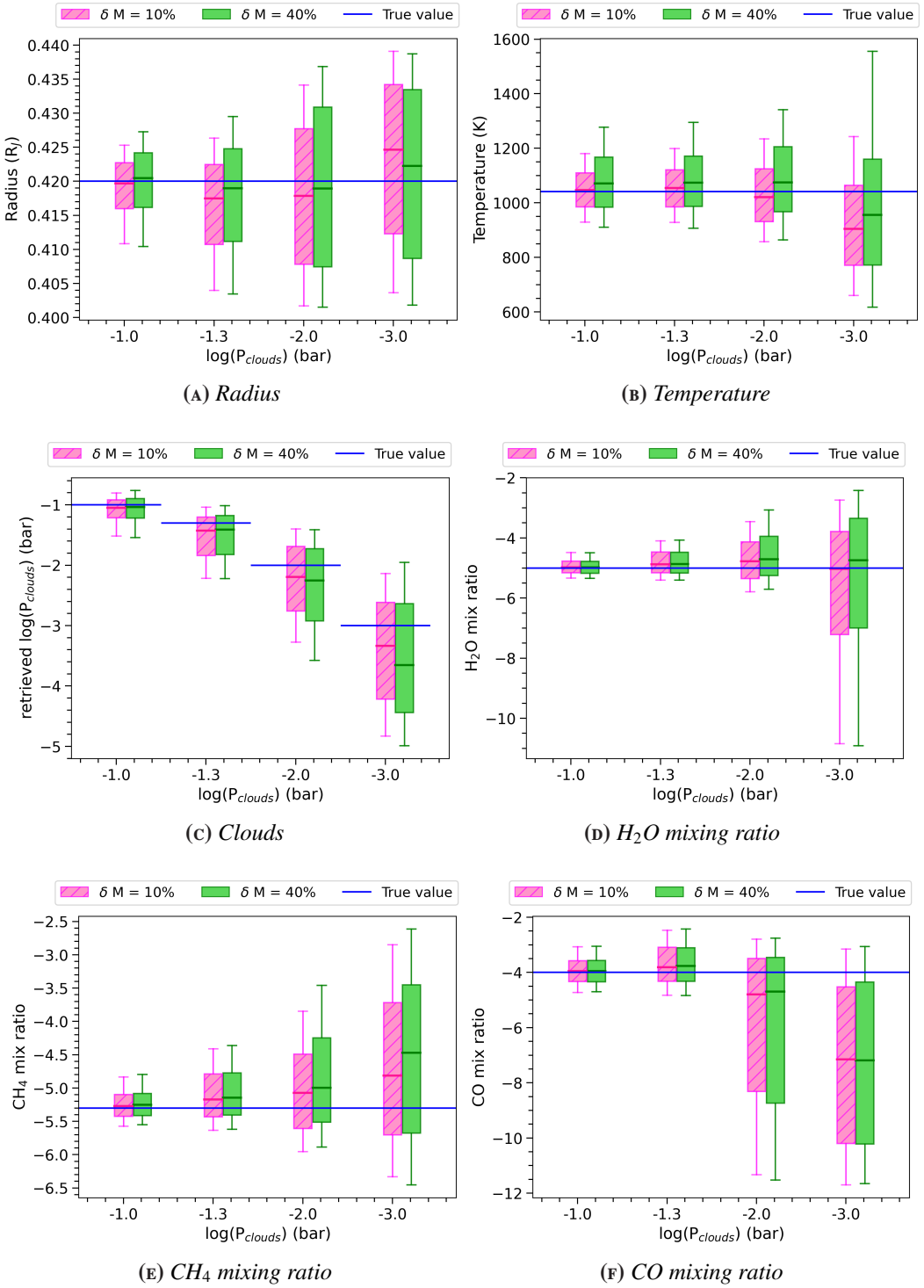

(A) *Radius*

(B) *Temperature*

(C) *Clouds*

(D) *H_2O mixing ratio*

(E) *CH_4 mixing ratio*

(F) *CO mixing ratio*

FIGURE 3.4: *Comparison between the results obtained from the retrieval performed for the case of a hot-Neptune around a G star when the mass is known with an uncertainty of 40% (in green) and 10% (in magenta) as a function of cloud pressure. The size of the box and the error bar represent the points within 1σ and 2σ of the median of the distribution (highlighted with solid-lines), respectively. The blue line is the input value.*

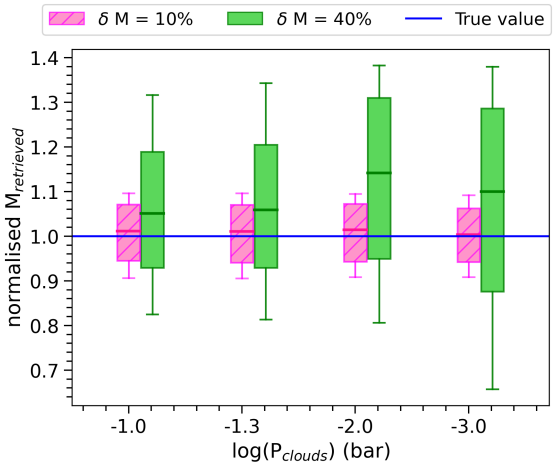

Figure 3.5: *Comparison between the normalised retrieved mass in the case of a hot-Neptune around a G star when the mass is estimated with an uncertainty of 40% (in green) and 10% (in magenta) as a function of cloud pressure. The size of the box and the error bar represent the points within 1σ and 2σ of the median of the distribution (highlighted with solid-lines), respectively. The blue line is the input value.*

3.2.3 Signal-to-noise ratio impact on the atmospheric retrieval at different wavelength ranges

Changeat et al. (2020) highlighted the importance of guaranteeing the adequate SNR when we observe heavy secondary atmosphere, by suggesting that an adequate SNR is necessary to estimate correctly the mass and the atmospheric composition through transit spectroscopy.

Here, I test the importance of the SNR for the primary atmosphere. To this purpose, in Fig. 3.6, I compare the results obtained in the previous section for an 8th-magnitude G star, with the results obtained for the same planet, orbiting around a 10.5th-magnitude star. Of course, a higher magnitude for the star implies a lower SNR. The results of this test are summarised in Table A.3 in Appendix A.

As expected, in the case of the 10.5th-magnitude star the uncertainties of all the fitted parameters increase with respect to the uncertainties obtained for the 8th-magnitude star case for all the cloud pressures. The retrieved values are within 1σ of the true values, except for the CO mixing ratio where the accuracy decreases at high altitude clouds and is not compatible (at 1σ) with the true value.

Focusing on the retrieval of the mass, see Fig. 3.7, it is clear that the mass is retrieved for all cases but with less accuracy and precision than the bright star case, however still within 1σ of the true value, in the case of 10.5th-magnitude star regardless of the height of the clouds.

In addition, I investigated the impact of the SNR of specific ranges of the spec-

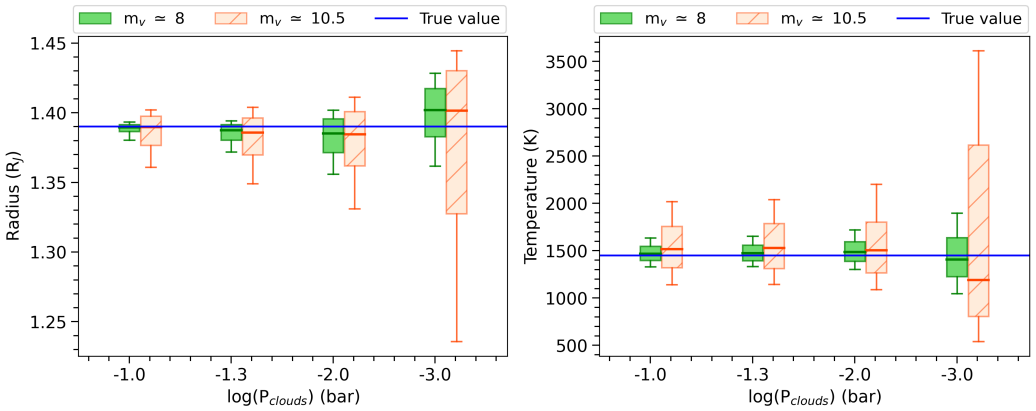

(A) *Radius*

(B) *Temperature*

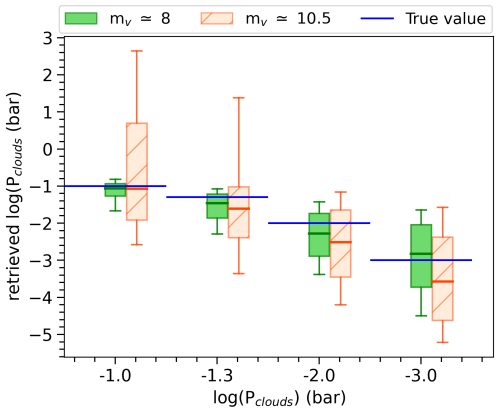

(C) *Clouds*

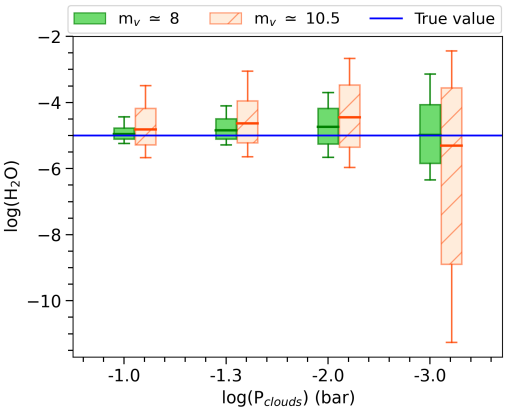

(D) *H_2O mixing ratio*

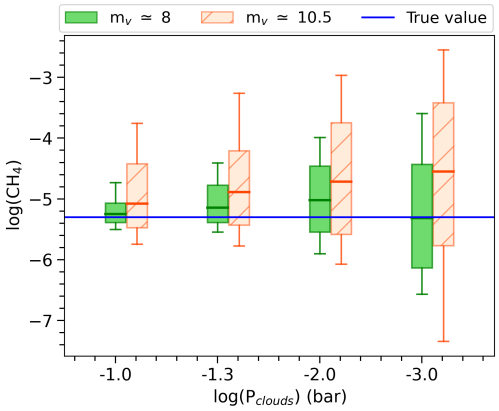

(E) *CH_4 mixing ratio*

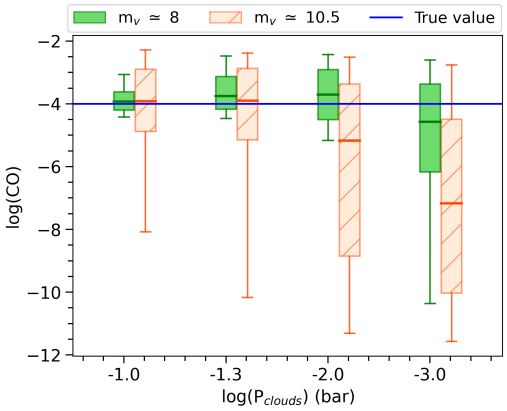

(F) *CO mixing ratio*

FIGURE 3.6: *Comparison between the results obtained from the retrieval performed for the case of a hot-Jupiter around an 8th-magnitude G star (in green) and around a 10.5th-magnitude G star (in orange) as a function of cloud pressure, assuming mass uncertainty of about 40%. The size of the box and the error bar represent the points within 1σ and 2σ of the median of the distribution (highlighted with red and orange solid-lines), respectively. The blue line is the input value.*

trum onto the atmospheric retrieval. I performed a retrieval analysis of a Jovian planet around a G star, considering a cloud pressure of 10^{-1} bar. I decided to split

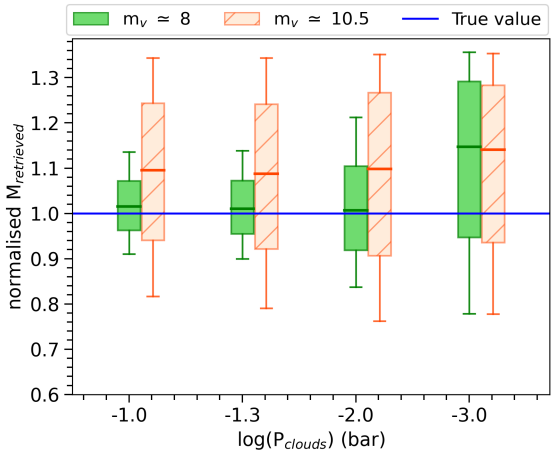

Figure 3.7: *Comparison between the retrieved mass for the case of a hot-Jupiter around an 8th-magnitude G star (in green) and around a 10.5th-magnitude G star (in orange) as a function of cloud pressure (mass uncertainty of about 40%). Scale colours is the same adopted for Fig. 3.6.*

the spectrum into six different ranges (see Fig. 3.8), each of which is dominated by different atmospheric features, to understand which range of the spectrum provides the main contribution to the retrieval.

For each retrieval, I changed the error bars of the points within one of the six ranges of the spectrum from $\delta = 3 \times 10^{-5}$ (the yellow band in Fig. 3.9) to $\delta = 5 \times 10^{-5}$ (the green boxes) and $\delta = 10^{-4}$ (the orange boxes).

Also, to better understand the contribution of the spectrum at low wavelengths,

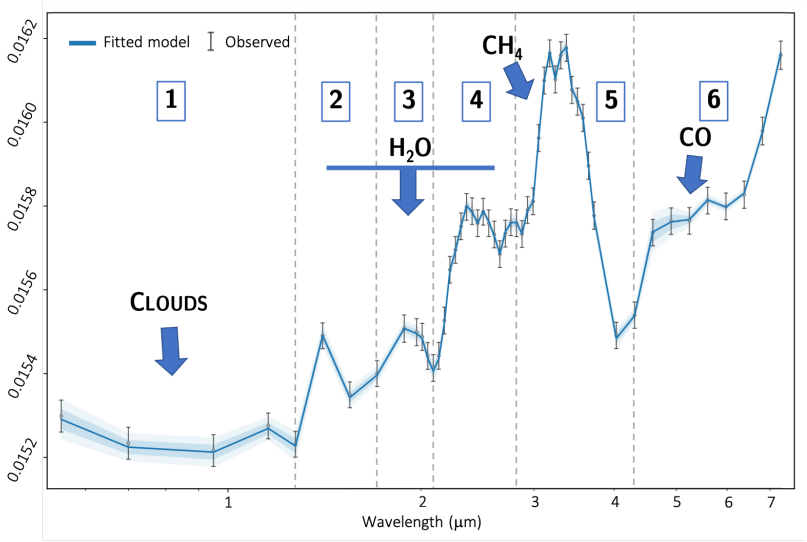

Figure 3.8: *Example of the spectrum obtained for a primordial atmosphere case with a cloud pressure of 10^{-1} bar. We highlighted the range of the spectrum in which we expected the main contribution of H_2O, CH_4 and CO. We selected six different ranges of the spectrum and we increased the SNR in each of them to investigate the contribution of each range on the retrieval (the points at the edge of the ranges belong to both of the adjacent selected sections).*

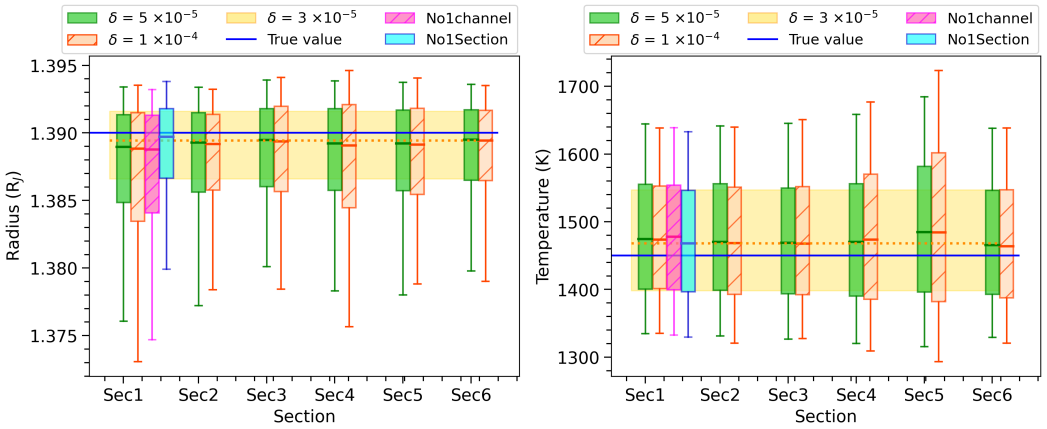

(A) *Radius* (B) *Temperature*

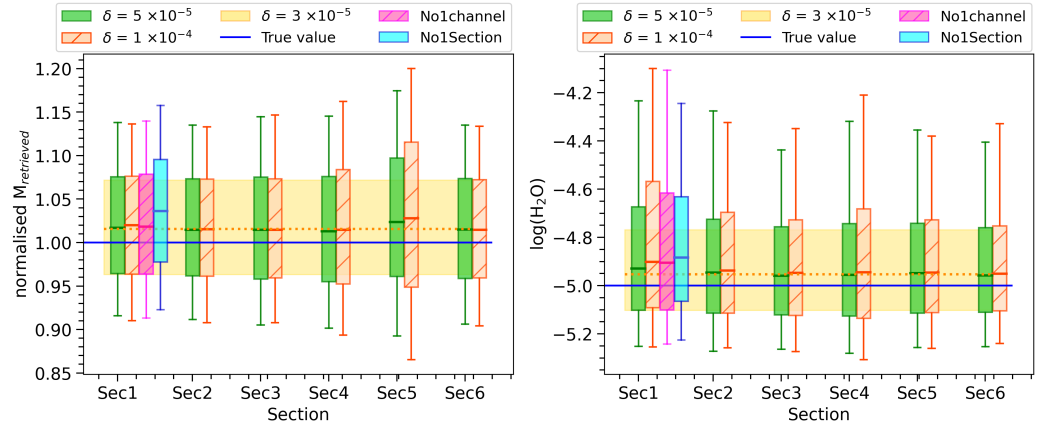

(C) *Mass* (D) *H_2O mixing ratio*

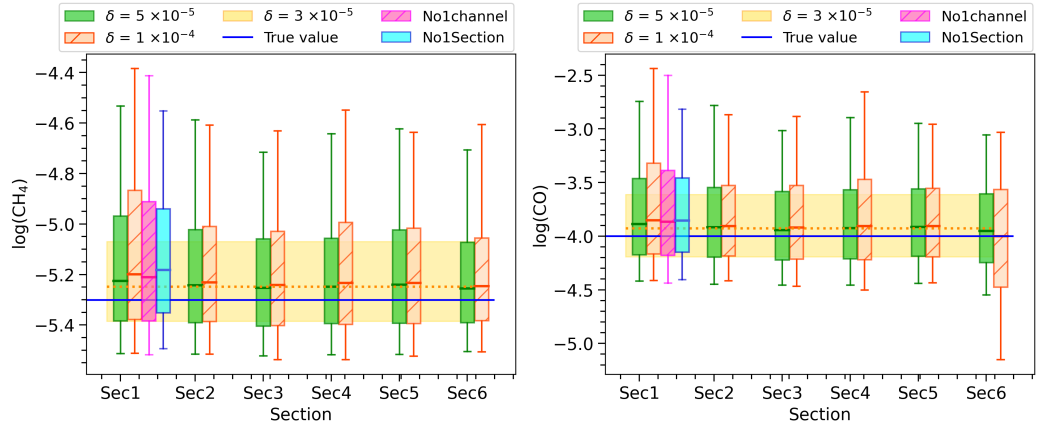

(E) *CH_4 mixing ratio* (F) *CO mixing ratio*

FIGURE 3.9: *Test of the impact of the SNR in each of the selected range of the spectrum performed on the primordial atmosphere of the hot-Jupiter around a 8th-magnitude G star. In green the retrieval performed considering an error of 5×10^{-5}. In orange the retrieval obtained with an error of 1×10^{-4}. The yellow band highlights the values retrieved in the original case ($\delta \simeq 3 \times 10^{-5}$). The magenta and cyan boxes represent the distributions of the values obtained by performing the retrieval without the first point or without the entire section 1 of Fig. 3.8, respectively. The blue line highlights the true value.*

I tested other two cases: in the first case we totally excluded the first point (the magenta box in Fig. 3.9), in the second case we excluded all the points of the first section (the cyan box).

Fig. 3.10 suggests that we are not able to correctly retrieve the cloud pressure when we entirely exclude the points of the first section. This result confirms that the wavelength range between 0.5 and 2 μ contains information of the features of the clouds, as also suggested by Yip et al. (2021a,b). This result highlights the importance of the continuous wavelength coverage of the blue end of the spectrum that allows us to fit for more complicated cloud models and probe the presence of species such as H_2O and CH_4.

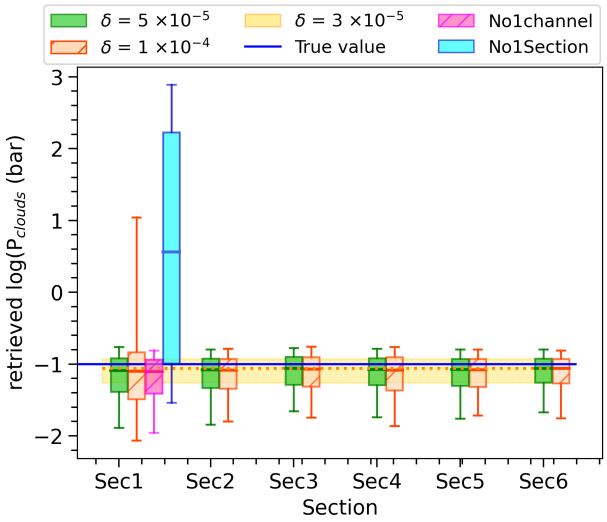

Figure 3.10: *Impact of the SNR in each of the selected range of the spectrum on the retrieved cloud pressure. The scale colour and the description of the figure are the same adopted in Fig. 3.9*

.

For all the other parameters, except for the temperature, we can see an increase of the uncertainties with a decrease in the SNR in the first section. Since, in the first section, the main contribution to the spectrum is due to the clouds component, this result suggests that all the parameters of the retrieval, excepted the temperature, are impacted by the cloud pressure knowledge. However, whilst the cloud is harder to constrain, in case at low-altitude clouds, we are still able to constrain the atmospheric parameters, which is encouraging if there are cases where we cannot use the shortwave region.

3.2.4 Secondary Atmosphere

The atmospheric retrieval of Earths and super-Earths is challenging because the mean molecular weight, μ, is unconstrained (with the assumption of $\mu \sim 2.3$ no

longer valid). Furthermore, diatomic background gases, such as H_2 and N_2 referred to as spectrally inactive gases, do not exhibit strong vibrational absorptions bands, so they have not directly observable features in the spectrum. Additionally, lower-mass planets tend to not have precise mass measurements.

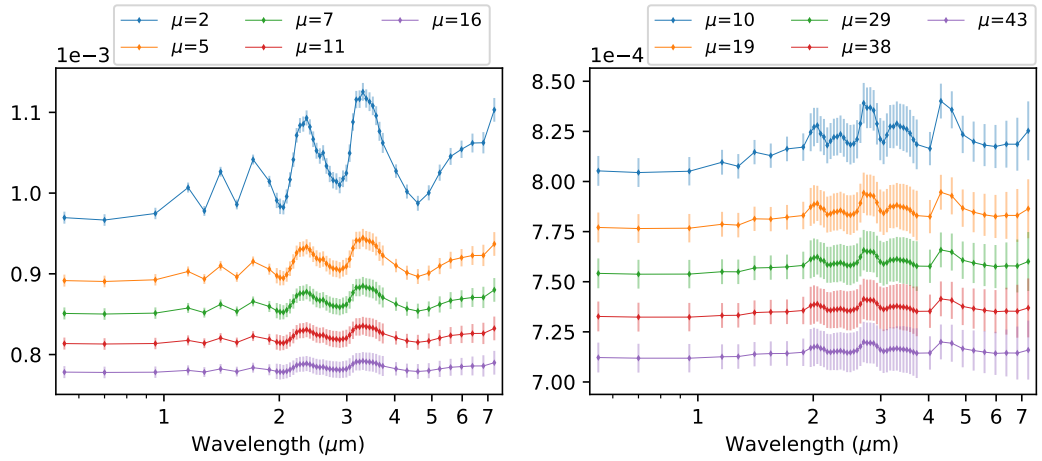

(A) N_2-dominated (B) CO_2-dominated

Figure 3.11: *Comparison between the Ariel simulated spectra obtained considering different mean molecular weights. (a) N_2-dominated (b) CO_2-dominated. The spectra are stacked to better compare them.*

To investigate how the mass uncertainties could impact the retrieval of low-mass planets, I considered a secondary atmosphere consisting of elements heavier than H/He. The super-Earth simulated here is based on HD 97658b. The parameters used in my model are reported in Table 3.2.

I considered a N_2-dominated atmosphere and used the inactive gas N_2 to increase the mean molecular weight of the atmosphere and simulate a heavy atmosphere around a rocky planet. I also included H_2O and CH_4 as trace gases fixing their absolute abundances at 10^{-4} and 6×10^{-4}, respectively. The rest of the atmosphere is filled with a combination of H_2 and He.

I considered four different scenarios with different values for the mean molecular weight (μ = 2.3, N_2/He = 10^{-10}; μ = 5.2, N_2/He = 1; μ = 7.6, N_2/He = 2; μ = 11.1, N_2/He = 4) to explore different compositions of the atmosphere. The highest considered mean molecular weight was selected to have atmospheric features detectable by an instrument such as Ariel.

In Fig. 3.11a I compared different Ariel simulated spectra of HD 97658b obtained considering different mean molecular weights (μ = 2.3, 5.2, 7.6, 11.1, 16). It can be seen that for $\mu > 11.1$ the spectrum is almost flat and the atmospheric features are not detectable any more. However, other worst-case scenarios could exist.

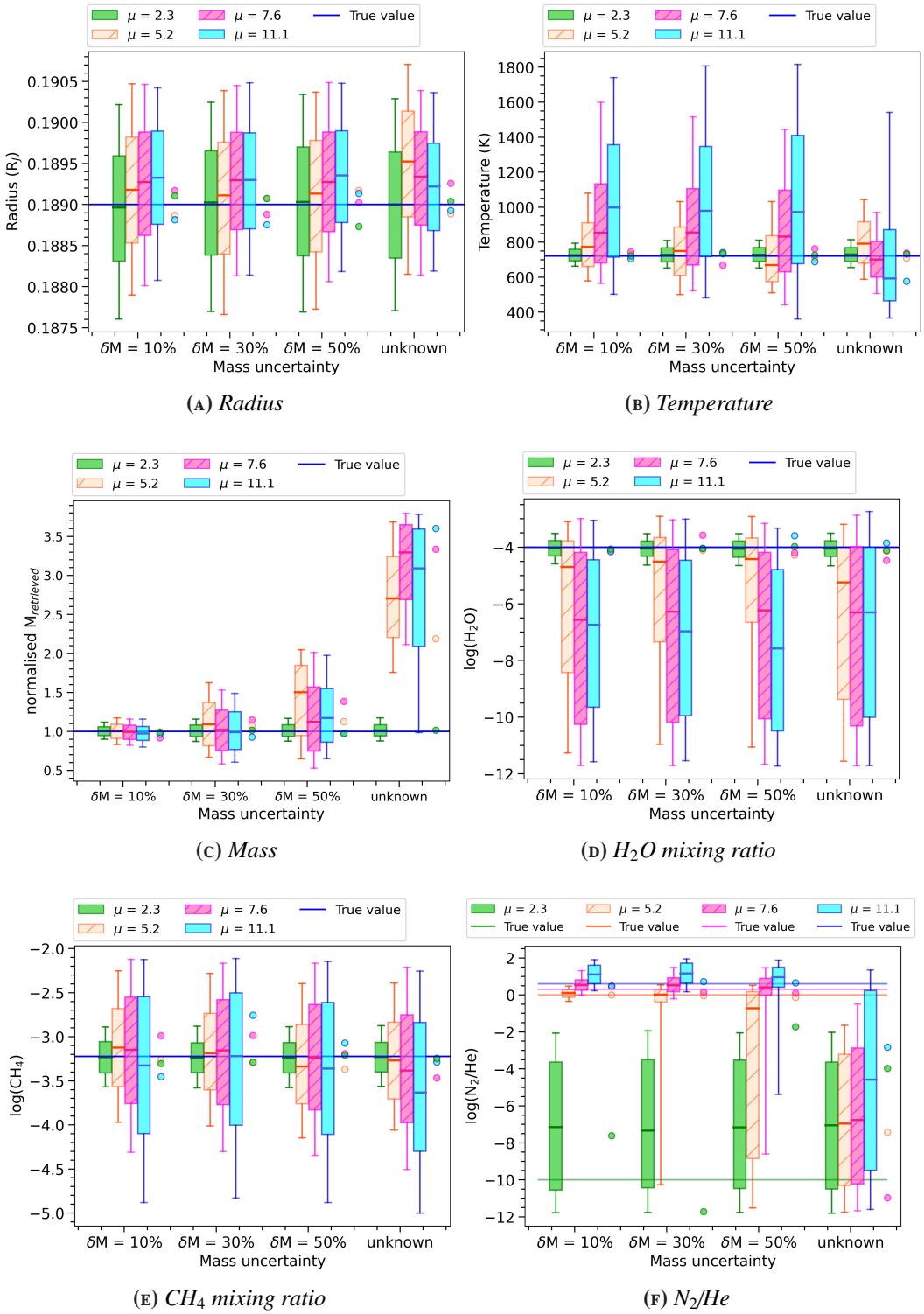

(A) *Radius* (B) *Temperature*

(C) *Mass* (D) H_2O *mixing ratio*

(E) CH_4 *mixing ratio* (F) N_2/*He*

Figure 3.12: *Impact of the mass uncertainties on the retrieval for different scenarios of heavy clear sky N_2-dominated secondary atmospheres represented by increasing values of μ (2.3 in green, 5.2 in orange, 7.6 in magenta and 11.1 in cyan). The blue lines highlight the true values. The points alongside the boxes highlight the MAP parameters obtained for each analysed case. The size of the box and the vertical segments represent the points within 1σ and 2σ of the median of the distribution (highlighted with solid lines), respectively.*

For instance, a pure Venus-like CO_2 atmosphere would not be detectable without impacting the scientific objectives of the Ariel mission. To understand the limits in detecting secondary atmospheres, in Fig. 3.11b we compared different spectra simulated for the same target supposing a CO_2 dominated secondary atmosphere (μ = 10, 19, 29, 38, 43). In these cases, we have a worse SNR than the N_2 dominated case. The spectra are dominated by the noise and the atmospheric features are undetectable starting from $\mu \simeq 29$ and this prevents us from an accurate atmospheric retrieval. It is also clear that in this case the mean molecular weight at which the atmospheric features are undetectable is higher than that obtained in the case of a N_2-dominated atmosphere. However, this result is not surprising because CO_2 is an active gas and, as we will show in Sec. 3.2.5, the retrieval is easier in the presence of a main gas producing spectral signatures. For these reasons, I limited my analyses to the hybrid case, where H_2 remains in large enough quantities to allow for good Tier 2 observations with Ariel.

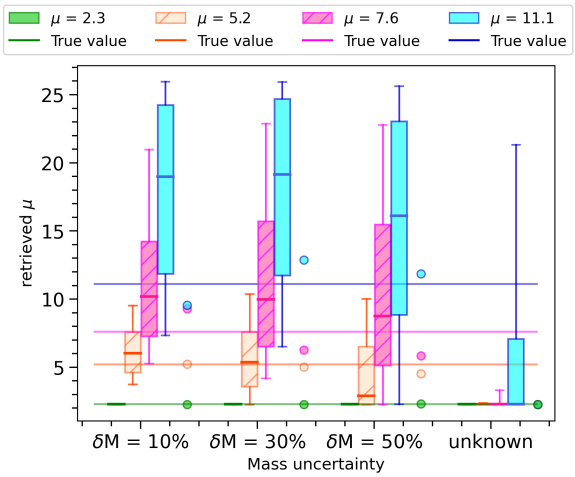

Figure 3.13: *Impact of the mass uncertainties on the retrieved mean molecular weight for different scenarios of heavy clear sky N_2-dominated secondary atmospheres represented by increasing values of μ (2.3 in green, 5.2 in orange, 7.6 in magenta and 11.1 in cyan). The scale colour and the description of the figure are the same adopted in Fig. 3.12*

.

In order to test the impact of the mass uncertainties I also performed the retrieval considering a mass uncertainty of about 10%, 30%, and 50%, along with a case where the mass is totally unknown (by using a very large boundary for the mass parameter).

In Fig. 3.12 I show the impact of the mass uncertainties on the atmospheric retrievals of different scenarios where I considered heavy secondary atmospheres represented by increasing values of μ. For comparison, I report also the case with μ = 2.3. In Appendix A.4 I summarised the results and in Appendix A.1 I reported

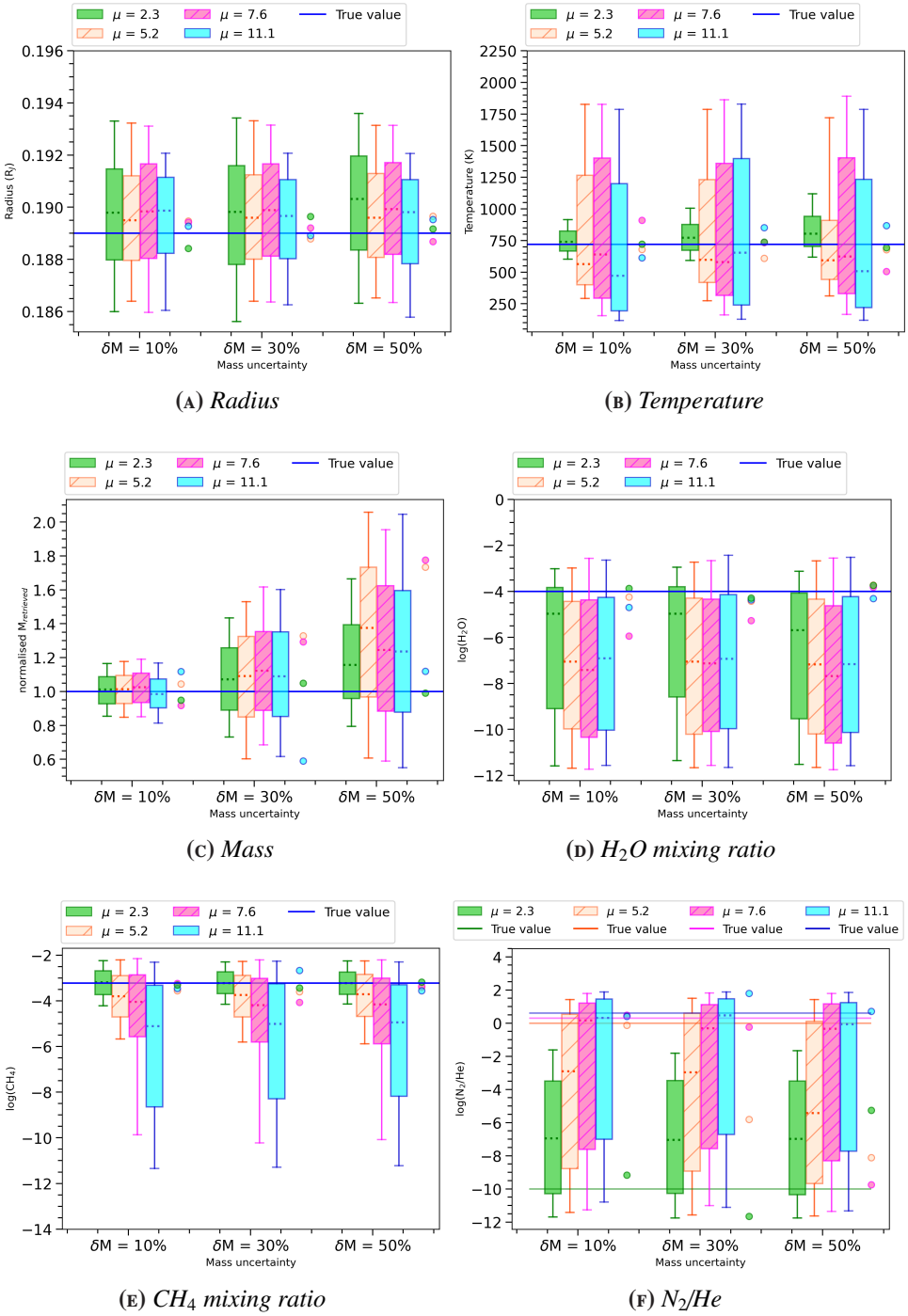

(A) *Radius* (B) *Temperature*

(C) *Mass* (D) H_2O *mixing ratio*

(E) CH_4 *mixing ratio* (F) N_2*/He*

Figure 3.14: *Impact of the mass uncertainties on the retrieval for different scenarios of heavy clear sky N_2-dominated secondary atmospheres of a hot-Jupiter around a 10.5th-magnitude G star, represented by increasing values of μ (2.3 in green, 5.2 in orange, 7.6 in magenta and 11.1 in cyan). The blue lines highlight the true values. The points alongside the boxes highlight the MAP parameters obtained for each analysed case. The size of the box and the vertical segments represent the points within 1σ and 2σ of the median of the distribution (highlighted with solid lines), respectively.*

some examples of corner plots obtained from these analyses.

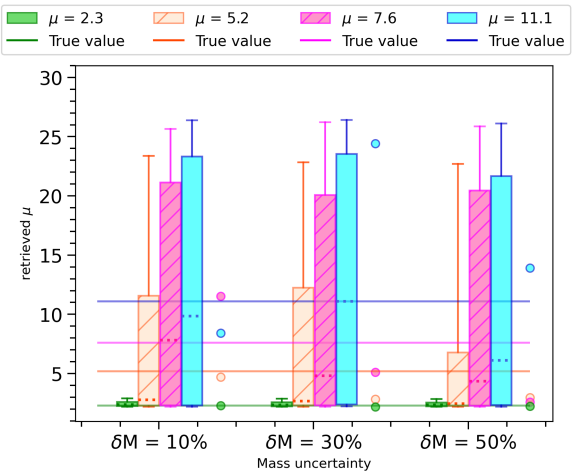

Figure 3.15: *Impact of the mass uncertainties on the retrieval of the mean molecular weight for different scenarios of heavy clear sky N_2-dominated secondary atmospheres of a hot-Jupiter around a 10.5th-magnitude G star, represented by increasing values of μ (2.3 in green, 5.2 in orange, 7.6 in magenta and 11.1 in cyan). The scale colour and the description of the figure are the same adopted in Fig. 3.14*

.

It can be seen that a mass estimation with an uncertainty equal to or lesser than 50% could help us to better constrain the mean molecular weight for all the tested cases with different mean molecular weights.

From this plot no significant differences appear in the retrieved atmospheric parameters obtained when performing the retrieval in cases where the mass is known with different uncertainties; this is not surprising, because for the high mean molecular weight atmosphere, the scale height is relatively small, so changes in the gravity will not produce such large differences in the spectrum. However, as expected, the retrieved mass shows a correlation with the mass uncertainty.

In Fig. 3.12 and following, I highlight the maximum-a-posteriori (MAP) parameters with circle points. In cases with higher values of μ some discrepancies appear in the temperature and H_2O retrieved values with respect to the true values, and in some cases, I obtained retrieved values that are not within 1σ of the true values. However, in these cases, even when I have a larger distribution, the MAP values obtained from the retrieval are totally consistent with the true values. In addition, some discrepancies appear in the retrieved MAP of N_2/He when $\mu = 2.3$. This result suggests that I am not able to constrain this ratio. In these cases I only define a possible range of values and some performed tests have demonstrated that this result does not depend on the choice of the prior limits.

Furthermore, from Fig. 3.13 it can be seen a slight trend between the mean molecular weight and the mass uncertainties. In particular, for a mass uncertainty

lower than 50% I am able to retrieve the mean molecular weight with higher accuracy (mostly if I consider the MAP values) with respect to the unknown mass cases, in particular for the heavier atmospheres and with a slight increase precision when I performed the retrieval with a mass uncertainty of 10%. This is probably due to the higher accuracy and precision in the retrieval of the N_2/He when I consider a mass uncertainty of 10%.

All these results suggest that I should be able to correctly retrieve the atmospheric parameters of a secondary atmosphere with a clear sky, even when the mass is known with an uncertainty of 50%, even when I considered the worst-case scenario to assess the degeneracy between the mass and the mean molecular weight. My analysis, also, suggests that this degeneracy is intrinsic to secondary atmospheres and not directly connected with mass uncertainty. Despite this, and precisely by virtue of this degeneracy, a more accurate estimate of the mass obtained from an independent determination could help to break the degeneracy, thus increasing the accuracy in the determination of the abundances of the fill gases.

I also tested the atmospheric retrieval of an analogue scenario but considering a 10.5th-magnitude star however (see Fig. 3.14 and 3.15). The results obtained from this test are reported in Table A.5. In this case, I obtained similar results with respect to the previous case in which we considered an 8th-magnitude star. However, due to the lower SNR, I obtained larger uncertainties for all the parameters, including for those cases with lower mean molecular weight.

3.2.5 Cloudy Secondary Atmosphere

Finally, I investigated the case of cloudy secondary atmospheres.

Small planets might not have a H_2-dominated atmosphere and the dominant gas is often unknown. I decided to investigate three different scenarios: in the first, I considered a nitrogen-dominated atmosphere representative of a rocky planet to investigate the retrieval results and compare it with the case without clouds (see Sec. 3.2.4). Also, in order to provide evidence of the difference in the atmospheric retrieval when an active gas dominates in the transmission spectrum, I analysed the second and third scenarios, where I considered a H_2O-dominated and a CO-dominated atmosphere, respectively. Atmospheres dominated by species such as H_2O or CO would have traceable molecular features directly observable in the spectrum, as it can be seen from Fig. 3.16, where I compare the observed spectrum and the fitted model obtained for a N_2-, H_2O-, and CO-dominated atmosphere in the case of $\mu = 5.2$ and with a $P_{clouds} = 5 \times 10^{-2}$ bar. These cases represent a more favourable scenario for the inverse models with respect to the N_2-dominated ones.

In the tables in appendix A.4 I summarised the results obtained from the analysis

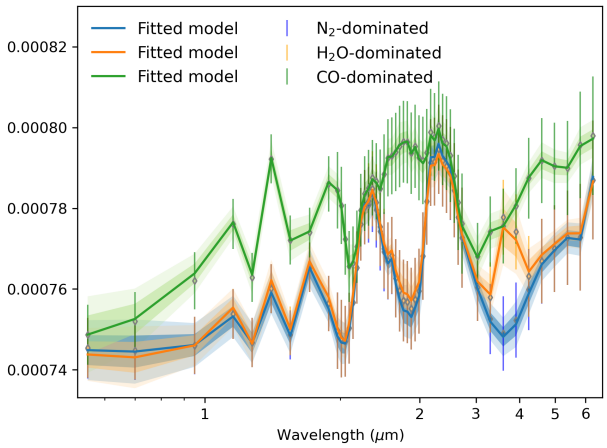

Figure 3.16: *Comparison between the observed spectrum and the fitted model obtained for a N_2-(blue), CO- (green) and H_2O-dominated (orange) atmospheres, in the case of μ = 5.2 and with a $P_{clouds} = 5 \times 10^{-2}$ bar.*

of the cloudy secondary atmosphere in the three different scenarios and in all the configuration of mean molecular weight for the cloud pressure 10^{-1} and 10^{-3} bar.

N_2-dominated Atmosphere Fig. 3.17 and Fig. 3.18 show the case $\mu = 5.2$, where I compare the results obtained for different cloud pressure. In this scenario, the atmosphere is light and presents a clear signal. From Fig. 3.18a it can be seen that with a mass uncertainty equal or lesser than 30%, I significantly increase the accuracy and the precision on the retrieval of N_2/He, in particular in cases with higher cloud pressure; however, if I consider the MAP values, I increase the accuracy also in the worst scenario with lower cloud pressure. These results are reflected in the determination of the mean molecular weight. Indeed, from Fig. 3.18b it may be noted that with a mass uncertainty equal or lesser than 30% I am able to retrieve the mean molecular weight and (as I would expect) the width of the values distributions increase (and, consequently, the uncertainties associated to the median values as well) while decreasing the cloud pressure. It seems that the mass uncertainty does not impact the retrievals of the CH_4 mixing ratio (Fig. 3.17f). The H_2O mixing ratio, see Fig. 3.17e, shows some discrepancies between the retrieved values and the true values, although the MAP values are compatible with the true values. However, these results do not show a correlation with the mass uncertainty, since they could be connected with the discrepancies shown in the cloud pressure retrieval (see Fig. 3.17d).

In Fig. 3.19 and 3.20 I considered the heaviest scenario (μ = 11.1). In this case I am not able to constrain the mean molecular weight. From Fig. 3.20b it can be seen

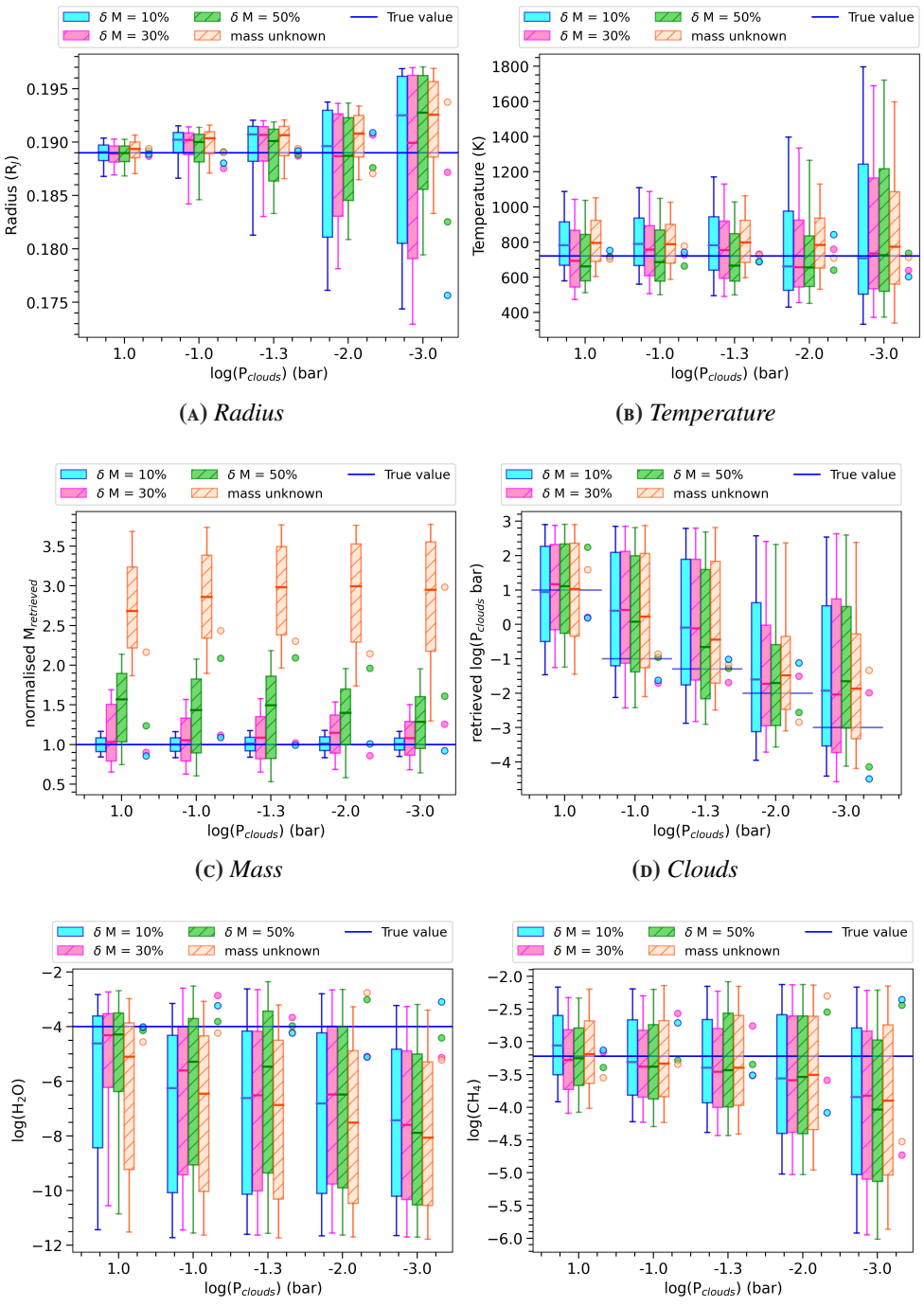

(A) *Radius* (B) *Temperature*

(C) *Mass* (D) *Clouds*

(E) *H_2O mixing ratio* (F) *CH_4 mixing ratio*

Figure 3.17: *Impact of the mass uncertainties on the retrieval for different scenarios of cloudy secondary N_2-dominated atmospheres in the case of μ=5.2. The different coloured boxes represent the different mass uncertainties. The blue lines highlight the true values. The points alongside the boxes highlight the MAP parameters obtained for each analysed case. The size of the box and the vertical segments represent the points within 1σ and 2σ of the median of the distribution (highlighted with solid-lines), respectively.*

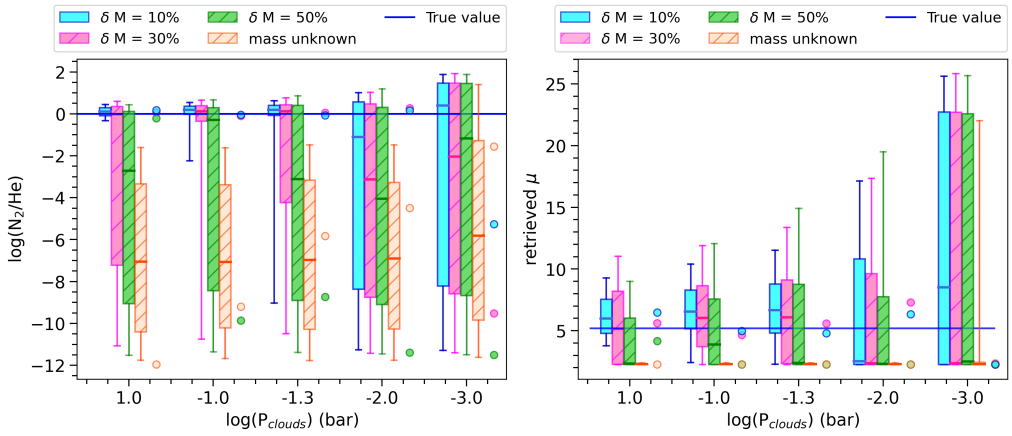

(A) N_2/He (B) μ

FIGURE 3.18: *Impact of the mass uncertainties on the retrieved N_2/He and mean molecular weight for different scenarios of cloudy secondary N_2-dominated atmospheres in the case of μ=5.2. The scale colour and the description of the figure are the same adopted in Fig. 3.17.*

that the retrieved μ tends to be larger than the true value, but these results are not correlated with the mass uncertainties. Additionally (and as expected), the retrieved μ present larger uncertainties when the cloud pressure decreases.

Fig. 3.19d suggests that the mass uncertainties do not impact the retrieved cloud pressure. Indeed, no significant discrepancies can be seen in the retrieved distribution with respect to the mass uncertainty. However, it can be noted a better compatibility between the true values and the MAP values when we considered a mass uncertainties of 10%.

With regards to the atmospheric parameters, the CH_4 mixing ratio is also adequately retrieved when the cloud pressure gets closer to 10^{-3} bar; whereas I am not able to accurately retrieve the H_2O mixing ratio, particularly for cloud pressure lower than 10^{-2} bar. Here, additional observations are needed to increase the SNR and to constrain the mean molecular weight.

H_2O and CO-dominated Atmosphere In Fig. 3.21 and Fig. 3.22 I show the results obtained from the retrieval of H_2O-dominated secondary atmosphere (μ = 5.2). In this case, the mass uncertainties do not significantly impact the retrieval. Here, I am able to constrain the H_2O/He with a slightly increased accuracy for lower mass uncertainties. Also, the cloud pressure and the mean molecular weight are adequately retrieved, even in cases with lower cloud pressure. In the worst scenario considered, when the cloud pressure gets closer to 10^{-3} bar, the retrieved μ is within 2σ of the true value, while the MAP value is closer to the true value.

Additionally, I performed the retrieval for our worst-case scenario, μ = 11.1

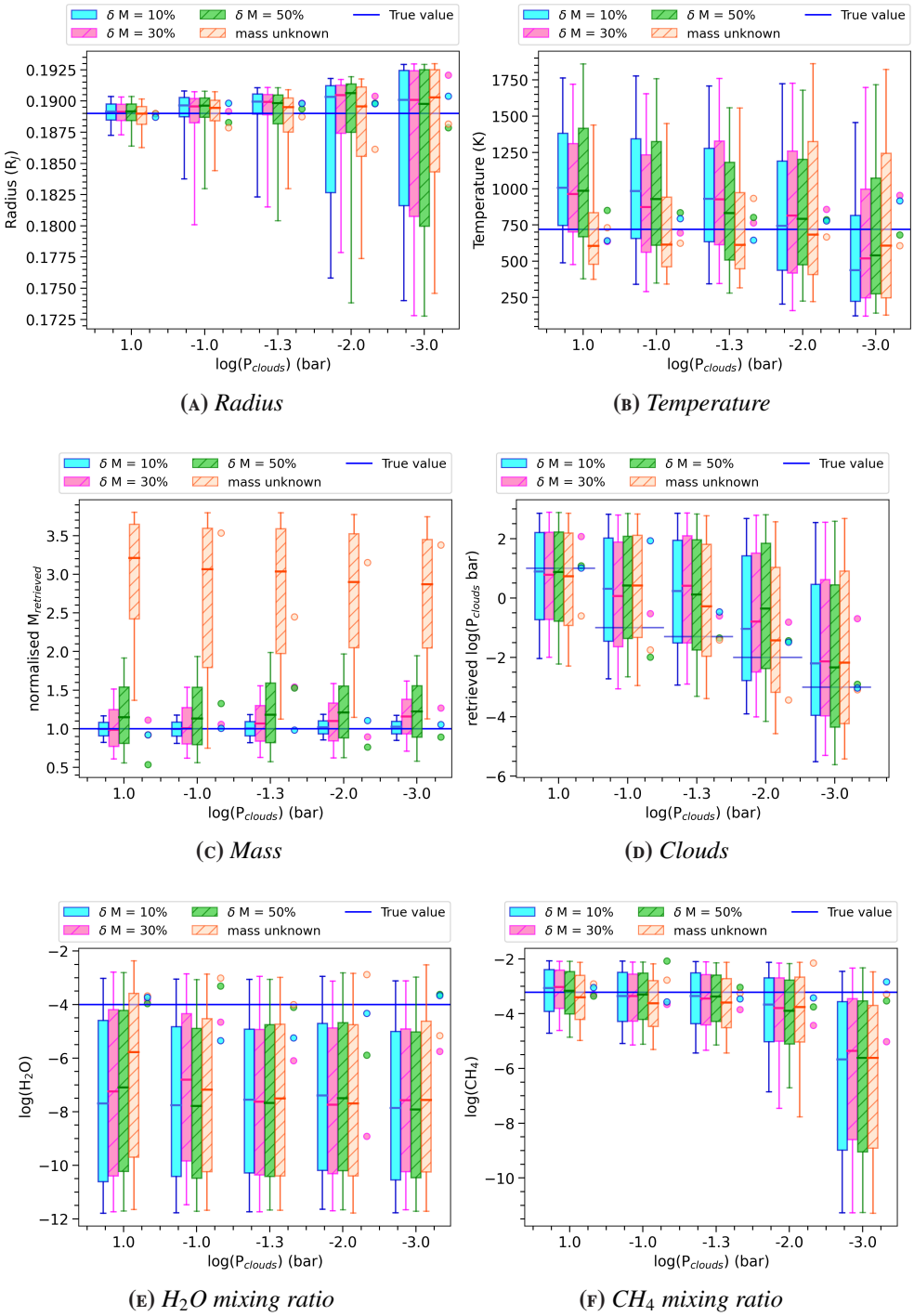

(A) *Radius* (B) *Temperature*

(C) *Mass* (D) *Clouds*

(E) *H_2O mixing ratio* (F) *CH_4 mixing ratio*

Figure 3.19: *Results obtained from the retrieval of N_2-dominated atmosphere in the case of μ=11.1. The different coloured boxes represent the different mass uncertainties. The blue lines highlight the true values. The points alongside the boxes highlight the MAP parameters obtained for each analysed case. The size of the box and the vertical segments represent the points within 1σ and 2σ of the median of the distribution (highlighted with solid-lines), respectively.*

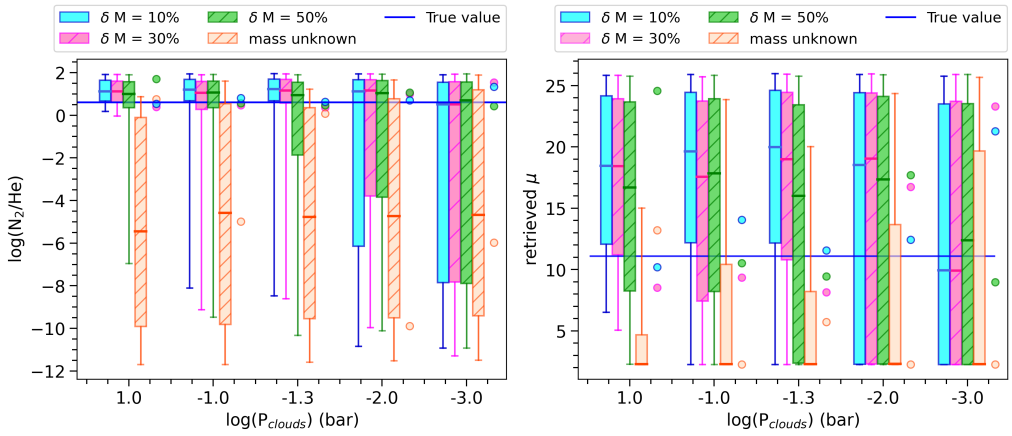

(A) N_2/He (B) μ

FIGURE 3.20: *Results obtained from the retrieved N_2/He and mean molecular weight of N_2-dominated atmosphere in the case of μ=11.1. The scale colour and the description of the figure are the same adopted in Fig. 3.19.*

(see Fig. A.5 in Appendix A.2). From this test, I confirmed that for this target more observations are needed in order to achieve an adequate SNR. The lower SNR values prevent from correctly retrieving the mean molecular weight, which for all cases is higher than the true value. The accuracy in the retrieved μ, namely, within 2σ of the true value, does not depend on the mass uncertainties. The uncertainties of the CH_4 increase by several orders of magnitude with respect to the case μ = 5.2. This is because, in the case of μ = 11.1, the water features tend to dominate the methane features present in the redder region of the spectrum, leading to greater uncertainty in the retrieval of CH_4.

An analogue behaviour is seen for the CO-dominated atmosphere (see Fig. 3.23 and Fig. 3.24 below and Fig. A.6 in Appendix A.2). In particular, in this scenario it can be noted a slight trend with the mass uncertainties in the retrieved CH_4 mixing ratio (see Fig. 3.23f). This increased accuracy in the retrieved CH_4 mixing ratio could be linked to the presence of a prominent CO feature in the redder part of the spectrum that allows to better describe and constrain the CH_4 component.

These results confirm that with a more favourable scenario, represented by an atmosphere with a main gas producing spectral signature, it is possible to better constrain the atmospheric parameters and the mean molecular weight. However, these results do not appear to be strongly correlated with the mass uncertainty, although in some cases, a better estimate of the mass can help to obtain more accurate retrievals.

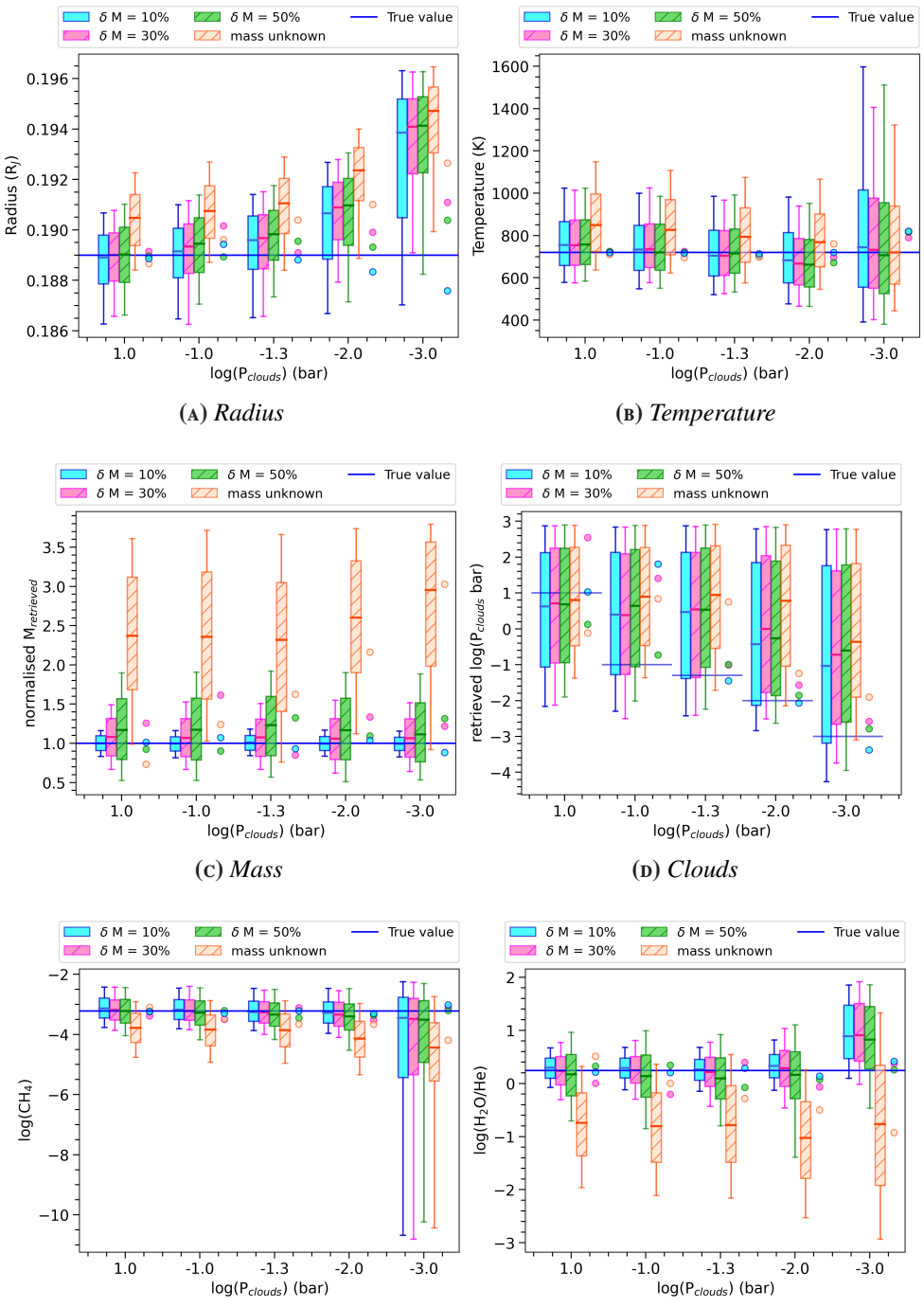

(A) *Radius* (B) *Temperature*

(C) *Mass* (D) *Clouds*

(E) *CH_4 mixing ratio* (F) *H_2O/He*

Figure 3.21: *Retrieval results obtained from different scenarios of cloudy secondary H_2O-dominated atmosphere in the case of μ=5.2. The different coloured boxes represent the different mass uncertainties. The blue lines highlight the true values. The points alongside the boxes highlight the MAP parameters obtained for each analysed case. The size of the box and the vertical segments represent the points within 1σ and 2σ of the median of the distribution (highlighted with solid-lines), respectively.*

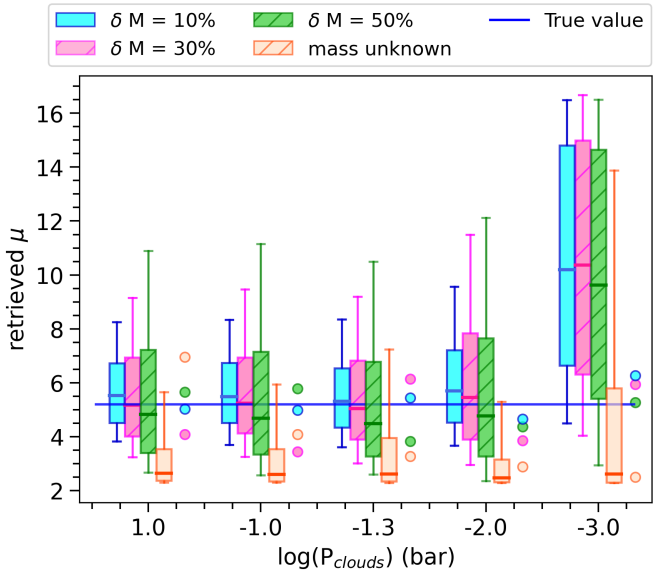

FIGURE 3.22: *Retrieval results for the retrieved mean molecular weight obtained from different scenarios of cloudy secondary H_2O-dominated atmosphere in the case of μ=5.2. The scale colour and the description of the figure are the same adopted in Fig. 3.21*

.

3.2.6 CONCLUSIONS AND FUTURE PROSPECTIVE

I detail my processes of performing several tests to investigate the impact of the planetary mass uncertainties in atmospheric retrieval and to identify the cases where mass measurements and their appropriate precision are needed in the presence of clear or cloudy and primary or secondary atmosphere, in the context of the ESA Ariel Mission.

I considered different scenarios to determine the level of planet mass precision required for robust atmospheric characterisation. I selected three representative targets from the Ariel MRS. For the primordial atmosphere, I considered a hot Jupiter and a hot Neptunian. In addition, I also tested the importance of the SNR on the retrievals and the role of the spectral bands. I also investigated the retrieval of a secondary atmosphere of a super-Earth, also in the presence of clouds. For each planet, I conducted the retrievals with varying levels of precision for the mass measurements. My conclusions are as follows:

1. In the hot-Jupiter case it is possible to accurately retrieve the atmospheric composition of the atmosphere with an accuracy that does not depends on the mass uncertainty. In the worst-case scenario analysed here, when the cloud pressure gets closer to 10^{-3} bar, there is a small discrepancy in the retrieval of the radius that disappears when I performed the retrieval considering a mass uncertainty of about 40% or lower. For all the other parameters, the uncer-

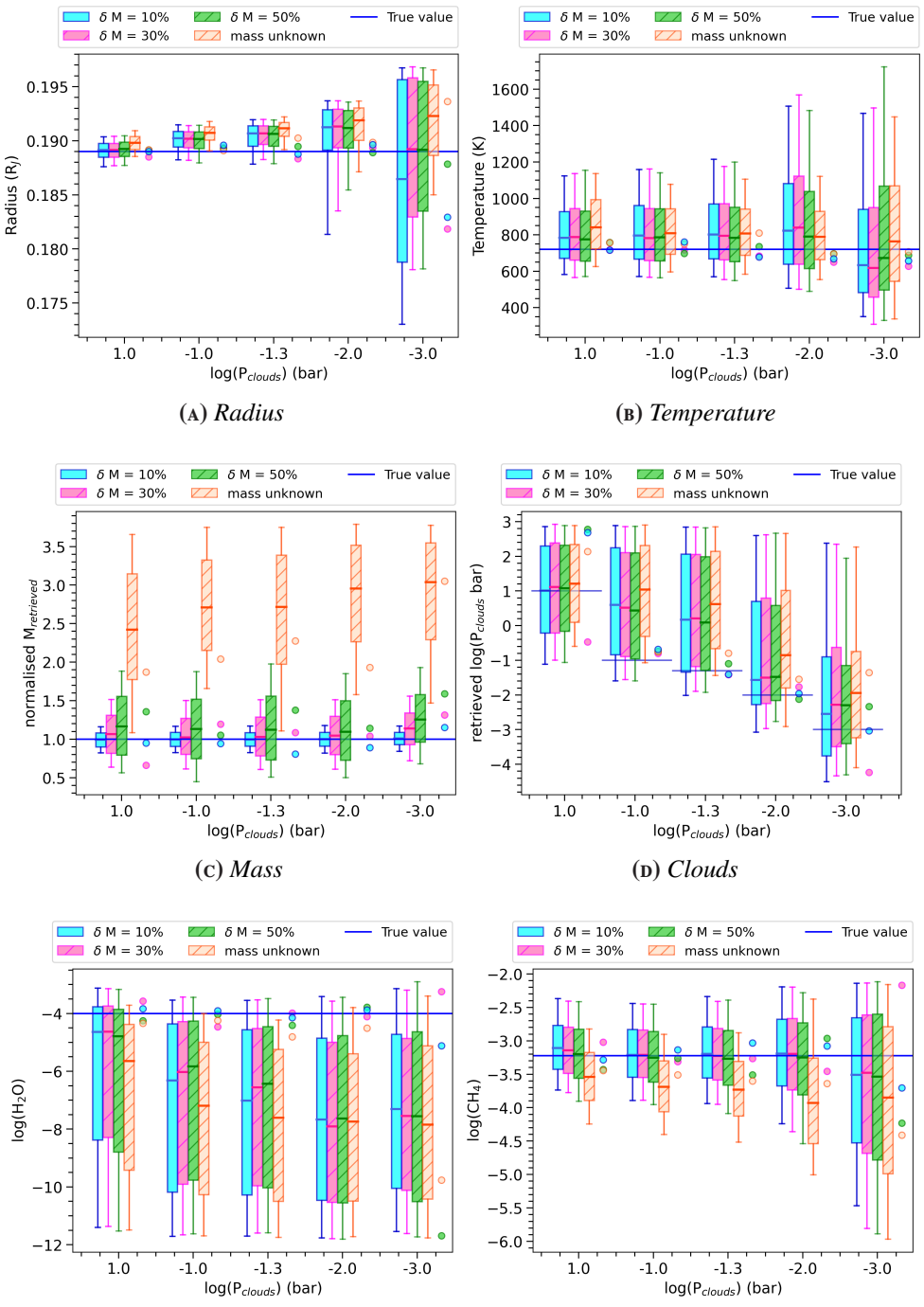

(A) *Radius* (B) *Temperature*

(C) *Mass* (D) *Clouds*

(E) H_2O *mixing ratio* (F) CH_4 *mixing ratio*

Figure 3.23: *Retrieval results obtained from different scenarios of cloudy secondary CO-dominated atmosphere in the case of μ=5.2. The different coloured boxes represent the different mass uncertainties. The blue lines highlight the true values. The points alongside the boxes highlight the MAP parameters obtained for each analysed case. The size of the box and the vertical segments represent the points within 1σ and 2σ of the median of the distribution (highlighted with solid-lines), respectively.*

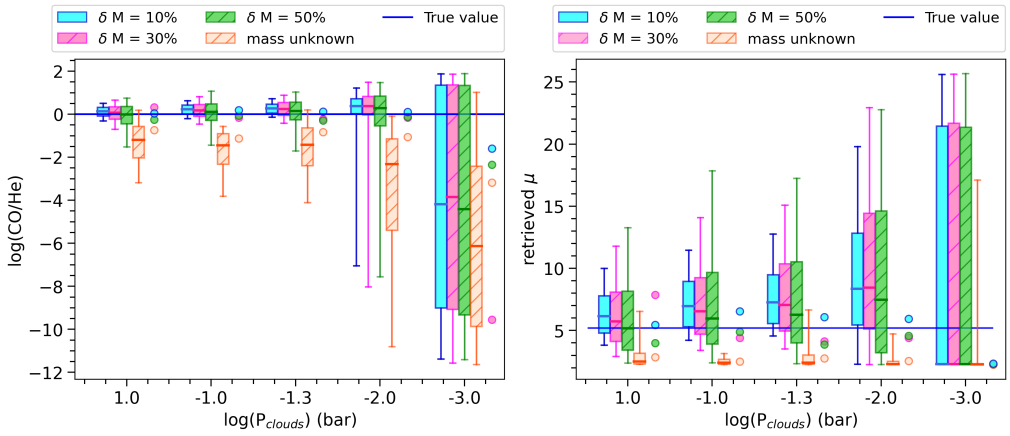

(A) *CO/He* (B) μ

FIGURE 3.24: *Retrieval results of the retrieved CO/He and mean molecular weight obtained from different scenarios of cloudy secondary CO-dominated atmosphere in the case of μ=5.2. The scale colour and the description of the figure are the same adopted in Fig. 3.23.*

tainties increase for high altitude clouds, which can be partially mitigated by increasing the SNR.

2. I could use the atmospheric analysis to estimate the mass of hot-Jupiters with greater precision; for example, I can increase the precision level of the mass estimation from 40% to 10-25% depending on the presence of clouds.

3. For faint stars the uncertainties of all the fitted parameters increase, confirming the relevance of S/N, independently from the knowledge on the mass.

4. Analogue considerations can be made about the hot-Neptunian case. I note increased uncertainties in the presence of high-altitude clouds and, in particular, a worse estimation of the CO mixing ratio and of the temperature when the cloud pressure gets closer to 10^{-3} bar. However, these results are independent from the planetary mass uncertainties.

5. Studying how the SNR at different wavelength ranges impact the retrieval highlights the importance of blue end of the Ariel spectrum, without which it is not possible to retrieve the cloud pressure, bringing on less accurate determination of other relevant parameters.

6. In the N_2-dominated secondary atmosphere case, when the presence of clouds is not considered, a minimum knowledge of the mass (of about 50%) significantly improves the accuracy and precision of the retrieval. Furthermore, a slight additional improvement is observed when considering a more precise estimation of the mass.

7. For a cloudy N_2-dominated secondary atmosphere, an estimation of the mass with an uncertainty of about 50% is needed to correctly retrieve the mean molecular weight. The uncertainties of all the parameters increase for a cloud pressure lower than 10^{-2} bar. A better estimation of the mass could moderately helps in the determination of the atmospheric parameters, in particular with regard to increasing the accuracy of the maximum probability values.

8. The test performed for a H_2O- and CO-dominated atmosphere highlights that in the presence of a main gas producing spectral signatures, it is possible to better constrain the atmospheric parameters and the mean molecular weight. Additionally, in this case, a minimum uncertainty of 50% on the mass is sufficient to measure the atmospheric parameters.

My analysis indicates that, even in the worst-case scenarios investigated in this work, it is sufficient to have a 50% mass precision level to obtain an accurate atmospheric characterisation. This implies that next-generation transmission spectra contain information about planetary mass (see also de Wit and Seager (2013)) and, thus, even a priori uncertainty as larger as 50% on the mass does not affect retrieval. On the other hand, going into an atmospheric characterisation without any knowledge of a planetary mass could compromise the ability to retrieve the atmospheric composition in cloudy primary atmospheres and in secondary atmospheres.

These results can be used in the preparation and target prioritisation of RV surveys supporting atmospheric characterisation studies.

The work presented here is a step forward towards the preparation of the Ariel mission. From this point of view, I scheduled other works, summarised below, that will allow to define the information that we will be able to obtain from the atmospheric retrieval:

- The analysis of the planetary mass uncertainty on the atmospherical retrieval using different chemistry models;

- The impact of a new clouds model on atmospheric retrieval;

In the preparation of the Ariel mission, this work can help in defining the strategy of a RV monitoring for those targets included in the MRS still lacking of a measurement of their mass. To this purpose, I will reproduce this analysis and quantify the impact of the mass uncertainty on the atmospheric retrieval for all the targets of Ariel MRS. This is already a work in progress and in the following section I show the results already obtained for some of the selected targets of the Ariel MRS.

CHAPTER 4

Analysis of targets of the MRS of Ariel

Based on the results described in the previous chapter about the impact of the planetary mass uncertainties on the accuracy of atmospheric retrieval and in preparation for the Ariel mission, in this chapter I analyse a sub-sample from the Ariel Mission reference sample (MRS).

According to Edwards and Tinetti (2022), the Ariel MRS will contain a selection of planets that could be observed in the prime mission lifetime. Approximately 2000 targets will be included in the MRS and half of them will actually be investigated by Ariel. To maximise the science return of Ariel, the observations will be performed in four tiers (Tinetti et al., 2021). Tiers 1-3 are devoted to transiting planets. Each one will produce spectra with a different binning to achieve the required signal-to-noise ratio and will include a decreasing number of targets, aiming to obtain unprecedented statistics of the planetary atmospheres and a full characterisation for a number of benchmark cases. Each tier requires a different number of transits. In the analysis described below, I will take into account the number of transits required for the Tier-2 derived by Edwards and Tinetti (2022). Note that the number of transits required is based on the requirement to achieve SNR ~ 7 and the assumption of a clear-sky primordial atmosphere, which could not be the case for many planets. Furthermore, the physical parameters used to describe the star-planet systems are constantly being updated, and for this reason, I adopted the stellar and planetary parameters from the recent literature that do not necessarily match those used by Edwards and Tinetti (2022). In some cases, I will explore different parameters available in the literature. For this reason, the estimated number of transits could not guarantee an adequate SNR.

From the following analysis, we expect to be able to define in which scenarios and for which targets the current planetary mass estimate is sufficiently accurate and precise to obtain an accurate atmospheric retrieval, in which cases we need a better mass estimate and to what level of precision. In addition, in preparation for the Ariel mission, it will provide useful indications for the selection of the targets

to be observed from Ariel in the various tiers. Indeed, in cases where, in light of the new estimates of stellar and planetary parameters obtained from the literature, the currently required number of transits is not sufficient to achieve an adequate SNR, the following analysis could suggests in which cases a higher number of transits could lead us to a more robust atmospheric characterisation, or in which cases it is more recommended to discard the target for the next tier.

To this purpose, I selected different targets from Ariel MRS, based on the radius and the mass of the planet and the spectral type of the host star as in Edwards and Tinetti (2022), in order to cover a large range of mass-radius distribution. In particular, I selected the following targets and I separated them into two classes, Neptunian planets (primordial atmosphere) and sub-Neptunes and super-Earth (secondary atmosphere) using a threshold value for the mass (M = 10 $M_{\oplus}$):

- Neptunian planets:
  - HD 3167 c ($\delta M \simeq 8\%$)
  - HD 152843 b ($\delta M \simeq 55\%$)
  - TOI-1130 b ($\delta M \simeq 100\%$)
  - AUMic c (three different configurations: $\delta M \simeq 85\%$ (Martioli et al., 2021), mass upper limit (Cale et al., 2021) and $\delta M \simeq 30\%$ (Zicher et al., 2022))
  - HD 106315 c ($\delta M \simeq 25\%$)
  - TOI-451 d ($\delta M \simeq 100\%$)
  - KOI-94 c (two different configurations, see Section 4.1.7)
  - Kepler-450 b ($\delta M \simeq 60\%$)
  - TOI-1728 b ($\delta M \simeq 20\%$)
  - HATS-37A b ($\delta M \simeq 42\%$)
- Sub-Neptunes and Super-Earths:
  - GJ 9827 c ($\delta M \simeq 25\%$)
  - LTT 1445A b (two different configurations: $\delta M \simeq 90\%$ (Winters et al., 2019) and $\delta M \simeq 10\%$ (Winters et al., 2022))
  - K2-3 c ($\delta M \simeq 40\%$)
  - K2-138 g ($\delta M \simeq 121\%$)
  - K2-32 d ($\delta M \simeq 40\%$)

– HIP 41378 b ($\delta M \simeq 100\%$)

– TOI-269 b ($\delta M \simeq 16\%$)

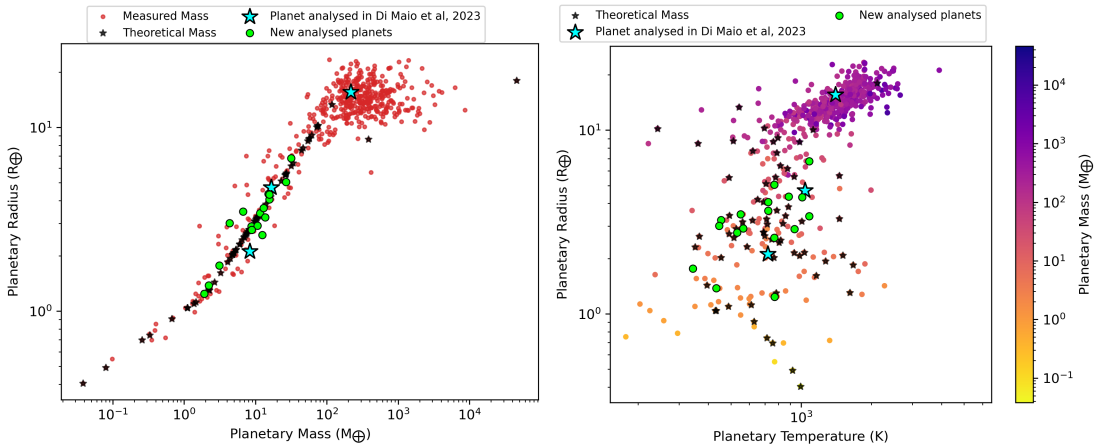

(A) *Mass-Radius distribution* (B) *Temperature-Radius distribution*

FIGURE 4.1: *(a) Mass-radius distribution of Ariel MRS (Edwards and Tinetti, 2022). I highlighted with black stars the planets for which we have a theoretical mass estimate based on the mass-radius relation. (b) Temperature-radius distribution of Ariel MRS (Edwards and Tinetti, 2022). The points are coloured following a colour scale from yellow to blue as a function of the mass of the planets. I highlighted the planets analysed in Di Maio, C. et al. (2023) with cyan stars and the the new subsample selected from the MRS, as in Edwards and Tinetti (2022), with green dots.*

In Figure 4.1 I show the mass-radius and radius-temperature distributions for the planets included in the Ariel MRS. In Figures 4.1a and 4.1b I highlighted with black stars the planets of the Ariel MRS for which we have a theoretical mass estimate based on the mass-radius relation (Chen and Kipping, 2017). In addition, I highlighted with cyan stars the planets analysed in Di Maio, C. et al. (2023) and with green dots the neptunian planets and the super-Earths, selected from the MRS for a more detailed analysis. In Figure 4.1b I also used a colour scale to evidence the planetary mass distribution. In Tables 4.1 and 4.2 I listed all the stellar and planetary parameters used to reproduce the forward models and simulate the spectra for the selected targets, as observed by Ariel, and original number of observations required for the Tier-2 as derived by Edwards and Tinetti (2022).

I performed the retrieval for the selected Neptunian planets and super-Earths simulating the spectrum of a primordial and N_2-dominated secondary atmosphere, respectively, as observed by Ariel. I convolved the high resolution forward spectra through the instrument model by using ArielRad (ArielRad v. 2.4.6, Mugnai et al. (2020), Ariel Payload v. 0.0.5, ExoRad v. 2.1.94). To simulate the Ariel Tier-2 performance, I took into account the number of transits required for the Tier-2 (see Table 4.1 and Table 4.2) to obtain the expected SNR.

Table 4.1: *Stellar and planetary parameters used to produce the forward models for the analysed neptunian planets selected from the MRS of Ariel. The number of transits required for Tier-2 as derived by Edwards and Tinetti (2022) is reported in the last column.*

Star	M_* ($M_\odot$)	R_* ($R_\odot$)	log g_* (cgs)	T_{eff} (K)	[Fe/H]	Distance (pc)
HD3167	$0.852^{+0.026(a)}_{-0.015}$	$0.871 \pm 0.006^{(a)}$	$4.47 \pm 0.12^{(a)}$	$5300 \pm 73^{(a)}$	$0.037 \pm 0.048^{(a)}$	$47.29^{+0.15(b)}_{-0.15}$
HD 152843	$1.15 \pm 0.4^{(c)}$	$1.43 \pm 0.2^{(c)}$	$4.19 \pm 0.03^{(c)}$	$6310 \pm 100^{(c)}$	$-0.16 \pm 0.05^{(c)}$	$107.898^{+0.318(b)}_{-0.316}$
TOI-1130	$0.684^{+0.016(d)}_{-0.02}$	$0.871 \pm 0.06^{(d)}$	$4.600^{+0.020(d)}_{-0.018}$	$4250 \pm 67^{(d)}$	$> 0.2^{(d)}$	$58.2609^{+0.1700(b)}_{-0.1691}$
AUMic	$0.50 \pm 0.03^{(e)}$	$0.75^{+0.029(e)}_{-0.03}$	$4.39 \pm 0.03^{(f)}$	$3700 \pm 100^{(e)}$	-	$9.722100 \pm 0.004625^{(b)}$
AUMic	$0.50 \pm 0.03^{(f)}$	$0.75 \pm 0.03^{(f)}$	$4.39 \pm 0.03^{(f)}$	$3700 \pm 100^{(f)}$	-	$9.722100 \pm 0.004625^{(b)}$
AUMic	$0.50 \pm 0.03^{(g)}$	$0.75 \pm 0.03^{(f)}$	$4.39 \pm 0.03^{(f)}$	$3700 \pm 100^{(f)}$	-	$9.722100 \pm 0.004625^{(b)}$
HD 106315	$1.091 \pm 0.036^{(h)}$	$1.296 \pm 0.058^{(h)}$	$4.252 \pm 0.043^{(h)}$	$6327 \pm 48^{(h)}$	$-0.311 \pm 0.079^{(h)}$	$109.353^{+0.691(b)}_{-0.681}$
TOI-451	$0.950 \pm 0.02^{(i)}$	$0.879 \pm 0.032^{(i)}$	$4.56^{+0.07(b)}_{-0.08}$	$5550 \pm 56^{(i)}$	-	$123.739^{+0.386(b)}_{-0.384}$
KOI-94	$1.277 \pm 0.5^{(j)}$	$1.52 \pm 0.14^{(j)}$	$4.181 \pm 0.066^{(j)}$	$6128 \pm 58^{(j)}$	$0.0228 \pm 0.0020^{(j)}$	$477.051^{+5.000(b)}_{-4.899}$
Kepler-450	$1.334^{+0.023(k)}_{-0.022}$	$1.600^{+0.028(k)}_{-0.008}$	$4.08^{+0.11(b)}_{-0.08}$	$6197^{+130(b)}_{-187}$	$0.128 \pm 0.014^{(b)}$	$455.982^{+5.189(b)}_{-5.074}$
TOI-1728	$0.646^{+0.023(l)}_{-0.022}$	$0.6243^{+0.0100(l)}_{-0.0097}$	$4.67 \pm 0.05^{(l)}$	$3975 \pm 77^{(l)}$	$0.09 \pm 0.13^{(l)}$	$60.80^{+0.14(l)}_{-0.13}$
HATS-37A	$0.843^{+0.017(m)}_{-0.012}$	$0.877^{+0.019(m)}_{-0.012}$	$4.478 \pm 0.017^{(m)}$	$5326 \pm 44^{(m)}$	$0.051 \pm 0.029^{(m)}$	$211.1 \pm 2.5^{(m)}$
Planet	**M_p (M_J)**	**R_p (R_J)**	**T_p (K)**	**a (AU)**	**T_{14} (h)**	**Tier-2 Transit number (Nobs)**
HD3167 c	$0.03357^{+0.00267(a)}_{-0.00255}$	$0.2608^{+0.0000157(a)}_{-0.0000154}$	$565.0^{+8.6(a)}_{-8.5}$	$0.1783 \pm 0.0025^{(a)}$	$4.869^{+0.026(a)}_{-0.025}$	26
HD 152843 b	$0.03637^{+0.02070(c)}_{-0.01932}$	$0.304^{+0.012(c)}_{-0.011}$	$1084.646972^{(n)}$	$0.1053^{+0.0030(c)}_{-0.0031}$	$5.53 \pm 0.11^{(c)}$	44
TOI-1130 b	$0.0407^{(*)}$	$0.326 \pm 0.009^{(d)}$	$810 \pm 15^{(d)}$	$0.04394^{+0.00035(d)}_{-0.00038}$	$2.30^{+0.18(d)}_{-0.14}$	19
AUMic c	$0.0428 \pm 0.0359^{(e)}$	$0.289 \pm 0.014^{(e)}$	$454 \pm 16^{(e)}$	$0.1101 \pm 0.0022^{(e)}$	$4.5 \pm 0.8^{(e)}$	6
AUMic c	$0.0698 \pm 0.0211^{(f)}$	$0.249^{+0.028(o)}_{-0.027}$	$454 \pm 16^{(e)}$	$0.1101 \pm 0.0022^{(e)}$	$4.5 \pm 0.8^{(e)}$	6
AUMic c	$\leq 0.063^{(g)}$	$0.249^{+0.028(o)}_{-0.027}$	$454 \pm 16^{(e)}$	$0.1101 \pm 0.0022^{(g)}$	$4.5 \pm 0.8^{(e)}$	6
HD 106315 c	$0.0478 \pm 0.0116^{(h)}$	$0.388 \pm 0.021^{(h)}$	$886 \pm 20^{(h)}$	$0.1536 \pm 0.0017^{(h)}$	$4.638 \pm 0.072^{(h)}$	9
TOI-451 d	$0.049^{(*)}$	$0.363 \pm 0.013^{(i)}$	$722^{+9\ (i)}_{-11}$	$0.1208^{+0.0048(i)}_{-0.0052}$	$4.097 \pm 0.024^{(i)}$	51
KOI-94 c	$0.049^{+0.018(j)}_{-0.049}$	$0.385 \pm 0.037^{(j)}$	$1012^{(j)}$	$0.1013 \pm 0.0013^{(j)}$	$5.2291 \pm 0.0237^{(p)}$	127
Kepler-450 b	$0.0610^{+0.0349(k)}_{-0.0214}$	$0.54272 \pm 0.00020^{(k)}$	$767^{(q)}$	$0.2004^{(k)}$	$8.1223 \pm 0.0132^{(p)}$	103
TOI-1728 b	$0.08426^{+0.01708(l)}_{-0.01614}$	$0.451^{+0.014(l)}_{-0.015}$	$767 \pm 8^{(l)}$	$0.0391 \pm 0.0009^{(l)}$	$1.96 \pm 0.03^{(l)}$	12
HATS-37A b	$0.099 \pm 0.042^{(m)}$	$0.606 \pm 0.016^{(m)}$	$1085^{+16(m)}_{-12}$	$0.04914^{+0.00033(m)}_{-0.00023}$	$2.914^{+0.024(m)}_{-0.024}$	17

Notes. [(a)] Bourrier et al. (2022) , [(b)] Stassun et al. (2019) , [(c)] Eisner et al. (2021) , [(d)] Huang et al. (2020) , [(e)] Martioli et al. (2021) , [(f)] Zicher et al. (2022) , [(g)] Cale et al. (2021) , [(h)] Barros et al. (2017) , [(i)] Newton et al. (2021) , [(j)] Weiss et al. (2013) , [(k)] Yoffe et al. (2021) , [(l)] Kanodia et al. (2020) , [(m)] Jordan et al. (2020) , [(n)] Edwards and Tinetti (2022) , [(o)] Gilbert et al. (2022) , [(p)] Morton et al. (2016) , [(q)] Coughlin et al. (2016) , [(*)] Mass-Radius relationship

Table 4.2: *Stellar and planetary parameters used to produce the forward models for the analysed super-Earths selected from the MRS of Ariel. The number of transits required for Tier-2 as derived by Edwards and Tinetti (2022) is reported in the last column.*

Star	M_* ($M_\odot$)	R_* ($R_\odot$)	log g_* (cgs)	T_{eff} (K)	[Fe/H]	Distance (pc)
GJ9827	$0.606^{+0.020}_{-0.014}$ [a]	$0.5994^{+0.0081}_{-0.0085}$ [a]	$4.657^{+0.015}_{-0.010}$ [a]	4340^{+40}_{-53} [a]	-0.28 ± 0.09 [a]	$29.66^{+0.05}_{-0.05}$ [b]
LTT1445A	0.256± 0.014 [c]	$0.276^{+0.024}_{-0.019}$ [c]	$4.967^{+0.061}_{-0.075}$ [c]	3337 ± 150 [c]	-0.34 ± 0.08 [c]	6.869 ± 0.004 [b]
LTT1445A	0.257± 0.014 [d]	$0.265^{+0.011}_{-0.010}$ [d]	-	3340 ± 150 [d]	-0.34 ± 0.09 [d]	6.869 ± 0.004 [b]
K2-3	0.62±0.06 [e]	0.60±0.06 [e]	4.66±0.5 [e]	3835±70 [e]	-0.01±40.09 [e]	44.07±0.11 [b]
K2-138	$0.935^{+0.019}_{-0.023}$ [f]	$0.863^{+0.031}_{-0.018}$ [f]	$4.54^{+0.02}_{-0.04}$ [f]	$5356.3^{+41.8}_{-13.1}$ [f]	$0.134^{+0.128}_{-0.176}$ [f]	$202.59^{+2.03}_{-1.99}$ [b]
K2-32	0.83±0.02 [g]	0.86 ± 0.02 [g]	4.49 ±0.03 [g]	5271^{+39}_{-35} [g]	-0.06 ±0.03 [g]	$157.68^{+1.31}_{-1.29}$ [b]
HIP 41378	$1.15^{+0.064}_{-0.06}$ [h]	1.40±0.19 [h]	4.18±0.1 [i]	6199±50 [h]	-0.11±0.08 [i]	$106.289^{+0.676}_{-0.668}$ [b]
TOI-269	0.3917± 0.0095 [j]	0.398± 0.012 [j]	4.831 ± 0.029 [j]	3514 ± 70 [j]	-0.29 ± 0.12 [j]	$57.02^{+0.08}_{-0.08}$ [b]
Planet	**M_p (M_J)**	**R_p (R_J)**	**T_p (K)**	**a (AU)**	**T_{14} (h)**	**Tier-2 Transit number (Nobs)**
GJ9827 c	0.00604 ± 0.00154 [k]	0.1070 ± 0.0041 [k]	771^{+31}_{-18} [l]	0.03896 ± 0.00040 [k]	1.825 ± 0.037 [a]	11
LTT1445A b	$0.0069^{+0.0053}_{-0.0066}$ [c]	$0.123^{+0.012}_{-0.011}$ [c]	433^{+28}_{-27} [c]	$0.03807^{+0.00068}_{-0.00071}$ [c]	1.38 ± 0.03 [c]	4
LTT1445A b	$0.00903^{+0.00082}_{-0.00079}$ [d]	$0.1164^{+0.0059}_{-0.0054}$ [d]	424 ± 21 [d]	$0.03813^{+0.00068}_{-0.00070}$ [d]	$1.367^{+0.017}_{0.016}$ [d]	4
K2-3 c	$0.0098^{+0.0041}_{-0.0038}$ [e]	0.158±0.016 [e]	344±29 [m]	$0.1413^{+0.0044}_{-0.0047}$ [e]	$3.633^{+0.491}_{-0.191}$ [m]	95
K2-138 g	$0.0136^{+0.0165}_{-0.03219}$ [f]	$0.2688^{+0.0270}_{-0.0224}$ [f]	445^{+31}_{-30} 25 [n]	$0.23109^{+0.00154}_{-0.00196}$ [f]	$4.75^{+0.80}_{-1.42}$ [f]	106
K2-32 d	0.021 ±0.008 [g]	$0.3108^{+0.0100}_{-0.0115}$ [g]	550^{+8}_{-9} 25 [g]	$0.18422^{+0.00152}_{-0.00144}$ [g]	$4.888^{+0.051}_{-0.048}$ [g]	50
HIP 41378 b	0.027*	0.259±0.039 [h]	937.14 [o]	0.1287 [i]	4.95 [i]	83
TOI-269 b	0.02777 ± 0.0044 [j]	0.247 ± 0.011 [j]	531 ± 25 [j]	0.0345 ± 0.0015 [j]	0.92 ± 0.06 [j]	73

Notes. [a] Rice et al. (2019) , [b] Stassun et al. (2019) , [c] Winters et al. (2019) , [d] Winters et al. (2022) , [e] Damasso et al. (2018) , [f] Lopez et al. (2019) , [g] Lillo-Box et al. (2020) , [h] Vanderburg et al. (2016) , [i] Edwards and Tinetti (2022) , [j] Cointepas et al. (2021) , [k] Kosiarek et al. (2021) , [l] Prieto-Arranz et al. (2018) , [m] Sinukoff et al. (2016) , [n] Hardegree-Ullman et al. (2021) , [o] Morton et al. (2016) ,

The forward spectra were obtained using H_2O, CH_4 and CO as trace gases, with mixing ratios of 10^{-5}, 5×10^{-6} and 10^{-4}, respectively, for the primordial atmospheres. For the secondary atmosphere, in the forward spectra I considered two different scenarios with different values of the mean molecular weight (μ = 2.3, N_2/He = 10^{-10}; μ = 7.6, N_2/He = 2) and I used H_2O and CH_4 as trace gases (H_2O mixing ratio = 10^{-4} and CH_4 mixing ratio = 6×10^{-4}) to explore different atmospheric compositions (see a more detailed description of spectral retrieval in Section 2.4.2). In the next sections I will describe the analysed targets in detail and summarise the results of retrievals. In order to evaluate the goodness of the analysis, I defined two parameters related to systematic (acc.) and random (prec.) uncertainties, as shown below:

- Acc. (=accuracy) and MAP Acc. (= maximum-a-posteriori accuracy):
  - for linear parameters, such as planetary mass, radius, and temperature, is calculated as follows:

$$acc. = \left| \frac{true - ret}{true} \right| * 100 \tag{4.1}$$

    where *true* is the input value, and *ret* is the median (or the MAP) value of the posterior distribution.
  - for logarithmic parameters, such as the cloud pressure and the atmospheric components, the accuracy (and MAP-accuracy) is calculated as the difference between the *true* and the *ret* values of the median and MAP of the distributions.
- Prec. (=precision): for linear parameters, left and right precisions are calculated as:

$$prec = \left| \frac{q_{50} - q}{q_{50}} \right| * 100 \tag{4.2}$$

  where q_{50} is the 50% quantile of the a posterior distribution, while q represents the quantiles at 16% and 84%, for left and right precisions, respectively. For logarithmic parameters, the left and right precisions are calculated by considering only the difference between q_{50} and q.

In order to evaluate the parameters obtained from the retrieval in terms of accuracy and precision, as defined above, I selected three thresholds as specified in the Table 4.3, to classify the results. In the following sections, I evaluated the retrieved values as accurate/moderately accurate/not accurate and precise/moderately precise/not precise, highlighting the values with the corresponding colours (white/orange/red).

Table 4.3: *Evaluation criteria for the accuracy and precision of the retrieved parameters.*

	Acc./MAP-Acc.			Prec.		
Param	Accurate	Moderately Acc.	Not Accurate	Precise	Moderately Prec.	Not Precise
Linear	<20%	20%-50%	>50%	<20%	20%-50%	>50%
Logarithmic	< 1 decades	1-2 decades	> 2 decades	< 1 decades	1-2 decades	> 2 decades

Notes. Linear parameters are evaluated in percentage terms, while the logarithmic parameters are evaluated in terms of the difference of orders of magnitude between the input value and the retrieved (or MAP) value.

The results of this analysis are summarised for each target in additional tables reported in Appendix B.

4.1 Neptunians - Primordial atmospheres

4.1.1 HD3167 c

HD 3167 system is of particular interest as it hosts four known planets (Vanderburg et al., 2016; Christiansen et al., 2017; Gandolfi et al., 2017; Bourrier et al., 2022): HD 3167 b (P = 0.96 d, R_p = 1.627 $^{+0.083}_{-0.058}$ $R_\oplus$, M_p = 4.73± $^{+0.28}_{-0.29}$ $M_\oplus$), HD 3167 d (P = 8.51 d, $M_p \sin i$ = 5.03±0.50 $M_\oplus$), HD 3167 e (P = 102.09 d, $M_p \sin i$ = 9.74 $^{+1.20}_{-1.15}$ $M_\oplus$) and HD 3167 c (P = 29.84 d, $R_p = 2.923^{+0.098}_{-0.109}$ $R_\oplus$, $M_p = 10.67^{+0.85}_{-0.81}$ $M_\oplus$).

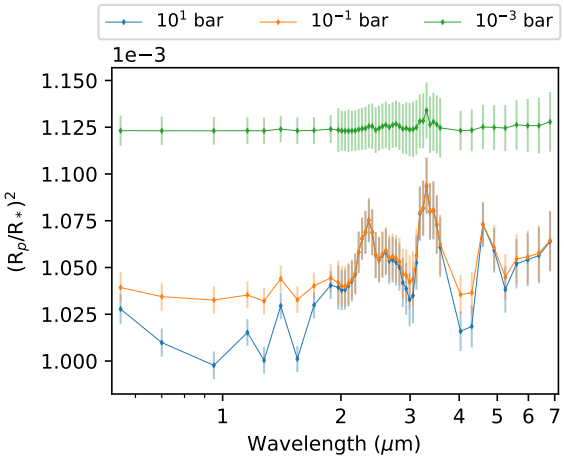

Figure 4.2: *Simulated spectra of HD3167 c as observed by Ariel, obtained considering different cloud pressures.*

According to Bourrier et al. (2022), the planetary mass of HD3167 c has an estimated uncertainty of about 8%. Given the high precision of this mass estimation, I investigated the accuracy of the retrieval for different cloudy scenarios. Figure 4.2 shows the simulated spectra of HD3167 c for the number of transits required for Tier-2 (N_{obs} = 26), at cloud pressures (P_{clouds} = 10^{1}, 10^{-1}, 10^{-3} bar). Characteristics of the target and host star are listed in Table 4.2.

The results of the retrieval are summarised in Table B.1 and Figure 4.3.

As shown in Figure 4.3 we are able to accurately retrieve all the atmospheric components when $P_{clouds} \geq 10^{-1}$ bar, while H_2O and CO are not accurately and not precisely retrieved in the presence of high altitude clouds. However, the MAP value is accurately retrieved in all the tested scenario excepted for the CO mixing ratio when $P_{clouds} = 10^{-3}$ bar, where the MAP retrieved value is moderately accurate.

In Figure 4.3c I showed the retrieved cloud pressure for the different considered scenarios. It can be seen that all the retrieved distributions are perfectly distinguishable, as confirmed by the Kolmogorov-Smirnov test (KS test) ($p_{value} << 0.05$) performed between the three distributions (10^{-1} - 10^{1} bar, 10^{-1} - 10^{-3} bar,10^{-1} - 10^{-3} bar). Consequently, I performed the retrieval on the simulated spectra of HD 1367 c, assuming the number of transits required by Tier-1 (N_{obs} = 4, see Figure 4.4a). As can be seen in Figure 4.4b and also confirmed by the KS test, we are able to discriminate between the different cloudy scenarios since the Tier-1. This results suggests that a valid observing strategy could be to test the cloudy conditions since during the Tier-1 and, in case of high altitude clouds probably plan to reach a higher SNR increasing the number of transits.

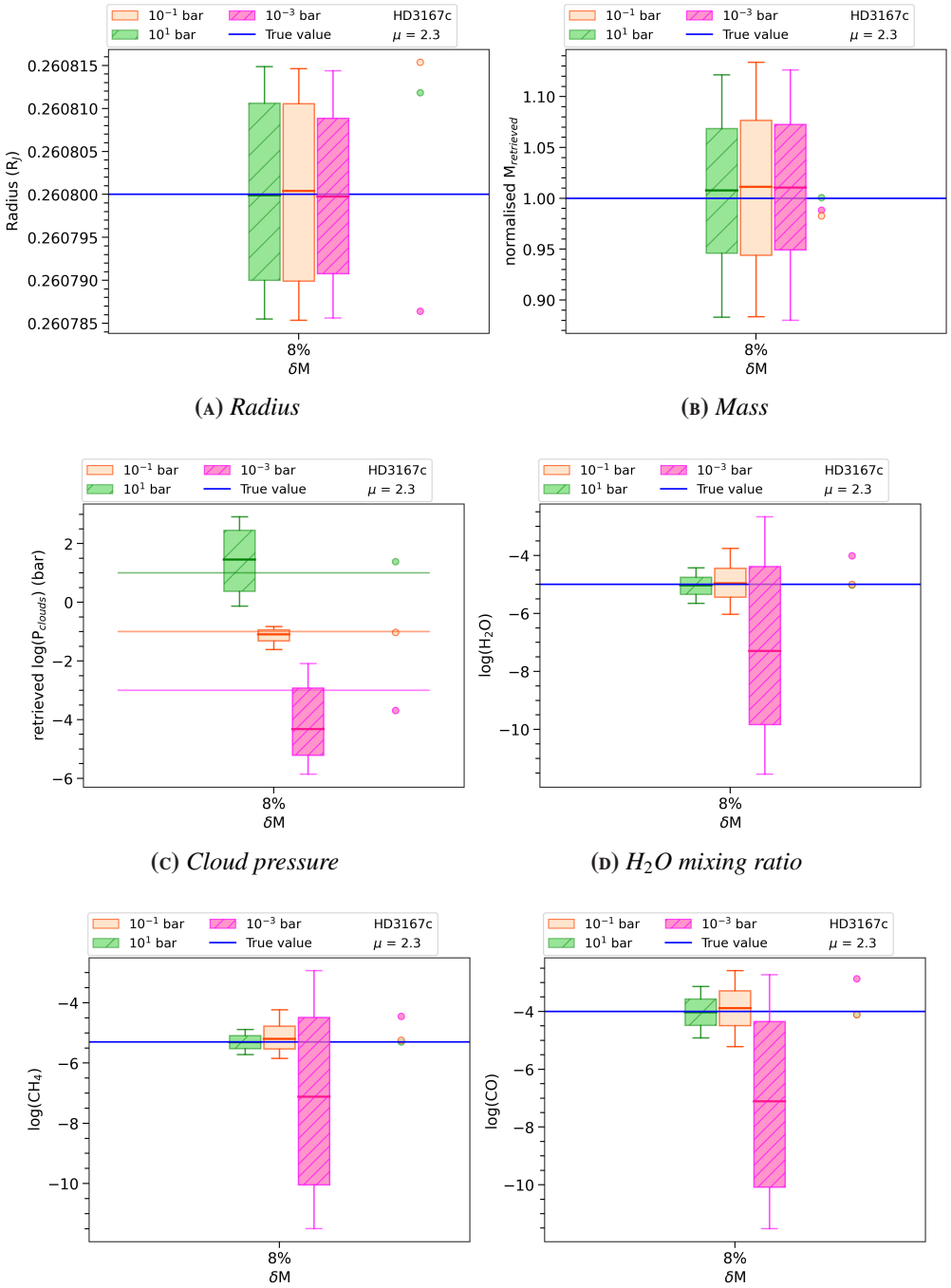

(A) *Radius* (B) *Mass*

(C) *Cloud pressure* (D) *H_2O mixing ratio*

(E) *CH_4 mixing ratio* (F) *CO mixing ratio*

FIGURE 4.3: *Impact of mass uncertainties on the retrieval performed for the hypothetical primordial atmosphere of HD 3167 c for different cloud pressures (P_{clouds} = 10^{1} bar in green, P_{clouds} = 10^{-1} bar in orange, and P_{clouds} = 10^{-3} bar in magenta) as a function of the mass uncertainty. The blue line highlights the input value. The points alongside the boxes highlight the MAP values obtained for each analysed case. The size of the boxes and the vertical segments represent the points within 1σ and 2σ of the median of the distribution (highlighted with solid lines), respectively.*

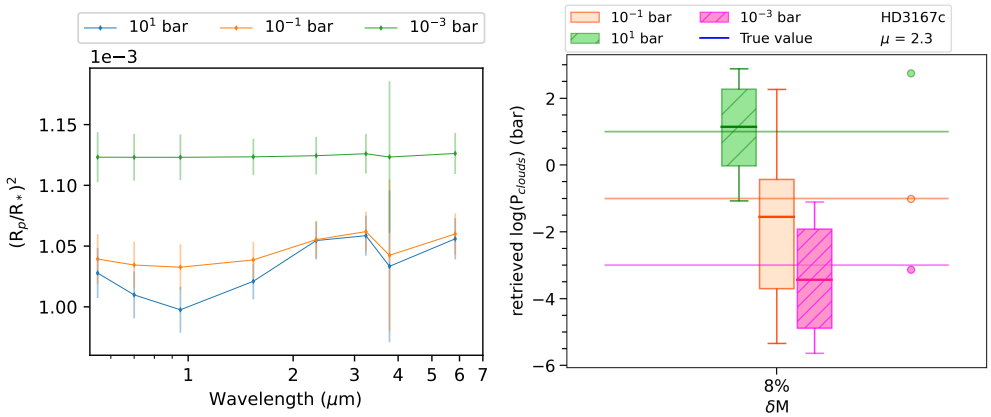

(A) *Tier-1* (B) *Cloud pressure*

Figure 4.4: *(A) Spectra of HD3167 c, as observed by Ariel, obtained considering different cloudy scenarios and assuming the number of transits required for Tier-1. (B) Comparison between the retrieved cloud pressure of HD3167 b obtained for different cloud pressures as a function of the mass uncertainty. Colour scale and description of Figure B are the same as in Figure 4.3.*

4.1.2 HD 152843 b

HD 152843 b ($M_b = 11.56^{+6.58}_{-6.14}$ $M_\oplus$, $R_b = 3.41\ ^{+0.14}_{-0.12}$ $R_\oplus$) is a Neptune-like exoplanet discovered by Eisner et al. (2021) using data from TESS. It is the inner planet of a two-planet system orbiting a bright (V = 8.85 mag) early G dwarf (1.43 $R_\odot$, 1.15 $M_\odot$).

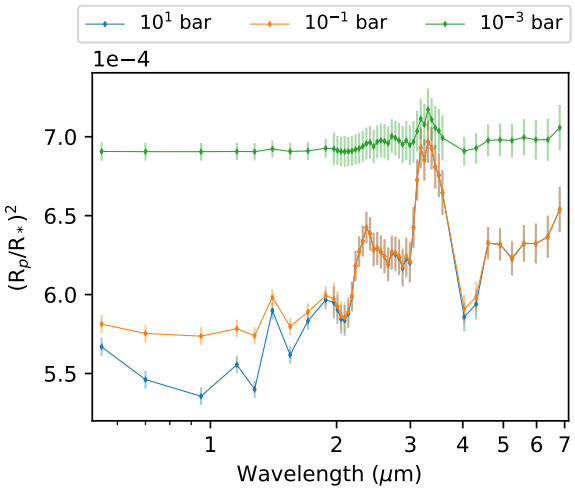

Figure 4.5: *Simulated spectra of HD 152843 b, as observed by Ariel, obtained considering different cloud pressures.*

Since Eisner et al. (2021) estimated the mass of HD 152843 b from radial velocity measurements with a mass uncertainty of about 55%, I performed the retrieval with a planetary level of precision of 10%, 30%, and 55% to test the contribution of the planetary mass uncertainty to the retrieval, taking into account the number of transits required for the Tier-2 (N_{obs} = 44, Edwards and Tinetti 2022). The main parameters used to simulate the spectra are given in Table 4.1.

In Table B.2 and in Figure 4.6 I summarised the results of the retrieval. As in the previous cases, the main discrepancies appear for the atmospheric components in the presence of high clouds, in particular for the retrieved CO mixing ratio, where the retrieved value is not accurate and not precise. However, also in this case, we can assert that the mass uncertainty does not impact the results.

Also in this case I have verified that the KS test confirms that the Tier-1 (N_{obs} = 5, Figure 4.7a) is able to identify the cloudy scenario for this planet, allowing to take an informed decision if include the planet in Tier-2 sample.

We can also see from Figure 4.6b that if we know the mass with an uncertainty of 55%, we can refine the mass with a mass uncertainty of less than 30% if $P_{clouds} \geq 10^{-1}$ bar.

These results suggest that we could be able to accurately determine the atmospheric composition based on the available mass.

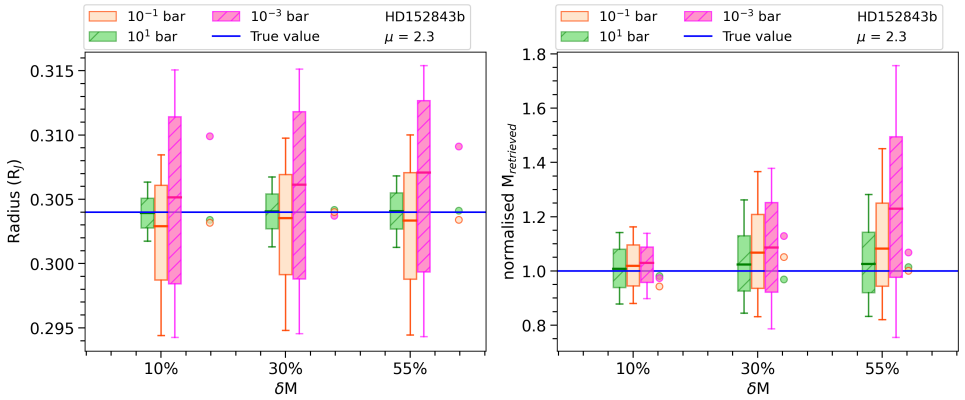

(A) *Radius* (B) *Mass*

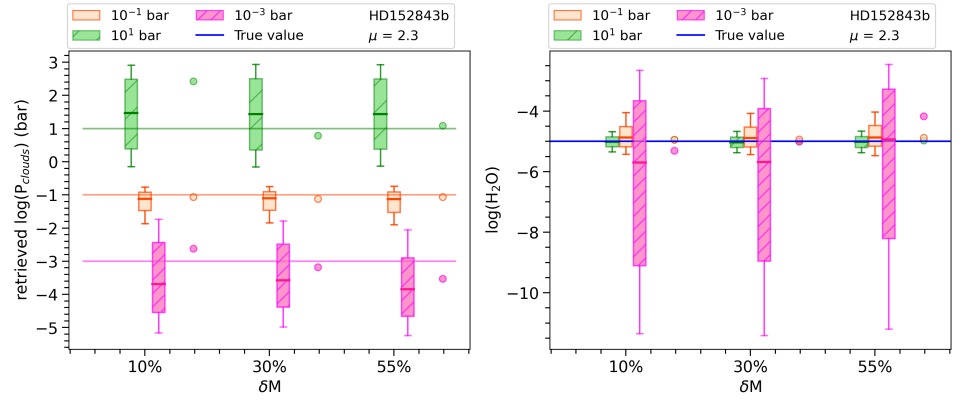

(C) *Cloud pressure* (D) *H_2O mixing ratio*

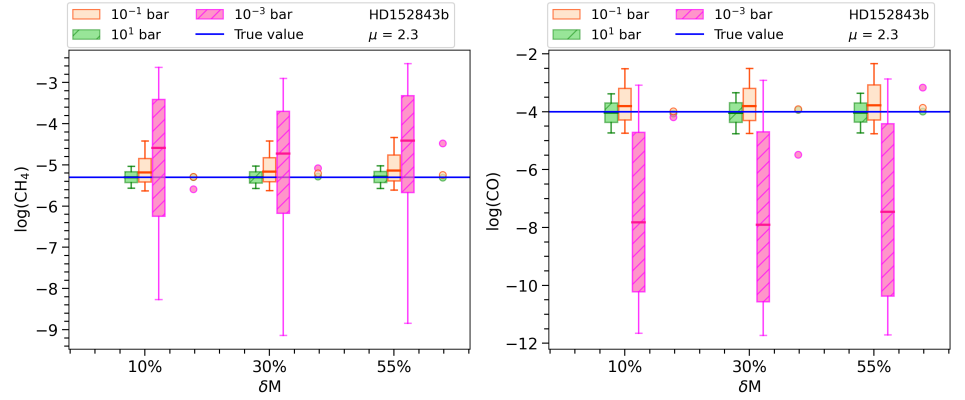

(E) *CH_4 mixing ratio* (F) *CO mixing ratio*

FIGURE 4.6: *Impact of mass uncertainties on the retrieval performed for the hypothetical primordial atmosphere of HD 152843 b for different cloud pressures. The colour scale and description of the figure are the same as in Figure 4.3.*

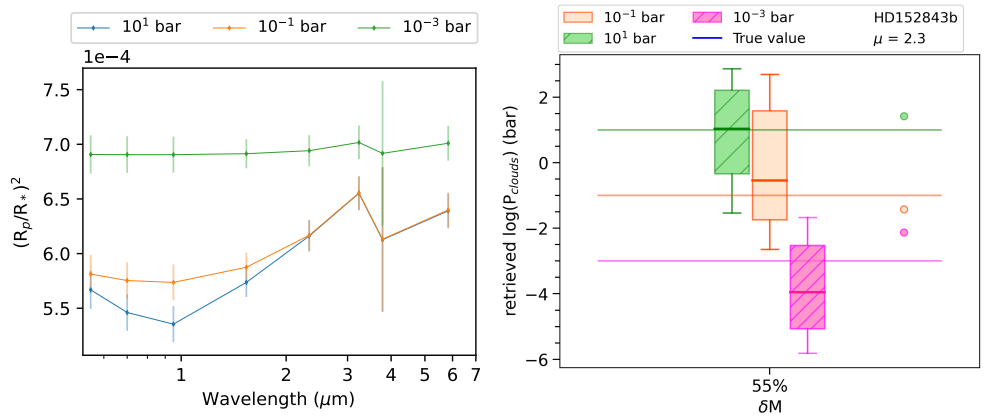

(A) *Tier-1* (B) *Cloud pressure*

Figure 4.7: *(A) Spectra of HD152843 b, as observed by Ariel, obtained considering different cloudy scenarios and assuming the number of transits required for Tier-1. (B) Comparison between the retrieved cloud pressure of HD152843 b obtained for different cloud pressures as a function of the mass uncertainty. Colour scale and description of Figure B are the same as in Figure 4.3.*

4.1.3 TOI-1130 b

TOI-1130 is a K7 star, relatively bright at near-infrared wavelengths (K_s = 8.3351), making it a good target for transit spectroscopy to study planetary atmospheres. Huang et al. (2020) found that it has two transiting: a Neptune-sized planet (3.65 ± 0.10 $R_\oplus$) with a period of 4.1 days, and a hot Jupiter ($1.50^{+0.27}_{-0.22}$ R_J) with a period of 8.4 days. Precise radial-velocity observations show that the mass of the hot Jupiter is $0.974^{+0.043}_{-0.044}$ M_J. Since the mass of the neptunian planet, TOI-1130 b, was estimated from a mass-radius relation, I assumed an uncertainty of 100% and performed the retrieval with uncertainties of 30%, 50%, and 100%.

Figure 4.8 shows the simulated spectra for different cloud pressures, obtained with TauREx using the number of transits required for Tier-2 (N_{obs} = 19) in order to simulate the noise.

The results of the retrieval are summarised in Table B.3 and shown in Figure 4.9. The results of the retrieval are similar to those obtained for the previous targets. In particular, when $P_{clouds} \geq 10^{-1}$ bar, I retrieved the CH_4 mixing ratio from a mass uncertainty of 100%, but with moderate accuracy compared to the other cloudy scenarios. A better mass estimate (e.g. δM = 50%) allows us to increase the precision of the retrieved CH_4 value even in the presence of high altitude clouds. We also note a slight increase in the accuracy of the retrieved H_2O mixing ratio with a mass uncertainty of 50%. The CO mixing ratio is the component of the atmosphere that is more difficult to constrain, since the reddest region of the spectrum, characterised

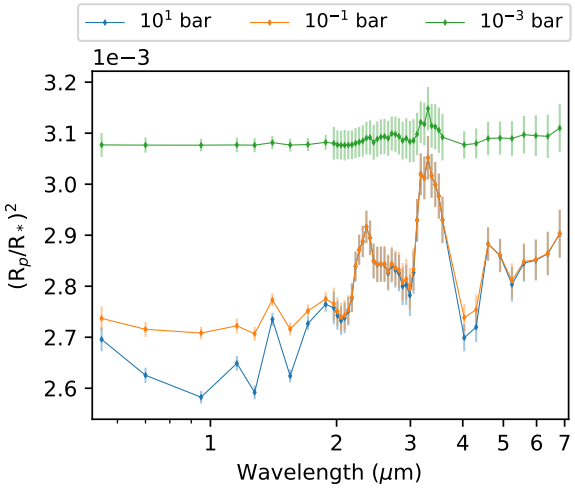

Figure 4.8: *Simulated spectra of TOI-1130 b, as observed by Ariel, obtained considering different cloud pressures.*

by the CO band, is dominated by the noise.

The test, performed assuming the number of transits required for the Tier-1 (N_{obs} = 1, see Figure 4.10a) confirmed that we could be able to characterise the cloud pressure with the Tier-1 (see Figure 4.10b), and, consequently, given that the number of transits actually required for the Tier-2 is not very time-consuming, the Ariel team could evaluate the possibility of increasing the number of observations required for the Tier-2 to improve the accuracy of the retrieval in the presence of high altitude clouds.

Additionally, Figure 4.9b highlights our capability to refine the planetary mass using TauREx. In particular, for this target, we are able to refine the mass to within 40% when $P_{clouds} = 10^{-1}$ bar, providing an initial mass uncertainty of about 100%.

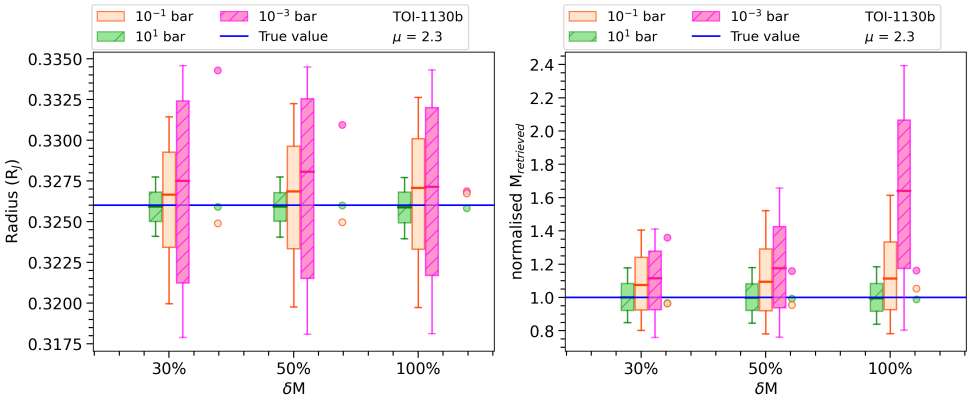

(A) *Radius* (B) *Mass*

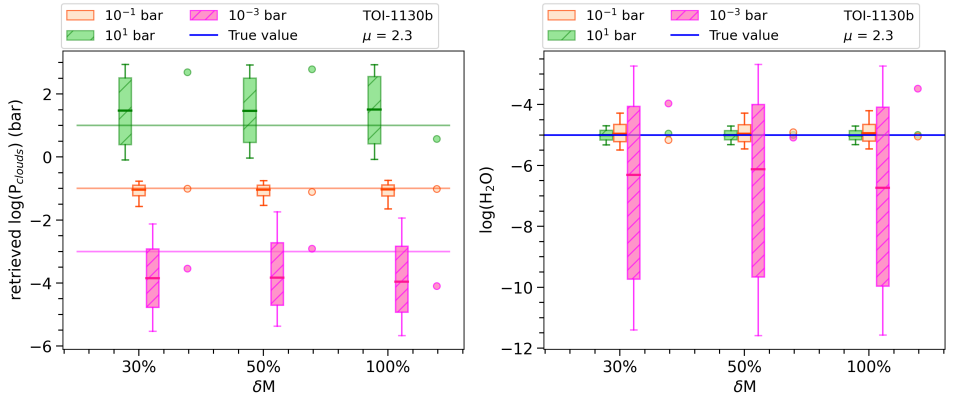

(C) *Cloud pressure* (D) *H_2O mixing ratio*

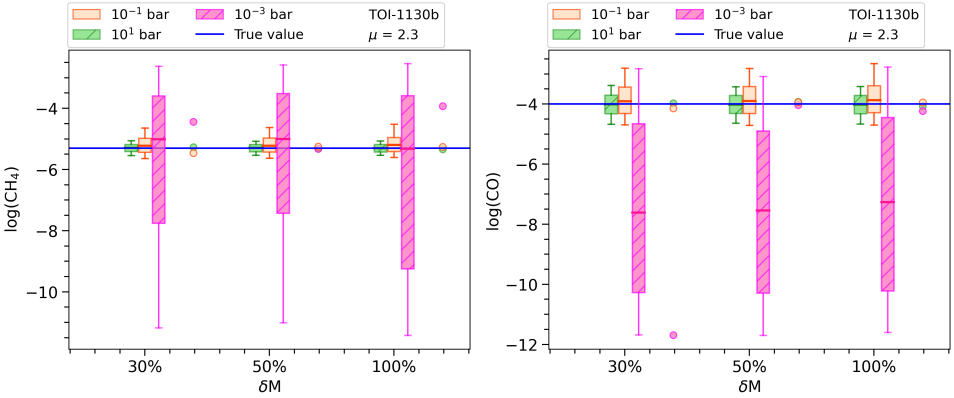

(E) *CH_4 mixing ratio* (F) *CO mixing ratio*

FIGURE 4.9: *Impact of mass uncertainties on the retrieval performed for the hypothetical primordial atmosphere of TOI-1130 b for different cloud pressures (P_{clouds} = 10^{1} bar in green, P_{clouds} = 10^{-1} bar in orange, and P_{clouds} = 10^{-3} bar in magenta) as a function of the mass uncertainty. Colour scale and description of the figure are the same as in Figure 4.3.*

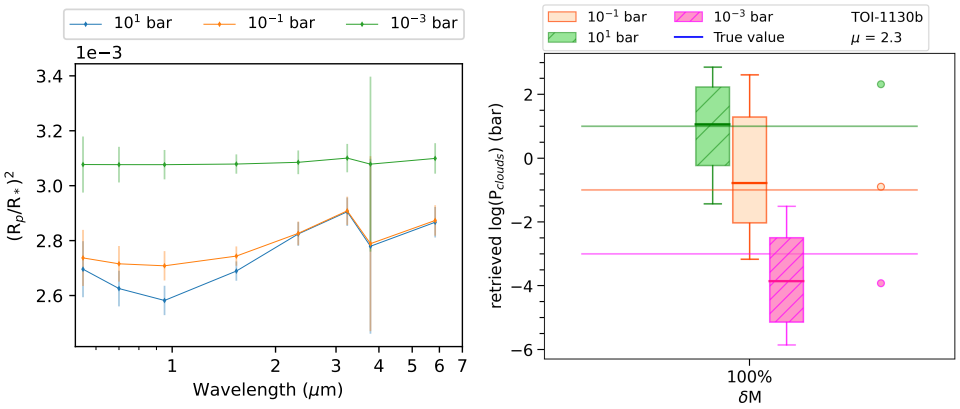

(A) *Tier-1* (B) *Cloud pressure*

Figure 4.10: *(A) Spectra of TOI-1130 b, as observed by Ariel, obtained considering different cloudy scenarios and assuming the number of transits required for Tier-1. (B) Comparison between the retrieved cloud pressure of TOI-1130 b obtained for different cloud pressures as a function of the mass uncertainty. Colour scale and description of Figure B are the same as in Figure 4.3.*

4.1.4 AUMic c

AU Mic is a young (22 Myr, Mamajek and Bell (2014)) nearby (∼ 10 pc, Gaia Collaboration et al. (2018)) and active pre-main-sequence M1 dwarf (Plavchan et al., 2020). AU Mic hosts an edge-on debris disk (Pecaut and Mamajek, 2013) and therefore the probability of planetary transit is higher than for other systems. The star is very active, then the derived planetary parameters are strongly dependent on the techniques adopted to correct the stellar activity.

Using photometric observations from TESS, Plavchan et al. (2020) discovered an ≈ 8.46 days Neptune-sized planet ($R_b = 4.38^{+0.18}_{-0.18}$ $R_\oplus$) in transit.

With further observations of AU Mic from the TESS extended mission Martioli et al. (2021) determined that AU Mic c is a smaller Neptune-sized planet (R_c = 3.24± 0.16 $R_\oplus$, M_c = 13.6 ± 11.4 $M_\oplus$) with a period of ≈18.86 days. Also, Cale et al. (2021) provided a 5σ upper limit to the mass of AU Mic c of $M_c \leq 20.13$ $M_\oplus$ from the analysis of several years of multi-wavelength RV observations of AU Mic. Finally, Zicher et al. (2022) estimated the mass of AU Mic c (M_c = 22.2 ± 6.7 $M_\oplus$) by analysing 91 observations provided by HARPS with a multidimensional Gaussian Process framework. The main characteristics of AU Mic c and its host star are reported in Table 4.1.

Due to the multiple mass estimates available in the literature, I performed the retrieval using different sets of parameters obtained from Martioli et al. (2021) (δ M ≃ 85%), Cale et al. (2021) (mass upper limit), and Zicher et al. (2022) (δ M ≃

30%).

I simulated the spectra taking into account the number of transits required for the Tier-2 (N_{obs} = 6, Edwards and Tinetti (2022)) and performed the retrieval assuming a mass uncertainty of 30%, 50%, and 85% for the set of parameters obtained by Martioli et al. (2021), and 10%, 20% and 30% for Zicher et al. (2022). Also, since Cale et al. (2021) proposed only an upper limit for the planetary mass, I created the forward spectra using the parameters obtained by Cale et al. (2021), assuming a planetary mass of 0.03020 M_J (value initially proposed by Cale et al. 2021, lower than the upper limit, and then discarded after further analysis) and then I performed the retrieval using a linear prior from 10^{-5} M_J to the mass upper limit.

Figure 4.11 shows a comparison between the simulated spectra obtained with the different sets of parameters and for different cloud pressures.

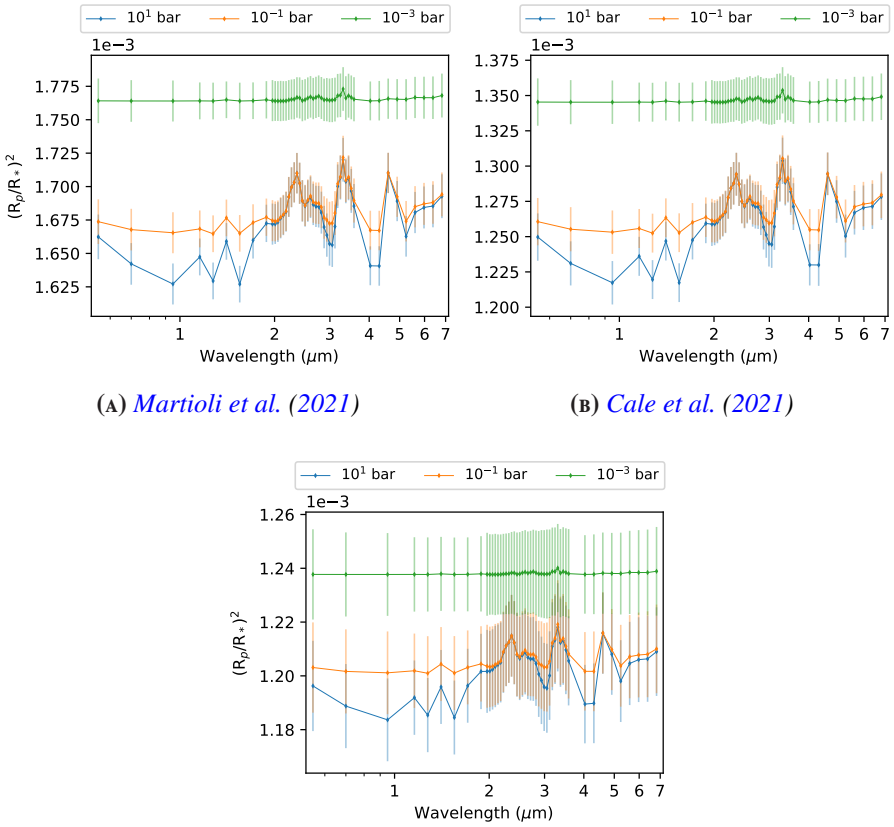

(A) *Martioli et al. (2021)*

(B) *Cale et al. (2021)*

(C) *Zicher et al. (2022)*

Figure 4.11: *Simulated spectra of AU Mic c provided considering the set of parameters obtained from (a) Martioli et al. (2021) (b) Cale et al. (2021) and (c) Zicher et al. (2022) obtained for different cloud pressures, taking into account the number of observations required for the Tier-2.*

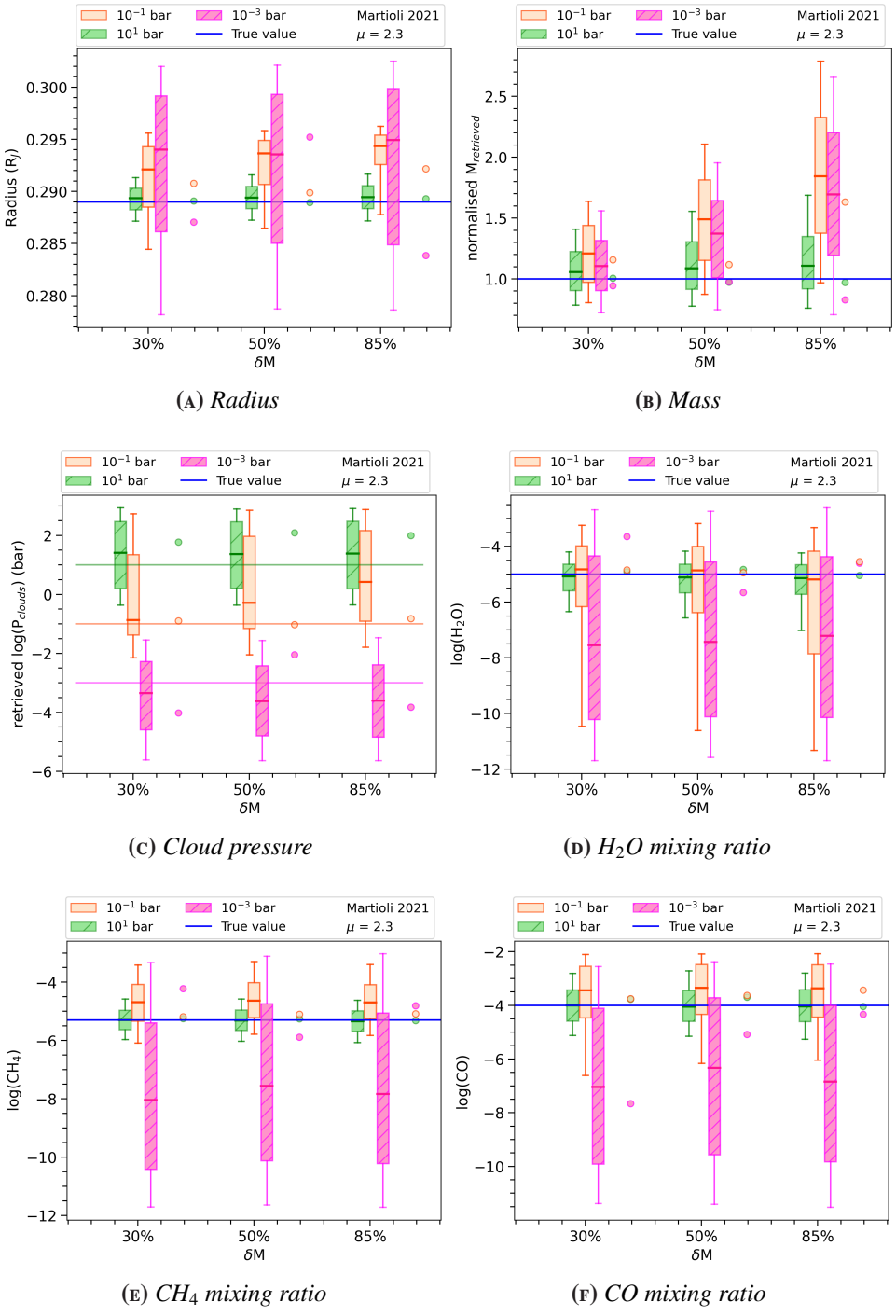

(A) *Radius* (B) *Mass*

(C) *Cloud pressure* (D) *H_2O mixing ratio*

(E) *CH_4 mixing ratio* (F) *CO mixing ratio*

FIGURE 4.12: *Impact of the mass uncertainties on the retrieval performed for the hypothetical primordial atmosphere of AU Mic c simulated using the set of parameters provided by Martioli et al. (2021) for different cloud pressures. Description of the figure are the same as in Figure 4.3.*

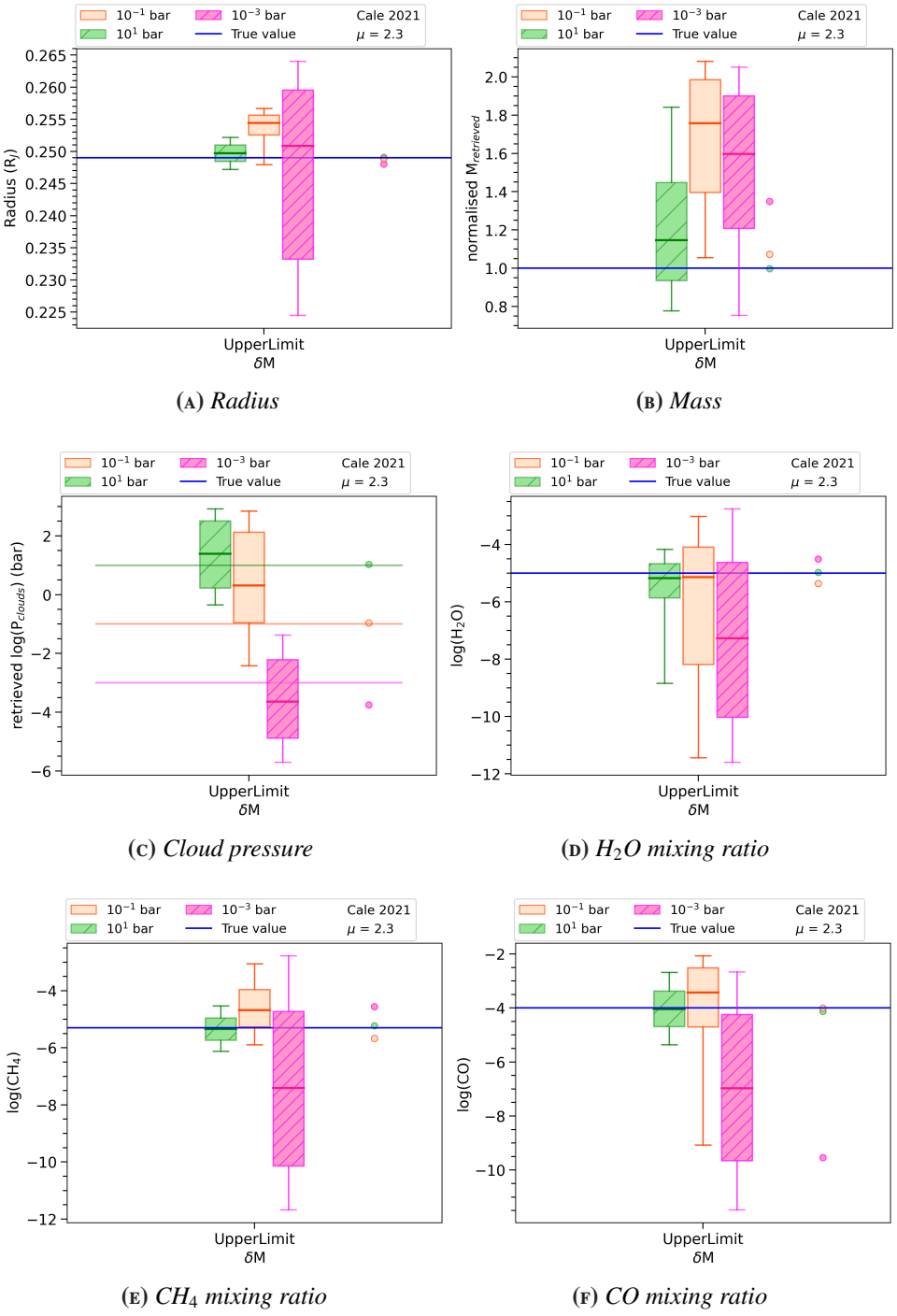

(A) *Radius* (B) *Mass*

(C) *Cloud pressure* (D) *H_2O mixing ratio*

(E) *CH_4 mixing ratio* (F) *CO mixing ratio*

FIGURE 4.13: *Impact of the mass uncertainties on the retrieval performed for the hypothetical primordial atmosphere of AU Mic c simulated using the set of parameters provided by Cale et al. (2021) for different cloud pressures. Colour scale and description of the figure are the same as in Fig. 4.3.*

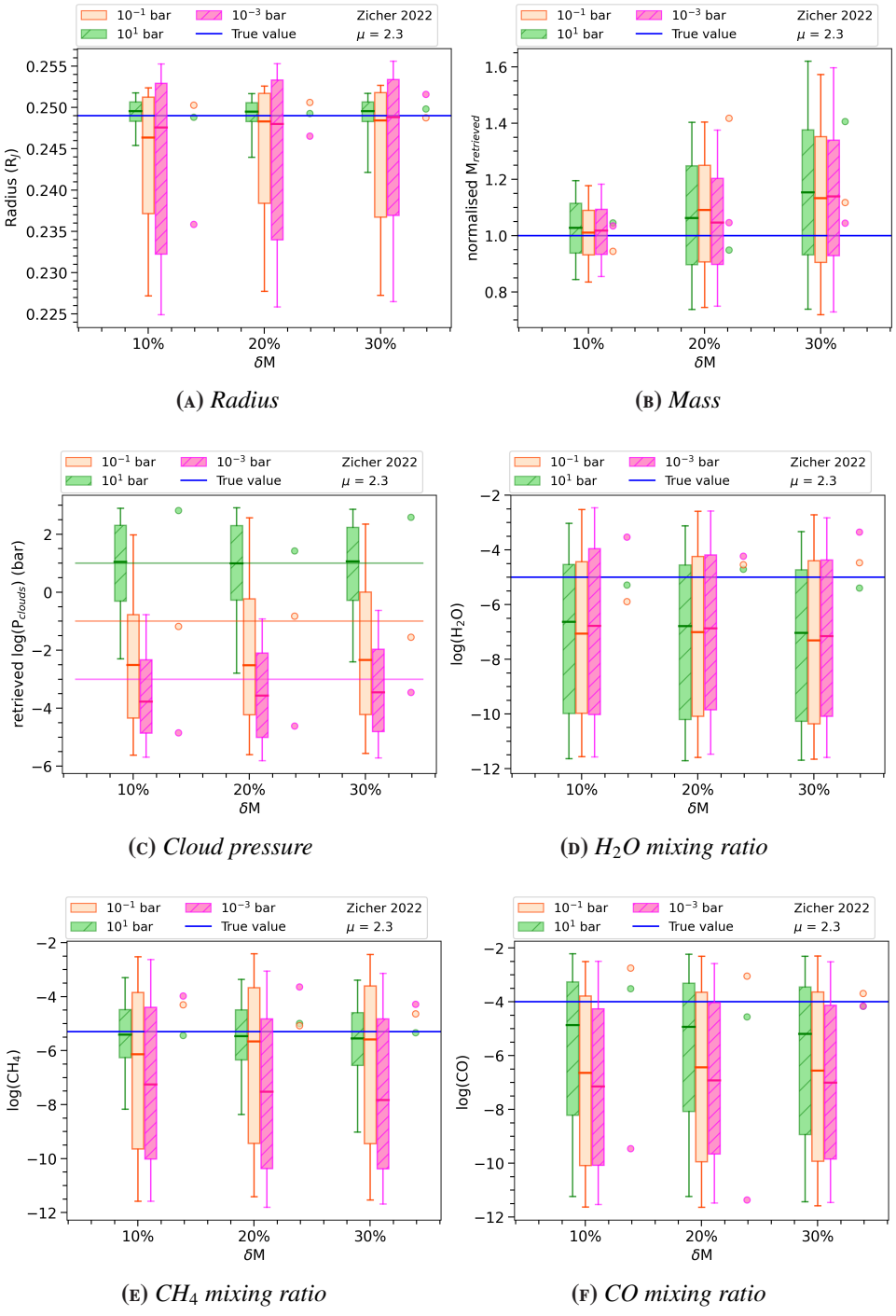

(A) *Radius* (B) *Mass*

(C) *Cloud pressure* (D) H_2O *mixing ratio*

(E) CH_4 *mixing ratio* (F) *CO mixing ratio*

FIGURE 4.14: *Impact of the mass uncertainties on the retrieval performed for the hypothetical primordial atmosphere of AU Mic c simulated using the set of parameters provided by Zicher et al. (2022) for different cloud pressures. Colour scale and description of the figure are the same as in Fig. 4.3.*

As we can note from Figure 4.11, the simulated spectra obtained using the parameters provided by Zicher et al. (2022) are dominated by the noise, even with low altitude clouds. We can observe an analogous behaviour from the simulated spectrum obtained using the parameters obtained from Martioli et al. (2021) and Cale et al. (2021) when $P_{clouds} = 10^{-3}$ bar. In Figures 4.12, 4.13 and 4.14 are summarised the results obtained from the retrievals of each tested case (see also the tables in Section B.4).

Comparing the three different configurations we see that the better results are obtained using the Martioli et al. (2021) and Cale et al. (2021) parameters, corresponding to the case with low gravity values, where we are able to accurately retrieve all the atmospheric components in the clear sky case and in the presence of low altitude clouds, while when $P_{clouds} = 10^{-3}$ bar the retrieved values are not accurate and not precise. These results are not strongly dependent from the mass estimation. We note that in the Martioli et al. (2021) case, we slightly increase the precision of the retrieved H_2O mixing ratio considering a mass uncertainty of 50% with respect to the retrieval obtained for $\delta M = 85\%$. Additionally, a mass uncertainty of 30% allows us to increase the accuracy in the retrieved P_{clouds} (see Figure 4.12c). The worst result is obtained using the Zicher et al. (2022) parameters, where we are able to accurately retrieve only the CH_4 mixing ratio in the presence of low altitude clouds.

The test performed using the Cale et al. (2021) configuration highlights that we are able to retrieve the atmosphere composition even when we only have an upper limit for the planetary mass. Indeed, in this configuration, when $P_{clouds} = 10^{-1}$ bar, we are not able to accurately retrieve the planetary mass, since we obtained an accurate determination considering the MAP value. However, we obtained accurate values for the trace gases. As in the previous cases, not accurate retrieved values are obtained in the presence of high altitude clouds.

The case of AU Mic c outlines how the capability to detect the planetary atmosphere depends on the true mass value that determines the scale height and then the SNR. The mass determination is strongly dependent on the methods adopted for stellar activity correction. In the presence of strong activity, as in AU Mic, the measured mass can be very different from the true value and its error strongly underestimated. For this reason, I decided to test our capabilities to obtain an accurate retrieval assuming minimum information on the mass. According to the values obtained from the literature, I considered a uniform prior with the maximum value obtained by Zicher et al. (2022) ($M_p = 28.9\ M_\oplus$) as the mass upper limit. I performed the retrieval for two different cases, assuming two different values for the

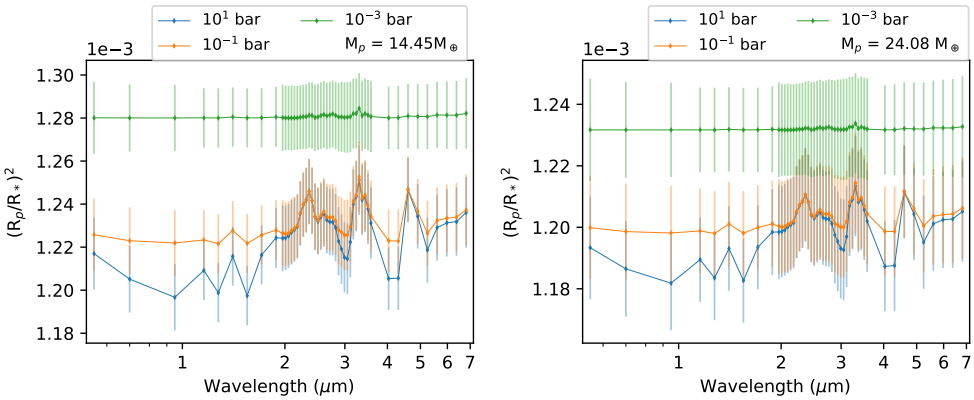

(A) $M_p = 14.45M_\oplus$ (B) $M_p = 24.08M_\oplus$

Figure 4.15: *Spectra of AU Mic c, as observed by Ariel, assuming (A) $M_p = 14.45M_\oplus$ (B) $M_p = 24.08M_\oplus$, considering the number of transits required for Tier-2 ($N_{obs} = 6$).*

input mass (see the simulated spectra in Figure 4.15). In the first test, I assumed an input planetary mass of $M_p = 14.45M_\oplus$, while in the second test $M_p = 24.08M_\oplus$. In both tests, TauREx explored the planetary mass parameter space with a linear prior.

The results of these tests suggest (see *LINEAR* results in Tables B.7 and B.8, and Figures 4.17 and 4.18) that we are not able to retrieve the atmospheric composition accurately. However, the retrieved mass is more constrained compared to the prior boundaries, so I used the retrieved mass distribution to iterate the procedure to apply an additional constraint on the planetary mass. Consequently, I performed another retrieval for both considered cases, assuming a Gaussian prior for the planetary mass, defined by mean and sigma values obtained in the previous retrieval (see *GAUSSIAN* results in Tables B.7 and B.8, and Figures 4.18 and 4.18).

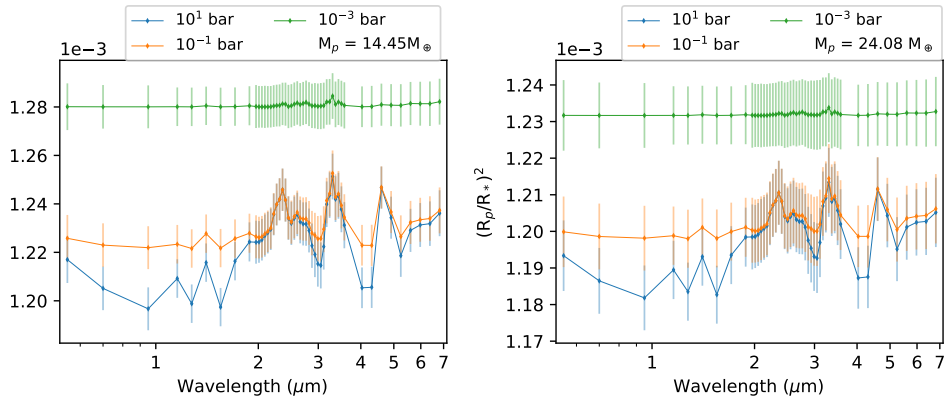

(A) $M_p = 14.45M_\oplus$ - $N_{obs} = 18$ (B) $M_p = 24.08M_\oplus$ - $N_{obs} = 18$

Figure 4.16: *Spectra of AU Mic c, as observed by Ariel, assuming (A) $M_p = 14.45M_\oplus$ (B) $M_p = 24.08M_\oplus$, considering three times the number of transits required for Tier-2 ($N_{obs} = 18$).*

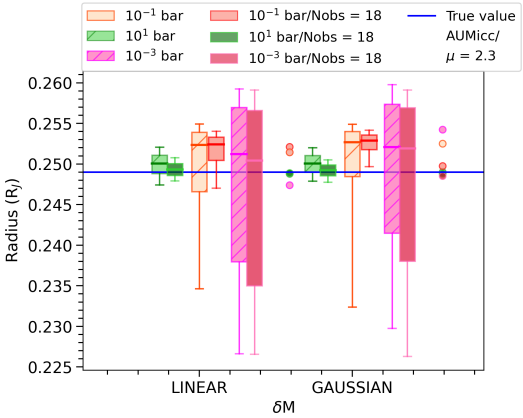

(A) *Radius*

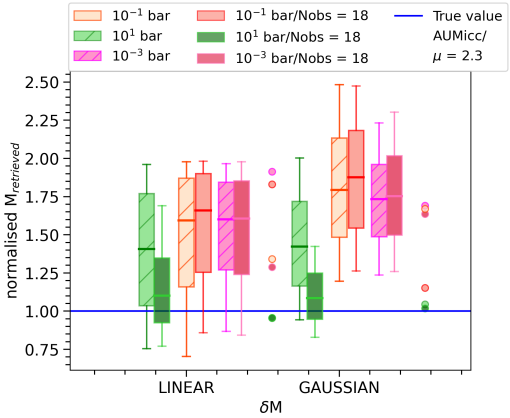

(B) *Mass*

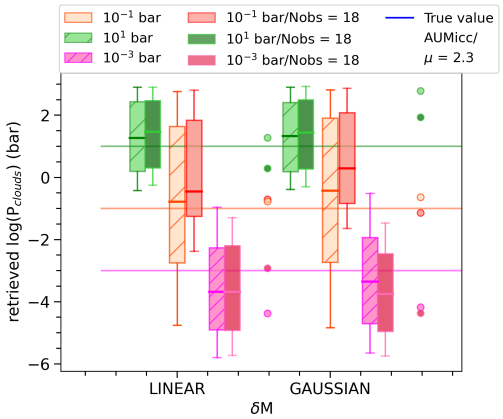

(C) *Cloud pressure*

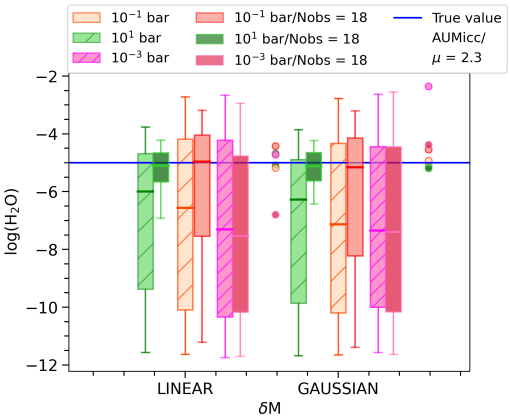

(D) *H_2O mixing ratio*

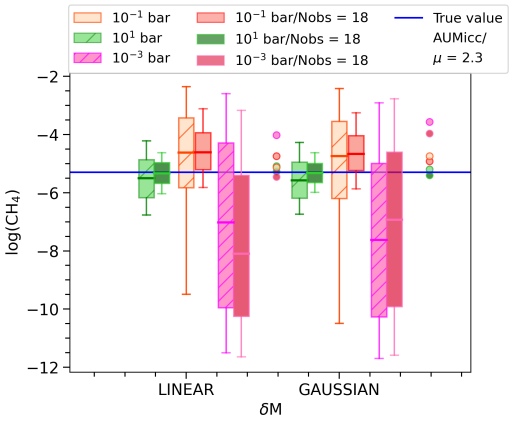

(E) *CH_4 mixing ratio*

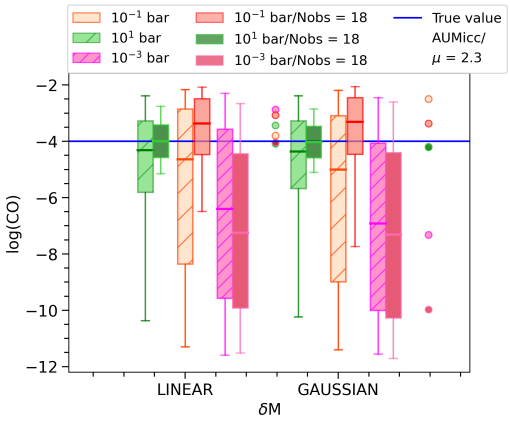

(F) *CO mixing ratio*

FIGURE 4.17: *Results of the retrieval performed on the hypothetical atmosphere of AU Mic c, assuming $M_p = 14.45 M_\oplus$ and using LINEAR and GAUSSIAN prior boundaries for the planetary mass, for different cloud pressures. I highlighted with darker colour the results obtained assuming $N_{obs} = 18$. Description of the figures are the same as in Fig. 4.3.*

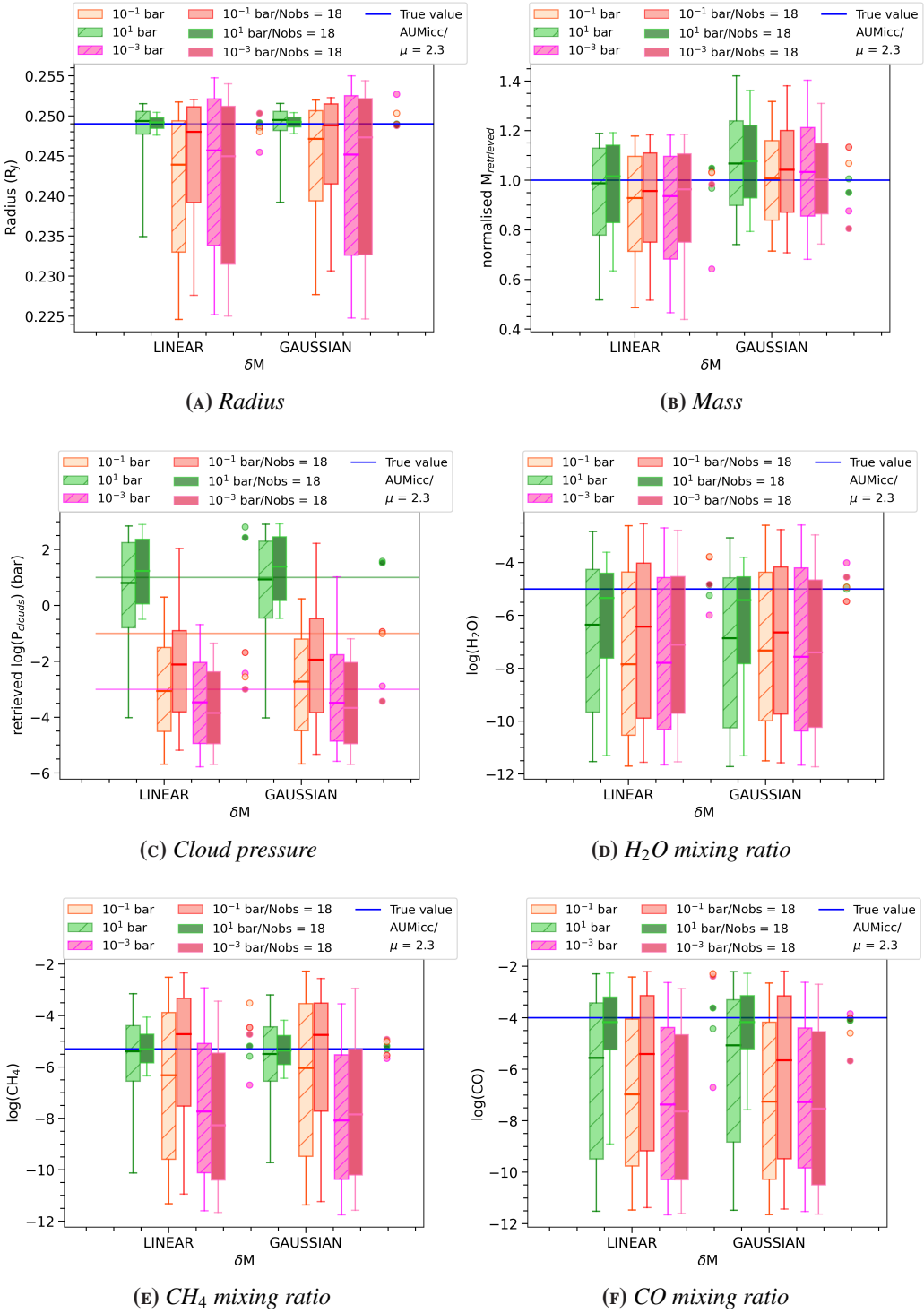

(A) *Radius* (B) *Mass*

(C) *Cloud pressure* (D) H_2O *mixing ratio*

(E) CH_4 *mixing ratio* (F) *CO mixing ratio*

FIGURE 4.18: *Results of the retrieval performed on the hypothetical atmosphere of AU Mic c, assuming a planetary mass* $M_p = 24.08 M_\oplus$ *and using a LINEAR and GAUSSIAN prior boundaries for the planetary mass, for different cloud pressures. Colour scale and description of the figure are the same as in Fig. 4.17.*

We observe that despite the gaussian constraint, similar results were obtained compared to the "linear" case.

This indicates that the results of the retrieval are not related to our knowledge of the planetary mass, but rather the SNR is the main factor. As can be seen from Figure 4.15, the spectra are dominated by noise and the limited number of transits is not sufficient to achieve the necessary SNR. To verify this hypothesis, spectra were simulated with three times the number of transits required for the Tier-2 (N_{obs} = 18, see Figure 4.16) and the retrieval was performed using *LINEAR* and *GAUSSIAN* priors, as in previous tests. As seen from Tables B.7 and B.8 and Figures 4.17 and 4.18, a higher number of transits improves the precision, and in some cases the accuracy, of the atmospheric parameters, particularly when $P_{clouds} = 10^1$ bar. However, three times the number of transits required for Tier-2 is still not enough to increase the SNR and achieve accurate retrieval.

In conclusion, these tests suggest that using TauREx, we can improve our knowledge of the mass and estimate the atmospheric composition of a clear sky atmosphere, given that the mass of the target is not well-constrained. However, in the presence of low altitude clouds, we need to increase the number of transits required for Tier-2 to obtain accurate results.

4.1.5 HD106315 c

HD 106315 is a F5V type star with $T_{eff} \approx 6260$ K, and a V = 9.0 mag, hosting a multiplanetary system. The inner planet, HD 106315b, has a period of 9.55 days and a radius of $R_p \sim 0.218 R_J$, while HD 106315c, the outer planet, has a period of 21.05 days and a radius of $R_p \sim 0.388 R_J$ (Barros et al., 2017). Here I focus my analysis on planet c (M_c = 15.2 ± 3.7 $M_\oplus$). Its main properties and those of its host star are summarised in Table 4.1. Barros et al. (2017) estimated the planetary mass with an uncertainty of about 25%. To test the impact of the mass uncertainty on the atmospheric retrieval, I performed the analysis assuming mass uncertainties of 25%, 20% and 10%.

Figure 4.19 shows the simulated spectra obtained taking into account the number of transits required for the Tier-2 (N_{obs} = 23) to achieve the needed SNR as in Edwards and Tinetti (2022), and assuming different cloudy scenarios. It can be seen from Figure 4.19 that in the worst considered cloudy scenario, the noise dominates the spectrum and the trace gases that produce spectral signatures are barely visible. Therefore, in cases such as this, it could be important to characterise the presence of clouds in the planetary atmosphere already at Tier-1 and, in the case of high altitude clouds, evaluate the opportunity of excluding the target from Tier-2 or decide

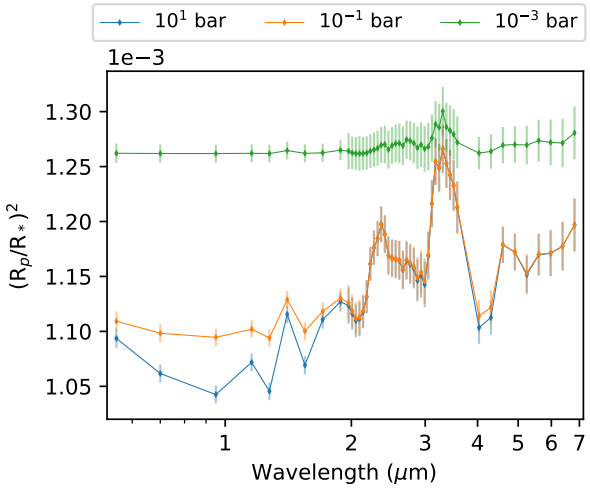

Figure 4.19: *Simulated spectra of HD106315 c, as observed by Ariel, obtained considering different cloud pressures.*

to increase the number of transits required.

The results of the retrieval analysis are reported in Table B.9 and also shown in Figure 4.20. All atmospheric parameters are accurately retrieved in the clear sky case and for low altitude clouds. A moderately accurate and not precise estimation of the retrieved H_2O was obtained in the low-pressure cloudy case ($P_{clouds} = 10^{-3}$ bar), where the retrieved 1σ distributions include values from 10^{-4} to 10^{-10} bar, while, according to the definitions described above, the retrieved CO is not accurate and not precise when $P_{clouds} = 10^{-3}$ bar. However, all these results are not impacted by the mass uncertainty, but by SNR, that is determined by cloud altitude.

It is therefore of great interest to investigate our ability to discriminate between different cloudy scenarios using Tier-1 observations. This information would allow us to evaluate the goodness of the Tier-2 observations of this target, and to make a decision to either exclude it in case of high altitude clouds or to increase the number of transits to improve the SNR. For this reason, I performed the retrieval assuming the number of observations required for the Tier-1 ($N_{obs} = 3$, reported in Edwards and Tinetti 2022), as shown in Figure 4.21a. In this case, although for $P_{clouds} = 10^{-1}$ bar the retrieved distribution is wider compared to the previous test (see Figure 4.21b), the KS test, performed between the three distributions (10^{-1} - 10^{1} bar, 10^{-1} - 10^{-3} bar,10^{-1} - 10^{-3} bar), confirmed ($p_{value} << 0.05$) that it would be possible to discriminate the cloudy scenario using the Tier-1 observations.

In conclusion, these results suggest that a valid observing strategy could be to test the cloudy conditions of this target during the Tier-1. In the case of high altitude clouds, we could evaluate the possibility of increasing the number of transits required for Tier-2.

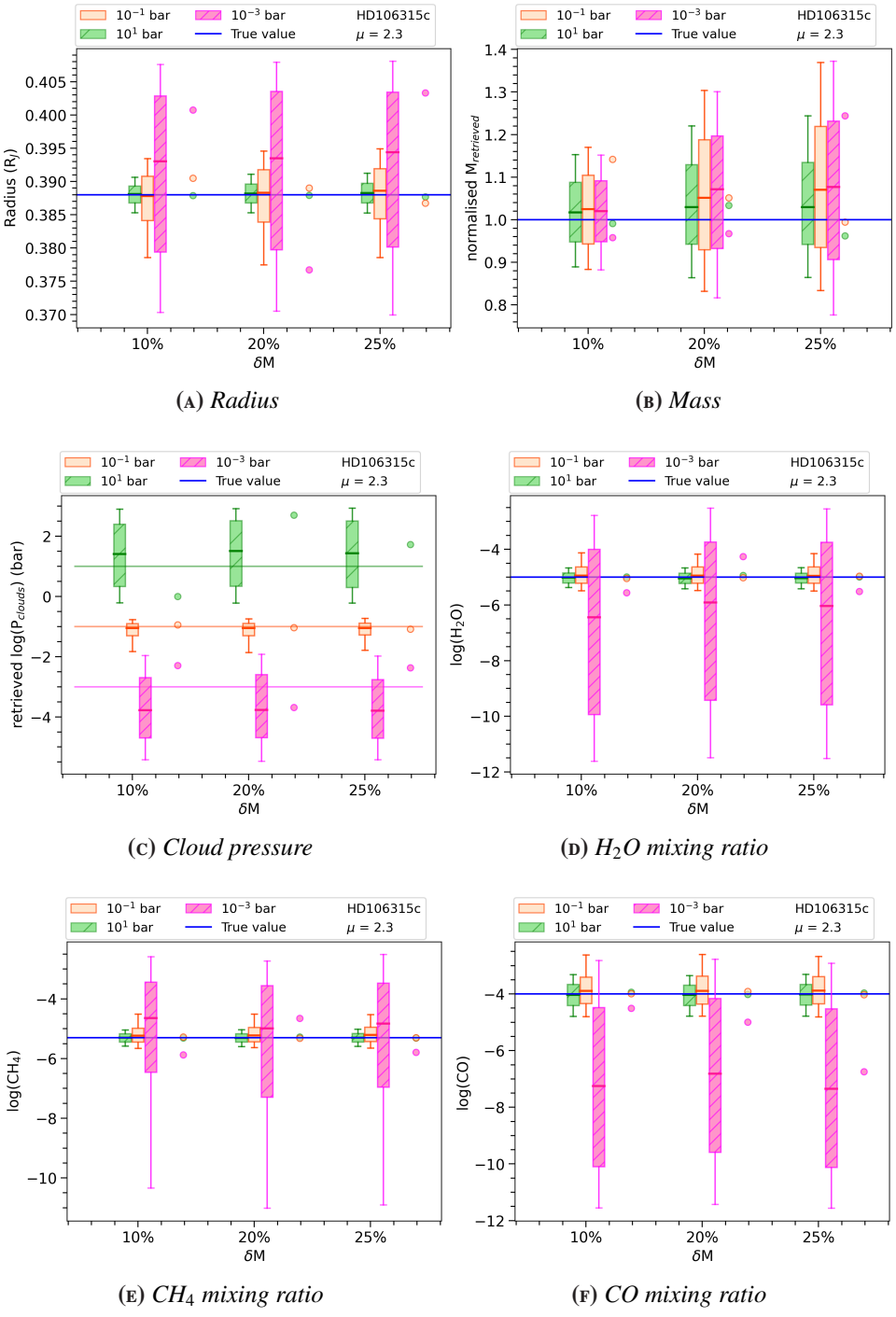

(A) *Radius* (B) *Mass*

(C) *Cloud pressure* (D) *H_2O mixing ratio*

(E) *CH_4 mixing ratio* (F) *CO mixing ratio*

FIGURE 4.20: *Impact of mass uncertainties on the retrieval performed for the hypothetical primordial atmosphere of HD106315 c for different cloud pressures (P_{clouds} = 10^{1} bar in green, P_{clouds} = 10^{-1} bar in orange, and P_{clouds} = 10^{-3} bar in magenta) as a function of the mass uncertainty. Colour scale and description of the figure are the same as in Fig. 4.3.*

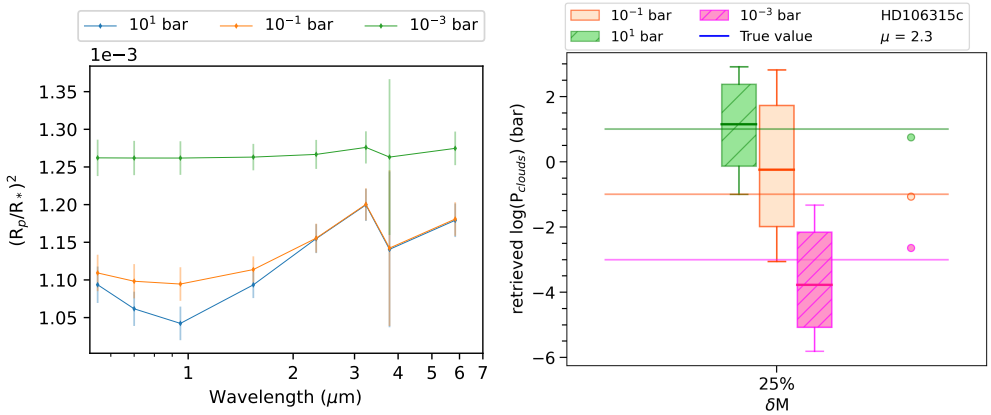

(A) *Tier-1* (B) *Cloud pressure*

Figure 4.21: *(A) Spectra of HD106315 c, as observed by Ariel, obtained considering different cloudy scenarios and assuming the number of transits required for Tier-1. (B) Comparison between the retrieved cloud pressures of HD106315 c obtained for different cloud pressures as a function of the mass uncertainty. Colour scale and description of Figure B are the same as in Figure 4.3.*

4.1.6 TOI-451 d

TOI 451 is a member of the 120 Myr old Pisces–Eridanus stream (Psc–Eri). Newton et al. (2021) found that TOI 451 is a young solar-mass star and has a comoving companion, TOI 451 B (Gaia DR2 4844691297067064576). They also confirmed a three-planet system around TOI 451. TOI 451 b, c, and d are hot planets in close orbits around their host star. The inner planet, TOI 451 b, has a period of 1.9 days

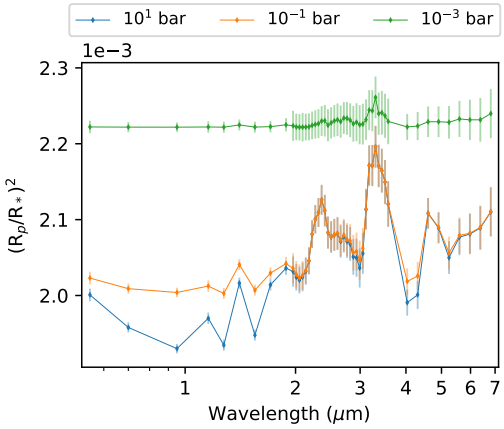

Figure 4.22: *Simulated spectra of TOI-451 d, as observed by Ariel, obtained considering different cloud pressures.*

and a radius of 1.9 $R_\oplus$. The two outer planets have radii of 3.1 and 4.1 $R_\oplus$. As they are young and hot (T_{eq} = 720 to 1500 K, assuming 0 albedo) and could be low mass, their observed radii may be impacted by high-altitude hazes (Gao and Zhang, 2020).

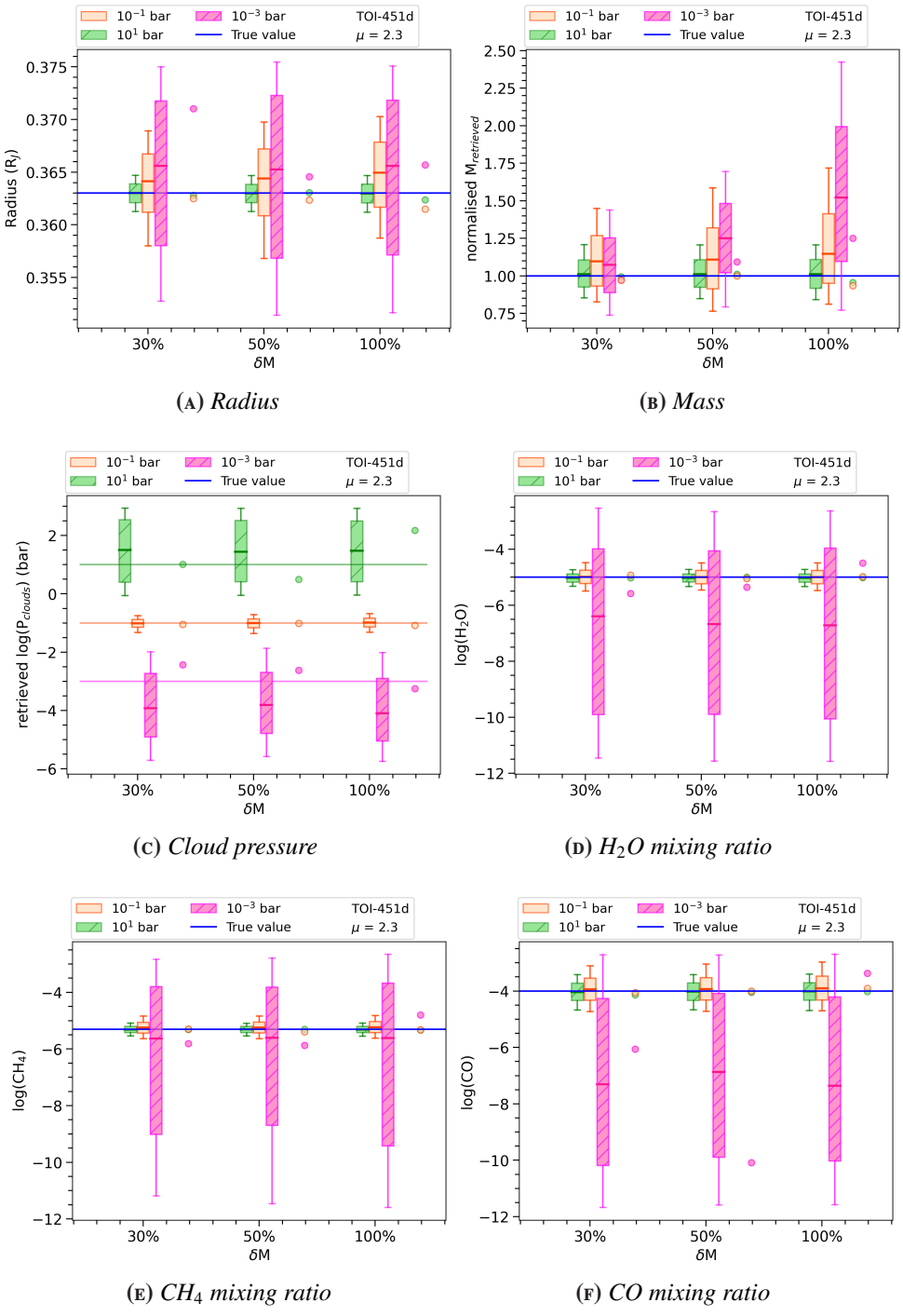

(A) *Radius* (B) *Mass*

(C) *Cloud pressure* (D) *H_2O mixing ratio*

(E) *CH_4 mixing ratio* (F) *CO mixing ratio*

FIGURE 4.23: *Impact of mass uncertainties on the retrieval performed for the hypothetical primordial atmosphere of TOI-451 d for different cloud pressures ($P_{clouds} = 10^{1}$ bar in green, $P_{clouds} = 10^{-1}$ bar in orange, and $P_{clouds} = 10^{-3}$ bar in magenta) as a function of the mass uncertainty. Colour scale and description of the figure are the same as in Fig. 4.3.*

The planetary masses were estimated using the non-parametric mass-radius relation from Ning et al. (2018). This assumes that these young planets obey the same mass–radius relation as older stars, which may be inaccurate. Since the mass of TOI-451 d (M_d = 15.57 $M_\oplus$) was estimated from a mass-radius relation, I assumed an uncertainty of 100% and performed the retrieval with uncertainties of 30%, 50%, and 100%. I simulated the spectra taking into account the number of transits required for the Tier-2 (N_{obs} = 51).

The results of the retrieval are summarised in Table B.10. As shown in Figure 4.23, we are able to accurately retrieve the atmospheric composition for this target when $P_{clouds} \geq 10^{-1}$ bar. In the presence of high clouds, the retrievals are moderately precise and accurate, in particular for the CO mixing ratio, where the median value of the retrieved distribution is several orders of magnitude lower than the true value, with a very large distribution. These results are not correlated with the mass uncertainty and are likely due to the lower SNR when $P_{clouds} = 10^{-3}$ bar, as we can see from Figure 4.22.

In addition, we can see from Figure 4.23c that the three distributions obtained from the different cloudy configurations are not compatible with each other, and this result is also not affected by the mass uncertainty. Consequently, I tested if we are able to estimate the cloudy scenarios of this target from Tier-1 (N_{obs} = 4) in order to recommend the target for the next tiers as a function of the retrieved cloudy configuration. From Figure 4.24b we can note that we could be able to discriminate the cloudy scenarios from Tier-1, and therefore we could decide to increase the number of observations in order to accurately retrieve the CO mixing ratio.

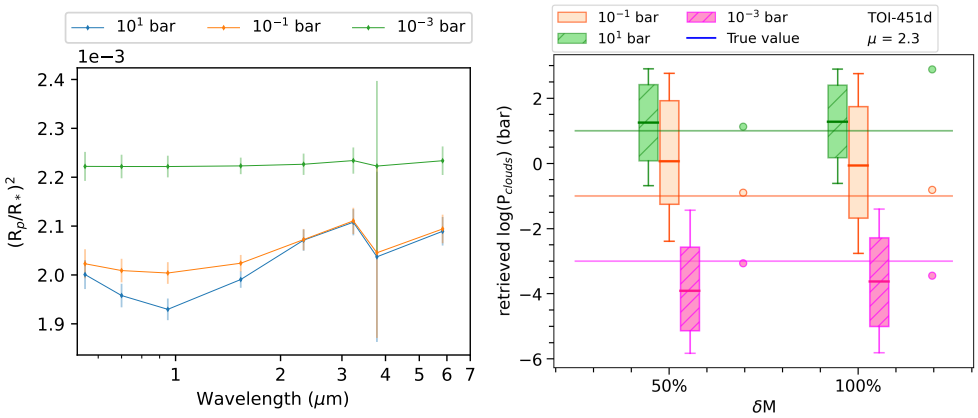

(A) *Tier-1* (B) *Cloud pressure*

Figure 4.24: *(A) Spectra of TOI-451 d, as observed by Ariel, obtained considering different cloudy scenarios and assuming the number of transit required for Tier-1. (B) Comparison between the retrieved cloud pressure of TOI-451 d obtained for different cloud pressures as a function of the mass uncertainty. Colour scale and description of Figure B are the same as in Figure 4.3.*

We also note that by using TauREx for $P_{clouds} > 10^{-1}$ bar we are able to refine the mass to within 50%, giving an initial mass uncertainty of 100% (see Figure 4.23b).

4.1.7 KOI-94 c

The Kepler Object of Interest (KOI) 94 system is a multi-transiting planetary system consisting of four transiting planets with periods of about 3.7, 10, 22, and 54 days. It was discovered by the Kepler space telescope (Borucki et al., 2010; Batalha et al., 2013) and its properties were reported by Weiss et al. (2013). KOI-94 b has a mass of 10.5 ± 4.6 $M_\oplus$ and a radius of 1.71 ± 0.16 $R_\oplus$, while KOI-94 c has a estimated mass of $15.6^{+5.7}_{-15.6}$ $M_\oplus$ and a radius of 4.32 ± 0.41 $R_\oplus$. KOI-94 d has a mass of 106 ± 11 $M_\oplus$ and a radius of 11.27 ± 1.06 $R_\oplus$. KOI-94 e has a mass of 35^{+18}_{-28} $M_\oplus$ and a radius of 6.56 ± 0.62 $R_\oplus$.

Since the wide uncertainty on the mass estimation, and since our capability to detect the planetary atmosphere depends on the true mass value as I already demonstrated in AU Mic (see Section 4.1.4), I simulated the spectra of KOI-94 c using the parameters given in Table 4.2, supposing two different values for the planetary mass (M_p = 8 $M_\oplus$ and M_p = 16 $M_\oplus$). For both tests I considered different cloudy scenarios (see Figure 4.25), taking into account the number of transits required for the Tier-2 (N_{obs} = 127).

Then, I performed the retrieval using a linear prior for the planetary mass with an upper limit at 21.3 $M_\oplus$. The results of the retrieval are reported in Figure 4.26 and summarised in Table B.11.

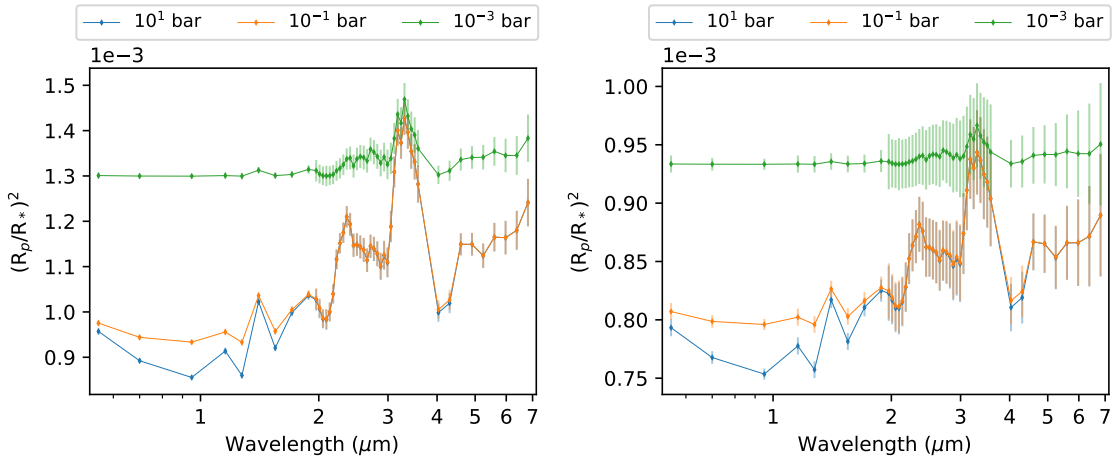

(A) $M_p = 8M\oplus$ (B) $M_p = 16M\oplus$

Figure 4.25: *Simulated spectra of KOI-94 c, as observed by Ariel, obtained for the two considered value of mass and at different cloud pressures.*

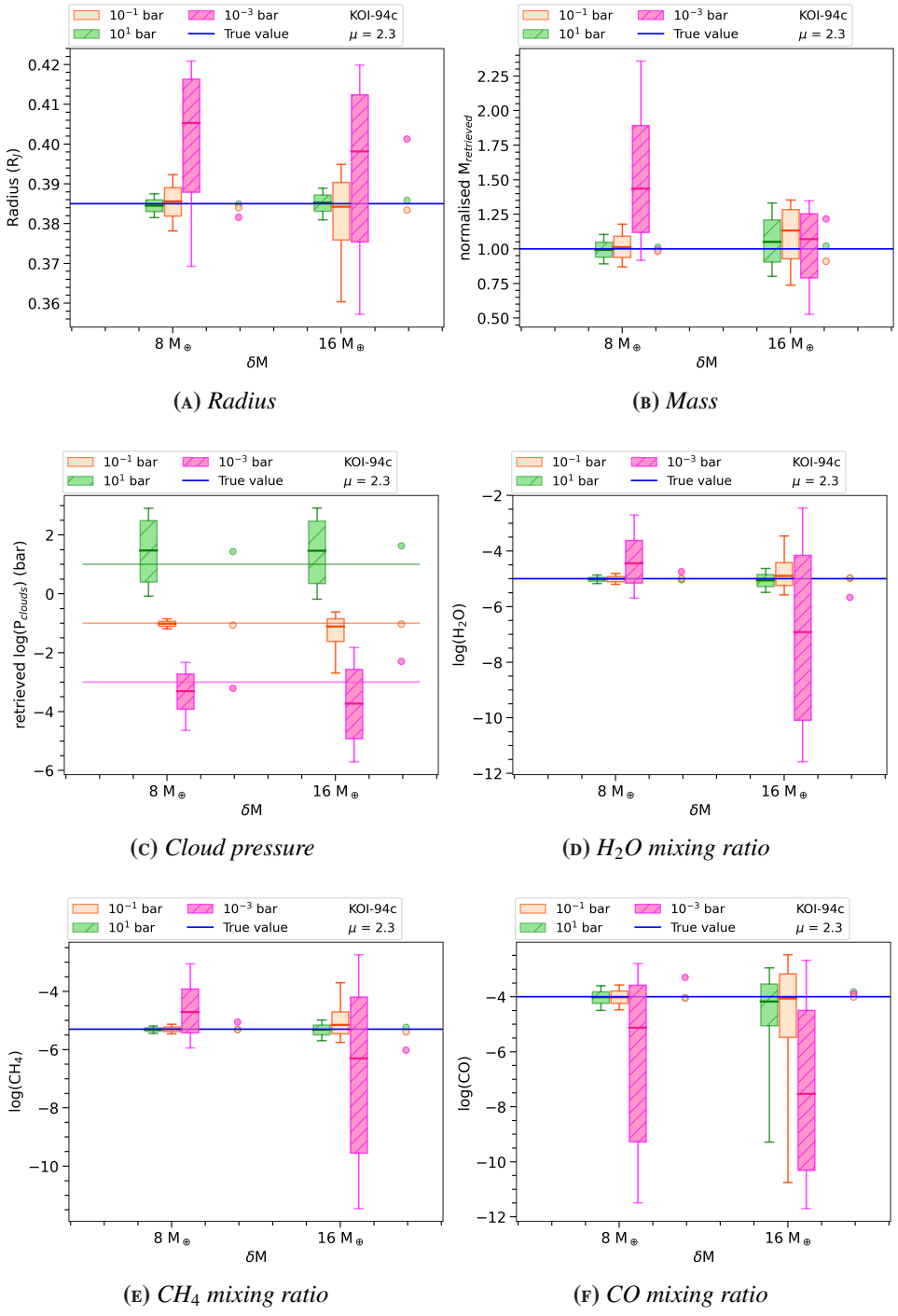

(A) *Radius* (B) *Mass*

(C) *Cloud pressure* (D) *H_2O mixing ratio*

(E) *CH_4 mixing ratio* (F) *CO mixing ratio*

FIGURE 4.26: *Impact of mass uncertainties on the retrieval performed for the hypothetical primordial atmosphere of KOI-94 c for different cloud pressures for the two different supposed values of the planetary mass. Colour scale and description of the figure are the same as in Fig. 4.3.*

As we seen in the case of AU Mic c, I obtained higher accuracy in the retrieved atmospheric parameters for M_p = 8 $M_\oplus$, corresponding to the low gravity case. In particular, in the case of M_p = 8 $M_\oplus$, all the atmospheric parameters are accurately retrieved even in the presence of high altitude clouds, with the exception of the CO

mixing ratio that is moderately accurately retrieved when $P_{clouds} = 10^{-3}$ bar. On the other hand, in the case of $M_p = 16\ M_\oplus$, we accurately retrieved the atmospheric composition when $P_{clouds} \geq 10^{-1}$. In the presence of high altitude clouds we moderately accurately retrieved the CH_4 mixing ratio while we are not able to accurately retrieved the other atmospheric components.

Additionally, as shown in Figure 4.26c, we are able to discriminate the cloudy scenario, as confirmed by the KS test ($p_{value} << 0.05$). Also in this case I have verified that the KS test confirms that the Tier-1 ($N_{obs} = 8$, see Figure 4.27) is able to identify the cloudy conditions for this planet, allowing to take informed decision if include the planet in Tier-2 sample.

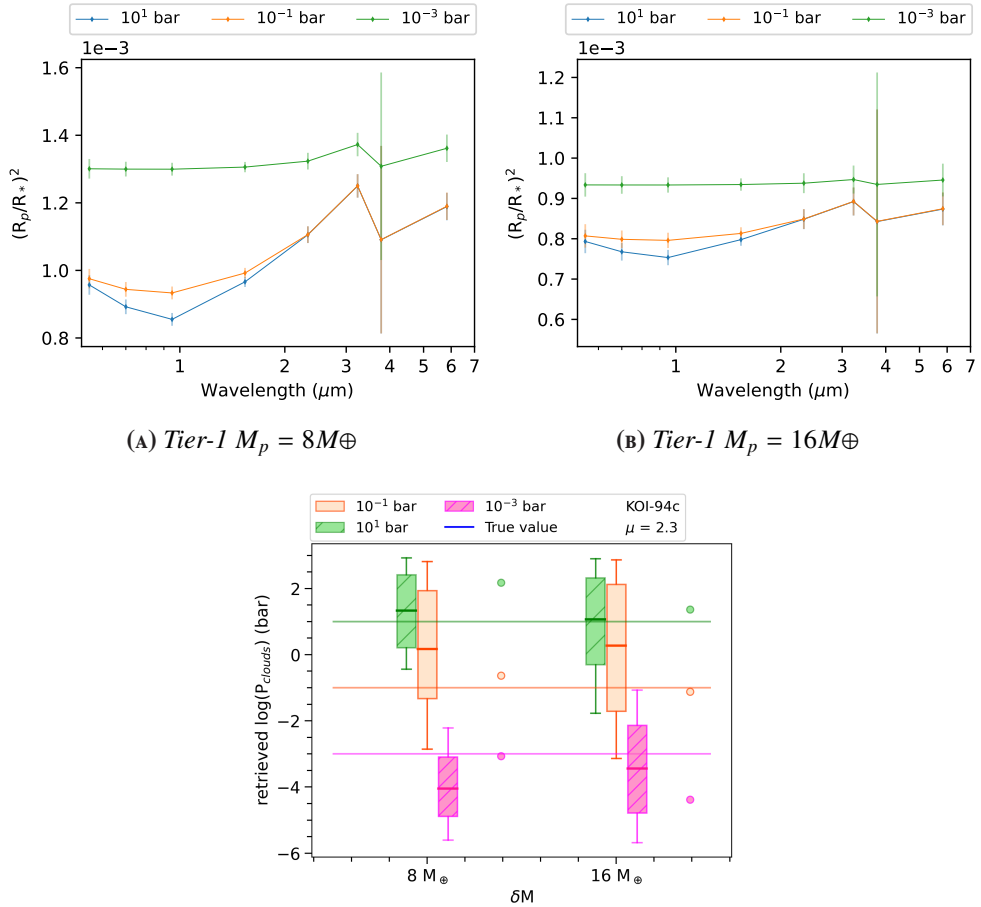

(A) *Tier-1* $M_p = 8M\oplus$

(B) *Tier-1* $M_p = 16M\oplus$

(C) *Cloud pressure*

FIGURE 4.27: *(Top panels) Spectra of KOI-94 c, as observed by Ariel, obtained considering different cloudy scenarios and assuming the number of transit required for Tier-1 for the two different values of planetary mass. (Bottom panel) Comparison between the retrieved cloud pressure of KOI-94 c obtained for different cloud pressures as a function of the mass. Colour scale and description of Figure B are the same as in Figure 4.3.*

4.1.8 Kepler-450 b

Kepler-450 is a three-planet system. The first mass constraint for this system were obtained by Yoffe et al. (2021). In Table 4.1 I reported the main properties of Kepler-450 and its planet Kepler-450 b ($M_b = 19.4^{+11.1}_{-6.8} M_\oplus$, $R_b = 6.0834 \pm 0.0022 R_\oplus$). Since Yoffe et al. (2021) estimated the mass of Kepler-450b with an uncertainty of about 60%, I investigated the contribution of the planetary mass uncertainty considering a mass precision level of 60%, 50% and 30%. I simulated the spectra assuming the number of transits required for the Tier-2 ($N_{obs} = 99$) to obtain the needed SNR (see the simulated spectra in Figure 4.28).

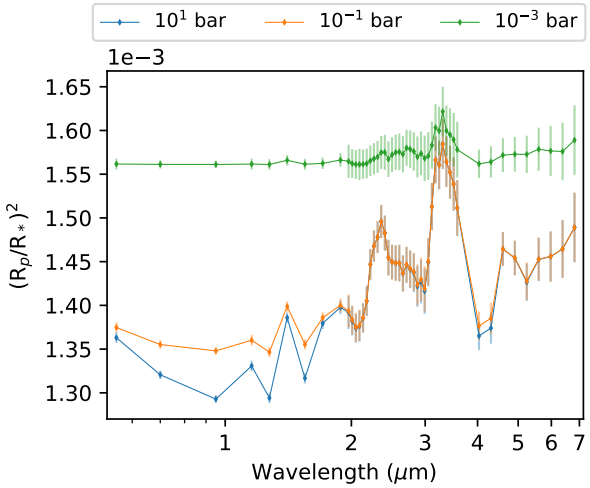

Figure 4.28: *Spectra of Kepler-450 b, as observed by Ariel, obtained considering different cloud pressures.*

In Figure 4.29 and Table B.12 I summarised the results of the retrieval. For high pressure clouds, all the quantities are well recovered with the exception of the case of $P_{clouds} = 10^{-3}$ bar, for which I obtained moderately precise retrieved parameters. In particular, according to the criteria of accuracy and precision described above, I obtained a not accurate retrieved CO mixing ratio for high altitude clouds. The mass uncertainty does not impact the results even in the worst considered scenario. All these results suggest that for this target is not particularly useful to further improve the mass measurement.

Also, as we can note from Figure 4.29b, with TauREx we are able to increase the precision of the mass estimate and refine the mass to within $\approx 10\%$ in the case of $P_{clouds} \geq 10^{-1}$ bar, giving an initial mass uncertainty of 60%.

In Figure 4.29c I showed the retrieved cloud pressure as a function of the mass uncertainty for the different considered scenarios. It can be seen that all the retrieved distributions are incompatible and therefore perfectly distinguishable. This result

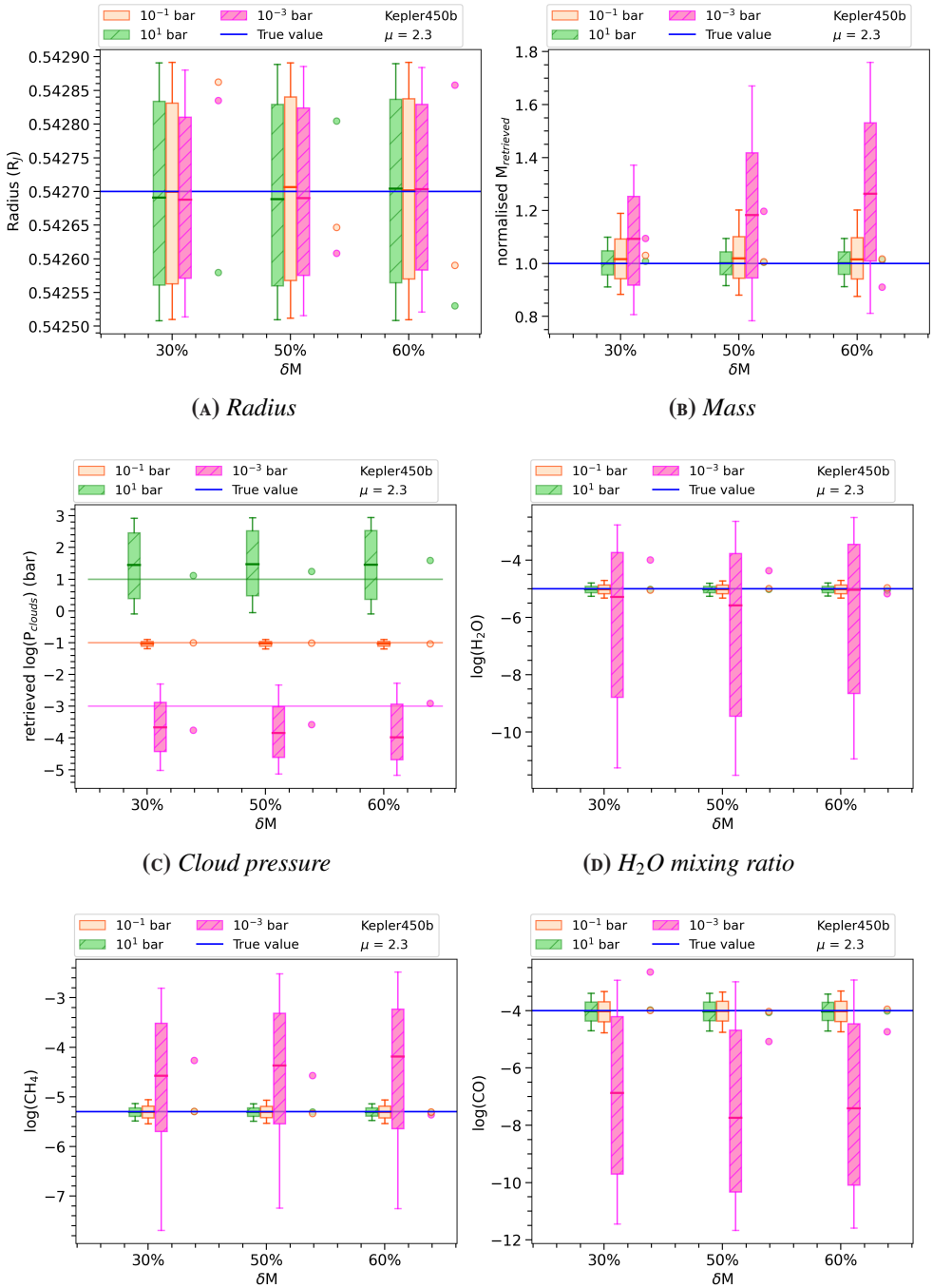

(A) *Radius* (B) *Mass*

(C) *Cloud pressure* (D) *H_2O mixing ratio*

(E) *CH_4 mixing ratio* (F) *CO mixing ratio*

FIGURE 4.29: *Impact of mass uncertainties on the retrieval performed for the hypothetical primordial atmosphere of Kepler-450 b for different cloud pressures as a function of the mass uncertainty. Colour scale and description of the figure are the same as in Fig. 4.3.*

is confirmed by the KS test, which suggests that the cloud pressure distributions derive from different samples ($p_{value} << 0.05$). I also performed the retrieval on the simulated spectra of Kepler-450 b, assuming the number of observations required by Tier-1 (N_{obs} = 6, see Figure 4.30a). As can be seen in Figure 4.30b and also

confirmed by the KS test, we are able to discriminate between the different cloudy scenarios since the Tier-1.

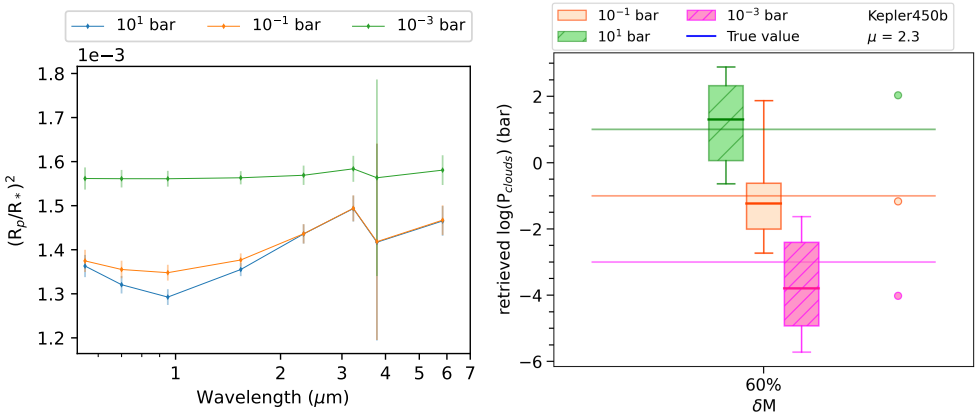

(A) *Tier-1* (B) *Cloud pressure*

Figure 4.30: *(A) Spectra of Kepler-450 b, as observed by Ariel, obtained considering different cloudy scenarios and assuming the number of transits required for Tier-1. (B) Comparison between the retrieved cloud pressure of Kepler-450 b obtained for different cloud pressures as a function of the mass uncertainty. Colour scale and description of Figure B are the same as in Figure 4.3.*

In light of these results, the analysis we will perform on the Tier-1 observations and the cloud pressure estimate will allow us to assess the feasibility of this target. In the case of high altitude clouds, probably to plan to reach a higher SNR increasing the number of transits will result in a too demanding observation to include the target in the final Ariel sample.

4.1.9 TOI-1728 b

The transiting planet candidate TOI-1728 b of the star TOI-1728 was confirmed by Kanodia et al. (2020). The star and planet characteristics are listed in Table 4.1. The estimated planetary mass of TOI-1728 b ($M_b = 26.78^{+5.43}_{-5.13} M_\oplus$, $R_b = 5.05^{+0.16}_{-0.17} R_\oplus$) has a uncertainty of approximately 20% (Kanodia et al., 2020). I examined the effect of this uncertainty by assuming mass uncertainties of 20% and 10%. The simulated spectra for different cloud pressures and with 14 observations (required for Tier-2) are shown in Figure 4.31.

The results of the retrieval are reported in Figure 4.32 and summarised in Table B.13. Also in this case the precision on the mass does not impact the results and the KS test test on the cloud distribution obtained from the Tier-1 planned transits ($N_{obs} = 1$, see Figure 4.33) allow to derive the cloud distribution to decide the strategy to be adopted in Tier-2.

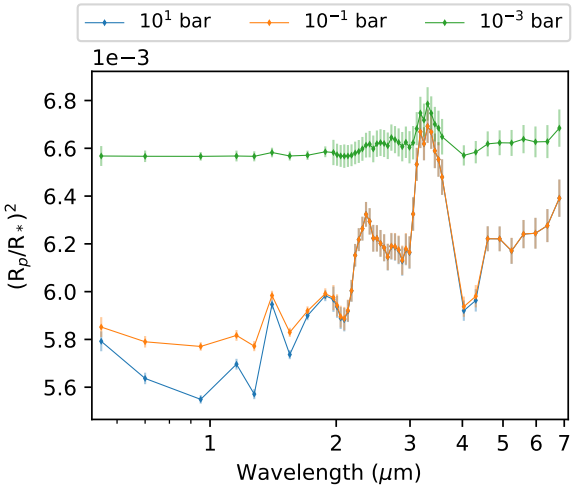

Figure 4.31: *Spectra of TOI-1728 b, as observed by Ariel, obtained considering different cloud pressures.*

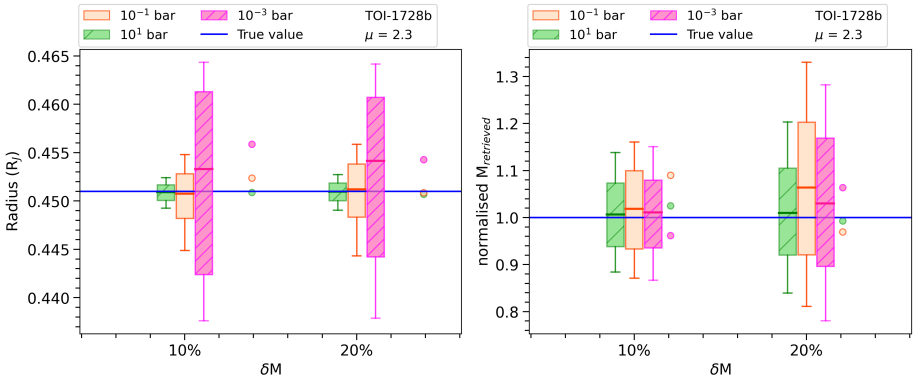

(A) *Radius*

(B) *Mass*

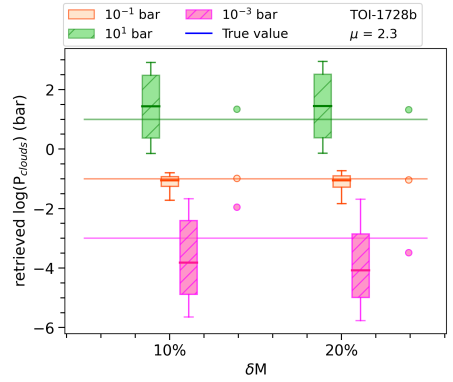

(C) *Cloud pressure*

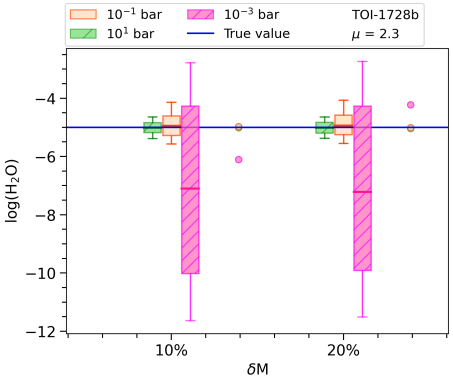

(D) H_2O *mixing ratio*

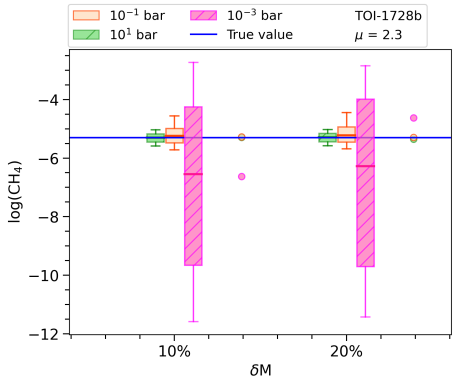

(E) CH_4 *mixing ratio*

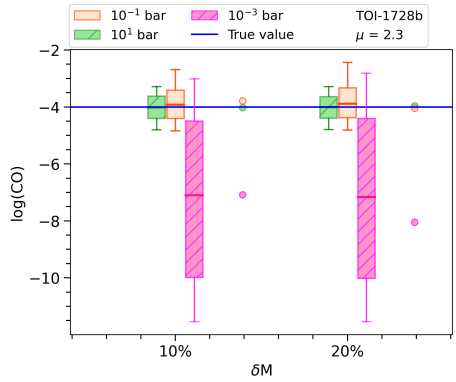

(F) *CO mixing ratio*

FIGURE 4.32: *Impact of the mass uncertainties on the retrieval performed for the hypothetical primordial atmosphere of TOI-1728 b for different cloud pressures. Colour scale and description of the figure are the same as in Figure 4.3.*

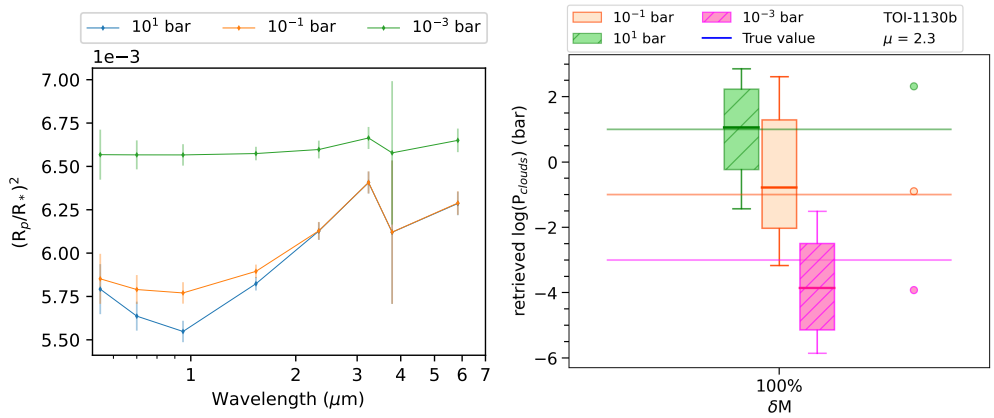

(A) *Tier-1* (B) *Cloud pressure*

FIGURE 4.33: *(A) Spectra of TOI-1728 b, as observed by Ariel, obtained considering different cloudy scenarios and assuming the number of transits required for Tier-1. (B) Comparison between the retrieved cloud pressure of TOI-1728 b obtained for different cloud pressures as a function of the mass uncertainty. Colour scale and description of Figure B are the same as in Figure 4.3.*

4.1.10 HATS-37A B

The distribution of the parameters of the discovered planets is far from homogeneous. This is due to observational biases and variations in the intrinsic occurrence of planets as a function of their physical parameters and those of their host stars. An example of intrinsically low occurrence rates is the so-called Neptune desert, a term coined by Mazeh et al. (2016) to describe a wedge in the period-mass or period-radius diagram where close-in (P ≤ 5 days) planets with radii similar to Neptune are very rare and essentially nonexistent for P≤ 3 days.

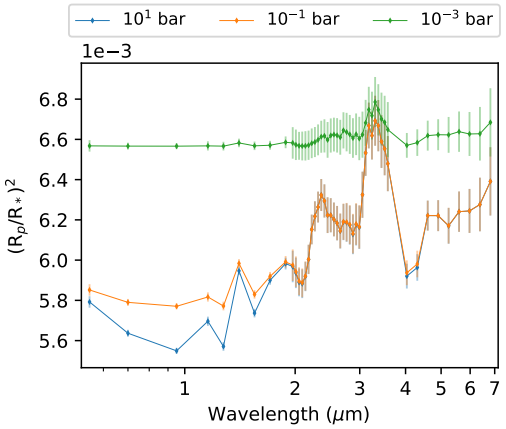

FIGURE 4.34: *Spectra of HATS-37A b, as observed by Ariel, obtained considering different cloud pressures.*

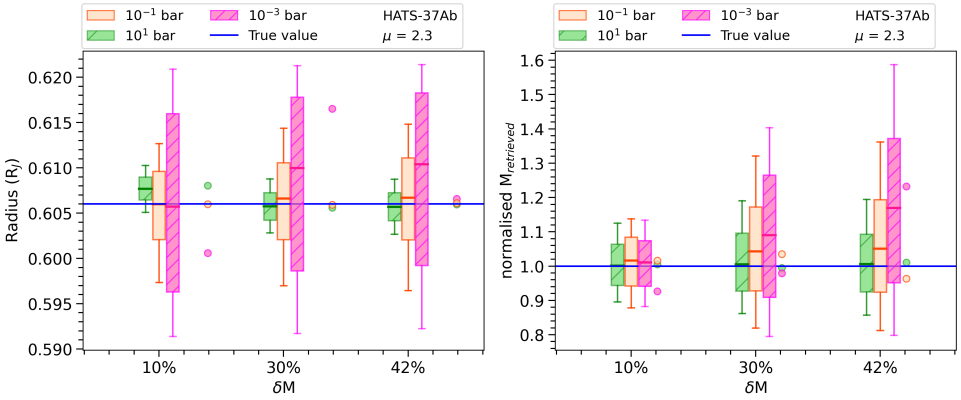

(A) *Radius* (B) *Mass*

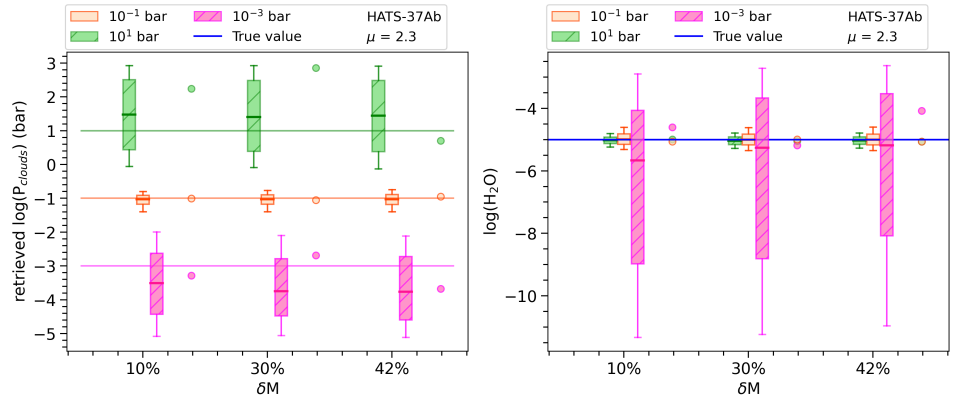

(C) *Cloud pressure* (D) *H_2O mixing ratio*

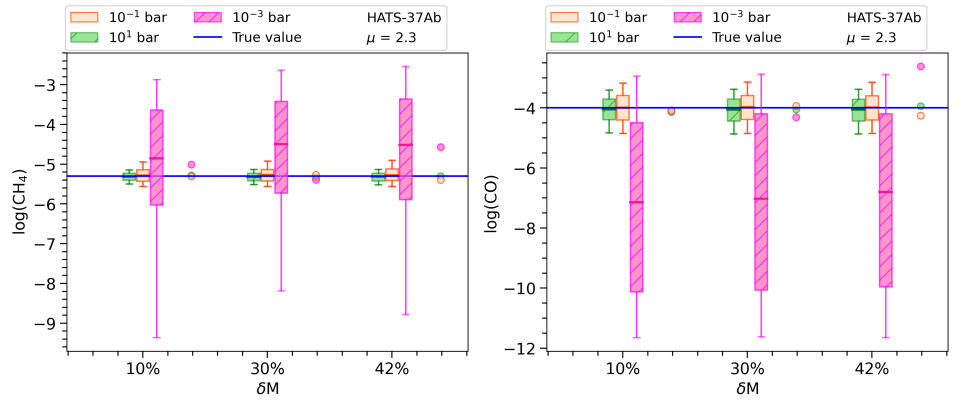

(E) *CH_4 mixing ratio* (F) *CO mixing ratio*

FIGURE 4.35: *Impact of mass uncertainties on the retrieval performed for the hypothetical primordial atmosphere of HATS-37A b for different cloud pressures as a function of the mass uncertainty. Colour scale and description of the figure are the same as in Fig. 4.3.*

Jordan et al. (2020) reported the discovery by the HATSouth survey of two transiting Neptunes in the desert. HATS-37A b is a Neptune-like exoplanet orbiting a G-type star. It has a estimated mass $M_p = 31.5 \pm 13.3 M_\oplus$ and a radius $R_p = 6.79 \pm 0.18 R_\oplus$. The host star HATS-37A has an apparent magnitude of 12.3, and an absolute magnitude of 5.6. It is 0.8 times more massive and 0.9 times larger than our Sun. These objects for their rare frequency are therefore very interesting for Ariel.

In Fig 4.34 I showed an example of the simulated spectra of HATS-37A b at different cloud pressures, taking into account the number of transits required for Tier-2 ($N_{obs} = 20$).

Since Jordan et al. (2020) estimated the mass of HATS-37A b with an uncertainty of $\approx 42\%$ I performed the retrieval considering mass uncertainties of 42%, 30% and 10%. I reported the results obtained for the primordial atmosphere of HATS-37A b in Figure 4.35 and I also summarised them in Table B.14.

When the cloud pressure gets closer to 10^{-3} bar, the estimation of the atmospheric parameters is moderately precise for the CH_4, the most prominent detectable features on the spectrum, and not precise and accurate for the other atmospheric components, such as H_2O and CO. However, these results do not depend on the mass uncertainty and suggest that a mass uncertainty of 42% is sufficient to retrieve the atmospheric parameters, in particular for $P_{clouds} > 10^{-3}$ bar.

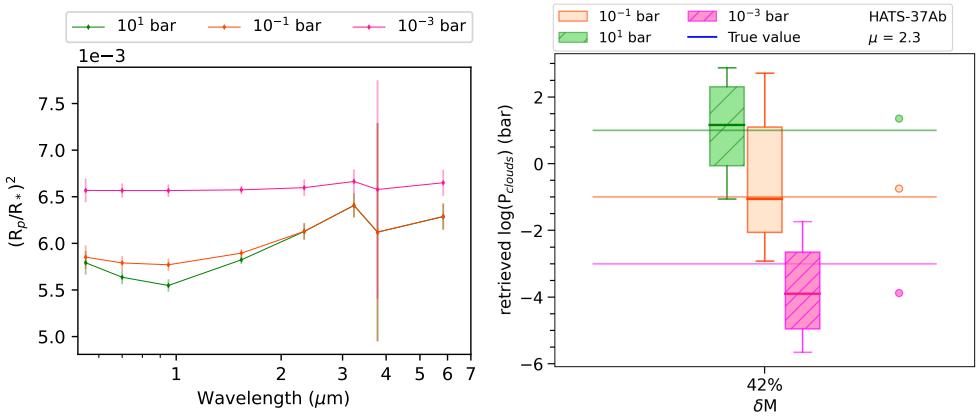

(A) *Tier-1* (B) *Cloud pressure*

Figure 4.36: *(A) Spectra of HATS-37A b as observed by Ariel obtained considering different cloudy scenarios and assuming the number of transits required for Tier-1. (B) Comparison between the retrieved cloud pressure of HATS-37A b obtained for different cloud pressures as a function of the mass uncertainty. Colour scale and description of Figure B are the same as in Figure 4.3.*

For high altitude clouds, it is difficult to constrain the atmospheric composition. However, also in this case we will be able to determine the cloud height from Tier-1

(N_{obs} = 1, Figures 4.36a and 4.36b), as confirmed by the KS test (p_{value} << 0.05), to take a decision if observe the target in Tier-2.

From Figure 4.35b we can also note that we could estimate the mass with more precision than what we already know using TauREx. For example, we can refine the mass to within 20% in the case of $P_{clouds} = 10^{-1}$ bar, giving an initial mass uncertainty of 42%.

4.2 Sub-Neptunes and super-Earths - Secondary atmospheres

In this section, I analysed the sub-Neptunes and super-Earths selected from the MRS of Ariel. The atmospheric retrieval of these kinds of planets is challenging because the mean molecular weight, μ, is unconstrained. Small planets might not have a H_2-dominated atmosphere and the dominant gas is often unknown. For the selected targets the forward spectra were obtained using H_2O and CH_4 as trace gases, with mixing ratios of 10^{-4} and 6×10^{-4}, and supposing different values of the mean molecular weight (μ = 2.3, N_2/He = 10^{-10}; μ = 7.6, N_2/He = 2) to explore different atmospheric compositions. I considered N_2-dominated atmosphere and used the N_2 to increase the mean molecular weight of the atmosphere. That is, as demonstrated in Di Maio, C. et al. (2023), one of the most unfavourable scenarios since diatomic background gases, such as H_2 and N_2 referred to as spectrally inactive gases, do not exhibit strong vibrational absorptions bands, so they do not produce traceable features directly observable in the spectrum.

The comparison between the results obtained in the two different atmospheric cases could allows to test our capability to discriminate between primordial (μ = 2.3) and secondary atmosphere.

4.2.1 GJ9827 c

GJ 9827 is known to host three super-Earths with radii between approximately 1 and 2 $R_\oplus$, and with orbital period of 1.21, 3.65 and 6.21 days (Niraula et al., 2017; Rodriguez et al., 2018). The star has a V-band magnitude of 10.25, a mass of 0.606 $M_\odot$, and a radius of 0.63 $R_\odot$. The characteristics of the star and its orbiting planet, GJ 9827 c (M_c = 1.92 ± 0.49 $M_\oplus$, R_c = 1.201 ± 0.046 $R_\oplus$), are listed in Table 4.2. Kosiarek et al. (2021) estimated the mass of GJ 9827 c with an uncertainty of about 25%. I investigated the impact of this uncertainty by considering precision levels of 25%, 20% , and 10%. The simulated spectra were obtained taking into account the

number of transits required for the Tier-2 (N_{obs} = 11).

In Figure 4.37, I showed the simulated spectra for different cloud pressures, obtained using the parameters listed in Table 4.2.

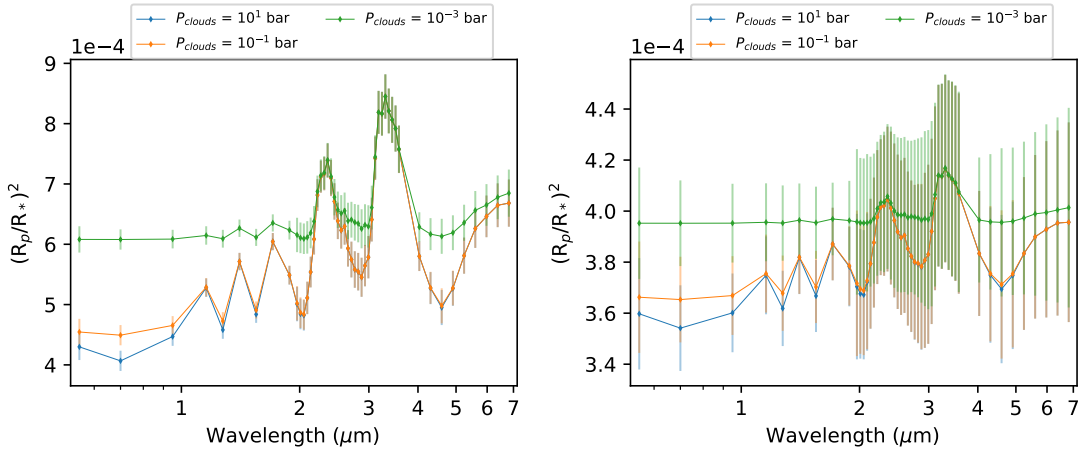

(A) μ = 2.3 (B) μ = 7.6

Figure 4.37: *Simulated spectra of GJ 9827 c as observed by Ariel, obtained considering different cloud pressures and mean molecular weights.*

As can be seen in Figure 4.38 and Table B.15, for μ = 2.3 we are able to accurately retrieve all the parameters, while some discrepancies appear in the atmospheric retrieval for the heaviest atmosphere scenario (μ = 7.6). In particular, for μ = 2.3 we are able to accurate retrieve the CH_4 mixing ratio when $P_{clouds} \geq 10^{-1}$ bar, while we not accurately retrieved the H_2O and the mean molecular weight in all the tested cloudy scenarios. However, all these results are not dependent on the mass uncertainties (see light coloured boxes in Figure 4.38).

These discrepancies and the inability to constrain the atmospheric components are due to the lower SNR in the simulated spectra obtained with the greatest considered mean molecular weight. Indeed, as shown in Figure 4.37b, when the atmosphere is dominated by N_2 (μ = 7.6, N_2/He = 2) and the cloud pressure decreases, the spectra are dominated by the noise, making it difficult to detect the spectral features of H_2O and CH_4. To test the impact of the SNR and to understand if the composition of the atmosphere can be better constrained with an increased SNR, a retrieval was performed assuming N_{obs} = 22, a number of transits twice than required for the Tier-2. The results of this test are shown in Figure 4.38 with dark coloured boxes and summarised in Table B.16.

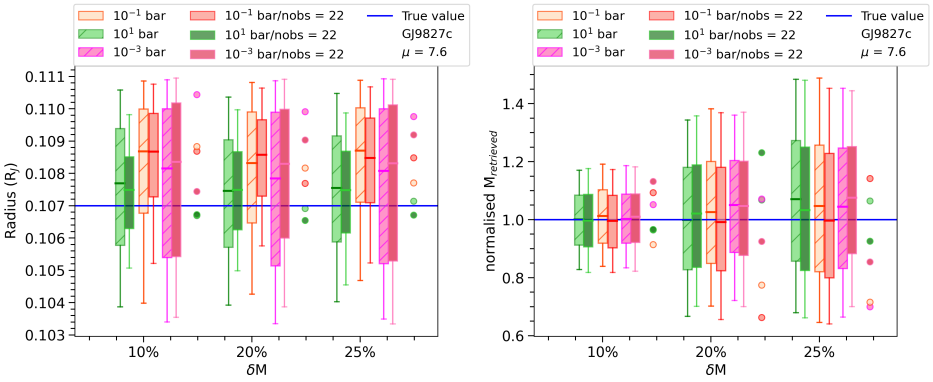

(A) *Radius* (B) *Mass*

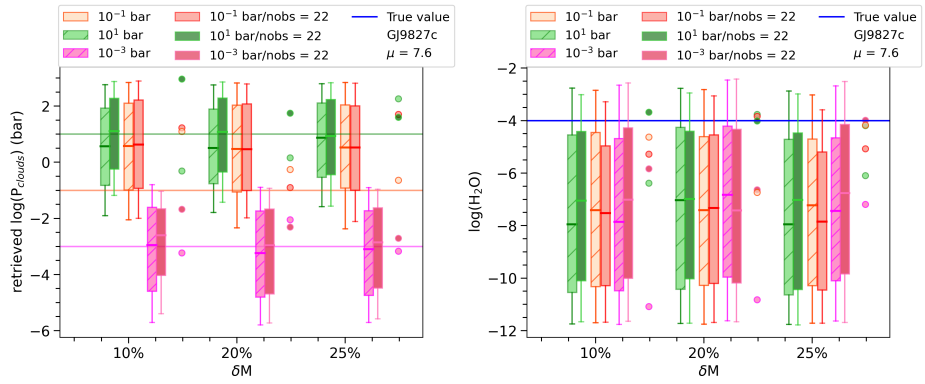

(C) *Cloud pressure* (D) *H_2O mixing ratio*

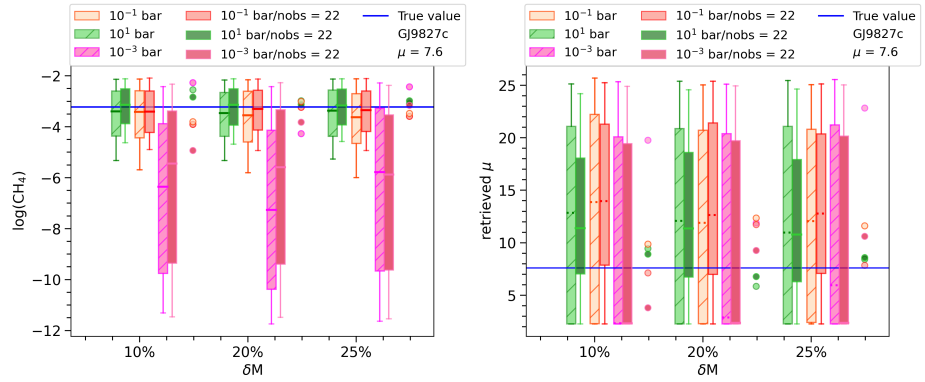

(E) *CH_4 mixing ratio* (F) *μ*

FIGURE 4.38: *Impact of mass uncertainties and number of transits on the retrieval of hypothetical N_2-dominated secondary atmosphere of GJ9827 c (μ = 7.6) with different cloud pressures (P_{clouds} = 10^1 bar in green, P_{clouds} = 10^{-1} bar in orange and P_{clouds} = 10^{-3} bar in magenta) as a function of mass uncertainty. The darker colours represent the results with N_{obs} = 22, a number of transits two times higher than Tier-2 requirement. The blue line highlights the input value. Points alongside the boxes show the MAP (maximum-a-posteriori) for each case. The size of the boxes and the vertical segments represent the points within 1σ and 2σ of the median of the distribution (highlighted with solid lines), respectively.*

We observe that even when N_{obs} = 22, we are not able to retrieve the H_2O mixing ratio accurately. However, when comparing the results to those obtained with N_{obs}

= 11, we see an improvement in the accuracy of the MAP retrieved values. Furthermore, in the clear-sky case, we are able to retrieve the mean molecular weight with moderate accuracy and precision. The improved SNR allow us to accurately retrieve the MAP values of the mean molecular weight, with moderate accurate values for high altitude clouds.

These results suggest that for this target, the precision level of 25% for the planetary mass is sufficient, and an increased precision in the mass estimation does not improve our accuracy in atmospheric retrieval. On the other hand, an increased number of transits, two times (or more) greater than the current requirements for Tier-2, is highly recommended to accurately characterise the atmospheric composition.

The results obtained for the two different values of mean molecular weight suggest that we are able to distinguish between primordial and secondary atmospheres. In the primordial case, we were able to precisely determine the mean molecular weight. However, for the case where μ = 7.6, the wide range of mean molecular weight distributions suggests the presence of a secondary atmosphere, although we are unable to accurately and precisely determine its composition.

For this target, I also verified that the Tier-1 planet transits (N_{obs} = 1) are sufficient to discriminate between different cloudy conditions and between the primordial and secondary atmosphere ($p_{value} << 0.05$ for both cases and comparing all the tested scenarios).

4.2.2 LTT1445A b

LTT 1445 is a hierarchical triple M-dwarf star system located at 6.86 pc away (Gaia Collaboration et al., 2016; Lindegren et al., 2021). The primary star, LTT 1445 A, with a mass of 0.257 $M_\odot$ and a radius of 0.268 $R_\odot$, is the most massive member of this triple system and is known to host the transiting planet LTT 1445A b, with an orbital period of 5.36 days. This makes it the second-closest known transiting exoplanet system, and the closest one with a M-dwarf host. LTT 1445 A and its orbiting planet were characterised by Winters et al. (2019, 2022). In the first study, they estimated the planetary mass with an uncertainty of about 90% ($M_p = 2.2^{+1.7}_{-2.1}$ $M_\oplus$, $R_b = 1.38^{+0.13}_{-0.12}$ $R_\oplus$), while in the most recent work, they obtained a more precise estimation of the mass of the planet ($M_b = 2.87^{+0.26}_{-0.25}$ $M_\oplus$, $\delta M \approx 10\%$). The main characteristics of this target and its host star are reported in Table 4.2.

In Fig 4.39 I showed the simulated spectra of LTT1445A b with different mean molecular weights, assuming different cloudy scenarios. I compared the simulated spectra obtained using the parameters from Winters et al. (2019) and Winters et al.

(2022) in Figure 4.40. For both cases, I assumed the number of transits required for Tier-2 (N_{obs} = 4), which was estimated based on the parameters from Winters et al. (2019). This may not guarantee the needed SNR in the simulated spectra obtained assuming the parameters estimated by Winters et al. (2022).

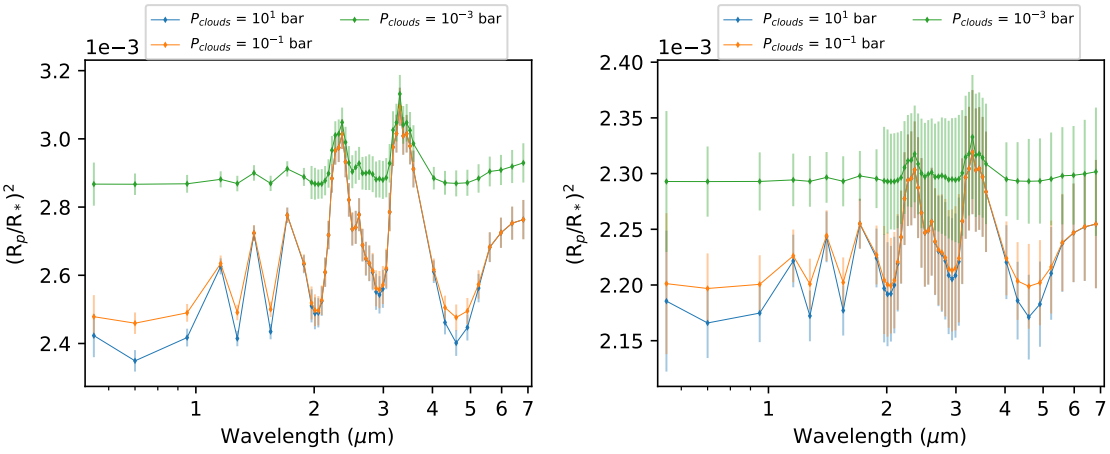

(A) μ = 2.3 (B) μ = 7.6

Figure 4.39: *Simulated spectra of LTT1445A b as observed by Ariel, obtained considering different cloud pressures and mean molecular weights, using the Winters et al. (2019) parameters.*

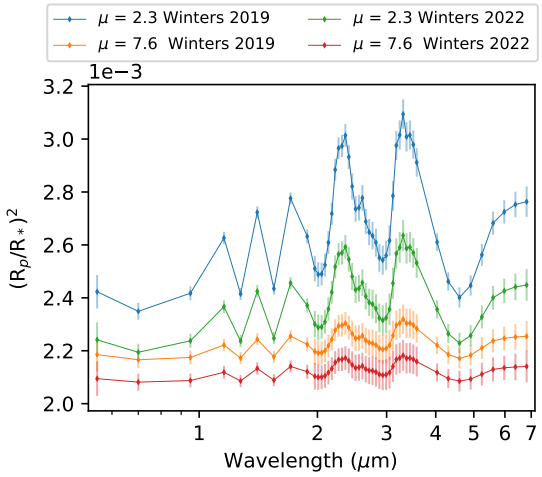

Figure 4.40: *Simulated spectra of LTT1445A b as observed by Ariel, for different mean molecular weights, obtained using the parameters from Winters et al. (2019) and Winters et al. (2022), and supposing a clear sky N_2-dominated secondary atmosphere.*

As seen in Figure 4.39, in the scenario with the highest cloud pressure (P_{clouds} = 10^{-3} bar, shown in green) and mean molecular weight, the clouds dominate the spectrum, making it nearly flat. In this situation, with both high cloud pressure and high mean molecular weight, the SNR is lower and spectral features are difficult to detect.

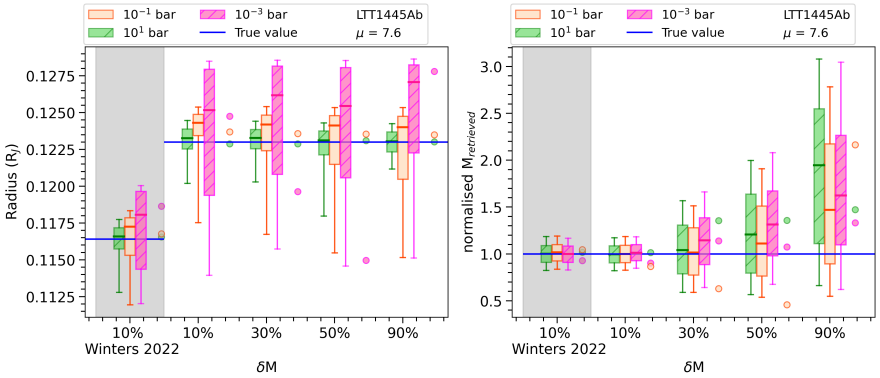

(A) *Radius* (B) *Mass*

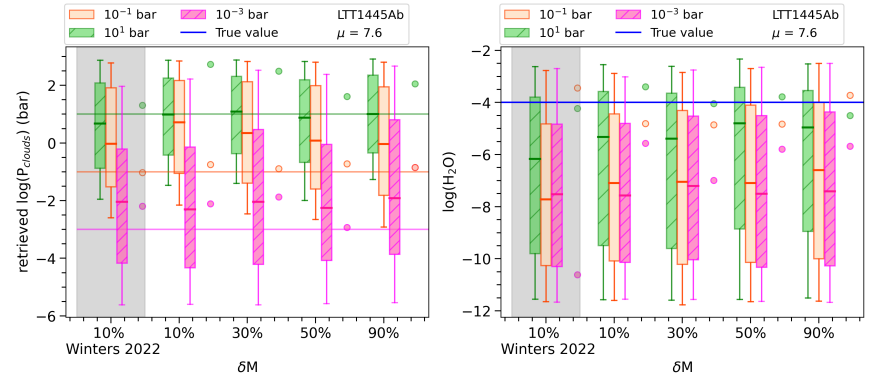

(C) *Cloud pressure* (D) *H_2O mixing ratio*

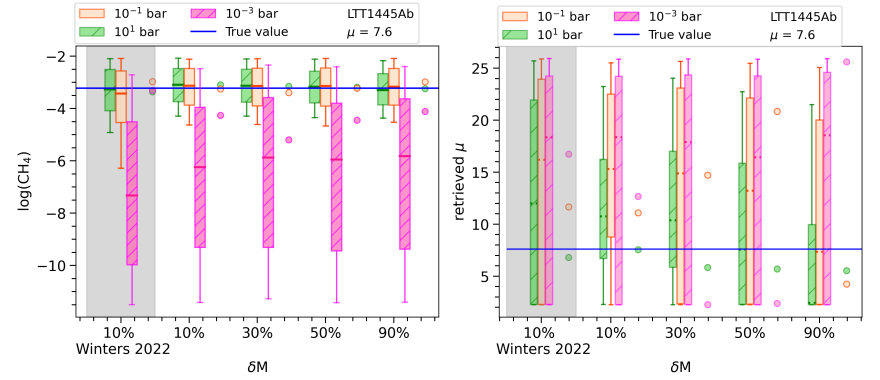

(E) *CH_4 mixing ratio* (F) *μ*

Figure 4.41: *Impact of the mass uncertainties on the retrieval performed for the hypothetical N_2-dominated secondary atmosphere of LTT1445A b (μ = 7.6) for different cloud pressures (P_{clouds} = 10^1 bar in green, P_{clouds} = 10^{-1} bar in orange and P_{clouds} = 10^{-3} bar in magenta) as a function of the mass uncertainty. The blue line highlights the input value. The points alongside the boxes highlight the MAP values obtained for each analysed case. The size of the boxes and the vertical segments represent the points within 1σ and 2σ of the median of the distribution (highlighted with solid lines), respectively.*

Figure 4.40 also shows that the main spectral features in the spectra generated using the parameters from Winters et al. (2022) are less distinct and the SNR is lower for both mean molecular weight values compared to the spectra generated using the parameters from Winters et al. (2019). The reason for these discrepancies is the determination of the stellar and planetary radii. Specially, the parameters from Winters et al. (2022) result in $R_p^2/R_*^2 \simeq 0.199$, while the parameters from Winters et al. (2022) result in $R_p^2/R_*^2 \simeq 0.193$. Given these differences, it is reasonable to expect less accurate atmospheric parameter determination from retrievals performed on simulated spectra obtained using the parameters from Winters et al. (2022). Also, demonstrated in previous cases, it could depend on the gravity of the planet, that determines the scale height and then the SNR, and that is lower if we considered the Winters et al. (2019) parameters.

Figure 4.41 shows the results obtained using the parameters from Winters et al. (2019) with different mass uncertainties of 90%, 50%, 30% and 10%. Additionally, I conducted a similar test using the parameters obtained from Winters et al. (2022) with a mass uncertainty of 10% (represented in the gray section of the plots). The results are summarised in Tables B.17 and B.18.

From Table B.17 , we can see that for $\mu = 7.6$, the H_2O mixing ratio cannot be accurately retrieved even with a mass uncertainty of 30% or 10%. The accuracy improves in the clear-sky atmosphere and when considering the MAP values. The CH_4 is easier to detect, and we can accurately retrieve this parameter when $P_{clouds} \geq 10^{-1}$ bar, with some discrepancies appearing in the presence of high altitude clouds. The mean molecular weight is moderately accurately retrieved in the clear-sky case, but cannot be retrieved in the presence of clouds.

These results are not impacted by the knowledge of the mass, as confirmed by the test with a mass uncertainty of 10% (see Table B.18). The results of the retrieval performed on the spectra simulated using the parameter of Winters et al. (2022) (shown in the grey part of the plots) are not better, and in some cases, they are even worse compared to the results obtained using the Winters et al. (2019) parameters. In particular, the H_2O and mean molecular weight parameters go from being moderately accurate to inaccurate in the clear-sky case. This is due to the lower SNR of the Winters et al. (2022) spectra compared to the SNR of the Winters et al. (2019) spectra.

These results highlight the importance of ensuring adequate SNR and suggest that, in this case, an increased number of transits may be necessary to improve the accuracy of the results, despite the excellent mass estimate performed by Winters et al. (2022).

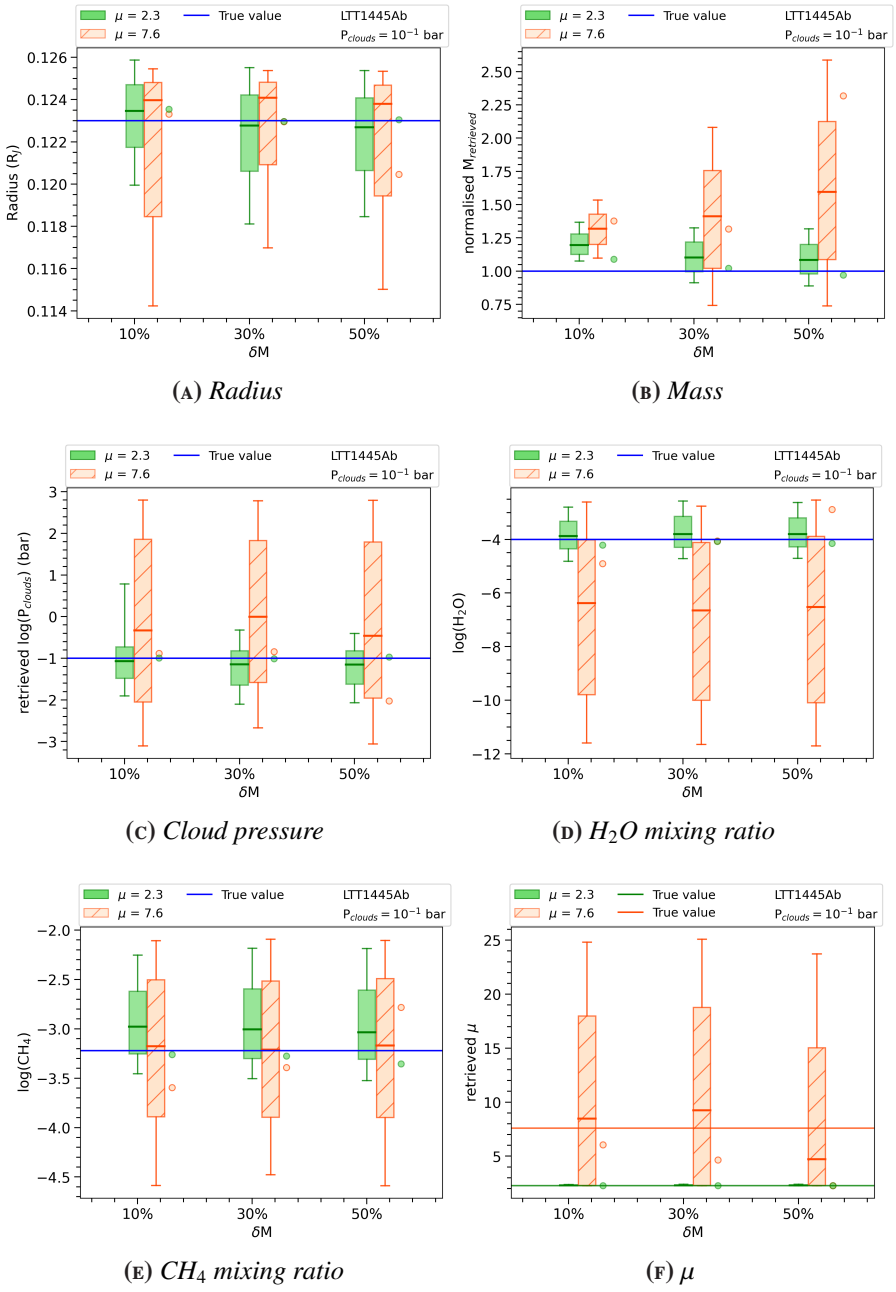

(A) *Radius* (B) *Mass*

(C) *Cloud pressure* (D) H_2O *mixing ratio*

(E) CH_4 *mixing ratio* (F) μ

Figure 4.42: *Impact of the mass uncertainties on the retrieval performed on the simulated spectra of LTT1445A b obtained considering* $P_{clouds} = 10^{-1}$ *bar, and assuming the Winters et al. (2019) parameters and exploring the parameters space using a gaussian prior for the planetary mass centred at the planetary mass obtained by Winters et al. (2022). In green the results obtained assuming a primordial atmosphere* ($\mu = 2.3$)*, in orange the results obtained for the secondary atmosphere* ($\mu = 7.6$)*. The horizontal lines highlight the input values. The size of the boxes and the vertical segments represent the points within* 1σ *and* 2σ *of the median of the distribution (highlighted with solid lines), respectively.*

Since the two different mass estimation, I tested our capability of accurately retrieving the atmospheric composition when we have minimum or wrong information about the mass. I simulated the spectra assuming the mass obtained by Winters et al. (2019) and considering an intermediate cloudy scenario ($P_{clouds} = 10^{-1}$ bar), and then I performed the retrieval exploring the parameters space around the planetary mass obtained by Winters et al. (2022) with a gaussian prior and with different mass uncertainties (10%, 30%, and 50%).

As we can see from Figure 4.42, and also from Table B.19, we are able to accurately retrieve the atmospheric composition in the case of a primordial atmosphere. For $\mu = 7.6$, we accurately and precisely retrieved the CH_4 mixing ratio, while the retrieved H_2O is not accurate and precise, despite we might increase the accuracy considering the MAP values. A better estimation of the mass seems to increase our accuracy in the determination of the mean molecular weight, despite is still not precise. As we note from Figure 4.42f, these results suggest that we are able to discriminate between the primary or secondary atmosphere, although we are not always able to accurately estimate the mean molecular weight in secondary atmosphere cases.

4.2.3 K2-3 c

M dwarfs that host temperate rocky planets exhibit a wide range of physical properties that can impact habitability.

Furthermore, the fact that these temperate planets are located at different distances from host stars spanning various spectral subtypes makes their comparative characterisation particularly interesting. Unfortunately, many of these planets either do not transit or their parent star is too faint for detailed follow-up, making it challenging to robustly characterise these planets and study their interior structures and compositions. In this context, the planetary system around K2-3 (EPIC 201367065), a nearby (45 pc) M0 dwarf (V = 12 mag; J = 9.4 mag), presents an interesting opportunity for follow-up studies. K2 mission observations showed that K2-3 hosts at least three transiting small planets (Crossfield et al., 2015): K2-3 b ($R_p = 2\ R_\oplus$, $P_{orb} = 10$ days), K2-3 c ($R_p = 1.7\ R_\oplus$, $P_{orb} = 24.6$ days), and K2-3 d ($R_p = 1.6\ R_\oplus$, $P_{orb} = 45.5$ days).

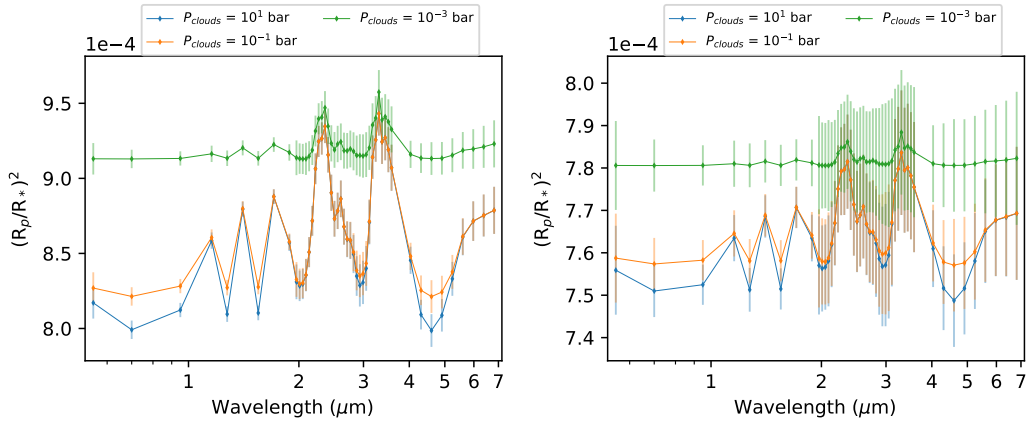

(A) μ = 2.3 (B) μ = 7.6

Figure 4.43: *Simulated spectra of K2-3 c as observed by Ariel, obtained considering different cloud pressures and mean molecular weights.*

Using Gaussian process regression on radial velocity time series, Damasso et al. (2018) were able to derive masses for both planet b (M_b = 6.6 ± 1.1 $M_\oplus$ - $\delta M \simeq$ 40%) and planet c (M_c = 3.1 $^{+1.3}_{-1.2}$ $M_\oplus$). The main properties of K2-3 c and its host star are listed in Table 4.2.

To test the impact of planetary mass uncertainty, I performed retrievals assuming the precision of 10%, 30%, and 40%. I simulated the spectra of K2-3 c assuming the number of transits required for Tier-2 (N_{obs} = 95). All the results are summarised in Table B.23 and in Figure 4.44.

As in the previous case, for the primordial case we are able to accurately retrieve all the atmospheric parameters. For μ = 7.6, the most prominent spectral features of CH_4 between 3 and 4 μm, can be accurately retrieved when $P_{clouds} =\geq 10^{-1}$ bar, and also the H_2O is accurately retrieved in the clear sky case, but with not accurate precision. Furthermore, in the clearsky case we are able to moderately accurately retrieve the mean molecular weight, and the accuracy increase considering the MAP values. Additionally, in the presence of clouds we are not able to retrieve the H_2O and the mean molecular weight.

However, in light of these results, we can discriminate if the planet has a secondary atmosphere despite the wide range of the 1σ distribution of the derived μ (see Figure 4.44f). I also verified our capability to discriminate between the primary and secondary atmosphere and the cloudy condition since the Tier-1 (N_{obs} = 7, $p_{value} << 0.05$).

These results are not correlated with the planetary mass uncertainty, so the current mass estimate is sufficient to retrieve the composition of the atmosphere in non-extreme cases of clouds and mean molecular weight.

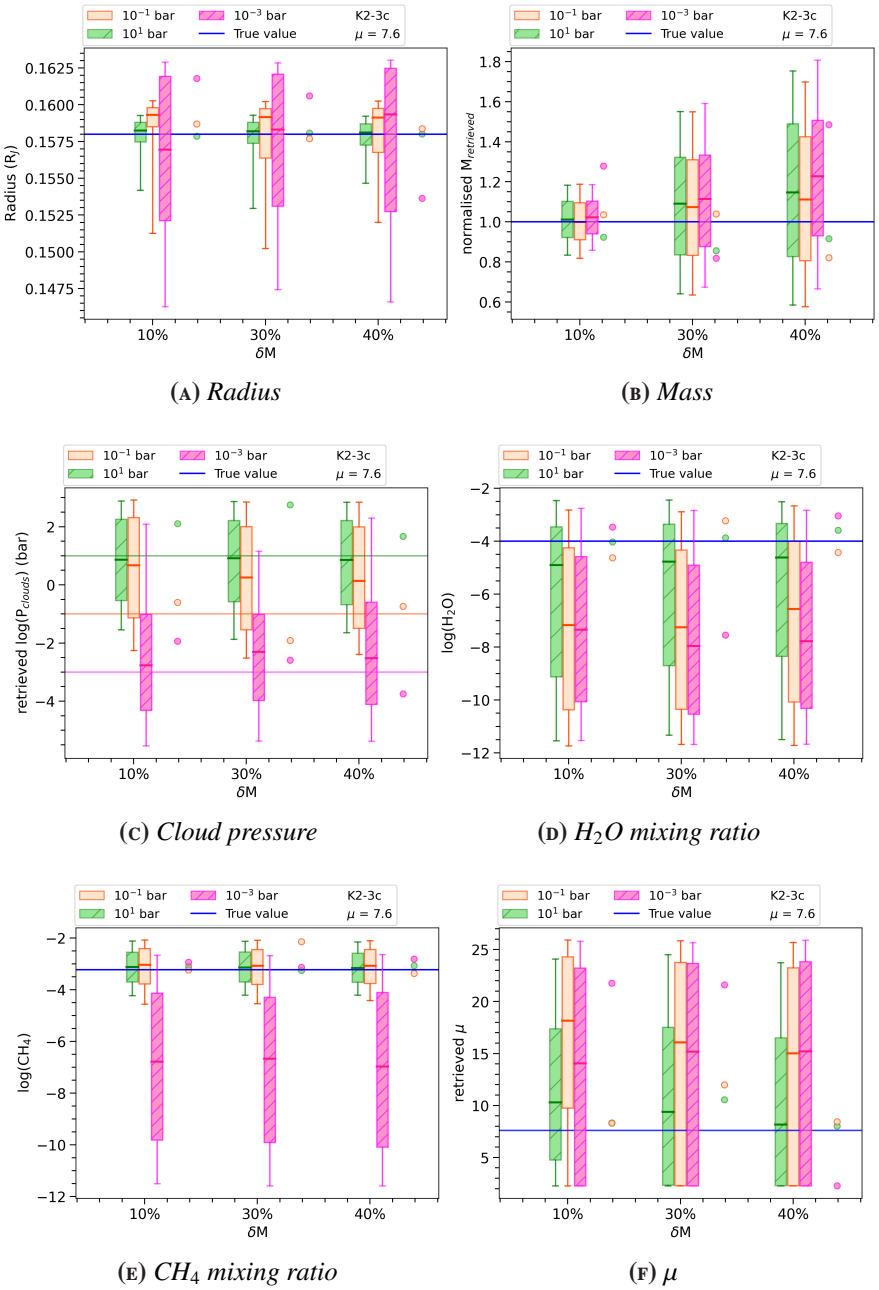

(A) *Radius* (B) *Mass*

(C) *Cloud pressure* (D) H_2O *mixing ratio*

(E) CH_4 *mixing ratio* (F) μ

FIGURE 4.44: *Impact of the mass uncertainties on the retrieval performed for the hypothetical N_2-dominated secondary atmosphere of K2-3 c (μ = 7.6) for different cloud pressures. Colour scale and description of the figure are the same in Fig. 4.3.*

4.2.4 K2-138 g

K2-138 is a moderately bright (V = 12.2, K = 10.3) main-sequence K star. It hosts seven small transiting planets, with sizes ranging from 1.6 to 3.3 $R_\oplus$, in a compact configuration, with orbital periods of 2.35, 3.56, 5.40, 8.26, 12.76 and 41.96 days. Table 4.2 summarises the parameters of the star and the outer planet K2-138 g ($M_g = 4.32^{+5.26}_{-3.03}$ $M_\oplus$, $R_g = 3.013^{+0.303}_{-0.251}$ $R_\oplus$) used for the retrieval.

Figure 4.45 shows the simulated spectra of K2-138 g, considering different mean molecular weights and cloud pressures, while taking into account the number of transits required for Tier-2 (N_{obs} = 106) to simulate the necessary SNR.

From Figure 4.45b, we can see that the number of transits required for this target provides a high SNR, and, under these conditions, the spectra do not appear to be dominated by the noise, allowing the features of H_2O and CH_4 to be detected in the simulated spectra with μ = 7.6, even in the worst cloudy considered scenario.

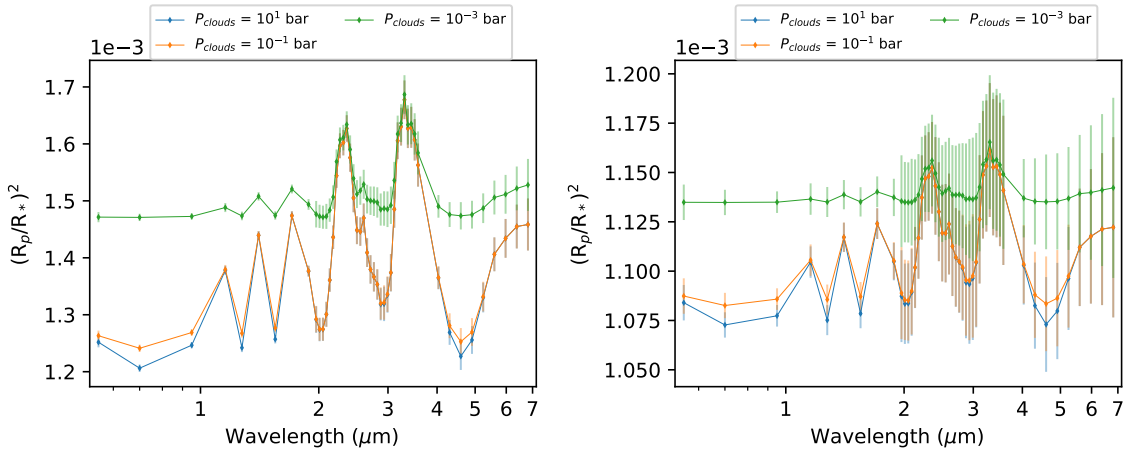

(A) μ = 2.3 (B) μ = 7.6

Figure 4.45: *Simulated spectra of K2-138 g, as observed by Ariel, obtained considering different cloud pressures and mean molecular weights.*

Since the mass of the outer planet was estimated by Lopez et al. (2019) with an uncertainty of about 121%, I performed the retrieval assuming mass uncertainties of 30%, 50%, and 121%. The results of the retrieval are summarised in Table B.21 and in Figure 4.46).

We can see that a mass uncertainty of 50% leads to a more accurate retrieval of the planetary mass (see Figure 4.46b). This trend has a slight effect on the retrieved mean molecular weight, particularly when μ = 7.6. In this case, the accuracy of the μ is increased when $P_{clouds} \geq 10^{-1}$ bar (see Figure 4.46f). However, the level precision of the mass does not seem to significantly impact the retrieved values for

the trace gases (see Figures 4.46d and 4.46e).

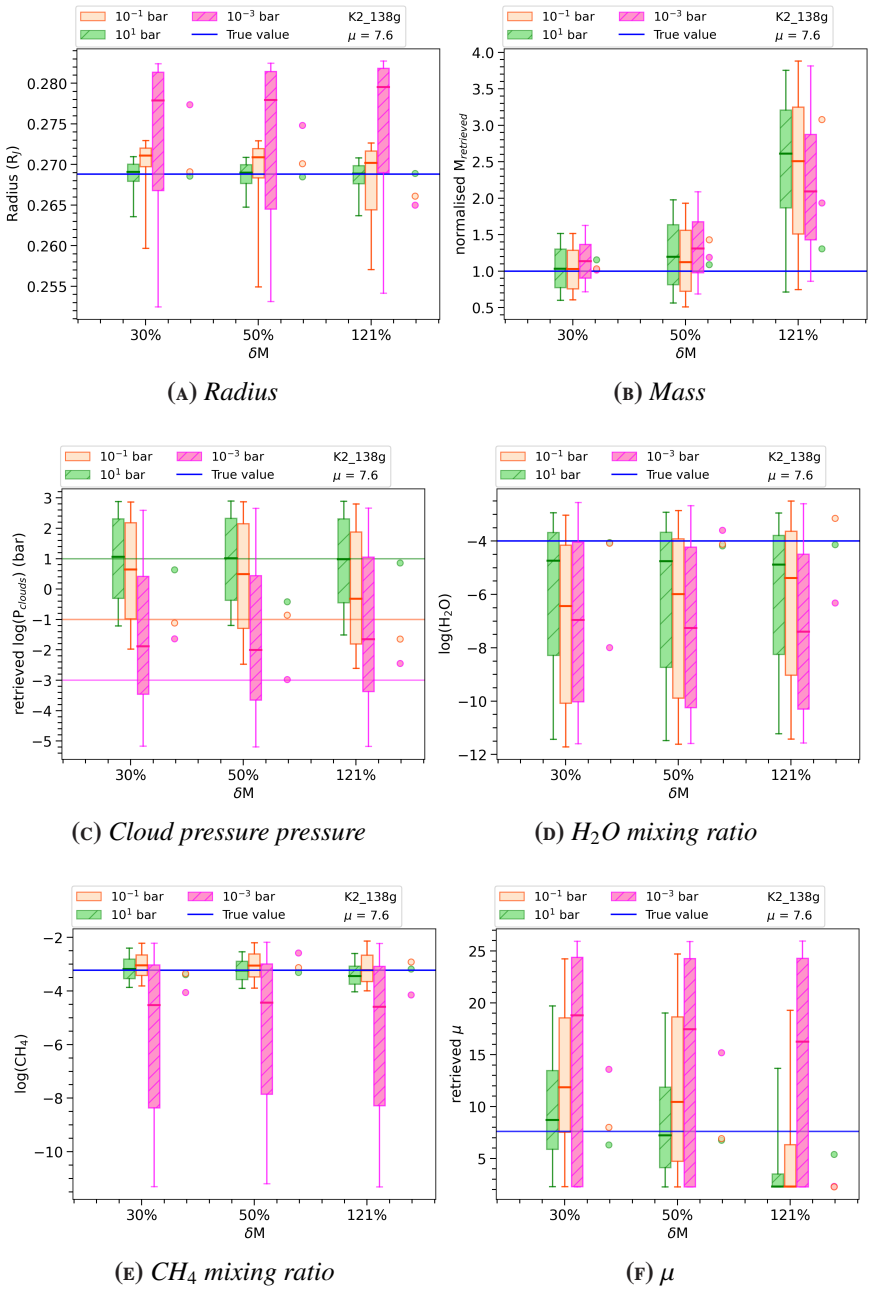

(A) *Radius* (B) *Mass*

(C) *Cloud pressure pressure* (D) *H_2O mixing ratio*

(E) *CH_4 mixing ratio* (F) *μ*

FIGURE 4.46: *Impact of the mass uncertainties on the retrieval performed for the hypothetical N_2-dominated secondary atmosphere of K2-138 g (μ = 7.6) for different cloud pressures. Colour scale and description of the figure are the same in Fig. 4.3.*

From Figure 4.46c, it appears that we might be able to distinguish between no/low and high altitude clouds. I also verified that the Tier-1 planet observations (N_{obs} = 7) are sufficient to discriminate between different cloudy conditions and between primordial and secondary atmosphere cases (p_{value} << 0.05). In light of this evaluation, made during the first tier of the mission, we may decide to either

slightly increase the number of transits, despite it already being time-consuming with a Tier-2 N_{obs} = 106, in order to achieve a higher SNR or to exclude this target from the Tier-2. In any case, an improvement to δM ≈ 50% is necessary for this target if we want to constrain the μ value.

4.2.5 K2-32 d

K2-32 harbours three planets, K2-32 b, K2-32 c, and K2-32 d, with orbital periods of 8.99 days, 20.66 days, and 31.7 days, respectively. The planets were first confirmed in the study by Sinukoff et al. (2016). The physical properties and parameters used to simulate the spectra of K2-32 d are listed in Table 4.2. The number

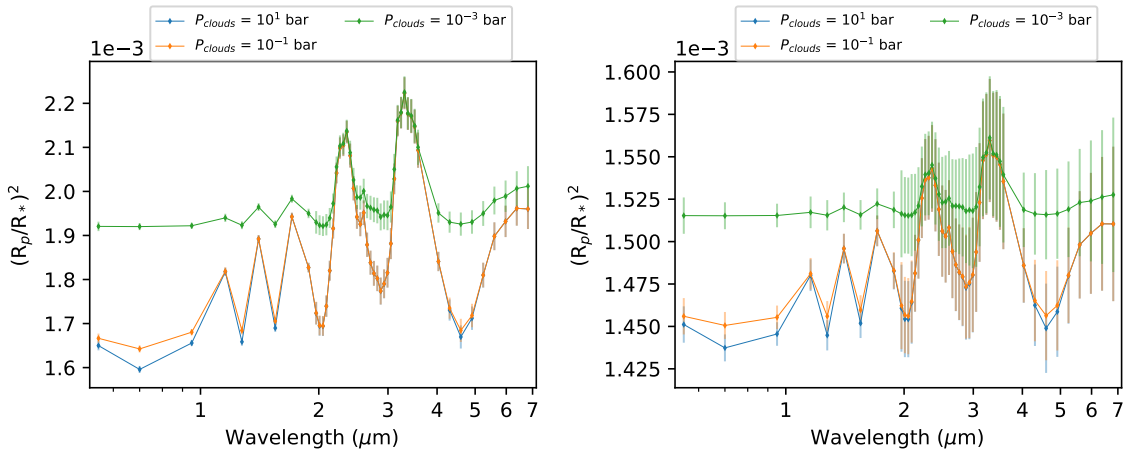

(A) μ = 2.3 (B) μ = 7.6

Figure 4.47: *Simulated spectra of K2-32 d, as observed by Ariel, obtained considering different cloud pressures and mean molecular weights.*

of transits required for Tier-2 (N_{obs} = 50) was taken into account when simulating the spectra. In 2020, Lillo-Box et al. (2020) estimated the mass of K2-32 d with an uncertainty of 38%. To evaluate the impact of this uncertainty on the atmospheric retrieval, I performed the retrieval with planetary mass uncertainties of 20%, 30%, and 38%.

The comparison between the simulated spectra assuming different mean molecular weights and cloud pressures is shown in Figure 4.47. The results of the atmospheric retrieval are presented in Table B.22 and in Figure 4.48.

The number of transits required for Tier-2 provides a high SNR, allowing us to distinguish the spectral features of H_2O and CH_4 even in the presence of high altitude clouds. Thus, a high level of accuracy in the atmospheric retrieval of these components can be expected.

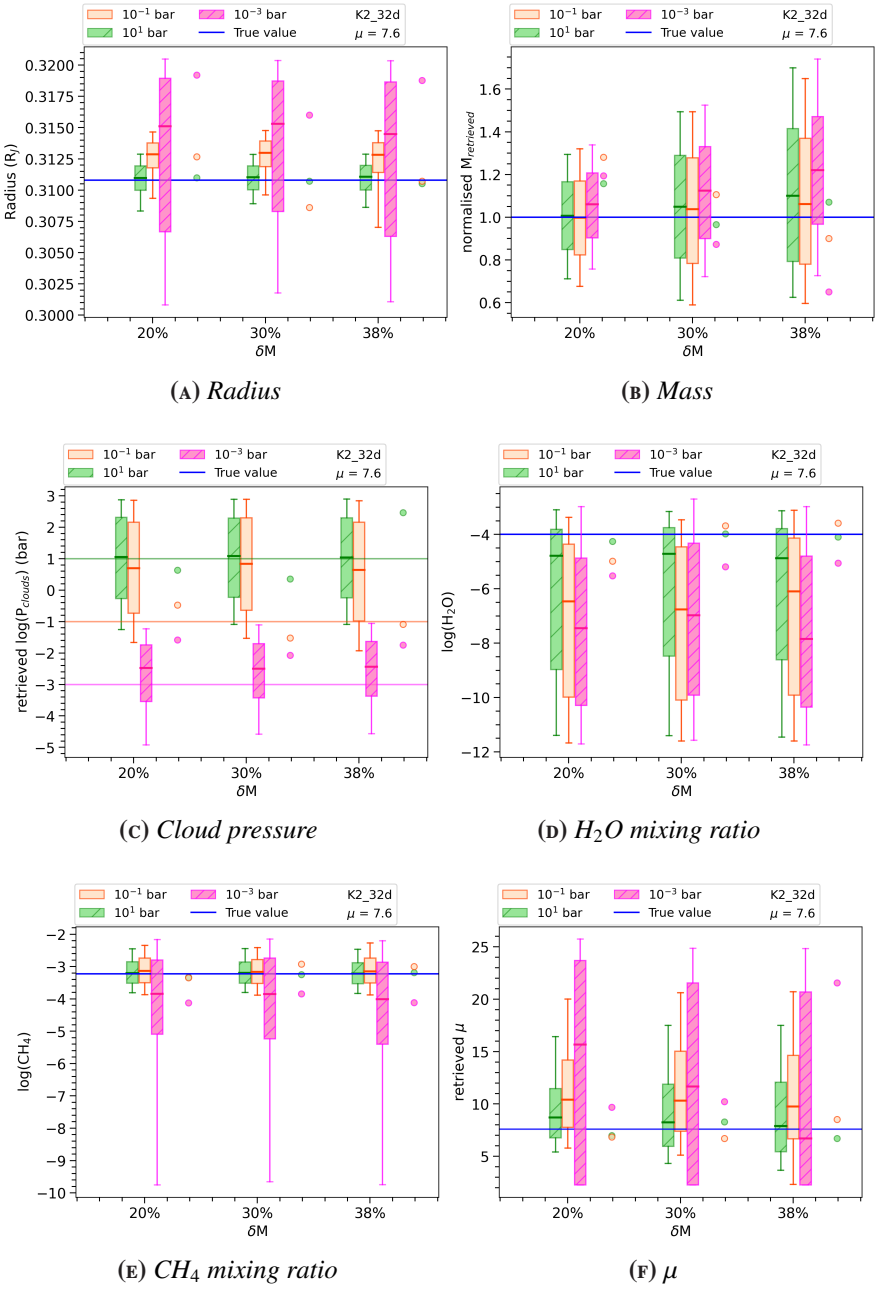

(A) *Radius* (B) *Mass*

(C) *Cloud pressure* (D) *H_2O mixing ratio*

(E) *CH_4 mixing ratio* (F) *μ*

FIGURE 4.48: *Impact of the mass uncertainties on the retrieval performed for the hypothetical N_2-dominated secondary atmosphere of K2-32 d (μ = 7.6) for different cloud pressures. Colour scale and description of the figure are the same in Fig. 4.3.*

In the case of μ = 7.6, I was able to accurately retrieve the CH_4 mixing ratio in all of the tested cloudy scenarios, and with moderate precision when cloud pressure approached 10^{-3} bar. However, I was unable to determine the H_2O mixing ratio, except for the clear-sky scenario, and these results appear to be independent of planetary mass uncertainty (see Figures 4.48d and 4.48e). The mean molecular weight was accurately or moderately accurately, and moderately precisely retrieved

when cloud pressure was equal to or greater than 10^{-1} bar, while it could not be retrieved in the presence of high altitude clouds (Figure 4.48f).

In conclusion, for this target, the mass estimation is sufficient to characterise the atmosphere in the case of low altitude clouds. However, in the presence of high altitude clouds, we may not be able to accurately retrieve the atmospheric composition independently from the planetary mass uncertainty estimation.

I also performed the retrieval for the simulated spectra obtained assuming the number of transits required for the Tier-1 (N_{obs} = 3) and verified that since the first tier we are able to discriminate between the primordial and secondary atmosphere and between different cloudy scenarios.

4.2.6 HIP41378 b

HIP 41378 is a slightly metal-poor, late F-type star located 116 ± 18 pc from Earth, with moderate rotation ($v \sin i \simeq 7$ km s^{-1}), and a brightness of 8.9 in V magnitude and 7.7 in K magnitude, making it one of the brightest planet host stars discovered by Kepler or K2. The planetary system around HIP 41378 is complex, consisting of two sub-Neptune planets and three larger planets in longer orbits. The innermost planet, HIP 41378 b, has a 15.6-day orbital period and a radius of 2.9 $R_\oplus$.

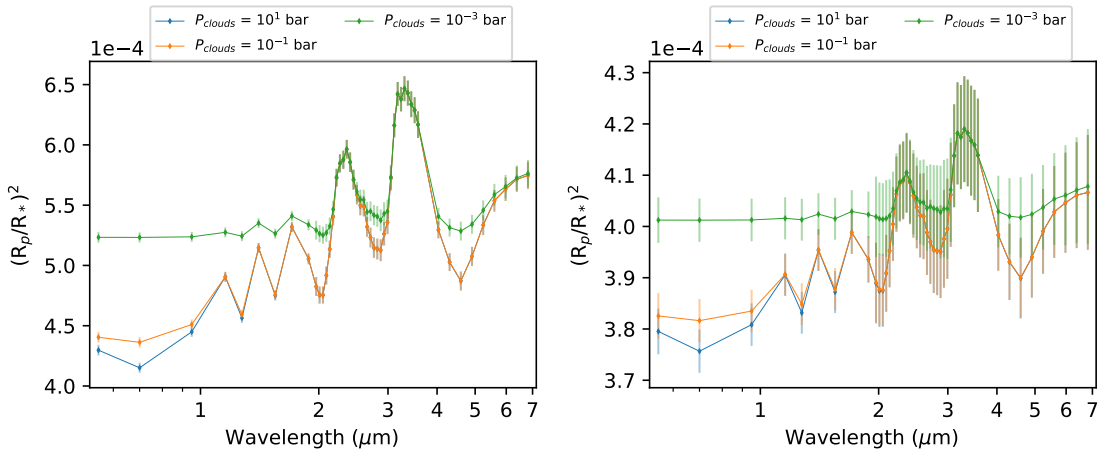

(a) μ = 2.3 (b) μ = 7.6

Figure 4.49: *Simulated spectra of HIP 41378 b as observed by Ariel based on different cloud pressures and mean molecular weights.*

The mass of this planet was estimated using a mass-radius relation. For this reason, I assumed an uncertainty of 100% and I performed the retrieval considering uncertainties of 30%, 50%, and 100%. To simulate the Ariel spectrum ArielRad was used to calculate the SNR based on the number of transits required fro the Tier-

2 (N_{obs} = 83). The key parameters of HIP 41378 b and its host star are listed in Table 4.2.

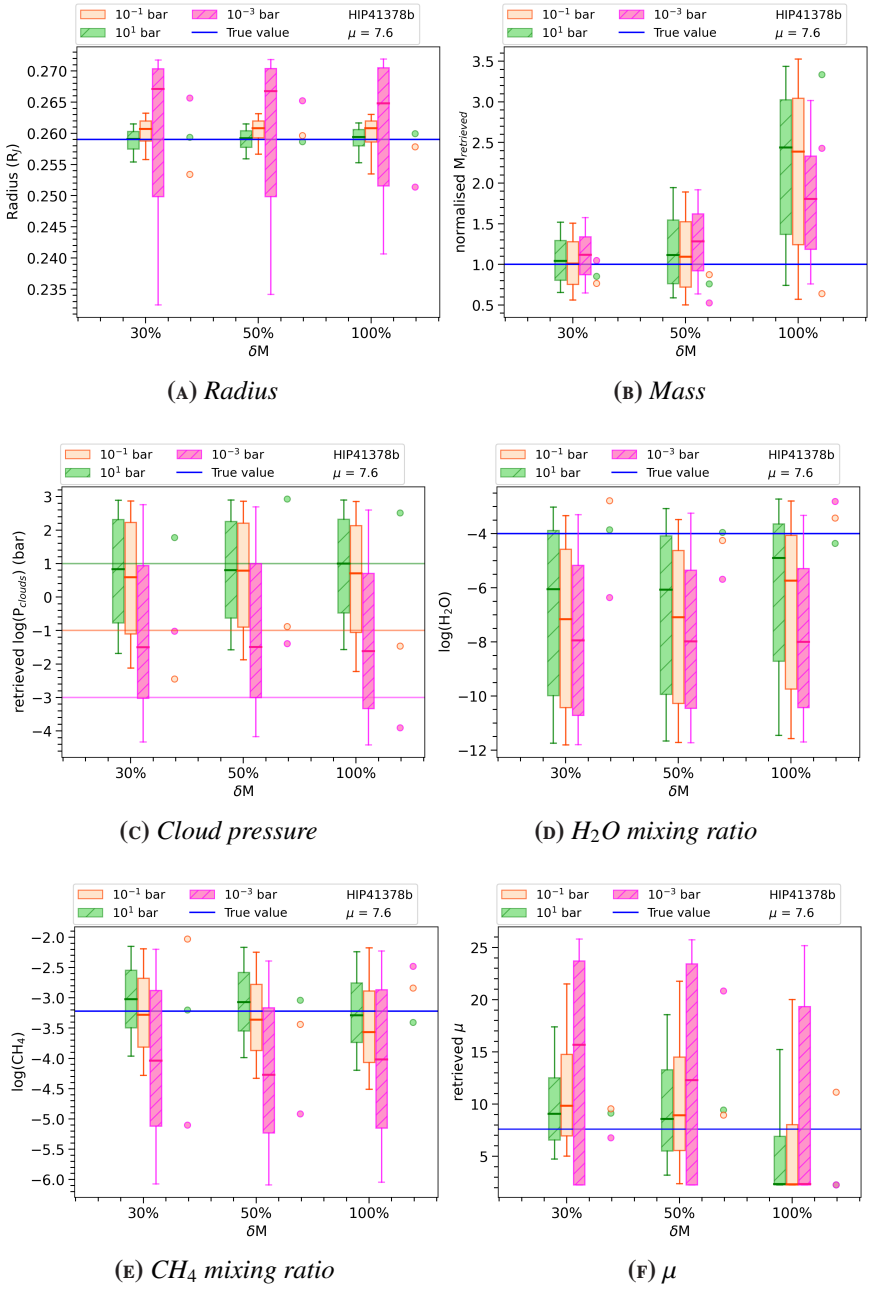

(A) *Radius* (B) *Mass*

(C) *Cloud pressure* (D) *H_2O mixing ratio*

(E) *CH_4 mixing ratio* (F) μ

Figure 4.50: *Impact of mass uncertainties on the retrieval performed for the hypothetical N_2-dominated secondary atmosphere of HIP41378 b (μ = 7.6) for different cloud pressures as a function of the mass uncertainty. Colour scale and description of the figure are the same in Fig. 4.3.*

Table B.20 and Figure 4.50 summarise the results of the retrievals. For the case with μ = 7.6 we are able to accurately retrieve the CH_4 mixing ratio, while the H_2O cannot be constrained. Figure 4.50f shows that a mass uncertainty of 50% is necessary to retrieve the mean molecular weight, but in the presence of high altitude

clouds, even a mass uncertainty of 30% is not sufficient. Additionally, discrepancies are evident in the retrieved cloud pressure (Figure 4.50c). In presence of the clouds we are able to moderately accurately and moderately precisely retrieved the cloud pressure. However, with the KS test I verified that we are able to discriminate between the different cloudy conditions since from the Tier-1 (N_{obs} = 9).

These results suggest that improving the precision of the mass estimate to a uncertainty of about 50% is necessary to determine the presence of a secondary atmosphere. Although improving the SNR would also be beneficial, given the large number of transits required for the Tier-2, it would be time-consuming. In light of these considerations, a preliminary study during Tier-1 could provide some insight into the cloud scenario, enabling us to distinguish between a clear-sky or low altitude cloud scenario ($P_{clouds} > 10^{-1}$ bar) and a high altitude clouds scenario ($P_{clouds} = 10^{-3}$ bar). In the latter case, given the difficulties in retrieving the mean molecular weight in the presence of high altitude clouds, it may be necessary to evaluate if excluding this target from the Tier-2.

4.2.7 TOI-269 b

TOI-269 is an M dwarf located at a distance of 57.023 ± 0.076 pc (Gaia Collaboration et al., 2018; Lindegren et al., 2018). According to Cointepas et al. (2021), the star has a mass of M_* = 0.3917 ± 0.0095 $M_\odot$ and a radius of R_* = 0.398 ± 0.012 $R_\odot$, which are the same values given in the TESS Input Catalog (TIC-v8; Stassun et al. (2019)).

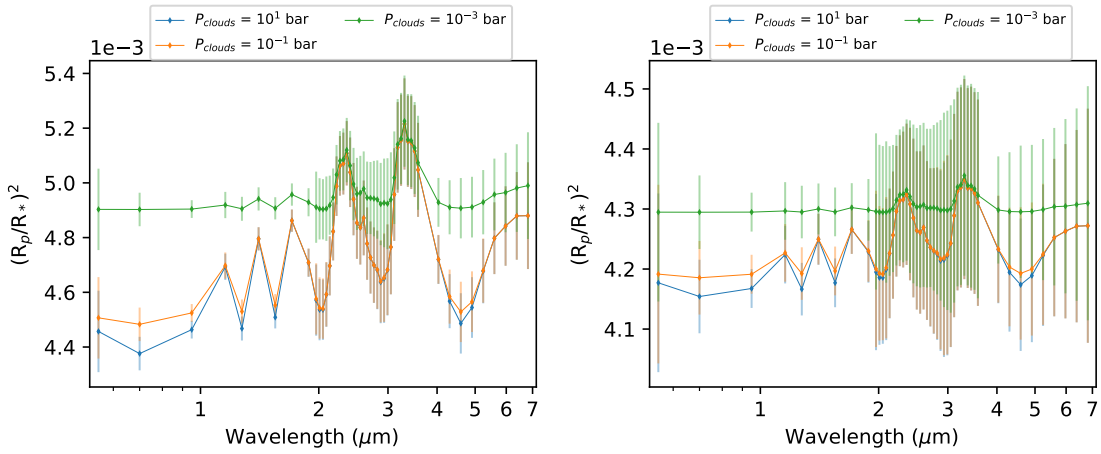

(a) μ = 2.3 (b) μ = 7.6

Figure 4.51: *Simulated spectra of TOI-269 b as observed by Ariel, obtained considering different cloud pressures and mean molecular weights.*

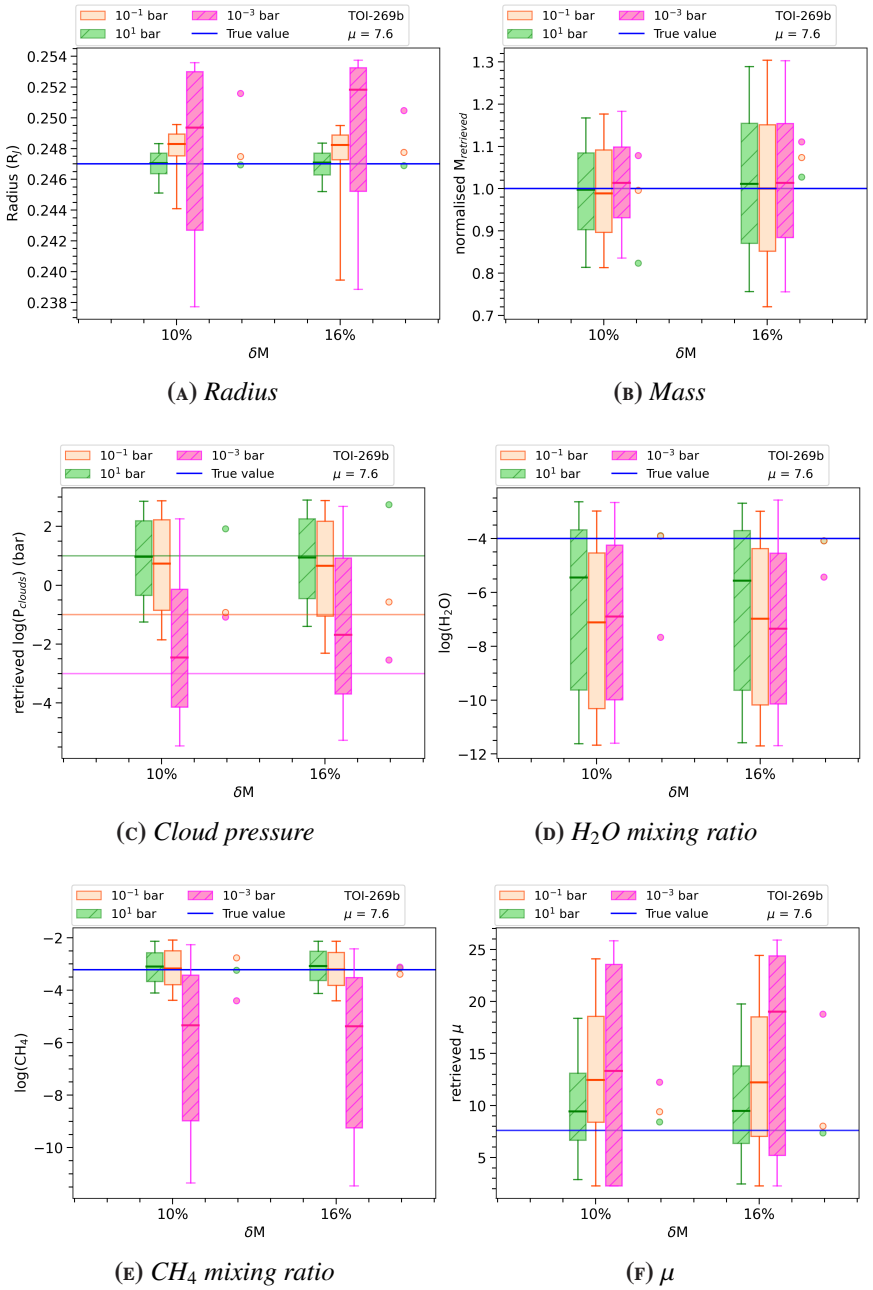

(A) *Radius* (B) *Mass*

(C) *Cloud pressure* (D) H_2O *mixing ratio*

(E) CH_4 *mixing ratio* (F) μ

FIGURE 4.52: *Impact of the mass uncertainties on the retrieval performed for the hypothetical N_2-dominated secondary atmosphere of TOI-269 b (μ = 7.6) for different cloud pressures. Colour scale and description of the figure are the same in Fig. 4.3.*

They also obtained an effective temperature T_{eff} = 3514 ± 70 K. It hosts a transiting sub-Neptune close to the transition between super-Earths and sub-Neptunes (M_p = 8.80 ± 1.40 $M_\oplus$, R_p = 2.77 ± 0.12 $R_\oplus$). All the parameters used in the retrieval and to estimate the noise from ArielRad are listed in Table 4.2. In Figure 4.51 I showed the spectra simulated taking into account the noise obtained from ArielRad obtained assuming the number of transits required for the Tier-2 (N_{obs} = 73), considering different mean molecular weights and cloud pressures.

Since Cointepas et al. (2021) reported a mass estimation with a precision level of about 16%, I performed the retrieval analysis with mass uncertainties of 16% and 10%. The results are reported in Figure 4.52 and also summarised in Table B.24.

In the case of μ = 2.3 we are able to accurately retrieve the atmospheric composition, with a moderately accurately and moderately precisely estimation of the H_2O in the presence of high altitude clouds. For μ = 7.6 discrepancies in the retrieved value for the trace gases are noted. In particular, we are able to accurately retrieve the CH_4 mixing ratio for $P_{clouds} \geq 10^{-1}$ bar, while we obtained a not accurate estimation in the presence of high altitude clouds. On the other hand, the accuracy of the H_2O mixing ratio retrieval is good for the MAP values and poor for the distributions, with a moderately accurately value obtained also in the clear-sky case. The mean molecular weight is difficult to constrain, and the retrieved value is moderately accurate in the clear-sky case, while is not accurate in the presence of clouds.

In conclusion, for this target, the precision of the mass estimate is sufficient to accurately retrieve the atmospheric composition in non-extreme scenarios, while an increased number of transits could contribute to an improvement in the accuracy of the results. However, I verified with the KS test that we are able to discriminate between different cloudy conditions and between primordial or secondary atmosphere cases since the Tier-1 (N_{obs} = 4), allowing to take an informed decision if include the planet in Tier-2 sample.

4.3 Summary and conclusions

The analysis performed on the selected subsample allowed me to explore a number of different situations that can occur in Ariel observations with the goal to establish for the various scenarios the way to proceed to obtain useful Ariel observations. The main results obtained from this analysis primarily concern the role of the precision on the mass estimation and the SNR. I explored also the impact of a wrong mass estimation. In particular, the results confirmed that a minimum mass uncertainty

better than 50% is not particularly useful for accurate retrieval of the atmospheric composition. Generally, the retrieval is more accurate in cases of primary atmospheres, even in the presence of high altitude clouds. For secondary atmospheres, the retrieval is less accurate compared to primary cases.

For each retrieved quantity I estimate accuracy and uncertainty. In general, the retrieval is moderately accurate in the presence of clouds, with the CH_4 mixing ratio almost always being accurately retrieved. However, the spectral features that are most difficult to determine are H_2O and the CO mixing ratio for the primordial cases, which is almost never recovered in the most extreme scenarios. For these reasons, a preliminary feasibility analysis of the targets during Tier-1 is strongly recommended. In many of the targets that were tested, our capability to retrieve the cloudy configuration or the presence of a secondary atmosphere during Tier-1 was successful.

It is important to highlight that for the sub-Neptunes and super-Earths, the analysis was performed considering N_2-dominated secondary atmospheres. As demonstrated in Di Maio, C. et al. (2023), this is one of the worst-case scenarios. However, different cases, such as H_2O- or CO-dominated secondary atmospheres, which are characterised by traceable molecular features directly observable in the spectrum, represent more favourable cases for the inverse models. This results in more accurate retrievals compared to the N_2-dominated ones.

Furthermore, the most important parameter that seems to impact all the retrieved components is the SNR. The analysis described in this chapter highlights the extreme importance of ensuring adequate SNR, particularly in secondary atmosphere cases and in the presence of clouds. This is connected with the estimation of the mass, as the capability to detect the planetary atmosphere depends on the true mass value, which determines the scale height and, subsequently, the SNR.

In this context, it is important to establish the Ariel main goal for each target. If our aim is to characterise the presence of the atmosphere, but we are not interested in an accurate estimation of its components, low SNR may still allow us to achieve our goal. However, for an accurate determination of the atmospheric components, adequate SNR is of primary importance. For this reason, we may have to exclude some targets that would require a number of transits too large to be fitted into the Ariel schedule.

I reported below some indications for each target:

- Neptunians:
  - In all explored cases, starting from Tier-1 observations, according to Edwards and Tinetti (2022), it is possible to identify the presence of

high clouds.

- Trace gases:
  - CH_4 mixing ratio is accurately recovered in all cases when $\delta M \leq 50\%$ and $P_{clouds} \geq 10^{-1}$ bar;
  - H_2O mixing ratio is accurately retrieved when $P_{clouds} \geq 10^{-1}$ bar, except for AU Mic c spectra simulated using the Zicher et al. (2022) parameters. For HD 152843 b, Kepler-450 b, and HATS-37A b, the retrieval is accurate even in the presence of high altitude clouds. The retrieval of H_2O becomes more accurate for low gravity planets, as confirmed by the analysis performed on KOI-94 c, and on AU MIC c, where double of transits required for Tier-2 (Edwards and Tinetti, 2022) allow to increase the accuracy of the retrieval.
  - CO mixing ratio is the most difficult parameter to be constrained. It is retrieved in all the cases when $P_{clouds} \geq 10^{-1}$ bar.

- sub-Neptunes and super-Earths:
  - In all explored cases, we are able to distinguish between primordial and secondary atmospheres and between different cloudy conditions, even when assuming the number of transits required for Tier-1, according to Edwards and Tinetti (2022). This is an important result that will be useful in the Ariel target scheduling.
  - For $\mu = 2.3$ all the atmospheric parameters are accurately retrieved, including the mean molecular weight, with the exception of LTT1445A b spectra obtained assuming the Winters et al. (2019) parameters, and of TOI-269 b spectra, where in the presence of high altitude clouds the H_2O is not accurately and moderately accurately retrieved, respectively.
  - For $\mu = 7.6$ cases:
    - the CH_4 mixing ratio is generally accurately retrieved when $P_{clouds} \geq 10^{-1}$ bar. It is not accurately retrieved in the presence of high altitude clouds, except for K2-32 d spectra where it is accurately and moderately precisely retrieved even in the worst cloudy scenario.
    - the H_2O mixing ratio is more difficult to be constrained. In particular, we are able to accurately/moderately accurately retrieve it in the clearsky case and when $\delta M \leq 50\%$, for LTT 1445A b, K2-138 g, and K2-32 d.

· the mean molecular weight is the parameter that shows the most complex behaviour as a function of cloudy scenarios and mass uncertainty estimation. In general, it is accurately or moderately accurately retrieved for the clear sky case and for $\delta M \leq 50\%$. In some cases, we obtain moderately accurate retrieval in the presence of low altitude clouds (e.g., HIP 41378 b, K2-32 d), while it was difficult to be constrained when $P_{clouds} = 10^{-3}$ bar. It is important to highlight that increased accuracy could be obtained by increasing the number of transits required and thus the SNR. For example, in the case of GJ9827 c, doubling the number of transits assumed by Edwards and Tinetti (2022) resulted in a moderately accurate retrieval of the μ value in the clearsky case.

– An important test was also performed on LTT 1445A b, to check not only the effect of mass uncertainty but also the impact of a wrong estimate or no information. In the forward model, we assumed an input value for the planetary mass that was not necessarily within the prior boundaries of the retrieval. Nevertheless, we were able to retrieve all atmospheric composition parameters in the case of $\mu = 2.3$. For the $\mu = 7.6$, we obtained an accurate determination of the CH_4 mixing ratio and a moderately accurate retrieval for the mean molecular weight.

CHAPTER 5

Optimised radial velocity and spot modelling

The intrinsic variability that characterises young active stars poses one of the main challenges in detecting and characterising exoplanets using Doppler spectroscopy. Stellar activity can induce Radial velocity (RV) signals that mimic the presence of planetary companions, making it crucial to account for the activity of the star during the RVs extraction. Active stars are often fast rotators and in this work, I present a method to optimise the RVs extraction of fast rotating stars, based on the cross correlation function (CCF) technique. I developed the `SpotCCF` model, which accounts the presence of multiple spots on the stellar surface by adapting the equation of the rotational broadening.

The content of this chapter is part of an article in preparation with the title "The GAPS programme at TNG. Optimised radial velocity and spot modelling in young-active stars".

The method described in this chapter was also applied to extract the RVs of the active M dwarf TOI-5375, as discussed in the paper entitled "The GAPS programme at TNG. XLVII. A massive brown dwarf orbiting the active M dwarf TOI-5375" (Maldonado et al., 2023), which has been accepted for publication to the Astronomy & Astrophysics journal, and I am a co-author.

5.1 Introduction

Since the discovery of the first exoplanet approximately 30 years ago, numerous research groups and resources have been dedicated to the discovery and characterisation of new exoplanets. Advances in instruments and the development of improved analysis techniques have paved the way for the detection of Earth-like exoplanets, rocky planets orbiting in the habitable zone of their star.

One of the main methods used to detect and characterise planetary companions is Doppler spectroscopy, which measures the RV variations of the star due to the presence of the planet (see Section 1.2.2). This technique pioneered the discovery

of 51 Peg b (Mayor and Queloz, 1995), the first exoplanet found orbiting a main sequence star. However, a major challenge in the search for exoplanets is the intrinsic variability of the stars. Late-type main-sequence stars exhibit observable evidence of magnetic activity, which manifests in various phenomena such as starspots, chromospheric plages, heating of the chromosphere and corona, and impulsive flares. Starspots are regions on the stellar photosphere where magnetic field lines obstruct the convective welling up of hot plasma, resulting in colder areas compared to the surrounding photosphere (Schrijver et al., 1989; Skumanich et al., 1975; Solanki et al., 2006; He et al., 2018; Choudhuri, 2017). In general, stellar activity produces temperature inhomogeneities in the stellar surface and a quenching of the convective blueshifts of photospheric spectral lines that effect the RV and therefore on the search for exoplanets: the observed stellar light contain the signal induced by exoplanets as well as the stellar variability, which can be large enough to overshadow the planetary signal. In some cases, instead, the radial velocity periodicity induced by stellar activity and rotation may produce spurious signals that mimic the planet signatures.

The study of the physical properties of the exoplanets, along with the physical characterisation of their host stars, is one of the main steps towards understanding the formation and evolution mechanisms of the planetary systems, which are currently a matter of extensive debate.

In this regard, studying planetary systems at young ages can provide valuable insights into the processes of formation and migration, as well as the physical evolution and evaporation of planets under high-energy irradiation. Although the high level of the stellar activity makes more challenging the search of the new exoplanets candidates, it's crucial to monitor and study young (< 20 Myr) and intermediate age (<700 Myr) stars to search for planets in formation or at the early stage of their evolution within the timescales of migration.

Additionally, stellar rotation plays a key role in the generation and amplification of surface magnetic field, and numerous studies have searched for relationships between magnetic activity and stellar rotation (e.g., Noyes et al., 1984; Rutten and Schrijver, 1987; Pizzolato et al., 2002; Schrijver and Zwaan, 2000; Pizzolato et al., 2003). The rotation-activity relationship was considered to be an indirect one, through stellar age. Skumanich (1972)'s work was the first to suggest a relationship between rotation velocity, chromospheric emission and stellar age, showing a decay of the rotation velocity and chromospheric emission as the inverse square root of the age.

The extraction of radial velocities from the high-resolution spectrographs HARPS

and HARPS-N observations is typically performed by using the HARPS Data Reduction Software (DRS) pipeline (Pepe et al., 2002) or the HARPS Template-Enhanced Radial velocity Re-analysis Application (TERRA) pipeline (Anglada-Escudé and Butler, 2012).

The DRS pipeline extracts the RVs from the cross correlation function (CCF). The CCF is computed by correlating the measured spectrum with a weighted binary mask, and is constructed by shifting the mask as a function of the Doppler velocity. The binary mask consists of a set of boxcar functions (a rectangle shaped function that has a constant value over a specific range and is zero elsewhere) centred at the nominal wavelength of absorption lines that are present in the stellar spectrum. The boxcar functions can have different weights depending on how much RV information is contained on each line. The weight in the mask is larger for the deepest and narrowest lines (Pepe et al., 2002). The resulting CCF is a function describing somehow a flux weighted "mean" profile of the stellar absorption lines transmitted by the mask. The minimum of the CCF as a function of the Doppler offset is the desired RV measurement. The shape of the CCF is usually fitted to find the stellar radial velocity using the Gaussian profile (Baranne et al., 1996; Pepe et al., 2002).

The CCF method is the standard approach for precise RV measurements of FGK-type stars. These classes of stars are known to have a number of resolved and unblended absorption lines in the visible spectra which makes them ideal to be represented by a weighted binary mask. In the M stars, instead, due to their lower temperatures, the spectra display a forest of lines that in most cases are blended, making their identification and consequentially the construction of a mask, more challenging. Similar problems are present for rotating stars.

On the other hand, the TERRA pipeline uses in a least-squares matching of a full spectrum template to the observations for RV extraction (Anglada-Escudé and Butler, 2012; Astudillo-Defru et al., 2015). Many studies have shown that the method used by TERRA provides a significant improvement in accuracy compared to the CCF, especially when applied to M dwarfs, as it utilises more Doppler information from the stellar spectrum (Anglada-Escudé and Butler, 2012; Perger et al., 2017).

Recently, different methods have been proposed to improve the RV extraction, including approaches that utilise Gaussian processes (Rajpaul et al., 2020). However, the CCF continues to be useful for studying the stellar activity of stars, including M dwarfs.

Young stars are often characterised by high levels of stellar activity, and they are also rapidly rotating stars. As a result, the spectral lines in their spectra are distorted due to the rotational broadening, which dominates over other broadening

effects. Consequently, the shape of the CCF profile cannot be accurately described by a Gaussian fit, as assumed by the DRS pipeline, but rather by a rotation profile. Furthermore, since the CCF profile gathers information from each individual spectral line selected in the mask, average changes in the individual line profiles due to stellar activity are reflected in changes in the CCF shape. The net result is that the average CCF profile changes from one observation to another, depending on the instantaneous spot configuration, rendering the use of a reference template, as done in TERRA, incorrect.

Many authors have attempted to correct for stellar activity when extracting and analysing the radial velocity using several approaches (Collier Cameron et al., 2021; Lafarga et al., 2020; Meunier and Lagrange, 2020; Meunier et al., 2017, 2010; Zhao and Tinney, 2020; Dumusque, 2018, 2016; Dumusque et al., 2014; Aigrain et al., 2017, 2012). In this work I present `SpotCCF`, a new method I developed for the RV extraction based on the CCF fitting. `SpotCCF` is specifically designed for active stars with a significant rotational broadening of the order of few tens of km s^{-1} and was turned on the HARPS-N observations of V1298 Tau, a very young fast rotating star.

This chapter is organised as follows. I describe the target in Section 5.2. I detail the model in Section 5.3. The CCFs correction and the RVs extraction follow in Section 5.4 and 5.5. Section 5.6 presents the analysis of the RVs time series and the comparison with the TERRA dataset. In Section 5.7 I test the detection sensitivity by direct injection of a planetary signal into the data. The spots characterisation is discussed in Section 5.8. Conclusions follows in Section 5.9.

5.2 V1298 Tau

V1298 Tau is a young solar-mass K1 star, relatively bright with a visual magnitude of 10.1 (David et al., 2019a; Suárez Mascareño et al., 2021). Its estimated effective temperature is 5050 ± 100 K, with solar metallicity, and a luminosity of 0.954 ± 0.040 $L_\odot$ (Suárez Mascareño et al., 2021). The logarithmic surface gravity is 4.246 ± 0.034 dex (David et al., 2019a). It is located at a distance of 108.6 ± 0.7 pc in the Taurus region and belongs to the Group 29 stellar association (Oh et al., 2017).

V1298Tau was observed in 2015 by NASA's K2 mission (Howell et al., 2014), which led to the discovery of four transiting planets, all with sizes ranging from Neptune to Jupiter (David et al., 2019a,b). The three inner planets have well-constrained orbital periods of about 24.1396 ± 0.0018, 8.24958 ± 0.00072 and 12.4032 ± 0.0015 days, and radii of $0.916^{+0.052}_{-0.047}$, $0.499^{+0.032}_{-0.029}$ and $0.572^{+0.040}_{-0.035}$ R_J, re-

spectively. The outer planet, e, has a more uncertain orbital period (40-120 days) as it was detected with a single transit event, and a radius of $0.780^{+0.075}_{-0.064}$ R_J.

Given the youth of the system and its potential to provide insights into the initial conditions of close-in planetary systems (e.g., Owen, 2020; Poppenhaeger et al., 2021), extensive follow-up observations have been conducted on V1298 Tau. These efforts include attempts to constrain planet masses through radial velocities (Beichman et al., 2019; Suárez Mascareño et al., 2021), measurement of the spin-orbit alignments of planet c (Feinstein et al., 2021) and planet b (Gaidos et al., 2022; Johnson et al., 2022), measurement or constraint of atmospheric mass-loss rates for the innermost planets (Schlawin et al., 2021; Vissapragada et al., 2021; Maggio et al., 2022), and an approved program to study planetary atmospheres using the James Webb Space Telescope (Desert et al., 2021).

V1298 Tau is a highly active star that exhibits significant radial velocity (RV) variations, principally caused by stellar activity. It is a fast rotating star, with a line-of-sight projected equatorial rotational velocity $v \sin i$ of 23 ± 2 km s^{-1} (David et al., 2019a), and displays a broadened cross-correlation function (CCF) profile. This derived rotation velocity is consistent with the value of 23.8 ± 0.5 reported by (Suárez Mascareño et al., 2021). The main stellar parameters of V1298 Tau, along with information about its planets, are listed in Table 5.1.

Table 5.1: *V1298Tau main parameters*

V1298 Tau	
Spectral type	K1
$M_\star (M_\odot)$ [(a)]	1.170 ± 0.060
$R_\star (R_\odot)$ [(a)]	1.278 ± 0.0.070
log g (dex) [(b)]	4.246 ± 0.034
Age (Myr)[(a)]	20 ± 10
$T_{\rm eff}$ (K) [(a)]	5050 ± 100
distance (pc)[(c)]	∼ 108.5 ± 0.7
$v \sin i$ (km s^{-1})[(a)]	23.8 ± 0.5
$P_{\rm phot}$ (d)[(b)]	2.865 ± 0.012

Notes. [(a)] Suárez Mascareño et al. (2021) [(b)] David et al. (2019a) [(c)] Gaia Collaboration et al. (2021) .

I analysed a total of 311 spectra of V1298 Tau, obtained with the HARPS-N spectrograph (Cosentino et al., 2014), a cross-dispersed high-resolution and high-stability échelle spectrograph at the Telescopio Nazionale Galileo (TNG). HARPS-N has a resolving power of R ∼ 115 000 and covers a spectral range of 3830-6930 Å (see Chapter 2.1). These spectra were collected in the context of the Global Architecture of Planetary System (GAPS) programme (Covino et al., 2013) between

March 2019 and March 2023.

5.3 Modelling of CCF profiles in presence of spots

The aim of this work is to develop a model (`SpotCCF`) that represents the CCF profile of active stars with $v \sin i$ values of several tens of km s^{-1}, where the CCF is strongly deformed. In such cases, the spectral lines are distorted due to the rotational broadening, which has a characteristic shape that dominates the spectral line profiles when rotation is the main broadening effect. As a result, the CCF is not accurately described by the Gaussian fit, as employed by the HARPS/HARPS-N DRS pipeline, but rather by a rotation profile.

Assuming the star to be spherical and rotating as a rigid body, a synthetic spectrum can be obtained through the convolution of the spectrum of a non-rotating star with the rotational profile $G(\Delta\lambda)$ described by Gray's equation (Gray, 2018).

$$G(\Delta\lambda) = G(v_z) = \begin{cases} \dfrac{1}{v_L} \dfrac{\int_{-y_1}^{+y_1} I_c dy/R}{\oint I_c \cos\theta d\omega} & \text{if } |v_z| \leq v_L \text{ or } |\Delta\lambda| \leq \Delta\lambda_L \\ 0 & \text{if } |v_z| > v_L \text{ or } |\Delta\lambda| > \Delta\lambda_L \end{cases} \tag{5.1}$$

with $v_L = v \sin i$ where v is the equatorial rotation velocity, and i is the angle of inclination with respect to line-of-sight. v_z represents the $\Delta\lambda$ shift from the line centre expressed in kilometres per second. The continuum intensity is denoted as I_c, while R represents the stellar radius. The stellar disc can be divided into strips parallel to the projection of the spin axis on the disc itself, and the Doppler shift is constant along each strip, with the highest shift at the limbs with value $v_L = v \sin i$. The integration limits, y_1, represent the extremes of the projected stellar disc in the orthogonal plane where the projections are defined, considering that the origin is in the star centre.

Here, I evaluate $G(\Delta\lambda)$ assuming the limb darkening law proposed by Claret (2000), which is the most precise analytical representation of the limb darkening to date (Howarth, 2011; Morello et al., 2017).

$$\frac{I_\lambda(\mu)}{I_\lambda(1)} = 1 - \sum_{n=1}^{4} a_{n,\lambda}(1 - \mu^{n/2}) \tag{5.2}$$

where λ indicates a specific spectral bin/passband; $\mu = \cos\theta$, being θ the angle between the line of sight and the normal inward direct the stellar surface (see Figure 5.1). The stellar intensity is denoted with $I_\lambda(\mu)$, while $I_\lambda(1)$ is the intensity at the

centre of the disc ($\mu = 1$). The limb darkening coefficients are indicated with $a_{n,\lambda}$.

This equation describe how the intensity changes at a given distance from the centre of the stellar disk, since the variable μ is related to the radial coordinate in the projected stellar disc by the relation $r = \sqrt{1-\mu^2}$, where $r = 0$ at the centre and $r = 1$ at the stellar limb.

The limb darkening coefficients are derived using the database `PHOENIX_2012_13` (Claret et al., 2012, 2013) of the `ExoTETHyS` package (Morello et al., 2020).

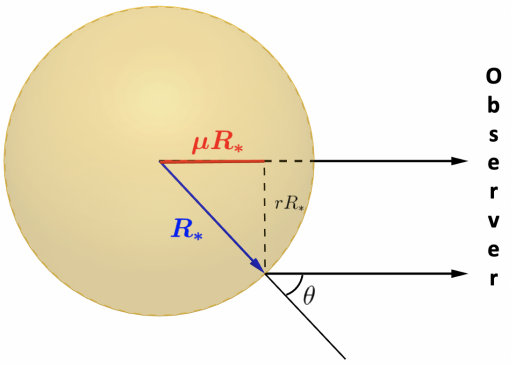

Figure 5.1: *Illustration of the limb darkening geometry. θ is the angle between the observer and the normal to the stellar surface in the observation point.*

Stars with high $v \sin i$ show higher stellar activity level than other stars. For this reason, to take into account the activity level of the star, the presence of one or more spots on the stellar disc was included in the model. In the following work, I limit the presence of surface inhomogeneities to dark spots; in the future I plan to introduce further structures (i.e. faculae) and to take into account for a temperature different from zero for the spots.

In Fig 5.2 I sketch the correspondence between position within the Doppler-shift distribution and longitude on the star for an equator-on aspect of view. Surface features that alter the amount of the light coming from specific longitude bands will introduce structures into the rotational profile. In the simplest case, a dark spot reduces the contribution to the light in one of the strips, as illustrated in Fig 5.2. This produces a dip or notch in the rotation function $G(\Delta\lambda)$ at the Doppler shift corresponding to that strip. The bump appears on the short-wavelength side of the profile as the spot becomes visible on the approaching limb. It migrates across the profile, growing stronger as the spot becomes more nearly face-on, reaching its largest size as the spot crosses the star's meridian. As the bump continues on the receding side of the disc, the same pattern is played in reverse, the bump fading in size and moving to its maximum positive Doppler shifts.

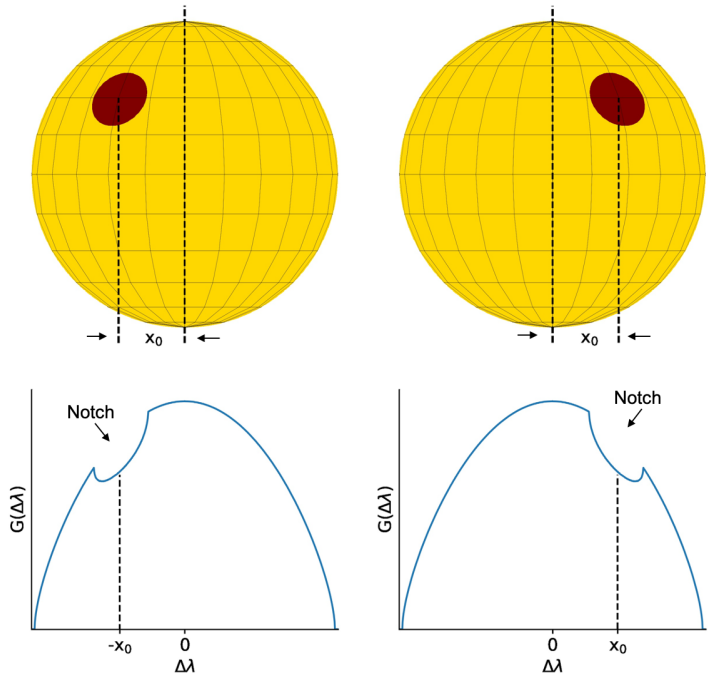

Figure 5.2: *The upper panels show the spot with its centre in the position (-x_0,y_0) of the projected stellar disc. The rotation of the star brings the spot centre to the new position on the disc (x_0,y_0). The lower panels show the rotation profile modified by the presence of the spot. The position in the Doppler-shift distribution corresponding to the spot (that is darker than the surrounding area), produces a notch or dip. As rotation carries the spot across the stellar disc, the position of the notch moves across the Doppler-shift distribution and its strength changes with the projected area of the spot and for the effect of the limb darkening. Figure adapted from Gray (2018).*

More generally, the Doppler shift for a spot of latitude l and longitude L is given by

$$\Delta\lambda = v \sin i \cos l \sin L \text{ km s}^{-1} \tag{5.3}$$

To take into account the presence of the spot I adapted Gray's formula (Eq. 5.1) changing the integration limits and computing a rotational profile only across the portion of the disc covered by the spot. In this way, I obtained the analytical expression of the Gray's formula for the spot, $G_{spot}(\Delta\lambda)$.

So, by subtracting the Gray rotational profile of the spot, $G_{spot}(\Delta\lambda)$, from the rotation profile calculated on the entire disc $G(\Delta\lambda)$, I obtain the final rotation profile $G_f(\Delta\lambda)$, which takes into account the presence of the spot.

$$G_f(\Delta\lambda) = norm[G(\Delta\lambda) - G_{spot}(\Delta\lambda)] \tag{5.4}$$

where *norm* is a normalisation parameter.

However, the analytical calculation of this function is computationally demanding, which is why a numerical model was developed. I constructed a photospheric

stellar model, where the star is treated as a spherical object that is mapped onto a Cartesian coordinate system, with a grid of 999 pixels in the range [-1;1], and each spot is represented as a spherical cap with a radius matching that of the spot. The stellar flux contribution is calculated for each pixel on the stellar map, with no contribution from the pixels representing the spots. Finally, the calculated flux contribution is integrated across each strip of the stellar disc.

To model the CCF, it is necessary to establish the latitude and longitude of the centre of the spot, as well as the filling factor, to identify the points where the $G_{spot}(\Delta\lambda)$ should be calculated, or in the case of the stellar map, the pixels of the grid representing the spot.

If we use a coordinate system where z-axis is along the line of sight, x and y identify the orthogonal plane where the projections are defined and the origin is the star centre, the projected spot centre is in the position (x_0,y_0)

$$\begin{cases} x_0 = \cos(l)\sin(L) \\ y_0 = \sin(l)\sin(i) - \cos(l)\cos(L)\cos(i) \end{cases} \tag{5.5}$$

with l and L are the latitude and longitude of the spot, respectively, and i is the inclination of the stellar spin to the line of sight z (see a detailed derivation in Appendix C). Since we are assuming a spot with a circular shape, its projection on the stellar disc will be an ellipse with semi-axes $a = R_{spot}$ and $b = R_{spot}\cos(l)\sin(L)$, where R_{spot} is the radius of the spot in stellar radii units. The spot filling factor is $ff = R_{spot}^2$ while the filling factor projected on the stellar disc is the area covered by the ellipse, $ff_p = ab = R_{spot}^2\sqrt{1-r^2}$, where $r = \sqrt{x_0^2 + y_0^2}$ is the projected distance of the spot from the star centre.

I used the relation between the rotational period of the star and the filling factor obtained by (Messina et al., 2001) to choose the boundaries of the filling factor of the spot, considering $P_{rot} = \dfrac{2\pi R_*}{v}$.

The numerical integration does not take into account the wings of the CCF profile because in those points the function is not defined. For this reason, the $G_f(\Delta\lambda)$ has been convolved with a Lorentzian function, L($\Delta\lambda$), that takes into account the wings in the CCF profile, given by

$$L(\Delta\lambda, \gamma) = \frac{1}{\pi\gamma}\left[\frac{\gamma^2}{\Delta\lambda^2 + \gamma^2}\right] \tag{5.6}$$

where γ is the scale parameter which specifies the half-width at half-maximum.

Finally, the model used to fit the CCF profile was described by

$$Model = G_f(\Delta\lambda) * L(\Delta\lambda) \tag{5.7}$$

5.4 CCFs correction

In some cases, especially for faint targets, the fiber B of the spectrograph is used to acquire the sky spectrum, in order to obtain an optimal subtraction of the detector noise and background. The DRS pipeline computes also the cross-correlation function (CCF) of the sky spectrum obtained using the fiber B, referred to as CCF_B. Some of the V1298 Tau CCF profiles that were analysed exhibited anomalous deformations that were also present in the CCF_B (see an example in Figure 5.3). These

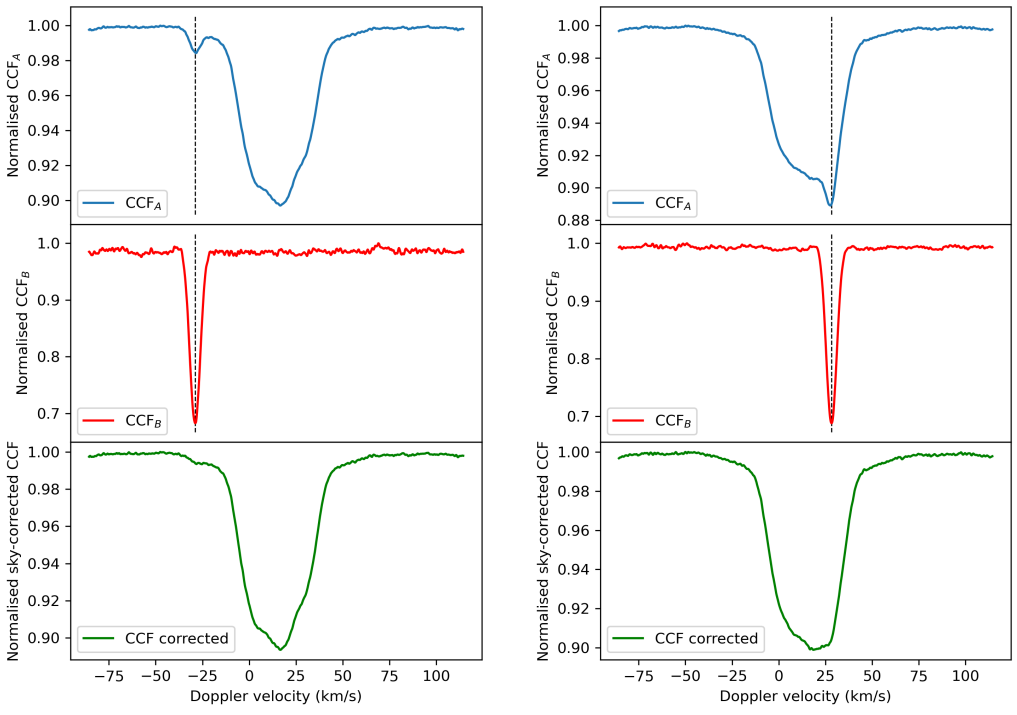

(a) *Wings deformation* (b) *Core deformation*

Figure 5.3: *Two examples of CCF profile distorted by the effect of the moon illumination. The top panel shows the CCF profile of the fiber A. The CCF profile of fiber B, CCF_B, is reported in the middle panel. The black dashed vertical lines highlight the deformations in both profiles. In the bottom panel the sky-corrected CCF.*

types of deformations could appear in the wings or even the core of the CCF profile, leading to incorrect radial velocity estimations and/or introducing spurious signals.

According to Malavolta et al. (2017), these deformations may be caused by moon illumination. To correct for these deformations in all the CCF profiles, I followed the procedure described in Malavolta et al. (2017). Firstly, I recalculated the CCF_B using the same flux correction coefficients as those used for the target CCF_A during the specific acquisition. Next, the CCF_B was subtracted from the corresponding CCF_A. The outcome of this process is the sky-corrected CCF profile (lower panel of Figure 5.3).

5.5 EXTRACTION OF THE RADIAL VELOCITIES AND SPOT PARAMETERS

The CCF profiles of V1298 Tau, corrected for sky effects, exhibit multiple deformations as shown in Figure 5.4.

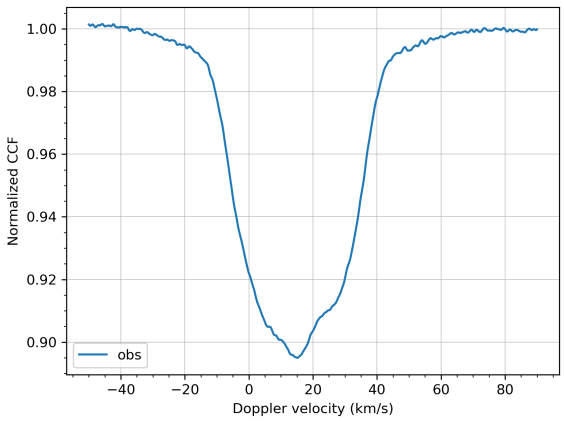

FIGURE 5.4: *Example of a normalised CCF profile of V1298 Tau. It can be observed that the deformed profile is due to the presence of one or multiple spots.*

I applied `SpotCCF` to the CCF profiles of V1298 tau in two steps. In the first step, I used a model that accounted for the presence of one spot on the stellar disc, which I refer to as the "One-spot model". I explored the full (hyper-)parameter space using the Monte Carlo (MC) nested sampler and Bayesian inference tool `MultiNest` v3.10 (Feroz et al., 2019), with the `pyMutliNest` wrapper (Buchner, 2016). The priors used in all the analyses described below are summarised in Table 5.2. The MC sampler was set up to run with 5120 live points for both One-spot and Two-spots models and with a sampling efficiency of 0.5 for all cases considered in

this study. The log-likelihood function to be minimised is expressed as:

$$\ln p(y_n, t_n, \theta) = -\frac{1}{2}\sum_{n=1}^{N}\frac{[y_n - f_\theta(t_n)]^2}{\sigma_j^2} - \frac{1}{2}\ln[2\pi(\sigma_j^2)] \tag{5.8}$$

where y_n and t_n are the values of the CCF profile and the Doppler velocities, respectively; θ is the array of model parameters, $f_\theta(t)$ is the model function, N are the number of CCF points, and σ_j is the white noise term (jitter).

In general, there are four parameters for the star ($v \sin i$, RV, γ, i), three parameters for each spot (latitude, longitude, R_{spot}), a normalisation parameter, and the jitter σ_j

Table 5.2: *Priors parameters of the model used for RVs extraction of V1298 Tau.*

V1298 Tau		
Parameter	Prior	Description
norm	$\mathcal{LU}(10^{-4}, 10^2)$	Normalisation parameter
Stellar parameters		
RV (km s^{-1})	$\mathcal{U}(10, 20)$	Centroid of CCF profile
v sin i (km s^{-1})	24.74 (fixed)	Width of CCF profile
γ (km s^{-1})	$\mathcal{U}(10^{-2}, 10^2)$	Lorentzian parameter
i (rad)	$\pi/2$ (fixed)	Inclinational angle
Spot parameters		
latitude (rad)	$\mathcal{U}\left(0, \frac{\pi}{2}\right)$	
longitude (rad)	$\mathcal{U}(-\pi, \pi)$	
$\sqrt{ff}$	$\mathcal{LU}(10^{-2}, 0.5)$	

Notes. Notes. The prior labels of $\mathcal{N}$, $\mathcal{U}$ and $\mathcal{LU}$ represent normal, uniform and loguniform distribution, respectively. Longitude and latitude are uniformly distributed in the interval.

To establish the priors for the parameters $v \sin i$, γ, and i, which should be consistent across all observations, I conducted a series of tests in which I allowed these parameters to vary within a range around their literature values. In particular, I kept $v \sin i$ fixed at 24.74 km s^{-1}, the value most frequently obtained in previous tests, and the inclination of the rotation axis to the line-of-sight i at 90 degrees (a reasonable estimate derived from the value of v sin i). Additionally, I constrained the latitude of the spots of V1298 Tau to the upper hemisphere of the star, given the inclination of its rotation axis to the line-of-sight. This star is observed close to equator-on, such that a spot in the upper or, symmetrically, in the lower hemisphere of the star, with the same longitude and filling factor, contributes equally to the CCF

profile. The spot radius, normalised to the stellar radius, was allowed to vary in the range $[10^{-2}, 0.5]$ to prevent spots that were too small to be resolved by the mapping resolution, or too large and covering the entire stellar surface.

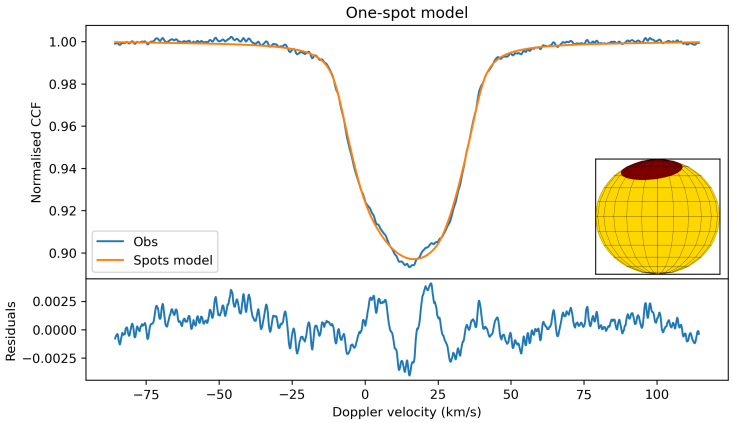

(A) *One-spot model*

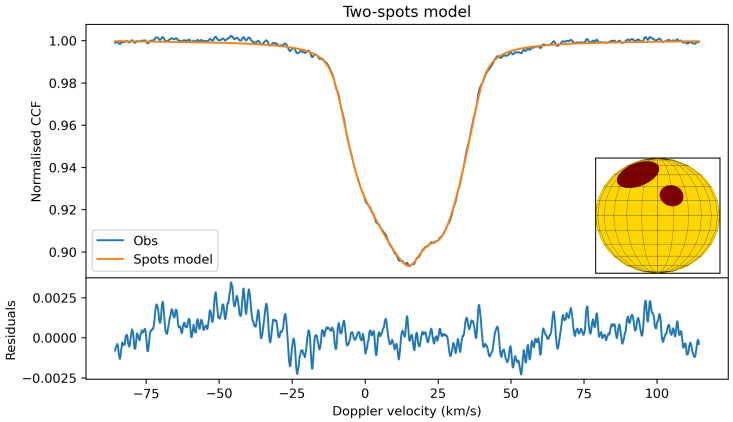

(B) *Two-spots model*

Figure 5.5: *Examples of CCF profiles of V1298 Tau fitted with "One-spot model" (A) and "Two-spots model" (B) and the corresponding residuals (in bottom panels). The inset of each plot shows the location of the spots on the stellar disc, as defined by the fit of both models; the grid indicates longitudes and latitudes from -90 to 90 degrees with 15-degree intervals.*

In the second step, I used a model that accounted for the presence of two different spots on the stellar surface (hereafter, "Two-spots model") to fit the CCF. Note that this multi-spots model also considered cases where spots were entirely or partially overlapping. I adopted the same priors as the "One-spot model", which are detailed in Table 5.2. The logarithmic Bayesian evidence, $\log E$, was used as an estimate of the goodness of the model. There is strong evidence in supporting the "Two-spots model" for all the analysed CCF profiles of V1298 Tau.

In Figure 5.5, I show an example of a CCF profile of V1298Tau fitted with "One-spot model" and "Two-spots model", and the corresponding spots configuration. As an example, Figure 5.6 shows the corner plot of the best-fit parameters acquired

from fitting a CCF profile of V1298 Tau using the Two-spots model. Here, σ_J is the jitter noise, which refers to the noise level to be added to the model as an additional parameter to account for unmodelled contributions or other factors not considered by the model.

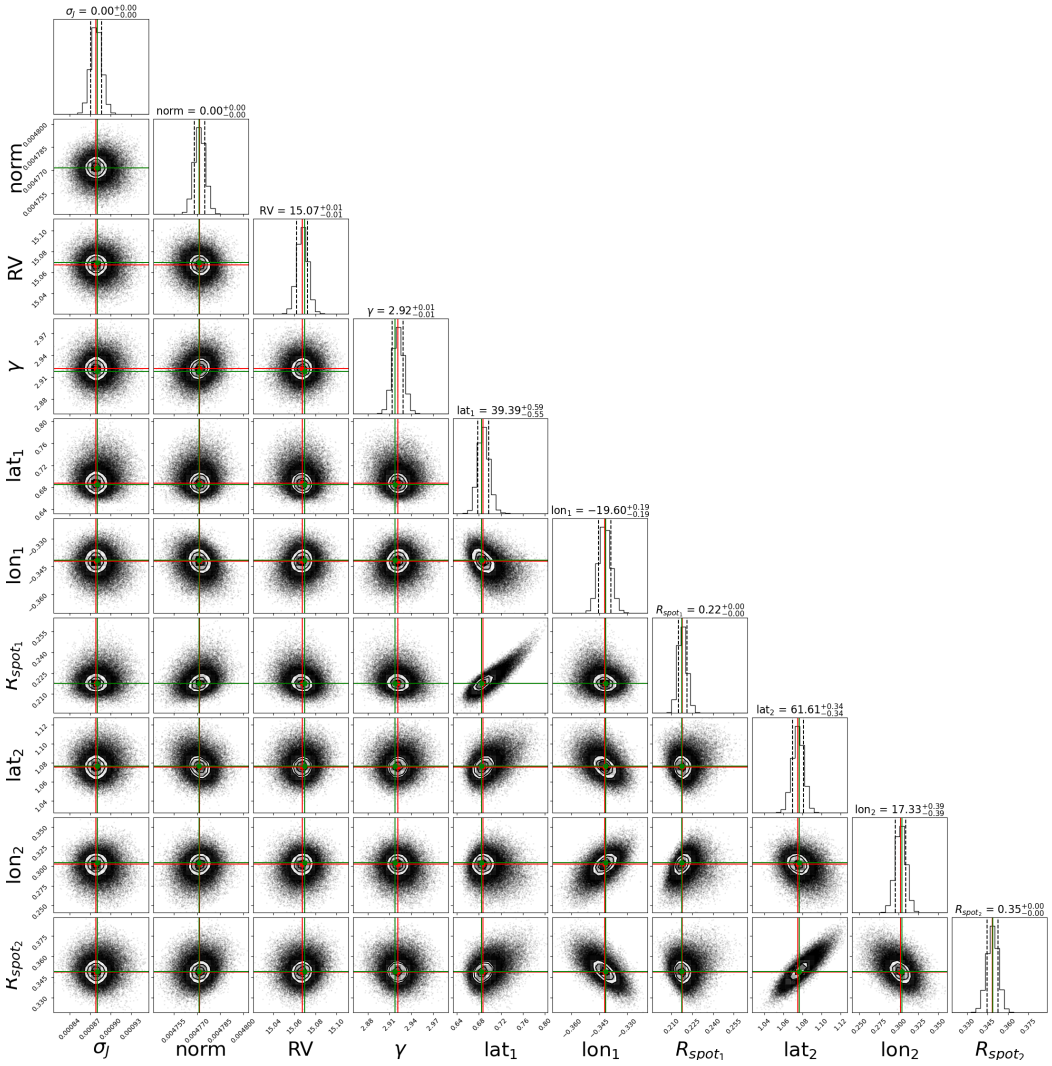

FIGURE 5.6: *Examples of corner plot of the best-fit parameters obtained from the fitting of a CCF profile of V1298 Tau with the "Two-spots model". The red and green lines mark the median and the maximum-a-posteriori values, respectively, while the dashed black lines are the 16$^{\text{th}}$ and 84$^{\text{th}}$ quantiles. The median values are reported in the title of each histogram. The latitude and longitude scales are in radians.*

5.6 RADIAL VELOCITY TIME SERIES ANALYSIS

The two pipelines that usually have been used to extract the RVs of HARPS/HARPS-N observation are the DRS and the TERRA pipeline (see Section 2.2). Figure 5.7 shows a comparison on the capabilities of the TERRA and DRS pipelines for the

extraction of the HARPS-N RVs of V1298 Tau. It can be seen that the root mean square (RMS) of the RV measurements obtained with TERRA is around 240 m s^{-1}, about 650 m s^{-1} smaller that the value obtained with the DRS (RMS_{DRS}) ≈ 890 m s^{-1}). By assuming that smaller RMS of the RV measurements corresponds to smaller RV noise RMS, we can conclude that the TERRA RVs should be preferred. This result confirmed that TERRA pipeline is preferred for the radial velocity extraction in case of active stars, showing complex profiles.

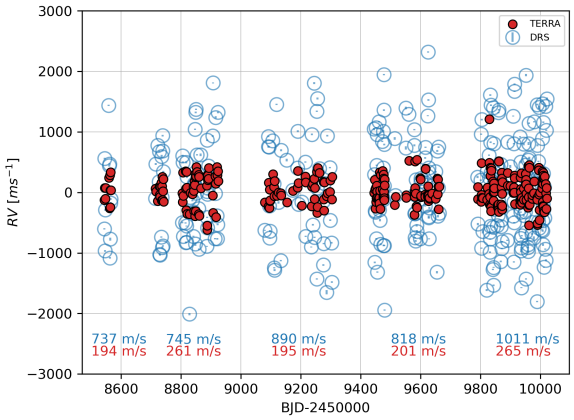

Figure 5.7: *Comparison between radial velocity measurement obtained with the DRS pipeline (blue empty dots) and TERRA RVs (red points). For each season I indicate the RMS of the corresponding RV subsample, in blue the RMS of the RVs extracted from DRS and in red the RMS of the TERRA RVs.*

To extract the RVs of V1298 Tau I applied the `SpotCCF` to model the CCF profiles of this target, selecting the best model based on Bayesian evidence values, typically the Two-spots model. I compared the RV time series obtained with `SpotCCF` to the RVs obtained with TERRA pipeline (see Figure 5.8). The RMS of the RVs obtained with `SpotCCF` is significantly smaller (between 40% and 60%) than the RMS obtained with TERRA, with the largest decrease observed during the second season.

To search for periodicity in the RV data obtained with `SpotCCF`, I used the generalized Lomb-Scargle periodogram (GLS, Zechmeister and Kürster 2009). The periodogram, see Figure 5.9a, identifies a significant frequency at 0.34716 ± 0.00005 d^{-1} (period of 2.8806 ± 0.0004 d), corresponding to the rotational period, P_{rot}, of the star, and the ±1 d^{-1} alias (frequency of about 0.65 d^{-1}). Figure 5.9b shows the periodogram of the RVs obtained with TERRA pipeline. In this case as well, the periodogram identifies a significant frequency at the P_{rot} of the star. However, the frequency at first harmonic of the P_{rot} of the star, which is present the TERRA periodogram, disappears in the `SpotCCF` periodogram. The results of the sinusoidal fit from both periodograms are summarised in Table 5.3.

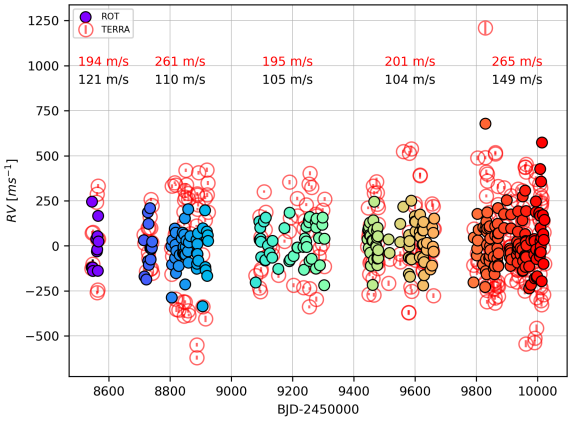

FIGURE 5.8: *Comparison between radial velocity measurement obtained with the* `SpotCCF` *(coloured filled points) and TERRA RVs (red empty points). For each season I indicate the RMS of the corresponding RV subsample, in red the RMS of the RVs extracted from TERRA and in black the RMS of the* `SpotCCF` *RVs.*

TABLE 5.3: *Summary of the sinusoidal fits obtained from the periodograms applied to the V1298 Tau RVs derived with* `SpotCCF` *and TERRA.*

Parameter	SpotCCF	TERRA
Weighted RMS of dataset (m s^{-1})	115.29	199.27
RMS of residuals (m s^{-1})	101.12	182.49
Mean weighted internal error (m s^{-1})	6.08	8.79
Best sine frequency (d^{-1})	0.34716 ± 0.00005	0.34722 ± 0.00006
Best sine period (d)	2.8806 ± 0.0004	2.8800 ± 0.0005
Amplitude (m s^{-1})	79 ± 8	115 ± 15

The comparison of the results obtained from the two periodograms shows that both datasets present a significant frequency at the P_{rot} of the star. However, the RV semi-amplitude obtained from `SpotCCF` is about 30% lower that the one obtained with TERRA, and the RMS of the residuals obtained from the subtraction of the best sinusoid from `SpotCCF` RVs is about 45% lower than the TERRA RMS of the residuals. Furthermore, from the comparison of the phase-fold residuals obtained in the two different cases (see the bottom right panel in Figure 5.9a and 5.9b) it can be noted that the modulation present in the residuals of TERRA disappears in the phase-fold residuals of `SpotCCF`. This is also confirmed by the periodogram, as the the `SpotCCF` periodogram appears cleaner and the rotational period seems better identified. This may be explained with a substantial removal of a number of rotation related frequency by `SpotCCF`.

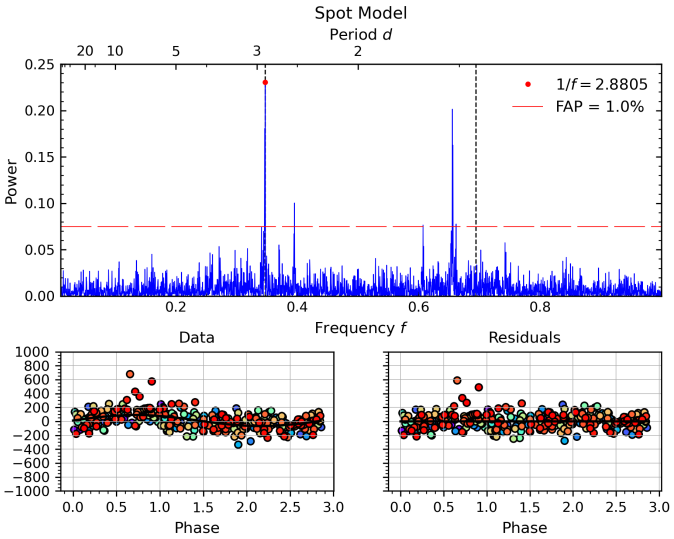

(A) *SpotCCF dataset*

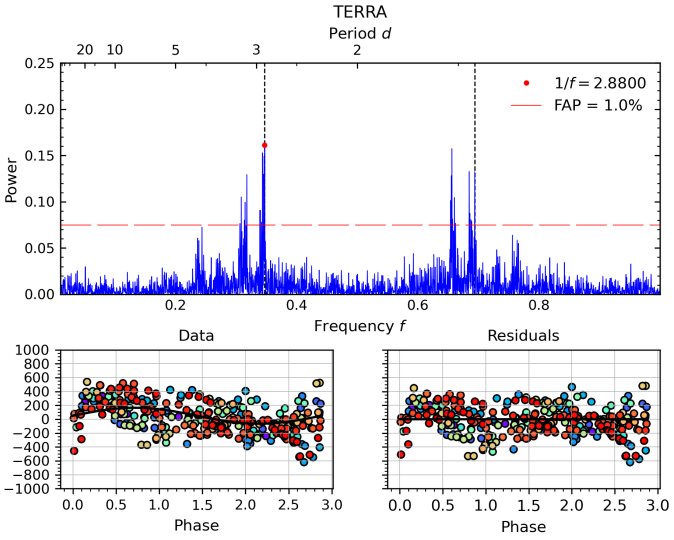

(B) *TERRA dataset*

FIGURE 5.9: *GLS periodogram of the V1298 Tau RVs obtained with the* SpotCCF *and the TERRA pipeline. The red dots highlight the maximum power and the dashed red line indicate the FAP at 1.0% (upper panels). The vertical dashed black line highlights the P_{rot} of the star. In the bottom panels I showed the RVs (left) and the residuals (right) phase folded with the dominant period.*

I performed an additional test by calculating the GLS periodograms for both the original data and residuals obtained after recursive pre-whitening, as shown in Figure 5.10, for both datasets. The periodogram of TERRA RVs (shown in the upper panel) exhibits a complex structure centred around the stellar rotation frequency, with signals related to stellar activity (at the rotational frequency or its harmonics) prominently dominating the periodograms even after four iterations of pre-whitening. However, the periodogram of the SpotCCF RVs does not display harmonics of the rotation frequency, and the signal at the stellar rotational frequency

disappears after the second pre-whitening step.

Previous analyses strongly support that the SpotCCF model efficiently removes part of the contribution from the stellar activity related to the rotation.

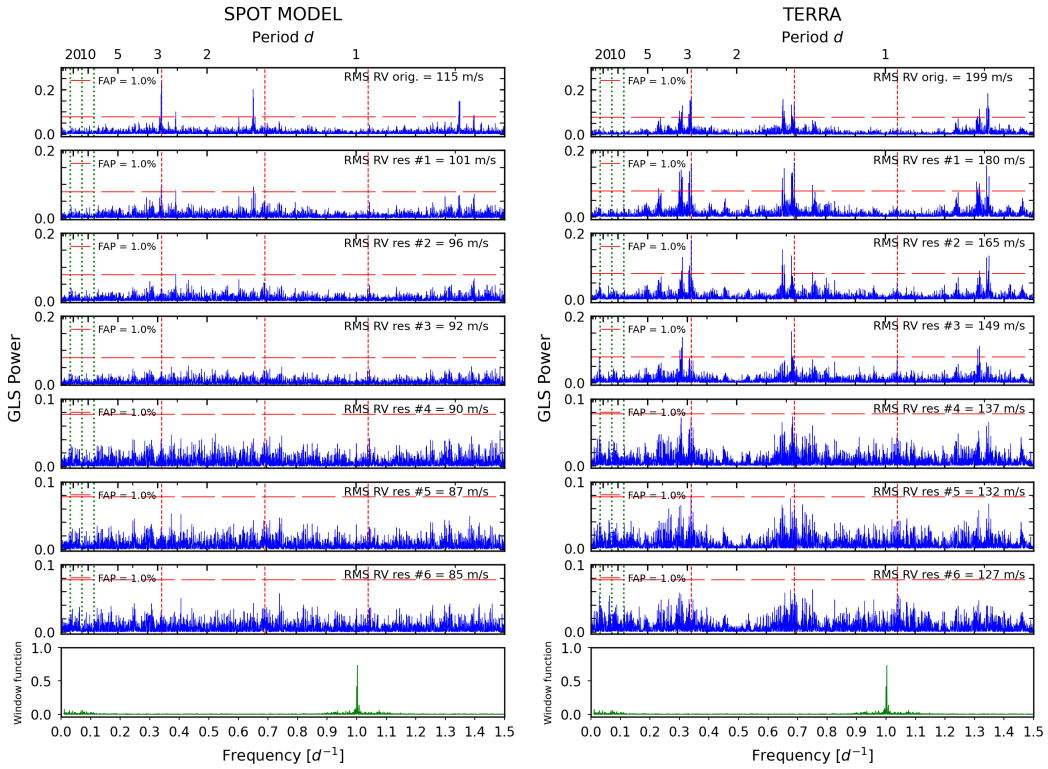

(A) *SpotCCF dataset* (B) *TERRA dataset*

FIGURE 5.10: *GLS periodogram of the V1298 Tau RVs obtained with the SpotCCF and the TERRA pipeline and their residuals after recursive pre-whitening. For each panel: the vertical and dashed black lines indicate the stellar rotation frequency and its harmonics; the green lines mark the orbital frequency of the planetary companions, and the horizontal red dashed line highlights the FAP at 1.0%. Each panel reports the RMS of the dataset. In the bottom panel I show the window function.*

5.7 DETECTION SENSITIVITY BY DIRECT INJECTION OF THE PLANETARY SIGNAL INTO THE DATA

To obtain further validation of the SpotCCF method I tested the ability to recover a planetary signal of a putative planet around V1298 Tau. To this purpose, I created different datasets by injecting a planetary signal with an orbital period of 4.9 days [1] and using different amplitudes (K = 37, 75, 100, 150 m s^{-1}) in the RV dataset

[1] Please note that the injected planet has a different period than the transiting planets, which enables good control over the amplitude of the signal.

obtained with SpotCCF and with the TERRA pipeline, respectively. Before proceeding, I tested the reliability of the method by injecting the signal on the CCFs verifying that the two procedures give the same radial velocity. To simulate a planetary signal, the CCFs were blue or redshifted with the desired amplitude, period and phase. I then performed the fit for all the shifted CCFs and the results were perfectly compatible with the fit obtained with the original CCFs. For this reason, and since the fit of CCFs is computationally demanding, I chose to inject the planetary signal directly into the original RVs time series.

The GLS periodogram was computed for each dataset. Figure 5.11 shows the comparison between the periodograms of the RVs+planet (injected at different amplitude) obtained from the original SpotCCF RVs (left panel) and from the original TERRA dataset (right panel). In both datasets (SpotCCF and TERRA) the GLS periodogram finds a significant peak at the rotational period of the star. From the second row of the figure it can be seen the periodogram for the RVs with the planet injection at different amplitude.

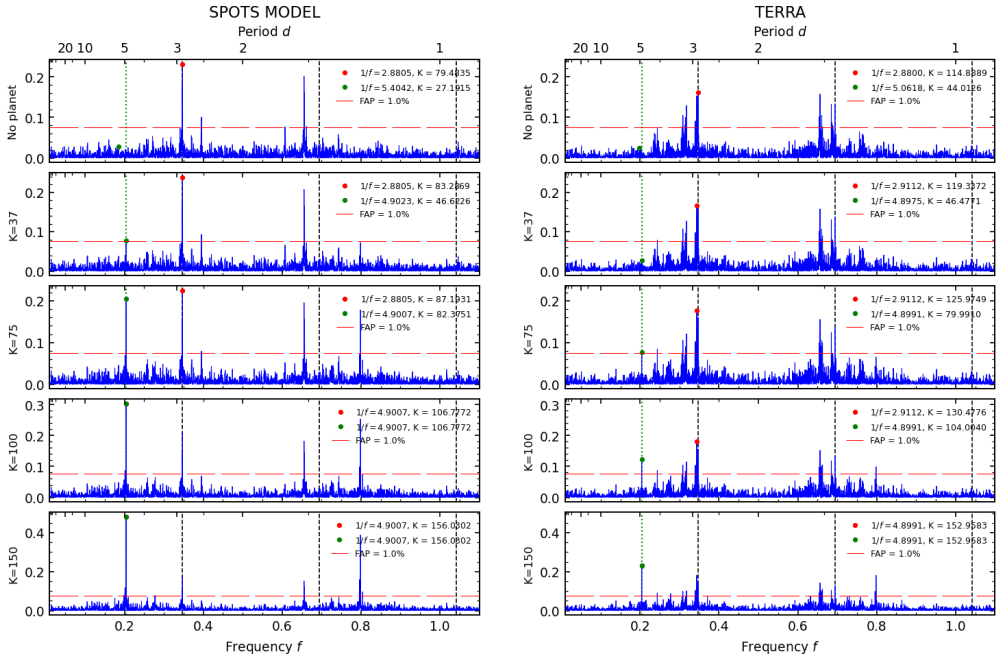

Figure 5.11: *Comparison between the GLS periodograms of the V1298 Tau RVs obtained with the SpotCCF (left panels) and the TERRA pipeline (right panels) where I injected a planetary signal at P_{orb} = 4.9 d, with different amplitude (from top to bottom K=0, 37, 75, 100, 150 m s−1), For each figure: the vertical and dashed black lines indicate the stellar rotation frequency and its harmonics; the green line marks the orbital frequency of the injected planet' the red dashed horizontal line highlights the FAP at 1.0%. The upper panel shows the original dataset without planet injection .*

The GLS periodogram finds a significant peak (FAP < 1.0%) at the orbital period of the injected planet with K ≈ 37 m s^{-1} (corresponding to M sin i ≈ 0.35 M_J) for the RVs obtained with SpotCCF. An analogous peak is significant for the TERRA

RVs only for an injected planet with K $\approx$ 75 m s^{-1} (corresponding to M sin $i \approx 0.70$ M_J).

This test demonstrates that using this method, it is possible to reliably detect a lower-massive planet, with an amplitude of the injected signal lower than what is required for the signal to be identified in the TERRA dataset. This result is consistent with the finding that the `SpotCCF` model reduces systematic effects caused by stellar activity.

5.8 SPOT CHARACTERISATION

The fit of the CCFs profile with `SpotCCF` allows characterising the spots present on the stellar surface, in particular the position and size of the spots, using the parameters latitude and longitude, and the area covered by the spots, using the projected filling factor (ff$_p$).

To analyse the spot properties I make the raw assumption that the spot system consists of a bigger (Spot A) and a smaller (Spot B) spot evolving separately.

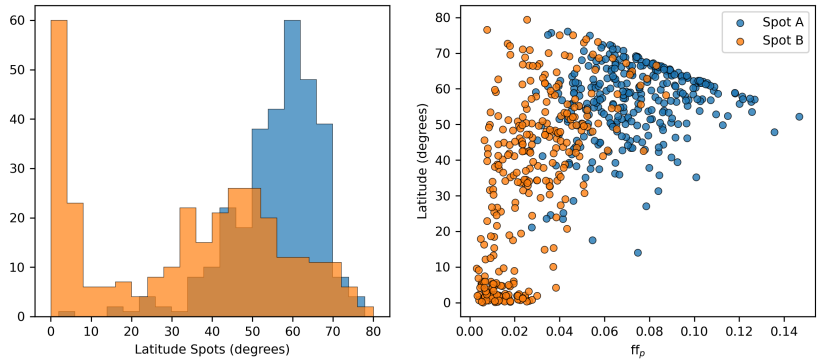

FIGURE 5.12: *(Left panel) Distribution of the latitude values obtained for spots of V1298 Tau. (Right panel) Latitude vs ff$_p$. The blue points indicate the spot with the highest ff$_p$ (Spot A), while the orange points are the spots with the lowest ff$_p$ (Spot B).*

In Figure 5.12 I show the distribution of the latitudes (left panel) and the relation between the latitude of the spots and the projected filling factor obtained for V1298 Tau (right panel).

There is an indication of two main peaks, with larger spots (ff$_p$ > 0.06) preferentially in the range ($\approx$ 45-90) degrees, and smaller spots (ff$_p$ < 0.02) in the range (0-10) degrees. The linear limit that characterises the larger spots is attributable to the upper limit of the spot radius boundary.

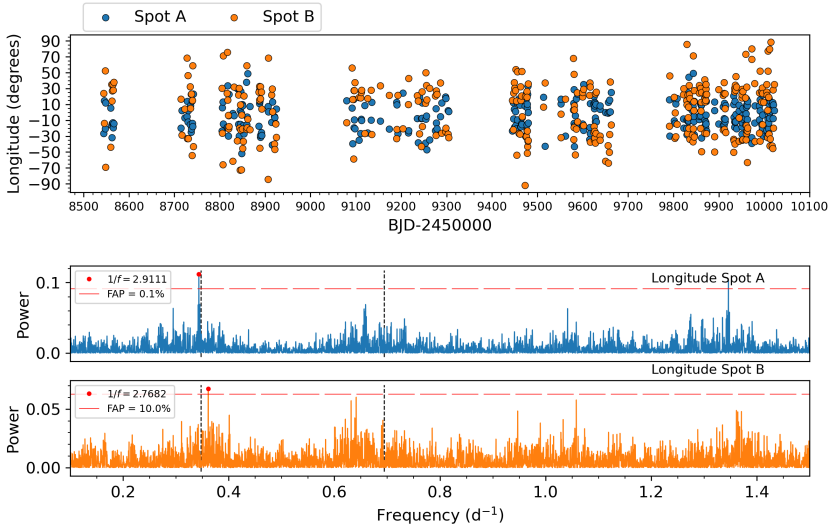

FIGURE 5.13: *(Upper panel) V1298 Tau longitude time-series. The blue points indicate the spot with the highest ff_p (Spot A), while the orange points are the spots with the lowest ff_p (Spot B). (Lower panels) GLS periodogram performed for the longitude values obtained for Spot A and Spot B, respectively. The red horizontal line indicates the false alarm probability (FAP) level at 0.1% and 10%, respectively. the black dashed lines highlight the rotational period of the star and its harmonic.*

The upper panel of Figure 5.13 shows the longitude time-series for Spot A and Spot B, in blue and orange respectively, and the lower panels show the GLS periodograms performed for each spot, respectively. A significant peak at 2.91 days, near the rotational period of the star is identified for Spot A with a FAP $\leq$ 0.1%, while a lower significant peak (FAP $\leq$ 10%) at 2.77 days is identified for Spot B.

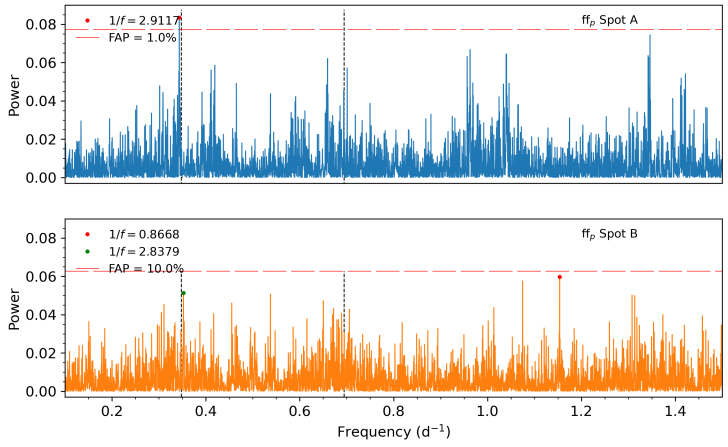

FIGURE 5.14: *GLS periodogram of the projected filling factor of Spot A (upper panel) and Spot B (lower panel). The red horizontal line indicates the false alarm probability (FAP) level at 1% and 10%, respectively. The black dashed lines highlight the rotational period of the star and its harmonic.*

The GLS periodogram of the projected filling factor of the two spot distributions

is shown in Figure 5.14. Even in this case a significant peak (FAP ≤ 1%) is identified for Spot A at 2.91 days, while Spot B shows a lower significant peak (FAP ≈ 10%, 2.84 days).

The lower significance of the peaks observed for Spot B is not surprising, as Spot A is larger and therefore contributes more significantly to the CCF profile, making it easier to detect. However, since Spot B is smaller, when there are more than two spots on the stellar surface, there can be multiple configurations for Spot B. Furthermore, the definition of "large" and "small" spots are relative to number of cases where "small" spots are really "large", but smaller than the other one.

However, I decided to make a further selection for the spots in order to test the potential influence of differential rotational velocity. As such, I categorised the spots into two groups: larger spots located between latitudes 60-90 degrees (referred as Spot A at≥ 60°), and smaller spots located between latitudes 0-40 degrees (Spot B at≤ 40°). This eliminates the "small" spots at high latitudes.

Figure 5.15 illustrates this new selection, depicting the distribution of latitude as a function of the ff_p.

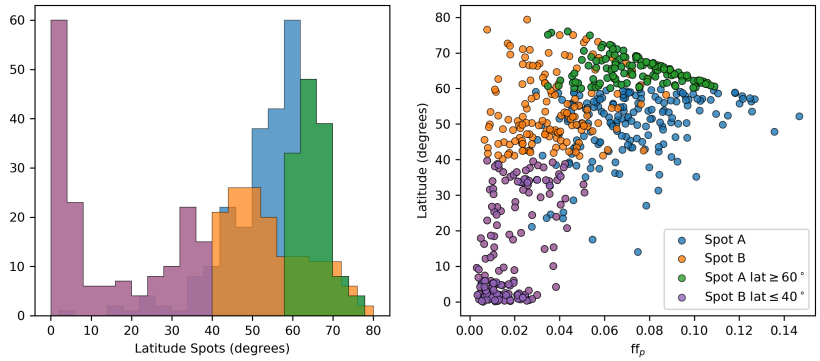

Figure 5.15: *(Left panel) Distribution of latitude values obtained for spots of V1298 Tau. (Right panel) Latitude vs ff_p. Blue points represent the spot with the highest ff_p (Spot A), while orange points indicate the spots with the lowest ff_p (Spot B). Purple points and distribution represent Spot B with latitude values lower than 40 degrees, while green points and distribution indicate Spot A with latitude values higher than 60 degrees.*

The GLS periodogram was performed on the projected filling factor distribution of the two spots (see Figure 5.16). The analysis revealed a significant peak (FAP ≤ 1%) for the Spot A and Spot B, at periods of 3.24 and 2.53 days, respectively. These periods may provide a strong suggestion of a differential rotational velocity of the star, with a higher velocity at lower latitudes and lower rotational velocity at higher latitudes. Additionally, it can be observed that the peak at 3.24 days is one of the peaks near the rotational period of the star in the TERRA periodogram, which was removed by the `SpotCCF` method.

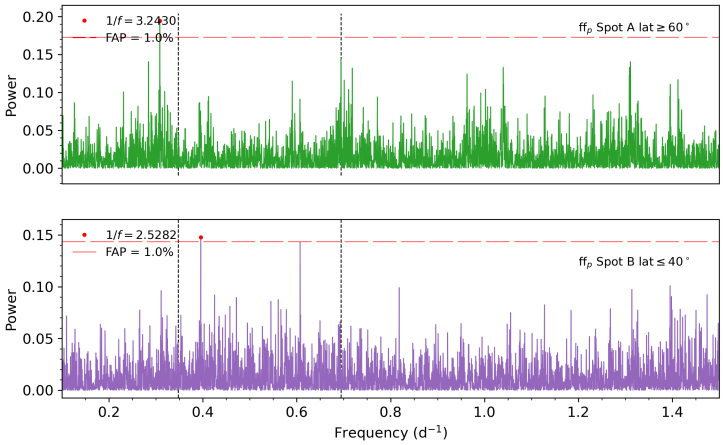

FIGURE 5.16: *GLS periodogram of the projected filling factor of Spot A with latitude higher than 60 degrees (upper panel) and Spot B with latitude lower than 40 degrees (lower panel). The red horizontal line indicates the false alarm probability (FAP) level at 1%. The black dashed lines highlight the rotational period of the star and its harmonic.*

Furthermore, I analysed the total area covered by the spots, $\mathrm{ff}_{p_{tot}}$, which was obtained by adding the ff_p of each individual spot. The upper panel of Figure 5.17b shows the $\mathrm{ff}_{p_{tot}}$ times-series. In Figure 5.17a I reported the distribution obtained

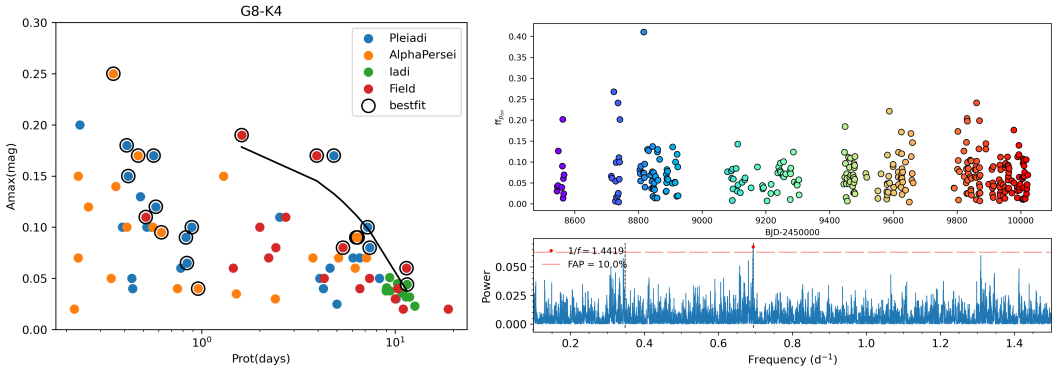

(A) (B)

FIGURE 5.17: *(A) A_{max} vs rotation period. The light curve maximum amplitude A_{max} can be adopted as suitable indicator of a lower limit of the star maximum spotlessness. Adapted from Messina et al. (2001). (B) Total projected filling factor time-series of V1298 Tau (upper panel) and corresponding GLS periodogram (lower panel). The points are coloured following a colour scale from blue to red as a function of the observation time. The red horizontal line in the periodogram indicates the FAP level at 10%, while the black dashed lines highlight the rotational period of the star and its harmonic.*

by Messina et al. (2001) for G8-K4 type stars. Here, the authors have depicted the light curve maximum amplitude as a function of the rotational period of the star, suggesting that it can be adopted as suitable indicator of a lower limit of the star maximum spottedness. According to this figure, a star like V1298 Tau, with a

rotational period of about 3 days, has approximately 15% of its surface covered by spots. It is worth noting that the range of total projected filling factor obtained for V1298 Tau is consistent with the value proposed by Messina et al. (2001).

The GLS periodogram of the $ff_{p_{tot}}$ time-series reveals a peak corresponding to the second harmonic of the P_{rot} of the star (FAP $\leq$ 10%).

Furthermore, as additional validation, I compare the spot configuration of observations obtained on the same nights.

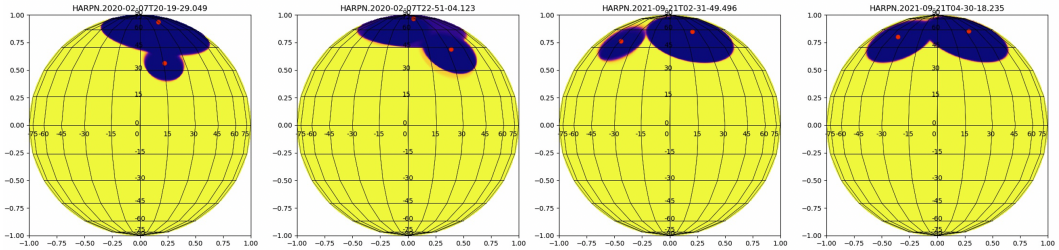

(A) *2020-02-07 Δ T = 2.53 h* (B) *2021-09-21 Δ T = 1.97 h*

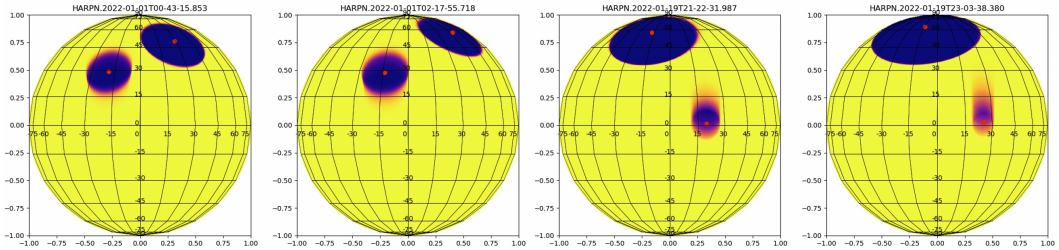

(C) *2022-01-01 Δ T = 1.58 h* (D) *2022-01-19 Δ T = 1.69 h*

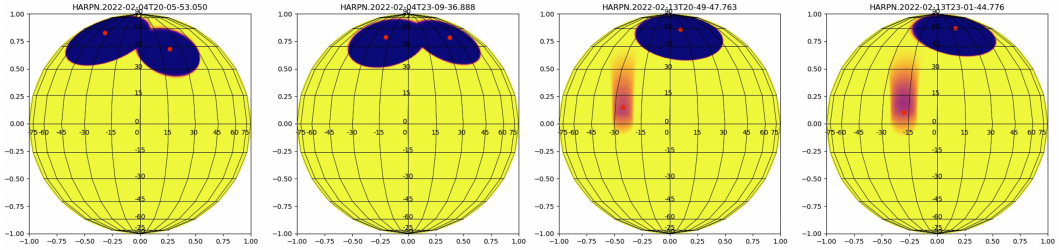

(E) *2022-02-04 Δ T = 3.06 h* (F) *2022-02-13 Δ T = 2.20 h*

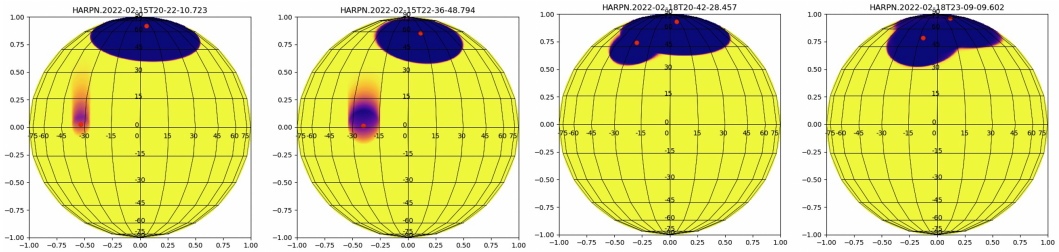

(G) *2022-02-15Δ T = 2.24 h* (H) *2022-02-18 Δ T = 2.45 h*

FIGURE 5.18: *Spot configuration of pairs of observations obtained at few hours of distance.*

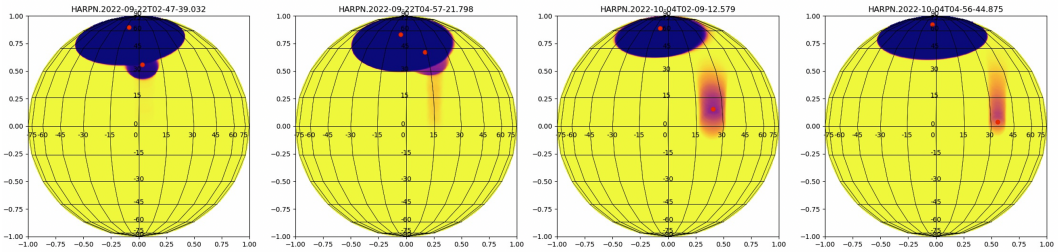

(I) *2022-09-22Δ T = 2.16 h* (J) *2022-10-04 Δ T = 2.79 h*

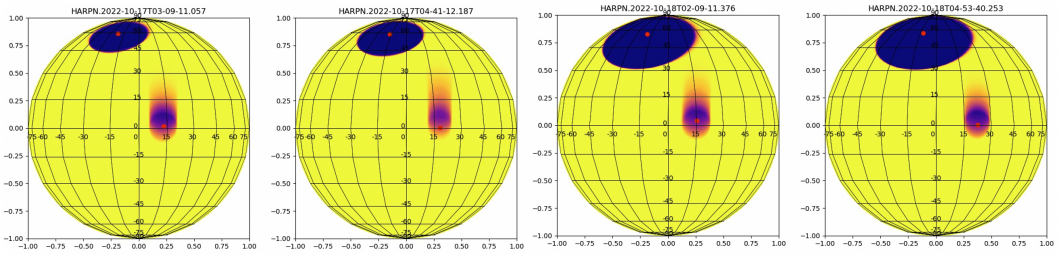

(K) *2022-10-17Δ T = 1.53 h* (L) *2022-10-18 Δ T = 2.74 h*

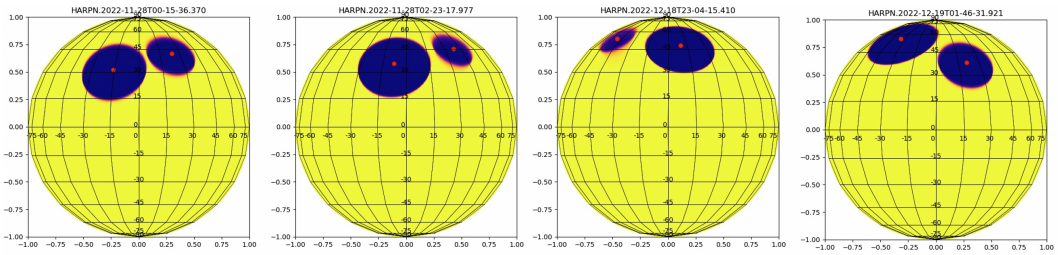

(M) *2022-11-28Δ T = 2.13 h* (N) *2022-12-19 Δ T = 2.70 h*

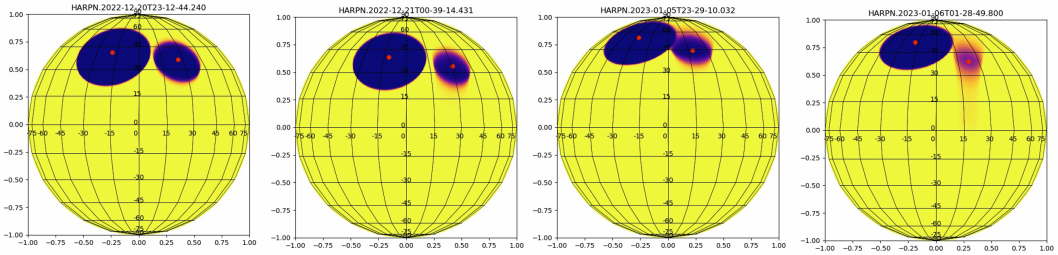

(O) *2022-12-20Δ T = 1.44 h* (P) *2023-01-05 Δ T = 2.00 h*

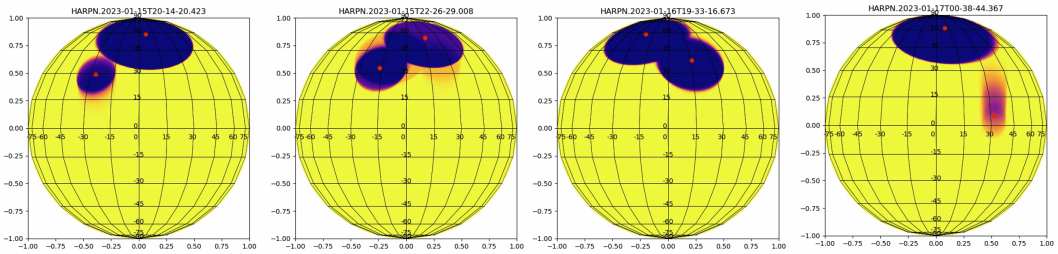

(Q) *2023-01-15 Δ T = 2.20 h* (R) *2023-01-16 Δ T = 5.09 h*

FIGURE 5.18: *Spot configuration of pairs of observations obtained at a few hours of distance (continued).*

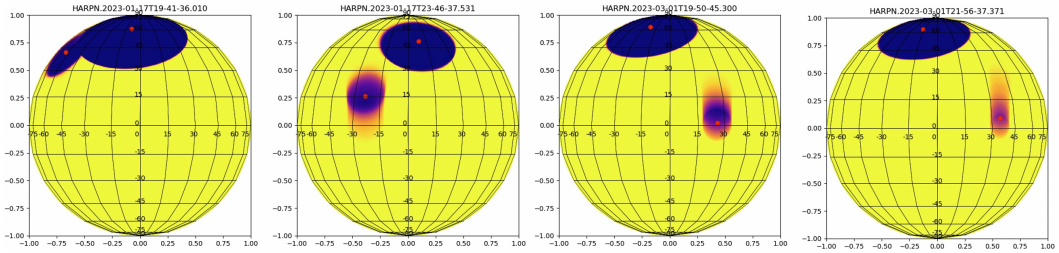

(S) *2023-01-17* $\Delta T = 2.10$ *h* (T) *2023-03-01* $\Delta T = 2.13$ *h*

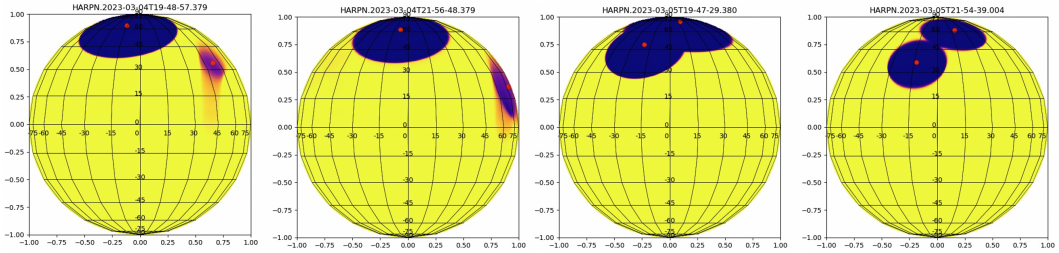

(U) *2023-03-04* $\Delta T = 2.13$ *h* (V) *2023-03-05* $\Delta T = 2.12$ *h*

FIGURE 5.18: *Spot configuration of pairs of observations obtained at a few hours of distance (continued).*

In Figure 5.18 I present the spot configurations obtained from pairs of observations taken at very few hours of separation. Specifically, I compare the spot configurations obtained from observations taken during the same night, but a few hours apart. It is important to note that each observation was analysed independently, and obtaining the same configuration of spots on the same night (with very few exceptions in 2023/01/16 and 2023/01/17) serves as a confirmation of the reliability of the method.

Figure 5.19 also shows a comparison between the spot configuration obtained with `SpotCCF`, applied to the HARPS-N data, and the maps obtained from an independent analysis conducted by Petralia et al. (2023, in preparation) of the data obtained with the TESS, simultaneously with the HARPS-N observations. The authors used a stellar activity model to fit the photometric light curve. assuming a model with 4 spots on the entire stellar sphere, rotating on the stellar surface with a period of P = 2.97 d (Suárez Mascareño et al., 2021), thus ignoring the effect due to the differential rotation. In their model, the spots do not evolve over time in size and do not migrate in latitude. They fit pieces of the observed light curves lasting at most one period. In each interval, the spots, which are initially visible on the stellar hemisphere at the initial time t_0, rotate during the stellar period.

Their 4-spot model on the entire surface of the star is consistent with the model presented here, which assumes two spots on the visible stellar hemisphere (in front of the observer). Both HARPS-N and TESS observations suggest the presence of

a large high-latitude dominant spot. It is not surprising; in fact, other studies have already suggested and demonstrated that highly active stars can exhibit a strong magnetic field in their polar caps, resulting in the formation of polar spots (e.g., Vogt et al., 1999; Schrijver and Title, 2001; Işık et al., 2018). Additionally, it is important to note that the TESS configurations at a given time are obtained by imposing a temporal coherence with the same fitted period and no spot evolution, while the HARPS-N configuration is derived from a snapshot spectroscopic observation at a given time.

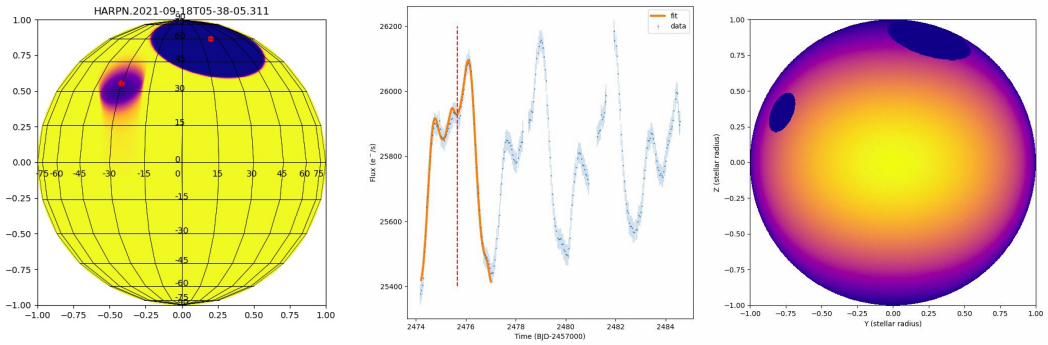

(A) *HARPS-N 2021-09-18* (B) *TESS 2021-09-18*

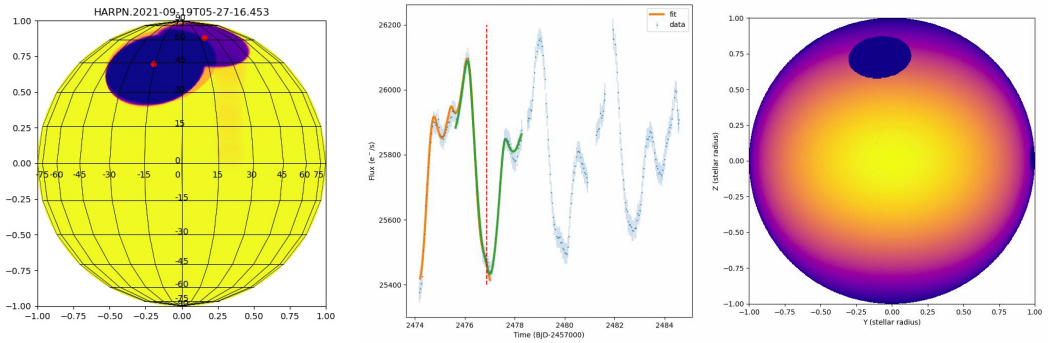

(C) *HARPS-N 2021-09-19* (D) *TESS 2021-09-19*

FIGURE 5.19: *Comparison between spot configuration of V1298 Tau obtained from simulations HARPS-N observation, with* `SpotCCF` *model (left panel) and TESS observation, by fitting the photometric light curve (right panel, courtesy of Petralia).*

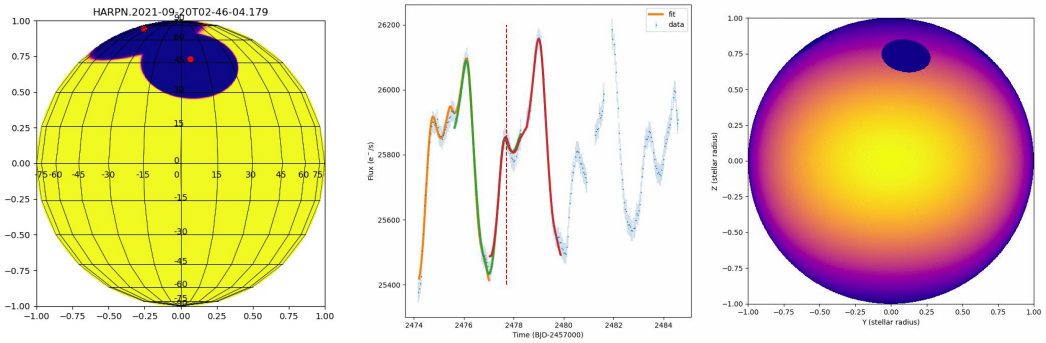

(E) *HARPS-N 2021-09-20* (F) *TESS 2021-09-20*

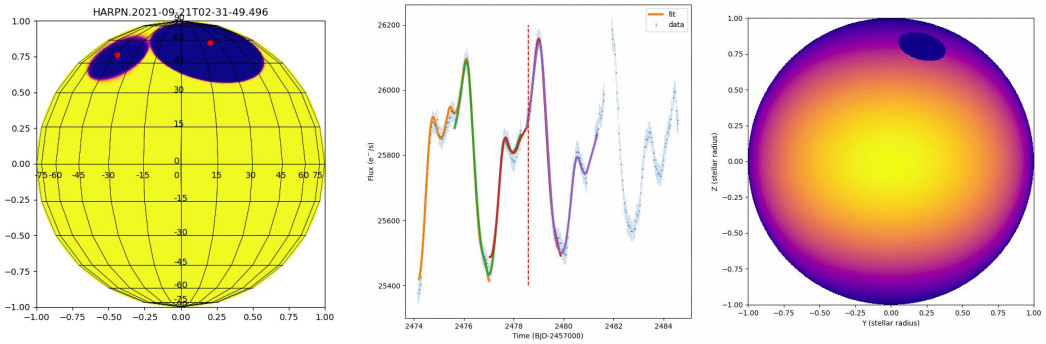

(G) *HARPS-N 2021-09-21* (H) *TESS 2021-09-21*

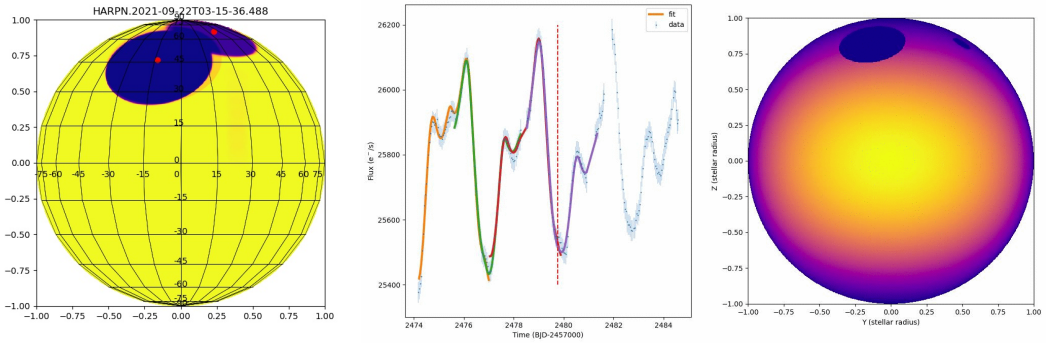

(I) *HARPS-N 2021-09-22* (J) *TESS 2021-09-22*

FIGURE 5.19: *Comparison between spot configuration of V1298 Tau obtained from simulations HARPS-N observation, with* `SpotCCF` *model (left panel) and TESS observation, by fitting the photometric light curve (right panel, courtesy of Petralia) (continued).*

5.9 DISCUSSION AND FUTURE PERSPECTIVES

In this chapter, I described the `SpotCCF`, which is a stellar photosphere model fit I developed for radial velocities extraction in young-active stars based on the cross-correlation function technique. This model takes into account the deformations of

the CCF due to the presence of multiple spots on the stellar disc, in presence of significant rotation. To test the validity of my model, I analysed V1298 Tau HARPS-N observations, which exhibit distorted CCF profiles due to the high activity level of this target. The original CCF profiles produced by the DRS pipeline were corrected for anomalous deformations present in the wings and in the core of the line, as well as in the CCF_B of the sky spectrum obtained using fiber B.

Then, I analysed over 300 HARPS-N observations of V1298 Tau using a Two-spots model. From the parameters through the fit performed on the CCF profiles, I extracted information about the spots, including latitude, longitude and the area covered by each spot. To analyse the spot properties, I separated the high latitude spots (Spot A, $ff_p \geq 0.04$ and latitude $\geq 60°$) and the smaller low latitude spots (Spot B, $ff_p < 0.04$ and latitude ≤ 50 °). Under this assumption, the GLS periodogram of the filling factor of Spot A and Spot B showed significant peaks (FAP $\leq 1\%$) at 3.24 and 2.53 days, respectively, suggesting a differential rotation velocity of the star, with lower rotation at higher latitudes.

The average total area covered by the spots is consistent with the range proposed by Messina et al. (2001). The GLS periodogram of the total projected filling factor, $ff_{p_{tot}}$, showed a significant peak at the $P_{rot}/2$ with a FAP $\leq 10\%$, indicating that the features identified in the CCF profiles are actually effects of few inhomogeneities (spots) on the stellar surface modulated by the rotation.

The consistency of the spot configuration obtained from different observations taken during the same night, but a few hours apart, confirms the reliability of the method. Moreover, similar spot configurations obtained from simultaneous HARPS-N and TESS observations, modelled with independent methods, provide strong evidence for the robustness of the method.

The `SpotCCF` model applied to the HARPS-N observations of V1298 Tau provided accurate RVs measurements. I compared these RVs with those obtained using the TERRA pipeline to light the benefits of the proposed method. I observed that the RVs obtained with my model showed lower dispersion, with a decrease ranging from 40% to 60% in each season, compared to the TERRA dataset. Additionally, a search for periodicities in the RV dataset revealed a significant peak at the rotational period of the star, with reduced RV amplitude for the `SpotCCF` RVs (about 30% lower than those obtained with TERRA) and reduced dispersion in the residuals. These results suggest that the new method for RVs extraction effectively mitigates the contribution of stellar activity modulated with stellar rotation. This thesis is further supported by the GLS periodogram performed on the `SpotCCF` dataset and on its residuals obtained after recursive pre-whitening, which show the removal of the

peak at the harmonics of the rotation frequency, since after the first pre-whitening, still present in the periodogram of the TERRA dataset.

I also tested the detection sensitivity of the method by directly injecting a hypothetical planetary signal (P_{orb} = 4.9 days) into the data. The results obtained from the GLS periodogram suggest that from the RV times series obtained with my method, a planet with an amplitude of the injected signal lower (K $\approx$ 37 m s^{-1}) than that necessary for the signal to be identified in the TERRA dataset (K $\geq$ 75 m s^{-1}), can reliably detected.

All the results of this work confirm that the developed method can optimise the radial velocity extraction in young/active stars, improving sensitivity and ability to recover planetary signals and reducing the probability of identifying signals that are actually due to stellar activity but can be mistaken as planetary signals.

I plan to apply the method proposed in this study to other targets that exhibit high values of v sin i, in order to assess the applicability range of the model. Furthermore, I could apply my `SpotCCF` model to individual spectral lines that are predominantly affected by rotational broadening and distorted by the presence of spots, in order to more accurately characterise the line profiles.

CHAPTER 6

Spectroscopic monitoring of AD Leonis

Understanding stellar activity in M dwarfs is fundamental to improving our knowledge of the physics of stellar atmospheres and for planet search programmes. High levels of stellar activity (also frequently associated with flare events) can cause additional variations in the stellar emission that contaminate the signal induced by a planet and that needs to be corrected. The study of activity indicators in active stars can improve our capability of modelling the signal generated by magnetic activity.

The content of this chapter has been published in the journal *Astronomy & Astrophysics*, volume 642, as the article with the title "The GAPS programme at TNG. XXVI. Magnetic activity in M stars: spectroscopic monitoring of AD Leonis" (Di Maio et al., 2020).

6.1 Introduction

Magnetic activity in late-type main-sequence stars is observable evidence of the stellar magnetic fields. The generation and intensification of surface magnetic fields in solar stars are generally due to a complex dynamo mechanism, whose efficiency is determined by the interaction between differential rotation and subphotospheric convection into the stellar interior and in which meridional circulation plays an important role (Brun et al., 2015; Brun and Browning, 2017; Charbonneau, 2020). Magnetic fields reach the stellar surface and manifest themselves in a variety of phenomena that we call stellar activity: starspots, chromospheric plages, heating of the chromosphere and corona, and impulsive flares. Starspots are a manifestation of magnetic field lines going through the stellar photosphere and obstructing the convective welling up of hot plasma, producing these cool spots that are darker than the surrounding photosphere. Chromospheric plage regions correspond to enhanced network magnetic field and facula regions in the photosphere, which might surround sunspots, but are not necessarily associated with them. Heating of the stellar chromosphere and corona generates chromospheric emission lines. Impul-

sive flares are visible in all regions of the spectrum and are due to the reconnection of magnetic field lines (Skumanich et al., 1975; Schrijver et al., 1989; Solanki et al., 2006; Choudhuri, 2017; He et al., 2018).

M stars are small cool main-sequence stars with effective temperatures in the range 2400 - 3800 K and radii between 0.10 and 0.63 $R_{\odot}$; they represent 75% of the stars in the solar neighbourhood (Reid et al., 2002; Henry et al., 2006). They are known to generate the strongest photospheric magnetic fields among main-sequence stars (Saar and Linsky, 1985; Reiners et al., 2009; Shulyak et al., 2017), showing magnetic activity as spots, flares, plages, and other brightness inhomogeneities.

In recent years the exoplanet community have started to monitor samples of M dwarfs, aiming to search for habitable planets around these stars. From an observational point of view, there are more chances of finding an Earth-like planet in the habitable zone as the host star's mass decreases. Therefore, M dwarfs are extremely interesting targets for planet discovery (Gomes da Silva et al., 2012). However, magnetic activity increases with decreasing stellar mass (Hawley et al., 1996; West et al., 2008; Newton et al., 2017).

Stellar activity has effects on the search of exoplanets: in some cases the radial velocity periodicity, induced by stellar activity and rotation, may produce spurious signals that mimic planetary signals. This was the case, for example, of AD Leonis, for which Tuomi et al. (2018) proposed the existence of a planet, while Reiners et al. (2013) and Bonfils et al. (2013) have interpreted the RV signal present in the AD Leo spectra as being due to magnetic activity; this thesis has also been recently confirmed by Carleo et al. (2020). They use a multi-wavelength approach (visible and near-infrared) to show that the signal is of stellar origin. Therefore, a detailed study of magnetic activity in active M stars could improve our capability of modelling the signal generated by magnetic activity and increase our possibilities of finding new exoplanet candidates.

In addition, stars with high levels of magnetic activity show flares more frequently than inactive stars (Kowalski et al., 2009). The large amounts of energy released by flares could potentially affect the structure and temperature regime of exoplanetary atmospheres, thereby affecting the size of the habitable zone (Lammer et al., 2007). It is therefore crucial to better understand and quantify the activity of M dwarfs in terms of strength and variability.

Chromospheric activity is usually observed in the cores of the Ca II H&K lines and the H I Balmer lines. Other common optical activity indicators include lines such as the Na $D_{1,2}$ doublet, the Mg I b triplet, or the Ca II infrared triplet. Simultaneous analysis of the different indicators of magnetic activity could increase our

knowledge of the chromospheric structure and the radial-velocity variations (e.g., Montes et al., 2000; Stelzer et al., 2013; Maldonado et al., 2017; Lanza et al., 2018; Maldonado et al., 2019). The common approach is to study the relationship between pairs of fluxes of different lines.

The aim of this work is to understand the behaviour of stellar chromospheres for M stars with high levels of activity. To this end, I focus my study on one M dwarf, AD Leonis, a very close active star, which was analysed through spectroscopic monitoring in the optical band. I present an analysis of fluxes and profiles of the main optical activity indicators such as chromospheric lines of H I, He I, Na I, and Ca II.

This chapter is organised as follows. I describe the target in Section 6.2 and the observations in Section 6.4. I detail my procedure in Section 6.5. Section 6.6 presents the analysis of the different spectral lines sensitive to the activity. A flare analysis is discussed in Section 6.7. Conclusions follow in Section 6.8.

6.2 AD Leonis

AD Leonis (AD Leo, GJ 388, BD +20 2465) is classified as dM4.5e (Tuomi et al., 2018) and is located in the immediate solar neighbourhood, at a distance of $\sim$ 4.97 pc (Gaia Collaboration et al., 2018). Shkolnik et al. (2012) estimated a radial velocity of 12.5 $\pm$ 0.2 km s^{-1}. Bonfils et al. (2013) estimated a mass of 0.42 $M_\odot$ and a luminosity of 0.023 $L_\odot$. The star has a radius of 0.436 $\pm$ 0.049 $R_\odot$ and effective temperature of 3414 $\pm$ 100 K (Houdebine et al., 2016). Neves et al. (2012) estimated the metallicity of AD Leo to be [Fe/H] = 0.07, while Rojas-Ayala et al. (2012) gave a value of 0.28 $\pm$ 0.17.

Based on spectropolarimetry, Morin et al. (2008) reported a stellar rotation period of 2.2399 $\pm$ 0.0006 days; they also gave alternative solutions at periods of 2.2264 and 2.2537 days. The strongest evidence in favour of the short rotation period of AD Leo comes from the Microvariability and Oscillations of Stars (MOST) photometric observations. MOST observations were reported to contain strong evidence for a periodicity of $2.23^{+0.36}_{-0.27}$ days (Hunt-Walker et al., 2012) caused by 'spots distributed at different longitudes or, possibly, that the modulation is caused by varying surface coverage of a large polar spot or a spot that is viewed nearly pole on'. This suggests a young age, estimated to be 25-300 Myr by Shkolnik et al. (2012).

Houdebine et al. (2016) reported a value for $v \sin i$ of AD Leo equal to 2.63 km s^{-1} that produced a projected rotation period of $8.38^{+1.2}_{-1.1}$ days. Thus, since the rotation period of the star is 2.23 days, the star is oriented nearly pole-on with an

inclination of $\sim$ 15 degrees, confirming the value reported by Morin et al. (2008) and Reiners et al. (2012).

AD Leo has been observed to be variable on longer timescales as well. Buccino et al. (2014) reported an approximately 7 yr activity cycle based on ASAS optical photometry and CASLEO spectroscopy. Even though the period reported in the ASAS photometry has a rather modest statistical significance with a false alarm probability (FAP) of the order of 8%, together with the spectroscopic data it indicates the presence of an approximately seven-year activity cycle in a convincing manner.

AD Leo hosts a magnetic field with properties similar to those observed for fully convective stars (Morin et al., 2008). A high-resolution infrared spectrum of AD Leo, obtained with the Kitt Peak 4 m Fourier Transform Spectrometer, clearly shows the presence of strong magnetic fields (Saar and Linsky, 1985). Lavail et al. (2018) inspected circularly polarised spectra and estimate an average large-scale magnetic field of $\sim 300-330$ G. Line broadenings in unpolarised spectra, also determined by small-scale field structures, reveal instead a stronger overall magnetic field (3100 G, Shulyak et al. 2017).

Since AD Leo is a magnetically active star, its emission from the upper layers of the atmosphere (chromosphere and corona) is intense. In particular, in the optical band AD Leo is characterised by Hα, Hβ, and Ca II H&K lines in emission, with variable line profiles (shape and intensity) that depend on the activity level at the time of observation, and by the presence of phenomena directly related to the stellar magnetic activity such as flares. It is well known for its frequent (Pettersen et al., 1984; Henry et al., 2006) and strong flares (e.g., Hawley and Pettersen, 1991) that have been observed and studied in the optical, extreme UV, and X-ray wavelength ranges (e.g., Hawley et al., 1995; Mauas and Falchi, 1996; Favata et al., 2000; Hawley et al., 2003; van den Besselaar et al., 2003). The most important properties of this star are shown in Table 6.1.

6.3 Activity indicators

High-resolution spectroscopy of activity diagnostics has been revealed to be a powerful tool to improve our understanding of stellar chromospheres; optically thick photospheric lines with broad absorption wings have core emission features that are strictly linked to the chromosphere's thermal structure. High-resolution spectra are required to resolve these emission features and to characterise their complex profiles that often consist of emission peaks with a self-reversed dip at the line centre.

Table 6.1: *AD Leonis main parameters*

AD Leonis	
Spectral type [(a)]	M4.5e
$M_\star(M_\odot)$ [(b)]	~ 0.42
$R_\star(R_\odot)$ [(c)]	0.436 ± 0.049
log g	~ 4.8
d (pc)[(d)]	$\sim 4.9660 \pm 0.0017$
$L_\star(L_\odot)$ [(b)]	~ 0.023
$T_{\rm eff}$ (K) [(c)]	3414 ± 100
$v \sin i$ (km s^{-1}) [(c)]	~ 2.63
$P_{\rm phot}$ (d)[(e)]	~ 2.23
[Fe/H] [(f)]	0.28 ± 0.17
RV (km s^{-1}) [(g)]	12.5 ± 0.2
B_{pol} (G) [(h)]	$\sim 300 - 330$
B_{unpol} (G) [(i)]	~ 3100

Notes. [(a)] Tuomi et al. (2018) [(b)] Bonfils et al. (2013) [(c)] Houdebine et al. (2016) [(d)] Gaia Collaboration et al. (2018) [(e)] Morin et al. (2008) [(f)] Rojas-Ayala et al. (2012) [(g)] Shkolnik et al. (2012) [(h)] Lavail et al. (2018) [(i)] Shulyak et al. (2017) .

In particular, I analysed the fluxes and profiles of the H I Balmer series, He I, Na I, and Ca II H&K.

Hα and Ca II K are two of the strongest optical emission lines in active M dwarf chromospheres. Across the M spectral class, there is a range of emission strength in Ca II K, and a wide variety of both absorption and emission in Hα. The Hα core appears to trace hotter regions of the chromosphere ($\geq$ 7000 K), while Ca II K is formed in the cooler regions between the temperature minimum and $\sim$ 6000 K (Giampapa et al., 1982; Cram and Mullan, 1985; Walkowicz and Hawley, 2009). Thus, Hα and Ca II K together offer complementary information on the chromospheric structure.

The Ca II H (3968.47 Å) and K (3933.66 Å) lines are very useful diagnostics of the solar chromosphere. The emission cores of the H&K lines are weak for very quiet regions on the Sun, but can exceed the local continuum in brightness for active stars, particularly for active M dwarfs that have a weak continuum. For FGK stars, the H&K lines show emission cores inside very broad absorption wings because Ca II is the primary ionisation stage in the photospheres and lower chromospheres of these warm stars. For M stars, Ca I is the dominant ionisation stage in the photosphere and lower chromosphere, and as a consequence, the H&K lines for these stars do not have broad absorption wings (Linsky, 2017).

Observations of the solar surface indicate that the inhomogeneities on the surface may be due to contributions from different regions and phenomena; Ca II K core emission corresponds spatially to regions of concentrated magnetic field, such

as active plage regions and bright network grains, while Hα chromospheric emission and absorption can be produced in filaments protruding from active regions, in spots across the network of the quiet Sun, and in enhanced emission from bright points during flares (Hasan and van Ballegooijen, 2008; Rutten, 2006, 2007). Consequently, examining the relationship between the Ca II and Balmer lines can throw light on the nature of magnetic structures.

Scandariato et al. (2017), extending a previous study by Martínez-Arnáiz et al. (2010), analysed the short-term chromospheric variability and the flux excess emitted in the Ca II H&K and Hα lines of a sample of 71 early-type M dwarfs with different levels of activity (inactive and moderately active stars). They show that the Ca II H&K flux excesses are strongly linearly correlated. When comparing the Ca II H&K with the Hα chromospheric line flux they found significantly more scatter, mostly for the most active stars. The same sample of inactive and moderately active stars was analysed by Maldonado et al. (2017), who focused on average trends.

The sodium resonance doublet is an important photospheric and chromospheric diagnostic. The typical profile of Na I doublet shows extended wings and narrow cores. Active dwarfs with Hα in emission have been shown to exhibit a distinctive core emission of probable chromospheric origin (e.g., Giampapa et al., 1978; Worden et al., 1981; Panagi et al., 1991). Pettersen (1989) was the first to detect the important chromospheric contribution of the Na I $D_{1,2}$ lines in the core for active M dwarfs. A complete study of the formation of the Na I $D_{1,2}$ lines proposed by Andretta et al. (1997) confirmed that these lines are promising diagnostics of the lower-middle chromosphere. Houdebine et al. (2009) also shows that the main chromospheric contribution of these indicators arises in a narrow line core, but they also note some differences in the inner wings, suggesting that magnetic activity could also affect the upper photosphere.

The He I D_3 (5875.62 Å) is also an interesting diagnostic because it is formed in the lower transition region and it is mostly detected in very active stars. All these chromospheric lines are used in planet search programmes to identify stellar activity, and they are all correlated to some extent with the RV jitter (e.g., Gomes da Silva et al., 2012).

Here, I present a study of all these chromospheric lines and their variability due to magnetic activity, focusing our attention on a specific M dwarf, well known for its high level of magnetic activity.

6.4 Observations

The high-resolution spectra of AD Leo analysed in this work were obtained with two different instruments. I analysed 33 high-resolution spectra of AD Leo collected with HARPS (Mayor et al., 2003), the fibre echelle spectrograph installed on the 3.6 m European Southern Observatory (ESO) telescope in the La Silla Observatory, Chile, obtained from January to May 2006. In addition, I considered 63 HARPS-N (Cosentino et al., 2012) spectra collected in the context of the Global Architecture of Planetary System (GAPS) programme (Covino et al., 2013) [1]. HARPS-N observations were performed in two different observing seasons: from April to June 2018 and from November 2018 to January 2019. All the data used in this work are listed in Table D.1.

The two instruments have very similar performance with a resolving power of R ~ 120000 (HARPS) and R ~ 115000 (HARPS-N) and a spectral coverage of 378-691 nm and 383-693 nm, respectively. The spectra are provided already reduced using ESO/HARPS-N standard calibration pipelines.

6.5 Analysis of the observations

I identified a number of lines sensitive to activity, listed in Table 6.2. A strong emission is detected, even during the quiescent state of the star, for the Hα, Hβ, Ca II H&K lines; an intermediate emission above the continuum is observed for the He lines (He I D_3, He I 4026 Å and He I 4471 Å); and the Na I doublet (D_1 & D_2) shows emission in the core of the line profile.

These lines result from different excitation potentials, so their formation requires different physical conditions that occur in different parts of the active atmosphere of AD Leo. As a result, changes in equivalent width and/or in line profile of these lines can be explained by a direct or indirect impact of the magnetic activity on the whole stellar atmosphere and on its time variability.

As a measure of the chromospheric activity strength, I measured the excess fluxes, as described in the next sections. To measure the emission caused by activity, I chose wavelength integration ranges that are sufficiently broad for the broadest emission even in case of a strong flaring event. These ranges were set after a visual inspection of the spectra and are reported in Table 6.2 for each line I considered.

[1] AD Leo was originally part of the search of planets around young stars of the GAPS 2 programme since a candidate planet around was proposed by Tuomi et al. (2018) and then discarded by Carleo et al. (2020)

In addition, other lines known as good indicators of chromospheric activity, such as the Mg I b_1, b_2, b_4 lines and Fe I at 5270 Å, were analysed, showing the same behaviour as the other lines studied in this work, even though their emission above the continuum is less intense than for the other lines, and for this reason they are not reported.

Table 6.2: *Rest wavelength and integration ranges for the selected lines. Blue and red integration ranges were chosen to fit the continuum.*

Line	λ (Å)	Blue integration ranges (Å)	W (Å)	Red integration ranges (Å)
Ca II K	3933.66	3932.20 - 3933.20	3933.20 - 3934.50	3934.50 - 3935.00
Ca II H	3968.47	3967.70 - 3968.00	3968.00 - 3969.10	3969.10 - 3969.30
He I 4026	4026.19	4025.40 - 4026.10	4026.10 - 4026.70	4026.70 - 4027.00
He I 4471	4471.48	4470.00 - 4471.40	4471.40 - 4471.85	4471.85 - 4473.00
Hβ	4861.35	4858.70 - 4859.60	4859.60 - 4864.00	4864.00 - 4864.20
He I 5876	5875.62	5875.30 - 5875.42	5875.28 - 5876.80	5876.90 - 5877.00
Na I D_2	5889.95	5889.50 - 5889.80	5889.80 - 5890.70	5890.70 - 5891.00
Na I D_1	5895.92	5895.70 - 5895.80	5895.90 - 5896.50	5896.60 - 5896.70
Hα	6562.79	6553.00 - 6555.00	6555.00 - 6570.00	6570.00 - 6572.00

6.5.1 Flux rescaling

The HARPS and HARPS-N spectra are not calibrated in flux; therefore, they have arbitrary units. The spectra provided by the Data Reduction Software (DRS) show night-to-night variations in the continuum level at different wavelengths, due to atmospheric differential absorption and instrumental effects. To correct them, and to scale the observed spectra to the same flux reference, in order to be able to compare the intensity of the analysed lines, I compare them with synthetic spectra from the BT-Settl spectral library provided by Allard et al. (2011)[2] with $T_{\rm eff}$, log(g), and [Fe/H] corresponding to stellar parameters (see Table 6.1) in analogy to the procedure adopted to compute the excess fluxes provided by Scandariato et al. (2017). Both the observed and the model spectra were degraded to low resolution, convolving them with a Gaussian kernel with $\sigma = 80$ Å, in order to avoid discrepancies between the observed and the model lines profiles. Finally, the observed-to-model flux ratio was used to rescale the observed high-resolution spectra.

The flux calibration procedure may be less accurate in the case of strong emission lines, sensitive to the magnetic activity, because the model does not take into account the chromospheric emission; therefore, to obtain a more precise calibration in those areas, they are removed during this procedure.

[2] I adopt the CIFIST2011 models (https://phoenix.ens-lyon.fr/Grids/BT-Settl/CIFIST2011bc/SPECTRA/)

I used the flux calibrated spectra to calculate the flux for each line according to Equation (6.1) with the same integration ranges listed in Table 6.2. This equation provides an estimate of the flux of the line above the continuum, assuming that the continuum follows a linear trend (see Figure 6.1). This value gives a measure similar to the Equivalent width (EW), but less influenced by continuum flux estimation. This is important for lines located in spectral regions where the continuum is very low, and hence its relative uncertainty is very high. The flux line is computed as

$$F_{line} = \sum_{i=1}^{i=n} F_i d\lambda - \frac{(F_{c,b} + F_{c,r})}{2} W, \tag{6.1}$$

where dλ is the width of the wavelength bin; F_i is the observed flux in the bin i of the line; n is the number of bins within the line region, defined as $W/d\lambda$; $F_{c,b}$ and $F_{c,r}$ are the flux values measured at the extremes of the integration range on the blue and red side of the line, respectively; and W is the wavelength range used for the integration, corresponding to the full line width (see Table 6.2).

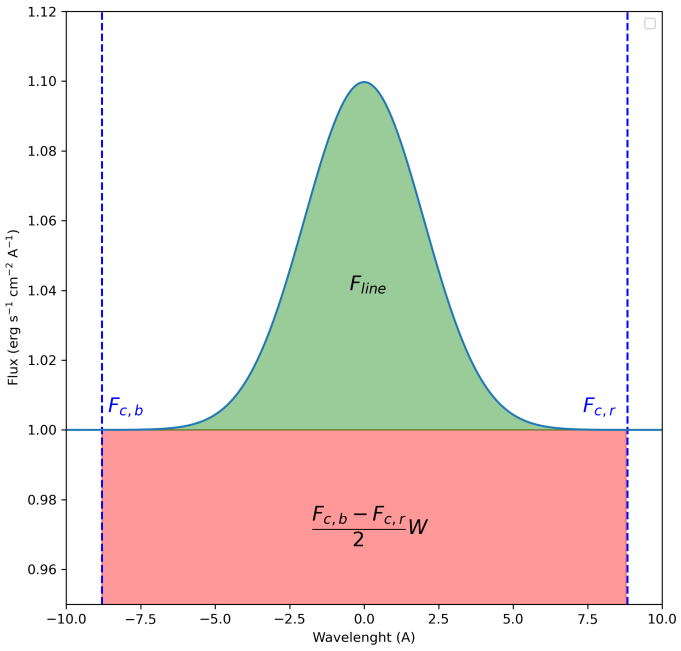

Figure 6.1: *Illustration of the flux calculated for a hypothetical spectral line. The blue lines indicate the flux values measured at the endpoints of the integration range on the blue and red sides of the spectral line, respectively. The red area shows the region above the continuum, while the green area represents the integrated flux of the spectral line.*

Several tests were done to find the most accurate method for determining the continuum flux F_c. I chose to fit the continuum (in the blue and red integration

ranges defined in Table 6.2) with a linear function. This method shows that the continuum flux is, with good approximation, constant over the considered range in most of the analysed spectra; however, some spectra show a slope and the linear fit allows us to take it into account. The error of the continuum flux, $\delta F_{c,i}$, was estimated by applying the standard error propagation theory on the uncertainties of the fit parameters.

There are no obvious estimates for the statistical error of the observed flux, δF_i. The spectrum is affected by the presence of numerous minor lines that are not variable in time, and that characterise every part of the spectrum. Since these lines are too numerous to be isolated, and since they can affect the spectrum in the continuum and in the profile of the line, I can assume that the δF_i is the standard deviation with respect to the continuum flux calculated in the N points outside the line (Equation 6.2):

$$\delta F_i = \sqrt{\frac{\sum_i (F_i - F_{c,i})^2}{N-1}}. \tag{6.2}$$

The F_{line} uncertainty was estimated using Equation 6.3, assuming $d\lambda = 0.01$ Å:

$$\delta F_{line} = \sqrt{\sum_i \left(\delta F_i \, d\lambda\right)^2 + \left(\delta F_{c,b}^2 + \delta F_{c,r}^2\right)\left(\frac{W}{2}\right)^2 + \delta F_{range}^2}\,. \tag{6.3}$$

Here F_{range} takes into account the possible effects due to the selection of the ranges used to estimate the continuum (δW). This value was calculated as the half difference between the maximum and minimum values of the continuum flux obtained with three different ranges for the continuum measurements.

6.5.2 Time series and line flux variability

Figure 6.2 shows the temporal variations of the analysed activity indicators. In particular, Figure 6.2 shows the variability of the integrated line flux of the analysed lines with time. The left panel shows HARPS data obtained in 2006; the middle and right panels show two different observing seasons of the HARPS-N dataset performed in 2018.

Several conclusions can be drawn from this figure. First, I can confirm that the flux on the stellar surface for the analysed lines is variable on both short (hours, days) and long (months, years) timescales during the entire observed time. Second, during the second season of 2018 (right panel) a flare is observed: two points, corresponding to two observations obtained two hours apart, highlight this phenomenon

and allow us to follow its evolution. A more detailed analysis of the flare is described in Section 6.7. Three other possible flare events are detected during 2006 (left panel). Moreover, observing the time series of the analysed activity indicators, I can assert that AD Leo was more active in 2018 than in 2006. Unexpectedly, despite the lower activity level, the time series of Ca II H&K show a higher flux in 2006 (see the average of the logarithmic flux $<F_\lambda>$ in Figure 6.2 and the histograms in Figure 6.3).

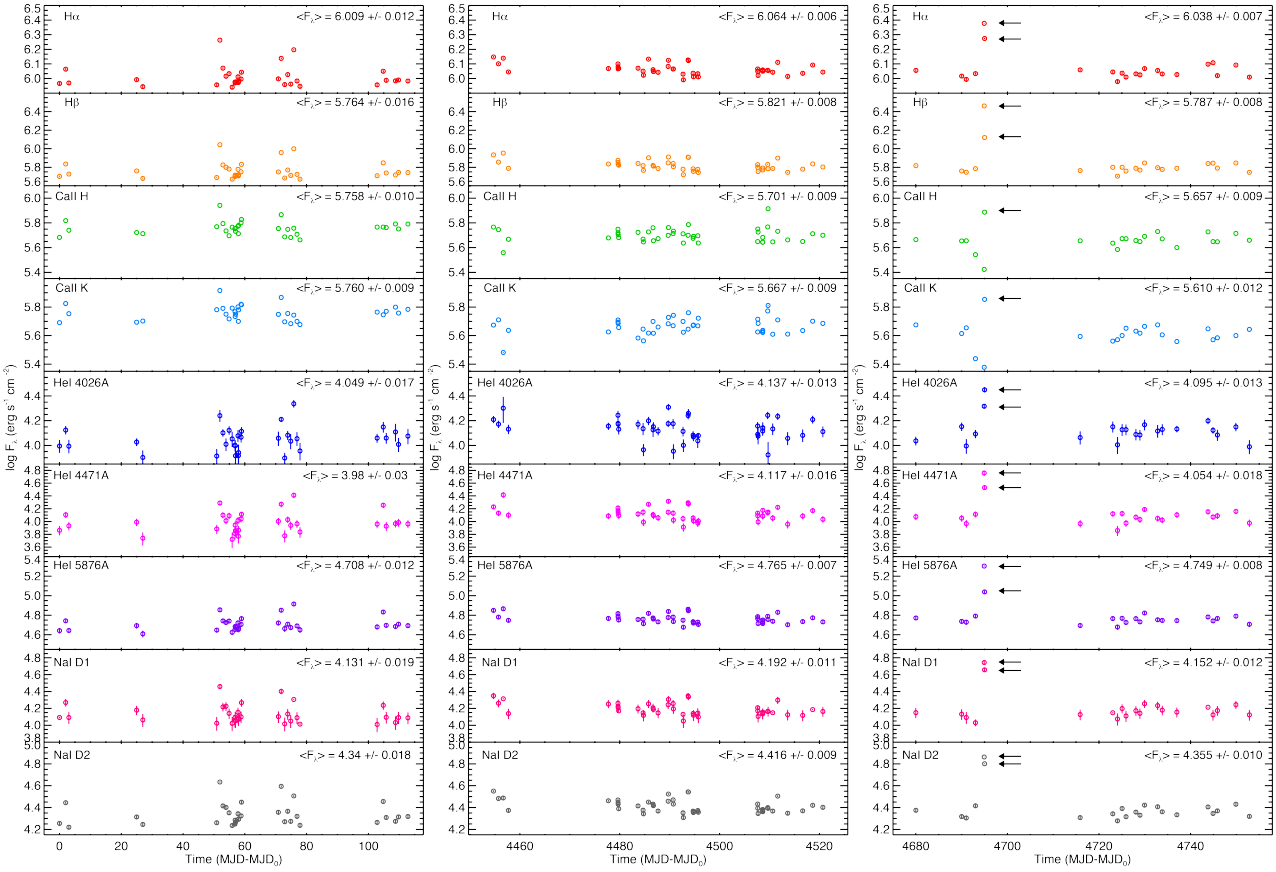

FIGURE 6.2: *Line flux vs time (MJD_0 is the start time of observations in 2006). Data obtained in 2006 are shown in the left panel. Data obtained in 2018 are shown in the middle and right panels. $<F_\lambda>$ is the average of the logarithmic flux of each activity indicator for each season (for the second season of 2018 these values exclude the flare event points). Black arrows mark the points relative to the flare event. The error bars are shown in the plots, but for most of the points are too small to be visible.*

6.6 FLUX-FLUX RELATIONSHIP

In the following, I analyse the relationships between the chromospheric fluxes of different activity indicators. I inspect the presence of a correlation based on Spearman's rank-order correlation coefficient (ρ). Figure 6.3 shows the correlations be-

tween the fluxes obtained from observations in 2018 (dark blue points) and those in 2006 (red points), and the results of the statistical tests separated for the two seasons are provided in Table 6.3.

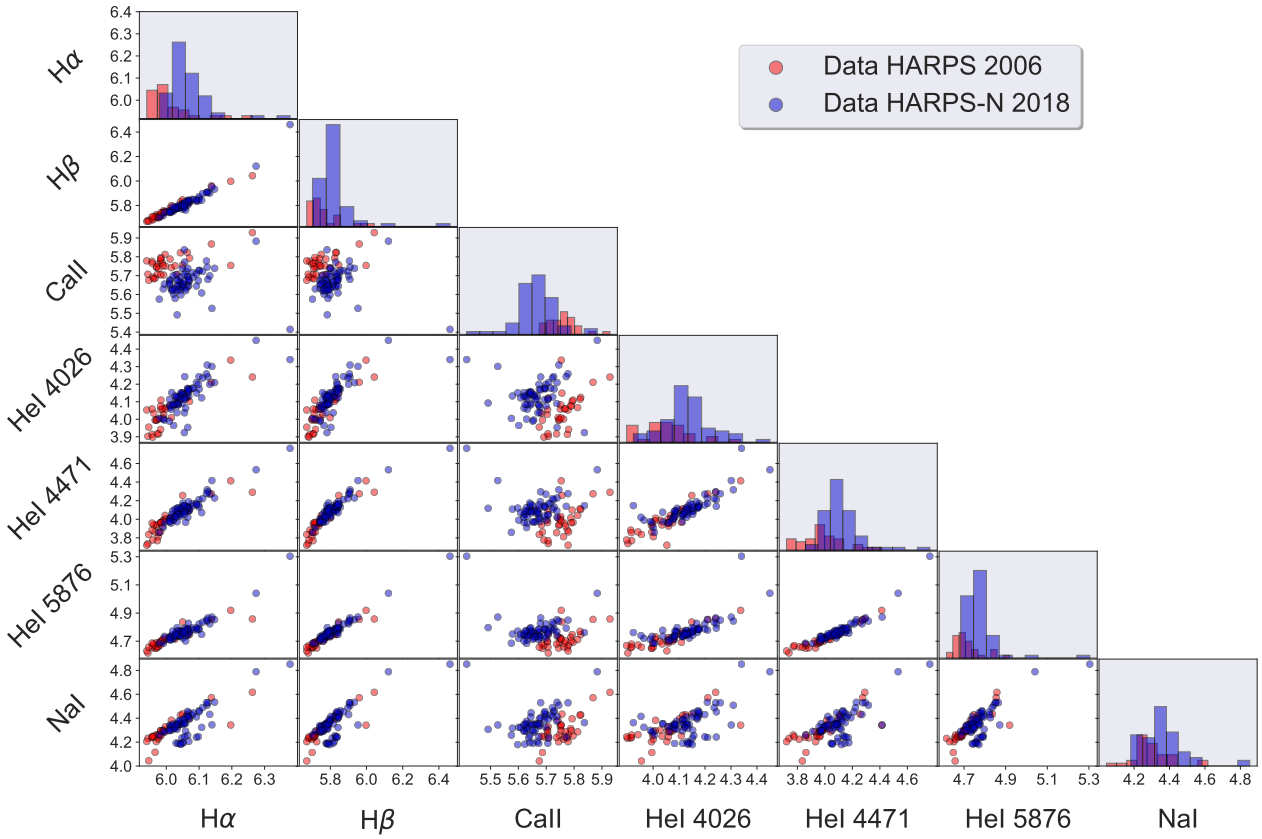

Figure 6.3: *Correlation plot of flux (logarithmic scale) between different activity indicators. The diagonal panels show the histogram of the flux of each indicator. It can be seen that most of the indicators show a significant correlation in both datasets. Here, the* Ca II *values are derived from the combined contributions of the* Ca II *H and K lines. Correlations with* Ca II *are less significant and more scattered. This figure also shows less activity of the star in 2006 (red points) than in 2018 (blue points). However, the flux of* Ca II *is higher in 2006 than in 2018. This result can be interpreted as a major surface coverage of plages and filaments during the observations in 2006.*

It can be seen that most of the indicators show a significant correlation ($P < 1\%$) in both datasets. The Ca II K line has a peculiar behaviour, with a weak correlation ($1\% < P < 3\%$) in the 2006 season and no correlation ($P > 3\%$) in 2018 with the other indicators. The correlation between most of the analysed lines implies that they have a similar origin and are likely formed from the same material or from the same region of the star's atmosphere.

I evaluated the same correlations excluding the points relative to the flare to verify their impact. I found that they do not influence the correlations among the indices.

Table 6.3: *Statistical analysis of chromospheric activity indicators fluxes. In the third and fourth columns are reported the Spearman coefficient ρ and the value of the probability of a null hypothesis for the dataset of 2006. In the last two columns I reported the same values for the dataset of 2018. Weak correlations are reported in brackets, no correlations are shown in boldface.*

X-index	Y-index	ρ_{2006} [a]	$P_{\rho 2006}$ [b]	ρ_{2018}	$P_{\rho 2018}$
Hα	Hβ	0.965	0.000006 %	0.941	0 %
Hα	Ca II H	0.518	0.34 %	0.490	0.01 %
Hα	Ca II K	(0.438)	(1.33 %)	**0.233**	**6.4 %**
Hα	Ca II	0.494	0.5 %	0.409	0.12 %
Hα	He I 4026	0.816	0.0004 %	0.769	0 %
Hα	He I 4471	0.920	0.000018 %	0.831	0 %
Hα	He I 5876	0.953	0.000006 %	0.802	0 %
Hα	Na I	0.932	0.000012 %	0.585	0.0003 %
Hβ	Ca II H	0.532	0.26 %	0.459	0.027 %
Hβ	Ca II K	(0.433)	(1.43 %)	**0.212**	**9.26 %**
Hβ	Ca II	0.489	0.6 %	0.390	0.2 %
Hβ	He I 4026	0.821	0.0003 %	0.831	0 %
Hβ	He I 4471	0.952	0.000006 %	0.886	0 %
Hβ	He I 5876	0.948	0.000006 %	0.901	0 %
Hβ	Na I	0.933	0.000012 %	0.601	0.00018 %
Ca II H	Ca II K	0.928	0.000018 %	0.771	0 %
Ca II H	He I 4026	0.597	0.07 %	0.338	0.73 %
Ca II H	He I 4471	0.543	0.21 %	0.379	0.26 %
Ca II H	He I 5876	0.517	0.3 %	0.408	0.12 %
Ca II H	Na I	0.517	0.43 %	0.520	0.004 %
Ca II K	He I 4026	0.511	0.38 %	**0.123**	**33 %**
Ca II K	He I 4471	(0.422)	(1.69 %)	**0.187**	**14 %**
Ca II K	He I 5876	(0.409)	(2.1 %)	**0.191**	**13 %**
Ca II K	Na I	(0.404)	(2.2 %)	0.327	0.94 %
Ca II	He I 4026	0.591	0.08 %	**0.268**	**3.37 %**
Ca II	He I 4471	0.494	0.52 %	0.336	0.76 %
Ca II	He I 5876	0.479	0.69 %	0.344	0.63 %
Ca II	Na I	0.478	0.69 %	0.479	0.014 %
He I 4026	He I 4471	0.86	0.00009 %	0.844	0 %
He I 4026	He I 5876	0.842	0.00019 %	0.808	0 %
He I 4026	Na I	0.777	0.0011 %	0.397	0.16 %
He I 4471	He I 5876	0.943	0.000012 %	0.919	0 %
He I 4471	Na I	0.887	0.00005 %	0.478	0.015 %
He I 5876	Na I	0.947	0.000006 %	0.536	0.002 %
Na I D1	Na I D2	0.867	0.00001 %	0.893	0 %

Notes. [a] Rank correlation for two populations [b] P-value denotes the two-sided significance of its deviation from 0 by random chance, i.e. a small value indicates significant correlation .

Finally, I verified that the correlation among the activity indices for the whole dataset is maintained when I join data obtained 12 years apart, with the only exception of the Ca II H&K index, for which there is no correlation with the other indices.

In addition, I estimated the Balmer decrements (Hα, Hβ), which are indicators of the physical conditions of the emitting regions (e.g., Landman and Mongillo, 1979; Chester, 1991). Maldonado et al. (2017) showed the Balmer decrement as a function of the effective temperature and overplotted the typical values of solar plages. This result ($\sim$ 1.76) is compatible with values of solar plages, suggesting that AD Leo is dominated by them.

The comparison between Hα (or Hβ) and Ca II (Ca II H&K) fluxes shows that the correlation between these two indicators is less significant and more scattered than the correlations between the other lines.

This result is consistent with the hypothesis that the phenomena that produce the two lines are actually connected, but the materials that generate them are in different regions of the atmosphere. Moreover, I also tested the correlations between the indicators excluding the measurements taken during the flare. These further tests return a value only slightly more significant than the previous one.

The result obtained from the test is consistent with those presented by Scandariato et al. (2017), who show that Hα and Ca II H&K are correlated and that the correlation is more scattered for the most active stars. Specifically, in Figure 6.4, the blue bubbles represent an envelope of the results obtained by Scandariato et al. (2017), while the orange points are the values obtained for AD Leo in this study.

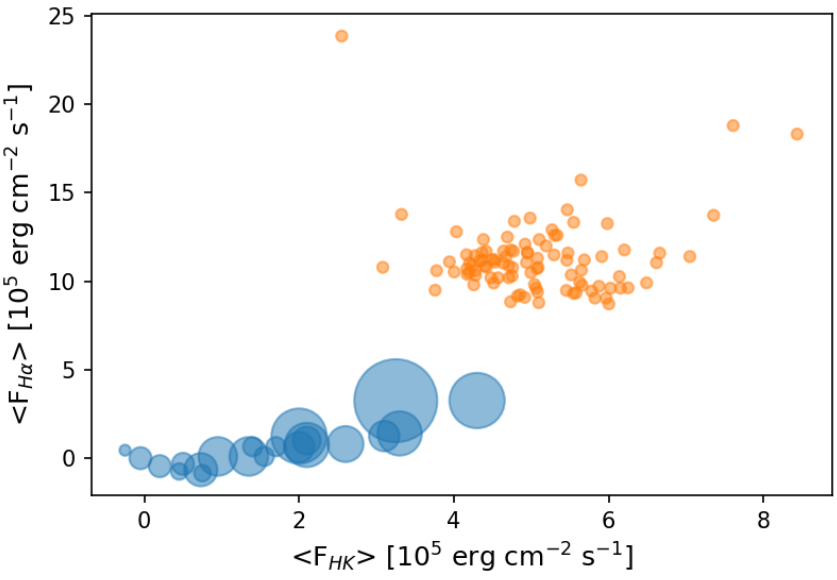

Figure 6.4: *Plot of F_{HK} vs $F_{H\alpha}$. The blue bubbles map the region populated by the stars analysed by* **?***, and the orange points are the flux values obtained for AD Leo in this study.*

Furthermore, although all the other activity indicators are more intense in 2018, the flux of Ca II H&K is higher in 2006 than in 2018. By considering the model of Meunier and Delfosse (2009), which affirms that Ca II core emission is connected to the active plage regions and bright network grains, while the Hα line is produced from all the inhomogeneities present on the stellar surface, the result can be interpreted with a major surface coverage of plages and filaments during the observations on 2006. Even though the Balmer decrement suggests that AD Leo is dominated by plages, this ratio does not allow us to distinguish between the two observing seasons.

6.7 Flare analysis

Solar and stellar flares are observable evidence of magnetic energy released on short timescales. The magnetic reconnection plays a key role in the reconfiguration of the magnetic field lines and the conversion of magnetic energy into kinetic and thermal energies of plasma (Forbes and Acton, 1996; Priest and Forbes, 2000). The impulsive X-ray and UV emissions associated with stellar flares can affect the stellar atmosphere.

The most extreme solar flare that hit Earth was recorded in 1859 (Carrington, 1859). It released a flare energy of 10^{32} erg. Stellar flares are expected to be generated by the same mechanism as solar flares with a wider range of energy radiation and timescale (e.g., Benz and Güdel, 2010; Doyle et al., 2018). Over short timescales of minutes to a few hours, they emit energy ranging from 10^{23} erg (called nanoflares) (e.g., Parnell and Jupp, 2000) to $10^{33} - 10^{38}$ erg (called superflares) (e.g., Shibayama et al., 2013).

From the standard solar flare model, flares are formed by accelerated non-thermal electrons that propagate downward and heat the chromosphere. As a consequence, the heated chromospheric material moves upward (evaporation), filling the coronal loop above. This material then cools down radiating away its excess energy, and finally moves downward (condensation), going back to the lower layers of the stellar atmosphere (Yokoyama and Shibata, 1998). Because of the high temperatures and large motions of the flaring material, chromospheric emission lines during flares appear much broader than in the quiescent state of the star.

In the right panels of Figure 6.2 I indicate with black arrows two consecutive points obtained during the second observing season of 2018, where the flux of all activity indicators is significantly higher than the quiescent state of the star. Therefore, it is reasonable to assume the presence of a flare. Since the two spectra were

obtained two hours apart, I have the possibility to follow roughly the temporal evolution of the flare. It can be supposed that the first observation during the flare is relative to the maximum phase of the flare, while the second point, with a lower value of flux than the first one, was obtained during the decaying phase of the flare.

The observed profiles of some selected spectral lines sensitive to stellar activity are broadened during the flare. This can be due to the motion of material inside the magnetic loop.

I considered a number of lines where the broadening is more evident (Hα, Hβ, He I 4471 Å, He I 5876 Å) and I fitted each profile with two Gaussian components (see Crespo-Chacón et al., 2006; Fuhrmeister et al., 2018). The Balmer lines show a self-reversal absorption in the core, but this behaviour was not taken into account because it does not have a significant contribution to the following analysis of the flare. The fit with two components results in a reasonably good description of the line profile even in the most asymmetric cases. In general, the Balmer lines display two distinct phases, called the impulsive and the gradual phases, with broader profiles during the impulsive phase and narrower profiles during the gradual phase. I do not consider the Ca II H&K even if they are strong emission lines because they are not significatively influenced by the flare and they do not show broadening. Because the flare event is supposed to be generated in different regions with respect to the plages, the fact that Ca II lines are not broadened is consistent with the hypothesis that this indicator is influenced by the presence of plages and that AD Leo is dominated by them. The results of the fit (the redshift and the sigma) for the narrow and the broad components are provided in Table 6.4.

Figure 6.5 shows the fits that I made on spectra obtained during the flare. The red dotted line corresponds to the spectrum obtained during the maximum phase of the flare (ID 79), and the blue dotted line to the spectrum obtained during the decaying phase (ID 80) of the flare. The orange and light blue Gaussians represent the broader components for the observation ID 79 and ID 80, respectively, while the purple (ID 79) and green (ID 80) are the narrow components obtained from the fit.

The spectra in Figure 6.5 show that the broadening of Balmer lines is larger than that of the helium lines. The broad components of the Balmer and helium lines are more redshifted than the narrow components. Doyle et al. (2018) observed a similar effect during a flare on YZ CMi and suggest the presence of material inside the loop corresponding to different flare kernels that brighten successively one after another. Each downflow would produce a redshifted contribution to the Balmer lines.

Moreover, Figure 6.5 shows symmetric broadening during the decay phase (light blue component), for Hα and Hβ, with σ of the order of hundreds of km/s. This

Table 6.4: *Fitted value of redshifts δv and sigma σ(δv) of the narrow and broad components for ID 79 and ID 80 spectra taken during the flare. The errors resulting from the fit are ≤ 0.1%.*

ID obs 79				
Line	Narrow		Broad	
	δv (km s^{-1})	$\sigma(\delta v)$ (km s^{-1})	δv (km s^{-1})	$\sigma(\delta v)$ (km s^{-1})
Hα	0.55	31.10	1.77	155.38
Hβ	1.50	26.51	4.31	129.03
He I 4471	0.68	7.93	15.77	16.73
He I 5876	2.06	8.21	10.13	15.49
ID obs 80				
Line	Narrow		Broad	
	δv (km s^{-1})	$\sigma(\delta v)$ (km s^{-1})	δv (km s^{-1})	$\sigma(\delta v)$ (km s^{-1})
Hα	0.68	28.82	29.52	170.99
Hβ	1.48	22.34	34.95	86.30
He I 4471	0.96	6.38	21.49	11.00
He I 5876	0.28	8.72	15.78	9.35

symmetric broadening can be interpreted with the presence of material inside the magnetic loop that undergoes blueshift and redshift simultaneously. Since the exposure time (900 seconds) of the observations acquired with HARPS-N is shorter than the evolution time of the flare, it can be concluded that the possibility of monitoring the same material before it rises uphill inside the loop and then descends is excluded. This result can be explained instead as the presence of turbulent motion that can be dominant with respect to the coherent motion of the material (uphill or downhill) (see Montes and Ramsey, 1999; Fuhrmeister et al., 2005). Hα monitors the lower regions of the magnetic loop; in this region, due to the high density of the material, the turbulent motion can be dominant with respect to the coherent motion of the material, which instead follows the magnetic field lines. Globally, the lines are shifted due to the coherent motion, but the broadening due to the turbulence is much larger and dominates the shape of the line.

On the contrary, Figure 6.5 (right panels) shows an asymmetrical broadening of helium lines with velocity of the order of tens of km s^{-1}. This asymmetric broadening might be present even in the Balmer lines, but it is clearly smaller than the symmetric broadening shown in Hα and Hβ and for these reasons it cannot be detected. It is possible to suppose that the helium lines monitor an upper region of the loop higher than Hα. If in the lower chromospheric regions the kinetic energy density of the turbulent motion is probably comparable to the magnetic energy density,

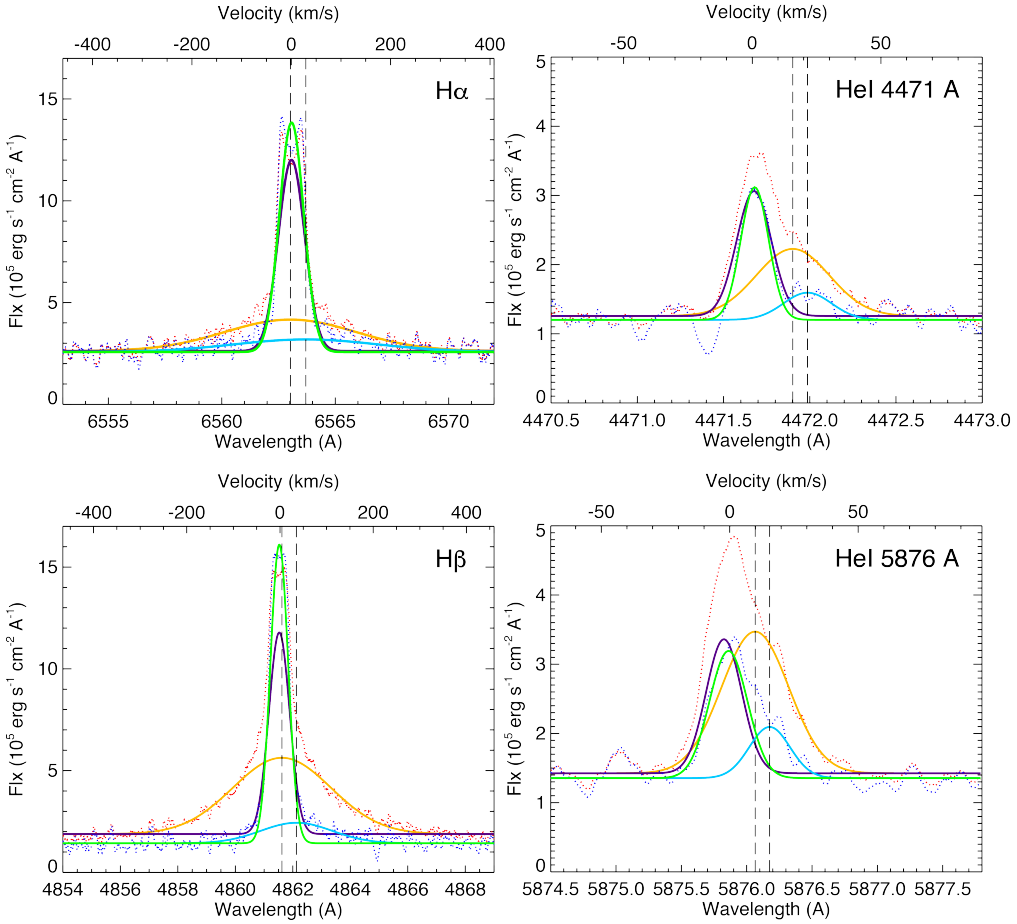

Figure 6.5: *Spectrum ID 79 for the flare's maximum phase (red dotted line) and spectrum ID 80 for the decay phase (blue dotted line). Gaussian fit with broad and narrow components, respectively in orange and purple for ID 79 and in green and light blue for ID 80. The black dashed line shows the centre of each broad component.*

in the upper regions the magnetic energy density dominates the kinetic energy density making the motion of the plasma less turbulent and inducing it to move along the magnetic field lines. This effect leads to a decrease in the line broadening and emphasises the radial velocity shift.

In addition, despite the low temporal resolution, I identified a delay of a flare event for the Ca II H&K and He I at 4026 Å with respect to the Balmer lines. The moment at which a line reaches its maximum is related to the temperature that characterises the formation of the line, and therefore it is also related to the height at which the line is formed. Therefore, it can be supposed that this delay, also observed by Crespo-Chacón et al. (2006), confirms that these lines monitor different regions of the stellar atmosphere with respect to the Balmer lines.

I also tried to estimate the luminosity and the energy released during the flare. According to our data, the line luminosity, estimated by analysing the lines during the flare, is significantly higher than the luminosity of the quiescent state of the

star. The energy released ($\sim 10^{30}$ erg to $\sim 1.4 \times 10^{32}$ erg for the Balmer lines) is consistent with the presence of a particularly intense flare event, stronger than the flares detected by Crespo-Chacón et al. (2006) who obtained an energy released value of the order of 10^{29} erg. In support of the results, I mention that Guenther et al. (2019), observing AD Leo for 222 hours with the Echelle spectrograph of the 2 m telescope Alfred-Jensch-Teleskope in Tautenburg, detected 22 flares, the largest of which emitted 2.9 10^{31} erg in Hα and 1.8 10^{32} erg in Hβ. Muheki et al. (2020), analysing more than 2000 spectra of AD Leo collected with the same telescope in the context of the flare-search programme of the Thüringer Landessternwarte, also detected numerous flares; the largest one emitted 8.32 10^{31} erg in Hβ and 2.12 10^{32} erg in Hα. Results from both studies are comparable to the energy released by our flare.

6.7.1 Delay of flare

Figure 6.6 shows the time series of normalised fluxes with respect to the quiescent state of the star. By inspecting the time series of most activity indicators it can be seen the two points related to the flare where the flux decreases going from ID 79 to ID 80, two hours later, except for the He I 4026 Å and Ca II lines.

In spite of the low temporal resolution, it can be seen that He I 4026 Å and Ca II lines show a delay with respect to the other lines. Crespo-Chacón et al. (2006) reported a delay (up to 5 ± 3 minutes) for the Ca II and He I 4026 Å lines in some weak and short flares observed on AD Leonis. Our flare is much more intense and it is possible that this effect is enhanced with respect to the case of weaker flares. Houdebine (2003) studied the dynamics of flares on dMe stars and show that the rise and decay times in the Ca II line are usually longer than the rise and decay times in the Balmer lines.

6.7.2 Luminosity and released energy

In order to estimate the flare energy released in the observed chromospheric lines, I have converted the observed flux to luminosity. The luminosity values obtained are provided in Table 6.5 as L_{max} for the considered lines. I calculated the value of luminosity for the quiescent state of the star, L_{quiet}, provided in Table 6.5, using the quiescent flux obtained from the average of the points outside the flare (red dashed lines in Figure 6.6). Despite the low temporal resolution I estimated the released energy by approximating the temporal evolution of the flare with a vertical ascent phase and a phase of linear decay.

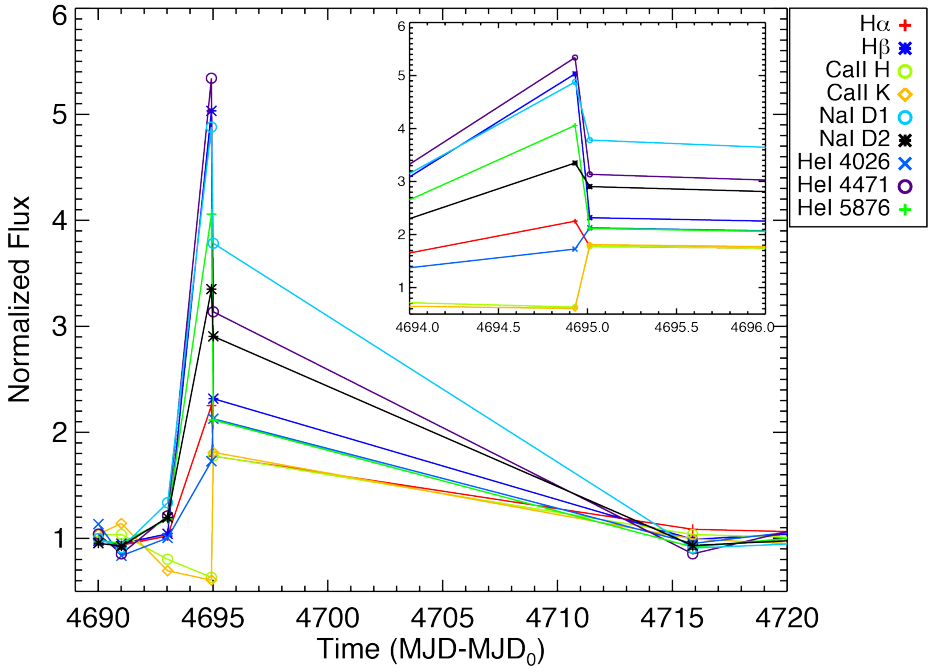

Figure 6.6: *Time series of the normalised flux of analysed activity indicators to evidence the flare. MJD_0 = 53758.244, time of the first observation obtained in 2006. The inset shows the zoom of the time series during the flares. Shown is the delay on the flare event in the* Ca II *H and K lines and in* He I *at 4026 Å. Also shown are the pre-flare dips on the time series of these indicators.*

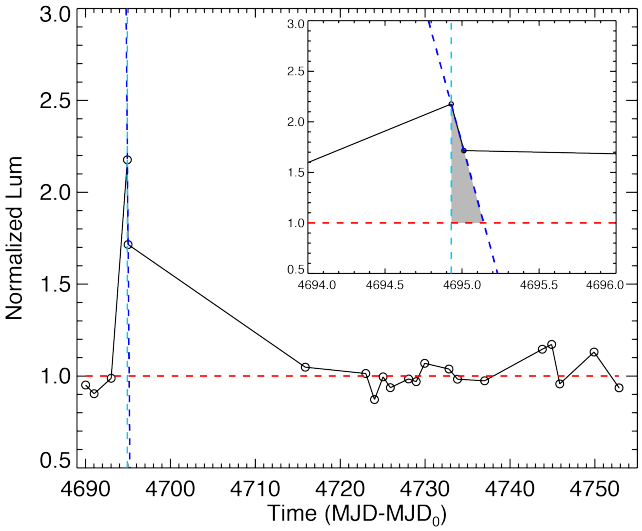

Figure 6.7: *Example of the triangle used to calculate the energy released during the flare in a given line. The dashed light blue line, parallel to the ordinate axis and passing through the point of flare maximum, represents the rising phase of the flare; the dashed blue line, passing through the two points corresponding to the two observations performed two hours apart, approximately the decay phase of the flare. The dashed red line shows the quiescent state of the star. MJD_0 = 53758.244, time of the first observation obtained in 2006. The inset shows the zoom-in on the triangle.*

Considering the characteristic timescale of the flares (from a few minutes to a few hours), it is unlikely that the flare ends in the next point, obtained with an observation carried out 20 days after the start of the flare. Therefore, I have drawn a straight line passing through the two points corresponding to the two observations performed two hours apart (dashed blue line) to reconstruct the shape of the flare (see Figure 6.7). The rising phase of the flare is approximated with one straight line (dashed light blue line) parallel to the ordinate axis and passing through the point of flare maximum. From the area of this triangle, I have obtained the value of energy released during the flare provided in Table 6.5. This is likely a conservative estimate since it cannot be determined whether the true flare maximum was observed.

For the lines where the flare shows a delay, it is not possible to calculate the released energy using the previous technique mentioned as there is only one point related to the flare.

Table 6.5: *Value of maximum flux corresponding to the flare, value of luminosity for the quiescent state of the star and in correspondence of the maximum of the flare, and value of energy released during the flare. The errors take into account the error on the stellar radius, which has the greatest influence on the final values.*

Line	F_{max} (10^5 erg s^{-1} cm^{-2})	L_{quiet} (10^{26} erg s^{-1})	L_{max} (10^{26} erg s^{-1})	Energy (10^{30} erg)
Ca II K	7.155 ± 0.016	47 ± 11	83 ± 19	-
Ca II H	7.730 ± 0.007	53 ± 12	89 ± 20	-
He I 4026	0.282 ± 0.012	1.5 ± 0.3	3 ± 0.7	-
He I 4471	0.58 ± 0.06	1.3 ± 0.3	6.7 ± 1.7	3.7 ± 1.2
Hβ	28.9 ± 0.4	71 ± 16	334 ± 75	137 ± 40
He I 5876	2.01 ± 0.03	6.6 ± 1.5	23 ± 5	9 ± 3
Na I D2	0.730 ± 0.007	2.6 ± 0.6	8.4 ± 1.9	11 ± 4
Na I D1	0.56 ± 0.02	1.7 ± 0.4	6.4 ± 1.5	7 ± 2
Hα	23.86 ± 0.13	127 ± 28	276 ± 62	136 ± 62

It can be seen that the luminosity of the maximum of the flare is greater than the luminosity of the quiescent state of the star by a factor of between ~ 2 and ~ 5. These results suggest that the ratio L_{max}/L_{quiet} is higher for the lines that are thought to originate in the upper layers of the stellar atmosphere, like the helium lines.

6.8 Summary and conclusions

In this study, I analysed the spectra of AD Leo using two datasets HARPS and HARPS-N spectra, obtained 12 years apart. I measured the line profiles and the intensities of the sensitive activity indicators, such as Hα, Hβ, Ca II H&K, He I at

4026 Å, 4471 Å, and 5876 Å, and Na I doublet. I derived the fluxes of these lines and evaluated the correlations between them.

By analysing the time variability of the fluxes I found a higher level of activity during 2018 than in 2006, except for the Ca II H&K indicator that shows a higher flux in 2006. As suggested by Hasan and van Ballegooijen (2008) and Rutten (2006, 2007), the Ca II core emission originates from regions of the concentrated magnetic field, such as active plages and bright grain networks. According to this, the long-term variability of Ca II suggests that the star had a larger coverage of plages during the observations of 2006 than in 2018. Furthermore, the Balmer decrements (Hα/Hβ), calculated for the three observing seasons, are compatible with the typical values of solar plages showed by Maldonado et al. (2017), confirming that the stellar surface is probably covered by a distribution of plages.

I searched for the correlation among the activity indicators measured in this work. All lines show a good correlation with each other, except for the Ca II, particularly the K line, indicating that the processes and regions of the formation of this line differ from other lines. Many studies (e.g., Walkowicz and Hawley, 2009; Cincunegui et al., 2007) suggest that there is a correlation between Hα and Ca II K flux obtained for a sample of different stars of different spectral types. However, Cincunegui et al. (2007) have declared that 'when we investigate this relation for individual observations of a particular star, the general trend is lost and each star shows a particular behaviour, ranging from tight correlations with different slopes, to anti-correlations, including cases where no correlations are found'. Walkowicz and Hawley (2009) compared the equivalent width of Hα to the Ca II K surface flux measured from a sample of M stars. They found a positive correlation between the measurements of these indicators when comparing different stars, with a wide range of scatter for the more active stars. Furthermore, they obtained multiple measurements of EW of Balmer lines and Ca II K in AD Leo and showed that for individual active stars these two lines are not necessarily correlated in time-resolved observations. The flux values obtained here for Ca II H&K and Hα follow the extrapolation of the trend shown in Figure 10 of Maldonado et al. (2017), confirming that the same trend continues at a high activity level.

I also detected the presence of a flare during the second season of HARPS-N data. Crespo-Chacón et al. (2006) monitored AD Leo for four nights in 2001 and observed a large number of short and weak flares occurring very frequently. I measured the EWs[3] of the analysed lines to compare our results to the published ones.

[3]The EWs were measured with a procedure similar to that of fluxes (see Sect. 6.5.1), except for the normalisation, and the results are provided in Appendix D.

The range of EW values that I obtained during the entire observed time identified as the 'quiescent' state of the star is consistent with the variability of Balmer lines EWs obtained by Crespo-Chacón et al. (2006). Moreover, the surface fluxes of the Balmer lines at flare maximum (F_{max}) obtained by Crespo-Chacón et al. (2006) are an order of magnitude lower than our results (see Table 6.5). This implies, also due to our low temporal resolution, that it is not possible to resolve less intense flares and that what is commonly referred quiescent state is indeed the superposition of several weak flares. The flare that I observed is a stronger and more uncommon event. In this work, I presented a detailed analysis of the profile of selected emission lines to study dynamic processes occurring during this phenomenon. In particular, I analysed the profiles of Hα, Hβ, and He I at 4471 Å and 5876 Å from two spectra collected during the flare and obtained two hours apart, showing a significant broadening, while no evidence of broadening is present in the Ca II lines. I fitted the profiles combining a broad and a narrow Gaussian component, finding that the broader one is redshifted with a velocity of the order of tens of km s^{-1}. This redshift can be interpreted as the presence of material going downhill inside the magnetic loop, according to the solar flare model. Globally, the shape of these lines, especially for the Balmer lines, is symmetrically broadened with σ of the order of hundreds of km s^{-1}. Since Hα monitors the lower regions of the magnetic loop, it can be supposed that in this region, because of the high density of the material, the turbulent motion can be dominant over the coherent motion of the material that follows the magnetic field lines. Consequently, it is reasonable to assume that the Balmer lines are also redshifted due to the coherent motion of the material, but that this redshift is hidden by the broadening due to the turbulence that is much larger and dominates the shape of the lines.

CHAPTER 7

Summary and conclusions

The main focus of this PhD thesis is the significance of estimating precise and accurate planetary mass and its effects on exoplanetary science.

The planetary mass of an exoplanet is a crucial factor that determines various properties such as internal structure, formation, evolution, and atmospheric characteristics. In the first part of the thesis, I analysed the impact of precision and accuracy in mass measurement on atmospheric retrievals. This study is a step forward towards the preparation of the ESA M4 Ariel mission, which will be the first dedicated mission to study the atmospheres of a large population of exoplanets. The mission aims to characterise the thermal structures, chemical composition, cloud properties and dynamic processes of about 1000 exoplanets, ranging from Jupiters and Neptunes down to super-Earth size, orbiting different types of stars.

After an introduction to problems, techniques and tools used for the study of exoplanets, in Chapter 3, I conducted an analysis of the impact of the planetary mass uncertainties on the atmospheric retrievals. Specifically, I identified scenarios where precise mass measurements are necessary, considering both clear or cloudy atmospheres, as well as primary or secondary atmospheres. This analysis was based on three representative targets from the Ariel MRS, including a hot Jupiter and a hot Neptunian as cases of primordial atmospheres, and a super-Earth as an example of a secondary atmosphere. The outcomes of this study suggest that a minimum knowledge of the planetary mass of about 50% is necessary in order to obtain an accurate atmospheric characterisation.

In Chapter 4, I expanded the previous analyses by studying a sub-sample of 17 targets from the Ariel MRS. I considered various scenarios to explore a number of different situations that occur in Ariel observations, with the goal of establishing the best approach for obtaining useful Ariel observations. The main focus of this analysis was on the role of mass estimation precision and accuracy, and signal-to-noise ratio (SNR) in obtaining accurate results. Additionally, I investigated the impact of incorrect mass estimation. The results confirmed that a minimum mass uncertainty better than 50% is not particularly useful for accurately retrieving the atmospheric composition, which is more accurate in cases of primary atmospheres, even in the

presence of high altitude clouds, than in cases of secondary atmospheres. For each retrieved quantity, I estimated both accuracy and precision. Generally, moderately accurate retrievals can be achieved in the presence of clouds, with CH_4 mixing ratio being accurately retrieved in most cases. However, determining spectral features of H_2O and CO in primordial cases, especially in extreme scenarios, is more challenging. For these reasons, I successfully tested our capability to retrieve the cloudy configuration or the presence of a secondary atmosphere during Tier-1. On the other hand, the analysis described in this chapter highlights the crucial importance of ensuring adequate SNR, and how this is connected with the estimation of the mass, as the capability to detect the planetary atmosphere depends on the true mass value, which determines the scale height of the atmosphere and, subsequently, the SNR.

The analysis presented in the first two chapters can be extended to include all the MRS of Ariel, exploring different other scenarios. It would also be interesting to compare the results obtained from simulated spectra as observed by Ariel with high-resolution spectra from space-based telescopes, such as JWST spectra. With the different instrumental configurations available with JWST, I will be able to test the impact of the planetary mass uncertainty on atmospheric retrieval considering different resolutions and different spectral coverages. By comparing the results with those obtained from the Ariel simulated spectra, I will be able to understand how different wavelength bands and different spectral resolutions may impact the results.

Having the ability to obtain independent observations with different spectral coverages and resolutions will allow me to determine the most efficient instrumental configuration for retrieving atmospheric parameters that are less dependent on mass uncertainty and accuracy. This study will complement those performed on simulated spectra of Ariel and will serve as preparation for future synergies that these two instruments may have in the study of exoplanetary atmospheres. This analysis was the base for the preparation of an observing proposal for the JWST Cycle 2, in which I aim to obtain a near-infrared transmission spectrum of TOI-942b, a hot Neptune-size exoplanet and probing the presence of the atmosphere by performing the atmospheric retrieval. This target is an example of a young planet that has the potential to deliver key insights on the formation and evolution of a close-in planet: due to the uncertainty on the stellar age and the mass upper limits, different evolution pathways could be possible.

Given the importance of mass estimation, the second part of this PhD thesis focuses on the challenges associated with the detection and mass characterization of exoplanets, particularly those caused by stellar activity.

In Chapter 5, I described the `SpotCCF`, a photospheric stellar model that I de-

veloped to optimise the extraction of radial velocities in the presence of active fast rotating stars. This model is based on the cross-correlation function (CCF) technique and takes into account the contribution of stellar activity by considering the presence of multiple spots on the stellar surface. The method described in this chapter was applied to extract the radial velocities of the active young star V1298 Tau.

The results obtained from this work confirm that the developed method can optimise radial velocity extraction. The radial velocities (RVs) obtained with the `SpotCCF` showed lower dispersion, ranging from 40% to 60% reduction in each observational season, compared to the TERRA dataset (that already improve significantly the standard DRS method). A search for periodicity in the RV dataset revealed a prominent peak at the rotational period of the star, with RV amplitude for the `SpotCCF` RVs about 30% lower than those obtained with TERRA, and reduced dispersion in the residuals. These results confirm that the new method for RV extraction effectively mitigates the contribution of stellar activity modulated with stellar rotation, as supported by the periodogram performed on residuals after recursive pre-whitening. This method improves sensitivity and ability to recover planetary signals and reduces the probability of identifying signals that are actually due to stellar activity but can be mistaken as planetary signals.

The `SpotCCF` allows for the modelling of spots on the stellar surface and provides information about the position of the spots (latitude and longitude) as well as the total surface coverage by them. The robustness of the model is ensured by consistent spot configurations obtained from an independent analysis of pairs of observations taken during the same night, and by comparison of the spot configurations obtained from an independent model analysis of simultaneous TESS observations. Additionally, the analysis of the properties of the spots provides evidence to support the hypothesis of a differential rotational velocity of the star.

Given the potential of this developed method, I plan to apply it to numerous other targets with varying levels of activity and exhibiting high values of v sin i, in order to assess the applicability range of the model. I may also apply the model to individual spectral lines that are predominantly affected by rotational broadening and distorted by the presence of spots, to more accurately characterise the line profiles.

In Chapter 6, I focused my study on understanding stellar activity in M dwarfs, which is crucial for improving our understanding of the physics of stellar atmospheres and for planet search programs. High levels of stellar activity, often associated with flare events, can cause additional variations in stellar emissions that contaminate the signals induced by planets and need to be corrected. In this context,

studying activity indicators in active stars can enhance our capability to model the signals generated by magnetic activity.

Specifically, I analysed HARPS and HARPS-N observations of AD Leonis, measuring the line profiles and intensities of sensitive activity indicators such as the Balmer lines, Ca II H&K, helium lines, and the sodium doublet. I derived the fluxes of these lines and evaluated the correlations between them. One of the main outcomes of this analysis was regarding the surface coverage of the stellar surface. As suggested by the Balmer decrement, AD Leo appears to be dominated by plages and filaments. The behaviour of Ca II also provides evidence to support the hypothesis of higher plages coverage in 2006 compared to 2018. Additionally, through a detailed analysis of selected line profiles, I investigated flares and evaluated the mass motion during the events.

Globally, this PhD thesis highlights the importance of planetary mass characterisation and the complexity of their determination due to the effects of stellar variability. In the context of the Ariel mission, it highlights the importance of a detailed and individual analysis of each target of the mission reference sample, to be able to accurately select the Tier-2 targets and characterise their planetary atmosphere. It also shows how this work cannot be disentangled from a detailed study of the stellar variability that is crucial in the determination of the planetary mass, both in its accuracy and precision.

Appendices

APPENDIX A

Additional material for Chapter 3

The corner plot reported below show the results obtained from retrieval performed on clear sky primordial atmosphere (μ = 2.3), where TauREx is able to fit the N_2/He, and on clear sky secondary N_2-dominated secondary atmosphere cases considered in this work (μ = 5.2, 7.6, 11.1) when the mass in known with an uncertainty of 50%.

A.1 N_2-DOMINATED CLEAR SKY SECONDARY ATMOSPHERE δM=50% (SECT. 3.2.4)

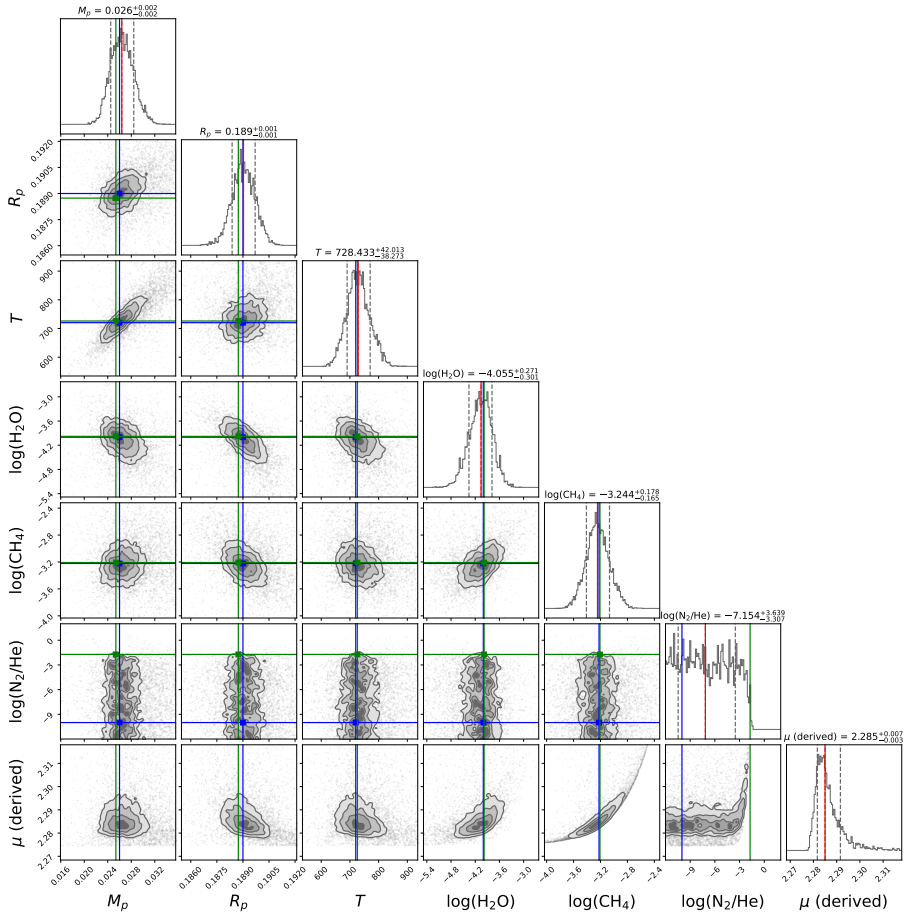

FIGURE A.1: *Retrieval results obtained for clear sky atmosphere in the case of μ=2.3 and δM = 50%. The blue, green and red vertical solid lines highlight the true, MAP and median values, respectively, while the vertical dashed-lines represent the values at 1σ from the median.*

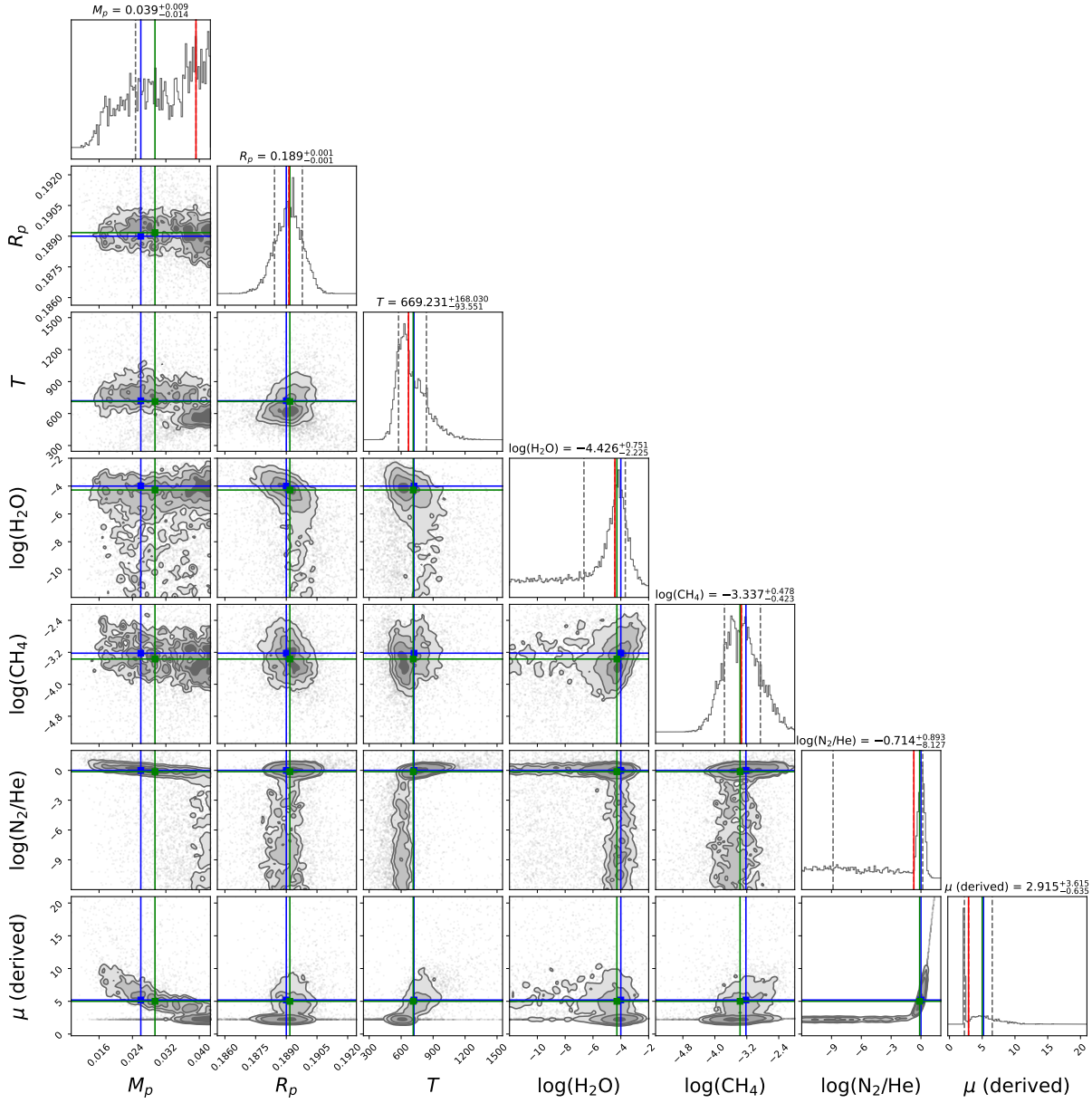

Figure A.2: *Retrieval results obtained for N_2-dominated clear sky secondary atmosphere in the case of μ=5.2 and δM = 50%. The blue, green and red vertical solid lines highlight the true, MAP and median values, respectively, while the vertical dashed-lines represent the values at 1σ from the median.*

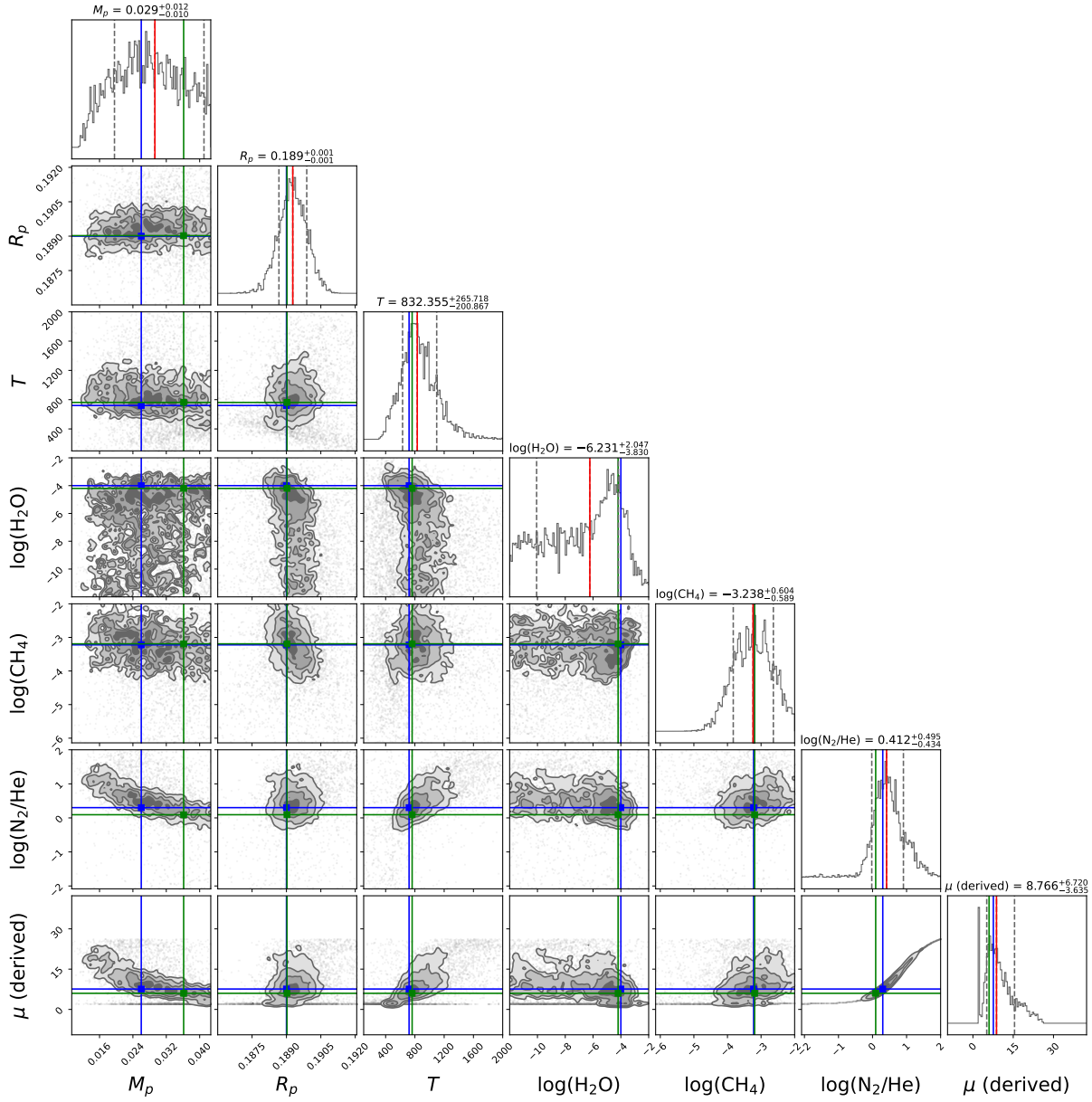

FIGURE A.3: *Retrieval results obtained for N_2-dominated clear sky secondary atmosphere in the case of μ=7.6 and δM = 50%. The blue, green and red vertical solid lines highlight the true, MAP and median values, respectively, while the vertical dashed-lines represent the values at 1σ from the median.*

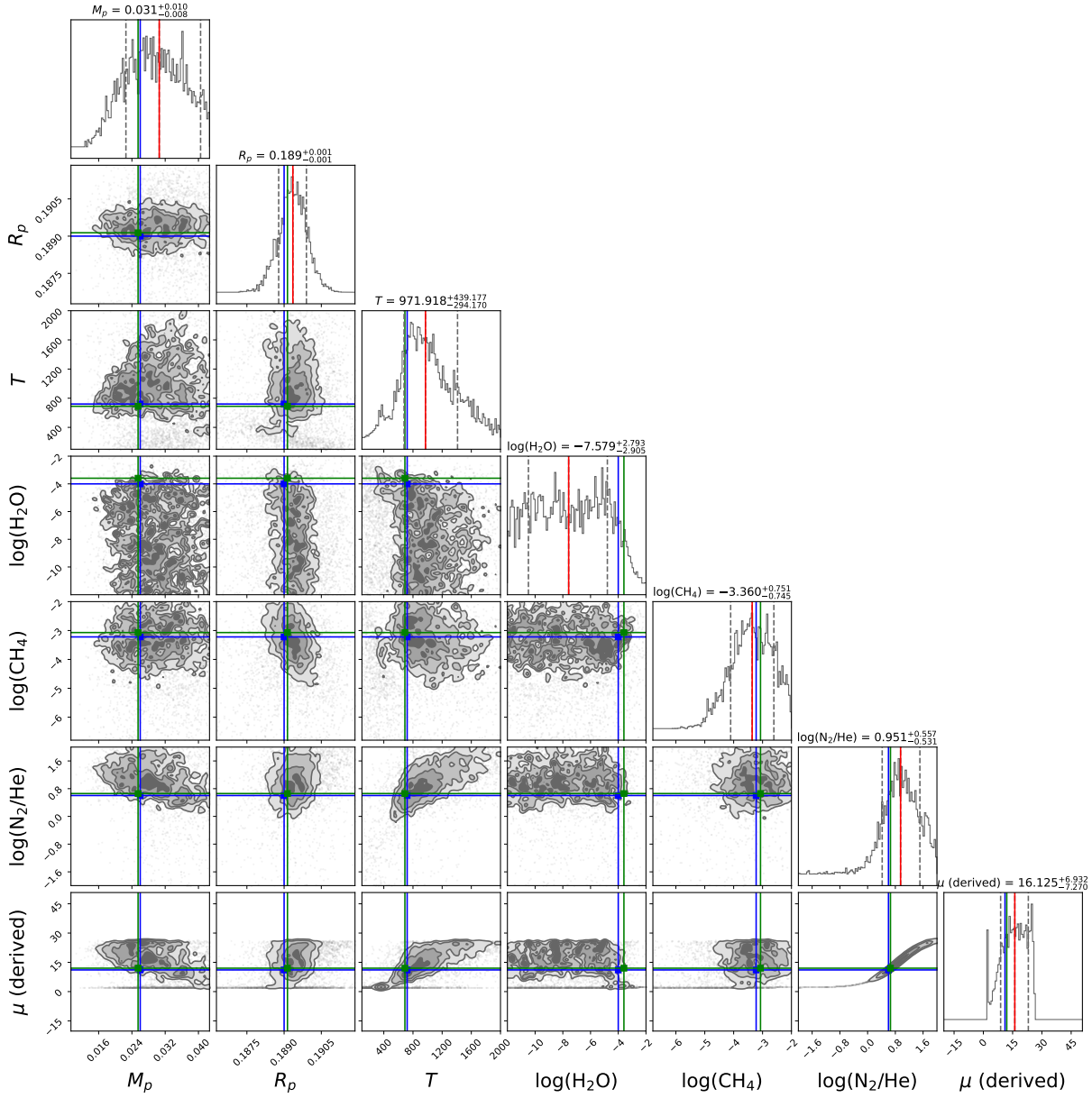

Figure A.4: *Retrieval results obtained for N_2-dominated clear sky secondary atmosphere in the case of μ=11.1 and δM = 50%. The blue, green and red vertical solid lines highlight the true, MAP and median values, respectively, while the vertical dashed-lines represent the values at 1σ from the median.*

A.2 H_2O- AND CO-DOMINATED ATMOSPHERES FOR μ = 11.1 (SECT. 3.2.5)

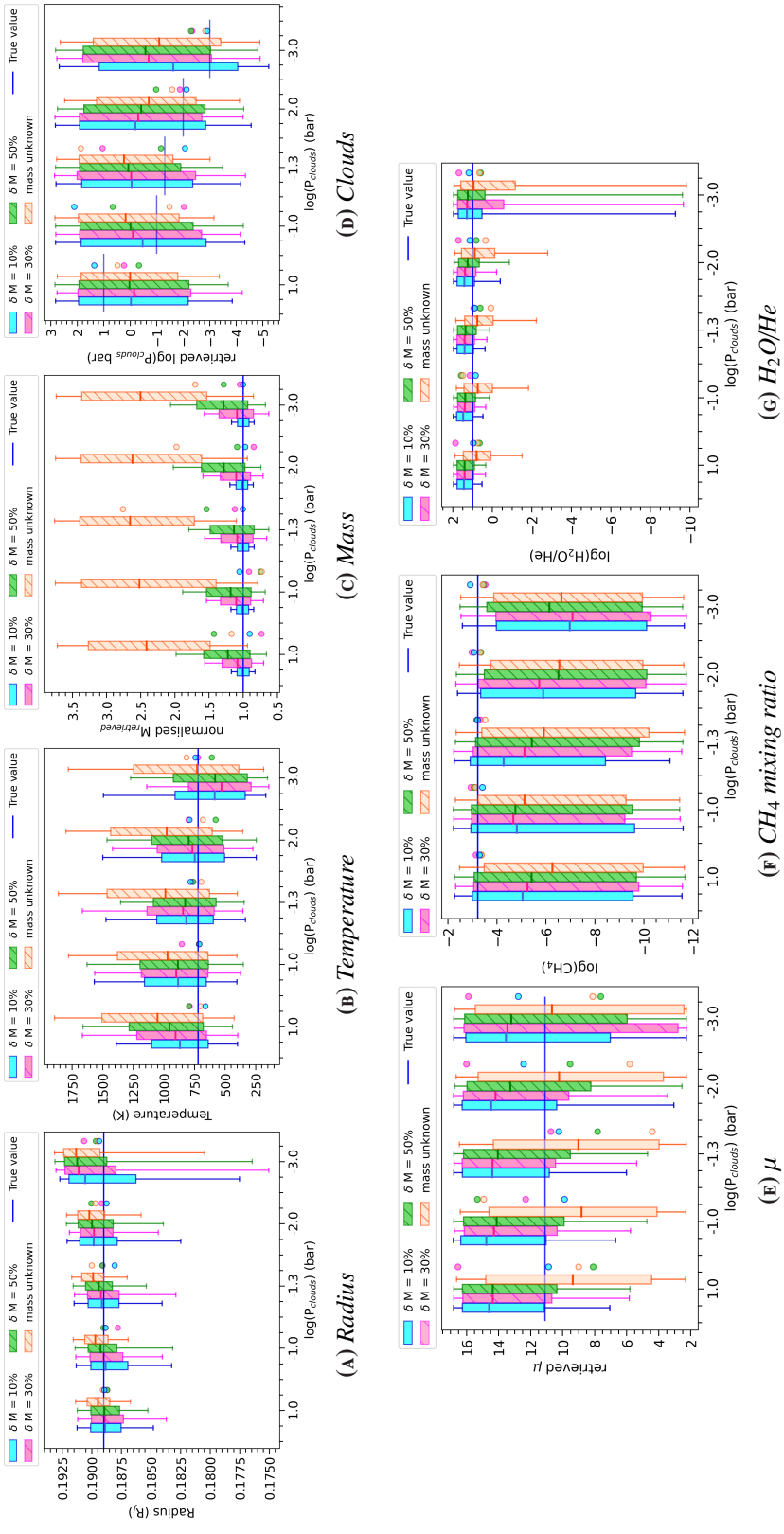

FIGURE A.5: *Retrieval results obtained for different scenarios of cloudy secondary H_2O-dominated atmosphere in the case of μ=11.1. The different coloured boxes represent the different mass uncertainties. The blue lines highlight the true values. The points alongside the boxes highlight the MAP parameters obtained for each analysed case. The size of the box and the vertical segments represent the points within 1σ and 2σ of the median of the distribution (highlighted with solid-lines), respectively.*

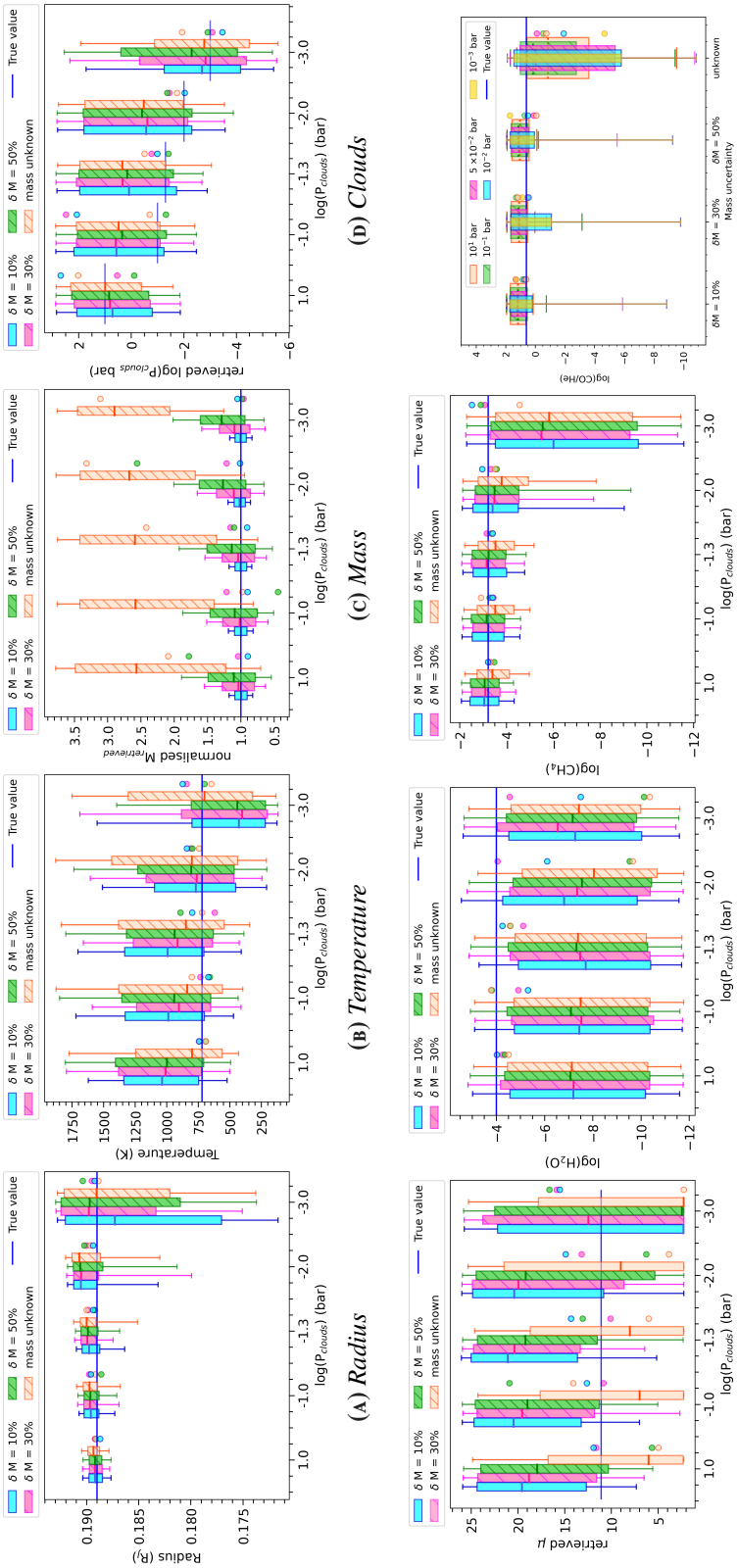

FIGURE A.6: *Retrieval results obtained for different scenarios of cloudy secondary CO-dominated atmosphere in the case of μ=11.1. The different coloured boxes represent the different mass uncertainties. The blue lines highlight the true values. The points alongside the boxes highlight the MAP (maximum-a-posteriori) parameters obtained for each analysed case. The size of the box and the vertical segments represent the points within 1σ and 2σ of the median of the distribution (highlighted with solid-lines), respectively.*

A.3 TABLES WITH THE RESULTS OF THE ANALYSIS OF SECT. 3.2.2

Tables below summarised the results obtained from the retrieval performed for a hot-Jupiter and hot neptune around a 8th-magnitude G star. In table A.3 we compare the results obtained from retrievals performed for different magnitude of star. Green boxes highlight the retrieved values within 1σ; values out of 1σ distribution but within 2σ are highlighted in red boxes.

TABLE A.1: *Results from the retrieval performed for a hot-Jupiter around a G star when we the mass is totally unknown and when we known it with an uncertainty of about 40% and 10%.*

G star with a Hot-Jupiter									
	Mass totally unknown			**δ M $\simeq$ 40%**			**δ M $\simeq$ 10%**		
	Clear Sky	Clouds		Clear Sky	Clouds		Clear Sky	Clouds	
Parameters		Low	High		Low	High		Low	High
Mass	<5%	< 10%	>50%	< 2 %	< 10%	< 30%	< 2%	< 10%	$\simeq$ 10%
Radius	√	√	X	√	√	~	√	√	√
Temperature	√	√	√	√	√	√	√	√	√
H_2O	√	√	√	√	√	√	√	√	√
CH_4	√	√	√	√	√	√	√	√	√
CO	√	√	√	√	√	√	√	√	√
Clouds	√	√	~	√	√	√	√	√	√

TABLE A.2: *Results from the retrieval performed for a neptunian planet around a G star when we know the mass with an uncertainty of about 40% and 10%.*

G star with a Neptunian planet						
	δ M $\simeq$ 40%			**δ M $\simeq$ 10%**		
	Clear Sky	Clouds		Clear Sky	Clouds	
Parameters		Low	High		Low	High
Mass	< 2 %	< 20%	< 30%	< 2%	< 10%	$\simeq$ 10%
Radius	√	√	√	√	√	√
Temperature	√	√	~	√	√	~
H_2O	√	√	√	√	√	√
CH_4	√	√	~	√	√	~
CO	√	√	X	√	√	X
Clouds	√	√	√	√	√	√

Table A.3: *Results from the retrieval performed for a hot-Jupiter around a 8th-magnitude G star and a 10.5th-magnitude G star.*

Hot-Jupiter around different magnitude G star (mass uncertainty 40%)						
	$m_v \simeq 8$			**$m_v \simeq 10.5$**		
	Clear Sky	Clouds		Clear Sky	Clouds	
Parameters		Low	High		Low	High
Mass	< 2 %	< 10%	< 30%	< 10%	≃ 20%	≃ 30%
Radius	√	√	~	√	√	√
Temperature	√	√	√	√	√	√
H_2O	√	√	√	√	√	~
CH_4	√	√	√	√	√	~
CO	√	√	√	√	√	X
Clouds	√	√	√	√	√	~

A.4 Tables with the results of the analysis of Sect. 3.2.4

Table A.4: *Retrieved values from the analyses performed on a clear sky N_2-dominated secondary atmosphere of a super-Earth around an 8th magnitude M star in the different scenarios considered in this study.*

N_2-dominated secondary atmosphere of a super-Earth around an 8th magnitude M star					
Parameter	True value	μ = 2.3			
δM		10%	30%	50%	Unknown
Mass	0.026	$0.026^{+0.001}_{-0.001}$ [0.026]	$0.026^{+0.002}_{-0.002}$ [0.026]	$0.026^{+0.002}_{-0.002}$ [0.025]	$0.026^{+0.002}_{-0.002}$ [0.027]
Radius	0.189	$0.189^{+0.001}_{-0.001}$ [0.189]	$0.189^{+0.001}_{-0.001}$ [0.189]	$0.189^{+0.001}_{-0.001}$ [0.189]	$0.189^{+0.001}_{-0.001}$ [0.189]
Temperature	720.33	725^{+34}_{-31} [722]	728^{+40}_{-41} [734]	728^{+42}_{-38} [726]	730^{+40}_{-39} [732]
log(H_2O)	-4	$-4^{+0.3}_{-0.3}$ [−4]	$-4.1^{+0.3}_{-0.3}$ [−4.0]	$-4.1^{+0.3}_{-0.3}$ [−4.0]	$-4.0^{+0.3}_{-0.3}$ [−4.1]
log(CH_4)	-3.22	$-3.2^{+0.2}_{-0.2}$ [−3.3]	$-3.24^{+0.17}_{-0.17}$ [−3.29]	$-3.24^{+0.18}_{-0.17}$ [−3.21]	$-3.2^{+0.2}_{-0.2}$ [−3.2]
log(N_2/He)	-10	-7^{+4}_{-3} [−8]	-7^{+4}_{-3} [−12]	-7^{+4}_{-3} [−2]	-7^{+3}_{-3} [−4]
μ	2.3	$2.285^{+0.007}_{-0.004}$ [2.261]	$2.285^{+0.007}_{-0.003}$ [2.261]	$2.285^{+0.007}_{-0.003}$ [2.324]	$2.285^{+0.006}_{-0.003}$ [2.261]
		μ = 5.2			
Mass	0.026	$0.026^{+0.002}_{-0.002}$ [0.026]	$0.028^{+0.007}_{-0.007}$ [0.028]	$0.039^{+0.009}_{-0.014}$ [0.029]	$0.071^{+0.014}_{-0.013}$ [0.057]
Radius	0.189	$0.189^{+0.001}_{-0.001}$ [0.189]	$0.189^{+0.001}_{-0.001}$ [0.189]	$0.189^{+0.001}_{-0.001}$ [0.189]	$0.190^{+0.001}_{-0.001}$ [0.189]
Temperature	720.33	773^{+138}_{-111} [731]	750^{+137}_{-138} [739]	669^{+168}_{-94} [713]	791^{+126}_{-110} [709]
log(H_2O)	-4	$-4.7^{+0.9}_{-3.7}$ [−4.1]	$-4.5^{+0.9}_{-2.8}$ [−4.1]	$-4.4^{+0.8}_{-2.2}$ [−4.3]	-5^{+1}_{-4} [−4]
log(CH_4)	-3.22	$-3.1^{+0.4}_{-0.4}$ [−3.3]	$-3.2^{+0.5}_{-0.4}$ [−3.3]	$-3.3^{+0.5}_{-0.4}$ [−3.4]	$-3.3^{+0.4}_{-0.4}$ [−3.3]
log(N_2/He)	0	$0.12^{+0.18}_{-0.23}$ [−0.001]	$0.018^{+0.281}_{-0.404}$ [−0.035]	$-0.7^{+0.9}_{-8.1}$ [−0.1]	-7^{+4}_{-3} [−7]
μ	5.2	6^{+2}_{-2} [5.2]	5^{+2}_{-2} [5]	$2.9^{+4}_{-0.6}$ [5]	$2.285^{+0.022}_{-0.007}$ [2.261]
		μ = 7.6			
Mass	0.026	$0.026^{+0.002}_{-0.002}$ [0.024]	$0.027^{+0.007}_{-0.007}$ [0.030]	$0.029^{+0.012}_{-0.01}$ [−0.036]	$0.086^{+0.009}_{-0.016}$ [0.087]
Radius	0.189	$0.189^{+0.001}_{-0.001}$ [0.189]	$0.189^{+0.001}_{-0.001}$ [0.189]	$0.189^{+0.001}_{-0.001}$ [0.189]	$0.189^{+0.001}_{-0.001}$ [0.189]
Temperature	720.33	854^{+279}_{-172} [745]	855^{+251}_{-185} [668]	832^{+266}_{-200} [762]	701^{+103}_{-100} [738]
log(H_2O)	-4	-7^{+2}_{-4} [−4]	-6^{+2}_{-4} [−4]	-6^{+2}_{-4} [−4]	-6^{+2}_{-4} [−4]
log(CH_4)	-3.22	$-3.1^{+0.6}_{-0.6}$ [−3.0]	$-3.2^{+0.6}_{-0.6}$ [−3.0]	$-3.2^{+0.6}_{-0.6}$ [−3.2]	$-3.4^{+0.6}_{-0.6}$ [−3.5]
log(N_2/He)	0.3	$0.5^{+0.3}_{-0.3}$ [0.5]	$0.5^{+0.4}_{-0.3}$ [0.2]	$0.4^{+0.5}_{-0.4}$ [−0.1]	-7^{+4}_{-3} [−11]
μ	7.6	10^{+4}_{-3} [9]	10^{+6}_{-3} [6]	9^{+7}_{-4} [6]	$2.284^{+0.050}_{-0.007}$ [2.261]
		μ = 11.1			
Mass	0.026	$0.025^{+0.002}_{-0.002}$ [0.025]	$0.026^{+0.007}_{-0.006}$ [0.024]	$0.031^{+0.01}_{-0.008}$ [0.025]	$0.081^{+0.013}_{-0.026}$ [0.094]
Radius	0.189	$0.189^{+0.001}_{-0.001}$ [0.189]	$0.189^{+0.001}_{-0.001}$ [0.189]	$0.189^{+0.001}_{-0.001}$ [0.189]	$0.189^{+0.001}_{-0.001}$ [0.189]
Temperature	720.33	998^{+359}_{-283} [706]	979^{+369}_{-260} [741]	972^{+439}_{-294} [689]	593^{+280}_{-128} [576]
log(H_2O)	-4	-7^{+2}_{-3} [−4]	-7^{+3}_{-3} [−4]	-8^{+3}_{-3} [−4]	-6^{+2}_{-4} [−4]
log(CH_4)	-3.22	$-3.3^{+0.8}_{-0.8}$ [−3.5]	$-3.2^{+0.7}_{-0.8}$ [−2.8]	$-3.4^{+0.8}_{-0.7}$ [−3.1]	$-3.6^{+0.8}_{-0.7}$ [−3.3]
log(N_2/He)	0.6	$1.1^{+0.5}_{-0.5}$ [0.5]	$1.2^{+0.6}_{-0.5}$ [0.7]	$1.0^{+0.6}_{-0.5}$ [0.7]	-5^{+5}_{-5} [−3]
μ	11.1	19^{+5}_{-7} [10]	19^{+6}_{-7} [13]	16^{+7}_{-7} [12]	$2.30^{+4.79}_{-0.02}$ [2.27]

Notes. I report the median values with its 1σ error and the MAP values in square brackets.

Table A.5: *Retrieved values obtained from the analyses performed on a clear sky N_2-dominated secondary atmosphere of a super-Earth around a 10.5th magnitude M star in the different scenarios considered here.*

N_2-dominated secondary atmosphere of a super-Earth around a 10.5th magnitude M star				
Parameter	True value	μ = 2.3		
δM		10%	30%	50%
Mass	0.026	$0.026^{+0.002}_{-0.002}$ [0.025]	$0.028^{+0.005}_{-0.005}$ [0.027]	$0.030^{+0.006}_{-0.005}$ [0.026]
Radius	0.189	$0.190^{+0.002}_{-0.002}$ [0.188]	$0.190^{+0.002}_{-0.002}$ [0.190]	$0.190^{+0.002}_{-0.002}$ [0.189]
Temperature	720.33	740^{+86}_{-73} [722]	772^{+105}_{-99} [737]	803^{+138}_{-100} [693]
log(H_2O)	-4	$-5.0^{+1.1}_{-4.1}$[-3.9]	$-5.0^{+1.2}_{-3.6}$[-4.3]	$-5.7^{+1.6}_{-3.9}$[-3.7]
log(CH_4)	-3.22	$-3.2^{+0.5}_{-0.5}$ [-3.3]	$-3.2^{+0.5}_{-0.5}$ [-3.43]	$-3.2^{+0.5}_{-0.5}$ [-3.2]
H_2/He	6.67	5^{+3}_{-3} [6]	6^{+3}_{-3} [10]	6^{+3}_{-3} [8]
log(N_2/He)	-10	-7^{+3}_{-3} [-9]	-7^{+4}_{-3} [-11.7]	-7^{+4}_{-3} [-5]
μ	2.3	$2.38^{+0.25}_{-0.12}$ [2.29]	$2.34^{+0.24}_{-0.10}$ [2.18]	$2.35^{+0.21}_{-0.11}$ [2.22]
		μ = 5.2		
Mass	0.026	$0.026^{+0.002}_{-0.002}$ [0.027]	$0.028^{+0.006}_{-0.006}$ [0.035]	$0.036^{+0.009}_{-0.011}$ [0.05]
Radius	0.189	$0.189^{+0.002}_{-0.002}$ [0.189]	$0.190^{+0.002}_{-0.002}$ [0.189]	$0.190^{+0.002}_{-0.002}$ [0.190]
Temperature	720.33	564^{+703}_{-162} [680]	597^{+636}_{-179} [610]	594^{+317}_{-150} [678]
log(H_2O)	-4	-7^{+3}_{-3}[-4]	-7^{+3}_{-3}[-4]	-7^{+3}_{-3}[-4]
log(CH_4)	-3.22	$-3.8^{+0.9}_{-0.9}$ [-3.6]	$-3.8^{+0.9}_{-1.0}$ [-3.6]	$-3.71^{+0.87}_{-0.10}$ [-3.4]
H_2/He	6.67	5^{+3}_{-2} [6]	5^{+3}_{-2} [1.4]	5^{+3}_{-3} [1]
log(N_2/He)	0	-3^{+3}_{-6} [-0.1]	-3^{+4}_{-6} [-5.8]	-5^{+6}_{-4} [-8]
μ	5.2	$2.8^{+8.8}_{-0.5}$ [4.7]	$2.7^{+9.6}_{-0.4}$ [2.8]	$2.5^{+4.3}_{-0.2}$ [3.0]
		μ = 7.6		
Mass	0.026	$0.027^{+0.002}_{-0.002}$ [0.024]	$0.029^{+0.006}_{-0.006}$ [0.034]	$0.033^{+0.010}_{-0.009}$ [0.046]
Radius	0.189	$0.190^{+0.002}_{-0.002}$ [0.189]	$0.190^{+0.002}_{-0.002}$ [0.189]	$0.190^{+0.002}_{-0.002}$ [0.189]
Temperature	720.33	639^{+762}_{-345} [910]	580^{+781}_{-263} [733]	624^{+780}_{-293} [505]
log(H_2O)	-4	-7^{+3}_{-3}[-6]	-7^{+3}_{-3}[-5]	-8^{+3}_{-3}[-4]
log(CH_4)	-3.22	$-4.1^{+1.2}_{-1.5}$ [-3.2]	$-4.2^{+1.2}_{-1.6}$ [-4.1]	$-4.2^{+1.2}_{-1.7}$ [-3.4]
H_2/He	6.67	6^{+3}_{-3} [4]	5^{+3}_{-2} [4]	5^{+3}_{-3} [2.5]
log(N_2/He)	0.3	$0.2^{+1.1}_{-7.8}$ [0.5]	$-0.3^{+1.4}_{-7.3}$ [-0.2]	$-0.34^{+1.5}_{-7.9}$ [-1]
μ	7.6	8^{+13}_{-6} [11.5]	5^{+15}_{-2} [5.1]	4^{+16}_{-2} [2.6]
		μ = 11.1		
Mass	0.026	$0.026^{+0.002}_{-0.002}$ [0.029]	$0.028^{+0.007}_{-0.006}$ [0.015]	$0.032^{+0.009}_{-0.009}$ [0.029]
Radius	0.189	$0.190^{+0.001}_{-0.002}$ [0.189]	$0.190^{+0.001}_{-0.002}$ [0.189]	$0.190^{+0.001}_{-0.002}$ [0.190]
Temperature	720.33	471^{+728}_{-276} [612]	654^{+745}_{-412} [852]	507^{+726}_{-286} [867]
log(H_2O)	-4	-7^{+3}_{-3}[-5]	-7^{+3}_{-3}[-4.4]	-7^{+3}_{-3}[-4.3]
log(CH_4)	-3.22	-5^{+2}_{-4}[-3.5]	-5^{+2}_{-3} [-2.7]	$-4.9^{+1.7}_{-3.2}$ [-3.6]
H_2/He	6.67	5^{+3}_{-2} [7]	5^{+3}_{-3} [9]	5^{+3}_{-3} [5.4]
log(N_2/He)	0.6	$0.3^{+1.1}_{-7.3}$ [0.4]	$-0.5^{+1.0}_{-7.2}$ [-1.8]	$-0.10^{+1.3}_{-7.7}$ [0.7]
μ	11.1	10^{+14}_{-8} [8.4]	11^{+12}_{-9} [24]	6^{+16}_{-4} [13.9]

Notes. I report the median values with its 1σ error and the MAP values in square brackets.

Table A.6: *Retrieved values obtained from the analyses performed on a N_2-dominated cloudy secondary atmosphere (P_{clouds} = 10^{-1} bar) of a super-Earth around an 8th magnitude M star in the different scenarios considered here.*

N_2-dominated cloudy secondary atmosphere of a super-Earth around an 8th magnitude M star (P_{clouds} = 10^{-1} bar)					
Parameter	True value	μ = 2.3			
δM		10%	30%	50%	Unknown
Mass	0.026	$0.026^{+0.002}_{-0.002}$ [0.025]	$0.026^{+0.002}_{-0.002}$ [0.026]	$0.026^{+0.002}_{-0.002}$ [0.026]	$0.026^{+0.002}_{-0.002}$ [0.026]
Radius	0.189	$0.189^{+0.002}_{-0.003}$ [0.189]	$0.189^{+0.002}_{-0.003}$ [0.187]	$0.189^{+0.002}_{-0.003}$ [0.188]	$0.189^{+0.002}_{-0.003}$ [0.189]
Temperature	720.33	727^{+37}_{-35} [712]	729^{+41}_{-40} [721]	728^{+44}_{-41} [715]	730^{+44}_{-43} [718]
log(H_2O)	-4	$-3.9^{+0.7}_{-0.5}$ [−4.2]	$-4.0^{+0.7}_{-0.6}$ [−3.6]	$-4.0^{+0.7}_{-0.6}$ [−3.8]	$-4.0^{+0.7}_{-0.6}$ [−4.0]
log(CH_4)	-3.22	$-3.1^{+0.5}_{-0.4}$ [−3.4]	$-3.1^{+0.5}_{-0.4}$ [−2.9]	$-3.2^{+0.6}_{-0.3}$ [−3.1]	$-3.1^{+0.6}_{-0.4}$ [−3.2]
log(N_2/He)	-10	-7^{+3}_{-3} [−7]	-7^{+4}_{-3} [−5]	-7^{+3}_{-3} [−9]	-7^{+3}_{-3} [−11]
log(P_{clouds})	-1	$-1.1^{+0.6}_{-0.6}$ [−0.9]	$-1.1^{+0.7}_{-0.7}$ [−1.4]	$-1.1^{+0.7}_{-0.7}$ [−1.1]	$-1.1^{+0.7}_{-0.7}$ [−1.0]
μ	2.3	$2.289^{+0.035}_{-0.008}$ [2.261]	$2.289^{+0.037}_{-0.009}$ [2.261]	$2.288^{+0.033}_{-0.008}$ [2.261]	$2.289^{+0.044}_{-0.009}$ [2.261]
		μ = 5.2			
Mass	0.026	$0.026^{+0.002}_{-0.002}$ [0.028]	$0.027^{+0.007}_{-0.007}$ [0.029]	$0.037^{+0.01}_{-0.014}$ [0.054]	$0.075^{+0.014}_{-0.014}$ [0.064]
Radius	0.189	$0.19^{+0.001}_{-0.001}$ [0.188]	$0.190^{+0.001}_{-0.001}$ [0.188]	$0.190^{+0.001}_{-0.002}$ [0.189]	$0.190^{+0.001}_{-0.001}$ [0.189]
Temperature	720	789^{+148}_{-122} [743]	757^{+137}_{-148} [728]	685^{+184}_{-107} [665]	788^{+113}_{-108} [777]
log(H_2O)	-4	-6^{+2}_{-4} [−3]	$-5.6^{+1.6}_{-3.8}$ [−2.9]	-5^{+2}_{-4} [−4]	-6^{+2}_{-4} [−4]
log(CH_4)	-3.22	$-3.3^{+0.6}_{-0.5}$ [−3]	$-3.4^{+0.6}_{-0.5}$ [−2.6]	$-3.4^{+0.6}_{-0.5}$ [−3.3]	$-3.3^{+0.7}_{-0.5}$ [−3.3]
log(N_2/He)	0	$0.18^{+0.19}_{-0.20}$ [−0.04]	$0.12^{+0.29}_{-0.46}$ [−0.10]	$-0.3^{+0.6}_{-8.1}$ [−9.9]	-7^{+4}_{-3} [−9]
log(P_{clouds})	-1	$0.4^{+1.7}_{-1.6}$ [−1.6]	$0.4^{+1.7}_{-1.5}$ [−1.7]	$0.08^{+1.92}_{-1.45}$ [−0.96]	$0.2^{+1.8}_{-1.5}$ [−0.9]
μ	5.2	$6.6^{+1.7}_{-1.4}$ [5.0]	6^{+3}_{-2} [5]	$3.9^{+3.7}_{-1.6}$ [2.3]	$2.284^{+0.037}_{-0.006}$ [2.261]
		μ = 7.6			
Mass	0.026	$0.026^{+0.002}_{-0.002}$ [0.028]	$0.027^{+0.007}_{-0.006}$ [0.025]	$0.027^{+0.011}_{-0.009}$ [0.037]	$0.085^{+0.010}_{-0.014}$ [0.084]
Radius	0.189	$0.190^{+0.001}_{-0.001}$ [0.189]	$0.190^{+0.001}_{-0.001}$ [0.189]	$0.190^{+0.001}_{-0.001}$ [0.189]	$0.190^{+0.001}_{-0.001}$ [0.187]
Temperature	720.33	896^{+328}_{-240} [791]	849^{+276}_{-182} [778]	860^{+291}_{-199} [831]	681^{+117}_{-108} [778]
log(H_2O)	-4	-7^{+3}_{-3} [−4]	-8^{+3}_{-3} [−4]	-8^{+3}_{-3} [−4]	-6^{+2}_{-4} [−3]
log(CH_4)	-3.22	$-3.3^{+0.7}_{-0.7}$ [−2.7]	$-3.3^{+0.7}_{-0.6}$ [−2.9]	$-3.3^{+0.7}_{-0.7}$ [−3.4]	$-3.4^{+0.8}_{-0.7}$ [−2.4]
log(N_2/He)	0.3	$0.6^{+0.4}_{-0.3}$ [0.4]	$0.6^{+0.4}_{-0.3}$ [0.5]	$0.6^{+0.6}_{-0.5}$ [0.2]	-6^{+4}_{-4} [−6]
log(P_{clouds})	-1	$0.5^{+1.6}_{-1.6}$ [−1.3]	$0.7^{+1.5}_{-1.5}$ [−0.8]	$0.6^{+1.6}_{-1.6}$ [−1.0]	$0.06^{+1.86}_{-1.63}$ [−2.21]
μ	7.6	12^{+5}_{-4} [9]	11^{+6}_{-4} [10]	11^{+8}_{-5} [6]	$2.285^{+0.069}_{-0.009}$ [2.261]
		μ = 11.1			
Mass	0.026	$0.026^{+0.002}_{-0.002}$ [0.026]	$0.026^{+0.007}_{-0.005}$ [0.028]	$0.030^{+0.011}_{-0.009}$ [0.035]	$0.080^{+0.014}_{-0.033}$ [0.092]
Radius	0.189	$0.190^{+0.001}_{-0.001}$ [0.190]	$0.19^{+0.001}_{-0.001}$ [0.189]	$0.190^{+0.001}_{-0.001}$ [0.188]	$0.189^{+0.001}_{-0.001}$ [0.188]
Temperature	720.33	984^{+361}_{-326} [793]	873^{+360}_{-311} [696]	929^{+397}_{-318} [836]	615^{+327}_{-152} [624]
log(H_2O)	-4	-8^{+3}_{-3} [−5]	-7^{+2}_{-3} [−5]	-8^{+3}_{-3} [−3]	-7^{+3}_{-3} [−3]
log(CH_4)	-3.22	$-3.4^{+0.9}_{-0.9}$ [−3.6]	$-3.4^{+0.8}_{-0.9}$ [−3.7]	$-3.3^{+0.8}_{-0.9}$ [−2.1]	$-3.6^{+0.8}_{-0.8}$ [−2.8]
log(N_2/He)	0.6	$1.2^{+0.5}_{-0.5}$ [0.8]	$1.1^{+0.5}_{-0.8}$ [0.5]	$1.1^{+0.5}_{-0.7}$ [0.6]	-5^{+5}_{-5} [−5]
log(P_{clouds})	-1	$0.3^{+1.7}_{-1.8}$ [1.9]	$0.07^{+1.82}_{-1.70}$ [−0.53]	$0.4^{+1.7}_{-1.8}$ [−2.0]	$0.4^{+1.7}_{-1.7}$ [−1.7]
μ	11.1	20^{+5}_{-7} [14]	18^{+6}_{-10} [9]	18^{+6}_{-10} [11]	$2.30^{+8.14}_{-0.02}$ [2.26]

Notes. I report the median values with its 1σ error and the MAP values in square brackets.

Table A.7: *Retrieved values obtained from the analyses performed on a N_2-dominated cloudy secondary atmosphere (P_{clouds} = 10^{-3} bar) of a super-Earth around an 8th magnitude M star in the different scenarios considered here.*

N_2-dominated cloudy secondary atmosphere of a super-Earth around an 8th magnitude M star (P_{clouds} = 10^{-3} bar)					
Parameter	True value	μ = 2.3			
δM		10%	30%	50%	Unknown
Mass	0.026	$0.026^{+0.002}_{-0.002}$ [0.026]	$0.029^{+0.005}_{-0.004}$ [0.028]	$0.031^{+0.007}_{-0.006}$ [0.025]	$0.038^{+0.009}_{-0.006}$ [0.028]
Radius	0.189	$0.191^{+0.004}_{-0.006}$ [0.187]	$0.193^{+0.005}_{-0.005}$ [0.196]	$0.193^{+0.004}_{-0.006}$ [0.188]	$0.198^{+0.003}_{-0.004}$ [0.191]
Temperature	720.33	727^{+61}_{-57} [743]	747^{+72}_{-68} [738]	768^{+78}_{-74} [722]	813^{+111}_{-77} [743]
log(H_2O)	-4	-6^{+2}_{-4} [−4]	$-5.8^{+1.6}_{-3.9}$ [−5.3]	$-5.7^{+1.6}_{-3.5}$ [−4.0]	-7^{+2}_{-3} [−4]
log(CH_4)	-3.22	$-3.6^{+1.0}_{-0.9}$ [−3.0]	$-3.7^{+0.9}_{-0.9}$ [−4.4]	$-3.6^{+0.9}_{-1.0}$ [−3.3]	$-4.1^{+0.8}_{-0.7}$ [−3.6]
log(N_2/He)	-10	-7^{+3}_{-3} [−10]	-7^{+3}_{-3} [−4]	$-6.7^{+3.4}_{-3.4}$ [−10.8]	-7^{+3}_{-3} [−9]
log(P_{clouds})	-3	$-2.6^{+0.875}_{-1.013}$ [−3.303]	$-2.5^{+0.9}_{-1.0}$ [−1.7]	$-2.5^{+0.9}_{-0.9}$ [−3.0]	$-1.9^{+0.6}_{-0.8}$ [−2.6]
μ	2.3	$2.281^{+0.036}_{-0.005}$ [2.261]	$2.280^{+0.028}_{-0.005}$ [2.262]	$2.281^{+0.029}_{-0.005}$ [2.261]	$2.277^{+0.010}_{-0.001}$ [2.261]
		μ = 5.2			
Mass	0.026	$0.026^{+0.002}_{-0.002}$ [0.024]	$0.028^{+0.006}_{-0.006}$ [0.033]	$0.034^{+0.008}_{-0.009}$ [0.042]	$0.077^{+0.016}_{-0.02}$ [0.078]
Radius	0.189	$0.193^{+0.004}_{-0.012}$ [0.176]	$0.190^{+0.006}_{-0.011}$ [0.187]	$0.193^{+0.004}_{-0.007}$ [0.183]	$0.193^{+0.003}_{-0.004}$ [0.194]
Temperature	720	708^{+536}_{-204} [604]	736^{+429}_{-202} [640]	725^{+493}_{-205} [736]	773^{+314}_{-212} [713]
log(H_2O)	-4	-7^{+3}_{-3} [−3]	-8^{+3}_{-3} [−5]	-8^{+3}_{-3} [−4]	-8^{+3}_{-2} [−5]
log(CH_4)	-3.22	$-3.8^{+1.1}_{-1.2}$ [−2.4]	$-3.8^{+1.0}_{-1.3}$ [−4.7]	$-4.0^{+1.1}_{-1.1}$ [−2.4]	$-3.9^{+1.2}_{-1.1}$ [−4.5]
log(N_2/He)	0	$0.4^{+1.1}_{-8.6}$ [−5.3]	-2^{+4}_{-7} [−10]	$-1.2^{+2.6}_{-7.5}$ [−11.5]	-6^{+5}_{-4} [−2]
log(P_{clouds})	-3	-2^{+2}_{-2} [−4]	$-2.0^{+2.8}_{-1.7}$ [−2.0]	$-1.7^{+2.2}_{-1.4}$ [−4.1]	$-1.9^{+1.6}_{-1.5}$ [−1.3]
μ	5.2	9^{+14}_{-6} [2.261]	$2.4^{+20.4}_{-0.1}$ [2.3]	$2.5^{+20.1}_{-0.2}$ [2.261]	$2.283^{+0.184}_{-0.008}$ [2.355]
		μ = 7.6			
Mass	0.026	$0.026^{+0.002}_{-0.002}$ [0.025]	$0.028^{+0.006}_{-0.006}$ [0.023]	$0.034^{+0.009}_{-0.009}$ [0.032]	$0.077^{+0.015}_{-0.022}$ [0.070]
Radius	0.189	$0.191^{+0.003}_{-0.012}$ [0.176]	$0.193^{+0.002}_{-0.009}$ [0.192]	$0.193^{+0.001}_{-0.009}$ [0.19]	$0.192^{+0.002}_{-0.005}$ [0.187]
Temperature	720.33	585^{+403}_{-262} [549]	597^{+395}_{-272} [880]	730^{+531}_{-343} [920]	656^{+533}_{-312} [681]
log(H_2O)	-4	-7^{+3}_{-3} [−3]	-8^{+3}_{-3} [−5]	-8^{+3}_{-3} [−5]	-8^{+3}_{-3} [−8]
log(CH_4)	-3.22	$-4.2^{+1.4}_{-2.3}$ [−2.4]	$-4.5^{+1.4}_{-2.5}$ [−3.9]	-5^{+2}_{-2} [−3]	$-4.4^{+1.5}_{-2.1}$ [−2.8]
log(N_2/He)	0.3	$0.4^{+1.1}_{-9.0}$ [−4.9]	$0.8^{+0.8}_{-8.6}$ [0.9]	$0.9^{+0.7}_{-8.3}$ [0.5]	-4^{+5}_{-5} [−9]
log(P_{clouds})	-3	$-2.4^{+3.1}_{-1.6}$ [−4.5]	$-1.7^{+3.0}_{-1.9}$ [−1.9]	$-1.3^{+2.7}_{-1.7}$ [−3.2]	$-1.7^{+2.4}_{-1.8}$ [−3.6]
μ	7.6	9^{+14}_{-7} [2.261]	14^{+10}_{-12} [15]	16^{+8}_{-13} [10]	$2.30^{+16.11}_{-0.02}$ [2.26]
		μ = 11.1			
Mass	0.026	$0.027^{+0.002}_{-0.002}$ [0.028]	$0.030^{+0.006}_{-0.006}$ [0.033]	$0.032^{+0.009}_{-0.009}$ [0.023]	$0.075^{+0.015}_{-0.021}$ [0.088]
Radius	0.189	$0.190^{+0.002}_{-0.008}$ [0.190]	$0.19^{+0.002}_{-0.009}$ [0.192]	$0.19^{+0.003}_{-0.01}$ [0.188]	$0.19^{+0.002}_{-0.006}$ [0.188]
Temperature	720.33	438^{+377}_{-214} [916]	519^{+479}_{-270} [954]	540^{+533}_{-263} [682]	608^{+636}_{-359} [607]
log(H_2O)	-4	-8^{+3}_{-3} [−4]	-8^{+3}_{-3} [−6]	-8^{+3}_{-3} [−4]	-8^{+3}_{-3} [−5]
log(CH_4)	-3.22	-6^{+2}_{-3} [−3]	-5^{+2}_{-3} [−5]	-6^{+2}_{-3} [−4]	-6^{+2}_{-3} [−3]
log(N_2/He)	0.6	$0.5^{+1.0}_{-8.4}$ [1.3]	$0.5^{+1.1}_{-8.3}$ [1.5]	$0.7^{+0.9}_{-8.6}$ [0.4]	-5^{+6}_{-5} [−6]
log(P_{clouds})	-3	$-2.2^{+2.7}_{-1.7}$ [−3.0]	$-2.1^{+2.8}_{-1.8}$ [−0.7]	-2^{+3}_{-2} [−3]	-2^{+3}_{-2} [−3]
μ	11.1	10^{+14}_{-8} [21]	10^{+14}_{-8} [23]	12^{+11}_{-10} [9]	$2.29^{+17.39}_{-0.01}$ [2.26]

Notes. I report the median values with its 1σ error and the MAP values in square brackets.

Table A.8: *Retrieved values obtained from the analyses performed on a H_2O-dominated cloudy secondary atmosphere ($P_{clouds} = 10^{-1}$ bar) of a super-Earth around an 8th magnitude M star in the different considered scenarios.*

H_2O-dominated cloudy secondary atmosphere of a super-Earth around an 8th magnitude M star ($P_{clouds} = 10^{-1}$ bar)					
Parameter	True value	$\mu = 2.3$			
δM		10%	30%	50%	Unknown
Mass	0.026	$0.027^{+0.002}_{-0.002}$ [0.026]	$0.027^{+0.003}_{-0.002}$ [0.027]	$0.027^{+0.003}_{-0.003}$ [0.027]	$0.027^{+0.003}_{-0.003}$ [0.027]
Radius	0.189	$0.191^{+0.001}_{-0.001}$ [0.190]	$0.191^{+0.001}_{-0.001}$ [0.189]	$0.191^{+0.001}_{-0.002}$ [0.190]	$0.191^{+0.001}_{-0.001}$ [0.19]
Temperature	720.33	704^{+39}_{-35} [703]	715^{+49}_{-45} [724]	717^{+53}_{-46} [725]	$717.815^{+52.961}_{-49.599}$ [713.822]
log(CH_4)	-3.22	$-3.5^{+0.3}_{-0.2}$ [−3.3]	$-3.5^{+0.3}_{-0.2}$ [−3.2]	$-3.5^{+0.3}_{-0.2}$ [−3.4]	$-3.502^{+0.276}_{-0.24}$ [−3.411]
log(H_2O/He)	-1.22	$-1.6^{+0.4}_{-0.3}$ [−1.3]	$-1.6^{+0.4}_{-0.3}$ [−1.2]	$-1.6^{+0.4}_{-0.3}$ [−1.5]	$-1.594^{+0.349}_{-0.313}$ [−1.436]
log(P_{clouds})	-1	$0.6^{+1.7}_{-1.4}$ [−0.9]	$0.5^{+1.7}_{-1.3}$ [−0.9]	$0.5^{+1.7}_{-1.4}$ [−0.8]	$0.534^{+1.657}_{-1.358}$ [−0.693]
μ	2.3	$2.34^{+0.08}_{-0.03}$ [2.35]	$2.33^{+0.08}_{-0.03}$ [2.38]	$2.33^{+0.09}_{-0.03}$ [2.33]	$2.331^{+0.067}_{-0.029}$ [2.336]
		$\mu = 5.2$			
Mass	0.026	$0.026^{+0.002}_{-0.002}$ [0.028]	$0.028^{+0.006}_{-0.006}$ [0.042]	$0.031^{+0.011}_{-0.010}$ [0.024]	$0.062^{+0.022}_{-0.021}$ [0.032]
Radius	0.189	$0.189^{+0.001}_{-0.001}$ [0.189]	$0.189^{+0.001}_{-0.001}$ [0.190]	$0.189^{+0.001}_{-0.001}$ [0.189]	$0.191^{+0.001}_{-0.001}$ [0.190]
Temperature	720	733^{+115}_{-98} [716]	735^{+121}_{-86} [725]	720^{+134}_{-84} [719]	826^{+144}_{-118} [696]
log(CH_4)	-3.22	$-3.2^{+0.3}_{-0.3}$ [−3.3]	$-3.2^{+0.4}_{-0.3}$ [−3.5]	$-3.3^{+0.4}_{-0.4}$ [−3.2]	$-3.8^{+0.5}_{-0.5}$ [−3.5]
log(H_2O/He)	0.24	$0.29^{+0.19}_{-0.19}$ [0.21]	$0.2^{+0.3}_{-0.2}$ [−0.2]	$0.14^{+0.40}_{-0.39}$ [0.34]	$-0.804^{+0.629}_{-0.679}$ [0.003]
log(P_{clouds})	-1	$0.4^{+1.7}_{-1.7}$ [1.8]	$0.4^{+1.7}_{-1.7}$ [1.4]	$0.6^{+1.6}_{-1.7}$ [−0.7]	$0.9^{+1.4}_{-1.4}$ [0.8]
μ	5.2	$5.5^{+1.3}_{-1.0}$ [5.0]	$5.2^{+1.7}_{-1.1}$ [3.4]	$4.7^{+2.5}_{-1.3}$ [5.8]	$2.6^{+0.9}_{-0.3}$ [4.1]
		$\mu = 7.6$			
Mass	0.026	$0.026^{+0.002}_{-0.002}$ [0.027]	$0.026^{+0.007}_{-0.006}$ [0.017]	$0.026^{+0.011}_{-0.008}$ [0.023]	$0.070^{+0.021}_{-0.029}$ [0.063]
Radius	0.189	$0.189^{+0.001}_{-0.001}$ [0.189]	$0.189^{+0.001}_{-0.001}$ [0.188]	$0.189^{+0.001}_{-0.001}$ [0.189]	$0.190^{+0.001}_{-0.001}$ [0.190]
Temperature	720.33	842^{+298}_{-196} [723]	844^{+277}_{-189} [736]	820^{+266}_{-176} [669]	787^{+167}_{-131} [759]
log(CH_4)	-3.22	$-3.3^{+0.6}_{-0.6}$ [−3.2]	$-3.2^{+0.6}_{-1.0}$ [−3.1]	$-3.2^{+0.6}_{-0.8}$ [−3.2]	$-4.0^{+0.8}_{-1.0}$ [−3.6]
log(H_2O/He)	0.59	$0.9^{+0.6}_{-0.4}$ [0.6]	$0.9^{+0.6}_{-0.4}$ [1.0]	$0.9^{+0.6}_{-0.5}$ [0.7]	$-0.3^{+0.8}_{-0.9}$ [−0.2]
log(P_{clouds})	-1	$0.2^{+2}_{-1.9}$ [2.4]	$0.13^{+1.82}_{-1.88}$ [−1.74]	$0.3^{+1.7}_{-1.8}$ [1.8]	$1.1^{+1.2}_{-1.6}$ [1.9]
μ	7.6	10^{+5}_{-3} [8]	10^{+4}_{-4} [11]	10^{+5}_{-4} [8]	$3.2^{+3.2}_{-0.8}$ [3.4]
		$\mu = 11.1$			
Mass	0.026	$0.026^{+0.002}_{-0.002}$ [0.028]	$0.029^{+0.006}_{-0.006}$ [0.024]	$0.031^{+0.009}_{-0.008}$ [0.020]	$0.066^{+0.022}_{-0.029}$ [0.019]
Radius	0.189	$0.189^{+0.001}_{-0.002}$ [0.189]	$0.189^{+0.001}_{-0.002}$ [0.188]	$0.189^{+0.001}_{-0.001}$ [0.189]	$0.190^{+0.001}_{-0.001}$ [0.189]
Temperature	720.33	883^{+277}_{-229} [712]	899^{+286}_{-259} [854]	886^{+311}_{-249} [715]	970^{+411}_{-329} [713]
log(CH_4)	-3.22	-5^{+2}_{-5} [−3]	-5^{+2}_{-5} [−3]	-5^{+2}_{-5} [−3]	-5^{+2}_{-4} [−3]
log(H_2O/He)	0.996	$1.5^{+0.3}_{-0.5}$ [0.9]	$1.4^{+0.4}_{-0.5}$ [1.1]	$1.4^{+0.4}_{-0.5}$ [1.6]	$0.7^{+0.7}_{-0.7}$ [1.5]
log(P_{clouds})	-1	$-0.5^{+2.3}_{-2.4}$ [2.1]	$-0.10^{+2.02}_{-2.59}$ [−2.02]	$-0.01^{+1.91}_{-2.36}$ [0.66]	$0.2^{+1.8}_{-2.0}$ [−1.5]
μ	11.1	15^{+2}_{-4} [10]	14^{+2}_{-4} [12]	14^{+2}_{-4} [15]	9^{+6}_{-5} [15]

Notes. I report the median values with its 1σ error and the MAP values in square brackets.

Table A.9: *Retrieved values obtained from the analyses performed on a H_2O-dominated cloudy secondary atmosphere (P_{clouds} = 10^{-3} bar) of a super-Earth around an 8th magnitude M star in the different scenarios considered here.*

H_2O-dominated cloudy secondary atmosphere of a super-Earth around an 8th magnitude M star (P_{clouds} = 10^{-3} bar)					
Parameter	True value	μ = 2.3			
δM		10%	30%	50%	Unknown
Mass	0.026	$0.026^{+0.002}_{-0.002}$ [0.024]	$0.029^{+0.005}_{-0.005}$ [0.024]	$0.032^{+0.006}_{-0.005}$ [0.024]	$0.034^{+0.011}_{-0.007}$ [0.029]
Radius	0.189	$0.191^{+0.003}_{-0.004}$ [0.188]	$0.192^{+0.004}_{-0.004}$ [0.187]	$0.194^{+0.003}_{-0.004}$ [0.187]	$0.194^{+0.004}_{-0.004}$ [0.191]
Temperature	720.33	711^{+63}_{-53} [715]	736^{+72}_{-68} [715]	758^{+80}_{-74} [721]	774^{+101}_{-82} [737]
log(CH_4)	-3.22	$-3.7^{+0.5}_{-0.7}$ [−3.0]	$-3.7^{+0.5}_{-0.7}$ [−3]	$-3.8^{+0.5}_{-0.7}$ [−3.0]	$-3.7^{+0.6}_{-0.6}$ [−3.4]
log(H_2O/He)	-1.22	$-1.7^{+0.6}_{-0.9}$ [−0.9]	$-1.8^{+0.6}_{-0.8}$ [−1.4]	$-1.9^{+0.6}_{-0.8}$ [−1.0]	$-1.8^{+0.7}_{-0.8}$ [−1.4]
log(P_{clouds})	-3	$-2.5^{+0.6}_{-0.6}$ [−3.2]	$-2.4^{+0.7}_{-0.6}$ [−3.0]	$-2.3^{+0.7}_{-0.6}$ [−3.3]	$-2.3^{+0.7}_{-0.6}$ [−2.8]
μ	2.3	$2.32^{+0.12}_{-0.04}$ [2.50]	$2.31^{+0.11}_{-0.03}$ [2.35]	$2.30^{+0.08}_{-0.02}$ [2.45]	$2.31^{+0.11}_{-0.03}$ [2.34]
		μ = 5.2			
Mass	0.026	$0.026^{+0.002}_{-0.002}$ [0.023]	$0.028^{+0.006}_{-0.006}$ [0.032]	$0.029^{+0.011}_{-0.009}$ [0.034]	$0.077^{+0.016}_{-0.025}$ [0.079]
Radius	0.189	$0.194^{+0.001}_{-0.003}$ [0.188]	$0.194^{+0.001}_{-0.002}$ [0.191]	$0.194^{+0.001}_{-0.002}$ [0.190]	$0.195^{+0.001}_{-0.002}$ [0.193]
Temperature	720.33	744^{+273}_{-188} [820]	733^{+245}_{-181} [790]	707^{+248}_{-181} [816]	720^{+219}_{-150} [820]
log(CH_4)	-3.22	$-3.5^{+0.7}_{-2.0}$ [−3.0]	$-3.5^{+0.7}_{-1.9}$ [−3.1]	$-3.5^{+0.6}_{-1.4}$ [−3.2]	$-4.4^{+0.8}_{-1.1}$ [−4.2]
log(H_2O/He)	0.24	$0.9^{+0.6}_{-0.4}$ [0.4]	$0.9^{+0.6}_{-0.5}$ [0.4]	$0.8^{+0.6}_{-0.5}$ [0.3]	$-0.8^{+1.1}_{-1.2}$ [−0.9]
log(P_{clouds})	-3	$-1.0^{+2.8}_{-2.1}$ [−3.4]	$-0.7^{+2.3}_{-1.9}$ [−2.6]	$-0.6^{+2.4}_{-2.0}$ [−2.8]	$-0.4^{+2.2}_{-1.5}$ [−1.9]
μ	5.2	10^{+5}_{-4} [6]	10^{+5}_{-4} [6]	10^{+5}_{-4} [5]	$2.6^{+3.2}_{-0.3}$ [2.5]
		μ = 7.6			
Mass	0.026	$0.026^{+0.002}_{-0.002}$ [0.025]	$0.029^{+0.006}_{-0.005}$ [0.033]	$0.030^{+0.011}_{-0.009}$ [0.021]	$0.071^{+0.019}_{-0.028}$ [0.098]
Radius	0.189	$0.192^{+0.001}_{-0.002}$ [0.190]	$0.192^{+0.001}_{-0.002}$ [0.188]	$0.193^{+0.001}_{-0.002}$ [0.191]	$0.193^{+0.001}_{-0.002}$ [0.192]
Temperature	720.33	695^{+252}_{-216} [657]	722^{+288}_{-257} [1011]	708^{+277}_{-262} [708]	826^{+523}_{-301} [793]
log(CH_4)	-3.22	-5^{+2}_{-4} [−3]	-6^{+2}_{-4} [−3]	-5^{+2}_{-4} [−3]	-6^{+2}_{-3} [−4]
log(H_2O/He)	0.59	$1.4^{+0.4}_{-0.5}$ [0.6]	$1.3^{+0.4}_{-0.5}$ [0.7]	$1.2^{+0.5}_{-0.6}$ [1.4]	$0.60^{+0.84}_{-1.32}$ [−0.15]
log(P_{clouds})	-3	$-0.4^{+2.3}_{-2.4}$ [−2.6]	$-0.4^{+2.2}_{-2.8}$ [−3.8]	$-0.3^{+2.1}_{-2.3}$ [−2.5]	$-0.6^{+2.3}_{-1.8}$ [−1.6]
μ	7.6	14^{+2}_{-4} [8]	14^{+2}_{-5} [8]	13^{+3}_{-5} [14]	8^{+7}_{-5} [4]
		μ = 11.1			
Mass	0.026	$0.026^{+0.002}_{-0.002}$ [0.026]	$0.028^{+0.007}_{-0.006}$ [0.027]	$0.034^{+0.010}_{-0.009}$ [0.034]	$0.065^{+0.023}_{-0.025}$ [0.044]
Radius	0.189	$0.191^{+0.001}_{-0.004}$ [0.189]	$0.191^{+0.001}_{-0.003}$ [0.191]	$0.191^{+0.001}_{-0.003}$ [0.190]	$0.191^{+0.001}_{-0.002}$ [0.190]
Temperature	720.33	584^{+326}_{-248} [742]	530^{+271}_{-242} [722]	581^{+342}_{-263} [609]	729^{+520}_{-342} [815]
log(CH_4)	-3.22	-7^{+3}_{-3} [−3]	-7^{+3}_{-3} [−4]	-6^{+3}_{-4} [−3]	-7^{+3}_{-3} [−3]
log(H_2O/He)	0.996	$1.3^{+0.4}_{-0.8}$ [1.2]	$1.3^{+0.5}_{-1.8}$ [1.7]	$1.2^{+0.5}_{-0.9}$ [0.6]	$0.9^{+0.7}_{-2.1}$ [0.7]
log(P_{clouds})	-3	$-1.6^{+2.8}_{-2.4}$ [−2.9]	$-0.7^{+2.5}_{-2.4}$ [−2.3]	$-0.6^{+2.4}_{-2.5}$ [−2.3]	$-1.1^{+2.5}_{-2.3}$ [−2.8]
μ	11.1	14^{+3}_{-7} [13]	13^{+3}_{-11} [16]	13^{+3}_{-7} [8]	11^{+5}_{-8} [8]

Notes. I report the median values with its 1σ error and the MAP values in square brackets.

Table A.10: *Retrieved values obtained from the analyses performed on a CO-dominated cloudy secondary atmosphere (P_{clouds} = 10^{-1} bar) of a super-Earth around an 8th magnitude M star in the different considered scenarios.*

CO-dominated cloudy secondary atmosphere of a super-Earth around an 8th magnitude M star (P_{clouds} = 10^{-1} bar)					
Parameter	True value	μ = 2.3			
δM		10%	30%	50%	Unknown
Mass	0.026	$0.026^{+0.002}_{-0.002}$ [0.026]	$0.026^{+0.002}_{-0.002}$ [0.026]	$0.026^{+0.002}_{-0.002}$ [0.026]	$0.026^{+0.002}_{-0.002}$ [0.027]
Radius	0.189	$0.188^{+0.002}_{-0.003}$ [0.189]	$0.189^{+0.002}_{-0.003}$ [0.189]	$0.188^{+0.002}_{-0.003}$ [0.189]	$0.189^{+0.002}_{-0.003}$ [0.190]
Temperature	720.33	728^{+36}_{-34} [714]	731^{+44}_{-42} [718]	732^{+43}_{-42} [727]	729^{+45}_{-39} [735]
log(H_2O)	-4	$-3.8^{+0.7}_{-0.6}$ [−4.0]	$-3.9^{+0.7}_{-0.6}$ [−4.0]	$-3.9^{+0.7}_{-0.6}$ [−4.0]	$-3.9^{+0.7}_{-0.6}$ [−4.3]
log(CH_4)	-3.22	$-3.1^{+0.6}_{-0.4}$ [−3.2]	$-3.1^{+0.6}_{-0.4}$ [−3.3]	$-3.1^{+0.6}_{-0.4}$ [−3.2]	$-3.1^{+0.6}_{-0.4}$ [−3.4]
log(CO/He)	-10	-8^{+3}_{-3} [−7]	-8^{+3}_{-3} [−6]	-8^{+3}_{-3} [−12]	-8^{+3}_{-3} [−11]
log(P_{clouds})	-1	$-1.2^{+0.6}_{-0.7}$ [−1.0]	$-1.1^{+0.6}_{-0.7}$ [−1.0]	$-1.2^{+0.6}_{-0.7}$ [−1.0]	$-1.1^{+0.7}_{-0.7}$ [−0.9]
μ	2.3	$2.29^{+0.043}_{-0.009}$ [2.261]	$2.289^{+0.041}_{-0.009}$ [2.261]	$2.290^{+0.045}_{-0.009}$ [2.261]	$2.288^{+0.041}_{-0.008}$ [2.261]
		μ = 5.2			
Mass	0.026	$0.026^{+0.002}_{-0.002}$ [0.025]	$0.027^{+0.006}_{-0.006}$ [0.031]	$0.030^{+0.010}_{-0.010}$ [0.027]	$0.071^{+0.016}_{-0.015}$ [0.053]
Radius	0.189	$0.190^{+0.001}_{-0.001}$ [0.190]	$0.190^{+0.001}_{-0.001}$ [0.189]	$0.190^{+0.001}_{-0.001}$ [0.189]	$0.191^{+0.001}_{-0.001}$ [0.189]
Temperature	720.33	796^{+167}_{-128} [761]	781^{+164}_{-123} [717]	785^{+158}_{-129} [698]	809^{+134}_{-114} [749]
log(H_2O)	-4	-6^{+2}_{-4} [−4]	-6^{+2}_{-4} [−4]	-6^{+2}_{-4} [−4]	-7^{+2}_{-3} [−4]
log(CH_4)	-3.22	$-3.2^{+0.4}_{-0.3}$ [−3.1]	$-3.2^{+0.4}_{-0.3}$ [−3.3]	$-3.3^{+0.4}_{-0.4}$ [−3.3]	$-3.7^{+0.4}_{-0.4}$ [−3.5]
log(CO/He)	0	$0.2^{+0.2}_{-0.2}$ [0.2]	$0.18^{+0.27}_{-0.28}$ [−0.16]	$0.11^{+0.38}_{-0.39}$ [−0.06]	$-1.5^{+0.6}_{-0.9}$ [−1.1]
log(P_{clouds})	-1	$0.6^{+1.6}_{-1.4}$ [−0.7]	$0.5^{+1.6}_{-1.4}$ [−0.8]	$0.4^{+1.7}_{-1.4}$ [−0.7]	$1.0^{+1.3}_{-1.3}$ [−0.7]
μ	5.2	7^{+2}_{-2} [7]	7^{+3}_{-2} [4]	6^{+4}_{-2} [5]	$2.40^{+0.30}_{-0.10}$ [2.51]
		μ = 7.6			
Mass	0.026	$0.026^{+0.002}_{-0.002}$ [0.024]	$0.026^{+0.006}_{-0.006}$ [0.033]	$0.027^{+0.011}_{-0.009}$ [0.026]	$0.074^{+0.017}_{-0.032}$ [0.026]
Radius	0.189	$0.190^{+0.001}_{-0.001}$ [0.189]	$0.190^{+0.001}_{-0.001}$ [0.189]	$0.190^{+0.001}_{-0.001}$ [0.189]	$0.190^{+0.001}_{-0.001}$ [0.190]
Temperature	720.33	888^{+352}_{-210} [688]	913^{+326}_{-193} [804]	864^{+295}_{-199} [725]	751^{+218}_{-134} [705]
log(H_2O)	-4	-8^{+3}_{-3} [−4]	-8^{+3}_{-3} [−4]	-7^{+3}_{-3} [−4]	-7^{+2}_{-3} [−5]
log(CH_4)	-3.22	$-3.2^{+0.5}_{-0.5}$ [−3.5]	$-3.2^{+0.5}_{-0.5}$ [−3.4]	$-3.2^{+0.5}_{-0.5}$ [−3.2]	$-3.6^{+0.6}_{-0.5}$ [−3.4]
log(CO/He)	0.3	$0.7^{+0.4}_{-0.3}$ [0.3]	$0.7^{+0.5}_{-0.4}$ [0.2]	$0.6^{+0.5}_{-0.4}$ [0.4]	$-0.7^{+0.9}_{-1.6}$ [0.4]
log(P_{clouds})	-1	$0.6^{+1.6}_{-1.5}$ [−0.9]	$0.7^{+1.5}_{-1.7}$ [−1.1]	$0.6^{+1.5}_{-1.6}$ [−1.1]	$0.8^{+1.4}_{-1.4}$ [−0.3]
μ	7.6	12^{+6}_{-4} [8]	12^{+7}_{-4} [7]	12^{+8}_{-5} [8]	$3.0^{+3.9}_{-0.7}$ [8.3]
		μ = 11.1			
Mass	0.026	$0.026^{+0.002}_{-0.002}$ [0.024]	$0.027^{+0.007}_{-0.006}$ [0.032]	$0.028^{+0.010}_{-0.009}$ [0.012]	$0.067^{+0.022}_{-0.031}$ [0.026]
Radius	0.189	$0.190^{+0.001}_{-0.001}$ [0.19]	$0.190^{+0.001}_{-0.001}$ [0.190]	$0.190^{+0.001}_{-0.001}$ [0.189]	$0.190^{+0.001}_{-0.001}$ [0.189]
Temperature	720.33	988^{+343}_{-285} [671]	905^{+335}_{-252} [734]	941^{+417}_{-290} [659]	839^{+544}_{-279} [803]
log(H_2O)	-4	-7^{+3}_{-3} [−5]	-8^{+3}_{-3} [−5]	-7^{+3}_{-3} [−4]	-7^{+3}_{-3} [−4]
log(CH_4)	-3.22	$-3.2^{+0.7}_{-0.7}$ [−3.4]	$-3.2^{+0.7}_{-0.7}$ [−3.44]	$-3.2^{+0.7}_{-0.8}$ [−3.3]	$-3.5^{+0.8}_{-0.8}$ [−2.9]
log(CO/He)	0.6	$1.3^{+0.5}_{-0.5}$ [0.7]	$1.2^{+0.5}_{-0.5}$ [0.6]	$1.2^{+0.5}_{-0.5}$ [1.3]	$0.2^{+0.8}_{-2.9}$ [0.8]
log(P_{clouds})	-1	$0.6^{+1.6}_{-1.8}$ [2.1]	$0.6^{+1.5}_{-1.7}$ [2.5]	$0.3^{+1.7}_{-1.7}$ [−1.3]	$0.5^{+1.6}_{-1.6}$ [−0.7]
μ	11.1	20^{+4}_{-7} [13]	20^{+5}_{-8} [11]	19^{+6}_{-8} [21]	7^{+11}_{-5} [14]

Notes. I report the median values with its 1σ error and the MAP values in square brackets.

Table A.11: *Retrieved values obtained from the analyses performed on a CO-dominated cloudy secondary atmosphere (P_{clouds} = 10^{-3} bar) of a super-Earth around an 8th magnitude M star in the different considered scenarios.*

CO-dominated cloudy secondary atmosphere of a super-Earth around an 8th magnitude M star (P_{clouds} = 10^{-3} bar)					
Parameter	True value	μ = 2.3			
δM		10%	30%	50%	Unknown
Mass	0.026	$0.026^{+0.002}_{-0.002}$ [0.026]	$0.029^{+0.005}_{-0.005}$ [0.028]	$0.031^{+0.007}_{-0.006}$ [0.026]	$0.037^{+0.009}_{-0.007}$ [0.027]
Radius	0.189	$0.191^{+0.005}_{-0.005}$ [0.191]	$0.192^{+0.005}_{-0.006}$ [0.191]	$0.193^{+0.005}_{-0.006}$ [0.189]	$0.196^{+0.004}_{-0.004}$ [0.191]
Temperature	720.33	727^{+62}_{-58} [715]	751^{+66}_{-67} [721]	762^{+83}_{-73} [722]	813^{+105}_{-87} [742]
log(H_2O)	-4	$-5.4^{+1.5}_{-3.5}$ [−4.6]	-6^{+2}_{-3} [−4]	-6^{+2}_{-3} [−4]	-6^{+2}_{-4} [−4]
log(CH_4)	-3.22	$-3.5^{+0.9}_{-1.0}$ [−3.7]	$-3.5^{+0.8}_{-1.0}$ [−3.4]	$-3.5^{+0.9}_{-1.0}$ [−3.3]	$-3.8^{+0.9}_{-0.8}$ [−3.6]
log(CO/He)	-10	-7^{+3}_{-3} [−9]	-8^{+3}_{-3} [−10]	-8^{+3}_{-3} [−5]	-7^{+3}_{-3} [−8]
log(P_{clouds})	-3	$-2.7^{+1.0}_{-0.9}$ [−2.5]	$-2.6^{+0.9}_{-1.0}$ [−2.7]	$-2.6^{+1.0}_{-0.9}$ [−2.9]	$-2.2^{+0.8}_{-0.9}$ [−2.7]
μ	2.3	$2.28^{+0.033}_{-0.005}$ [2.261]	$2.281^{+0.032}_{-0.005}$ [2.261]	$2.280^{+0.030}_{-0.004}$ [2.261]	$2.278^{+0.018}_{-0.002}$ [2.261]
		μ = 5.2			
Mass	0.026	$0.026^{+0.002}_{-0.002}$ [0.03]	$0.030^{+0.005}_{-0.006}$ [0.034]	$0.033^{+0.008}_{-0.008}$ [0.041]	$0.079^{+0.013}_{-0.020}$ [0.080]
Radius	0.189	$0.186^{+0.009}_{-0.008}$ [0.183]	$0.189^{+0.007}_{-0.006}$ [0.182]	$0.189^{+0.006}_{-0.006}$ [0.188]	$0.192^{+0.003}_{-0.004}$ [0.194]
Temperature	720.33	633^{+308}_{-150} [657]	618^{+332}_{-160} [628]	672^{+395}_{-174} [687]	763.3^{+306}_{-218} [707]
log(H_2O)	-4	-7^{+3}_{-3} [−5]	-8^{+3}_{-3} [−3]	-8^{+3}_{-3} [−12]	-8^{+3}_{-3} [−10]
log(CH_4)	-3.22	$-3.5^{+0.9}_{-1.0}$ [−3.7]	$-3.5^{+0.87}_{-1.2}$ [−2.2]	$-3.5^{+0.9}_{-1.2}$ [−4.2]	$-3.85^{+1.06}_{-1.14}$ [−4.41]
log(CO/He)	0	-4^{+6}_{-5} [−2]	-4^{+5}_{-5} [−10]	-4^{+6}_{-5} [−2]	-6^{+4}_{-4} [−3]
log(P_{clouds})	-3	$-2.5^{+1.6}_{-1.2}$ [−3.0]	$-2.3^{+1.7}_{-1.2}$ [−4.2]	$-2.3^{+1.1}_{-1.1}$ [−2.3]	$-1.9^{+1.2}_{-1.3}$ [−1.4]
μ	5.2	$2.294^{+19.17}_{-0.018}$ [2.345]	$2.30^{+19.38}_{-0.03}$ [2.26]	$2.29^{+19.07}_{-0.02}$ [2.28]	$2.280^{+0.066}_{-0.005}$ [2.263]
		μ = 7.6			
Mass	0.026	$0.026^{+0.002}_{-0.002}$ [0.025]	$0.029^{+0.006}_{-0.005}$ [0.035]	$0.034^{+0.008}_{-0.008}$ [0.021]	$0.074^{+0.016}_{-0.024}$ [0.093]
Radius	0.189	$0.191^{+0.003}_{-0.009}$ [0.189]	$0.189^{+0.004}_{-0.008}$ [0.177]	$0.192^{+0.002}_{-0.006}$ [0.189]	$0.191^{+0.003}_{-0.007}$ [0.190]
Temperature	720.33	574^{+466}_{-292} [833]	499^{+306}_{-227} [670]	575^{+437}_{-290} [731]	596^{+533}_{-315} [700]
log(H_2O)	-4	-7^{+3}_{-3} [−11]	-7^{+3}_{-3} [−10]	-7^{+3}_{-3} [−6]	-7^{+3}_{-3} [−5]
log(CH_4)	-3.22	$-4.1^{+1.2}_{-3.8}$ [−3.0]	$-4.1^{+1.3}_{-2.7}$ [−2.2]	$-4.2^{+1.3}_{-2.6}$ [−2.8]	$-4.3^{+1.3}_{-2.5}$ [−3.2]
log(CO/He)	0.3	$0.9^{+0.7}_{-8.5}$ [0.6]	-3^{+5}_{-6} [−9]	$0.4^{+1.1}_{-8.6}$ [0.6]	$-6.3^{+6.5}_{-3.6}$ [−1.3]
log(P_{clouds})	-3	$-2.5^{+3.1}_{-1.5}$ [−3.2]	-2^{+2}_{-2} [−5]	$-1.9^{+2.2}_{-1.5}$ [−3.5]	-2^{+2}_{-2} [−3]
μ	7.6	15^{+9}_{-13} [10]	$2.31^{+19.86}_{-0.04}$ [2.26]	9^{+14}_{-7} [11]	$2.281^{+4.478}_{-0.006}$ [2.422]
		μ = 11.1			
Mass	0.026	$0.026^{+0.002}_{-0.002}$ [0.027]	$0.029^{+0.006}_{-0.006}$ [0.025]	$0.034^{+0.008}_{-0.009}$ [0.026]	$0.076^{+0.015}_{-0.022}$ [0.081]
Radius	0.189	$0.187^{+0.005}_{-0.010}$ [0.189]	$0.190^{+0.003}_{-0.006}$ [0.190]	$0.190^{+0.003}_{-0.009}$ [0.190]	$0.189^{+0.003}_{-0.007}$ [0.189]
Temperature	720.33	428^{+373}_{-208} [875]	402^{+484}_{-198} [842]	441^{+365}_{-222} [702]	701^{+606}_{-380} [648]
log(H_2O)	-4	-7^{+3}_{-3} [−7]	-7^{+3}_{-3} [−5]	-7^{+3}_{-3} [−10]	-7^{+3}_{-3} [−10]
log(CH_4)	-3.22	-6^{+2}_{-4} [−3]	-5^{+2}_{-4} [−3]	-6^{+2}_{-4} [−3]	-6^{+2}_{-4} [−5]
log(CO/He)	0.6	$-4.0^{+5.4}_{-4.6}$ [0.9]	$0.7^{+0.9}_{-8.5}$ [0.9]	$-1.2^{+2.7}_{-7.3}$ [1.0]	-5^{+6}_{-4} [−3]
log(P_{clouds})	-3	$-2.7^{+1.5}_{-1.5}$ [−3.5]	-3^{+3}_{-2} [−3]	-2^{+3}_{-2} [−3]	-3^{+2}_{-2} [−2]
μ	11.1	$2.29^{+19.91}_{-0.01}$ [15.53]	12^{+11}_{-10} [16]	$2.5^{+20.0}_{-0.2}$ [16.7]	$2.278^{+15.539}_{-0.003}$ [2.262]

Notes. I report the median values with its 1σ error and the MAP values in square brackets.

APPENDIX B

Additional material for Chapter 4

B.1 HD3167 c

TABLE B.1: *Results obtained from the retrieval performed on the simulated spectra of HD3167c*

HD3167c				
Param	P_{clouds} (bar)	δM = 8%		
		Acc.	MAP Acc.	Prec.
Mass	1	0.77	0.08	6.11/6.04
	-1	1.12	1.72	6.64/6.47
	-3	1.06	1.17	6.06/6.14
Radius	1	<0.01	<0.01	<0.01/<0.01
	-1	<0.01	0.01	<0.01/<0.01
	-3	<0.01	0.01	<0.01/<0.01
Temp	1	0.74	0.24	7.13/7.27
	-1	1.58	2.17	9.84/9.4
	-3	24.24	14.67	14.57/36.65
P_{clouds}	1	0.45	0.38	1.07/1.0
	-1	0.09	0.03	0.22/0.15
	-3	1.32	0.69	0.89/1.4
H_2O	1	0.04	0.02	0.3/0.29
	-1	0.04	0.01	0.47/0.52
	-3	2.3	0.99	2.53/2.91
CH_4	1	0.01	<0.01	0.21/0.22
	-1	0.1	0.06	0.33/0.43
	-3	1.82	0.86	2.92/2.63
CO	1	0.02	0.11	0.45/0.46
	-1	0.12	0.1	0.6/0.6
	-3	3.11	1.13	2.96/2.77

B.2 HD 152843 b

Table B.2: *Results of the retrieval performed on the simulated spectra of HD152843 b*

HD152843 b										
Param	P_{clouds} (bar)	δM = 10%			δM = 30%			δM = 55%		
		Acc.	MAP Acc.	Prec.	Acc.	MAP Acc.	Prec.	Acc.	MAP Acc.	Prec.
Mass	1	0.72	1.8	6.75/7.29	2.37	3.1	9.54/10.36	2.52	1.44	10.26/11.47
	-1	1.89	5.72	7.27/7.53	6.73	5.14	12.31/13.28	8.2	0.04	12.74/15.51
	-3	2.95	2.6	6.9/5.66	8.64	12.94	15.07/15.28	22.89	6.87	20.51/21.65
Radius	1	0.02	0.19	0.38/0.38	0.02	0.06	0.44/0.45	0.03	0.04	0.46/0.47
	-1	0.36	0.27	1.38/1.05	0.15	0.01	1.45/1.12	0.21	0.19	1.5/1.23
	-3	0.38	1.94	2.2/2.06	0.7	0.09	2.39/1.86	1.01	1.68	2.51/1.83
Temp	1	0.57	0.78	5.61/6.44	1.74	3.58	7.04/8.72	1.81	0.81	8.05/8.86
	-1	0.82	3.86	6.82/7.46	3.55	2.49	8.96/9.94	4.36	0.51	9.04/11.62
	-3	14.01	5.29	17.08/38.21	7.33	8.12	18.09/27.68	0.99	14.82	22.29/26.99
P_{clouds}	1	0.46	1.42	1.08/1.03	0.43	0.22	1.08/1.07	0.44	0.08	1.06/1.06
	-1	0.12	0.06	0.35/0.2	0.1	0.12	0.36/0.2	0.13	0.07	0.4/0.22
	-3	0.69	0.38	0.85/1.26	0.58	0.18	0.8/1.09	0.84	0.53	0.81/0.95
H_2O	1	0.02	0.05	0.16/0.17	0.03	0.01	0.17/0.17	0.02	0.03	0.18/0.18
	-1	0.12	0.06	0.3/0.37	0.11	0.07	0.3/0.36	0.13	0.12	0.29/0.4
	-3	0.7	0.31	3.4/2.04	0.68	<0.01	3.27/1.77	0.06	0.82	3.27/1.66
CH_4	1	<0.01	0.01	0.13/0.14	<0.01	0.02	0.13/0.14	0.01	<0.01	0.13/0.13
	-1	0.12	0.01	0.23/0.34	0.14	0.1	0.24/0.34	0.17	0.06	0.25/0.38
	-3	0.71	0.29	1.66/1.18	0.58	0.22	1.45/1.03	0.89	0.83	1.26/1.1
CO	1	0.03	0.06	0.34/0.33	0.04	0.06	0.32/0.35	0.03	0.01	0.33/0.34
	-1	0.19	0.01	0.48/0.62	0.19	0.09	0.49/0.62	0.22	0.13	0.5/0.71
	-3	3.83	0.19	2.39/3.11	3.91	1.49	2.66/3.21	3.46	0.83	2.91/3.04

B.3 TOI-1130 b

Table B.3: *Results of the retrieval performed on the simulated spectra of TOI-1130 b*

TOI-1130 b										
Param	P_{clouds} (bar)	δM = 30%			δM = 50%			δM = 100%		
		Acc.	MAP Acc.	Prec.	Acc.	MAP Acc.	Prec.	Acc.	MAP Acc.	Prec.
Mass	1	0.03	3.33	7.83/8.45	0.21	0.62	7.61/8.43	0.45	1.17	7.87/8.98
	-1	7.44	3.5	13.8/15.52	9.38	4.57	15.85/18.16	11.31	5.37	16.72/19.9
	-3	11.55	35.96	16.84/14.56	17.54	15.81	20.18/21.34	63.99	16.15	28.36/25.99
Radius	1	0.02	0.03	0.28/0.28	0.02	<0.01	0.27/0.27	0.04	0.05	0.29/0.29
	-1	0.2	0.34	0.98/0.8	0.26	0.32	1.07/0.85	0.33	0.23	1.15/0.93
	-3	0.46	2.54	1.91/1.5	0.63	1.51	1.99/1.36	0.35	0.26	1.66/1.49
Temp	1	0.25	3.46	6.2/5.77	0.04	0.58	5.82/5.93	0.17	0.25	6.28/5.87
	-1	2.36	2.66	7.88/9.64	3.35	2.51	8.48/10.2	4.1	2.33	9.11/10.32
	-3	9.24	5.25	23.3/25.99	5.58	3.34	21.98/30.7	29.13	11.11	27.59/37.52
P_{clouds}	1	0.47	1.69	1.08/1.05	0.46	1.79	1.0/1.04	0.51	0.43	1.09/1.05
	-1	0.04	0.01	0.18/0.14	0.04	0.1	0.19/0.15	0.03	0.01	0.2/0.15
	-3	0.85	0.54	0.92/0.93	0.83	0.09	0.87/1.11	0.96	1.09	0.96/1.13
H_2O	1	<0.01	0.05	0.16/0.16	0.01	<0.01	0.15/0.15	0.01	0.01	0.14/0.16
	-1	0.04	0.16	0.26/0.3	0.04	0.09	0.26/0.31	0.06	0.04	0.25/0.29
	-3	1.31	1.04	3.42/2.25	1.12	0.08	3.54/2.12	1.73	1.53	3.23/2.64
CH_4	1	0.01	0.03	0.12/0.11	0.01	0.02	0.12/0.11	<0.01	0.04	0.12/0.12
	-1	0.08	0.16	0.21/0.25	0.08	0.05	0.21/0.26	0.1	0.04	0.21/0.25
	-3	0.29	0.86	2.74/1.42	0.3	0.02	2.42/1.49	0.02	1.38	3.92/1.73
CO	1	0.01	0.03	0.31/0.31	0.01	0.07	0.3/0.3	0.02	0.07	0.3/0.31
	-1	0.09	0.14	0.4/0.47	0.1	0.06	0.42/0.48	0.13	0.06	0.41/0.49
	-3	3.62	7.69	2.65/2.96	3.54	0.03	2.75/2.65	3.27	0.23	2.95/2.82

B.4 AU Mic c

B.4.1 Martioli et al. (2021)

Table B.4: *Results of the retrieval performed on the simulated spectra of AU Mic obtained using the parameters from Martioli et al. (2021)*

AU Mic c (Martioli et al., 2021)										
Param	P_{clouds} (bar)	δM = 30%			δM = 50%			δM = 85%		
		Acc.	MAP Acc.	Prec.	Acc.	MAP Acc.	Prec.	Acc.	MAP Acc.	Prec.
Mass	1	5.55	0.69	14.19/16.13	8.61	2.64	15.74/20.17	10.69	2.91	16.91/21.86
	-1	20.93	15.71	19.55/19.03	48.92	11.73	22.58/21.85	84.3	63.25	25.33/26.4
	-3	10.46	5.58	18.12/19.11	37.14	2.23	26.29/19.98	69.46	17.06	29.47/30.03
Radius	1	0.12	0.03	0.38/0.33	0.14	0.02	0.36/0.37	0.16	0.1	0.38/0.38
	-1	1.07	0.62	1.23/0.76	1.61	0.3	1.02/0.43	1.85	1.1	0.59/0.37
	-3	1.73	0.67	2.68/1.75	1.57	2.15	2.9/1.97	2.05	1.78	3.4/1.67
Temp	1	2.12	0.76	14.07/15.46	4.49	2.55	15.2/17.88	6.29	5.16	15.84/19.13
	-1	17.26	3.68	23.96/30.3	13.62	0.1	22.35/25.42	4.97	11.4	21.28/21.8
	-3	26.16	16.11	42.45/61.8	15.56	18.38	42.19/64.47	7.56	9.66	39.37/78.2
P_{clouds}	1	0.41	0.78	1.21/1.06	0.37	1.09	1.16/1.09	0.39	1.0	1.19/1.1
	-1	0.13	0.1	0.51/2.22	0.72	0.02	0.87/2.25	1.43	0.18	1.34/1.74
	-3	0.35	1.02	1.24/1.07	0.62	0.96	1.17/1.2	0.6	0.82	1.24/1.21
H_2O	1	0.08	0.09	0.51/0.44	0.11	0.17	0.56/0.48	0.14	0.04	0.58/0.49
	-1	0.18	0.16	1.33/0.84	0.13	0.05	1.51/0.87	0.19	0.45	2.67/1.02
	-3	2.55	1.35	2.67/3.21	2.43	0.66	2.69/2.87	2.22	0.39	2.93/2.85
CH_4	1	<0.01	0.06	0.33/0.34	0.02	0.05	0.33/0.36	0.04	0.01	0.34/0.37
	-1	0.62	0.12	0.65/0.62	0.67	0.2	0.58/0.62	0.61	0.22	0.56/0.61
	-3	2.74	1.08	2.38/2.64	2.25	0.59	2.56/2.81	2.53	0.5	2.38/2.77
CO	1	<0.01	0.23	0.59/0.58	0.05	0.3	0.54/0.61	0.04	0.04	0.57/0.62
	-1	0.56	0.25	1.02/0.9	0.65	0.37	0.98/0.87	0.64	0.57	1.07/0.88
	-3	3.04	3.66	2.87/2.94	2.32	1.08	3.24/2.61	2.85	0.33	2.98/2.85

B.4.2 Cale et al. (2021)

Table B.5: *Results of the retrieval performed on the simulated spectra of AU Mic obtained using the parameters from Cale et al. (2021)*

AU Mic c (Cale et al., 2021)				
Param	P_{clouds} (bar)	*LinearPrior – UpperLimit*		
		Acc.	MAP Acc.	Prec.
Mass	1	14.62	0.2	18.31/26.31
	-1	75.73	7.31	20.51/12.97
	-3	59.62	34.87	24.31/19.1
Radius	1	0.28	0.03	0.5/0.52
	-1	2.19	0.06	0.73/0.47
	-3	0.75	0.4	7.02/3.48
Temp	1	7.96	2.22	16.97/21.43
	-1	10.06	14.59	22.47/25.06
	-3	24.08	19.52	48.93/91.48
P_{clouds}	1	0.39	0.03	1.16/1.12
	-1	1.32	0.04	1.27/1.81
	-3	0.64	0.75	1.24/1.43
H_2O	1	0.18	0.03	0.68/0.51
	-1	0.14	0.36	3.04/1.05
	-3	2.27	0.49	2.75/2.64
CH_4	1	0.04	0.07	0.38/0.39
	-1	0.62	0.37	0.58/0.72
	-3	2.1	0.74	2.74/2.68
CO	1	0.05	0.13	0.64/0.68
	-1	0.57	0.01	1.27/0.92
	-3	2.97	5.54	2.68/2.74

B.4.3 Zicher et al. (2022)

Table B.6: *Results of the retrieval performed on the simulated spectra of AU Mic obtained using the parameters from Zicher et al. (2022)*

AU Mic c (Zicher et al., 2022)										
Param	P_{clouds} (bar)	δM = 10%			δM = 20%			δM = 30%		
		Acc.	MAP Acc.	Prec.	Acc.	MAP Acc.	Prec.	Acc.	MAP Acc.	Prec.
Mass	1	2.75	4.56	8.66/8.54	6.27	5.09	15.55/17.51	15.36	40.58	19.22/19.31
	-1	1.09	5.58	7.8/7.9	9.09	41.72	16.83/14.62	13.32	11.81	20.13/19.32
	-3	1.74	3.51	8.22/7.47	4.63	4.61	14.16/15.06	13.96	4.45	18.42/17.59
Radius	1	0.22	0.08	0.49/0.45	0.19	0.11	0.47/0.44	0.22	0.33	0.5/0.44
	-1	1.06	0.51	3.73/1.98	0.28	0.65	3.98/1.37	0.23	0.09	4.71/1.35
	-3	0.57	5.28	6.18/2.17	0.4	0.99	5.65/2.15	0.08	1.03	4.77/1.84
Temp	1	8.58	10.44	33.57/38.39	4.14	14.78	33.1/40.41	3.52	15.51	35.27/44.23
	-1	1.05	35.14	52.16/108.81	21.46	10.33	49.54/163.06	15.64	0.16	50.34/154.19
	-3	10.66	99.95	54.8/138.81	5.49	0.45	55.59/144.88	3.06	38.22	50.36/152.29
P_{clouds}	1	0.04	1.82	1.35/1.26	0.01	0.42	1.27/1.3	0.06	1.59	1.34/1.18
	-1	1.51	0.18	1.83/1.73	1.52	0.18	1.7/2.3	1.34	0.55	1.87/2.35
	-3	0.77	1.85	1.08/1.44	0.57	1.61	1.44/1.47	0.46	0.46	1.35/1.49
H_2O	1	1.63	0.28	3.35/2.1	1.79	0.3	3.41/2.24	2.04	0.39	3.22/2.32
	-1	2.06	0.89	2.91/2.64	2.01	0.46	3.07/2.77	2.31	0.53	3.05/2.91
	-3	1.78	1.47	3.24/2.83	1.87	0.78	2.97/2.69	2.15	1.65	2.92/2.79
CH_4	1	0.11	0.14	0.85/0.93	0.17	0.31	0.88/0.98	0.25	0.04	1.0/0.96
	-1	0.84	1.0	3.5/2.3	0.36	0.22	3.77/2.0	0.29	0.66	3.85/1.98
	-3	1.96	1.32	2.75/2.86	2.22	1.66	2.84/2.7	2.53	1.02	2.54/3.0
CO	1	0.87	0.49	3.34/1.61	0.93	0.56	3.15/1.62	1.19	0.16	3.74/1.75
	-1	2.64	1.25	3.44/2.86	2.43	0.95	3.5/2.79	2.56	0.31	3.36/2.93
	-3	3.15	5.46	2.93/2.89	2.93	7.36	2.73/2.91	3.01	0.15	2.83/2.89

B.4.4 $M_p = 14.45 M_\oplus$

Table B.7: *Results obtained from the retrieval performed on the simulated spectra of AU Mic assuming a planetary mass of $14.45 M_\oplus$*

AU Mic c - M_p = 14.45 $M_\oplus$													
		Nobs = 6						Nobs = 18					
Param	P_{clouds} (bar)	Linear			Gaussian			Linear			Gaussian		
		Acc.	MAP Acc.	Prec.	Acc.	MAP Acc.	Prec.	Acc.	MAP Acc.	Prec.	Acc.	MAP Acc.	Prec.
Mass	1	40.64	4.43	26.32/25.86	42.22	4.43	18.11/20.89	10.08	4.28	16.05/22.56	8.6	1.93	12.78/15.1
	-1	59.46	34.11	27.24/17.37	79.32	66.9	17.25/19.02	65.84	83.05	24.37/14.61	87.61	15.24	17.71/16.4
	-3	60.12	91.34	20.65/15.19	73.27	69.05	14.11/13.16	60.6	28.81	22.74/15.38	75.29	63.65	14.47/15.1
Radius	1	0.42	0.08	0.49/0.42	0.43	<0.01	0.43/0.4	0.12	0.04	0.28/0.31	0.1	0.07	0.27/0.27
	-1	1.35	0.99	2.28/0.62	1.48	1.41	1.67/0.52	1.37	1.25	0.78/0.36	1.56	0.31	0.44/0.27
	-3	0.9	0.65	5.27/2.28	1.24	2.1	4.2/2.1	0.57	0.98	6.15/2.47	1.16	0.2	5.5/2.0
Temp	1	18.75	5.45	24.33/34.7	24.23	4.2	22.43/29.29	5.06	3.0	15.69/20.03	4.85	6.05	13.15/15.77
	-1	18.89	8.48	38.7/58.13	12.06	10.19	36.74/63.14	13.95	0.65	22.36/29.07	9.95	3.92	21.5/24.73
	-3	8.37	64.02	53.53/130.75	14.15	24.97	50.16/128.09	20.17	3.98	53.52/139.0	9.6	26.58	47.68/158.58
P_{clouds}	1	0.27	0.28	1.08/1.17	0.33	1.78	1.13/1.09	0.47	0.71	1.16/1.0	0.44	0.93	1.17/1.06
	-1	0.22	0.22	1.97/2.42	0.57	0.37	2.3/2.34	0.54	0.29	0.79/2.3	1.29	0.13	1.13/1.79
	-3	0.68	1.37	1.23/1.42	0.36	1.17	1.35/1.43	0.69	0.08	1.23/1.5	0.75	1.37	1.2/1.3
H_2O	1	0.99	0.33	3.39/1.31	1.28	0.1	3.58/1.39	0.1	0.08	0.56/0.45	0.12	0.19	0.5/0.47
	-1	1.56	0.18	3.53/2.39	2.14	0.07	3.06/2.8	0.04	0.58	2.58/0.92	0.16	0.46	3.06/1.02
	-3	2.31	0.28	3.02/3.09	2.35	2.64	2.66/2.9	2.54	1.79	2.63/2.77	2.39	0.62	2.77/2.94
CH_4	1	0.2	0.22	0.66/0.64	0.27	0.1	0.61/0.63	0.03	0.03	0.35/0.36	0.03	0.1	0.33/0.34
	-1	0.68	0.17	1.21/1.19	0.56	0.56	1.46/1.19	0.69	0.56	0.6/0.67	0.64	0.38	0.56/0.62
	-3	1.72	1.29	2.93/2.73	2.32	1.74	2.65/2.63	2.8	0.15	2.15/2.7	1.63	1.34	2.99/2.32
CO	1	0.32	0.57	1.49/1.05	0.37	0.19	1.31/1.1	<0.01	0.08	0.57/0.58	0.03	0.21	0.56/0.56
	-1	0.64	0.21	3.71/1.79	1.01	1.5	3.98/1.92	0.63	0.93	1.1/0.88	0.69	0.63	1.15/0.86
	-3	2.41	1.13	3.17/2.84	2.92	3.32	3.08/2.85	3.24	0.04	2.68/2.8	3.31	5.97	2.96/2.91

Notes. Linear: TauREx is able to retrieved the mass in a linear boundary range from 0 to 28.9 $M_\oplus$. Gaussian: retrieval performed using a gaussian prior for the planetary mass using the parameter obtained in the linear retrieval as median and standard deviation values.

B.4.5 $M_p = 24.08 M_\oplus$

Table B.8: *Results obtained from the retrieval performed on the simulated spectra of AU Mic assuming a planetary mass of $24.08 M_\oplus$*

AU Mic c - M_p = 24.08 $M_\oplus$													
		Nobs = 6						Nobs = 18					
Param	P_{clouds} (bar)	Linear			Gaussian			Linear			Gaussian		
		Acc.	MAP Acc.	Prec.	Acc.	MAP Acc.	Prec.	Acc.	MAP Acc.	Prec.	Acc.	MAP Acc.	Prec.
Mass	1	1.56	4.92	18.35/12.4	7.64	4.95	13.72/13.53	1.24	3.16	21.12/14.45	6.76	0.59	15.79/16.12
	-1	4.34	3.33	21.47/16.08	4.26	13.35	16.42/15.22	7.14	3.13	23.14/18.07	0.7	6.83	16.68/15.17
	-3	3.7	1.59	21.99/14.88	0.31	19.46	13.8/14.59	6.42	35.74	27.06/17.17	3.37	12.38	17.15/17.29
Radius	1	0.08	0.07	0.29/0.24	0.1	0.07	0.24/0.25	0.14	0.18	0.65/0.5	0.2	<0.01	0.53/0.43
	-1	0.39	0.16	3.56/1.26	0.07	0.03	2.93/1.07	2.04	0.39	4.47/2.25	0.75	0.53	3.12/1.43
	-3	1.61	0.54	5.49/2.55	0.67	0.08	5.92/1.96	1.33	1.42	4.82/2.63	1.53	1.5	5.11/3.01
Temp	1	5.33	3.33	21.4/26.35	1.64	1.82	19.97/22.4	13.73	12.26	38.81/48.79	7.02	0.16	34.13/44.49
	-1	20.04	5.17	49.18/113.38	20.53	20.26	48.15/101.16	9.99	16.04	50.18/134.93	9.94	26.13	46.06/103.01
	-3	20.25	17.07	54.53/142.39	13.2	24.83	50.28/138.1	14.9	13.24	54.23/115.05	38.45	57.18	57.97/110.46
P_{clouds}	1	0.24	1.43	1.17/1.14	0.39	0.53	1.21/1.07	0.2	1.82	1.6/1.46	0.07	0.59	1.38/1.37
	-1	1.12	0.68	1.68/1.22	0.94	0.07	1.9/1.47	2.06	1.55	1.44/1.56	1.73	<0.01	1.75/1.53
	-3	0.85	0.01	1.1/1.48	0.67	0.42	1.28/1.63	0.47	0.57	1.47/1.43	0.49	0.12	1.36/1.73
H_2O	1	0.34	0.16	2.27/0.94	0.42	0.08	2.4/0.89	1.35	0.23	3.3/2.1	1.87	<0.01	3.38/2.29
	-1	1.42	1.21	3.46/2.41	1.64	0.46	3.09/2.48	2.85	1.23	2.69/3.49	2.33	0.07	2.65/2.96
	-3	2.11	0.18	2.59/2.58	2.41	0.46	2.83/2.75	2.79	0.99	2.52/3.23	2.56	0.99	2.8/3.37
CH_4	1	0.01	0.12	0.53/0.58	0.07	0.12	0.53/0.59	0.09	0.28	1.16/1.01	0.19	<0.01	1.05/1.06
	-1	0.58	0.84	2.79/1.4	0.55	0.24	2.97/1.24	1.02	1.79	3.26/2.45	0.73	0.3	3.43/2.5
	-3	2.97	0.58	2.12/2.81	2.55	0.38	2.34/2.56	2.43	1.4	2.38/2.65	2.78	0.37	2.28/2.56
CO	1	0.17	0.38	1.07/0.99	0.17	0.11	1.04/1.03	1.56	0.42	3.92/2.14	1.07	<0.01	3.75/1.78
	-1	1.41	1.7	3.75/2.27	1.65	0.01	3.82/2.5	2.97	1.72	2.78/2.92	3.26	0.6	3.0/3.09
	-3	3.65	1.61	2.64/2.99	3.53	1.67	2.95/3.0	3.37	2.71	2.91/2.99	3.27	0.16	2.56/2.87

Notes. Linear: TauREx is able to retrieved the mass in a linear boundary range from 0 to 28.9 $M_\oplus$. Gaussian: retrieval performed using a gaussian prior for the planetary mass using the parameter obtained in the linear retrieval as median and standard deviation values.

B.5 HD106315 c

Table B.9: *Results of the retrieval performed on the simulated spectra of HD106315c*

HD106315c										
Param	P_{clouds} (bar)	δM = 10%			δM = 20%			δM = 25%		
		Acc.	MAP Acc.	Prec.	Acc.	MAP Acc.	Prec.	Acc.	MAP Acc.	Prec.
Mass	1	1.72	0.91	6.79/6.98	2.97	3.35	8.44/9.67	2.92	3.8	8.46/10.24
	-1	2.47	14.15	7.96/7.77	5.13	5.15	11.6/12.97	7.0	0.55	12.65/13.93
	-3	2.01	4.22	7.01/6.97	7.14	3.24	12.99/11.71	7.7	24.4	15.81/14.34
Radius	1	0.02	0.03	0.34/0.31	0.05	0.02	0.36/0.37	0.07	0.08	0.38/0.38
	-1	0.05	0.64	0.94/0.78	0.07	0.26	1.13/0.9	0.15	0.33	1.08/0.86
	-3	1.29	3.29	3.47/2.5	1.41	2.9	3.48/2.56	1.65	3.95	3.6/2.3
Temp	1	4.51	2.44	5.48/6.37	5.79	5.88	6.64/7.29	5.57	0.35	6.28/7.73
	-1	3.99	9.94	6.92/7.84	5.57	5.57	8.29/8.74	6.2	5.17	8.21/9.46
	-3	16.22	8.88	20.97/23.66	13.27	4.01	25.09/29.99	14.33	9.06	22.81/26.82
P_{clouds}	1	0.41	1.0	1.07/0.99	0.51	1.7	1.17/1.01	0.43	0.72	1.13/1.08
	-1	0.05	0.05	0.24/0.15	0.05	0.03	0.25/0.16	0.05	0.09	0.23/0.16
	-3	0.78	0.71	0.91/1.09	0.77	0.69	0.92/1.18	0.8	0.63	0.91/1.03
H_2O	1	0.02	0.01	0.18/0.17	0.04	0.07	0.18/0.18	0.03	0.01	0.18/0.18
	-1	0.06	0.05	0.28/0.31	0.05	0.02	0.27/0.31	0.05	0.03	0.26/0.32
	-3	1.45	0.56	3.49/2.45	0.91	0.74	3.51/2.18	1.04	0.52	3.54/2.3
CH_4	1	<0.01	0.01	0.14/0.14	0.01	0.02	0.14/0.14	<0.01	0.01	0.14/0.14
	-1	0.07	0.02	0.22/0.25	0.08	0.01	0.21/0.26	0.09	<0.01	0.21/0.27
	-3	0.66	0.57	1.82/1.2	0.31	0.65	2.3/1.44	0.48	0.49	2.13/1.35
CO	1	0.03	0.06	0.37/0.37	0.04	0.01	0.37/0.35	0.01	0.04	0.37/0.36
	-1	0.11	0.01	0.44/0.49	0.1	0.09	0.46/0.53	0.11	0.03	0.46/0.5
	-3	3.25	0.51	2.85/2.77	2.82	0.99	2.77/2.66	3.35	2.74	2.77/2.83

B.6 TOI-451 d

Table B.10: *Results of the retrieval performed on the simulated spectra of TOI-451 d*

TOI-451 d										
Param	P_{clouds} (bar)	δM = 30%			δM = 50%			δM = 100%		
		Acc.	MAP Acc.	Prec.	Acc.	MAP Acc.	Prec.	Acc.	MAP Acc.	Prec.
Mass	1	1.18	0.59	8.5/9.44	1.05	1.11	8.57/9.69	1.09	4.32	9.18/9.77
	-1	9.58	2.91	14.81/15.75	10.74	0.03	17.42/19.18	14.71	6.49	17.05/23.27
	-3	7.31	2.92	17.18/16.84	25.0	9.4	18.3/18.57	52.21	25.11	27.98/31.06
Radius	1	<0.01	0.06	0.25/0.25	0.01	0.02	0.24/0.24	0.01	0.18	0.25/0.25
	-1	0.31	0.14	0.81/0.71	0.38	0.18	0.96/0.77	0.54	0.42	0.9/0.8
	-3	0.71	2.21	2.07/1.69	0.62	0.43	2.31/1.92	0.71	0.74	2.31/1.71
Temp	1	1.08	0.43	6.55/7.18	1.11	0.63	6.59/7.59	1.22	1.29	6.96/7.41
	-1	3.09	0.91	8.33/9.1	3.72	3.68	9.24/9.53	5.12	1.7	9.54/10.65
	-3	16.65	11.59	25.04/34.91	1.29	14.6	24.34/33.27	10.24	8.49	28.1/56.97
P_{clouds}	1	0.5	0.02	1.1/1.04	0.44	0.51	1.02/1.08	0.48	1.17	1.06/1.02
	-1	0.01	0.04	0.13/0.14	0.01	0.01	0.15/0.14	0.02	0.08	0.15/0.16
	-3	0.92	0.57	0.98/1.19	0.81	0.38	0.97/1.12	1.09	0.25	0.95/1.19
H_2O	1	0.02	0.03	0.15/0.14	0.02	<0.01	0.15/0.14	0.02	0.02	0.15/0.14
	-1	0.02	0.07	0.23/0.24	<0.01	0.05	0.23/0.24	<0.01	0.02	0.23/0.24
	-3	1.39	0.58	3.51/2.41	1.68	0.35	3.21/2.62	1.72	0.51	3.34/2.76
CH_4	1	0.01	0.02	0.11/0.11	0.01	0.01	0.12/0.11	0.01	0.03	0.11/0.11
	-1	0.06	0.01	0.19/0.19	0.05	0.09	0.18/0.2	0.07	0.02	0.19/0.2
	-3	0.34	0.51	3.37/1.84	0.31	0.57	3.08/1.79	0.32	0.5	3.8/1.94
CO	1	0.04	0.14	0.3/0.32	0.02	0.05	0.31/0.32	0.01	0.02	0.31/0.31
	-1	0.06	0.05	0.38/0.4	0.06	0.01	0.38/0.41	0.09	0.1	0.4/0.44
	-3	3.3	2.06	2.88/3.05	2.87	6.08	3.02/2.79	3.36	0.63	2.67/3.15

B.7 KOI-94 c

Table B.11: *Results obtained from the retrieval performed on the simulated spectra of KOI-94 c assuming two different value of planetary mass.*

KOI-94c							
Param	P_{clouds} (bar)	$M_p = 8M_\oplus$			$M_p = 16M_\oplus$		
		Acc.	MAP Acc.	Prec.	Acc.	MAP Acc.	Prec.
Mass	1	0.67	1.32	5.32/5.65	5.14	2.23	13.84/15.08
	-1	1.17	1.88	7.26/7.91	13.17	8.83	17.93/13.55
	-3	43.58	0.74	22.03/31.82	7.02	21.7	26.17/17.24
Radius	1	0.14	0.01	0.37/0.4	0.06	0.24	0.55/0.51
	-1	0.15	0.24	0.95/0.89	0.2	0.4	2.17/1.59
	-3	5.27	0.89	4.29/2.71	3.42	4.24	5.71/3.58
Temp	1	0.01	1.69	4.34/4.68	4.67	1.64	11.27/12.21
	-1	0.53	0.58	5.03/5.54	6.42	4.54	13.18/15.65
	-3	11.15	2.21	14.54/22.25	29.58	6.71	36.07/53.34
P_{clouds}	1	0.47	0.44	1.07/1.02	0.46	0.64	1.11/1.01
	-1	0.02	0.06	0.08/0.08	0.11	0.03	0.5/0.27
	-3	0.31	0.21	0.61/0.59	0.73	0.71	1.19/1.17
H_2O	1	0.01	0.03	0.08/0.07	0.06	0.02	0.21/0.22
	-1	0.01	0.01	0.09/0.09	0.1	0.03	0.35/0.48
	-3	0.55	0.25	0.7/0.82	1.92	0.66	3.17/2.76
CH_4	1	0.01	0.01	0.06/0.06	0.02	0.07	0.17/0.17
	-1	<0.01	0.01	0.08/0.08	0.15	0.08	0.31/0.45
	-3	0.59	0.25	0.71/0.79	1.0	0.72	3.25/2.11
CO	1	0.02	0.05	0.22/0.21	0.17	0.18	0.87/0.64
	-1	0.01	0.03	0.22/0.22	0.06	0.01	1.41/0.89
	-3	1.12	0.71	4.15/1.55	3.53	0.1	2.77/3.04

B.8 Kepler-450b

Table B.12: *Results of the retrieval performed on the simulated spectra of Kepler-450b*

Kepler-450b										
Param	P_{clouds} (bar)	δM = 30%			δM = 50%			δM = 60%		
		Acc.	MAP Acc.	Prec.	Acc.	MAP Acc.	Prec.	Acc.	MAP Acc.	Prec.
Mass	1	1.05	0.85	5.01/4.8	0.95	2.12	4.72/5.03	1.3	0.3	4.99/4.81
	-1	1.42	1.58	7.13/7.97	1.54	2.14	7.4/8.74	1.72	0.49	7.56/8.75
	-3	5.17	9.76	14.64/16.99	18.55	28.11	19.32/19.99	28.9	3.38	24.58/22.81
Radius	1	<0.01	<0.01	0.02/0.03	<0.01	0.02	0.03/0.02	<0.01	0.03	0.02/0.03
	-1	<0.01	0.03	0.03/0.02	<0.01	0.03	0.02/0.02	<0.01	0.02	0.03/0.02
	-3	<0.01	0.01	0.02/0.02	<0.01	0.01	0.02/0.02	<0.01	0.01	0.02/0.02
Temp	1	1.03	0.77	5.42/5.75	1.2	2.92	5.2/5.51	1.46	0.25	5.56/5.48
	-1	1.52	2.34	7.44/7.8	1.19	1.58	7.3/8.92	1.68	0.63	7.9/8.68
	-3	7.66	8.34	18.92/24.92	0.23	26.26	19.91/20.94	2.97	7.99	22.8/35.23
P_{clouds}	1	0.42	1.25	1.0/1.09	0.42	1.61	1.05/1.05	0.47	0.34	1.07/0.99
	-1	0.03	0.05	0.08/0.07	0.03	0.03	0.08/0.07	0.03	0.06	0.08/0.07
	-3	0.62	0.08	0.78/0.8	0.85	0.05	0.74/0.83	0.94	0.5	0.71/1.01
H_2O	1	0.02	0.01	0.13/0.12	0.03	0.05	0.12/0.12	0.02	0.01	0.12/0.12
	-1	0.01	<0.01	0.17/0.17	0.01	0.03	0.17/0.17	0.01	0.02	0.17/0.16
	-3	0.44	0.11	3.32/1.7	0.28	0.16	3.35/1.63	0.46	0.44	3.58/1.85
CH_4	1	0.01	0.01	0.1/0.09	0.01	0.04	0.09/0.09	0.01	0.01	0.09/0.1
	-1	<0.01	0.02	0.12/0.13	<0.01	0.02	0.12/0.13	<0.01	0.01	0.13/0.13
	-3	0.43	0.04	1.31/1.19	0.82	0.07	1.3/1.03	0.81	0.67	1.52/1.04
CO	1	0.03	0.05	0.32/0.31	0.03	0.04	0.31/0.31	0.03	0.12	0.34/0.31
	-1	0.01	0.06	0.35/0.33	0.01	0.05	0.36/0.34	0.02	0.02	0.34/0.35
	-3	3.16	1.98	2.75/2.75	3.57	0.33	2.84/2.93	3.39	6.48	2.98/2.98

B.9 TOI-1728 b

Table B.13: *Results of the retrieval performed on the simulated spectra of TOI-1728 b.*

TOI-1728b							
Param	P_{clouds} (bar)	δM = 10%			δM = 20%		
		Acc.	MAP Acc.	Prec.	Acc.	MAP Acc.	Prec.
Mass	1	0.65	2.51	6.78/6.65	0.95	0.71	8.84/9.5
	-1	1.87	9.0	8.38/7.95	6.35	3.09	13.42/13.1
	-3	1.1	3.82	7.46/6.8	3.0	6.39	12.97/13.5
Radius	1	0.02	0.02	0.19/0.17	0.01	0.07	0.21/0.2
	-1	0.05	0.31	0.56/0.46	0.05	0.03	0.64/0.58
	-3	0.51	1.08	2.41/1.77	0.7	0.73	2.19/1.45
Temp	1	0.65	2.77	5.64/6.09	0.99	1.45	7.0/6.91
	-1	0.43	3.03	7.36/8.81	1.89	2.15	8.27/9.51
	-3	17.31	11.91	27.52/34.44	24.15	14.23	22.55/41.77
P_{clouds}	1	0.44	0.34	1.06/1.05	0.44	0.33	1.06/1.07
	-1	0.06	0.02	0.2/0.14	0.05	0.04	0.23/0.16
	-3	0.82	1.05	1.06/1.42	1.08	0.48	0.91/1.22
H_2O	1	0.01	0.01	0.17/0.18	0.01	0.04	0.18/0.19
	-1	0.05	0.02	0.33/0.34	0.06	0.01	0.3/0.37
	-3	2.1	1.1	2.92/2.84	2.22	0.77	2.7/2.94
CH_4	1	<0.01	0.01	0.15/0.13	0.01	0.05	0.15/0.14
	-1	0.06	0.03	0.24/0.26	0.08	<0.01	0.23/0.29
	-3	1.25	1.33	3.1/2.3	0.97	0.68	3.42/2.29
CO	1	0.01	0.03	0.39/0.4	0.01	0.05	0.38/0.37
	-1	0.08	0.21	0.48/0.52	0.12	0.04	0.49/0.56
	-3	3.1	3.08	2.88/2.61	3.16	4.04	2.86/2.76

B.10 HATS-37A b

Table B.14: *Results of the retrieval performed on the simulated spectra of HATS-37Ab*

HATS-37Ab										
Param	P_{clouds} (bar)	δM = 10%			δM = 30%			δM = 42%		
		Acc.	MAP Acc.	Prec.	Acc.	MAP Acc.	Prec.	Acc.	MAP Acc.	Prec.
Mass	1	0.13	0.55	5.76/6.28	0.51	0.53	7.75/9.09	0.6	1.1	8.06/8.63
	-1	1.6	1.64	7.29/6.76	4.29	3.52	11.04/12.43	5.08	3.69	12.03/13.62
	3	1.08	7.36	6.86/6.29	8.97	2.1	16.53/16.12	16.91	23.21	18.61/17.4
Radius	1	0.28	0.33	0.2/0.21	0.04	0.07	0.25/0.25	0.05	0.01	0.25/0.26
	-1	<0.01	<0.01	0.64/0.6	0.1	0.01	0.74/0.65	0.11	0.02	0.76/0.73
	3	0.04	0.89	1.55/1.7	0.65	1.73	1.86/1.29	0.72	0.1	1.83/1.3
Temp	1	0.59	0.02	4.93/5.39	1.57	2.04	6.59/7.02	1.86	1.52	6.39/6.97
	-1	2.64	1.22	6.26/7.0	0.98	0.35	7.86/9.36	0.62	4.72	7.91/9.86
	-3	13.35	9.94	14.06/19.16	14.35	12.66	17.86/28.33	6.05	3.31	20.41/21.55
P_{clouds}	1	0.48	1.24	1.04/1.03	0.4	1.86	1.01/1.08	0.44	0.3	1.06/1.05
	-1	0.03	<0.01	0.15/0.12	0.03	0.05	0.15/0.13	0.02	0.06	0.16/0.14
	3	0.51	0.28	0.92/0.88	0.75	0.31	0.72/0.97	0.76	0.67	0.83/1.04
H_2O	1	0.02	0.01	0.11/0.1	0.03	0.04	0.12/0.13	0.02	0.06	0.12/0.12
	-1	<0.01	0.07	0.15/0.18	<0.01	<0.01	0.16/0.17	<0.01	0.07	0.17/0.18
	3	0.66	0.4	3.31/1.6	0.26	0.18	3.55/1.6	0.18	0.92	2.89/1.66
CH_4	1	0.01	0.02	0.09/0.09	0.02	0.03	0.09/0.09	0.01	<0.01	0.1/0.09
	-1	0.01	0.01	0.14/0.15	0.03	0.03	0.15/0.15	0.02	0.09	0.13/0.16
	3	0.45	0.3	1.17/1.22	0.81	0.09	1.24/1.07	0.79	0.73	1.37/1.15
CO	1	0.05	0.13	0.35/0.35	0.06	0.05	0.37/0.36	0.05	0.06	0.38/0.35
	-1	0.01	0.09	0.41/0.4	0.02	0.07	0.4/0.39	0.01	0.26	0.41/0.39
	3	3.14	0.08	2.99/2.65	3.02	0.3	3.04/2.83	2.8	1.38	3.16/2.6

B.11 GJ9827 c

Table B.15: *Results of the retrieval performed on the simulated spectra of GJ9827c (N_{obs} = 11).*

GJ9827c											
Param	μ	P_{clouds} (bar)	δM = 10%			δM = 20%			δM = 25%		
			Acc.	MAP Acc.	Prec.	Acc.	MAP Acc.	Prec.	Acc.	MAP Acc.	Prec.
Mass	2.3	1	1.14	1.08	5.61/6.33	1.36	2.15	7.34/8.14	1.45	0.46	7.68/8.48
		-1	1.24	1.52	6.41/6.27	2.63	2.41	7.82/8.05	3.1	0.99	8.21/9.46
		-3	1.98	5.22	6.93/7.3	5.35	2.87	11.44/12.42	6.76	0.48	12.43/12.43
	7.6	1	0.11	3.54	8.85/8.39	0.11	6.82	17.15/18.21	7.04	6.5	19.94/18.95
		-1	1.3	8.59	9.29/8.92	2.59	22.57	17.2/17.06	4.67	28.46	21.55/20.11
		-3	0.24	5.23	8.3/8.59	5.08	7.1	15.56/14.62	4.41	30.01	20.31/19.47
Radius	2.3	1	0.15	0.33	1.46/1.49	0.1	0.1	1.57/1.41	0.14	0.13	1.57/1.47
		-1	1.95	0.2	3.0/1.27	2.08	1.36	3.03/1.22	1.93	0.87	2.83/1.33
		-3	0.18	2.03	2.48/2.41	0.39	0.22	2.6/2.28	0.24	3.83	2.61/2.44
	7.6	1	0.65	0.28	1.78/1.58	0.42	0.08	1.62/1.48	0.52	0.13	1.55/1.5
		-1	1.57	1.71	1.76/1.21	1.23	1.09	1.71/1.46	1.59	0.66	1.46/1.22
		-3	1.08	3.22	2.55/1.71	0.79	2.72	2.51/1.9	1.01	2.58	2.65/1.78
P_{clouds}	2.3	1	0.21	0.65	1.31/1.17	0.27	0.05	1.31/1.16	0.2	0.19	1.28/1.21
		-1	0.61	0.02	0.78/2.05	0.61	0.25	0.78/2.17	0.61	0.19	0.76/2.2
		-3	0.05	0.23	0.36/0.37	0.07	0.1	0.37/0.38	0.11	0.43	0.37/0.38
	7.6	1	0.43	1.31	1.39/1.37	0.5	0.84	1.27/1.4	0.13	1.26	1.41/1.24
		-1	1.58	2.1	1.56/1.53	1.47	0.74	1.52/1.56	1.52	0.36	1.44/1.52
		-3	0.05	0.23	1.64/1.35	0.24	0.95	1.57/1.5	0.1	0.17	1.64/1.38
H_2O	2.3	1	0.85	0.23	8.73/8.11	1.36	1.34	9.19/8.6	1.24	2.28	8.63/8.54
		-1	7.01	1.9	9.03/10.17	8.07	6.22	8.87/10.89	8.04	2.65	8.97/10.47
		-3	20.92	8.07	86.1/20.97	19.02	1.07	83.25/20.48	18.56	9.47	89.25/21.38
	7.6	1	98.69	59.63	32.64/42.81	75.88	6.06	48.13/39.51	98.74	52.39	33.79/40.78
		-1	85.24	15.65	39.23/39.96	85.43	68.3	38.5/37.84	80.62	4.31	42.3/34.93
		-3	96.38	177.0	33.44/40.37	70.75	170.49	45.76/38.34	86.0	79.71	35.76/37.43
CH_4	2.3	1	0.03	<0.01	0.24/0.25	0.02	0.03	0.23/0.24	0.02	0.07	0.23/0.25
		-1	0.15	0.11	0.25/0.37	0.17	0.17	0.24/0.38	0.15	0.16	0.24/0.35
		-3	0.07	0.21	0.46/0.45	0.11	0.08	0.5/0.44	0.15	0.35	0.48/0.46
	7.6	1	0.17	0.68	0.97/0.8	0.24	0.25	0.91/0.81	0.15	0.13	1.0/0.82
		-1	0.19	0.58	1.01/0.83	0.33	0.22	1.04/0.95	0.41	0.25	1.02/0.93
		-3	3.13	0.95	3.4/2.48	4.04	1.05	3.11/3.13	2.56	0.79	3.88/2.51
μ	2.3	1	0.59	1.47	0.23/0.42	0.61	1.71	0.2/0.43	0.61	1.7	0.21/0.44
		-1	0.77	1.71	0.15/0.55	0.78	1.71	0.14/0.55	0.77	1.71	0.15/0.5
		-3	0.57	1.71	0.34/0.95	0.52	1.71	0.39/1.01	0.46	1.7	0.43/1.2
	7.6	1	69.04	24.42	82.2/64.26	58.92	22.92	81.09/72.91	44.21	11.16	79.19/92.39
		-1	82.38	29.91	83.44/60.45	56.66	62.65	80.7/73.98	58.83	52.81	79.92/72.41
		-3	69.49	160.14	1.9/766.97	61.99	56.62	21.25/605.9	21.55	200.57	61.84/256.18

TABLE B.16: *Results of the retrieval performed on the simulated spectra of GJ9827c, obtained assuming twice the number of transits required for Tier-2.*

GJ9827c - Nobs = 22											
Param	μ	P_{clouds} (bar)	δM = 10%			δM = 20%			δM = 25%		
			Acc.	MAP Acc.	Prec.	Acc.	MAP Acc.	Prec.	Acc.	MAP Acc.	Prec.
Mass	7.6	1	0.37	3.35	9.0/9.17	2.11	23.13	18.16/16.45	3.26	7.39	20.11/21.13
		-1	0.43	9.37	9.26/8.89	0.87	33.71	16.88/19.13	0.36	14.24	19.71/23.28
		-3	1.0	13.23	8.71/7.86	4.74	7.49	16.23/14.72	7.57	14.51	17.92/16.44
Radius	7.6	1	0.46	0.26	1.11/0.95	0.46	0.43	1.15/1.1	0.45	0.27	1.23/1.12
		-1	1.56	1.58	1.28/1.09	1.47	0.65	1.17/1.0	1.38	1.39	1.28/1.14
		-3	1.27	0.41	2.7/1.69	1.21	1.9	2.12/1.56	1.22	2.05	2.79/1.67
P_{clouds}	7.6	1	0.11	1.96	1.35/1.17	0.08	0.75	1.42/1.21	0.06	0.6	1.38/1.3
		-1	1.63	2.23	1.55/1.6	1.46	0.1	1.47/1.61	1.52	2.71	1.52/1.49
		-3	0.39	1.32	1.42/0.95	0.04	0.69	1.73/1.3	0.15	0.29	1.63/1.23
H_2O	7.6	1	76.31	8.0	43.23/37.41	74.53	0.3	43.56/37.0	75.46	4.81	48.58/36.37
		-1	88.19	31.96	36.65/34.16	83.28	4.14	39.16/38.03	96.21	26.82	33.16/33.85
		-3	75.43	45.92	42.6/39.09	85.45	65.83	37.25/41.63	69.0	0.47	45.53/38.75
CH_4	7.6	1	0.09	0.39	0.74/0.63	0.08	0.1	0.8/0.63	0.06	0.25	0.76/0.65
		-1	0.19	0.69	0.81/0.82	0.08	0.01	0.83/0.74	0.12	0.37	0.83/0.76
		-3	2.22	1.71	3.91/2.06	2.37	0.6	3.8/2.26	2.65	0.07	3.74/2.35
μ	7.6	1	49.69	17.55	38.12/58.9	49.46	10.56	40.67/63.91	41.79	13.04	41.62/66.39
		-1	83.82	6.11	43.61/52.45	66.32	54.33	44.64/69.48	68.21	3.29	44.56/59.37
		-3	69.2	49.89	2.81/731.07	68.67	21.91	4.45/728.16	68.84	39.75	3.94/751.49

B.12 LTT1445 A b

Table B.17: *Results of the retrieval performed on the simulated spectra of LTT1445A b Winters et al. (2019).*

LTT1445A b Winters et al. (2019)												
Param	μ	P_{clouds} (bar)	δM = 30%			δM = 50%			δM = 90%			
			Acc.	MAP Acc.	Prec.	Acc.	MAP Acc.	Prec.	Acc.	MAP Acc.	Prec.	
Mass	2.3	1	3.01	1.31	7.25/8.5	3.03	0.81	7.37/8.64	3.3	0.78	7.39/8.59	
		-1	5.78	5.25	9.76/11.07	6.91	6.86	10.52/10.85	7.16	3.01	9.91/11.17	
		-3	10.85	6.16	18.01/17.3	24.38	1.44	19.75/25.05	44.13	13.49	26.01/31.98	
	7.6	1	3.98	35.55	24.29/25.85	20.72	35.83	34.16/35.72	94.56	47.34	42.97/30.99	
		-1	1.4	37.1	23.65/26.2	11.14	54.33	31.28/35.9	46.93	116.45	39.02/47.95	
		-3	14.43	13.98	22.53/21.23	31.46	7.36	25.43/27.29	62.29	33.09	32.33/39.63	
Radius	2.3	1	0.03	0.03	0.44/0.44	0.03	0.06	0.47/0.43	0.02	0.13	0.44/0.45	
		-1	0.44	0.61	1.86/1.19	0.35	0.44	1.93/1.18	0.3	0.03	1.76/1.12	
		-3	3.07	3.54	4.77/3.34	4.13	3.83	3.85/3.04	5.48	3.88	3.77/2.5	
	7.6	1	0.23	0.1	0.6/0.46	0.09	0.07	0.79/0.52	0.04	0.01	0.58/0.52	
		-1	0.96	0.47	1.43/0.53	0.91	0.44	2.12/0.55	0.82	0.4	2.84/0.6	
		-3	2.58	2.74	4.25/1.57	1.99	6.54	3.88/2.09	3.31	3.91	3.78/0.93	
P_{clouds}	2.3	1	0.31	1.63	1.19/1.14	0.33	0.49	1.16/1.15	0.33	0.13	1.2/1.14	
		-1	0.18	0.13	0.54/0.32	0.16	0.03	0.53/0.33	0.15	0.03	0.5/0.31	
		-3	0.48	0.76	0.93/0.82	0.5	0.86	0.92/0.77	0.5	0.71	0.79/0.78	
	7.6	1	0.09	1.5	1.45/1.23	0.12	0.61	1.55/1.32	<0.01	1.05	1.35/1.36	
		-1	1.35	0.11	1.73/1.78	1.08	0.28	1.67/1.91	0.96	0.15	1.78/1.98	
		-3	0.96	1.13	2.17/2.51	0.74	0.07	1.82/2.21	1.08	2.16	1.95/2.73	
H_2O	2.3	1	0.7	0.07	6.93/6.91	0.6	2.57	6.94/6.85	0.94	2.04	6.38/7.0	
		-1	5.24	4.43	11.69/18.19	4.84	1.41	12.14/18.06	4.72	1.21	12.18/16.94	
		-3	56.89	16.32	56.67/31.56	51.34	21.0	60.77/33.29	55.65	22.02	57.57/32.85	
	7.6	1	34.7	0.97	78.21/32.43	20.12	5.55	84.21/28.82	24.04	12.66	80.42/28.78	
		-1	76.15	21.41	44.87/38.91	77.29	20.77	42.88/42.19	64.87	6.99	51.52/39.55	
		-3	80.07	74.87	39.3/37.24	87.71	44.75	37.56/40.04	85.25	42.13	38.62/41.09	
CH_4	2.3	1	0.02	0.03	0.15/0.18	0.01	0.05	0.16/0.16	0.01	<0.01	0.16/0.16	
		-1	0.19	0.02	0.29/0.48	0.2	0.01	0.29/0.47	0.18	0.04	0.29/0.44	
		-3	0.39	0.72	0.86/0.85	0.3	0.75	0.83/0.89	0.19	0.65	0.93/0.81	
	7.6	1	0.09	0.07	0.63/0.63	0.05	0.04	0.61/0.61	0.08	0.02	0.55/0.64	
		-1	0.08	0.17	0.76/0.68	0.08	0.01	0.76/0.7	0.05	0.24	0.7/0.71	
		-3	2.66	1.98	3.42/2.3	2.73	1.23	3.48/2.17	2.6	0.89	3.55/2.2	
μ	2.3	1	0.65	0.83	0.15/0.29	0.64	1.71	0.15/0.27	0.63	1.71	0.15/0.28	
		-1	0.31	1.71	0.43/1.82	0.31	1.71	0.42/1.78	0.34	1.55	0.39/1.56	
		-3	0.87	1.71	0.19/1.24	0.81	1.71	0.24/1.71	0.75	1.71	0.31/1.78	
	7.6	1	36.56	23.33	43.56/63.94	0.57	25.07	69.65/109.92	67.94	27.14	6.47/309.34	
		-1	95.8	93.62	84.14/55.23	73.94	174.37	82.5/67.5	3.36	44.33	68.89/172.77	
		-3	135.23	70.25	87.25/36.35	116.31	68.6	86.16/47.68	143.87	237.02	87.71/32.7	

Table B.18: *Results of the retrieval performed on the simulated spectra of LTT1445A b using the set of parameters from Winters et al. (2019) and Winters et al. (2022), assuming a mass uncertainty of 10%.*

LTT1445A b Winters et al. (2019) vs Winters et al. (2022)								
Param	μ	P_{clouds} (bar)	δM = 10% Winters et al. (2019)			δM = 10% Winters et al. (2022)		
			Acc.	MAP Acc.	Prec.	Acc.	MAP Acc.	Prec.
Mass	2.3	1	1.36	0.61	5.54/6.07	2.24	0.78	7.61/7.23
		-1	3.2	3.36	6.99/6.3	3.43	6.48	7.74/7.51
		-3	0.84	2.3	8.1/7.88	0.48	0.91	7.76/7.55
	7.6	1	0.28	1.41	9.36/8.95	0.18	1.59	9.08/8.71
		-1	0.14	13.43	8.99/9.3	1.66	4.56	9.0/8.17
		-3	1.26	9.75	8.33/8.57	0.1	7.13	8.98/8.51
Radius	2.3	1	0.06	0.04	0.44/0.4	0.04	0.14	0.45/0.47
		-1	0.65	0.46	2.1/1.22	0.36	0.44	1.78/1.32
		-3	1.96	1.39	4.03/3.54	1.45	0.15	2.89/2.17
	7.6	1	0.21	0.1	0.59/0.51	0.16	0.13	0.73/0.51
		-1	1.06	0.57	0.68/0.47	0.73	0.32	1.65/0.52
		-3	1.76	1.42	4.62/2.22	1.43	1.93	3.14/1.34
P_{clouds}	2.3	1	0.26	1.02	1.13/1.17	0.33	0.05	1.24/1.08
		-1	0.22	0.11	0.59/0.34	0.2	0.12	0.65/0.54
		-3	0.39	0.3	0.86/0.88	0.37	0.02	0.81/0.94
	7.6	1	0.02	1.73	1.4/1.27	0.33	0.31	1.55/1.42
		-1	1.72	0.25	1.77/1.45	0.97	0.02	1.49/1.94
		-3	0.69	0.89	2.02/2.17	0.96	0.81	2.13/1.83
H_2O	2.3	1	0.36	0.49	6.63/6.46	1.16	1.71	11.54/11.23
		-1	6.57	2.46	12.71/20.7	5.18	6.79	21.38/21.6
		-3	56.89	4.86	55.14/31.16	82.58	4.3	39.77/37.79
	7.6	1	33.08	14.97	78.37/32.84	54.14	5.7	59.0/38.53
		-1	77.41	20.3	42.06/37.45	93.04	13.93	32.83/37.6
		-3	89.25	39.3	33.96/36.54	88.18	165.38	36.81/35.83
CH_4	2.3	1	0.02	0.04	0.15/0.17	0.01	0.02	0.23/0.26
		-1	0.2	0.02	0.3/0.53	0.22	0.01	0.42/0.54
		-3	0.36	0.26	0.9/0.84	0.41	0.11	1.2/0.92
	7.6	1	0.13	0.13	0.64/0.63	0.05	0.14	0.81/0.77
		-1	0.09	0.03	0.74/0.67	0.21	0.25	1.11/0.87
		-3	3.02	1.04	3.07/2.29	4.1	0.09	2.64/2.82
μ	2.3	1	0.64	1.7	0.14/0.29	0.61	1.71	0.21/0.59
		-1	0.3	1.69	0.43/2.12	0.21	1.7	0.6/2.4
		-3	0.85	1.71	0.21/1.28	0.88	1.71	0.2/1.43
	7.6	1	41.38	0.51	37.52/51.22	57.69	10.62	80.82/83.21
		-1	101.31	45.96	42.58/47.18	113.01	53.45	85.86/47.89
		-3	141.44	66.69	87.59/32.04	141.66	120.08	87.58/31.99

TABLE B.19: *Results obtained from the retrieval performed on the simulated spectra of LTT1445A b using the Winters et al. (2019) parameters and exploring the parameters space using a gaussian prior centred at the planetary mass assumed by Winters et al. (2022).*

LTT1445A b Winters et al. (2019)										
Param	μ	δM = 10%			δM = 30%			δM = 50%		
		Acc.	MAP Acc.	Prec.	Acc.	MAP Acc.	Prec.	Acc.	MAP Acc.	Prec.
Mass	2.3	19.59	8.91	5.81/7.06	10.19	2.12	9.58/10.66	8.38	3.03	9.59/10.83
	7.6	31.8	37.81	8.87/8.4	41.25	31.61	27.69/24.38	59.56	131.82	31.83/33.18
Radius	2.3	0.37	0.44	1.39/1.01	0.19	0.02	1.76/1.19	0.26	0.03	1.66/1.15
	7.6	0.79	0.25	4.44/0.68	0.88	0.04	2.55/0.6	0.64	2.07	3.51/0.72
Temp	2.3	10.6	5.98	5.11/4.35	6.4	2.67	5.79/6.41	5.53	0.53	5.97/6.75
	7.6	7.05	10.42	33.98/62.96	14.71	11.53	38.85/48.68	1.7	4.95	29.2/52.61
P_{clouds}	2.3	0.07	0.01	0.41/0.34	0.15	0.01	0.5/0.33	0.15	0.03	0.47/0.34
	7.6	0.67	0.12	1.72/2.19	1.0	0.16	1.58/1.83	0.54	1.03	1.49/2.25
H_2O	2.3	3.12	5.4	12.22/14.2	4.98	1.97	12.96/17.36	4.81	3.86	12.31/16.08
	7.6	59.38	22.68	53.64/37.03	66.29	1.57	50.39/38.16	63.22	27.9	54.51/40.48
CH_4	2.3	0.24	0.04	0.27/0.36	0.22	0.05	0.29/0.41	0.19	0.13	0.27/0.43
	7.6	0.05	0.37	0.71/0.67	0.01	0.17	0.68/0.7	0.05	0.44	0.73/0.68
μ	2.3	0.29	1.68	0.4/1.16	0.29	1.71	0.43/1.53	0.33	1.71	0.39/1.46
	7.6	11.4	20.31	73.03/112.33	21.55	38.78	75.25/103.39	38.04	70.25	51.55/219.65

B.13 HIP 41378 b

Table B.20: *Outcome of the retrieval performed on the simulated spectra of HIP 41378 b.*

HIP 41378 b											
Param	μ	P_{clouds} (bar)	δM = 30%			δM = 50%			δM = 100%		
			Acc.	MAP Acc.	Prec.	Acc.	MAP Acc.	Prec.	Acc.	MAP Acc.	Prec.
Mass	2.3	1	0.24	2.46	4.4/4.61	0.13	1.04	4.26/4.72	0.24	0.85	4.32/4.52
		-1	0.43	2.86	5.09/4.85	0.42	0.47	4.89/4.77	0.42	0.83	5.2/4.93
		-3	5.65	5.75	10.45/11.69	6.87	2.28	11.27/12.35	6.87	2.28	11.27/12.35
	7.6	1	4.35	14.54	22.87/24.21	11.57	23.94	31.59/38.77	143.94	233.5	43.81/24.11
		-1	0.92	23.36	25.17/26.71	9.39	12.61	33.91/39.42	138.68	35.98	47.89/27.62
		-3	11.97	5.0	21.93/19.74	28.41	47.2	28.07/26.23	80.5	142.82	34.27/29.2
Radius	2.3	1	0.08	0.04	0.46/0.42	0.08	0.08	0.44/0.4	0.09	0.01	0.45/0.41
		-1	0.7	0.62	2.46/1.14	0.67	0.63	2.5/1.17	0.7	0.5	2.42/1.15
		-3	3.4	2.32	4.94/3.45	3.52	1.7	4.46/3.43	3.52	1.7	4.46/3.43
	7.6	1	0.03	0.15	0.62/0.48	0.08	0.13	0.56/0.46	0.16	0.37	0.54/0.47
		-1	0.66	2.15	0.74/0.49	0.7	0.25	0.58/0.45	0.7	0.45	0.84/0.45
		-3	3.13	2.58	6.46/1.21	2.99	2.41	6.33/1.36	2.25	2.95	5.0/2.15
P_{clouds}	2.3	1	0.16	0.85	1.18/1.24	0.18	0.42	1.2/1.19	0.18	0.92	1.22/1.25
		-1	0.22	0.21	0.68/1.8	0.22	0.2	0.7/1.95	0.22	0.17	0.67/2.06
		-3	0.6	0.36	0.87/0.76	0.58	0.28	0.77/0.76	0.58	0.28	0.77/0.76
	7.6	1	0.17	0.78	1.6/1.49	0.2	1.93	1.43/1.45	<0.01	1.51	1.47/1.32
		-1	1.59	1.45	1.69/1.64	1.79	0.12	1.68/1.42	1.7	0.46	1.76/1.43
		-3	1.5	1.98	1.52/2.44	1.5	1.61	1.5/2.49	1.39	0.9	1.72/2.32
H_2O	2.3	1	0.48	0.02	4.21/4.42	0.45	0.45	4.25/4.24	0.58	2.0	4.28/4.4
		-1	4.17	3.69	7.32/12.24	3.77	1.84	7.78/12.21	3.87	1.48	7.69/12.13
		-3	15.54	6.99	16.95/17.65	15.79	5.24	16.29/17.01	15.79	5.24	16.29/17.01
	7.6	1	51.23	3.63	65.02/35.82	51.73	1.11	63.73/32.84	22.45	9.03	77.82/25.68
		-1	79.05	30.47	45.57/36.15	77.26	6.2	44.84/34.9	43.33	14.57	69.89/29.14
		-3	98.73	58.87	34.8/35.02	99.47	42.04	30.94/32.94	99.95	29.78	30.37/33.89
CH_4	2.3	1	0.01	0.04	0.11/0.11	0.02	<0.01	0.1/0.12	0.01	0.04	0.11/0.11
		-1	0.13	0.07	0.23/0.44	0.13	0.09	0.23/0.46	0.13	0.11	0.23/0.43
		-3	0.51	0.29	0.73/0.77	0.5	0.25	0.72/0.7	0.5	0.25	0.72/0.7
	7.6	1	0.2	0.02	0.47/0.48	0.15	0.18	0.47/0.49	0.07	0.18	0.45/0.54
		-1	0.06	1.19	0.53/0.6	0.14	0.22	0.51/0.58	0.34	0.38	0.5/0.68
		-3	0.81	1.88	1.08/1.16	1.05	1.69	0.96/1.1	0.8	0.74	1.13/1.15
μ	2.3	1	0.66	0.81	0.1/0.17	0.66	1.71	0.09/0.17	0.65	1.63	0.11/0.18
		-1	0.74	1.7	0.16/0.66	0.73	1.7	0.17/0.74	0.73	1.71	0.17/0.68
		-3	0.91	1.71	0.15/0.8	0.92	1.71	0.15/0.66	0.92	1.71	0.15/0.66
	7.6	1	19.41	20.17	27.66/38.1	12.87	24.12	35.76/55.02	69.35	70.25	2.13/196.61
		-1	29.4	25.69	29.14/50.15	17.28	17.68	37.7/62.83	69.51	46.67	1.74/246.51
		-3	106.24	10.95	85.47/51.19	61.77	174.18	81.49/90.48	69.18	70.25	2.86/725.35

B.14 K2-138 g

Table B.21: *Results of the retrieval performed on the simulated spectra of K2-138 g.*

K2-138 g												
Param	μ	P_{clouds} (bar)	δM = 30%			δM = 50%			δM = 121%		
			Acc.	MAP Acc.	Prec.	Acc.	MAP Acc.	Prec.	Acc.	MAP Acc.	Prec.
Mass	2.3	1	0.57	0.12	5.03/5.97	0.53	1.91	5.31/6.11	0.77	1.59	5.14/5.99
		-1	3.31	1.48	7.04/7.55	3.27	1.06	7.07/7.99	3.66	1.73	7.43/7.88
		-3	10.31	8.82	15.57/17.23	18.8	0.3	20.02/21.88	35.29	11.35	21.43/25.66
	7.6	1	3.36	15.62	25.16/26.14	19.75	8.75	31.89/36.77	160.98	30.64	28.48/22.99
		-1	2.89	3.08	26.35/24.93	12.4	43.1	35.41/38.91	150.83	207.87	39.78/29.5
		-3	13.44	1.61	20.23/20.43	30.83	19.0	25.13/28.21	109.14	93.43	31.64/37.46
Radius	2.3	1	0.14	0.06	0.31/0.3	0.13	0.19	0.32/0.31	0.13	0.18	0.32/0.31
		-1	0.17	0.06	0.76/0.76	0.2	0.02	0.76/0.75	0.21	0.02	0.77/0.77
		-3	1.84	3.38	4.56/3.99	3.21	1.64	5.03/3.73	5.19	3.3	4.55/2.97
	7.6	1	0.1	0.09	0.42/0.36	0.07	0.12	0.49/0.37	0.03	0.04	0.46/0.36
		-1	0.86	0.11	0.5/0.34	0.78	0.49	0.93/0.4	0.52	1.0	2.13/0.55
		-3	3.38	3.19	3.99/1.25	3.4	2.24	4.84/1.26	3.99	1.41	3.78/0.82
P_{clouds}	2.3	1	0.29	0.59	1.22/1.17	0.29	1.1	1.26/1.14	0.26	1.67	1.22/1.15
		-1	0.05	0.01	0.19/0.23	0.06	0.03	0.19/0.2	0.06	0.03	0.19/0.21
		-3	0.17	0.38	0.78/0.74	0.26	0.29	0.76/0.74	0.44	0.42	0.71/0.6
	7.6	1	0.06	0.37	1.36/1.26	0.01	1.41	1.37/1.32	0.02	0.14	1.43/1.33
		-1	1.65	0.11	1.63/1.54	1.49	0.14	1.78/1.67	0.68	0.65	1.48/2.2
		-3	1.11	1.36	1.57/2.3	1.0	0.02	1.65/2.44	1.35	0.55	1.72/2.71
H_2O	2.3	1	1.14	1.75	4.27/3.74	1.28	1.25	4.15/3.99	1.38	0.06	4.43/3.92
		-1	1.84	0.89	5.86/5.67	2.05	3.2	5.64/5.57	2.11	2.36	5.44/5.63
		-3	9.71	7.39	20.49/19.03	11.59	7.21	22.3/19.34	13.51	9.6	22.36/18.26
	7.6	1	18.51	1.31	74.83/22.5	18.95	4.46	83.57/22.92	22.11	3.38	68.95/22.55
		-1	60.96	2.03	56.48/35.56	49.67	2.88	65.07/34.56	34.61	21.26	67.54/32.6
		-3	73.94	99.73	44.02/42.06	81.57	10.23	40.97/41.87	84.99	57.96	39.13/39.26
CH_4	2.3	1	0.06	0.07	0.08/0.07	0.06	0.05	0.07/0.07	0.07	0.06	0.07/0.08
		-1	0.04	0.03	0.1/0.11	0.04	0.07	0.09/0.11	0.04	0.05	0.09/0.11
		-3	0.08	0.3	0.67/0.74	0.12	0.25	0.64/0.74	0.17	0.28	0.57/0.65
	7.6	1	0.04	0.17	0.35/0.37	0.01	0.09	0.34/0.35	0.22	0.04	0.3/0.37
		-1	0.18	0.12	0.38/0.4	0.17	0.09	0.42/0.44	<0.01	0.3	0.42/0.56
		-3	1.3	0.83	3.84/1.5	1.21	0.64	3.42/1.44	1.37	0.93	3.69/1.51
μ	2.3	1	0.7	1.7	0.07/0.1	0.7	1.71	0.06/0.1	0.7	1.71	0.06/0.1
		-1	0.68	1.68	0.09/0.17	0.68	1.71	0.09/0.19	0.68	1.71	0.09/0.17
		-3	0.63	1.71	0.37/1.71	0.7	1.71	0.31/1.67	0.74	1.71	0.26/1.12
	7.6	1	14.55	16.83	32.3/54.95	4.93	11.22	42.84/64.55	69.95	28.95	0.24/54.06
		-1	55.87	5.39	36.5/56.58	37.51	8.84	54.67/78.43	69.72	70.25	0.94/175.53
		-3	147.32	78.97	87.85/29.78	129.67	99.9	86.95/39.05	113.83	69.57	85.99/49.46

B.15 K2-32 d

Table B.22: *Results of the retrieval performed on the simulated spectra of K2-32 d.*

K2-32 d											
Param	μ	P_{clouds} (bar)	δM = 20%			δM = 30%			δM = 38%		
			Acc.	MAP Acc.	Prec.	Acc.	MAP Acc.	Prec.	Acc.	MAP Acc.	Prec.
Mass	2.3	1	0.25	0.22	4.5/4.96	0.24	1.32	4.49/4.78	0.26	0.3	4.34/4.83
		-1	1.7	2.88	5.65/5.51	2.03	1.47	5.32/5.95	1.44	1.12	5.31/5.76
		-3	3.29	4.51	9.96/10.32	4.94	0.71	11.45/13.13	5.24	4.73	12.15/13.53
	7.6	1	0.67	15.77	15.66/15.86	4.9	3.48	22.85/23.0	10.02	7.05	27.91/28.68
		-1	0.2	28.07	17.47/17.23	3.77	10.57	24.41/23.24	6.09	9.98	26.46/29.08
		-3	6.04	19.42	14.75/13.84	12.47	12.71	19.9/18.33	22.05	34.96	20.69/20.6
Radius	2.3	1	0.11	0.16	0.27/0.26	0.12	0.07	0.26/0.26	0.11	0.12	0.27/0.25
		-1	0.14	0.25	0.8/0.66	0.14	0.01	0.79/0.67	0.13	0.22	0.77/0.63
		-3	0.27	2.7	2.4/2.0	0.43	0.39	2.56/1.88	0.57	1.14	2.57/1.81
	7.6	1	0.05	0.06	0.31/0.31	0.07	0.03	0.32/0.3	0.09	0.09	0.34/0.3
		-1	0.67	0.6	0.34/0.29	0.7	0.7	0.35/0.3	0.65	0.03	0.45/0.31
		-3	1.39	2.71	2.67/1.22	1.45	1.67	2.22/1.09	1.18	2.56	2.6/1.33
P_{clouds}	2.3	1	0.27	1.18	1.2/1.17	0.27	0.11	1.2/1.17	0.36	0.2	1.23/1.11
		-1	0.06	0.01	0.24/0.24	0.06	0.01	0.25/0.24	0.05	0.02	0.23/0.24
		-3	0.01	0.6	0.5/0.47	0.04	0.07	0.47/0.46	0.02	0.15	0.46/0.47
	7.6	1	0.05	0.37	1.32/1.26	0.09	0.65	1.31/1.21	0.04	1.46	1.28/1.26
		-1	1.69	0.52	1.42/1.47	1.84	0.52	1.48/1.47	1.64	0.09	1.62/1.52
		-3	0.52	1.42	1.06/0.74	0.5	0.93	0.93/0.8	0.56	1.25	0.94/0.8
H_2O	2.3	1	1.29	1.84	3.75/4.05	1.05	1.05	3.85/3.67	1.23	0.58	3.84/3.72
		-1	2.1	0.5	5.58/6.65	1.89	2.03	5.62/6.26	1.51	0.03	5.74/5.87
		-3	2.01	11.56	14.53/14.03	1.27	3.42	15.1/13.97	1.95	3.92	14.44/13.52
	7.6	1	19.72	6.48	87.17/20.57	17.96	0.53	79.6/20.66	21.88	2.39	76.56/22.42
		-1	61.68	24.49	54.28/32.64	68.98	8.03	49.31/34.05	52.44	10.41	62.46/32.31
		-3	86.37	38.12	37.94/34.77	74.39	29.83	42.0/38.1	96.07	26.32	31.9/38.84
CH_4	2.3	1	0.05	0.05	0.07/0.07	0.06	0.07	0.07/0.08	0.05	0.04	0.07/0.07
		-1	0.05	0.03	0.1/0.14	0.04	0.05	0.11/0.13	0.04	0.04	0.11/0.13
		-3	0.05	0.52	0.52/0.52	0.1	0.04	0.5/0.47	0.09	0.1	0.55/0.47
	7.6	1	0.02	0.11	0.31/0.35	0.03	0.02	0.32/0.34	0.01	0.04	0.31/0.33
		-1	0.09	0.12	0.36/0.4	0.06	0.3	0.35/0.38	0.08	0.22	0.35/0.41
		-3	0.62	0.9	1.25/1.05	0.63	0.62	1.38/1.12	0.79	0.89	1.39/1.15
μ	2.3	1	0.7	1.41	0.07/0.11	0.7	1.71	0.06/0.1	0.7	1.71	0.06/0.11
		-1	0.69	1.7	0.1/0.24	0.68	1.71	0.1/0.21	0.68	1.71	0.1/0.23
		-3	0.56	1.65	0.37/1.16	0.51	1.71	0.39/1.09	0.51	1.68	0.41/1.15
	7.6	1	14.51	8.16	22.02/31.89	8.55	9.1	27.66/44.17	3.98	11.91	30.95/52.8
		-1	36.86	9.93	25.25/36.5	35.85	11.65	28.2/45.59	28.5	12.18	31.64/50.02
		-3	106.24	27.35	85.48/51.17	53.57	34.48	80.5/84.63	11.72	183.73	66.09/208.57

B.16 K2-3 c

Table B.23: *Results obtained from the retrieval performed on the simulated spectra of K2-3 c.*

K2-3 c												
Param	μ	P_{clouds} (bar)	δM = 10%			δM = 30%			δM = 40%			
			Acc.	MAP Acc.	Prec.	Acc.	MAP Acc.	Prec.	Acc.	MAP Acc.	Prec.	
Mass	2.3	1	1.8	0.78	6.81/7.07	3.97	1.38	8.9/10.15	3.83	2.23	9.03/10.08	
		-1	3.15	3.95	7.91/7.27	9.96	6.26	12.58/13.09	10.82	1.21	13.18/14.32	
		-3	1.52	0.05	8.1/7.5	12.31	17.7	19.68/17.53	11.77	18.34	19.5/21.6	
	7.6	1	1.14	7.63	8.84/9.05	9.12	14.4	23.4/21.25	14.72	8.37	27.97/29.86	
		-1	0.1	3.52	8.84/9.68	7.39	3.89	22.46/22.06	11.13	17.91	27.5/28.25	
		-3	2.23	27.82	7.97/7.95	11.36	18.13	21.27/19.8	22.8	48.55	24.22/22.72	
Radius	2.3	1	0.04	0.04	0.3/0.28	0.02	0.04	0.3/0.33	0.01	0.14	0.32/0.31	
		-1	0.17	0.18	1.17/0.7	0.03	0.16	1.15/0.85	0.1	0.12	1.09/0.84	
		-3	1.64	1.74	3.69/3.37	1.94	4.46	4.0/3.24	2.41	2.55	3.45/3.07	
	7.6	1	0.15	0.08	0.48/0.36	0.12	0.05	0.51/0.39	0.08	0.01	0.54/0.38	
		-1	0.83	0.44	0.5/0.32	0.74	0.2	1.75/0.36	0.71	0.24	1.48/0.4	
		-3	0.66	2.4	3.07/3.18	0.2	1.65	3.29/2.38	0.85	2.76	4.14/1.97	
P_{clouds}	2.3	1	0.29	0.71	1.17/1.15	0.33	1.46	1.16/1.13	0.35	0.06	1.18/1.12	
		-1	0.08	0.05	0.43/0.23	0.06	0.01	0.44/0.27	0.04	0.04	0.39/0.28	
		-3	0.45	0.53	0.94/0.82	0.36	0.75	1.04/0.89	0.47	0.4	0.94/0.75	
	7.6	1	0.14	1.1	1.4/1.4	0.09	1.75	1.49/1.3	0.14	0.67	1.54/1.35	
		-1	1.67	0.39	1.81/1.64	1.25	0.91	1.79/1.75	1.13	0.26	1.62/1.87	
		-3	0.23	1.06	1.55/1.76	0.7	0.41	1.67/1.29	0.48	0.75	1.58/1.93	
H_2O	2.3	1	1.47	1.07	6.75/6.4	1.48	1.45	6.85/6.48	1.75	1.01	6.55/6.78	
		-1	2.85	1.01	10.3/14.4	2.42	0.72	11.2/15.2	1.48	2.31	10.16/13.5	
		-3	66.56	11.94	49.18/34.41	76.85	16.27	44.36/36.76	60.29	9.51	54.44/34.85	
	7.6	1	22.55	0.73	86.12/29.5	19.38	3.34	82.14/29.74	15.48	10.31	80.68/27.99	
		-1	79.22	15.75	44.67/40.76	81.43	19.3	42.66/40.28	64.09	10.51	53.54/39.27	
		-3	83.62	13.36	37.06/37.6	99.08	88.64	32.29/38.44	94.45	23.96	32.59/38.4	
CH_4	2.3	1	0.06	0.08	0.13/0.15	0.04	0.05	0.14/0.14	0.04	0.04	0.15/0.15	
		-1	0.08	0.07	0.21/0.34	0.12	0.07	0.25/0.36	0.1	0.01	0.24/0.33	
		-3	0.3	0.56	0.87/0.83	0.23	0.6	0.85/0.94	0.26	0.22	0.83/0.83	
	7.6	1	0.1	0.13	0.58/0.58	0.08	0.03	0.56/0.61	0.06	0.16	0.55/0.58	
		-1	0.18	0.01	0.74/0.64	0.15	1.08	0.71/0.64	0.15	0.15	0.69/0.63	
		-3	3.56	0.29	3.03/2.66	3.45	0.09	3.23/2.38	3.75	0.41	3.12/2.86	
μ	2.3	1	0.68	1.71	0.12/0.24	0.67	1.71	0.13/0.24	0.66	1.69	0.14/0.24	
		-1	0.5	1.66	0.26/1.2	0.46	1.71	0.3/1.2	0.48	1.41	0.28/1.0	
		-3	0.79	1.69	0.27/2.47	0.75	1.7	0.3/2.2	0.74	1.71	0.32/2.07	
	7.6	1	35.45	9.45	53.79/68.91	23.31	38.94	75.09/87.02	7.34	5.62	71.82/102.32	
		-1	138.85	9.36	46.2/33.92	111.45	57.85	85.69/47.87	97.42	11.23	84.7/54.97	
		-3	85.01	186.4	83.82/65.13	99.61	184.23	85.0/56.01	99.88	70.21	85.02/56.82	

B.17 TOI-269 b

Table B.24: *Results obtained from the retrieval performed on the simulated spectra of TOI-269 b.*

TOI-269 b								
Param	μ	P_{clouds} (bar)	δM = 10%			δM = 16%		
			Acc.	MAP Acc.	Prec.	Acc.	MAP Acc.	Prec.
Mass	2.3	1	0.63	2.74	5.04/5.91	1.27	0.15	6.1/7.12
		-1	2.01	0.68	6.27/6.74	3.45	2.12	7.76/8.41
		-3	2.2	6.5	7.93/6.88	4.27	0.17	11.76/11.18
	7.6	1	0.27	17.65	9.43/8.77	1.15	2.75	13.93/14.17
		-1	1.12	0.38	9.31/10.42	0.02	7.38	14.82/15.12
		-3	1.37	7.82	8.14/8.39	1.34	11.09	12.72/13.92
Radius	2.3	1	0.1	0.13	0.27/0.24	0.09	0.1	0.28/0.28
		-1	0.42	0.04	1.61/0.99	0.22	0.01	1.54/0.96
		-3	0.83	2.33	2.51/2.27	1.16	0.7	2.52/1.96
	7.6	1	0.02	0.02	0.28/0.26	0.04	0.05	0.33/0.25
		-1	0.52	0.2	0.31/0.26	0.5	0.3	0.38/0.27
		-3	0.96	1.86	2.67/1.46	1.95	1.4	2.62/0.57
P_{clouds}	2.3	1	0.3	0.64	1.23/1.15	0.26	0.18	1.18/1.14
		-1	0.18	0.03	0.71/0.46	0.09	0.05	0.7/0.45
		-3	0.28	0.7	0.91/0.92	0.33	0.24	0.87/0.85
	7.6	1	0.04	0.92	1.3/1.23	0.05	1.74	1.4/1.32
		-1	1.74	0.08	1.58/1.49	1.66	0.43	1.71/1.52
		-3	0.54	1.92	1.68/2.33	1.31	0.46	2.01/2.61
H_2O	2.3	1	1.24	0.39	6.98/6.99	1.13	<0.01	7.58/6.97
		-1	5.94	2.71	15.57/21.57	2.97	2.33	14.98/19.94
		-3	46.85	18.9	61.14/31.21	40.22	10.37	67.73/28.31
	7.6	1	36.27	2.76	76.63/32.66	39.11	2.07	73.08/33.47
		-1	77.99	2.25	44.77/36.28	74.42	2.09	45.92/37.36
		-3	72.39	91.73	44.84/38.45	83.8	35.76	37.92/38.17
CH_4	2.3	1	0.05	0.1	0.14/0.16	0.04	0.04	0.14/0.15
		-1	0.17	0.11	0.32/0.62	0.11	0.01	0.28/0.59
		-3	0.23	0.65	0.95/0.87	0.28	0.24	0.86/0.87
	7.6	1	0.12	0.02	0.56/0.54	0.14	0.07	0.54/0.57
		-1	0.05	0.46	0.62/0.67	0.01	0.17	0.6/0.65
		-3	2.12	1.18	3.64/1.91	2.15	0.11	3.87/1.86
μ	2.3	1	0.68	1.71	0.12/0.25	0.67	1.71	0.13/0.24
		-1	0.29	1.71	0.48/2.52	0.46	1.71	0.34/1.96
		-3	0.74	1.71	0.33/1.73	0.79	1.71	0.26/1.55
	7.6	1	23.96	10.81	29.23/39.1	24.82	3.02	32.9/45.67
		-1	63.97	23.73	32.51/49.08	60.95	5.55	42.44/51.53
		-3	75.4	61.17	82.93/76.87	150.34	147.01	72.59/28.19

APPENDIX C

Additional material for Chapter 5

In this Appendix Equations 5.5 will be derived.

Let us consider a Cartesian orthogonal reference frame having its origin in the barycentre of the star O and the Z axis along the stellar spin axis. The XY plane is define in such a way as to contain the line of sight, indicated as z (see Figure C.1). Indicating the latitude and the longitude of a point P on the surface of the star with (ϕ,λ), it has the Cartesian coordinate

$$P \equiv (X, Y, Z) = R_*(\cos\phi\cos\lambda, \cos\phi\sin\lambda, \sin\phi) \tag{C.1}$$

where R_* is the radius of the star assumed to be spherically symmetric. In our fixes reference frame, the longitude λ is increasing versus the time t because of the stellar rotation. It changes according to

$$\lambda = \lambda_0 + \Omega_*(t - t_0) \tag{C.2}$$

where λ_0 is the longitude at the initial time t_0 and $\Omega_* \equiv 2\pi/P_{rot}$ is the stellar angular velocity of rotation with P_{rot} the rotation period.

To obtain the coordinate in the reference frame adopted in this work, we first make a rotation of the angle i around the Y axis, where i is the inclination of the stellar spin to the line of sight z. This brings the xy plane in the plane of the sky that is the same plane of the stellar disc. The equation of such a rotation are

$$x = X\cos i - Z\sin i \tag{C.3}$$
$$y = Y \tag{C.4}$$
$$z = X\sin i + Z\cos i \tag{C.5}$$

This gives

$$x = R_*(\cos\phi\cos i\cos\lambda - \sin\phi\sin i) \tag{C.6}$$
$$y = R_*\cos\phi\sin\lambda \tag{C.7}$$
$$z = R_*(\cos\phi\sin i\cos\lambda + \sin\phi\cos i) \tag{C.8}$$

The unit vector along the spin axis of the star in the $OXYZ$ reference frame is $\hat{\Omega}_* \equiv \hat{Z} \equiv (0, 0, 1)$. Transforming it to the $Oxyz$ reference frame, it becomes $(-\sin i, 0, \cos i)$. Since the z axis is directed along the line f sight, the projection of the spin axis onto the plane of the sky xy, that is, the plane of the stellar disc, is $(-\sin i, 0)$. The reference frame adopted in the model to describe the disc of the star has the x_0 axis orthogonal to the projection of the spin axis on the plane of the sky and the y_0 axis along that projection. This implies that our $x_0 = y$ and $y_0 = -x$ because the projection of the spin axis in the plane of the stellar disc is opposite to the orientation of our x axis, give that its component along our x axis is $-\sin i < 0$ for $0° \leq i \leq 180°$.

In conclusion, we find

$$x_0 = R_* \cos\phi \sin\lambda \tag{C.9}$$

$$y_0 = R_*(\sin\phi \sin i - \cos\phi \cos i \cos\lambda) \tag{C.10}$$

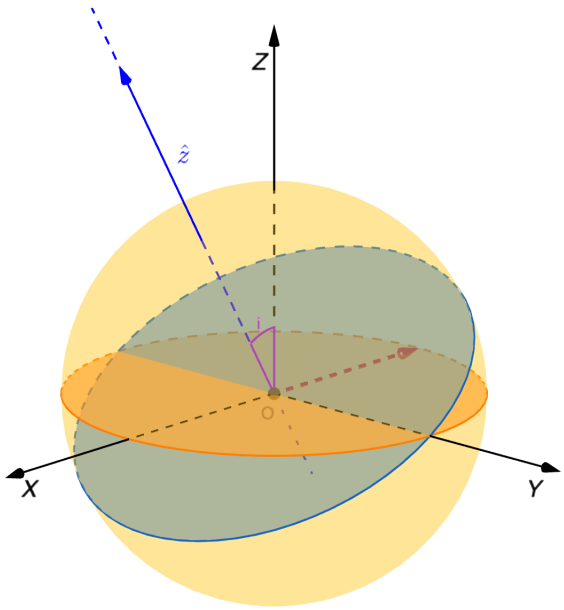

Figure C.1: *The OXYZ reference frame with its origin in the barycentre O of the star, the Z along the stellar spin axis Ω_*, and the XZ plane oriented as to contain the line of sight $\hat{z}$. The inclination of the stellar spin axis to the line of sight is indicated with i. The red vector indicate the projection of the rotation axis over the plan of the sky, that is the plane xy of the reference frame Oxyz, obtained from OXYZ by making a rotation of the angle i along the Y axis. Note that the projection of the spin axis onto the xy plane is opposite to the positive direction of the x axis because the angle i is taken positive (counter-clockwise) from the spin axis to the line of sight.*

APPENDIX D

Additional material for Chapter 6

D.1 Data

Table D.1: *HARPS and HARPS-N AD Leonis observations.*

Dataset HARPS and HARPS-N			
ID obs.	Date obs.	ID obs.	Date obs.
0	2006-01-23T05:50:40.777	49	2018-05-09T22:32:35.186
1	2006-01-25T05:51:44.132	50	2018-05-09T23:47:46.114
2	2006-01-26T06:28:08.689	51	2018-05-10T22:27:20.700
3	2006-02-17T05:08:51.940	52	2018-05-10T23:39:34.923
4	2006-02-19T05:10:02.902	53	2018-05-12T22:05:00.407
5	2006-03-15T03:35:31.947	54	2018-05-12T23:45:11.480
6	2006-03-16T03:59:36.755	55	2018-05-13T22:25:29.185
7	2006-03-17T03:57:09.285	56	2018-05-13T23:56:32.158
8	2006-03-18T03:41:26.807	57	2018-05-14T22:30:43.244
9	2006-03-19T03:33:55.815	58	2018-05-15T00:01:09.165
10	2006-03-20T03:27:16.811	59	2018-05-15T21:11:35.361
11	2006-03-21T01:26:51.761	60	2018-05-15T23:30:22.494
12	2006-03-21T02:40:26.046	61	2018-05-27T20:59:25.662
13	2006-03-21T05:24:18.323	62	2018-05-27T21:24:55.599
14	2006-03-22T00:48:00.516	63	2018-05-27T22:56:06.024
15	2006-03-22T03:29:23.648	64	2018-05-28T21:03:58.534
16	2006-03-22T05:04:07.360	65	2018-05-28T21:23:35.972
17	2006-03-23T00:57:34.300	66	2018-05-28T21:34:03.413
18	2006-03-23T03:57:20.767	67	2018-05-29T21:15:42.131
19	2006-04-04T02:31:22.549	68	2018-05-29T22:53:49.473
20	2006-04-05T00:43:43.084	69	2018-05-30T21:28:00.923
21	2006-04-06T03:50:55.581	70	2018-05-31T21:28:09.476
22	2006-04-07T03:22:37.338	71	2018-06-02T21:17:36.977
23	2006-04-08T02:49:45.071	72	2018-06-05T21:26:30.380
24	2006-04-09T02:26:12.065	73	2018-06-07T21:24:36.344
25	2006-04-10T03:30:17.109	74	2018-06-09T22:22:20.949
26	2006-04-11T02:34:49.554	75	2018-11-16T05:57:05.053
27	2006-05-06T02:04:42.614	76	2018-11-26T06:04:08.981
28	2006-05-08T01:30:29.280	77	2018-11-27T06:04:27.010
29	2006-05-09T00:39:34.279	78	2018-11-29T06:21:38.890
30	2006-05-12T00:51:00.460	79	2018-12-01T04:07:57.348
31	2006-05-13T00:17:03.541	80	2018-12-01T06:07:14.296
32	2006-05-16T01:21:13.214	81	2018-12-22T03:05:48.342
33	2018-04-04T22:41:25.606	82	2018-12-29T06:11:43.793
34	2018-04-05T22:45:01.749	83	2018-12-30T06:45:42.584
35	2018-04-06T21:39:55.987	84	2018-12-31T07:03:15.062
36	2018-04-07T22:36:04.836	85	2019-01-01T03:32:58.198
37	2018-04-27T23:11:22.072	86	2019-01-03T07:08:57.897
38	2018-04-29T21:16:07.356	87	2019-01-04T04:39:46.320
39	2018-04-29T21:34:24.920	88	2019-01-05T04:41:12.333
40	2018-04-29T22:03:09.306	89	2019-01-08T01:19:55.980
41	2018-04-30T00:48:30.207	90	2019-01-09T01:22:25.777
42	2018-05-03T21:36:00.027	91	2019-01-12T06:01:49.512
43	2018-05-04T21:55:50.636	92	2019-01-19T01:13:58.959
44	2018-05-04T23:46:58.038	93	2019-01-20T03:38:34.651
45	2018-05-05T23:58:38.798	94	2019-01-21T02:30:12.323
46	2018-05-06T21:50:35.356	95	2019-01-25T03:28:00.107
47	2018-05-06T23:32:25.529	96	2019-01-28T02:08:17.490
48	2018-05-07T22:04:47.710		

Table D.2: *Equivalent width of the analysed activity indicators obtained from HARPS Data 2006*

Equivalent Width HARPS Data 2006									
ID Obs.	EW$_{H\alpha}$ (Å)	EW$_{H\beta}$ (Å)	EW$_{CaIIH}$ (Å)	EW$_{CaIIK}$ (Å)	EW$_{CaII}$ (Å)	EW$_{HeI4026}$ (Å)	EW$_{HeI4471}$ (Å)	EW$_{HeI5876}$ (Å)	EW$_{NaI}$ (Å)
0	3.40 ± 0.09	3.43 ± 0.10	10.86 ± 0.09	18.92 ± 0.17	12.47 ± 0.08	0.407 ± 0.004	0.126 ± 0.016	0.059 ± 0.017	0.36 ± 0.03
1	4.30 ± 0.10	4.64 ± 0.09	10.8 ± 0.2	21.04 ± 0.15	18.11 ± 0.12	0.720 ± 0.012	0.163 ± 0.015	0.102 ± 0.017	0.45 ± 0.03
2	3.45 ± 0.09	3.60 ± 0.11	10.74 ± 0.04	18.6 ± 0.2	10.91 ± 0.04	0.439 ± 0.013	0.126 ± 0.017	0.069 ± 0.018	0.36 ± 0.02
3	3.68 ± 0.09	3.79 ± 0.08	9.50 ± 0.14	18.27 ± 0.19	12.41 ± 0.11	0.577 ± 0.014	0.131 ± 0.011	0.079 ± 0.018	0.40 ± 0.03
4	3.27 ± 0.09	3.24 ± 0.11	11.13 ± 0.06	18.24 ± 0.08	13.76 ± 0.05	0.489 ± 0.011	0.103 ± 0.015	0.045 ± 0.017	0.33 ± 0.03
5	3.35 ± 0.09	3.36 ± 0.10	10.25 ± 0.06	16.97 ± 0.09	12.16 ± 0.05	0.446 ± 0.013	0.107 ± 0.015	0.062 ± 0.017	0.37 ± 0.02
6	7.07 ± 0.10	7.09 ± 0.12	10.53 ± 0.17	21.2 ± 0.3	13.74 ± 0.14	1.020 ± 0.014	0.20 ± 0.02	0.155 ± 0.017	0.58 ± 0.03
7	4.39 ± 0.09	4.46 ± 0.09	10.10 ± 0.08	18.27 ± 0.08	13.89 ± 0.06	0.659 ± 0.013	0.157 ± 0.013	0.100 ± 0.017	0.45 ± 0.03
8	3.84 ± 0.09	4.15 ± 0.10	11.07 ± 0.09	20.6 ± 0.2	12.24 ± 0.09	0.661 ± 0.014	0.129 ± 0.017	0.083 ± 0.017	0.44 ± 0.03
9	4.00 ± 0.09	3.86 ± 0.08	7.76 ± 0.04	16.27 ± 0.07	9.96 ± 0.03	0.579 ± 0.013	0.162 ± 0.014	0.098 ± 0.017	0.45 ± 0.03
10	3.22 ± 0.09	3.20 ± 0.11	10.22 ± 0.08	20.23 ± 0.18	12.04 ± 0.08	0.409 ± 0.015	0.14 ± 0.02	0.043 ± 0.018	0.35 ± 0.02
11	3.50 ± 0.09	3.43 ± 0.09	9.34 ± 0.07	15.65 ± 0.13	10.70 ± 0.06	0.456 ± 0.014	0.125 ± 0.014	0.052 ± 0.017	0.37 ± 0.02
12	3.45 ± 0.10	3.53 ± 0.09	9.61 ± 0.03	18.20 ± 0.12	10.28 ± 0.03	0.491 ± 0.015	0.125 ± 0.014	0.070 ± 0.017	0.40 ± 0.03
13	3.49 ± 0.09	3.45 ± 0.11	10.56 ± 0.04	18.2 ± 0.3	10.69 ± 0.04	0.458 ± 0.014	0.11 ± 0.02	0.058 ± 0.017	0.40 ± 0.03
14	3.79 ± 0.10	4.03 ± 0.08	9.78 ± 0.15	17.7 ± 0.2	12.50 ± 0.12	0.534 ± 0.016	0.147 ± 0.017	0.083 ± 0.018	0.44 ± 0.03
15	3.47 ± 0.09	3.48 ± 0.10	10.68 ± 0.04	18.54 ± 0.10	11.85 ± 0.04	0.466 ± 0.016	0.11 ± 0.02	0.047 ± 0.018	0.37 ± 0.03
16	3.53 ± 0.09	3.55 ± 0.11	10.21 ± 0.11	17.9 ± 0.2	11.78 ± 0.09	0.461 ± 0.015	0.113 ± 0.018	0.060 ± 0.018	0.38 ± 0.02
17	3.65 ± 0.09	3.80 ± 0.09	9.89 ± 0.07	18.20 ± 0.06	14.14 ± 0.05	0.484 ± 0.017	0.147 ± 0.015	0.088 ± 0.018	0.42 ± 0.02
18	4.09 ± 0.09	4.52 ± 0.09	10.67 ± 0.05	18.29 ± 0.07	13.66 ± 0.04	0.695 ± 0.017	0.157 ± 0.015	0.104 ± 0.017	0.48 ± 0.03
19	3.68 ± 0.09	3.85 ± 0.10	10.33 ± 0.05	17.94 ± 0.06	13.51 ± 0.04	0.541 ± 0.015	0.142 ± 0.019	0.081 ± 0.017	0.44 ± 0.03
20	5.14 ± 0.09	5.48 ± 0.07	7.97 ± 0.06	15.2 ± 0.3	8.27 ± 0.06	0.914 ± 0.016	0.187 ± 0.012	0.147 ± 0.017	0.56 ± 0.03
21	3.37 ± 0.09	3.32 ± 0.11	11.69 ± 0.05	17.91 ± 0.09	13.23 ± 0.04	0.466 ± 0.013	0.108 ± 0.012	0.049 ± 0.017	0.39 ± 0.03
22	3.95 ± 0.09	3.98 ± 0.11	9.68 ± 0.10	16.51 ± 0.10	13.10 ± 0.07	0.560 ± 0.014	0.152 ± 0.013	0.087 ± 0.017	0.42 ± 0.02
23	3.38 ± 0.09	3.54 ± 0.10	10.17 ± 0.06	17.60 ± 0.08	13.00 ± 0.05	0.473 ± 0.013	0.137 ± 0.019	0.070 ± 0.018	0.39 ± 0.03
24	5.97 ± 0.09	5.49 ± 0.11	5.056 ± 0.011	14.69 ± 0.14	5.114 ± 0.011	0.611 ± 0.005	0.243 ± 0.019	0.199 ± 0.019	0.66 ± 0.03
25	3.57 ± 0.09	3.66 ± 0.11	10.95 ± 0.04	18.1 ± 0.2	11.17 ± 0.04	0.508 ± 0.013	0.138 ± 0.018	0.075 ± 0.018	0.41 ± 0.03
26	3.27 ± 0.09	3.23 ± 0.11	10.78 ± 0.06	17.75 ± 0.06	14.25 ± 0.04	0.346 ± 0.003	0.118 ± 0.018	0.056 ± 0.017	0.38 ± 0.03
27	3.37 ± 0.09	3.41 ± 0.10	9.99 ± 0.09	18.29 ± 0.10	13.64 ± 0.07	0.488 ± 0.011	0.141 ± 0.014	0.073 ± 0.018	0.40 ± 0.03
28	4.18 ± 0.09	4.49 ± 0.06	8.20 ± 0.10	18.9 ± 0.2	9.79 ± 0.09	0.709 ± 0.013	0.171 ± 0.018	0.143 ± 0.017	0.56 ± 0.03
29	3.62 ± 0.09	3.80 ± 0.09	10.10 ± 0.11	18.14 ± 0.05	16.51 ± 0.05	0.537 ± 0.012	0.144 ± 0.016	0.068 ± 0.018	0.41 ± 0.03
30	3.59 ± 0.09	3.51 ± 0.07	8.80 ± 0.02	15.90 ± 0.08	9.44 ± 0.02	0.483 ± 0.011	0.15 ± 0.03	0.074 ± 0.017	0.40 ± 0.03
31	3.63 ± 0.09	3.77 ± 0.10	10.46 ± 0.05	18.6 ± 0.2	10.81 ± 0.05	0.536 ± 0.012	0.125 ± 0.016	0.078 ± 0.018	0.43 ± 0.03
32	3.58 ± 0.09	3.75 ± 0.10	10.55 ± 0.06	17.9 ± 0.2	11.01 ± 0.06	0.539 ± 0.012	0.14 ± 0.02	0.074 ± 0.017	0.41 ± 0.03

Table D.3: *Equivalent width of the analysed activity indicators obtained from HARPS-N Data 2018*

Equivalent Width HARPS-N Data 2018									
ID Obs.	$EW_{H\alpha}$ (Å)	$EW_{H\beta}$ (Å)	EW_{CaIIH} (Å)	EW_{CaIIK} (Å)	EW_{CaII} (Å)	$EW_{HeI4026}$ (Å)	$EW_{HeI4471}$ (Å)	$EW_{HeI5876}$ (Å)	EW_{NaI} (Å)
33	5.23 ± 0.10	5.67 ± 0.15	12.95 ± 0.06	20.2 ± 0.3	13.29 ± 0.06	0.898 ± 0.013	0.190 ± 0.014	0.135 ± 0.017	0.59 ± 0.03
34	4.68 ± 0.09	4.79 ± 0.10	11.77 ± 0.07	20.04 ± 0.13	13.51 ± 0.06	0.770 ± 0.012	0.180 ± 0.014	0.110 ± 0.017	0.50 ± 0.03
35	5.12 ± 0.10	4.99 ± 0.06	8.7 ± 0.5	19.0 ± 1.5	9.5 ± 0.4	0.663 ± 0.017	0.20 ± 0.06	0.20 ± 0.02	0.60 ± 0.02
36	4.09 ± 0.09	4.10 ± 0.07	8.95 ± 0.03	15.74 ± 0.15	9.15 ± 0.03	0.594 ± 0.012	0.162 ± 0.015	0.100 ± 0.017	0.46 ± 0.03
37	4.32 ± 0.10	4.63 ± 0.09	11.63 ± 0.12	17.10 ± 0.10	14.87 ± 0.08	0.760 ± 0.011	0.174 ± 0.014	0.100 ± 0.017	0.48 ± 0.03
38	4.69 ± 0.10	4.99 ± 0.09	9.76 ± 0.06	18.74 ± 0.17	10.79 ± 0.06	0.780 ± 0.012	0.197 ± 0.019	0.130 ± 0.017	0.54 ± 0.03
39	4.47 ± 0.09	4.74 ± 0.10	10.90 ± 0.09	18.71 ± 0.18	12.50 ± 0.08	0.730 ± 0.012	0.179 ± 0.013	0.119 ± 0.016	0.50 ± 0.03
40	4.32 ± 0.09	4.63 ± 0.10	11.70 ± 0.05	20.15 ± 0.10	13.54 ± 0.05	0.686 ± 0.012	0.182 ± 0.013	0.110 ± 0.017	0.49 ± 0.03
41	4.34 ± 0.09	4.49 ± 0.09	10.51 ± 0.11	17.81 ± 0.12	14.00 ± 0.08	0.536 ± 0.008	0.165 ± 0.016	0.100 ± 0.017	0.46 ± 0.03
42	4.37 ± 0.10	4.57 ± 0.09	12.53 ± 0.08	16.0 ± 0.3	12.79 ± 0.08	0.650 ± 0.013	0.174 ± 0.018	0.104 ± 0.017	0.47 ± 0.02
43	4.17 ± 0.09	4.39 ± 0.08	9.20 ± 0.03	16.43 ± 0.09	9.93 ± 0.03	0.452 ± 0.003	0.165 ± 0.019	0.112 ± 0.018	0.47 ± 0.03
44	3.90 ± 0.09	3.91 ± 0.10	11.40 ± 0.14	16.4 ± 0.2	12.95 ± 0.12	0.591 ± 0.013	0.126 ± 0.017	0.078 ± 0.017	0.43 ± 0.03
45	5.06 ± 0.10	4.53 ± 0.06	5.24 ± 0.05	6.91 ± 0.08	5.70 ± 0.04	0.726 ± 0.013	0.20 ± 0.02	0.144 ± 0.016	0.52 ± 0.03
46	4.24 ± 0.09	4.53 ± 0.10	11.39 ± 0.08	17.47 ± 0.13	13.02 ± 0.07	0.686 ± 0.012	0.15 ± 0.02	0.103 ± 0.017	0.49 ± 0.03
47	4.11 ± 0.10	4.41 ± 0.10	12.27 ± 0.06	17.82 ± 0.15	13.00 ± 0.06	0.497 ± 0.004	0.170 ± 0.017	0.099 ± 0.017	0.47 ± 0.03
48	4.06 ± 0.09	4.24 ± 0.09	12.17 ± 0.05	18.28 ± 0.10	13.46 ± 0.05	0.613 ± 0.013	0.163 ± 0.014	0.094 ± 0.017	0.45 ± 0.03
49	4.49 ± 0.09	4.79 ± 0.09	11.02 ± 0.11	16.79 ± 0.19	12.47 ± 0.10	0.790 ± 0.010	0.182 ± 0.014	0.113 ± 0.016	0.49 ± 0.03
50	4.96 ± 0.10	5.19 ± 0.07	8.72 ± 0.03	18.04 ± 0.09	9.51 ± 0.03	0.899 ± 0.011	0.228 ± 0.015	0.166 ± 0.016	0.56 ± 0.03
51	4.30 ± 0.10	4.63 ± 0.09	10.81 ± 0.10	18.65 ± 0.19	12.38 ± 0.09	0.814 ± 0.011	0.183 ± 0.018	0.109 ± 0.017	0.50 ± 0.03
52	4.31 ± 0.10	4.45 ± 0.11	12.25 ± 0.19	16.3 ± 0.2	13.99 ± 0.14	0.750 ± 0.010	0.116 ± 0.017	0.085 ± 0.018	0.45 ± 0.03
53	3.97 ± 0.09	4.14 ± 0.08	10.19 ± 0.10	16.6 ± 0.2	11.39 ± 0.09	0.489 ± 0.006	0.152 ± 0.016	0.091 ± 0.018	0.47 ± 0.03
54	3.60 ± 0.10	3.64 ± 0.09	12.12 ± 0.14	16.97 ± 0.17	14.20 ± 0.11	0.563 ± 0.009	0.124 ± 0.015	0.067 ± 0.017	0.39 ± 0.03
55	5.00 ± 0.10	5.12 ± 0.06	7.78 ± 0.04	15.83 ± 0.13	8.32 ± 0.03	0.892 ± 0.010	0.203 ± 0.016	0.156 ± 0.017	0.59 ± 0.03
56	4.95 ± 0.10	5.45 ± 0.07	9.91 ± 0.04	16.8 ± 0.2	10.14 ± 0.04	0.906 ± 0.010	0.22 ± 0.02	0.150 ± 0.017	0.57 ± 0.03
57	4.01 ± 0.09	4.18 ± 0.10	11.71 ± 0.09	17.96 ± 0.14	13.56 ± 0.08	0.471 ± 0.004	0.148 ± 0.013	0.093 ± 0.017	0.45 ± 0.03
58	3.81 ± 0.10	3.94 ± 0.09	11.6 ± 0.3	17.35 ± 0.12	16.65 ± 0.11	0.610 ± 0.012	0.142 ± 0.013	0.083 ± 0.016	0.43 ± 0.03
59	3.98 ± 0.09	4.15 ± 0.10	12.01 ± 0.12	15.14 ± 0.12	13.54 ± 0.09	0.621 ± 0.012	0.136 ± 0.018	0.077 ± 0.017	0.45 ± 0.03
60	3.80 ± 0.10	3.87 ± 0.10	11.08 ± 0.06	13.63 ± 0.08	12.03 ± 0.05	0.628 ± 0.011	0.154 ± 0.014	0.082 ± 0.018	0.42 ± 0.03
61	4.33 ± 0.10	4.54 ± 0.09	9.92 ± 0.04	16.07 ± 0.16	10.30 ± 0.04	0.601 ± 0.007	0.178 ± 0.015	0.110 ± 0.016	0.50 ± 0.02
62	4.14 ± 0.09	4.33 ± 0.09	11.34 ± 0.07	17.9 ± 0.3	11.72 ± 0.07	0.659 ± 0.012	0.153 ± 0.016	0.099 ± 0.016	0.48 ± 0.03
63	3.88 ± 0.09	4.00 ± 0.10	12.0 ± 0.3	17.01 ± 0.17	15.49 ± 0.14	0.606 ± 0.012	0.15 ± 0.02	0.080 ± 0.017	0.43 ± 0.03
64	4.23 ± 0.09	4.17 ± 0.10	10.15 ± 0.08	17.47 ± 0.09	13.50 ± 0.06	0.614 ± 0.011	0.161 ± 0.015	0.099 ± 0.017	0.45 ± 0.03
65	4.13 ± 0.10	3.93 ± 0.09	9.48 ± 0.06	15.97 ± 0.12	10.87 ± 0.05	0.612 ± 0.011	0.161 ± 0.019	0.096 ± 0.017	0.43 ± 0.03
66	4.15 ± 0.10	3.96 ± 0.07	8.69 ± 0.09	18.1 ± 0.2	10.03 ± 0.08	0.465 ± 0.004	0.169 ± 0.018	0.119 ± 0.017	0.47 ± 0.03
67	4.22 ± 0.10	4.39 ± 0.11	13.1 ± 0.4	14.06 ± 0.10	14.00 ± 0.10	0.541 ± 0.006	0.19 ± 0.02	0.109 ± 0.018	0.51 ± 0.03
68	4.20 ± 0.10	4.31 ± 0.10	16.8 ± 1.9	12.6 ± 0.8	13.2 ± 0.7	0.561 ± 0.015	0.13 ± 0.05	0.121 ± 0.019	0.48 ± 0.03
69	4.09 ± 0.09	4.14 ± 0.09	10.07 ± 0.09	18.12 ± 0.11	13.31 ± 0.07	0.477 ± 0.005	0.165 ± 0.018	0.091 ± 0.017	0.45 ± 0.03
70	4.81 ± 0.09	5.28 ± 0.08	11.25 ± 0.04	18.52 ± 0.09	12.27 ± 0.03	0.859 ± 0.011	0.201 ± 0.014	0.134 ± 0.016	0.56 ± 0.03
71	3.80 ± 0.09	3.90 ± 0.10	12.03 ± 0.11	17.44 ± 0.16	13.82 ± 0.09	0.591 ± 0.013	0.138 ± 0.017	0.073 ± 0.018	0.42 ± 0.03
72	4.00 ± 0.09	4.08 ± 0.09	9.76 ± 0.03	17.12 ± 0.14	10.16 ± 0.03	0.642 ± 0.010	0.150 ± 0.018	0.099 ± 0.017	0.45 ± 0.03
73	4.59 ± 0.10	4.59 ± 0.07	8.60 ± 0.04	14.49 ± 0.09	9.71 ± 0.04	0.506 ± 0.003	0.187 ± 0.015	0.119 ± 0.016	0.48 ± 0.03
74	4.08 ± 0.09	4.33 ± 0.08	12.31 ± 0.07	19.27 ± 0.17	13.36 ± 0.07	0.686 ± 0.012	0.155 ± 0.016	0.088 ± 0.017	0.45 ± 0.03
75	4.21 ± 0.10	4.47 ± 0.10	11.93 ± 0.08	19.08 ± 0.17	13.26 ± 0.07	0.586 ± 0.013	0.139 ± 0.014	0.098 ± 0.018	0.49 ± 0.03
76	3.85 ± 0.10	4.01 ± 0.09	10.60 ± 0.04	17.86 ± 0.10	11.65 ± 0.04	0.552 ± 0.012	0.175 ± 0.015	0.091 ± 0.018	0.45 ± 0.03
77	3.64 ± 0.10	3.83 ± 0.10	10.75 ± 0.06	17.22 ± 0.08	12.95 ± 0.05	0.502 ± 0.013	0.123 ± 0.016	0.075 ± 0.017	0.45 ± 0.03
78	3.97 ± 0.09	3.77 ± 0.06	6.61 ± 0.07	11.14 ± 0.10	7.99 ± 0.06	0.427 ± 0.011	0.157 ± 0.014	0.104 ± 0.016	0.51 ± 0.03
79	8.97 ± 0.09	17.6 ± 0.5	1.699 ± 0.006	5.60 ± 0.08	1.73 ± 0.01	1.066 ± 0.006	0.239 ± 0.008	0.41 ± 0.04	1.44 ± 0.04
80	7.15 ± 0.11	8.13 ± 0.07	9.71 ± 0.02	19.8 ± 0.3	9.76 ± 0.02	1.467 ± 0.014	0.318 ± 0.019	0.27 ± 0.02	0.87 ± 0.04
81	4.19 ± 0.10	4.03 ± 0.10	11.07 ± 0.09	17.09 ± 0.09	13.98 ± 0.06	0.547 ± 0.012	0.144 ± 0.018	0.075 ± 0.017	0.42 ± 0.03
82	4.09 ± 0.10	4.19 ± 0.07	9.10 ± 0.05	16.43 ± 0.11	10.43 ± 0.05	0.461 ± 0.003	0.173 ± 0.019	0.107 ± 0.017	0.48 ± 0.03
83	3.49 ± 0.09	3.57 ± 0.10	10.99 ± 0.09	16.84 ± 0.09	13.86 ± 0.06	0.509 ± 0.013	0.13 ± 0.02	0.060 ± 0.018	0.40 ± 0.03
84	4.02 ± 0.10	4.29 ± 0.08	10.21 ± 0.08	17.41 ± 0.09	13.31 ± 0.06	0.651 ± 0.012	0.165 ± 0.019	0.107 ± 0.017	0.49 ± 0.03
85	3.75 ± 0.10	3.97 ± 0.09	11.13 ± 0.08	16.16 ± 0.12	12.60 ± 0.06	0.533 ± 0.013	0.165 ± 0.018	0.076 ± 0.017	0.45 ± 0.03
86	3.96 ± 0.10	4.21 ± 0.11	11.14 ± 0.11	18.7 ± 0.3	12.21 ± 0.11	0.591 ± 0.013	0.152 ± 0.017	0.096 ± 0.018	0.48 ± 0.03
87	3.90 ± 0.10	4.05 ± 0.10	11.04 ± 0.10	18.19 ± 0.10	14.37 ± 0.07	0.555 ± 0.012	0.152 ± 0.016	0.088 ± 0.017	0.45 ± 0.03
88	4.32 ± 0.10	4.79 ± 0.08	10.81 ± 0.04	19.07 ± 0.10	12.00 ± 0.04	0.682 ± 0.014	0.181 ± 0.019	0.124 ± 0.018	0.55 ± 0.03
89	4.17 ± 0.10	4.34 ± 0.11	12.24 ± 0.07	17.37 ± 0.12	13.68 ± 0.06	0.668 ± 0.013	0.159 ± 0.019	0.092 ± 0.017	0.48 ± 0.03
90	3.95 ± 0.10	4.16 ± 0.09	12.19 ± 0.11	18.13 ± 0.10	15.37 ± 0.08	0.599 ± 0.012	0.169 ± 0.018	0.086 ± 0.017	0.46 ± 0.03
91	3.93 ± 0.09	3.90 ± 0.06	6.80 ± 0.08	12.74 ± 0.14	8.42 ± 0.07	0.573 ± 0.012	0.166 ± 0.012	0.099 ± 0.016	0.45 ± 0.03
92	4.63 ± 0.10	4.67 ± 0.09	10.71 ± 0.18	17.5 ± 0.2	13.46 ± 0.14	0.534 ± 0.006	0.181 ± 0.013	0.112 ± 0.017	0.49 ± 0.03
93	4.79 ± 0.10	4.71 ± 0.08	9.88 ± 0.07	15.69 ± 0.11	11.54 ± 0.06	0.552 ± 0.014	0.160 ± 0.012	0.095 ± 0.017	0.45 ± 0.03
94	3.84 ± 0.10	4.13 ± 0.08	9.49 ± 0.03	15.88 ± 0.14	9.80 ± 0.03	0.582 ± 0.013	0.153 ± 0.016	0.099 ± 0.017	0.48 ± 0.03
95	4.60 ± 0.09	4.74 ± 0.10	10.74 ± 0.10	14.71 ± 0.13	12.34 ± 0.08	0.693 ± 0.015	0.166 ± 0.016	0.115 ± 0.017	0.50 ± 0.03
96	3.76 ± 0.09	3.87 ± 0.11	11.17 ± 0.13	16.24 ± 0.14	13.39 ± 0.10	0.547 ± 0.013	0.127 ± 0.017	0.076 ± 0.018	0.42 ± 0.03

Table D.4: *Fluxes of the analysed activity indicators obtained from HARPS Data 2006*

Fluxes HARPS Data 2006					
ID Obs.	$Flx_{H\alpha}$ (10^5 erg s^{-1} cm^{-2})	$Flx_{H\beta}$ (10^5 erg s^{-1} cm^{-2})	Flx_{CaIIH} (10^5 erg s^{-1} cm^{-2})	Flx_{CaIIK} (10^5 erg s^{-1} cm^{-2})	Flx_{CaII} (10^5 erg s^{-1} cm^{-2})
0	9.24 ± 0.19	5.03 ± 0.09	4.817 ± 0.008	4.905 ± 0.009	4.857 ± 0.006
1	11.59 ± 0.20	6.84 ± 0.08	6.580 ± 0.016	6.678 ± 0.008	6.661 ± 0.007
2	9.32 ± 0.19	5.33 ± 0.10	5.503 ± 0.007	5.668 ± 0.012	5.545 ± 0.006
3	9.82 ± 0.19	5.76 ± 0.08	5.274 ± 0.012	4.941 ± 0.008	5.042 ± 0.007
4	8.79 ± 0.19	4.78 ± 0.11	5.163 ± 0.007	5.035 ± 0.007	5.098 ± 0.005
5	9.05 ± 0.18	4.89 ± 0.10	5.876 ± 0.009	6.044 ± 0.008	5.968 ± 0.006
6	18.32 ± 0.18	11.05 ± 0.08	8.742 ± 0.017	8.242 ± 0.014	8.437 ± 0.011
7	11.77 ± 0.18	6.69 ± 0.09	6.230 ± 0.008	6.183 ± 0.007	6.204 ± 0.005
8	10.36 ± 0.19	6.31 ± 0.09	5.436 ± 0.008	5.623 ± 0.009	5.518 ± 0.006
9	10.79 ± 0.19	6.04 ± 0.08	4.966 ± 0.007	5.208 ± 0.007	5.089 ± 0.005
10	8.72 ± 0.19	4.70 ± 0.11	5.828 ± 0.008	6.205 ± 0.008	6.003 ± 0.006
11	9.45 ± 0.20	5.01 ± 0.09	5.683 ± 0.011	5.846 ± 0.009	5.781 ± 0.007
12	9.34 ± 0.20	5.19 ± 0.09	5.700 ± 0.007	5.417 ± 0.008	5.579 ± 0.006
13	9.48 ± 0.19	5.13 ± 0.10	5.400 ± 0.008	5.621 ± 0.013	5.455 ± 0.007
14	10.27 ± 0.20	6.00 ± 0.07	5.928 ± 0.014	6.325 ± 0.013	6.140 ± 0.010
15	9.39 ± 0.20	5.09 ± 0.10	5.163 ± 0.007	5.010 ± 0.007	5.082 ± 0.005
16	9.61 ± 0.18	5.25 ± 0.10	6.022 ± 0.010	6.027 ± 0.012	6.024 ± 0.008
17	9.91 ± 0.19	5.64 ± 0.09	6.324 ± 0.009	6.603 ± 0.007	6.491 ± 0.006
18	11.05 ± 0.18	6.78 ± 0.08	6.727 ± 0.009	6.550 ± 0.007	6.619 ± 0.005
19	9.94 ± 0.18	5.62 ± 0.09	5.681 ± 0.008	5.609 ± 0.005	5.627 ± 0.004
20	13.73 ± 0.18	9.09 ± 0.05	7.351 ± 0.014	7.37 ± 0.02	7.357 ± 0.012
21	9.09 ± 0.18	4.83 ± 0.11	4.864 ± 0.007	4.972 ± 0.007	4.916 ± 0.005
22	10.63 ± 0.18	5.89 ± 0.10	5.597 ± 0.010	5.687 ± 0.008	5.649 ± 0.006
23	9.16 ± 0.18	5.15 ± 0.10	4.810 ± 0.007	4.826 ± 0.005	4.821 ± 0.004
24	15.72 ± 0.17	9.99 ± 0.09	5.718 ± 0.010	5.539 ± 0.011	5.644 ± 0.007
25	9.61 ± 0.19	5.29 ± 0.10	5.102 ± 0.007	5.007 ± 0.009	5.063 ± 0.006
26	8.84 ± 0.18	4.70 ± 0.11	4.600 ± 0.008	4.755 ± 0.003	4.733 ± 0.003
27	9.05 ± 0.19	5.11 ± 0.09	5.836 ± 0.009	5.817 ± 0.006	5.823 ± 0.005
28	11.21 ± 0.18	7.04 ± 0.05	5.837 ± 0.013	5.566 ± 0.011	5.687 ± 0.008
29	9.72 ± 0.19	5.48 ± 0.08	5.785 ± 0.012	5.892 ± 0.005	5.876 ± 0.005
30	9.63 ± 0.18	5.21 ± 0.07	6.186 ± 0.008	6.303 ± 0.007	6.252 ± 0.005
31	9.77 ± 0.19	5.55 ± 0.09	5.635 ± 0.007	5.725 ± 0.012	5.657 ± 0.006
32	9.61 ± 0.18	5.53 ± 0.09	6.178 ± 0.007	6.085 ± 0.012	6.154 ± 0.006

Table D.5: *Fluxes of the analysed activity indicators obtained from HARPS Data 2006 (continued))*

Fluxes HARPS Data 2006				
ID Obs.	$Flx_{HeI4026}$ (10^5 erg s^{-1} cm^{-2})	$Flx_{HeI4471}$ (10^5 erg s^{-1} cm^{-2})	$Flx_{HeI5876}$ (10^5 erg s^{-1} cm^{-2})	Flx_{NaI} (10^5 erg s^{-1} cm^{-2})
0	0.099 ± 0.012	0.073 ± 0.012	0.44 ± 0.03	0.131 ± 0.003
1	0.133 ± 0.011	0.127 ± 0.014	0.55 ± 0.03	0.2686 ± 0.0060
2	0.099 ± 0.013	0.086 ± 0.013	0.44 ± 0.03	0.160 ± 0.007
3	0.106 ± 0.008	0.098 ± 0.013	0.49 ± 0.03	0.200 ± 0.006
4	0.080 ± 0.011	0.055 ± 0.013	0.41 ± 0.03	0.171 ± 0.006
5	0.082 ± 0.012	0.077 ± 0.013	0.44 ± 0.03	0.173 ± 0.007
6	0.174 ± 0.019	0.195 ± 0.018	0.72 ± 0.03	0.415 ± 0.007
7	0.126 ± 0.009	0.126 ± 0.014	0.55 ± 0.03	0.250 ± 0.007
8	0.102 ± 0.012	0.103 ± 0.013	0.53 ± 0.03	0.243 ± 0.007
9	0.132 ± 0.011	0.123 ± 0.015	0.55 ± 0.03	0.215 ± 0.007
10	0.113 ± 0.016	0.053 ± 0.014	0.42 ± 0.03	0.161 ± 0.008
11	0.100 ± 0.011	0.065 ± 0.013	0.45 ± 0.03	0.169 ± 0.007
12	0.099 ± 0.010	0.088 ± 0.013	0.48 ± 0.03	0.183 ± 0.008
13	0.082 ± 0.016	0.072 ± 0.013	0.47 ± 0.03	0.175 ± 0.007
14	0.120 ± 0.013	0.104 ± 0.013	0.53 ± 0.03	0.207 ± 0.008
15	0.083 ± 0.018	0.059 ± 0.014	0.45 ± 0.03	0.183 ± 0.008
16	0.087 ± 0.014	0.073 ± 0.013	0.46 ± 0.03	0.184 ± 0.008
17	0.117 ± 0.011	0.110 ± 0.013	0.51 ± 0.03	0.195 ± 0.009
18	0.130 ± 0.011	0.130 ± 0.014	0.58 ± 0.03	0.267 ± 0.008
19	0.114 ± 0.015	0.101 ± 0.013	0.53 ± 0.03	0.215 ± 0.007
20	0.163 ± 0.008	0.187 ± 0.019	0.71 ± 0.04	0.375 ± 0.007
21	0.079 ± 0.008	0.060 ± 0.013	0.46 ± 0.04	0.177 ± 0.007
22	0.121 ± 0.010	0.107 ± 0.013	0.51 ± 0.03	0.220 ± 0.007
23	0.108 ± 0.015	0.087 ± 0.013	0.47 ± 0.03	0.179 ± 0.007
24	0.217 ± 0.015	0.26 ± 0.03	0.82 ± 0.03	0.222 ± 0.003
25	0.113 ± 0.015	0.092 ± 0.013	0.49 ± 0.03	0.199 ± 0.007
26	0.090 ± 0.015	0.069 ± 0.013	0.45 ± 0.03	0.111 ± 0.003
27	0.115 ± 0.010	0.091 ± 0.013	0.48 ± 0.03	0.176 ± 0.006
28	0.141 ± 0.014	0.180 ± 0.018	0.68 ± 0.03	0.274 ± 0.007
29	0.115 ± 0.012	0.085 ± 0.013	0.50 ± 0.03	0.195 ± 0.007
30	0.129 ± 0.021	0.093 ± 0.012	0.48 ± 0.03	0.180 ± 0.006
31	0.102 ± 0.014	0.096 ± 0.014	0.51 ± 0.03	0.197 ± 0.006
32	0.119 ± 0.017	0.092 ± 0.013	0.49 ± 0.03	0.199 ± 0.007

Table D.6: *Fluxes of the analysed activity indicators obtained from HARPS Data 2018*

Fluxes HARPS-N Data 2018					
ID Obs.	$Flx_{H\alpha}$ (10^5 erg s^{-1} cm^{-2})	$Flx_{H\beta}$ (10^5 erg s^{-1} cm^{-2})	Flx_{CaIIH} (10^5 erg s^{-1} cm^{-2})	Flx_{CaIIK} (10^5 erg s^{-1} cm^{-2})	Flx_{CaII} (10^5 erg s^{-1} cm^{-2})
33	14.04 ± 0.19	8.58 ± 0.11	5.836 ± 0.007	4.717 ± 0.009	5.466 ± 0.005
34	12.60 ± 0.19	7.17 ± 0.08	5.565 ± 0.008	5.131 ± 0.007	5.335 ± 0.005
35	13.78 ± 0.18	8.97 ± 0.05	3.62 ± 0.03	3.03 ± 0.03	3.324 ± 0.018
36	11.08 ± 0.18	6.15 ± 0.07	4.653 ± 0.007	4.331 ± 0.009	4.533 ± 0.006
37	11.7 ± 0.2	6.84 ± 0.08	4.770 ± 0.009	4.224 ± 0.007	4.418 ± 0.005
38	12.6 ± 0.2	7.48 ± 0.08	5.609 ± 0.008	4.946 ± 0.008	5.303 ± 0.006
39	12.00 ± 0.18	7.11 ± 0.09	5.252 ± 0.008	5.120 ± 0.009	5.193 ± 0.006
40	11.64 ± 0.19	6.79 ± 0.08	5.080 ± 0.007	4.848 ± 0.007	4.952 ± 0.005
41	11.71 ± 0.19	6.64 ± 0.08	4.796 ± 0.009	4.535 ± 0.007	4.644 ± 0.006
42	11.77 ± 0.19	6.93 ± 0.09	5.293 ± 0.008	3.826 ± 0.011	4.737 ± 0.007
43	11.23 ± 0.18	6.57 ± 0.08	4.665 ± 0.007	4.420 ± 0.004	4.490 ± 0.004
44	10.53 ± 0.19	5.85 ± 0.09	4.428 ± 0.009	3.657 ± 0.008	4.005 ± 0.006
45	13.57 ± 0.19	7.98 ± 0.05	5.332 ± 0.009	4.146 ± 0.014	4.986 ± 0.008
46	11.49 ± 0.19	6.60 ± 0.08	5.761 ± 0.008	5.004 ± 0.006	5.295 ± 0.005
47	11.16 ± 0.19	6.49 ± 0.09	4.523 ± 0.007	4.135 ± 0.007	4.334 ± 0.005
48	11.03 ± 0.19	6.11 ± 0.08	4.708 ± 0.007	4.573 ± 0.007	4.638 ± 0.005
49	12.10 ± 0.19	7.04 ± 0.08	5.000 ± 0.009	4.816 ± 0.010	4.921 ± 0.007
50	13.33 ± 0.19	8.14 ± 0.05	5.781 ± 0.008	5.339 ± 0.007	5.549 ± 0.005
51	11.6 ± 0.2	6.91 ± 0.08	5.173 ± 0.008	4.667 ± 0.009	4.950 ± 0.006
52	11.6 ± 0.2	6.38 ± 0.10	5.412 ± 0.013	5.525 ± 0.012	5.475 ± 0.009
53	10.71 ± 0.19	6.01 ± 0.07	5.151 ± 0.008	5.003 ± 0.008	5.076 ± 0.006
54	9.8 ± 0.2	5.24 ± 0.08	4.334 ± 0.009	4.203 ± 0.008	4.258 ± 0.006
55	13.39 ± 0.19	8.12 ± 0.06	5.012 ± 0.007	4.416 ± 0.008	4.782 ± 0.005
56	13.26 ± 0.19	8.07 ± 0.05	6.108 ± 0.009	5.755 ± 0.012	5.984 ± 0.007
57	10.87 ± 0.19	6.07 ± 0.09	4.737 ± 0.008	4.686 ± 0.007	4.710 ± 0.005
58	10.3 ± 0.2	5.69 ± 0.08	4.910 ± 0.016	4.721 ± 0.007	4.753 ± 0.006
59	10.78 ± 0.19	5.99 ± 0.09	4.964 ± 0.009	4.660 ± 0.006	4.759 ± 0.005
60	10.2 ± 0.2	5.55 ± 0.09	4.335 ± 0.007	5.270 ± 0.009	4.710 ± 0.006
61	11.62 ± 0.19	6.73 ± 0.08	4.457 ± 0.008	4.222 ± 0.009	4.364 ± 0.006
62	11.19 ± 0.19	6.30 ± 0.08	5.628 ± 0.009	5.189 ± 0.011	5.461 ± 0.007
63	10.49 ± 0.19	5.68 ± 0.09	5.318 ± 0.013	4.849 ± 0.009	4.996 ± 0.007
64	11.45 ± 0.19	6.19 ± 0.09	4.398 ± 0.008	4.189 ± 0.007	4.274 ± 0.005
65	11.22 ± 0.19	5.91 ± 0.09	4.820 ± 0.009	4.297 ± 0.008	4.529 ± 0.006
66	11.2 ± 0.2	6.19 ± 0.07	4.405 ± 0.009	4.332 ± 0.009	4.371 ± 0.006
67	11.4 ± 0.2	6.77 ± 0.10	5.852 ± 0.018	5.921 ± 0.007	5.912 ± 0.007
68	11.4 ± 0.2	6.08 ± 0.08	8.21 ± 0.07	6.47 ± 0.05	7.05 ± 0.04
69	11.04 ± 0.19	6.12 ± 0.09	4.431 ± 0.009	4.069 ± 0.007	4.203 ± 0.005
70	12.91 ± 0.19	7.93 ± 0.07	5.395 ± 0.007	5.125 ± 0.007	5.270 ± 0.005
71	10.34 ± 0.19	5.57 ± 0.09	4.596 ± 0.009	4.078 ± 0.007	4.280 ± 0.006
72	10.86 ± 0.19	6.02 ± 0.08	4.463 ± 0.007	4.316 ± 0.008	4.400 ± 0.005
73	12.36 ± 0.19	6.86 ± 0.06	5.155 ± 0.007	5.021 ± 0.009	5.104 ± 0.005
74	11.06 ± 0.18	6.35 ± 0.07	5.011 ± 0.008	4.849 ± 0.008	4.939 ± 0.006
75	11.4 ± 0.2	6.57 ± 0.09	4.625 ± 0.007	4.731 ± 0.008	4.675 ± 0.005
76	10.39 ± 0.19	5.75 ± 0.08	4.507 ± 0.007	4.116 ± 0.003	4.173 ± 0.003
77	9.9 ± 0.2	5.58 ± 0.09	4.521 ± 0.007	4.511 ± 0.007	4.516 ± 0.005
78	10.79 ± 0.19	6.09 ± 0.06	3.491 ± 0.009	2.742 ± 0.009	3.082 ± 0.006
79	23.86 ± 0.15	28.9 ± 0.4	2.655 ± 0.011	2.387 ± 0.013	2.551 ± 0.008
80	18.8 ± 0.2	13.20 ± 0.04	7.705 ± 0.007	7.146 ± 0.016	7.610 ± 0.007
81	11.5 ± 0.2	5.81 ± 0.09	4.520 ± 0.008	3.928 ± 0.007	4.164 ± 0.005
82	11.1 ± 0.2	6.31 ± 0.06	4.327 ± 0.008	3.641 ± 0.007	3.943 ± 0.005
83	9.5 ± 0.2	5.06 ± 0.10	3.846 ± 0.007	3.725 ± 0.005	3.758 ± 0.004
84	10.9 ± 0.2	6.32 ± 0.07	4.705 ± 0.009	3.985 ± 0.006	4.239 ± 0.005
85	10.2 ± 0.2	5.74 ± 0.09	4.701 ± 0.008	4.483 ± 0.007	4.572 ± 0.005
86	10.8 ± 0.2	6.15 ± 0.10	4.547 ± 0.010	4.278 ± 0.010	4.421 ± 0.007
87	10.6 ± 0.2	5.88 ± 0.09	4.450 ± 0.008	4.137 ± 0.007	4.279 ± 0.005
88	11.7 ± 0.2	7.02 ± 0.07	4.910 ± 0.007	4.622 ± 0.007	4.770 ± 0.005
89	11.3 ± 0.2	6.25 ± 0.10	5.371 ± 0.007	4.734 ± 0.008	5.081 ± 0.005
90	10.7 ± 0.2	5.99 ± 0.08	4.685 ± 0.009	4.028 ± 0.005	4.168 ± 0.004
91	10.6 ± 0.2	6.16 ± 0.06	3.986 ± 0.011	3.618 ± 0.009	3.777 ± 0.007
92	12.5 ± 0.2	6.92 ± 0.08	5.339 ± 0.015	4.439 ± 0.009	4.692 ± 0.008
93	12.8 ± 0.2	6.99 ± 0.07	4.454 ± 0.008	3.722 ± 0.007	4.034 ± 0.005
94	10.5 ± 0.2	6.18 ± 0.08	4.439 ± 0.007	3.842 ± 0.008	4.198 ± 0.005
95	12.36 ± 0.18	7.02 ± 0.09	5.186 ± 0.011	3.982 ± 0.008	4.383 ± 0.006
96	10.2 ± 0.2	5.57 ± 0.10	4.569 ± 0.009	4.399 ± 0.008	4.479 ± 0.006

Table D.7: *Fluxes of the analysed activity indicators obtained from HARPS Data 2018 (continued)*

Fluxes HARPS-N Data 2018				
ID Obs.	$Flx_{HeI4026}$ (10^5 erg s^{-1} cm^{-2})	$Flx_{HeI4471}$ (10^5 erg s^{-1} cm^{-2})	$Flx_{HeI5876}$ (10^5 erg s^{-1} cm^{-2})	Flx_{NaI} (10^5 erg s^{-1} cm^{-2})
33	0.162 ± 0.011	0.169 ± 0.016	0.71 ± 0.03	0.343 ± 0.006
34	0.149 ± 0.010	0.135 ± 0.014	0.60 ± 0.03	0.292 ± 0.006
35	0.20 ± 0.05	0.26 ± 0.03	0.73 ± 0.02	0.220 ± 0.004
36	0.135 ± 0.012	0.126 ± 0.014	0.56 ± 0.03	0.226 ± 0.006
37	0.143 ± 0.010	0.122 ± 0.014	0.59 ± 0.03	0.280 ± 0.006
38	0.175 ± 0.016	0.163 ± 0.016	0.66 ± 0.03	0.284 ± 0.006
39	0.150 ± 0.010	0.147 ± 0.015	0.62 ± 0.03	0.268 ± 0.006
40	0.149 ± 0.010	0.136 ± 0.014	0.60 ± 0.03	0.259 ± 0.006
41	0.135 ± 0.013	0.124 ± 0.014	0.56 ± 0.03	0.162 ± 0.003
42	0.148 ± 0.013	0.131 ± 0.014	0.57 ± 0.03	0.249 ± 0.007
43	0.137 ± 0.016	0.140 ± 0.016	0.57 ± 0.03	0.154 ± 0.003
44	0.092 ± 0.010	0.098 ± 0.013	0.52 ± 0.03	0.211 ± 0.006
45	0.158 ± 0.013	0.186 ± 0.017	0.66 ± 0.03	0.271 ± 0.006
46	0.134 ± 0.017	0.128 ± 0.014	0.59 ± 0.03	0.258 ± 0.006
47	0.142 ± 0.012	0.124 ± 0.015	0.58 ± 0.03	0.171 ± 0.003
48	0.130 ± 0.010	0.115 ± 0.013	0.54 ± 0.03	0.223 ± 0.006
49	0.150 ± 0.010	0.140 ± 0.014	0.60 ± 0.03	0.277 ± 0.006
50	0.204 ± 0.012	0.208 ± 0.019	0.69 ± 0.03	0.323 ± 0.006
51	0.150 ± 0.014	0.135 ± 0.015	0.60 ± 0.03	0.285 ± 0.006
52	0.090 ± 0.013	0.105 ± 0.013	0.54 ± 0.03	0.261 ± 0.006
53	0.130 ± 0.012	0.111 ± 0.013	0.56 ± 0.03	0.156 ± 0.003
54	0.100 ± 0.012	0.082 ± 0.012	0.48 ± 0.03	0.196 ± 0.006
55	0.174 ± 0.012	0.196 ± 0.019	0.73 ± 0.03	0.339 ± 0.006
56	0.182 ± 0.015	0.188 ± 0.018	0.70 ± 0.03	0.338 ± 0.006
57	0.121 ± 0.009	0.113 ± 0.013	0.54 ± 0.03	0.153 ± 0.003
58	0.117 ± 0.009	0.103 ± 0.012	0.52 ± 0.03	0.217 ± 0.006
59	0.109 ± 0.014	0.094 ± 0.012	0.54 ± 0.03	0.226 ± 0.006
60	0.120 ± 0.006	0.101 ± 0.013	0.51 ± 0.03	0.219 ± 0.006
61	0.143 ± 0.011	0.135 ± 0.013	0.61 ± 0.03	0.180 ± 0.002
62	0.123 ± 0.012	0.123 ± 0.015	0.58 ± 0.03	0.238 ± 0.006
63	0.119 ± 0.017	0.099 ± 0.012	0.52 ± 0.03	0.213 ± 0.006
64	0.131 ± 0.011	0.122 ± 0.013	0.54 ± 0.03	0.227 ± 0.006
65	0.138 ± 0.016	0.121 ± 0.014	0.52 ± 0.03	0.222 ± 0.006
66	0.139 ± 0.014	0.149 ± 0.015	0.56 ± 0.03	0.156 ± 0.003
67	0.175 ± 0.012	0.138 ± 0.014	0.61 ± 0.03	0.173 ± 0.003
68	0.08 ± 0.02	0.140 ± 0.014	0.57 ± 0.03	0.232 ± 0.008
69	0.136 ± 0.015	0.113 ± 0.013	0.55 ± 0.03	0.154 ± 0.003
70	0.172 ± 0.011	0.167 ± 0.016	0.68 ± 0.03	0.309 ± 0.006
71	0.114 ± 0.014	0.091 ± 0.013	0.50 ± 0.03	0.214 ± 0.006
72	0.121 ± 0.014	0.122 ± 0.014	0.54 ± 0.03	0.225 ± 0.006
73	0.162 ± 0.012	0.148 ± 0.015	0.59 ± 0.03	0.173 ± 0.003
74	0.129 ± 0.013	0.108 ± 0.013	0.54 ± 0.03	0.242 ± 0.006
75	0.109 ± 0.009	0.119 ± 0.014	0.59 ± 0.03	0.227 ± 0.007
76	0.142 ± 0.011	0.113 ± 0.014	0.55 ± 0.03	0.201 ± 0.006
77	0.099 ± 0.014	0.093 ± 0.013	0.54 ± 0.04	0.192 ± 0.007
78	0.124 ± 0.010	0.130 ± 0.014	0.62 ± 0.03	0.208 ± 0.006
79	0.207 ± 0.007	0.57 ± 0.06	2.01 ± 0.03	0.713 ± 0.006
80	0.282 ± 0.014	0.34 ± 0.03	1.09 ± 0.03	0.615 ± 0.006
81	0.116 ± 0.014	0.093 ± 0.013	0.50 ± 0.03	0.196 ± 0.007
82	0.142 ± 0.015	0.132 ± 0.014	0.58 ± 0.03	0.152 ± 0.003
83	0.101 ± 0.016	0.072 ± 0.013	0.48 ± 0.03	0.182 ± 0.007
84	0.134 ± 0.015	0.133 ± 0.014	0.59 ± 0.03	0.237 ± 0.006
85	0.134 ± 0.014	0.094 ± 0.012	0.53 ± 0.03	0.198 ± 0.007
86	0.123 ± 0.013	0.117 ± 0.013	0.58 ± 0.03	0.219 ± 0.007
87	0.121 ± 0.012	0.107 ± 0.013	0.54 ± 0.03	0.205 ± 0.007
88	0.147 ± 0.015	0.155 ± 0.015	0.66 ± 0.03	0.255 ± 0.007
89	0.131 ± 0.015	0.112 ± 0.012	0.57 ± 0.03	0.246 ± 0.007
90	0.135 ± 0.014	0.105 ± 0.012	0.56 ± 0.03	0.222 ± 0.006
91	0.136 ± 0.008	0.127 ± 0.013	0.56 ± 0.03	0.208 ± 0.006
92	0.158 ± 0.010	0.142 ± 0.014	0.61 ± 0.03	0.177 ± 0.003
93	0.132 ± 0.008	0.118 ± 0.012	0.55 ± 0.03	0.211 ± 0.007
94	0.121 ± 0.013	0.123 ± 0.014	0.58 ± 0.03	0.224 ± 0.007
95	0.141 ± 0.011	0.144 ± 0.013	0.62 ± 0.03	0.258 ± 0.007
96	0.098 ± 0.013	0.095 ± 0.013	0.51 ± 0.03	0.200 ± 0.007

Bibliography

Abel, M., Frommhold, L., Li, X. et al. Collision-Induced Absorption by H2Pairs: From Hundreds to Thousands of Kelvin. *Journal of Physical Chemistry A*, 115 (25):6805–6812, June 2011. doi: 10.1021/jp109441f.

Abel, M., Frommhold, L., Li, X. et al. Infrared absorption by collisional H_2-He complexes at temperatures up to 9000 K and frequencies from 0 to 20 000 cm^{-1}. J. Chem. Phys., 136(4):044319–044319, Jan. 2012. doi: 10.1063/1.3676405.

Affer, L., Micela, G., Damasso, M. et al. HADES RV program with HARPS-N at the TNG GJ 3998: An early M-dwarf hosting a system of super-Earths. A&A, 593:A117, Oct. 2016. doi: 10.1051/0004-6361/201628690.

Aigrain, S., Pont, F. and Zucker, S. A simple method to estimate radial velocity variations due to stellar activity using photometry. MNRAS, 419(4):3147–3158, Feb. 2012. doi: 10.1111/j.1365-2966.2011.19960.x.

Aigrain, S., Parviainen, H., Roberts, S. et al. Robust, open-source removal of systematics in Kepler data. MNRAS, 471(1):759–769, Oct. 2017. doi: 10.1093/mnras/stx1422.

Al-Refaie, A.F., Changeat, Q., Waldmann, I.P. et al. TauREx 3: A fast, dynamic, and extendable framework for retrievals. *The Astrophysical Journal*, 917(1):37, aug 2021. doi: 10.3847/1538-4357/ac0252. URL https://doi.org/10.3847/1538-4357/ac0252.

Allard, F., Homeier, D. and Freytag, B. *Model Atmospheres From Very Low Mass Stars to Brown Dwarfs*, volume 448 of *Astronomical Society of the Pacific Conference Series*, page 91. 2011.

Andretta, V., Doyle, J.G. and Byrne, P.B. The NaI $\lambda\lambda$5890,5896 resonance doublet as chromospheric diagnostics in M dwarfs. A&A, 322:266–279, Jun 1997.

Anglada-Escudé, G. and Butler, R.P. The HARPS-TERRA Project. I. Description of the Algorithms, Performance, and New Measurements on a Few Remarkable Stars Observed by HARPS. ApJS, 200(2):15, June 2012. doi: 10.1088/0067-0049/200/2/15.

Astudillo-Defru, N., Bonfils, X., Delfosse, X. et al. The HARPS search for southern extra-solar planets. XXXVI. Planetary systems and stellar activity of the M dwarfs GJ 3293, GJ 3341, and GJ 3543. A&A, 575:A119, Mar. 2015. doi: 10.1051/0004-6361/201424253.

Baglin, A., Auvergne, M., Barge, P. et al. The CoRoT mission and its scientific objectives. In Dumitrache, C., Popescu, N.A., Suran, M.D. et al, editors, *Fifty Years of Romanian Astrophysics*, volume 895 of *American Institute of Physics Conference Series*, pages 201–209, Mar. 2007. doi: 10.1063/1.2720423.

Baranne, A., Queloz, D., Mayor, M. et al. ELODIE: A spectrograph for accurate radial velocity measurements. A&AS, 119:373–390, Oct. 1996.

Barman, T. Identification of Absorption Features in an Extrasolar Planet Atmosphere. ApJ, 661(2):L191–L194, June 2007. doi: 10.1086/518736.

Barnes, S.A. Ages for Illustrative Field Stars Using Gyrochronology: Viability, Limitations, and Errors. ApJ, 669(2):1167–1189, Nov. 2007. doi: 10.1086/519295.

Barning, F.J.M. The numerical analysis of the light-curve of 12 Lacertae. Bull. Astron. Inst. Netherlands, 17:22, Aug. 1963.

Barros, S.C.C., Gosselin, H., Lillo-Box, J. et al. Precise masses for the transiting planetary system HD 106315 with HARPS. A&A, 608:A25, Dec. 2017. doi: 10.1051/0004-6361/201731276.

Barstow, J.K., Aigrain, S., Irwin, P.G.J. et al. A Consistent Retrieval Analysis of 10 Hot Jupiters Observed in Transmission. ApJ, 834(1):50, Jan. 2017. doi: 10.3847/1538-4357/834/1/50.

Baruteau, C., Crida, A., Paardekooper, S.J. et al. Planet-Disk Interactions and Early Evolution of Planetary Systems. In Beuther, H., Klessen, R.S., Dullemond, C.P. et al, editors, *Protostars and Planets VI*, pages 667–689, Jan. 2014. doi: 10.2458/azu_uapress_9780816531240-ch029.

Batalha, N.E., Lewis, T., Fortney, J.J. et al. The Precision of Mass Measurements Required for Robust Atmospheric Characterization of Transiting Exoplanets. ApJ, 885(1):L25, Nov. 2019. doi: 10.3847/2041-8213/ab4909.

Batalha, N.M. Exploring exoplanet populations with NASA's Kepler Mission. *Proceedings of the National Academy of Science*, 111(35):12647–12654, Sept. 2014. doi: 10.1073/pnas.1304196111.

Batalha, N.M., Rowe, J.F., Bryson, S.T. et al. Planetary Candidates Observed by Kepler. III. Analysis of the First 16 Months of Data. ApJS, 204(2):24, Feb. 2013. doi: 10.1088/0067-0049/204/2/24.

Beaulieu, J.P., Bennett, D.P., Fouqué, P. et al. Discovery of a cool planet of 5.5 Earth masses through gravitational microlensing. Nature, 439(7075):437–440, Jan. 2006. doi: 10.1038/nature04441.

Beichman, C., Hirano, T., David, T.J. et al. A Mass Limit for the Young Transiting Planet V1298 Tau b. *Research Notes of the American Astronomical Society*, 3(6): 89, June 2019. doi: 10.3847/2515-5172/ab2c9d.

Benneke, B. and Seager, S. Atmospheric Retrieval for Super-Earths: Uniquely Constraining the Atmospheric Composition with Transmission Spectroscopy. ApJ, 753(2):100, July 2012. doi: 10.1088/0004-637X/753/2/100.

Benz, A.O. and Güdel, M. Physical Processes in Magnetically Driven Flares on the Sun, Stars, and Young Stellar Objects. ARA&A, 48:241–287, Sep 2010. doi: 10.1146/annurev-astro-082708-101757.

Blunt, S., Endl, M., Weiss, L.M. et al. Radial Velocity Discovery of an Eccentric Jovian World Orbiting at 18 au. AJ, 158(5):181, Nov. 2019. doi: 10.3847/1538-3881/ab3e63.

Bocchieri, A., Mugnai, L.V., Pascale, E. et al. Detecting molecules in Ariel Tier 1 transmission spectra. In *European Planetary Science Congress*, pages EPSC2022–416, Sept. 2022. doi: 10.5194/epsc2022-416.

Bond, I.A., Udalski, A., Jaroszyński, M. et al. OGLE 2003-BLG-235/MOA 2003-BLG-53: A Planetary Microlensing Event. ApJ, 606(2):L155–L158, May 2004. doi: 10.1086/420928.

Bonfils, X., Delfosse, X., Udry, S. et al. The HARPS search for southern extra-solar planets. XXXI. The M-dwarf sample. A&A, 549:A109, Jan 2013. doi: 10.1051/0004-6361/201014704.

Borucki, W.J., Koch, D., Jenkins, J. et al. Kepler's Optical Phase Curve of the Exoplanet HAT-P-7b. *Science*, 325(5941):709, Aug. 2009. doi: 10.1126/science.1178312.

Borucki, W.J., Koch, D. and Kepler Science Team. Kepler Planet Detection Mission: Highlights of the First Results. In *AAS/Division for Planetary Sciences Meeting Abstracts #42*, volume 42 of *AAS/Division for Planetary Sciences Meeting Abstracts*, page 47.03, Oct. 2010.

Borysow, A. Collision-induced absorption coefficients of H_2 pairs at temperatures from 60 K to 1000 K. A&A, 390:779–782, Aug. 2002. doi: 10.1051/0004-6361:20020555.

Borysow, A., Jorgensen, U.G. and Fu, Y. High-temperature (1000-7000 K) collision-induced absorption of H"2 pairs computed from the first principles, with application to cool and dense stellar atmospheres. J. Quant. Spec. Radiat. Transf., 68:235–255, Feb. 2001. doi: 10.1016/S0022-4073(00)00023-6.

Bourrier, V., Deline, A., Krenn, A. et al. A CHEOPS-enhanced view of the HD3167 system. *arXiv e-prints*, art. arXiv:2209.06937, Sept. 2022.

Boyajian, T.S., von Braun, K., van Belle, G. et al. Stellar Diameters and Temperatures. III. Main-sequence A, F, G, and K Stars: Additional High-precision Measurements and Empirical Relations. ApJ, 771(1):40, July 2013. doi: 10.1088/0004-637X/771/1/40.

Bridges, M., Feroz, F., Hobson, M.P. et al. Bayesian optimal reconstruction of the primordial power spectrum. MNRAS, 400(2):1075–1084, Dec. 2009. doi: 10.1111/j.1365-2966.2009.15525.x.

Brogi, M. and Line, M.R. Retrieving Temperatures and Abundances of Exoplanet Atmospheres with High-resolution Cross-correlation Spectroscopy. AJ, 157(3):114, Mar. 2019. doi: 10.3847/1538-3881/aaffd3.

Brown, E.L., Jeffers, S.V., Marsden, S.C. et al. Linking chromospheric activity and magnetic field properties for late-type dwarf stars. MNRAS, 514(3):4300–4319, Aug. 2022. doi: 10.1093/mnras/stac1291.

Brun, A.S. and Browning, M.K. Magnetism, dynamo action and the solar-stellar connection. *Living Reviews in Solar Physics*, 14(1):4, Sept. 2017. doi: 10.1007/s41116-017-0007-8.

Brun, A.S., García, R.A., Houdek, G. et al. The Solar-Stellar Connection. Space Sci. Rev., 196(1-4):303–356, Dec. 2015. doi: 10.1007/s11214-014-0117-8.

Bryden, G., Chen, X., Lin, D.N.C. et al. Tidally Induced Gap Formation in Protostellar Disks: Gap Clearing and Suppression of Protoplanetary Growth. ApJ, 514(1):344–367, Mar. 1999. doi: 10.1086/306917.

Buccino, A.P., Petrucci, R., Jofré, E. et al. Possible Chromospheric Activity Cycles in AD Leo. ApJ, 781(1):L9, Jan 2014. doi: 10.1088/2041-8205/781/1/L9.

Buchhave, L.A., Latham, D.W., Johansen, A. et al. An abundance of small exoplanets around stars with a wide range of metallicities. Nature, 486(7403):375–377, June 2012. doi: 10.1038/nature11121.

Buchner, J. PyMultiNest: Python interface for MultiNest. Astrophysics Source Code Library, record ascl:1606.005, June 2016.

Burrows, A. and Sharp, C.M. Chemical Equilibrium Abundances in Brown Dwarf and Extrasolar Giant Planet Atmospheres. ApJ, 512(2):843–863, Feb. 1999. doi: 10.1086/306811.

Burrows, A., Hubeny, I., Budaj, J. et al. Theoretical Spectral Models of the Planet HD 209458b with a Thermal Inversion and Water Emission Bands. ApJ, 668(2): L171–L174, Oct. 2007. doi: 10.1086/522834.

Burrows, A., Budaj, J. and Hubeny, I. Theoretical Spectra and Light Curves of Close-in Extrasolar Giant Planets and Comparison with Data. ApJ, 678(2):1436–1457, May 2008. doi: 10.1086/533518.

Butler, R.P. and Marcy, G.W. A Planet Orbiting 47 Ursae Majoris. ApJ, 464:L153, June 1996. doi: 10.1086/310102.

Butler, R.P., Marcy, G.W., Williams, E. et al. Three New "51 Pegasi-Type" Planets. ApJ, 474(2):L115–L118, Jan. 1997. doi: 10.1086/310444.

Butler, R.P., Marcy, G.W., Fischer, D.A. et al. Evidence for Multiple Companions to υ Andromedae. ApJ, 526(2):916–927, Dec. 1999. doi: 10.1086/308035.

Cale, B.L., Reefe, M., Plavchan, P. et al. Diving Beneath the Sea of Stellar Activity: Chromatic Radial Velocities of the Young AU Mic Planetary System. AJ, 162(6): 295, Dec. 2021. doi: 10.3847/1538-3881/ac2c80.

Campante, T.L., Barclay, T., Swift, J.J. et al. An Ancient Extrasolar System with Five Sub-Earth-size Planets. ApJ, 799(2):170, Feb. 2015. doi: 10.1088/0004-637X/799/2/170.

Carleo, I., Malavolta, L., Lanza, A.F. et al. The GAPS Programme at TNG. XXI. A GIARPS case study of known young planetary candidates: confirmation of HD 285507 b and refutation of AD Leonis b. A&A, 638:A5, June 2020. doi: 10.1051/0004-6361/201937369.

Carrington, R.C. Description of a Singular Appearance seen in the Sun on September 1, 1859. MNRAS, 20:13–15, Nov 1859. doi: 10.1093/mnras/20.1.13.

Chandrasekhar, S. Radiative transfer. *Quarterly Journal of the Royal Meteorological Society*, 76(330):498–499, Oct. 1950. doi: 10.1002/qj.49707633016.

Changeat, Q. On Spectroscopic Phase-curve Retrievals: H_2 Dissociation and Thermal Inversion in the Atmosphere of the Ultrahot Jupiter WASP-103 b. AJ, 163 (3):106, Mar. 2022. doi: 10.3847/1538-3881/ac4475.

Changeat, Q. and Edwards, B. The Hubble WFC3 Emission Spectrum of the Extremely Hot Jupiter KELT-9b. ApJ, 907(1):L22, Jan. 2021. doi: 10.3847/2041-8213/abd84f.

Changeat, Q., Keyte, L., Waldmann, I.P. et al. Impact of Planetary Mass Uncertainties on Exoplanet Atmospheric Retrievals. ApJ, 896(2):107, June 2020. doi: 10.3847/1538-4357/ab8f8b.

Changeat, Q., Edwards, B., Al-Refaie, A.F. et al. Five Key Exoplanet Questions Answered via the Analysis of 25 Hot-Jupiter Atmospheres in Eclipse. ApJS, 260 (1):3, May 2022. doi: 10.3847/1538-4365/ac5cc2.

Chaplin, W.J., Basu, S., Huber, D. et al. Asteroseismic Fundamental Properties of Solar-type Stars Observed by the NASA Kepler Mission. ApJS, 210(1):1, Jan. 2014. doi: 10.1088/0067-0049/210/1/1.

Charbonneau, D., Brown, T.M., Latham, D.W. et al. Detection of Planetary Transits Across a Sun-like Star. ApJ, 529(1):L45–L48, Jan. 2000. doi: 10.1086/312457.

Charbonneau, D., Brown, T.M., Noyes, R.W. et al. Detection of an Extrasolar Planet Atmosphere. ApJ, 568(1):377–384, Mar. 2002. doi: 10.1086/338770.

Charbonneau, D., Allen, L.E., Megeath, S.T. et al. Detection of Thermal Emission from an Extrasolar Planet. ApJ, 626(1):523–529, June 2005. doi: 10.1086/429991.

Charbonneau, P. Dynamo models of the solar cycle. *Living Reviews in Solar Physics*, 17(1):4, June 2020. doi: 10.1007/s41116-020-00025-6.

Chauvin, G., Lagrange, A.M., Dumas, C. et al. Giant planet companion to 2MASSW J1207334-393254. A&A, 438(2):L25–L28, Aug. 2005. doi: 10.1051/0004-6361:200500116.

Chen, J. and Kipping, D. Probabilistic Forecasting of the Masses and Radii of Other Worlds. ApJ, 834(1):17, Jan. 2017. doi: 10.3847/1538-4357/834/1/17.

Chester, M.M. *Testing the Solar Paradigm for Chromospheric Activity in RS CVN Binaries: Moderate Resolution Spectroscopy of Solar Active Regions*. PhD thesis, Pennsylvania State University, University Park., Jan. 1991.

Choudhuri, A.R. Starspots, stellar cycles and stellar flares: Lessons from solar dynamo models. *Science China Physics, Mechanics, and Astronomy*, 60(1):19601, Jan. 2017. doi: 10.1007/s11433-016-0413-7.

Christiansen, J.L., Vanderburg, A., Burt, J. et al. Three's Company: An Additional Non-transiting Super-Earth in the Bright HD 3167 System, and Masses for All Three Planets. AJ, 154(3):122, Sept. 2017. doi: 10.3847/1538-3881/aa832d.

Cincunegui, C., Díaz, R.F. and Mauas, P.J.D. Hα and the Ca II H and K lines as activity proxies for late-type stars. A&A, 469(1):309–317, July 2007. doi: 10.1051/0004-6361:20066503.

Claret, A. A new non-linear limb-darkening law for LTE stellar atmosphere models. Calculations for -5.0 <= log[M/H] <= +1, 2000 K <= T_{eff} <= 50000 K at several surface gravities. A&A, 363:1081–1190, Nov. 2000.

Claret, A., Hauschildt, P.H. and Witte, S. New limb-darkening coefficients for PHOENIX/1D model atmospheres. I. Calculations for 1500 K $\leq$ T_{eff} $\leq$ 4800 K Kepler, CoRot, Spitzer, uvby, UBVRIJHK, Sloan, and 2MASS photometric systems. A&A, 546:A14, Oct. 2012. doi: 10.1051/0004-6361/201219849.

Claret, A., Hauschildt, P.H. and Witte, S. New limb-darkening coefficients for Phoenix/1d model atmospheres. II. Calculations for 5000 K $\leq$ T_{eff} $\leq$ 10 000 K Kepler, CoRot, Spitzer, uvby, UBVRIJHK, Sloan, and 2MASS photometric systems. A&A, 552:A16, Apr. 2013. doi: 10.1051/0004-6361/201220942.

Cointepas, M., Almenara, J.M., Bonfils, X. et al. TOI-269 b: an eccentric sub-Neptune transiting a M2 dwarf revisited with ExTrA. A&A, 650:A145, June 2021. doi: 10.1051/0004-6361/202140328.

Collier Cameron, A., Ford, E.B., Shahaf, S. et al. Separating planetary reflex Doppler shifts from stellar variability in the wavelength domain. MNRAS, 505 (2):1699–1717, Aug. 2021. doi: 10.1093/mnras/stab1323.

Cosentino, R., Lovis, C., Pepe, F. et al. Harps-N: the new planet hunter at TNG. In McLean, I.S., Ramsay, S.K. and Takami, H., editors, *Ground-based and Airborne*

Instrumentation for Astronomy IV, volume 8446 of *Society of Photo-Optical Instrumentation Engineers (SPIE) Conference Series*, page 84461V, Sept. 2012. doi: 10.1117/12.925738.

Cosentino, R., Lovis, C., Pepe, F. et al. HARPS-N @ TNG, two year harvesting data: performances and results. In Ramsay, S.K., McLean, I.S. and Takami, H., editors, *Ground-based and Airborne Instrumentation for Astronomy V*, volume 9147 of *Society of Photo-Optical Instrumentation Engineers (SPIE) Conference Series*, page 91478C, July 2014. doi: 10.1117/12.2055813.

Coughlin, J.L., Mullally, F., Thompson, S.E. et al. Planetary Candidates Observed by Kepler. VII. The First Fully Uniform Catalog Based on the Entire 48-month Data Set (Q1-Q17 DR24). ApJS, 224(1):12, May 2016. doi: 10.3847/0067-0049/224/1/12.

Covino, E., Esposito, M., Barbieri, M. et al. The GAPS programme with HARPS-N at TNG. I. Observations of the Rossiter-McLaughlin effect and characterisation of the transiting system Qatar-1. A&A, 554:A28, Jun 2013. doi: 10.1051/0004-6361/201321298.

Cram, L.E. and Giampapa, M.S. Formation of Chromospheric Lines in Cool Dwarf Stars. ApJ, 323:316, Dec. 1987. doi: 10.1086/165829.

Cram, L.E. and Mullan, D.J. Model chromospheres of flare stars.I. Balmer-line profiles. ApJ, 234:579–587, Dec. 1979. doi: 10.1086/157532.

Cram, L.E. and Mullan, D.J. Formation of the H-alpha absorption line in the chromospheres of cool stars. ApJ, 294:626–633, Jul 1985. doi: 10.1086/163330.

Crespo-Chacón, I., Montes, D., García-Alvarez, D. et al. Analysis and modeling of high temporal resolution spectroscopic observations of flares on <ASTROBJ>AD Leonis</ASTROBJ>. A&A, 452(3):987–1000, Jun 2006. doi: 10.1051/0004-6361:20053615.

Crossfield, I.J.M., Petigura, E., Schlieder, J.E. et al. A Nearby M Star with Three Transiting Super-Earths Discovered by K2. ApJ, 804(1):10, May 2015. doi: 10.1088/0004-637X/804/1/10.

Damasso, M., Bonomo, A.S., Astudillo-Defru, N. et al. Eyes on K2-3: A system of three likely sub-Neptunes characterized with HARPS-N and HARPS. A&A, 615:A69, July 2018. doi: 10.1051/0004-6361/201732459.

David, T.J., Cody, A.M., Hedges, C.L. et al. A Warm Jupiter-sized Planet Transiting the Pre-main-sequence Star V1298 Tau. AJ, 158(2):79, Aug. 2019a. doi: 10.3847/1538-3881/ab290f.

David, T.J., Petigura, E.A., Luger, R. et al. Four Newborn Planets Transiting the Young Solar Analog V1298 Tau. ApJ, 885(1):L12, Nov. 2019b. doi: 10.3847/2041-8213/ab4c99.

de Wit, J. and Seager, S. Constraining Exoplanet Mass from Transmission Spectroscopy. *Science*, 342(6165):1473–1477, Dec. 2013. doi: 10.1126/science.1245450.

de Wit, J., Wakeford, H.R., Lewis, N.K. et al. Atmospheric reconnaissance of the habitable-zone Earth-sized planets orbiting TRAPPIST-1. *Nature Astronomy*, 2:214–219, Mar. 2018. doi: 10.1038/s41550-017-0374-z.

del Burgo, C. and Allende Prieto, C. Accurate parameters for HD 209458 and its planet from HST spectrophotometry. MNRAS, 463(2):1400–1408, Dec. 2016. doi: 10.1093/mnras/stw2005.

Deleuil, M., Aigrain, S., Moutou, C. et al. Planets, candidates, and binaries from the CoRoT/Exoplanet programme. The CoRoT transit catalogue. A&A, 619:A97, Nov. 2018. doi: 10.1051/0004-6361/201731068.

Desert, J.M., Adhiambo, V., Barat, S. et al. The nature, origin, and fate of two planets of a newborn system through the lens of their relative atmospheric properties. JWST Proposal. Cycle 1, ID. #2149, Mar. 2021.

Di Maio, C., Argiroffi, C., Micela, G. et al. The GAPS programme at TNG. XXVI. Magnetic activity in M stars: spectroscopic monitoring of AD Leonis. A&A, 642:A53, Oct. 2020. doi: 10.1051/0004-6361/202038011.

Di Maio, C., Changeat, Q., Benatti, S. et al. Analysis of the planetary mass uncertainties on the accuracy of atmospherical retrieval. *A&A*, 669:A150, 2023. doi: 10.1051/0004-6361/202244881. URL https://doi.org/10.1051/0004-6361/202244881.

Dorn, C., Khan, A., Heng, K. et al. Can we constrain the interior structure of rocky exoplanets from mass and radius measurements? A&A, 577:A83, May 2015. doi: 10.1051/0004-6361/201424915.

Doyle, J.G., Shetye, J., Antonova, A.E. et al. Stellar flare oscillations: evidence for oscillatory reconnection and evolution of MHD modes. MNRAS, 475(2): 2842–2851, Apr 2018. doi: 10.1093/mnras/sty032.

Drossart, P., Panek, E., Batista, V. et al. Transit spectroscopy : on the influence of stellar molecular lines in the retrieval of exoplanets atmospheric absorption. In *44th COSPAR Scientific Assembly. Held 16-24 July*, volume 44, page 565, July 2022.

Dumusque, X. Radial velocity fitting challenge. I. Simulating the data set including realistic stellar radial-velocity signals. A&A, 593:A5, Aug. 2016. doi: 10.1051/0004-6361/201628672.

Dumusque, X. Measuring precise radial velocities on individual spectral lines. I. Validation of the method and application to mitigate stellar activity. A&A, 620: A47, Nov. 2018. doi: 10.1051/0004-6361/201833795.

Dumusque, X., Boisse, I. and Santos, N.C. SOAP 2.0: A Tool to Estimate the Photometric and Radial Velocity Variations Induced by Stellar Spots and Plages. ApJ, 796(2):132, Dec. 2014. doi: 10.1088/0004-637X/796/2/132.

Edwards, B. and Tinetti, G. The Ariel Target List: The Impact of TESS and the Potential for Characterizing Multiple Planets within a System. AJ, 164(1):15, July 2022. doi: 10.3847/1538-3881/ac6bf9.

Edwards, B., Mugnai, L., Tinetti, G. et al. An Updated Study of Potential Targets for Ariel. AJ, 157(6):242, June 2019. doi: 10.3847/1538-3881/ab1cb9.

Edwards, B., Changeat, Q., Baeyens, R. et al. ARES I: WASP-76 b, A Tale of Two HST Spectra. AJ, 160(1):8, July 2020. doi: 10.3847/1538-3881/ab9225.

Eisner, N.L., Nicholson, B.A., Barragán, O. et al. Planet Hunters TESS III: two transiting planets around the bright G dwarf HD 152843. MNRAS, 505(2):1827–1840, Aug. 2021. doi: 10.1093/mnras/stab1253.

Elkins-Tanton, L.T. and Seager, S. Ranges of Atmospheric Mass and Composition of Super-Earth Exoplanets. ApJ, 685(2):1237–1246, Oct. 2008. doi: 10.1086/591433.

Ellis, T.G., Boyajian, T., von Braun, K. et al. Directly Determined Properties of HD 97658 from Interferometric Observations. AJ, 162(3):118, Sept. 2021. doi: 10.3847/1538-3881/ac141a.

Esposito, M., Armstrong, D.J., Gandolfi, D. et al. HD 219666 b: a hot-Neptune from TESS Sector 1. A&A, 623:A165, Mar. 2019. doi: 10.1051/0004-6361/201834853.

Favata, F. and Micela, G. Stellar Coronal Astronomy. Space Sci. Rev., 108(4): 577–708, Oct. 2003. doi: 10.1023/B:SPAC.0000007491.80144.21.

Favata, F., Micela, G. and Reale, F. The corona of the dMe flare star AD Leo. A&A, 354:1021–1035, Feb 2000.

Feinstein, A.D., Montet, B.T., Johnson, M.C. et al. H-alpha and Ca II Infrared Triplet Variations During a Transit of the 23 Myr Planet V1298 Tau c. AJ, 162 (5):213, Nov. 2021. doi: 10.3847/1538-3881/ac1f24.

Fellgett, P. A proposal for a radial velocity photometer. *Optica Acta: International Journal of Optics*, 2(1):9–16, 1955.

Feroz, F. and Hobson, M.P. Multimodal nested sampling: an efficient and robust alternative to Markov Chain Monte Carlo methods for astronomical data analyses. MNRAS, 384(2):449–463, Feb. 2008. doi: 10.1111/j.1365-2966.2007.12353.x.

Feroz, F., Hobson, M.P. and Bridges, M. MULTINEST: an efficient and robust Bayesian inference tool for cosmology and particle physics. MNRAS, 398(4): 1601–1614, Oct. 2009. doi: 10.1111/j.1365-2966.2009.14548.x.

Feroz, F., Hobson, M.P. and Trotta, R. Comment on "Bayesian evidence: can we beat MultiNest using traditional MCMC methods", by Rutger van Haasteren (arXiv:0911.2150). *arXiv e-prints*, art. arXiv:1001.0719, Jan. 2010.

Feroz, F., Balan, S.T. and Hobson, M.P. Bayesian evidence for two companions orbiting HIP 5158. MNRAS, 416(1):L104–L108, Sept. 2011a. doi: 10.1111/j.1745-3933.2011.01109.x.

Feroz, F., Balan, S.T. and Hobson, M.P. Detecting extrasolar planets from stellar radial velocities using Bayesian evidence. MNRAS, 415(4):3462–3472, Aug. 2011b. doi: 10.1111/j.1365-2966.2011.18962.x.

Feroz, F., Hobson, M.P., Cameron, E. et al. Importance Nested Sampling and the MultiNest Algorithm. *The Open Journal of Astrophysics*, 2(1):10, Nov. 2019. doi: 10.21105/astro.1306.2144.

Fischer, D.A. and Valenti, J. The Planet-Metallicity Correlation. ApJ, 622(2):1102–1117, Apr. 2005. doi: 10.1086/428383.

Fletcher, L.N., Gustafsson, M. and Orton, G.S. Hydrogen Dimers in Giant-planet Infrared Spectra. ApJS, 235(1):24, Mar. 2018. doi: 10.3847/1538-4365/aaa07a.

Forbes, T.G. and Acton, L.W. Reconnection and Field Line Shrinkage in Solar Flares. ApJ, 459:330, Mar 1996. doi: 10.1086/176896.

Fortney, J.J. The effect of condensates on the characterization of transiting planet atmospheres with transmission spectroscopy. MNRAS, 364(2):649–653, Dec. 2005. doi: 10.1111/j.1365-2966.2005.09587.x.

Fressin, F., Torres, G., Charbonneau, D. et al. The False Positive Rate of Kepler and the Occurrence of Planets. ApJ, 766(2):81, Apr. 2013. doi: 10.1088/0004-637X/766/2/81.

Fuhrmeister, B., Schmitt, J.H.M.M. and Hauschildt, P.H. Detection of red line asymmetries in LHS 2034. A&A, 436(2):677–686, Jun 2005. doi: 10.1051/0004-6361:20042518.

Fuhrmeister, B., Czesla, S., Schmitt, J.H.M.M. et al. The CARMENES search for exoplanets around M dwarfs. Wing asymmetries of Hα, Na I D, and He I lines. A&A, 615:A14, Jul 2018. doi: 10.1051/0004-6361/201732204.

Gaia Collaboration, Prusti, T., de Bruijne, J.H.J. et al. The Gaia mission. A&A, 595:A1, Nov. 2016. doi: 10.1051/0004-6361/201629272.

Gaia Collaboration, Brown, A.G.A., Vallenari, A. et al. Gaia Data Release 2. Summary of the contents and survey properties. A&A, 616:A1, Aug. 2018. doi: 10.1051/0004-6361/201833051.

Gaia Collaboration, Brown, A.G.A., Vallenari, A. et al. Gaia Early Data Release 3. Summary of the contents and survey properties. A&A, 649:A1, May 2021. doi: 10.1051/0004-6361/202039657.

Gaidos, E., Hirano, T., Beichman, C. et al. Zodiacal exoplanets in time - XIII. Planet orbits and atmospheres in the V1298 Tau system, a keystone in studies of early planetary evolution. MNRAS, 509(2):2969–2978, Jan. 2022. doi: 10.1093/mnras/stab3107.

Gandhi, S. and Madhusudhan, N. Retrieval of exoplanet emission spectra with HyDRA. MNRAS, 474(1):271–288, Feb. 2018. doi: 10.1093/mnras/stx2748.

Gandolfi, D., Barragán, O., Hatzes, A.P. et al. The Transiting Multi-planet System HD 3167: A 5.7 M $_\oplus$ Super-Earth and an 8.3 M $_\oplus$ Mini-Neptune. AJ, 154(3):123, Sept. 2017. doi: 10.3847/1538-3881/aa832a.

Gao, P. and Zhang, X. Deflating Super-puffs: Impact of Photochemical Hazes on the Observed Mass-Radius Relationship of Low-mass Planets. ApJ, 890(2):93, Feb. 2020. doi: 10.3847/1538-4357/ab6a9b.

Giampapa, M.S., Linsky, J.L., Schneeberger, T.J. et al. Chromospheric emission lines in the red spectrum of AD Leonis. I. The nonflare spectrum. ApJ, 226: 144–150, Nov 1978. doi: 10.1086/156594.

Giampapa, M.S., Worden, S.P. and Linsky, J.L. Stellar model chromospheres. XIII. M dwarf stars. ApJ, 258:740–760, July 1982. doi: 10.1086/160122.

Gilbert, E.A., Barclay, T., Quintana, E.V. et al. Flares, Rotation, and Planets of the AU Mic System from TESS Observations. AJ, 163(4):147, Apr. 2022. doi: 10.3847/1538-3881/ac23ca.

Goldreich, P. and Tremaine, S. Disk-satellite interactions. ApJ, 241:425–441, Oct. 1980. doi: 10.1086/158356.

Gomes da Silva, J., Santos, N.C., Bonfils, X. et al. Long-term magnetic activity of a sample of M-dwarf stars from the HARPS program . II. Activity and radial velocity. A&A, 541:A9, May 2012. doi: 10.1051/0004-6361/201118598.

Gordon, I., Rothman, L.S., Wilzewski, J.S. et al. HITRAN2016 : new and improved data and tools towards studies of planetary atmospheres. In *AAS/Division for Planetary Sciences Meeting Abstracts #48*, volume 48 of *AAS/Division for Planetary Sciences Meeting Abstracts*, page 421.13, Oct. 2016.

Gould, A. and Loeb, A. Discovering Planetary Systems through Gravitational Microlenses. ApJ, 396:104, Sept. 1992. doi: 10.1086/171700.

Graff, P., Feroz, F., Hobson, M.P. et al. BAMBI: blind accelerated multimodal Bayesian inference. MNRAS, 421(1):169–180, Mar. 2012. doi: 10.1111/j.1365-2966.2011.20288.x.

Grasset, O., Schneider, J. and Sotin, C. A Study of the Accuracy of Mass-Radius Relationships for Silicate-Rich and Ice-Rich Planets up to 100 Earth Masses. ApJ, 693(1):722–733, Mar. 2009. doi: 10.1088/0004-637X/693/1/722.

Gray, D.F. A Solar-flux Line-broadening Analysis. ApJ, 857(2):139, Apr. 2018. doi: 10.3847/1538-4357/aab8f2.

Greene, T.P., Line, M.R., Montero, C. et al. Characterizing Transiting Exoplanet Atmospheres with JWST. ApJ, 817(1):17, Jan. 2016. doi: 10.3847/0004-637X/817/1/17.

Griffin, R.F. A Photoelectric Radial-Velocity Spectrometer. ApJ, 148:465, May 1967. doi: 10.1086/149168.

Grillmair, C.J., Burrows, A., Charbonneau, D. et al. Strong water absorption in the dayside emission spectrum of the planet HD189733b. Nature, 456(7223): 767–769, Dec. 2008. doi: 10.1038/nature07574.

Güdel, M. X-ray astronomy of stellar coronae. A&A Rev., 12(2-3):71–237, Sept. 2004. doi: 10.1007/s00159-004-0023-2.

Guenther, E.W., Woeckel, D. and Muheki, P. Flares of M-stars in Upper Scorpius region and flares and CMEs of the active M-star AD Leo. *arXiv e-prints*, art. arXiv:1911.09922, Nov. 2019.

Hardegree-Ullman, K.K., Christiansen, J.L., Ciardi, D.R. et al. K2-138 g: Spitzer Spots a Sixth Planet for the Citizen Science System. AJ, 161(5):219, May 2021. doi: 10.3847/1538-3881/abeab0.

Hasan, S.S. and van Ballegooijen, A.A. Dynamics of the Solar Magnetic Network. II. Heating the Magnetized Chromosphere. ApJ, 680(2):1542–1552, Jun 2008. doi: 10.1086/587773.

Hawley, S.L. and Pettersen, B.R. The Great Flare of 1985 April 12 on AD Leonis. ApJ, 378:725, Sep 1991. doi: 10.1086/170474.

Hawley, S.L., Fisher, G.H., Simon, T. et al. Simultaneous Extreme-Ultraviolet Explorer and Optical Observations of AD Leonis: Evidence for Large Coronal Loops and the Neupert Effect in Stellar Flares. ApJ, 453:464, Nov 1995. doi: 10.1086/176408.

Hawley, S.L., Gizis, J.E. and Reid, I.N. The Palomar/MSU Nearby Star Spectroscopic Survey.II.The Southern M Dwarfs and Investigation of Magnetic Activity. AJ, 112:2799, Dec 1996. doi: 10.1086/118222.

Hawley, S.L., Allred, J.C., Johns-Krull, C.M. et al. Multiwavelength Observations of Flares on AD Leonis. ApJ, 597(1):535–554, Nov 2003. doi: 10.1086/378351.

He, H., Wang, H., Zhang, M. et al. Activity Analyses for Solar-type Stars Observed with Kepler. II. Magnetic Feature versus Flare Activity. ApJS, 236(1):7, May 2018. doi: 10.3847/1538-4365/aab779.

Henry, G.W., Marcy, G.W., Butler, R.P. et al. A Transiting "51 Peg-like" Planet. ApJ, 529(1):L41–L44, Jan. 2000. doi: 10.1086/312458.

Henry, T.J., Jao, W.C., Subasavage, J.P. et al. The Solar Neighborhood. XVII. Parallax Results from the CTIOPI 0.9 m Program: 20 New Members of the RECONS 10 Parsec Sample. AJ, 132(6):2360–2371, Dec 2006. doi: 10.1086/508233.

Hoeijmakers, H.J., Ehrenreich, D., Heng, K. et al. Atomic iron and titanium in the atmosphere of the exoplanet KELT-9b. Nature, 560(7719):453–455, Aug. 2018. doi: 10.1038/s41586-018-0401-y.

Høg, E., Fabricius, C., Makarov, V.V. et al. The Tycho-2 catalogue of the 2.5 million brightest stars. A&A, 355:L27–L30, Mar. 2000.

Horne, K. An optimal extraction algorithm for CCD spectroscopy. PASP, 98:609–617, June 1986. doi: 10.1086/131801.

Hou, F., Goodman, J., Hogg, D.W. et al. An Affine-invariant Sampler for Exoplanet Fitting and Discovery in Radial Velocity Data. ApJ, 745(2):198, Feb. 2012. doi: 10.1088/0004-637X/745/2/198.

Houdebine, E.R. Dynamics of flares on late type dMe stars. IV. Constraints from spectrophotometry in the visible. A&A, 397:1019–1034, Jan. 2003. doi: 10.1051/0004-6361:20021537.

Houdebine, E.R. and Stempels, H.C. Observation and modelling of main sequence stellar chromospheres. VI. $H_{alpha\_}$ and CaII line observations of M1 dwarfs and comparison with models. A&A, 326:1143–1166, Oct. 1997.

Houdebine, E.R., Junghans, K., Heanue, M.C. et al. Observation and modelling of main sequence star chromospheres. VIII. High resolution observations of M and K dwarf chromospheric lines. A&A, 503(3):929–944, Sept. 2009. doi: 10.1051/0004-6361/200811349.

Houdebine, E.R., Mullan, D.J., Paletou, F. et al. Rotation-Activity Correlations in K and M Dwarfs. I. Stellar Parameters and Compilations of v sin I and P/sin I for a Large Sample of Late-K and M Dwarfs. ApJ, 822(2):97, May 2016. doi: 10.3847/0004-637X/822/2/97.

Howard, A.W., Marcy, G.W., Johnson, J.A. et al. The Occurrence and Mass Distribution of Close-in Super-Earths, Neptunes, and Jupiters. *Science*, 330(6004): 653, Oct. 2010. doi: 10.1126/science.1194854.

Howard, A.W., Johnson, J.A., Marcy, G.W. et al. The NASA-UC Eta-Earth Program. III. A Super-Earth Orbiting HD 97658 and a Neptune-mass Planet Orbiting Gl 785. ApJ, 730(1):10, Mar. 2011. doi: 10.1088/0004-637X/730/1/10.

Howarth, I.D. New limb-darkening coefficients and synthetic photometry for model-atmosphere grids at Galactic, LMC and SMC abundances. MNRAS, 413 (3):1515–1523, May 2011. doi: 10.1111/j.1365-2966.2011.18122.x.

Howell, S.B., Everett, M.E., Sherry, W. et al. Speckle Camera Observations for the NASA Kepler Mission Follow-up Program. AJ, 142(1):19, July 2011. doi: 10.1088/0004-6256/142/1/19.

Howell, S.B., Sobeck, C., Haas, M. et al. The K2 Mission: Characterization and Early Results. PASP, 126(938):398, Apr. 2014. doi: 10.1086/676406.

Huang, C.X., Quinn, S.N., Vanderburg, A. et al. TESS Spots a Hot Jupiter with an Inner Transiting Neptune. ApJ, 892(1):L7, Mar. 2020. doi: 10.3847/2041-8213/ab7302.

Hunt-Walker, N.M., Hilton, E.J., Kowalski, A.F. et al. MOST Observations of the Flare Star AD Leo. PASP, 124(916):545, Jun 2012. doi: 10.1086/666495.

Işık, E., Solanki, S.K., Krivova, N.A. et al. Forward modelling of brightness variations in Sun-like stars. I. Emergence and surface transport of magnetic flux. A&A, 620:A177, Dec. 2018. doi: 10.1051/0004-6361/201833393.

Ida, S. and Lin, D.N.C. Toward a Deterministic Model of Planetary Formation. IV. Effects of Type I Migration. ApJ, 673(1):487–501, Jan. 2008. doi: 10.1086/523754.

Irwin, P.G.J., Teanby, N.A. and Davis, G.R. Vertical cloud structure of Uranus from UKIRT/UIST observations and changes seen during Northern Spring Equinox in 2007. In *European Planetary Science Congress 2008*, page 645, Sept. 2008.

Järvinen, S.P., Berdyugina, S.V., Korhonen, H. et al. EK Draconis. Magnetic activity in the photosphere and chromosphere. A&A, 472(3):887–895, Sept. 2007. doi: 10.1051/0004-6361:20077551.

Jeffreys, H. *The theory of probability*. OUP Oxford, 1998.

Johnson, J.A. *How Do You Find An Exoplanet?* 2016.

Johnson, J.A., Aller, K.M., Howard, A.W. et al. Giant Planet Occurrence in the Stellar Mass-Metallicity Plane. PASP, 122(894):905, Aug. 2010. doi: 10.1086/655775.

Johnson, M.C., David, T.J., Petigura, E.A. et al. An Aligned Orbit for the Young Planet V1298 Tau b. AJ, 163(6):247, June 2022. doi: 10.3847/1538-3881/ac6271.

Jordan, A., Bakos, G.Á., Bayliss, D. et al. HATS-37Ab and HATS-38b: Two Transiting Hot Neptunes in the Desert. AJ, 160(5):222, Nov. 2020. doi: 10.3847/1538-3881/aba530.

Kanodia, S., Cañas, C.I., Stefansson, G. et al. TOI-1728b: The Habitable-zone Planet Finder Confirms a Warm Super-Neptune Orbiting an M-dwarf Host. ApJ, 899(1):29, Aug. 2020. doi: 10.3847/1538-4357/aba0a2.

Karpenka, N.V., March, M.C., Feroz, F. et al. Bayesian constraints on dark matter halo properties using gravitationally lensed supernovae. MNRAS, 433(4):2693–2705, Aug. 2013. doi: 10.1093/mnras/sts700.

Knutson, H.A., Charbonneau, D., Allen, L.E. et al. The 3.6-8.0 μm Broadband Emission Spectrum of HD 209458b: Evidence for an Atmospheric Temperature Inversion. ApJ, 673(1):526–531, Jan. 2008. doi: 10.1086/523894.

Knutson, H.A., Charbonneau, D., Burrows, A. et al. Detection of A Temperature Inversion in the Broadband Infrared Emission Spectrum of TrES-4. ApJ, 691(1):866–874, Jan. 2009. doi: 10.1088/0004-637X/691/1/866.

Koch, D., Borucki, W., Basri, G. et al. The Kepler Mission and Eclipsing Binaries. In Hartkopf, W.I., Harmanec, P. and Guinan, E.F., editors, *Binary Stars as Critical Tools & Tests in Contemporary Astrophysics*, volume 240, pages 236–243, Aug. 2007. doi: 10.1017/S1743921307004085.

Kosiarek, M.R., Berardo, D.A., Crossfield, I.J.M. et al. Physical Parameters of the Multiplanet Systems HD 106315 and GJ 9827. AJ, 161(1):47, Jan. 2021. doi: 10.3847/1538-3881/abca39.

Kowalski, A.F., Hawley, S.L., Hilton, E.J. et al. M Dwarfs in Sloan Digital Sky Survey Stripe 82: Photometric Light Curves and Flare Rate Analysis. AJ, 138(2):633–648, Aug 2009. doi: 10.1088/0004-6256/138/2/633.

Kozai, Y. Secular perturbations of asteroids with high inclination and eccentricity. AJ, 67:591–598, Nov. 1962. doi: 10.1086/108790.

Kreidberg, L., Bean, J.L., Désert, J.M. et al. Clouds in the atmosphere of the super-Earth exoplanet GJ1214b. Nature, 505(7481):69–72, Jan. 2014. doi: 10.1038/nature12888.

Lafarga, M., Ribas, I., Lovis, C. et al. The CARMENES search for exoplanets around M dwarfs. Radial velocities and activity indicators from cross-correlation functions with weighted binary masks. A&A, 636:A36, Apr. 2020. doi: 10.1051/0004-6361/201937222.

Lammer, H., Lichtenegger, H.I.M., Kulikov, Y.N. et al. Coronal Mass Ejection (CME) Activity of Low Mass M Stars as An Important Factor for The Habitability of Terrestrial Exoplanets. II. CME-Induced Ion Pick Up of Earth-like Exoplanets in Close-In Habitable Zones. *Astrobiology*, 7(1):185–207, Feb. 2007. doi: 10.1089/ast.2006.0128.

Landman, D.A. and Mongillo, M. Halpha and Hbeta emission in quiescent prominences. ApJ, 230:581–589, June 1979. doi: 10.1086/157116.

Lanza, A.F., Malavolta, L., Benatti, S. et al. The GAPS Programme with HARPS-N at TNG. XVII. Line profile indicators and kernel regression as diagnostics of radial-velocity variations due to stellar activity in solar-like stars. A&A, 616: A155, Sep 2018. doi: 10.1051/0004-6361/201731010.

Lavail, A., Kochukhov, O. and Wade, G.A. A sudden change of the global magnetic field of the active M dwarf AD Leo revealed by full Stokes spectropolarimetric observations. MNRAS, 479(4):4836–4843, Oct. 2018. doi: 10.1093/mnras/sty1825.

Lavie, B., Mendonça, J.M., Mordasini, C. et al. HELIOS-RETRIEVAL: An Open-source, Nested Sampling Atmospheric Retrieval Code; Application to the HR 8799 Exoplanets and Inferred Constraints for Planet Formation. AJ, 154(3):91, Sept. 2017. doi: 10.3847/1538-3881/aa7ed8.

Lecavelier des Etangs, A. and Lissauer, J.J. The IAU working definition of an exoplanet. New A Rev., 94:101641, June 2022. doi: 10.1016/j.newar.2022.101641.

Li, G., Gordon, I.E., Rothman, L.S. et al. Rovibrational Line Lists for Nine Isotopologues of the CO Molecule in the X $^1\Sigma^+$ Ground Electronic State. ApJS, 216 (1):15, Jan. 2015. doi: 10.1088/0067-0049/216/1/15.

Lillo-Box, J., Lopez, T.A., Santerne, A. et al. Masses for the seven planets in K2-32 and K2-233. Four diverse planets in resonant chain and the first young rocky worlds. A&A, 640:A48, Aug. 2020. doi: 10.1051/0004-6361/202037896.

Lindegren, L., Hernández, J., Bombrun, A. et al. Gaia Data Release 2. The astrometric solution. A&A, 616:A2, Aug. 2018. doi: 10.1051/0004-6361/201832727.

Lindegren, L., Klioner, S.A., Hernández, J. et al. Gaia Early Data Release 3. The astrometric solution. A&A, 649:A2, May 2021. doi: 10.1051/0004-6361/202039709.

Line, M.R., Wolf, A.S., Zhang, X. et al. A Systematic Retrieval Analysis of Secondary Eclipse Spectra. I. A Comparison of Atmospheric Retrieval Techniques. ApJ, 775(2):137, Oct. 2013. doi: 10.1088/0004-637X/775/2/137.

Line, M.R., Teske, J., Burningham, B. et al. Uniform Atmospheric Retrieval Analysis of Ultracool Dwarfs. I. Characterizing Benchmarks, Gl 570D and HD 3651B. ApJ, 807(2):183, July 2015. doi: 10.1088/0004-637X/807/2/183.

Linsky, J.L. Stellar Model Chromospheres and Spectroscopic Diagnostics. ARA&A, 55(1):159–211, Aug 2017. doi: 10.1146/annurev-astro-091916-055327.

Linsky, J.L., Bornmann, P.L., Carpenter, K.G. et al. Outer atmospheres of cool stars. XII. A survey of IUE ultraviolet emission line spectra of cool dwarf stars. ApJ, 260:670–694, Sept. 1982. doi: 10.1086/160288.

Lomb, N.R. Least-Squares Frequency Analysis of Unequally Spaced Data. Ap&SS, 39(2):447–462, Feb. 1976. doi: 10.1007/BF00648343.

Lopez, E.D. and Fortney, J.J. The Role of Core Mass in Controlling Evaporation: The Kepler Radius Distribution and the Kepler-36 Density Dichotomy. ApJ, 776 (1):2, Oct. 2013. doi: 10.1088/0004-637X/776/1/2.

Lopez, T.A., Barros, S.C.C., Santerne, A. et al. Exoplanet characterisation in the longest known resonant chain: the K2-138 system seen by HARPS. A&A, 631: A90, Nov. 2019. doi: 10.1051/0004-6361/201936267.

MacDonald, R.J. and Madhusudhan, N. HD 209458b in new light: evidence of nitrogen chemistry, patchy clouds and sub-solar water. MNRAS, 469(2):1979–1996, Aug. 2017. doi: 10.1093/mnras/stx804.

Madhusudhan, N. and Seager, S. A Temperature and Abundance Retrieval Method for Exoplanet Atmospheres. ApJ, 707(1):24–39, Dec. 2009. doi: 10.1088/0004-637X/707/1/24.

Madhusudhan, N., Harrington, J., Stevenson, K.B. et al. A high C/O ratio and weak thermal inversion in the atmosphere of exoplanet WASP-12b. Nature, 469(7328): 64–67, Jan. 2011. doi: 10.1038/nature09602.

Maggio, A., Locci, D., Pillitteri, I. et al. New Constraints on the Future Evaporation of the Young Exoplanets in the V1298 Tau System. ApJ, 925(2):172, Feb. 2022. doi: 10.3847/1538-4357/ac4040.

Malavolta, L., Borsato, L., Granata, V. et al. The Kepler-19 System: A Thick-envelope Super-Earth with Two Neptune-mass Companions Characterized Using Radial Velocities and Transit Timing Variations. AJ, 153(5):224, May 2017. doi: 10.3847/1538-3881/aa6897.

Maldonado, J., Scandariato, G., Stelzer, B. et al. HADES RV Programme with HARPS-N at TNG . III. Flux-flux and activity-rotation relationships of early-M dwarfs. A&A, 598:A27, Feb 2017. doi: 10.1051/0004-6361/201629223.

Maldonado, J., Phillips, D.F., Dumusque, X. et al. Temporal evolution and correlations of optical activity indicators measured in Sun-as-a-star observations. A&A, 627:A118, Jul 2019. doi: 10.1051/0004-6361/201935233.

Maldonado, J., Petralia, A., Mantovan, G. et al. The GAPS programme at TNG XLIII. A massive brown dwarf orbiting the active M dwarf TOI-5375. *arXiv e-prints*, art. arXiv:2304.04477, Apr. 2023. doi: 10.48550/arXiv.2304.04477.

Mamajek, E.E. and Bell, C.P.M. On the age of the β Pictoris moving group. MNRAS, 445(3):2169–2180, Dec. 2014. doi: 10.1093/mnras/stu1894.

Mamajek, E.E. and Hillenbrand, L.A. Improved Age Estimation for Solar-Type Dwarfs Using Activity-Rotation Diagnostics. ApJ, 687(2):1264–1293, Nov. 2008. doi: 10.1086/591785.

Mao, S. and Paczynski, B. Gravitational Microlensing by Double Stars and Planetary Systems. ApJ, 374:L37, June 1991. doi: 10.1086/186066.

Marcy, G.W. and Butler, R.P. A Planetary Companion to 70 Virginis. ApJ, 464: L147, June 1996. doi: 10.1086/310096.

Markov, A. et al. Theory of algorithms. Springer, 1954.

Marois, C., Zuckerman, B., Konopacky, Q.M. et al. Images of a fourth planet orbiting HR 8799. Nature, 468(7327):1080–1083, Dec. 2010. doi: 10.1038/nature09684.

Martínez-Arnáiz, R., Maldonado, J., Montes, D. et al. Chromospheric activity and rotation of FGK stars in the solar vicinity. An estimation of the radial velocity jitter. A&A, 520:A79, Sept. 2010. doi: 10.1051/0004-6361/200913725.

Martioli, E., Hébrard, G., Correia, A.C.M. et al. New constraints on the planetary system around the young active star AU Mic. Two transiting warm Neptunes near mean-motion resonance. A&A, 649:A177, May 2021. doi: 10.1051/0004-6361/202040235.

Mauas, P.J.D. and Falchi, A. Atmospheric Models of Flare Stars: The Quiescent State of AD Leonis. A&A, 281:129–138, Jan. 1994. doi: 10.48550/arXiv.astro-ph/9308010.

Mauas, P.J.D. and Falchi, A. Atmospheric models of flare stars: the flaring state of AD Leonis. A&A, 310:245–258, Jun 1996.

Mayor, M. and Queloz, D. A Jupiter-mass companion to a solar-type star. Nature, 378(6555):355–359, Nov. 1995. doi: 10.1038/378355a0.

Mayor, M., Pepe, F., Queloz, D. et al. Setting New Standards with HARPS. *The Messenger*, 114:20–24, Dec 2003.

Mazeh, T., Naef, D., Torres, G. et al. The Spectroscopic Orbit of the Planetary Companion Transiting HD 209458. ApJ, 532(1):L55–L58, Mar. 2000. doi: 10.1086/312558.

Mazeh, T., Holczer, T. and Faigler, S. Dearth of short-period Neptunian exoplanets: A desert in period-mass and period-radius planes. A&A, 589:A75, May 2016. doi: 10.1051/0004-6361/201528065.

Messina, S., Rodonò, M. and Guinan, E.F. The "rotation-activity connection": Its extension to photospheric activity diagnostics. A&A, 366:215–228, Jan. 2001. doi: 10.1051/0004-6361:20000201.

Meunier, N. and Delfosse, X. On the correlation between Ca and Hα solar emission and consequences for stellar activity observations. A&A, 501(3):1103–1112, Jul 2009. doi: 10.1051/0004-6361/200911823.

Meunier, N. and Lagrange, A.M. Radial-velocity variations due to meridional flows in the Sun and solar-type stars: impact on exoplanet detectability. A&A, 638: A54, June 2020. doi: 10.1051/0004-6361/201937354.

Meunier, N., Desort, M. and Lagrange, A.M. Using the Sun to estimate Earth-like planets detection capabilities . II. Impact of plages. A&A, 512:A39, Mar. 2010. doi: 10.1051/0004-6361/200913551.

Meunier, N., Lagrange, A.M. and Borgniet, S. A new method of correcting radial velocity time series for inhomogeneous convection. A&A, 607:A6, Oct. 2017. doi: 10.1051/0004-6361/201630328.

Montes, D. and Ramsey, L.W. *A Long-Duration Flare on the X-ray/EUV Selected, Chromospherically Active Binary 2RE J0743+224*, volume 158 of *Astronomical Society of the Pacific Conference Series*, page 226. 1999.

Montes, D., Fernández-Figueroa, M.J., De Castro, E. et al. Multiwavelength optical observations of chromospherically active binary systems. III. High resolution echelle spectra from Ca II H & K to Ca II IRT. A&AS, 146:103–140, Oct 2000. doi: 10.1051/aas:2000359.

Morello, G., Tsiaras, A., Howarth, I.D. et al. High-precision Stellar Limb-darkening in Exoplanetary Transits. AJ, 154(3):111, Sept. 2017. doi: 10.3847/1538-3881/aa8405.

Morello, G., Claret, A., Martin-Lagarde, M. et al. The ExoTETHyS Package: Tools for Exoplanetary Transits around Host Stars. AJ, 159(2):75, Feb. 2020. doi: 10.3847/1538-3881/ab63dc.

Morin, J., Donati, J.F., Petit, P. et al. Large-scale magnetic topologies of mid M dwarfs. MNRAS, 390(2):567–581, Oct 2008. doi: 10.1111/j.1365-2966.2008.13809.x.

Morley, C.V., Fortney, J.J., Kempton, E.M.R. et al. Quantitatively Assessing the Role of Clouds in the Transmission Spectrum of GJ 1214b. ApJ, 775(1):33, Sept. 2013. doi: 10.1088/0004-637X/775/1/33.

Morton, T.D., Bryson, S.T., Coughlin, J.L. et al. False Positive Probabilities for all Kepler Objects of Interest: 1284 Newly Validated Planets and 428 Likely False Positives. ApJ, 822(2):86, May 2016. doi: 10.3847/0004-637X/822/2/86.

Mugnai, L.V., Pascale, E., Edwards, B. et al. ArielRad: the Ariel radiometric model. *Experimental Astronomy*, 50(2-3):303–328, Oct. 2020. doi: 10.1007/s10686-020-09676-7.

Muheki, P., Guenther, E.W., Mutabazi, T. et al. High-resolution spectroscopy of flares and CMES on AD Leo*. *arXiv e-prints*, art. arXiv:2003.06163, Mar. 2020.

Nelson, R.P., Papaloizou, J.C.B., Masset, F. et al. The migration and growth of protoplanets in protostellar discs. MNRAS, 318(1):18–36, Oct. 2000. doi: 10.1046/j.1365-8711.2000.03605.x.

Neves, V., Bonfils, X., Santos, N.C. et al. Metallicity of M dwarfs. II. A comparative study of photometric metallicity scales. A&A, 538:A25, Feb 2012. doi: 10.1051/0004-6361/201118115.

Newton, E.R., Irwin, J., Charbonneau, D. et al. The Hα Emission of Nearby M Dwarfs and its Relation to Stellar Rotation. ApJ, 834(1):85, Jan. 2017. doi: 10.3847/1538-4357/834/1/85.

Newton, E.R., Mann, A.W., Kraus, A.L. et al. TESS Hunt for Young and Maturing Exoplanets (THYME). IV. Three Small Planets Orbiting a 120 Myr Old Star in the Pisces-Eridanus Stream. AJ, 161(2):65, Feb. 2021. doi: 10.3847/1538-3881/abccc6.

Ning, B., Wolfgang, A. and Ghosh, S. Predicting Exoplanet Masses and Radii: A Nonparametric Approach. ApJ, 869(1):5, Dec. 2018. doi: 10.3847/1538-4357/aaeb31.

Niraula, P., Redfield, S., Dai, F. et al. Three Super-Earths Transiting the Nearby Star GJ 9827. AJ, 154(6):266, Dec. 2017. doi: 10.3847/1538-3881/aa957c.

Nissen, P.E. High-precision abundances of elements in solar twin stars. Trends with stellar age and elemental condensation temperature. A&A, 579:A52, July 2015. doi: 10.1051/0004-6361/201526269.

Nowak, M., Lacour, S., Lagrange, A.M. et al. Direct confirmation of the radial-velocity planet β Pictoris c. A&A, 642:L2, Oct. 2020. doi: 10.1051/0004-6361/202039039.

Noyes, R.W., Hartmann, L.W., Baliunas, S.L. et al. Rotation, convection, and magnetic activity in lower main-sequence stars. ApJ, 279:763–777, Apr. 1984. doi: 10.1086/161945.

Oh, S., Price-Whelan, A.M., Hogg, D.W. et al. Comoving Stars in Gaia DR1: An Abundance of Very Wide Separation Comoving Pairs. AJ, 153(6):257, June 2017. doi: 10.3847/1538-3881/aa6ffd.

Owen, J.E. Constraining the entropy of formation from young transiting planets. MNRAS, 498(4):5030–5040, Nov. 2020. doi: 10.1093/mnras/staa2784.

Panagi, P.M., Byrne, P.B. and Houdebine, E.R. High resolution observations of chromospheric lines in late-type dwarfs. A&AS, 90:437, Nov 1991.

Parnell, C.E. and Jupp, P.E. Statistical Analysis of the Energy Distribution of Nanoflares in the Quiet Sun. ApJ, 529(1):554–569, Jan 2000. doi: 10.1086/308271.

Pecaut, M.J. and Mamajek, E.E. Intrinsic Colors, Temperatures, and Bolometric Corrections of Pre-main-sequence Stars. ApJS, 208(1):9, Sept. 2013. doi: 10.1088/0067-0049/208/1/9.

Pepe, F., Mayor, M., Delabre, B. et al. HARPS: a new high-resolution spectrograph for the search of extrasolar planets. In Iye, M. and Moorwood, A.F., editors, *Optical and IR Telescope Instrumentation and Detectors*, volume 4008 of *Society of Photo-Optical Instrumentation Engineers (SPIE) Conference Series*, pages 582–592, Aug. 2000. doi: 10.1117/12.395516.

Pepe, F., Mayor, M., Galland, F. et al. The CORALIE survey for southern extra-solar planets VII. Two short-period Saturnian companions to <ASTROBJ>HD 108147</ASTROBJ> and <ASTROBJ>HD 168746</ASTROBJ>. A&A, 388:632–638, June 2002. doi: 10.1051/0004-6361:20020433.

Pepe, F., Cristiani, S., Rebolo, R. et al. ESPRESSO at VLT. On-sky performance and first results. A&A, 645:A96, Jan. 2021. doi: 10.1051/0004-6361/202038306.

Perger, M., García-Piquer, A., Ribas, I. et al. HADES RV Programme with HARPS-N at TNG. II. Data treatment and simulations. A&A, 598:A26, Feb. 2017. doi: 10.1051/0004-6361/201628985.

Perryman, M. *The Exoplanet Handbook*. 2014.

Petigura, E.A., Marcy, G.W., Winn, J.N. et al. The California-Kepler Survey. IV. Metal-rich Stars Host a Greater Diversity of Planets. AJ, 155(2):89, Feb. 2018. doi: 10.3847/1538-3881/aaa54c.

Pettersen, B.R. Chromospheric lines in red dwarf flare stars. III. A&A, 209:279–295, Jan 1989.

Pettersen, B.R., Coleman, L.A. and Evans, D.S. The flare activity of AD Leonis. ApJS, 54:375–386, Mar 1984. doi: 10.1086/190934.

Pizzolato, N., Maggio, A., Micela, G. et al. The stellar activity-rotation relationship revisited: Dependence of saturated and non-saturated X-ray emission regimes on spectral type for main-sequence stars. In Favata, F. and Drake, J.J., editors, *Stellar Coronae in the Chandra and XMM-NEWTON Era*, volume 277 of *Astronomical Society of the Pacific Conference Series*, page 557, Dec. 2002.

Pizzolato, N., Maggio, A., Micela, G. et al. The stellar activity-rotation relationship revisited: Dependence of saturated and non-saturated X-ray emission regimes on stellar mass for late-type dwarfs. A&A, 397:147–157, Jan. 2003. doi: 10.1051/0004-6361:20021560.

Plavchan, P., Barclay, T., Gagné, J. et al. A planet within the debris disk around the pre-main-sequence star AU Microscopii. Nature, 582(7813):497–500, June 2020. doi: 10.1038/s41586-020-2400-z.

Polyansky, O.L., Kyuberis, A.A., Zobov, N.F. et al. ExoMol molecular line lists XXX: a complete high-accuracy line list for water. MNRAS, 480(2):2597–2608, Oct. 2018. doi: 10.1093/mnras/sty1877.

Poppenhaeger, K., Ketzer, L. and Mallonn, M. X-ray irradiation and evaporation of the four young planets around V1298 Tau. MNRAS, 500(4):4560–4572, Jan. 2021. doi: 10.1093/mnras/staa1462.

Priest, E. and Forbes, T. *Magnetic reconnection. MHD theory and applications*. Cambridge University Press, United Kingdom, 2000. ISBN 0-521-48179-1.

Prieto-Arranz, J., Palle, E., Gandolfi, D. et al. Mass determination of the 1:3:5 near-resonant planets transiting GJ 9827 (K2-135). A&A, 618:A116, Oct. 2018. doi: 10.1051/0004-6361/201832872.

Rainer, M., Borsa, F. and Affer, L. Stellar masks and bisector's shape for M-type stars observed in the GAPS programme with HARPS-N at TNG. *Experimental Astronomy*, 49(1-2):73–84, Mar. 2020. doi: 10.1007/s10686-020-09654-z.

Rajpaul, V.M., Aigrain, S. and Buchhave, L.A. A robust, template-free approach to precise radial velocity extraction. MNRAS, 492(3):3960–3983, Mar. 2020. doi: 10.1093/mnras/stz3599.

Rasio, F.A. and Ford, E.B. Dynamical instabilities and the formation of extrasolar planetary systems. *Science*, 274:954–956, Nov. 1996. doi: 10.1126/science.274.5289.954.

Rauscher, E. and Marcy, G.W. Ca II H and K Chromospheric Emission Lines in Late-K and M Dwarfs. PASP, 118(842):617–635, Apr. 2006. doi: 10.1086/503021.

Reid, I.N., Gizis, J.E. and Hawley, S.L. The Palomar/MSU Nearby Star Spectroscopic Survey. IV. The Luminosity Function in the Solar Neighborhood and M Dwarf Kinematics. AJ, 124(5):2721–2738, Nov 2002. doi: 10.1086/343777.

Reiners, A., Basri, G. and Browning, M. Evidence for Magnetic Flux Saturation in Rapidly Rotating M Stars. ApJ, 692(1):538–545, Feb 2009. doi: 10.1088/0004-637X/692/1/538.

Reiners, A., Joshi, N. and Goldman, B. A Catalog of Rotation and Activity in Early-M Stars. AJ, 143(4):93, Apr. 2012. doi: 10.1088/0004-6256/143/4/93.

Reiners, A., Shulyak, D., Anglada-Escudé, G. et al. Radial velocity signatures of Zeeman broadening. A&A, 552:A103, Apr. 2013. doi: 10.1051/0004-6361/201220437.

Rice, K., Malavolta, L., Mayo, A. et al. Masses and radii for the three super-Earths orbiting GJ 9827, and implications for the composition of small exoplanets. MNRAS, 484(3):3731–3745, Apr. 2019. doi: 10.1093/mnras/stz130.

Richard, C., Gordon, I.E., Rothman, L.S. et al. New section of the HITRAN database: Collision-induced absorption (CIA). J. Quant. Spec. Radiat. Transf., 113(11):1276–1285, July 2012. doi: 10.1016/j.jqsrt.2011.11.004.

Richichi, A. Lunar occultation measurements of stellar angular diameters. *IAU Symposium*, 189:45–50, Jan. 1997.

Ricker, G.R., Winn, J.N., Vanderspek, R. et al. Transiting Exoplanet Survey Satellite (TESS). *Journal of Astronomical Telescopes, Instruments, and Systems*, 1:014003, Jan. 2015. doi: 10.1117/1.JATIS.1.1.014003.

Robinson, R.D., Cram, L.E. and Giampapa, M.S. Chromospheric H alpha and CA II Lines in Late-Type Stars. ApJS, 74:891, Dec. 1990. doi: 10.1086/191525.

Rocchetto, M. and Waldmann, I.P. Biases and degeneracies in the retrieval of exoplanetary atmospheres through transit spectroscopy. In *AAS/Division for Extreme*

Solar Systems Abstracts, volume 47 of *AAS/Division for Extreme Solar Systems Abstracts*, page 111.24, Dec. 2015.

Rodriguez, J.E., Vanderburg, A., Eastman, J.D. et al. A System of Three Super Earths Transiting the Late K-Dwarf GJ 9827 at 30 pc. AJ, 155(2):72, Feb. 2018. doi: 10.3847/1538-3881/aaa292.

Rogers, L.A. and Seager, S. Three Possible Origins for the Gas Layer on GJ 1214b. ApJ, 716(2):1208–1216, June 2010. doi: 10.1088/0004-637X/716/2/1208.

Rojas-Ayala, B., Covey, K.R., Muirhead, P.S. et al. Metallicity and Temperature Indicators in M Dwarf K-band Spectra: Testing New and Updated Calibrations with Observations of 133 Solar Neighborhood M Dwarfs. ApJ, 748(2):93, Apr 2012. doi: 10.1088/0004-637X/748/2/93.

Rothman, L.S. and Gordon, I.E. Status of the HITRAN and HITEMP databases. In *13th International HITRAN Conference*, page 49, June 2014. doi: 10.5281/zenodo.11207.

Roudier, G.M., Swain, M.R., Gudipati, M.S. et al. Disequilibrium Chemistry in Exoplanet Atmospheres Observed with the Hubble Space Telescope. AJ, 162(2):37, Aug. 2021. doi: 10.3847/1538-3881/abfdad.

Rutten, R.G.M. and Schrijver, C.J. Magnetic structure in cool stars. XIII - Appropriate units for the rotation-activity relation. A&A, 177(1-2):155–162, May 1987.

Rutten, R.J. *On the Nature of the Solar Chromosphere*, volume 354 of *Astronomical Society of the Pacific Conference Series*, page 276. 2006.

Rutten, R.J. *Observing the Solar Chromosphere*, volume 368 of *Astronomical Society of the Pacific Conference Series*, page 27. 2007.

Saar, S.H. and Linsky, J.L. The photospheric magnetic field of the dM3.5e flare star AD Leonis. ApJ, 299:L47–L50, Dec 1985. doi: 10.1086/184578.

Scandariato, G., Maldonado, J., Affer, L. et al. HADES RV Programme with HARPS-N at TNG. IV. Time resolved analysis of the Ca II H&K and Hα chromospheric emission of low-activity early-type M dwarfs. A&A, 598:A28, Feb. 2017. doi: 10.1051/0004-6361/201629382.

Scargle, J.D. Studies in astronomical time series analysis. II. Statistical aspects of spectral analysis of unevenly spaced data. ApJ, 263:835–853, Dec. 1982. doi: 10.1086/160554.

Schaefer, L. and Fegley, B. Chemistry of Silicate Atmospheres of Evaporating Super-Earths. ApJ, 703(2):L113–L117, Oct. 2009. doi: 10.1088/0004-637X/703/2/L113.

Schlawin, E., Ilyin, I., Feinstein, A.D. et al. H-α Variability of V1298 Tau c. *Research Notes of the American Astronomical Society*, 5(8):195, Aug. 2021. doi: 10.3847/2515-5172/ac1f2f.

Schöfer, P., Jeffers, S.V., Reiners, A. et al. The CARMENES search for exoplanets around M dwarfs. Activity indicators at visible and near-infrared wavelengths. A&A, 623:A44, Mar. 2019. doi: 10.1051/0004-6361/201834114.

Schrijver, C.J. and Title, A.M. On the Formation of Polar Spots in Sun-like Stars. ApJ, 551(2):1099–1106, Apr. 2001. doi: 10.1086/320237.

Schrijver, C.J. and Zwaan, C. Solar and stellar magnetic activity. *Cambridge Astrophysics Series*, 34, Jan. 2000.

Schrijver, C.J. and Zwaan, C. *Solar and Stellar Magnetic Activity*. Cambridge Astrophysics. Cambridge University Press, 2000. doi: 10.1017/CBO9780511546037.

Schrijver, C.J., Cote, J., Zwaan, C. et al. Relations between the Photospheric Magnetic Field and the Emission from the Outer Atmospheres of Cool Stars. I. The Solar CA II K Line Core Emission. ApJ, 337:964, Feb. 1989. doi: 10.1086/167168.

Schuster, A. On the investigation of hidden periodicities with application to a supposed 26 day period of meteorological phenomena. *Terrestrial Magnetism (Journal of Geophysical Research)*, 3(1):13, Jan. 1898. doi: 10.1029/TM003i001p00013.

Schwarz, H., Brogi, M., de Kok, R. et al. Evidence against a strong thermal inversion in HD 209458b from high-dispersion spectroscopy. A&A, 576:A111, Apr. 2015. doi: 10.1051/0004-6361/201425170.

Seager, S., Kuchner, M., Hier-Majumder, C.A. et al. Mass-Radius Relationships for Solid Exoplanets. ApJ, 669(2):1279–1297, Nov. 2007. doi: 10.1086/521346.

Sharp, C.M. and Burrows, A. Atomic and Molecular Opacities for Brown Dwarf and Giant Planet Atmospheres. ApJS, 168(1):140–166, Jan. 2007. doi: 10.1086/508708.

Shibayama, T., Maehara, H., Notsu, S. et al. Superflares on Solar-type Stars Observed with Kepler. I. Statistical Properties of Superflares. ApJS, 209(1):5, Nov 2013. doi: 10.1088/0067-0049/209/1/5.

Shkolnik, E.L., Anglada-Escudé, G., Liu, M.C. et al. Identifying the Young Low-mass Stars within 25 pc. II. Distances, Kinematics, and Group Membership. ApJ, 758(1):56, Oct 2012. doi: 10.1088/0004-637X/758/1/56.

Shulyak, D., Reiners, A., Engeln, A. et al. Strong dipole magnetic fields in fast rotating fully convective stars. *Nature Astronomy*, 1:0184, Aug. 2017. doi: 10.1038/s41550-017-0184.

Sing, D.K., Fortney, J.J., Nikolov, N. et al. A continuum from clear to cloudy hot-Jupiter exoplanets without primordial water depletion. Nature, 529(7584):59–62, Jan. 2016. doi: 10.1038/nature16068.

Sinukoff, E., Howard, A.W., Petigura, E.A. et al. Eleven Multiplanet Systems from K2 Campaigns 1 and 2 and the Masses of Two Hot Super-Earths. ApJ, 827(1):78, Aug. 2016. doi: 10.3847/0004-637X/827/1/78.

Skilling, J. Nested Sampling. In Fischer, R., Preuss, R. and Toussaint, U.V., editors, *Bayesian Inference and Maximum Entropy Methods in Science and Engineering: 24th International Workshop on Bayesian Inference and Maximum Entropy Methods in Science and Engineering*, volume 735 of *American Institute of Physics Conference Series*, pages 395–405, Nov. 2004. doi: 10.1063/1.1835238.

Skilling, J. Skilling, j.: Nested sampling for general bayesian computation. bayesian anal. 1(4), 833-860. *Bayesian Analysis*, 1:833–860, 12 2006. doi: 10.1214/06-BA127.

Skumanich, A. Time Scales for Ca II Emission Decay, Rotational Braking, and Lithium Depletion. ApJ, 171:565, Feb. 1972. doi: 10.1086/151310.

Skumanich, A., Smythe, C. and Frazier, E.N. On the statistical desription of inhomogeneities in the quiet solar atmosphere. I. Linear regression analysis and absolute calibration of multichannel observations of the Ca^+ emission network. ApJ, 200:747–764, Sept. 1975. doi: 10.1086/153846.

Solanki, S.K., Inhester, B. and Schüssler, M. The solar magnetic field. *Reports on Progress in Physics*, 69(3):563–668, Mar. 2006. doi: 10.1088/0034-4885/69/3/R02.

Sousa, S.G., Santos, N.C., Israelian, G. et al. Spectroscopic stellar parameters for 582 FGK stars in the HARPS volume-limited sample. Revising the metallicity-planet correlation. A&A, 533:A141, Sept. 2011. doi: 10.1051/0004-6361/201117699.

Sousa, S.G., Santos, N.C., Mortier, A. et al. Homogeneous spectroscopic parameters for bright planet host stars from the northern hemisphere . The impact on stellar and planetary mass. A&A, 576:A94, Apr. 2015. doi: 10.1051/0004-6361/201425227.

Sozzetti, A., Torres, G., Charbonneau, D. et al. Improving Stellar and Planetary Parameters of Transiting Planet Systems: The Case of TrES-2. ApJ, 664(2):1190–1198, Aug. 2007. doi: 10.1086/519214.

Spiegel, D.S., Burrows, A. and Milsom, J.A. The Deuterium-burning Mass Limit for Brown Dwarfs and Giant Planets. ApJ, 727(1):57, Jan. 2011. doi: 10.1088/0004-637X/727/1/57.

Stassun, K.G., Collins, K.A. and Gaudi, B.S. Accurate Empirical Radii and Masses of Planets and Their Host Stars with Gaia Parallaxes. AJ, 153(3):136, Mar. 2017. doi: 10.3847/1538-3881/aa5df3.

Stassun, K.G., Oelkers, R.J., Paegert, M. et al. The Revised TESS Input Catalog and Candidate Target List. AJ, 158(4):138, Oct. 2019. doi: 10.3847/1538-3881/ab3467.

Stauffer, J.R. and Hartmann, L.W. The Chromospheric Activity, Kinematics and Metallicities of Gliese Catalog M Dwarfs. In Zeilik, M. and Gibson, D.M., editors, *Cool Stars, Stellar Systems and the Sun*, volume 254, page 58. 1986. doi: 10.1007/3-540-16763-3_135.

Stelzer, B., Micela, G., Neuhäuser, R. et al. Age, mass and temperature dependence of X-ray activity on brown dwarfs . *Memorie della Societa Astronomica Italiana Supplementi*, 9:273, Jan. 2006.

Stelzer, B., Frasca, A., Alcalá, J.M. et al. X-shooter spectroscopy of young stellar objects. III. Photospheric and chromospheric properties of Class III objects. A&A, 558:A141, Oct 2013. doi: 10.1051/0004-6361/201321979.

Stevens, D.J. and Gaudi, B.S. A Posteriori Transit Probabilities. PASP, 125(930): 933, Aug. 2013. doi: 10.1086/672572.

Suárez Mascareño, A., Damasso, M., Lodieu, N. et al. Rapid contraction of giant planets orbiting the 20-million-year-old star V1298 Tau. *Nature Astronomy*, 6: 232–240, Dec. 2021. doi: 10.1038/s41550-021-01533-7.

Sundland, S.R., Pettersen, B.R., Hawley, S.L. et al. Radiation losses in chromospheric and transition region emission lines from AD Leo (dM4e). In Havnes, O., Pettersen, B.R., Schmitt, J.H.M.M. et al, editors, *Activity in Cool Star Envelopes*, volume 143, page 61, Jan. 1988. doi: 10.1007/978-94-009-2951-7_8.

Swain, M.R., Vasisht, G. and Tinetti, G. The presence of methane in the atmosphere of an extrasolar planet. Nature, 452(7185):329–331, Mar. 2008. doi: 10.1038/nature06823.

Takeda, G., Ford, E.B., Sills, A. et al. Structure and Evolution of Nearby Stars with Planets. II. Physical Properties of ~1000 Cool Stars from the SPOCS Catalog. ApJS, 168(2):297–318, Feb. 2007. doi: 10.1086/509763.

Tennyson, J., Yurchenko, S.N., Al-Refaie, A.F. et al. The exomol database: Molecular line lists for exoplanet and other hot atmospheres. *Journal of Molecular Spectroscopy*, 327:73–94, 2016. ISSN 0022-2852. doi: https://doi.org/10.1016/j.jms.2016.05.002. URL https://www.sciencedirect.com/science/article/pii/S0022285216300807. New Visions of Spectroscopic Databases, Volume II.

Tinetti, G., Vidal-Madjar, A., Liang, M.C. et al. Water vapour in the atmosphere of a transiting extrasolar planet. Nature, 448(7150):169–171, July 2007. doi: 10.1038/nature06002.

Tinetti, G., Tennyson, J., Griffith, C.A. et al. Water in exoplanets. *Philosophical Transactions of the Royal Society of London Series A*, 370(1968):2749–2764, June 2012. doi: 10.1098/rsta.2011.0338.

Tinetti, G., Drossart, P., Eccleston, P. et al. The science of ARIEL (Atmospheric Remote-sensing Infrared Exoplanet Large-survey). In MacEwen, H.A., Fazio, G.G., Lystrup, M. et al, editors, *Space Telescopes and Instrumentation 2016: Optical, Infrared, and Millimeter Wave*, volume 9904 of *Society of Photo-Optical Instrumentation Engineers (SPIE) Conference Series*, page 99041X, July 2016. doi: 10.1117/12.2232370.

Tinetti, G., Drossart, P., Eccleston, P. et al. A chemical survey of exoplanets with ARIEL. *Experimental Astronomy*, 46(1):135–209, Nov. 2018. doi: 10.1007/s10686-018-9598-x.

Tinetti, G., Eccleston, P., Haswell, C. et al. Ariel: Enabling planetary science across light-years. *arXiv e-prints*, art. arXiv:2104.04824, Apr. 2021.

Torres, G., Lacy, C.H., Marschall, L.A. et al. The Eclipsing Binary V1061 Cygni: Confronting Stellar Evolution Models for Active and Inactive Solar-Type Stars. ApJ, 640(2):1018–1038, Apr. 2006. doi: 10.1086/500188.

Torres, G., Andersen, J. and Giménez, A. Accurate masses and radii of normal stars: modern results and applications. A&A Rev., 18(1-2):67–126, Feb. 2010. doi: 10.1007/s00159-009-0025-1.

Traub, W.A. and Oppenheimer, B.R. Direct Imaging of Exoplanets. In Seager, S., editor, *Exoplanets*, pages 111–156. 2010.

Trotta, R. Forecasting the Bayes factor of a future observation. MNRAS, 378(3):819–824, July 2007. doi: 10.1111/j.1365-2966.2007.11861.x.

Trotta, R. Bayes in the sky: Bayesian inference and model selection in cosmology. *Contemporary Physics*, 49(2):71–104, Mar. 2008. doi: 10.1080/00107510802066753.

Trotta, R. Bayesian Methods in Cosmology. *arXiv e-prints*, art. arXiv:1701.01467, Jan. 2017.

Tsiaras, A., Waldmann, I.P., Tinetti, G. et al. Water vapour in the atmosphere of the habitable-zone eight-Earth-mass planet K2-18 b. *Nature Astronomy*, 3:1086–1091, Sept. 2019. doi: 10.1038/s41550-019-0878-9.

Tuomi, M., Jones, H.R.A., Barnes, J.R. et al. AD Leonis: Radial Velocity Signal of Stellar Rotation or Spin-Orbit Resonance? AJ, 155(5):192, May 2018. doi: 10.3847/1538-3881/aab09c.

van den Besselaar, E.J.M., Raassen, A.J.J., Mewe, R. et al. <ASTROBJ>AD Leonis</ASTROBJ>: Flares observed by XMM-Newton and Chandra. A&A, 411:587–593, Dec 2003. doi: 10.1051/0004-6361:20031398.

Vanderburg, A., Bieryla, A., Duev, D.A. et al. Two Small Planets Transiting HD 3167. ApJ, 829(1):L9, Sept. 2016. doi: 10.3847/2041-8205/829/1/L9.

Vissapragada, S., Stefánsson, G., Greklek-McKeon, M. et al. A Search for Planetary Metastable Helium Absorption in the V1298 Tau System. AJ, 162(5):222, Nov. 2021. doi: 10.3847/1538-3881/ac1bb0.

Vogt, S.S., Hatzes, A.P., Misch, A.A. et al. Doppler Imagery of the Spotted RS Canum Venaticorum Star HR 1099 (V711 Tauri) from 1981 to 1992. ApJS, 121 (2):547–589, Apr. 1999. doi: 10.1086/313195.

Waldmann, I.P., Rocchetto, M., Tinetti, G. et al. τ−REx. II. RETRIEVAL OF EMISSION SPECTRA. *The Astrophysical Journal*, 813(1):13, oct 2015a. doi: 10.1088/0004-637x/813/1/13. URL https://doi.org/10.1088/0004-637x/813/1/13.

Waldmann, I.P., Tinetti, G., Rocchetto, M. et al. TAU-REX i: A NEXT GENERATION RETRIEVAL CODE FOR EXOPLANETARY ATMOSPHERES. *The Astrophysical Journal*, 802(2):107, mar 2015b. doi: 10.1088/0004-637x/802/2/107. URL https://doi.org/10.1088/0004-637x/802/2/107.

Walkowicz, L.M. and Hawley, S.L. Tracers of Chromospheric Structure. I. Observations of Ca II K and Hα in M Dwarfs. AJ, 137(2):3297–3313, Feb. 2009. doi: 10.1088/0004-6256/137/2/3297.

Ward, W.R. Survival of Planetary Systems. ApJ, 482(2):L211–L214, June 1997. doi: 10.1086/310701.

Weiss, L.M. and Marcy, G.W. The Mass-Radius Relation for 65 Exoplanets Smaller than 4 Earth Radii. ApJ, 783(1):L6, Mar. 2014. doi: 10.1088/2041-8205/783/1/L6.

Weiss, L.M., Marcy, G.W., Rowe, J.F. et al. The Mass of KOI-94d and a Relation for Planet Radius, Mass, and Incident Flux. ApJ, 768(1):14, May 2013. doi: 10.1088/0004-637X/768/1/14.

Welbanks, L., Madhusudhan, N., Allard, N.F. et al. Mass-Metallicity Trends in Transiting Exoplanets from Atmospheric Abundances of H_2O, Na, and K. ApJ, 887(1):L20, Dec. 2019. doi: 10.3847/2041-8213/ab5a89.

West, A.A., Hawley, S.L., Walkowicz, L.M. et al. Spectroscopic Properties of Cool Stars in the Sloan Digital Sky Survey: An Analysis of Magnetic Activity and a Search for Subdwarfs. AJ, 128(1):426–436, July 2004. doi: 10.1086/421364.

West, A.A., Hawley, S.L., Bochanski, J.J. et al. Constraining the Age-Activity Relation for Cool Stars: The Sloan Digital Sky Survey Data Release 5 Low-Mass Star Spectroscopic Sample. AJ, 135(3):785–795, Mar. 2008. doi: 10.1088/0004-6256/135/3/785.

Winters, J.G., Medina, A.A., Irwin, J.M. et al. Three Red Suns in the Sky: A Transiting, Terrestrial Planet in a Triple M-dwarf System at 6.9 pc. AJ, 158(4):152, Oct. 2019. doi: 10.3847/1538-3881/ab364d.

Winters, J.G., Cloutier, R., Medina, A.A. et al. A Second Planet Transiting LTT 1445A and a Determination of the Masses of Both Worlds. AJ, 163(4):168, Apr. 2022. doi: 10.3847/1538-3881/ac50a9.

Wolszczan, A. and Frail, D.A. A planetary system around the millisecond pulsar PSR1257 + 12. Nature, 355(6356):145–147, Jan. 1992. doi: 10.1038/355145a0.

Worden, S.P., Schneeberger, T.J. and Giampapa, M.S. High-resolution profiles of chromospheric lines in M dwarf stars. ApJS, 46:159–175, Jun 1981. doi: 10.1086/190741.

Wright, J.T., Marcy, G.W., Howard, A.W. et al. The Frequency of Hot Jupiters Orbiting nearby Solar-type Stars. ApJ, 753(2):160, July 2012. doi: 10.1088/0004-637X/753/2/160.

Wright, N.J. and Drake, J.J. Solar-type dynamo behaviour in fully convective stars without a tachocline. Nature, 535(7613):526–528, July 2016. doi: 10.1038/nature18638.

Xia, F. and Fu, Y.N. The V-band Empirical Mass-luminosity Relation for Main Sequence Stars. Chinese Astron. Astrophys., 34(3):277–287, July 2010. doi: 10.1016/j.chinastron.2010.07.009.

Yip, K.H., Changeat, Q., Edwards, B. et al. On the Compatibility of Ground-based and Space-based Data: WASP-96 b, an Example. AJ, 161(1):4, Jan. 2021a. doi: 10.3847/1538-3881/abc179.

Yip, K.H., Changeat, Q., Nikolaou, N. et al. Peeking inside the Black Box: Interpreting Deep-learning Models for Exoplanet Atmospheric Retrievals. AJ, 162(5):195, Nov. 2021b. doi: 10.3847/1538-3881/ac1744.

Yoffe, G., Ofir, A. and Aharonson, O. A Simplified Photodynamical Model for Planetary Mass Determination in Low-eccentricity Multitransiting Systems. ApJ, 908(1):114, Feb. 2021. doi: 10.3847/1538-4357/abc87a.

Yokoyama, T. and Shibata, K. A Two-dimensional Magnetohydrodynamic Simulation of Chromospheric Evaporation in a Solar Flare Based on a Magnetic Reconnection Model. ApJ, 494(1):L113–L116, Feb 1998. doi: 10.1086/311174.

Young, A., Skumanich, A. and Harlan, E. Rapid rotation and H alpha emission anomalies among some members of the population of low-mass stars. ApJ, 282: 683–687, July 1984. doi: 10.1086/162248.

Yurchenko, S.N., Amundsen, D.S., Tennyson, J. et al. A hybrid line list for CH_4 and hot methane continuum. A&A, 605:A95, Sept. 2017. doi: 10.1051/0004-6361/201731026.

Zechmeister, M. and Kürster, M. The generalised Lomb-Scargle periodogram. A new formalism for the floating-mean and Keplerian periodograms. A&A, 496(2): 577–584, Mar. 2009. doi: 10.1051/0004-6361:200811296.

Zhao, J. and Tinney, C.G. FIESTA - disentangling stellar variability from exoplanets in the Fourier domain. MNRAS, 491(3):4131–4146, Jan. 2020. doi: 10.1093/mnras/stz3254.

Zhou, L., Ma, B., Wang, Y. et al. Hubble WFC3 Spectroscopy of the Rocky Planet L 98-59 b: No Evidence for a Cloud-free Primordial Atmosphere. AJ, 164(5): 203, Nov. 2022. doi: 10.3847/1538-3881/ac8fe9.

Zicher, N., Barragán, O., Klein, B. et al. One year of AU Mic with HARPS - I. Measuring the masses of the two transiting planets. MNRAS, 512(2):3060–3078, May 2022. doi: 10.1093/mnras/stac614.